Technische Universität München
Fakultät für Elektrotechnik und Informationstechnik

Antenna Field Measurements and Transformations in Arbitrary Echoic Environments

Josef Knapp

Vollständiger Abdruck der von der Fakultät für Elektrotechnik und Informationstechnik
der Technischen Universität München zur Erlangung des akademischen Grades eines

– Doktors der Ingenieurswissenschaften –

genehmigten Dissertation.

Vorsitzender:		Prof. Dr. Marc Tornow
Prüfer der Dissertation:	1.	Prof. Dr.-Ing. Thomas F. Eibert
	2.	Prof. Dr.-Ing. Ludger Klinkenbusch

Die Dissertation wurde am 09. 06. 2021 bei der Technischen Universität München eingereicht
und durch die Fakultät für Elektrotechnik und Informationstechnik am 18. 11. 2021
angenommen.

Danksagung

Es war ein besonderes Glück für mich, dass ich die vorliegende Arbeit als akademischer Mitarbeiter am Lehrstuhl für Hochfrequenztechnik der Technischen Universität München anfertigen konnte. Hier fand ich ein ideales Umfeld, das mir in vielerlei Hinsicht den Weg geebnet hat. Durch die umfangreiche Infrastruktur am Lehrstuhl sind mir viele Hürden erspart geblieben und einige Türen geöffnet worden. Noch viel wichtiger als die Infrastruktur am Lehrstuhl waren für mich jedoch die zahlreichen Menschen, die dieses Umfeld für mich so wertvoll gemacht haben.

Von ganzem Herzen danke ich meinem Doktorvater Prof. Dr.-Ing. Thomas Eibert, der mir stets eine Inspirationsquelle war und dessen Führung während meiner gesamten Zeit am Lehrstuhl es zu verdanken ist, dass ich mein fachliches Verständnis um große Teile erweitern konnte. Sehr dankbar bin ich für die vielen anregenden Gespräche mit Dr.-Ing. Uwe Siart inner- und außerhalb der Arbeitszeit sowie seine zahlreichen Hinweise im Bezug auf alle typografischen Belange. Überaus dankbar bin ich, schon wärend des Studiums in Jonas Kornprobst M.Sc.einen so idealen Diskussionspartner gefunden zu haben, der mich auch in der gesamten Zeit als Doktorand begleitet hat und dessen messerscharfer Verstand in jeder Diskussion dazu beigetragen hat, dass auch ich meinen Verstand immer weiter schärfen konnte. Vielen Dank auch dafür, dass er mir seine Expertise für das Probelesen der vorliegenden Arbeit zur Verfügung gestellt hat. Dipl.-Ing. Raimund A. M. Mauermayer danke ich dafür, dass er mir den Start in die akademische Welt erleichtert hat indem er mit großer Geduld alle fachlichen Fragen beantwortet hat, die insbesondere in der Anfangszeit meiner Laufbahn am Lehrstuhl immer wieder auftraten. Jun.-Prof. Dr.-Ing. Simon Adrian danke ich dafür, dass er mich über die Jahre als steter Begleiter im Büro, in gemeinsamen Lehrveranstaltungen aber auch in der Mathematik und Kultur auf spannende Abenteuer mitgenommen hat. Ich bin Alexander Paulus M.Sc. dankbar für seine besondere Rolle nicht nur als Zimmerkollege sondern auch als Partner in gemeinsamen Forschungsthemen und durch die Bereicherungen, die alle Diskussionen stets durch seine Anregungen erhalten haben. Vielen Dank auch für das aufmerksame Durchlesen der vorliegenden Arbeit und das überaus hilfreiche Feedback. Bernd Hofmann M.Sc. danke ich herzlich dafür, dass er mein Umfeld nicht nur am Lehrstuhl und während des Hauptseminars überaus angenehm mitgestaltete sondern ganz besonders auch das Umfeld im Homeoffice während der Corona-Pandemie in den vergangenen

Jahren. Mein Dank gilt an dieser Stelle ihm sowie auch Jonas Weindl M.Sc. für das Durchlesen der vorlegenden Arbeit. Meinen herzlichen Dank weiterhin an Prof. Dr.-Ing. Ludger Klinkenbusch für die Mitwirkung als Prüfer der Dissertation und Prof. Dr. Marc Tornow für den Vorsitz der Prüfungskommission.

Ein besonderes Dankeschön spreche ich meiner Familie aus. Sie ist ein wesentlicher Bestandteil des Umfeldes, über das ich mich über alle Maßen glücklich schätze. Ganz besonders danke ich meiner Frau für die stete Unterstützung sowie den liebevollen Großmut. Ohne diesen Rückhalt wäre meine Reise um ein Vielfaches stressiger ausgefallen.

München im Dezember 2021

Zusammenfassung

In der Antennenmesstechnik wird ein großer Aufwand betrieben, um den Einfluss von Streufeldern — eine bedeutende Fehlerquelle — zu minimieren. Das geschieht beispielsweise, indem die Wände von Antennenmesskammern mit Absorbern ausgekleidet werden, um eine möglichst reflexionsarme Umgebung zu schaffen. Die Einschränkungen, die ein solcher reflexionsarmer Messaufbau mit sich zieht, sind erheblich, was die Anwendungsmöglichkeiten von Antennenmessungen stark beschränkt.

In dieser Arbeit werden Echounterdrückungsmethoden beschrieben, die es ermöglichen, das unter Freiraumbedingungen abgestrahlte Feld einer Testantenne (AUT, engl. *antenna under test*) aus echobehafteten Messungen zu bestimmen. Die Ergebnisse dieser Arbeit schaffen damit die Grundlage für präzise Vermessungen der von einer AUT abgestrahlten Felder in bisher unerschlossenen Anwendungsszenarien, darunter auch Messungen in stark reflektierenden Umgebungen.

Ausgehend von einer umfassenden Darstellung der Übertragungsfunktion zwischen Sende- und Empfangsantenne wird eine formelle Beschreibung des Einflusses von Echos auf das Empfangssignal in unterschiedlichen Messszenarien entworfen. Die formelle Beschreibung erfolgt sowohl auf Basis von sphärischen Modenentwicklungen als auch mithilfe von äquivalenten Oberflächenströmen im Zusammenhang mit Greenschen Funktionen. Im Gegensatz zur gängigen Praxis, werden nicht nur Greensche Funktionen betrachtet, die aus auslaufenden Wellen bestehen, sondern auch solche, die über einlaufende oder stehende Wellen beschrieben werden. Auf diese Weise wird eine enge Analogie zwischen der Beschreibung mit sphärischen Moden und mit äquivalenten Oberflächenströmen ersichtlich.

Die Möglichkeiten, Streufelder anhand ihrer räumlichen Verteilungen von den idealen Freiraumfeldern der AUT zu trennen, werden für Messszenarien mit stationärer AUT und mit stationärer Sondenantenne ausführlich analysiert. Dazu werden Quellrekonstruktionsalgorithmen untersucht, die aus den Messsignalen äquivalente Quellen für das Antennenfeld entweder mit oder ohne Berücksichtigung zusätzlicher Echoquellen bestimmen sollen.

Es stellt sich heraus, dass für Messszenarien mit stationärer AUT die relative Lage vom Echo- zum Antennenvolumen maßgeblich ist für die Unterscheidbarkeit der erwünschten und unerwünschten Feldanteile. Die absolute Positionierung der AUT ist nicht relevant. Für ausreichend

große Abstände zwischen Antennen- und Echogebiet — wenn evaneszente Feldeffekte zwischen beiden Gebieten ausgeschlossen werden können — gelingt es, die Echoeinflüsse eindeutig von den idealen Antenneneinflüssen zu trennen.

Für Messszenarien mit stationärer Feldsonde und rotierender AUT wird im Rahmen dieser Arbeit erstmals das torusförmige äquivalente Quellgebiet der hypothetischen Echoquellen identifiziert, mit denen gewisse (jedoch niemals alle) Echoeinflüsse berücksichtigt werden können. Der Torus für die äquivalenten Echoquellen entfernt sich dabei von den Antennenquellen, je weiter die AUT vom Drehzentrum entfernt montiert wird. Die Ergebnisse der theoretischen Überlegungen für beide Szenarien (rotierende oder stationäre AUT) werden mithilfe von numerischen Simulationen untermauert. Da die unerwünschten Echoanteile in Szenarien mit rotierender AUT schwieriger zu entfernen sind als in Szenarien mit stationärer AUT, gilt es hier in besonderem Maße, die Echoeinflüsse in den Messergebnissen möglichst gering zu halten, was unter anderem durch das Synthetisieren virtueller Sondenarrays erreicht werden kann.

Schließlich werden die zeitharmonischen Echounterdrückungsmethoden mit Zeitbereichsmethoden kombiniert, um effektive Echounterdrückung auch in herausfordernden Umgebungen zu realisieren. Messungen mit in der Nähe der Antenne montierten Echoobjekten sowie Messkampagnen in der eigens aufgebauten *Moskitokammer*, die bewusst starke Streufeldeinflüsse erzeugt, zeigen, dass unter großem Mess- und Datenverarbeitungsaufwand das ideale Freiraumfeld der AUT mit zufriedenstellender Genauigkeit (ca. −40 dB Abweichung zur Referenzmessung) auch aus stark echobehafteten Messsignalen rekonstruiert werden kann.

Abstract

Parasitic echo fields are an influential error source in antenna measurements and their suppression and control requires a considerable amount of effort. For instance, the walls of antenna measurement chambers are covered with absorbers in order to create an ideally anechoic environment. The substantial restrictions of such an anechoic measurement setup limit the application of antenna measurements.

This thesis describes echo suppression methods which make it possible to determine the free-space radiated fields of an antenna under test (AUT) from echo distorted measurements. The results of this work are the basis for previously unaccessible application scenarios of antenna measurements, e.g., measurements in strongly reflective environments.

Starting from a comprehensive representation of the electromagnetic transmission between two antennas, a formal description of the echo influence on the receiving signal is derived for different measurement scenarios. The formal description is based on spherical mode expansions on the one hand, and on equivalent surface currents on the other hand. In contrast to available literature, not only Green's functions in the form of outward-radiating fields are considered but also Green's functions consisting of inward-traveling or standing waves. In this way, a close analogy between the descriptions based on spherical modes and equivalent surface currents becomes evident.

The possibilities to separate scattered fields from the desired free-space fields of the AUT are analyzed in detail for measurement scenarios with a stationary AUT or a stationary probe. Source reconstruction algorithms are investigated which aim to reconstruct equivalent AUT sources from the measurement samples either with or without considering additional sources for the echo.

In scenarios with a stationary AUT the relative position between echo and antenna is decisive for the separability of the desired and the undesired contributions. The absolute AUT position is irrelevant. For sufficiently large separation distances between the AUT and the echo — when evanescent fields can be precluded — the echo influences can be unambiguously distinguished from the ideal AUT influences. A torus shaped source region for the unphysical additional echo sources is identified for measurement scenarios with a stationary probe for the first time in this thesis. A certain portion (but not all) of the echo influences can be accounted for by these additional sources. The separation between the actual AUT sources and the auxiliary echo

sources increases with an increasing distance of the AUT from the rotation center. The theoretical results are supported by simulations for both scenarios (rotating or stationary AUT). Since it is harder to remove the echo influences in stationary probe scenarios than in stationary AUT scenarios, it is more important to avoid echo influences in the measurement samples. This is accomplished, e.g., by synthesizing virtual probe arrays.

Finally, frequency domain and time echo suppression methods are combined to achieve effective echo suppression even in challenging environments. Measurements with an echo object mounted in proximity of the AUT as well as measurements in the *Mosquito chamber* — a strongly reflective environment built on purpose for the investigation of echo effects — show that with enormous measurement and processing effort it is possible to determine the ideal free-space radiated field with satisfactory accuracy (about -40 dB deviation from the reference) even from measurements in strongly reflective environments.

Contents

1

Introduction

The common purpose of antennas is to enable the interaction of distant objects via electromagnetic fields, e.g., communication with a distant participant, remote sensing, or surveillance. Thus, the primary quantity of interest of antennas is their radiation behavior (for reciprocal antennas this is equivalent to the receiving behavior) under so-called far field (FF) conditions. While many parameters such as the input reflection or the radiation efficiency can be subject of antenna measurements, in this thesis, the focus lies on determining the radiated electromagnetic fields of an antenna under test (AUT). Usually, one is interested in the ideal AUT behavior, i.e., as if the AUT was placed in free-space without any disturbances from the environment. The ideal measurement environment, therefore, consists of an anechoic chamber large enough to allow the probe antenna to be located in the FF of the AUT but the efforts of building a large enough test range with the required suppression of environmental influences is often not feasible, either because the FF distance is too large to allow direct FF measurements or because echo influences cannot be avoided.

The problem of unfeasibly large FF distances can be handled by near field (NF) measurement techniques, where the desired FF characteristics are determined by a computational NF FF transformation (NFFFT). However, the problem with undesired environmental influences remains, as (even small) anechoic chambers are not perfect and echoes from walls or antenna positioning systems remain one of the major error influences in antenna measurements [Newell 1988]. To overcome the limitations imposed by the measurement chambers, powerful and flexible echo suppression algorithms are in need to obtain accurate results. In non-ideal environments, where absorbers may have a bad performance (e.g., at low frequencies) or are not feasible at all (e.g., in outdoor measurements, in in-situ measurements, or measurements in standard assembly halls) echo suppression becomes even more important.

The two key technologies — NFFFTs and echo suppression — are the subject of this thesis. The goal is to derive a comprehensive formal description of the complex radiation scenarios which may arise in various measurement setups. Based on this understanding of the physical mechanisms behind the measurements, algorithms shall be derived which can determine the free-space FFs of an AUT from (NF) measurements distorted by echoes from the environment.

The echo suppression methods must be capable of removing undesired echo contributions from antenna measurements in arbitrary non-anechoic environments — including strongly reflective environments[1] — with high accuracy. With a history of several decades, a large variety of algorithms exist to solve the tasks of NFFFT and echo suppression, often specialized to very particular measurement scenarios. Most of the algorithms are not general enough to handle very complex or strongly reflective environments and this thesis attempts to close relevant gaps in the literature to open up the possibility of performing accurate antenna measurements in many practically relevant applications.

An overview on the landscape of existing literature for NFFFT algorithms and echo suppression techniques is given in the next section, whereas many of the methods are analyzed in more detail in the main part of this thesis. A description of the scope and the outline of the thesis is given at the end of this chapter.

1.1. Overview of Existing Literature

The tasks of echo suppression and field transformation are closely related as both tasks are fundamentally linked to reconstructing feasible sources for the radiated fields of an AUT. While the distinction into NF and FF is sensible for an isolated antenna, such a distinction is not so clear in an echoic environment. In free-space, the antenna radiation in a sufficiently large distance is well approximated by a single plane wave, thus, the FF can be defined as the region, where the plane wave approximation of the AUT field is accurate enough for a certain application. Often the accuracy criterion is based on an estimate for the expected phase error in the FF approximation dependent on the size of the AUT [Hansen 1988, p. 21], [Balanis 2005, pp. 26ff.]. When echoes are present, the fields can usually not be approximated well by a single plane wave and consequently echo suppression techniques are often linked to NF measurement techniques and the related NFFFT techniques, even if the measurements were obtained in FF distance.

1.1.1. Field Transformation Algorithms

With the availability of computers powerful enough to handle measurements of reasonable size and with the development of new methods to calculate the FFs from NF samples, antenna NF measurements began to become popular in the second half of the last century, e.g., [Tice 1955; Johnson 1973]. An excellent overview over the historical development of NF antenna measurements is given in [Yaghjian 1986]. The basic idea behind NFFFTs is to express the AUT radiation by equivalent sources, which can consist of equivalent electric and/or magnetic currents [Petre 1992; Sarkar 1999; Álvarez 2007; Álvarez 2008; Eibert 2010] or coefficients of a modal field expansion [Sarkar 1997; Hansen 1988; Ludwig 1971; Kerns 1963]. The unknown coefficients of the equivalent field representation are determined in a way such that they match the sampled field values at the measurement positions, thereby creating an equivalent field description valid for the complete region of interest (in this sense, NFFFT algorithms can be interpreted as interpolating the field at the locations which were not sampled by a field probe).

In general, the coefficient determination step requires to invert a system of equations relating

---

[1] This might be interesting for instance in the context of antenna measurements in reverberation chambers [Gruber 2015].

the unknown source coefficients to the measured field samples. This is the reason, why modal field transformations were the first to be developed as the inverse of the resulting system of equations can be found analytically and computed very efficiently by means of fast Fourier transforms (FFTs) utilizing the orthogonality properties of the field modes in certain coordinate systems — e.g., planar, spherical or cylindrical coordinates [Yaghjian 1986]. The application of FFT based methods requires the measurements to be obtained regularly distributed on canonical measurement surfaces and often also specific properties of the utilized field probes are needed.

The receiving properties of the field probes play an important role in NF measurements. Due to their non-zero size, field probes do not measure the electric field at a single point but perform a spatial weighting of the incident fields over the complete probe volume [Eibert 2015]. Taking the realistic probe behavior into account in the system of equations for the determination of the source coefficients is called probe correction [Yaghjian 1986; Schmidt 2008a; Larsen 1977; Larsen 1984] and is generally possible for all above mentioned transformation methods, however, often the efficiency of the NFFFT method is lost as FFT based methods are no longer directly applicable, or additional measurement samples are needed [Hansen 2011b]. Certain less regular sampling strategies — e.g., spiral scans — are possible based on modal expansions [D’Agostino 2011; D’Agostino 2016; D’Agostino 2013].

Equivalent current based approaches are far more flexible concerning the placement of equivalent sources and measurement samples. In current based approaches, equivalent surface currents can be placed on an arbitrary closed Huygens surface around the AUT and the measurement samples can be irregularly distributed around the AUT [Quijano 2010a], provided the measurement samples contain sufficient information to characterize the important AUT radiation [Qureshi 2013b]. With the help of ideas from the multilevel fast multipole method (MLFMM) [Song 1995; Coifman 1993] based on a hierarchical domain decomposition scheme for the source and observation domains, the matrix-vector products relating source coefficients to the observed signals can be evaluated very efficiently. These matrix vector products can be used in an iterative solution of the system of equations for determining the source coefficients. A propagating plane wave expansion of the translation operator between the source and observation domains is the basis for the so-called Fast Irregular Antenna Field Transformation Algorithm (FIAFTA) [Eibert 2009; Eibert 2014; Eibert 2010; Eibert 2016b; Schmidt 2008a; Schmidt 2008b; Eibert 2005; Eibert 2016a], which forms the basis for all surface current based field transformations performed in this thesis.

1.1.2. Echo Suppression Methods

A variety of methods have been developed to separate undesired echo influences in the measurement data by means of processing techniques and a general summary can be found, e.g., in [Yinusa 2015]. It should be understood that, in order to extract the desired echo free signal from echoic measurements, the measurements require a certain amount of redundancy. Compared to anechoic environments, where a non-redundant number of measurements [Bucci 1996; Bucci 1991] can be used to characterize the AUT radiation, additional measurements are needed to identify and filter out the echo contributions [Foged 2013]. Redundancy in the measurements can be achieved by either measuring at more than one frequency, giving rise to time domain echo suppression techniques [Blech 2010b; Levitas 2006; Burrell 1973], or by obtaining measurement samples in more measurement positions than needed to obtain the AUT pattern under free-space conditions.

The additional samples in spatial domain are the basis for frequency-domain methods which ultimately aim to separate the AUT sources from the echo contributions based on spatial filtering. Finally, the echoic environment can be characterized in an additional preliminary measurement. The distortions in the measurements can be compensated by taking the previously measured chamber fields into account [Pogorzelski 2009; Pogorzelski 2010; Black 1995; Toivanen 2010; Toivanen 2009; Koh 2011].

Time-domain echo suppression methods utilize the fact that echo signals usually have a longer traveling time than the line of sight (LOS) signal. The direct path contributions can be separated from the echo contributions by identifying the different traveling times of the signal components. The longer traveling time of echo waves can be directly exploited in hardware by finishing the measurement before the first echo signal arrives at the probe [Levitas 2006; Blech 2008; Blech 2010b; Leibfritz 2006; Henderson 1989; Levitas 1996; Lestari 2005; Morales 2016; Young 1973]. More common is, however, to sample the signals sequentially at distinct frequencies and to obtain a time domain representation by various reconstruction methods. The most commonly used method to find a time domain representation of the frequency sequence is by means of an inverse fast Fourier transforma (IFFT)[2] [Loredo 2004; Tian 2008; Loredo 2009; Leather 2004b; Leather 2004a; Oppenheim 2010]. The major drawback of FFT based methods is the large required bandwidth — about ten times the reciprocal of the anticipated time domain step width was suggested in [Loredo 2004]. Naturally, several alternative reconstruction methods have been proposed to overcome the severe bandwidth requirements for time gating [Moon 2009; Sarkar 2016], most notably the matrix pencil method [Sarkar 1995; Fourestie 1999; Hua 1990a; Hua 1991; Hua 1990b; Fernández del Río 1996], which matches the frequency domain sequence to a sequence of exponentials, and a reconstruction of the time domain sequence with a sparsity constraint [Mauermayer 2016; Mauermayer 2017]. All time domain methods discussed here were applied directly to the probe output signals and have problems to separate signals with a similar run time, e.g., when a measurement sample was obtained in the shadow region of the echo object.

Complementary to time-domain methods, frequency-domain echo suppression methods separate the undesired echo contributions by spatial filtering. Frequency domain echo suppression algorithms can be further subdivided into current reconstruction methods [Quijano 2011a; Quijano 2011b; Cano 2010; Cano-Facila 2011; Garcia-Gonzalez 2011] and modal echo suppression methods [Hess 2006; Hess 2010a; Hess 2011; Hess 2010b; Gregson 2009; Gregson 2010a; Gregson 2011a; Gregson 2011b; Gregson 2011d; Gregson 2011c; Gregson 2013; Gregson 2010b; Gregson 2012a; Gregson 2012b; Gregson 2010c; Gregson 2017a; Gregson 2017b; Tian 2019] based on the type of equivalent sources for the AUT. In modal echo suppression methods, the AUT fields are expressed in terms of a field expansion into orthogonal modes [Yaghjian 1986; Hansen 1988], whereas the fields in current reconstruction methods are expressed by equivalent surface currents on a Huygens surface enclosing the AUT. The echo suppression in both methods is based on restricting the AUT fields to fields which can be radiated by an AUT of given size. The source reconstruction can be augmented by assuming additional sources which account for the echo distortions [Yinusa 2012b; Yinusa 2012a].

---

[2] In this work, the FFT is regarded as a computationally efficient implementation of the discrete Fourier transform, and likewise for their respective inverses. The terms FFT and *discrete Fourier transform* are used synonymously in the following.

Finally, the beneficial effects of using directive probes shall be mentioned [Hansen 1984]. By illuminating the echoes as little as possible, the echoes tend to have a small influence on the measurements. The beneficial effects can under certain circumstances be achieved by combining the measurement samples from different probe locations to form a virtual receiving array [Yinusa 2014; Dohler 2002; Dohler 2004; Dohler 2009]. These virtual beam forming methods are strongly related to the field synthesis problem [Clauzier 2015; Bucci 2013; Ford 2013; Laitinen 2010; Hill 1988; Haupt 2003b; Haupt 2003a; Mauermayer 2015; Knapp 2019c] in which a certain desired field distribution shall be achieved by optimizing the excitation of the elements of an antenna array.

1.2. Scope and Outline of the Thesis

The main objective of this thesis is the derivation and analysis of echo suppression algorithms for antenna measurements in arbitrary scattering scenarios. Many different echo suppression algorithms have already been presented in the literature, but the existing literature in the field of echo suppression algorithms is confusingly fragmented because usually the algorithms are only described isolated from each other and are applicable only in special cases. The range of applicable measurement scenarios for the specialized methods is not always well described and the requirements for an effective echo suppression are often obscure. The relation between different echo suppression methods — e.g., current and mode based algorithms — is not clear.

Therefore, the first task of the thesis is a unified description of existing methods based on a rigorous formal description of the antenna interaction in scattering scenarios. Throughout the thesis, the attempt is made to clarify the analogies between field descriptions based on spherical vector field modes and surface current based methods. Some properties of the fields can be more easily described by one or the other description, but the underlying physics is the same, independent on how it is described.

When the fields and interactions between the AUT and the probe antenna are correctly described, the formal expressions can be used to explain the working mechanisms behind existing echo suppression methods and estimate their expected performance in certain scenarios. Finally, different echo suppression methods can be combined to complement each other and thereby achieve field reconstructions with an accuracy beyond previously achieved echo suppression levels, even in strongly reflective environments.

This thesis is written for an audience with some experience in electromagnetics. Therefore, the text does not start with Maxwell's equations but it is assumed that the reader is already familiar with concepts like the curl-curl-equation for time harmonic fields. Every chapter is concluded with a chapter summary containing the relevant chore ideas from the chapter and also clarifying the contribution of this thesis to the literature.

The starting point for the formal description is a description of guided waves and free-space waves in Chapters 2 and 3, respectively. While the description of guided waves in Chapter 2 follows the paths which can be found in standard text books [Marcuvitz 1951; Collin 1990], the description of the free-space fields in Chapter 3 includes a discussion of Green's functions with an inward-traveling asymptotic boundary condition. These Green's functions are usually discarded in text books, as they are related to non-causal fields [Chew 1995; Jin 2015]. However, the analysis reveals striking similarities to a modal expansion into spherical waves, where both, inward- and outward-traveling waves are common [Hansen 1988]. The fields are systematically characterized into *purely radiated*, *purely absorbed*, *purely incident*, and *scattered* fields and their corresponding properties are revisited in terms of equivalent surface currents on the boundary of the observation volume and in terms of spherical vector waves, respectively.

In Chapter 4, antennas enter the scene as transformers between guided waves and free-space waves. The transformation between a forward-traveling wave on a waveguide into a transmitted field is described in terms of equivalent surface current based descriptions as well as in terms of spherical waves. In the same manner, also the reverse operating mode of an antenna — transforming an incident field into a backward-traveling wave on the waveguide — is revisited. In this regard, the role of an antenna as a scatterer is also briefly addressed.

Based on the results from previous chapters, the interaction between two antennas in the form of the S_{12}- and S_{21}-scattering parameters is treated in Chapter 5. Here, also the principles of NFFFT algorithms are detailed, both in terms of current reconstruction methods and spherical mode expansions, however, only for the case of an ideal anechoic environment at this point.

The formal treatment of echoes is introduced in Chapter 6. The echo influence is described by additional sources dependent on which of the two antennas is in transmitting or receiving mode. Despite the echo sources are different in both cases, the reciprocity relation $S_{12} = S_{21}$ still holds and, therefore, one can switch between the formal descriptions as one wishes. On the one hand, using the S_{12}-parameter description is advantageous in scenarios where the probe is stationary with respect to the echoic environment, because the echo sources can remain the same for all measurement positions. On the other hand, the S_{21}-parameter description can be beneficially employed for stationary AUT scenarios for the same reason.

Chapter 7 describes echo suppression methods in time domain. Although possible [Blech 2008; Blech 2010b; Levitas 2006], it is not common to obtain the measurements directly in time domain. Measurements are customarily obtained at distinct frequencies and a time domain signal is generated from the multi-frequency data. Chapter 7 investigates the relationship between the frequency domain samples of a signal and the resulting time domain representations using relevant reconstruction methods. Time domain echo suppression methods are usually applied directly to the measurement data before any further processing. As will be shown in later chapters, it is also possible to apply time gating at different steps of the processing chain, but the theoretical investigation in Chapter 7 is abstract enough to be applicable also to those cases.

Apart from providing a comprehensive view on the topic of echoic NF measurements, the main contribution of this thesis starts with the extensive analysis of frequency domain echo suppression techniques in Chapter 8. It is shown why it is important to differentiate between stationary probe and stationary AUT scenarios and both scenarios are investigated in detail. For stationary AUT scenarios, it is shown how AUT sources can be separated from echo sources and why a perfect separation of the undesired contributions can be unfeasible if the echo objects are too close to the AUT. A heuristic argument involving the anticipated degrees of freedom (DoFs) of the complete system containing AUT and echo is used to explain why echo influences can persist even when the echo objects are well separated from the AUT. The theoretical investigations are accompanied by numerical simulations. In the second part of Chapter 8, echoic scenarios with a stationary probe are investigated, which are historically linked to modal echo suppression techniques. The description by spherical field modes is particularly well suited to discuss the influences of a moving AUT. The success of modal echo suppression methods is explained on the basis of an analysis of the portion of the echo distortion which can be reconstructed by AUT sources. The source region of the additional sources accounting for the echoes is identified and shown to have a larger separation to the AUT sources the further the AUT is mounted away from the rotation center. Numerical simulations support the findings from the theoretical investigation. The chapter concludes with describing how the beneficial effect of directive probes can be synthesized by combining the probe output signals from different probe locations. The combination of probe signal acts as a virtual probe array which can be used to collect the measurement samples for a rotating AUT. Since the probe antenna as well as the AUT move in this scenario, it can be regarded as a hybrid case from the two previous scenarios. The effectiveness of the method is illustrated with a measurement example.

Two examples of particularly challenging measurement scenarios are presented in Chapter 9. These examples require a powerful combination of time domain and frequency domain methods to obtain acceptable reconstruction results for the AUT free-space fields. The first example consists of an echo object in close proximity to the AUT with a fixed position relative to the AUT. Since this scenario must be described by a moving probe, it is clear that conventional time gating cannot be effective for all measurement positions, as for some measurement positions, the probe is located in the shadow region of the echo object and no path length difference between the LOS path and the reflected path can be used for time gating. The proposed solution is to reconstruct equivalent surface currents on a tight Huygens surface around the AUT and the echo in frequency domain for many frequencies. Following the analysis from Chapter 8, the spatial separation should be possible if the echoes are not too close, but mutual interactions distort the actual current distribution on the AUT. These mutual interactions can be treated in a second step by time gating the reconstructed sources (as opposed to time gating the signals before the reconstruction step as was the case for all existing time gating techniques in the literature). The effectiveness of the proposed processing scheme is illustrated with a simulation and also with an actual measurement. The second example of a challenging measurement scenario consists of a strongly reflective environment called Mosquito chamber. Inside the anechoic chamber of the Technical University of Munich (TUM), a smaller chamber was built with walls consisting of a metallic mesh. All four chamber walls as well as the floor and the ceiling were covered by the metallic mesh, thus, the AUT and probe positioners were effectively placed inside a strongly reflective environment. The free-space radiated fields of three different AUTs covering the S-Band and the Ku-Band were determined from a large number of measurement samples obtained inside the Mosquito chamber. For example, a complete spherical measurement (by rotating the AUT) was obtained for more than 100 different probe positions. Time gating was combined with virtual array synthesis for the probes to achieve the echo suppression in this challenging environment. Finally, Chapter 10 concludes this work and summarizes the main results.

1.3. Notation

Throughout this thesis, a time dependency of $\mathrm{e}^{\mathrm{j}\omega t}$ is assumed and suppressed for all time harmonic fields and currents, if not stated otherwise. For quantities with a different time dependence, the time dependence is made explicit, when necessary (e.g., in Chapter 7). Physical vectors which have a meaningful interpretation in terms of a direction or location in the three-dimensional world, such as the electric field $\boldsymbol{E}$, the surface current density $\boldsymbol{J}$, or the location $\boldsymbol{r}$ are typeset in a bold, serif, and italic font. The vector spaces in which these vectors are situated are commonly

$\mathbb{R}^3$ or $\mathbb{C}^3$ (or two dimensional surfaces embedded in these spaces). For physical vectors, this thesis follows standard conventions, where either capital letters or minuscules can be used to denote a vector. The unit vectors in certain spatial directions are denoted by $\boldsymbol{e}_k$, where the index k indicates the direction (e.g., the vector $\boldsymbol{e}_x$ is the unit vector in x-direction).

Vectors in abstract linear algebra spaces which have a meaningful interpretation as either column or row vectors, such as a coefficient vector $\boldsymbol{\mathsf{x}} \in \mathbb{C}^{N\times 1}$ are typeset with minuscules in a bold, sans serif, and italic font. Notice the subtle difference in their definition space — $\mathbb{C}^{N\times 1}$ instead of $\mathbb{C}^N$ — in contrast to their physical counterparts. Matrices (e.g., $\boldsymbol{\mathsf{A}} \in \mathbb{C}^{M\times N}$ is a matrix) are written in capital letters in a bold, sans serif, and italic font.

Dyadic quantities such as the dyadic Green's function $\boldsymbol{\mathcal{G}}$ are written in a bold calligraphic font. The noun *dyadic* refers to a general tensor of order two (e.g., $\boldsymbol{\mathcal{D}} = c_{xx}\,\boldsymbol{e}_x\boldsymbol{e}_x + c_{xy}\,\boldsymbol{e}_x\boldsymbol{e}_y + c_{xz}\,\boldsymbol{e}_x\boldsymbol{e}_z + c_{yx}\,\boldsymbol{e}_y\boldsymbol{e}_x + c_{yy}\,\boldsymbol{e}_y\boldsymbol{e}_y + c_{yz}\,\boldsymbol{e}_y\boldsymbol{e}_z + c_{zx}\,\boldsymbol{e}_z\boldsymbol{e}_x + c_{zy}\,\boldsymbol{e}_z\boldsymbol{e}_y + c_{zz}\,\boldsymbol{e}_z\boldsymbol{e}_z$ is a dyadic), whereas the noun *dyad* specifically refers to a tensor of order two and rank one (e.g., $\boldsymbol{e}_x\boldsymbol{e}_z$ is a dyad). A dyad is the result of a dyadic product (or tensor product) $\boldsymbol{ab}$ between two vectors (the dyadic product has no multiplication symbol between the vectors in contrast to the scalar product $\boldsymbol{a}\cdot\boldsymbol{b}$ or the cross product $\boldsymbol{a}\times\boldsymbol{b}$).

Mathematical constants, such as π, the Euler constant e, the imaginary unit j, or the unit dyadic $\mathbf{I}$ are typeset in upright letters (notice that *physical* constants such as the speed of light c_0 are not considered to be *mathematical* constants and therefore denoted by italic letters). Similarly, mathematically well defined and established (generalized) functions such as $\sin(x)$ or the Dirac-Delta distribution $\delta(x)$ as well as mathematically well defined and established operators such as the derivative operators $\mathrm{d}(\cdot)/\mathrm{d}x$, the infinitesimal element $\mathrm{d}x$ or the Laplace operator Δ are typeset with upright symbols.

The volume element in a volume integral over the spatial variable $\boldsymbol{r}$ is denoted by $\mathrm{d}v$ (or $\mathrm{d}v'$ if the integration variable is $\boldsymbol{r}'$) and the corresponding surface element in a surface integral over the spatial variable $\boldsymbol{r}$ is denoted by $\mathrm{d}a$ (or $\mathrm{d}a'$ if the integration variable is $\boldsymbol{r}'$). The surface integral over the Ewald sphere in spectral domain, where the integration is performed over all directions in space indicated by the short hand notation $\hat{\boldsymbol{k}}$ has its surface element for the integration (in a slight abuse of notation) symbolically expressed by $\mathrm{d}\hat{\boldsymbol{k}}$.

2

Guided Waves

Antennas are devices which transform guided waves into free-space waves and vice versa. It is thus convenient to analyze guided waves before going on with the discussion about antennas. Waveguides[1] are structures, which support solutions of Maxwell's equations in the form

$$\boldsymbol{E}(x, y, z) = \boldsymbol{E}(x, y, 0)\, \mathrm{e}^{\pm\gamma z} \tag{2.1}$$

and

$$\boldsymbol{H}(x, y, z) = \boldsymbol{H}(x, y, 0)\, \mathrm{e}^{\pm\gamma z}\,, \tag{2.2}$$

where without loss of generality, the propagation direction was chosen along the z-axis [Marcuvitz 1951, p. 13]. For the upcoming analysis, the considerations are limited to shielded waveguides filled with a homogeneous medium. The cross section of the waveguide is surrounded by a perfect electrically conducting (PEC) enclosure. The limitation to this special case ensures that free-space waves can couple with the waveguide only via the antenna and that the field modes are either transverse electromagnetic (TEM) fields where neither the electric nor the magnetic field has a z-component, or transverse electric (TE) fields where only the magnetic field has a z-component, or transverse magnetic (TM) fields where only the electric field has a z-component [Marcuvitz 1951, p. 4]. Some possible cross sections for such waveguides are depicted in Fig. 2.1.

The finite cross section of the waveguide is defined as the area S in the xy-plane enclosed by the perfectly conducting hull[2]. The guided field modes have desirable orthogonality properties which can be exploited by mode matching techniques. The limitation to shielded waveguides is not severe, as the guided wave is anyhow eventually guided into a shielded waveguide in most practical applications, e.g., when the waveguide is connected to a vector network analyzer (usually by a coaxial cable).

---

[1] The term *waveguide* will be used as an umbrella term for all guiding structures, including tube like hollow waveguides and transmission lines.

[2] Open waveguides such as microstrip lines formally require to consider an infinite cross section for the guided wave. More details on open waveguides may be found for example in [Bladel 2007, pp. 882ff.].

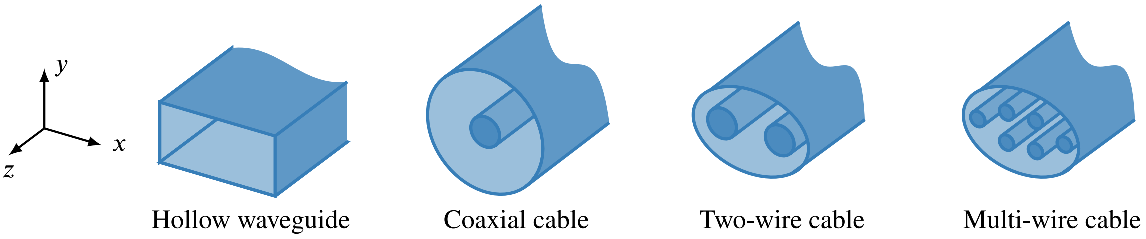

Fig. 2.1.: Cross sections of different examples of wave-guiding structures considered in this thesis. All waveguides have a PEC enclosure to avoid coupling with free-space waves and to ensure the orthogonality of the guided modes.

As will be shown in the following, the guided waves in the shielded waveguides can be expressed by a sum of orthogonal modes traveling in positive or negative z-direction [Marcuvitz 1951, p. 5]. For all waveguide modes, the transversal part of the backward-traveling modes in the reference plane at $z = 0$ is found from the corresponding transversal part of the forward-traveling mode by simply changing the sign of the magnetic field.

2.1. Transverse Electromagnetic Modes

The simplest kind of guided field modes are TEM modes. TEM waves which have neither an H-field nor an E-field component in z-direction can only exist inside a waveguide if there is at least one conductor inside the waveguide apart from the enclosing hull [Marcuvitz 1951, p. 4]. Coaxial cables and shielded two-wire cables fall into this category, for example (also multi-wire cables can be imagined but have little practical relevance). The TEM fields inside the waveguide can be expressed by [Collin 1990, pp. 174f., pp. 247ff.]

$$\boldsymbol{E}_\mathrm{t}(x, y, z) = -\nabla_\mathrm{t}\Phi(x, y)\,\mathrm{e}^{\pm \mathrm{j}k_0 z} \tag{2.3}$$

$$\boldsymbol{H}_\mathrm{t}(x, y, z) = \mp Y \boldsymbol{e}_z \times \boldsymbol{E}_\mathrm{t}(x, y, z) \ , \tag{2.4}$$

where $\nabla_\mathrm{t} = \boldsymbol{e}_x \left(\partial/\partial x\right) + \boldsymbol{e}_y \left(\partial/\partial y\right)$ is the transverse part of the Nabla operator [Marcuvitz 1951, p. 4], $k_0^2 = \omega^2\varepsilon\mu$ is the propagation constant, and $Y = \sqrt{\varepsilon/\mu}$ is the admittance of the homogeneous medium with permittivity ε and permeability μ between the conductors. The subscript “t” in $\boldsymbol{E}_\mathrm{t}$ and $\boldsymbol{H}_\mathrm{t}$ indicates that the vectors are transverse. No longitudinal field component (parallel to the z-axis) exists for TEM modes. The scalar generating function $\Phi(x, y)$ is a solution to the two-dimensional Laplace equation

$$\Delta_\mathrm{t}\,\Phi(x, y) = 0 \tag{2.5}$$

in the xy-plane subject to the boundary condition that the value of $\Phi(x, y)$ is constant along the border of any conductor (but the value may change from one conductor to the other) [Marcuvitz 1951, p. 4]. The symbol $\Delta_\mathrm{t} = \partial^2/\partial x^2 + \partial^2/\partial y^2$ denotes the transverse part of the Laplacian. It is necessary that Φ attains different values on at least two conductors to obtain a non-trivial solution for the electric field[3]. The upper signs of the expressions in (2.3) and (2.4) correspond

---

[3] Due to the maximum principle of solutions of the Laplace equation, the function $\Phi(x, y)$ must be constant if the same potential is enforced on all boundaries.

to a wave propagating in negative z-direction and the lower signs to a wave traveling in positive z-direction. Losses in the medium can be introduced by letting ε have a negative imaginary part, giving rise to an imaginary part in the propagation constant $k_0 = \beta - \mathrm{j}\alpha$.

If the waveguide has N separate conductors (including the surrounding tube), there are $N - 1$ possible independent propagating TEM modes, which are obtained by consecutively fixing the potential on one of the $N - 1$ internal conductors to $V_n \neq 0$ and setting the remaining conductors to a potential of 0 [Collin 1990, p. 248].

2.2. Transverse Electric Modes

When no additional conductor is present inside the conducting tube, the waveguide is called hollow waveguide. No TEM mode exists in a hollow waveguide but one can find infinitely many discrete solutions with a z-component of the magnetic field and no z-component of the electric field. These TE solutions also exist on all other waveguides considered in this work. The electric and magnetic fields of the TE modes can be expressed by [Collin 1990, pp. 330ff.]

$$\boldsymbol{H}_{\mathrm{t,TE}} = \pm\gamma\,\nabla_{\mathrm{t}}\psi_{\mathrm{TE}}\,\mathrm{e}^{\pm\gamma z} \tag{2.6}$$

$$H_{z,\mathrm{TE}} = -\Delta_{\mathrm{t}}\psi_{\mathrm{TE}}\,\mathrm{e}^{\pm\gamma z} \tag{2.7}$$

$$\boldsymbol{E}_{\mathrm{t,TE}} = \pm Z_{\mathrm{TE}}\,\boldsymbol{e}_z \times \boldsymbol{H}_{\mathrm{t,TE}} \tag{2.8}$$

with the TE wave impedance

$$Z_{\mathrm{TE}} = \frac{\mathrm{j}k_0 Z}{\gamma}\,. \tag{2.9}$$

The subscript “t” means the transverse part (only x- and y-component) of the fields and $Z = \sqrt{\mu/\varepsilon}$ is the material impedance of the material between the conductors.

The involved scalar generating function ψ_{TE} is a solution to the two-dimensional scalar Helmholtz equation

$$\Delta_{\mathrm{t}}\,\psi_{\mathrm{TE}} + k_c^2\,\psi_{\mathrm{TE}} = 0 \tag{2.10}$$

satisfying the boundary condition $\partial\psi_{\mathrm{TE}}/\partial\boldsymbol{n} = 0$ on the surface of the conductors. Due to the boundary condition, solutions for ψ_{TE} exist only for certain discrete eigenvalues $k_c > 0$. The value for γ is fixed for every TE solution by the relation

$$k_0^2 + \gamma^2 = k_c^2\,, \tag{2.11}$$

where $k_0^2 = \omega^2\varepsilon\mu$ is the hypothetical plane wave propagation constant for the material. A propagating wave is characterized by a purely imaginary γ in the lossless case, which happens for $k_0^2 > k_c^2$. If $k_0^2 < k_c^2$ in the lossless case, γ is purely real and the so-called evanescent wave is exponentially damped along its direction of propagation. Losses are considered by a negative imaginary part of ε, such that both, k_0 and γ become complex valued numbers with real and imaginary part. A real part of γ always indicates that the corresponding mode is damped along its propagation direction (either due to losses or due to the mode being evanescent) [Collin 1990, pp. 340ff.].

2.3. Transverse Magnetic Modes

Similar to the TE modes, a second set of infinitely many discrete solutions exists on a waveguide with a z-component of the electric field and no z-component of the magnetic field. These solutions are called TM modes and their electric and magnetic fields are expressed as[4] [Collin 1990, pp. 332f.]

$$\begin{aligned} \boldsymbol{E}_{\mathrm{t,TM}} &= -\gamma\,\nabla_{\mathrm{t}}\psi_{\mathrm{TM}}\,\mathrm{e}^{\pm\gamma z} && (2.12)\\ E_{z,\mathrm{TM}} &= \pm\Delta_{\mathrm{t}}\psi_{\mathrm{TM}}\,\mathrm{e}^{\pm\gamma z} && (2.13)\\ \boldsymbol{H}_{\mathrm{t,TM}} &= \mp Y_{\mathrm{TM}}\,\boldsymbol{e}_z \times \boldsymbol{E}_{\mathrm{t,TM}} && (2.14) \end{aligned}$$

with the TM wave admittance

$$Y_{\mathrm{TM}} = \frac{\mathrm{j}k_0}{\gamma Z}\,. \tag{2.15}$$

The subscript “t” means the transverse part (only x- and y-component) of the fields and $Z = \sqrt{\mu/\varepsilon}$ is the material impedance of the material between the conductors.

The involved scalar generating function ψ_{TM} is a solution to the two-dimensional scalar Helmholtz equation

$$\Delta_{\mathrm{t}}\psi_{\mathrm{TM}} + k_c^2\psi_{\mathrm{TM}} = 0 \tag{2.16}$$

satisfying the boundary condition $\psi_{\mathrm{TM}} = 0$ on the surface of the conductors. Due to the boundary condition, solutions for ψ_{TM} exist only for certain discrete eigenvalues $k_c > 0$. The value for γ is fixed for every TE solution by the relation

$$k_0^2 + \gamma^2 = k_c^2\,, \tag{2.17}$$

where $k_0^2 = \omega^2\varepsilon\mu$ is the hypothetical plane wave propagation constant for the material. A propagating wave is characterized by a purely imaginary γ in the lossless case, which happens for $k_0^2 > k_c^2$. If $k_0^2 < k_c^2$ in the lossless case, γ is purely real and the so-called evanescent wave is exponentially damped along its direction of propagation. Losses are considered by a negative imaginary part of ε, such that both, k_0 and γ become complex valued numbers with real and imaginary part. A real part of γ always indicates that the corresponding mode is damped along its propagation direction (either due to losses or due to the mode being evanescent) [Collin 1990, pp. 340ff.].

2.4. Orthogonality Properties of Waveguide Modes

The field modes of the previous sections have important orthogonality properties. This section follows the derivation in [Collin 1990, pp. 335ff.] which can be used to derive the orthogonality between any pair of TE and TM modes but also to derive the orthogonality between a possible TEM mode and any TE or TM mode.

---

[4] Notice that the signs are changed compared to [Collin 1990]. In the sign convention used here, we have for the transversal fields of the same mode propagating in opposite directions $\boldsymbol{E}_{\mathrm{t,TM}} = \boldsymbol{E}'_{\mathrm{t,TM}}$ and $\boldsymbol{H}_{\mathrm{t,TM}} = -\boldsymbol{H}'_{\mathrm{t,TM}}$ (The primed fields denote the mode propagating in opposite direction of the unprimed fields).

Let $\boldsymbol{E}_m$, $\boldsymbol{H}_m$ and $\boldsymbol{E}_n$, $\boldsymbol{H}_n$ be two independent electromagnetic fields corresponding to non-degenerate guided wave modes traveling in positive z-direction on a shielded waveguide. The corresponding transverse fields are denoted by $\boldsymbol{E}_{\mathrm{t},m}$, $\boldsymbol{H}_{\mathrm{t},m}$ and $\boldsymbol{E}_{\mathrm{t},n}$, $\boldsymbol{H}_{\mathrm{t},n}$.

The two waveguide modes have a z-dependency of $\mathrm{e}^{-\gamma_m z}$ and $\mathrm{e}^{-\gamma_n z}$, respectively. Because non-degenerate modes are assumed, $\gamma_m \neq \gamma_n$. Multiplying the four curl equations

$$\nabla \times \boldsymbol{E}_m = -\mathrm{j}\omega\mu \boldsymbol{H}_m \,, \tag{2.18}$$

$$\nabla \times \boldsymbol{E}_n = -\mathrm{j}\omega\mu \boldsymbol{H}_n \,, \tag{2.19}$$

$$\nabla \times \boldsymbol{H}_m = \mathrm{j}\omega\varepsilon \boldsymbol{E}_m \,, \tag{2.20}$$

$$\nabla \times \boldsymbol{H}_n = \mathrm{j}\omega\varepsilon \boldsymbol{E}_n \,, \tag{2.21}$$

with $\boldsymbol{H}_n$, $\boldsymbol{H}_m$, $\boldsymbol{E}_n$, and $\boldsymbol{E}_m$, respectively, and subtracting two equations each, one obtains

$$\boldsymbol{H}_n \cdot \nabla \times \boldsymbol{E}_m - \boldsymbol{H}_m \cdot \nabla \times \boldsymbol{E}_n = 0 \tag{2.22}$$

and

$$\boldsymbol{E}_n \cdot \nabla \times \boldsymbol{H}_m - \boldsymbol{E}_m \cdot \nabla \times \boldsymbol{H}_n = 0 \,. \tag{2.23}$$

Using the identity[5] $\boldsymbol{B} \cdot \nabla \times \boldsymbol{A} - \boldsymbol{A} \cdot \nabla \times \boldsymbol{B} = \nabla \cdot \boldsymbol{A} \times \boldsymbol{B}$ after adding (2.22) and (2.23) we have

$$\nabla \cdot \left(\boldsymbol{E}_m \times \boldsymbol{H}_n - \boldsymbol{E}_n \times \boldsymbol{H}_m\right) = 0 \tag{2.24}$$

$$\nabla_{\mathrm{t}} \cdot \left(\boldsymbol{E}_m \times \boldsymbol{H}_n - \boldsymbol{E}_n \times \boldsymbol{H}_m\right) + \boldsymbol{e}_z \cdot \frac{\partial}{\partial z}\left(\boldsymbol{E}_m \times \boldsymbol{H}_n - \boldsymbol{E}_n \times \boldsymbol{H}_m\right) = 0 \tag{2.25}$$

$$\nabla_{\mathrm{t}} \cdot \left(\boldsymbol{E}_m \times \boldsymbol{H}_n - \boldsymbol{E}_n \times \boldsymbol{H}_m\right) - \boldsymbol{e}_z \cdot \left(\gamma_m + \gamma_n\right)\left(\boldsymbol{E}_{\mathrm{t},m} \times \boldsymbol{H}_{\mathrm{t},n} - \boldsymbol{E}_{\mathrm{t},n} \times \boldsymbol{H}_{\mathrm{t},m}\right) = 0 \tag{2.26}$$

Integrating over the waveguide cross section S and exploiting the two-dimensional divergence theorem we have

$$\iint\limits_S \nabla_{\mathrm{t}} \cdot \left(\boldsymbol{E}_m \times \boldsymbol{H}_n - \boldsymbol{E}_n \times \boldsymbol{H}_m\right) \mathrm{d}a = \left(\gamma_m + \gamma_n\right) \iint\limits_S \boldsymbol{e}_z \cdot \left(\boldsymbol{E}_{\mathrm{t},m} \times \boldsymbol{H}_{\mathrm{t},n} - \boldsymbol{E}_{\mathrm{t},n} \times \boldsymbol{H}_{\mathrm{t},m}\right) \mathrm{d}a \tag{2.27}$$

$$\sum_{n=0}^{N} \oint\limits_{C_n} \boldsymbol{n} \cdot \left(\boldsymbol{E}_m \times \boldsymbol{H}_n - \boldsymbol{E}_n \times \boldsymbol{H}_m\right) \mathrm{d}\ell = \left(\gamma_m + \gamma_n\right) \iint\limits_S \boldsymbol{e}_z \cdot \left(\boldsymbol{E}_{\mathrm{t},m} \times \boldsymbol{H}_{\mathrm{t},n} - \boldsymbol{E}_{\mathrm{t},n} \times \boldsymbol{H}_{\mathrm{t},m}\right) \mathrm{d}a \tag{2.28}$$

$$0 = \left(\gamma_m + \gamma_n\right) \iint\limits_S \boldsymbol{e}_z \cdot \left(\boldsymbol{E}_{\mathrm{t},m} \times \boldsymbol{H}_{\mathrm{t},n} - \boldsymbol{E}_{\mathrm{t},n} \times \boldsymbol{H}_{\mathrm{t},m}\right) \mathrm{d}a \,. \tag{2.29}$$

The contour integrals vanish since $\boldsymbol{n} \times \boldsymbol{E}_m = \boldsymbol{n} \times \boldsymbol{E}_n = 0$ on the contours C_n which lie on the surfaces of the perfect conductors ($\boldsymbol{n}$ is the vector in the xy-plane which is orthogonal to C_n, pointing away from the surface enclosed by C_n). The same derivation can be carried out for the two modes $\boldsymbol{E}_m$, $\boldsymbol{H}_m$ and $\boldsymbol{E}'_n$, $\boldsymbol{H}'_n$, where $\boldsymbol{E}'_n$, $\boldsymbol{H}'_n$ is the same mode as above but traveling

---

[5] This identity can, e.g., be found in the very good appendix of [Bladel 2007].

into the opposite direction. Since $\boldsymbol{H}'_{\mathrm{t},n} = -\boldsymbol{H}_{\mathrm{t},n}$, $\boldsymbol{E}'_{\mathrm{t},n} = \boldsymbol{E}_{\mathrm{t},n}$ and with the z-dependency of the backward-traveling modes being $\mathrm{e}^{\mathrm{j}\gamma_n z}$ rather than $\mathrm{e}^{-\gamma_n z}$, one obtains

$$0 = \left(\gamma_m - \gamma_n\right) \iint\limits_S \boldsymbol{e}_z \cdot \left(-\boldsymbol{E}_{\mathrm{t},m} \times \boldsymbol{H}_{\mathrm{t},n} - \boldsymbol{E}_{\mathrm{t},n} \times \boldsymbol{H}_{\mathrm{t},m}\right) \,\mathrm{d}a\,. \tag{2.30}$$

Adding and subtracting (2.29) and (2.30) yields

$$\iint\limits_S \boldsymbol{e}_z \cdot \left(\boldsymbol{E}_{\mathrm{t},m} \times \boldsymbol{H}_{\mathrm{t},n}\right) \,\mathrm{d}a = 0 \tag{2.31}$$

and

$$\iint\limits_S \boldsymbol{e}_z \cdot \left(\boldsymbol{E}_{\mathrm{t},n} \times \boldsymbol{H}_{\mathrm{t},m}\right) \,\mathrm{d}a = 0\,, \tag{2.32}$$

which are the central orthogonality relations for guided modes on the shielded waveguide. Any two non-degenerate modes are proven to be orthogonal, even if they travel into opposite directions. Notice that one only gets insightful insights from this proof if $\gamma_m \neq \pm\gamma_n$, i.e., this proof only holds for non-degenerate modes. Losses inside the filling material of the waveguide can be expressed by an imaginary part of γ without a problem in the previous derivation, but losses in the enclosing waveguide walls lead to non-orthogonal waveguide modes in general. If the losses in the waveguide are small enough, the waveguide modes are approximately orthogonal, which is sufficient in most applications.

2.5. Degenerate Modes

Some waveguides can support more than one independent field mode with the same propagation constant γ. These modes are called *degenerate*. Degenerate modes are possible for example in multi-wire cables — in this case one can have more than one possible TEM mode — or in symmetrical hollow waveguides such as square or circular hollow waveguides — which may support multiple TE or TM waves with the same propagation constant.

Let $\boldsymbol{E}_{\mathrm{t},n}$, $\boldsymbol{H}_{\mathrm{t},n}$, $n = 1, \ldots, N$ with $N < \infty$ be a set of degenerate modes traveling in positive z-direction[6]. These modes have no obligation to be mutually orthogonal, since the proof given in the previous section does not apply for degenerate modes.

The non-orthogonal degenerate modes can always be replaced by an orthogonal set $\tilde{\boldsymbol{E}}_{\mathrm{t},n}$, $\tilde{\boldsymbol{H}}_{\mathrm{t},n}$, $n = 1, \ldots, N$ for example by a Gram-Schmidt orthogonalization [Collin 1990, pp. 333f.]

$$\tilde{\boldsymbol{E}}_{\mathrm{t},n} = \boldsymbol{E}_{\mathrm{t},n} - \sum_{m=1}^{n-1} \tilde{\boldsymbol{E}}_{\mathrm{t},m} \frac{\iint\limits_S \boldsymbol{e}_z \cdot \left(\boldsymbol{E}_{\mathrm{t},n} \times \tilde{\boldsymbol{H}}_{\mathrm{t},m}\right) \,\mathrm{d}a}{\iint\limits_S \boldsymbol{e}_z \cdot \left(\tilde{\boldsymbol{E}}_{\mathrm{t},m} \times \tilde{\boldsymbol{H}}_{\mathrm{t},m}\right) \,\mathrm{d}a}\,, \tag{2.33}$$

$$\tilde{\boldsymbol{H}}_{\mathrm{t},n} = \boldsymbol{H}_{\mathrm{t},n} - \sum_{m=1}^{n-1} \tilde{\boldsymbol{H}}_{\mathrm{t},m} \frac{\iint\limits_S \boldsymbol{e}_z \cdot \left(\tilde{\boldsymbol{E}}_{\mathrm{t},m} \times \boldsymbol{H}_{\mathrm{t},n}\right) \,\mathrm{d}a}{\iint\limits_S \boldsymbol{e}_z \cdot \left(\tilde{\boldsymbol{E}}_{\mathrm{t},m} \times \tilde{\boldsymbol{H}}_{\mathrm{t},m}\right) \,\mathrm{d}a}\,. \tag{2.34}$$

---

[6] The corresponding fields for the modes traveling into the opposite direction are found by reversing the sign of the magnetic field.

The orthogonalized modes $\tilde{\boldsymbol{E}}_{\mathrm{t},n}$, $\tilde{\boldsymbol{H}}_{\mathrm{t},n}$, $n = 1, \dots, N$ are still degenerate — they share the same propagation constant γ — but they also fulfill the orthogonality conditions (2.31) and (2.32). For the Gram-Schmidt orthogonalization to be applicable the number of degenerate modes must be finite. This is ensured by the surrounding PEC enclosure which was assumed in the beginning of the discussion about waveguides. In the following it is thus always assumed that the different field modes on a waveguide are mutually orthogonal, i.e., (2.31) and (2.32) hold true.

2.6. Mode Matching

The total field inside a waveguide can be expanded into normalized orthogonal forward- and backward-traveling waveguide modes in the manner of

$$\boldsymbol{E}(x,y,z) = \sum_{m=0}^{\infty} \left(\alpha_m \hat{\boldsymbol{E}}_m(x,y,0)\,\mathrm{e}^{-\gamma_m z} + \beta_m \hat{\boldsymbol{E}}'_m(x,y,0)\,\mathrm{e}^{+\gamma_m z} \right) \tag{2.35}$$

and

$$\boldsymbol{H}(x,y,z) = \sum_{m=0}^{\infty} \left(\alpha_m \hat{\boldsymbol{H}}_m(x,y,0)\,\mathrm{e}^{-\gamma_m z} + \beta_m \hat{\boldsymbol{H}}'_m(x,y,0)\,\mathrm{e}^{+\gamma_m z} \right) . \tag{2.36}$$

The hat above the field quantities denotes that they are divided by $\sqrt{\mathrm{W}}$, i.e., the normalized electric fields have units $[\hat{\boldsymbol{E}}_m] = \sqrt{\Omega}\,/\mathrm{m}$, the normalized magnetic fields have the units $[\hat{\boldsymbol{H}}_m] = 1/(\sqrt{\Omega}\,\mathrm{m})$, and the wave amplitudes α_m, β_m have the units $[\alpha_m] = [\beta_m] = \sqrt{\mathrm{W}}$.

Let $\boldsymbol{E}_\mathrm{t}$, $\boldsymbol{H}_\mathrm{t}$ be the transversal part of the total field. Using the orthogonality relations (2.31) and the relations $\hat{\boldsymbol{H}}'_{\mathrm{t},m}(x,y,0) = -\hat{\boldsymbol{H}}_{\mathrm{t},m}(x,y,0)$, $\hat{\boldsymbol{E}}'_{\mathrm{t},m}(x,y,0) = \hat{\boldsymbol{E}}_{\mathrm{t},m}(x,y,0)$ between the forward- and backward- traveling transversal fields of the same mode, the expansion coefficients are found by

$$\alpha_m = \frac{1}{2}\left(\frac{\iint\limits_S \boldsymbol{e}_z \cdot \left(\hat{\boldsymbol{E}}_{\mathrm{t},m} \times \boldsymbol{H}_\mathrm{t}\right)\,\mathrm{d}a + \iint\limits_S \boldsymbol{e}_z \cdot \left(\boldsymbol{E}_\mathrm{t} \times \hat{\boldsymbol{H}}_{\mathrm{t},m}\right)\,\mathrm{d}a}{\iint\limits_S \boldsymbol{e}_z \cdot \left(\hat{\boldsymbol{E}}_{\mathrm{t},m} \times \hat{\boldsymbol{H}}_{\mathrm{t},m}\right)\,\mathrm{d}a} \right) \tag{2.37}$$

and

$$\beta_m = \frac{1}{2}\left(\frac{\iint\limits_S \boldsymbol{e}_z \cdot \left(\hat{\boldsymbol{E}}_{\mathrm{t},m} \times \boldsymbol{H}_\mathrm{t}\right)\,\mathrm{d}a - \iint\limits_S \boldsymbol{e}_z \cdot \left(\boldsymbol{E}_\mathrm{t} \times \hat{\boldsymbol{H}}_{\mathrm{t},m}\right)\,\mathrm{d}a}{\iint\limits_S \boldsymbol{e}_z \cdot \left(\hat{\boldsymbol{E}}_{\mathrm{t},m} \times \hat{\boldsymbol{H}}_{\mathrm{t},m}\right)\,\mathrm{d}a} \right) , \tag{2.38}$$

where S is the cross section of the waveguide at an arbitrary fixed z-coordinate — usually $z = 0$.

Using the auxiliary surface currents

$$\hat{\boldsymbol{J}}_m(x,y) = \boldsymbol{e}_z \times \hat{\boldsymbol{H}}_{m\mathrm{t}}(x,y,0) \tag{2.39}$$

and

$$\hat{\boldsymbol{M}}_m(x,y) = -\boldsymbol{e}_z \times \hat{\boldsymbol{E}}_{m\mathrm{t}}(x,y,0) \tag{2.40}$$

we have

$$\alpha_m = \frac{1}{2} \frac{1}{\iint\limits_S \boldsymbol{e}_z \cdot \left(\hat{\boldsymbol{J}}_m \times \hat{\boldsymbol{M}}_m\right)\,\mathrm{d}a} \left(\iint\limits_S \left[\hat{\boldsymbol{M}}_m \cdot \boldsymbol{H} + \hat{\boldsymbol{J}}_m \cdot \boldsymbol{E}\right]\,\mathrm{d}a \right) \tag{2.41}$$

and

$$\beta_m = \frac{1}{2} \frac{1}{\iint\limits_S \boldsymbol{e}_z \cdot \left(\hat{\boldsymbol{J}}_m \times \hat{\boldsymbol{M}}_m\right) \mathrm{d}a} \left(\iint\limits_S \left[-\hat{\boldsymbol{M}}_m \cdot \boldsymbol{H} + \hat{\boldsymbol{J}}_m \cdot \boldsymbol{E} \right] \mathrm{d}a \right), \tag{2.42}$$

where α_m and β_m are the wave coefficients of the mode expansion of the total field in the waveguide with respect to the reference plane S at $z = 0$. The (normalized) auxiliary mode surface currents have the units $[\hat{\boldsymbol{J}}_m] = 1/(\sqrt{\Omega}\,\mathrm{m})$ and $[\hat{\boldsymbol{M}}_m] = \sqrt{\Omega}/\mathrm{m}$. The normalization integrals

$$\iint\limits_S \boldsymbol{e}_z \cdot \left(\hat{\boldsymbol{E}}_{\mathrm{t},m} \times \hat{\boldsymbol{H}}_{\mathrm{t},m}\right) \mathrm{d}a \tag{2.43}$$

or equivalently

$$\iint\limits_S \boldsymbol{e}_z \cdot \left(\hat{\boldsymbol{J}}_m \times \hat{\boldsymbol{M}}_m\right) \mathrm{d}a \tag{2.44}$$

are mode specific and do not depend on the total field to be expanded into the field modes.

If the waveguide modes are normalized such that the normalization condition

$$\iint\limits_S \boldsymbol{e}_z \cdot \left(\hat{\boldsymbol{E}}_{\mathrm{t},m}(x, y, z_0) \times \hat{\boldsymbol{H}}_{\mathrm{t},m}(x, y, z_0)\right) \mathrm{d}a = 1 \tag{2.45}$$

holds in the reference surface S at $z = 0$ then the wave amplitudes can be found by the simplified equations

$$\alpha_m = \frac{1}{2} \left(\iint\limits_S \left[\hat{\boldsymbol{M}}_m \cdot \boldsymbol{H} + \hat{\boldsymbol{J}}_m \cdot \boldsymbol{E} \right] \mathrm{d}a \right) \tag{2.46}$$

and

$$\beta_m = \frac{1}{2} \left(\iint\limits_S \left[-\hat{\boldsymbol{M}}_m \cdot \boldsymbol{H} + \hat{\boldsymbol{J}}_m \cdot \boldsymbol{E} \right] \mathrm{d}a \right). \tag{2.47}$$

In general, the normalization in (2.45) is not directly related to the time averaged power flow [Bladel 2007, p. 866]

$$P_m = \frac{1}{2} |\alpha_m|^2 \,\mathrm{Re} \left\{ \iint\limits_S \hat{\boldsymbol{E}}_{\mathrm{t},m} \times \hat{\boldsymbol{H}}^*_{\mathrm{t},m} \cdot \boldsymbol{e}_z \,\mathrm{d}a \right\} \tag{2.48}$$

of the mth mode through the surface S (due to the complex conjugation of $\hat{\boldsymbol{H}}_{\mathrm{t},m}$).

Only for propagating modes in lossless waveguides (where ε and μ are real and positive) the power normalization and the mode normalization in (2.45) are related [Bladel 2007, p. 866], [Collin 1990, p. 337]. The propagation constant γ is purely imaginary for propagating modes in this case and, thus, the transversal electric and magnetic fields of the waveguide modes in the reference surface S ($z = z_0$) can be chosen purely real as can be seen in (2.3) and (2.4) for the TEM case, in (2.6) and (2.8) for the TE case, and in (2.12) and (2.14) for the TM case. Thus, we have

$$\operatorname{Re}\left\{\iint\limits_S \boldsymbol{e}_z \cdot \left(\hat{\boldsymbol{E}}_{\mathrm{t},m}(x,y,z) \times \hat{\boldsymbol{H}}^*_{\mathrm{t},m}(x,y,z)\right) \,\mathrm{d}a\right\}$$
$$= \iint\limits_S \boldsymbol{e}_z \cdot \left(\hat{\boldsymbol{E}}_{\mathrm{t},m}\big(x,y,z_0\big) \times \hat{\boldsymbol{H}}_{\mathrm{t},m}\big(x,y,z_0\big)\right) \,\mathrm{d}a = 1\,. \tag{2.49}$$

for properly normalized traveling modes in a lossless waveguide[7]. The expansion coefficients α_m, β_m associated with the normalized field modes correspond to the definition of power wave amplitudes[8] in the scattering parameter description of N-ports [Kurokawa 1965]. In the lossless case, the total time averaged power transported in z-direction is the sum of the individual mode powers of the forward-traveling modes minus the sum of individual mode powers of the backward-traveling modes[9] [Kurokawa 1965].

It is often desired to have only one mode traveling on a waveguide (usually the fundamental mode with $m = 0$). In this case, only the mode coefficients of the operating mode are of interest and by careful design of the waveguide and the surrounding circuits it is ensured that only one traveling waveguide mode is traveling in either direction, e.g., by ensuring that all modes apart from the fundamental mode are evanescent. The derived orthogonality relations will prove to be very useful for the calculation of the received signal of an antenna impinged by an incident field. The received signal is exactly the expansion coefficient β_m of the fundamental mode traveling in backward direction on the waveguide.

2.7. Chapter Summary

The formal description of guided waves has been revisited in this chapter. The description has followed the paths which can be found in standard textbooks [Marcuvitz 1951; Collin 1990]. The guided modes are characterized by their transversal field components. The transversal electric fields are identical for forward- and backward-traveling field modes whereas the transversal magnetic field of the backward-traveling mode is the negative of its forward-traveling counterpart. The commonly measured scattering parameters are defined by the ratios of the expansion coefficients for forward- and backward-traveling fundamental field modes on the waveguide. The orthogonality relations in combination with the mode matching technique build the basis for determining the received signal of a receiving antenna from an arbitrary incident field.

---

[7] The expression for the transported power through the waveguide cross section is independent of the z-coordinate of the corresponding cross section plane. It holds not only for the reference plane.

[8] Only modes which correspond to traveling waves can be power normalized since evanescent modes do not transport a net power ($P_m = 0$ for evanescent modes), but the normalization (2.45) can also be used for evanescent waveguide modes.

[9] In the case of losses, the total transported power is no longer the sum of the powers transported by the individual modes but the orthogonality relations (2.31) and (2.32) remain valid.

3

Fields in the Vicinity of an Antenna

With the knowledge about the fields in the waveguide connected to an antenna, in this chapter the fields on the other end of the antenna — i.e., the free-space fields — are investigated. As such, the fields in the vicinity of the antenna volume V_{int} enclosed by the surface S_1 are characterized, as these are the fields which will be transformed into a guided wave (or vice versa) by the antenna. The considered situation is depicted in Fig. 3.1. The "vicinity of the antenna" is formally defined as the volume V which is located outside of V_{int} but may be bounded externally by a surface S_2. Thus, the volume of interest V is the volume bounded by the two non-intersecting closed surfaces S_1 internally and S_2 externally. The volume which is external to S_2 is called V_{ext}. The unit normals $\boldsymbol{n}_1$ and $\boldsymbol{n}_2$ on the surfaces S_1 and S_2 point toward the volume V. If desired, the surface S_2 can be shifted toward infinity in certain cases. Then the "vicinity of the antenna" is the whole space outside of V_{int}, i.e., $V = \mathbb{R}^3 \setminus V_{\text{int}}$. The region of interest V is considered to be source free and sources may be located only in V_{int} and V_{ext} or on the surfaces S_1 and S_2.

The fields in V may correspond to a situation in which the fields are *radiated* from the volume V_{int}, or are *absorbed* in the volume V_{int}, or are *scattered* in the volume V_{int}, or they may correspond to undisturbed *incident* fields. A precise definition of the terms *radiated*, *absorbed*, *incident*, and *scattered* fields will be provided at another point in this chapter. Of course, in general the total fields in the vicinity of the antenna volume are a superposition of these pure states, i.e., they correspond to a sum of radiated and absorbed fields, for example. It is helpful to find the characteristic properties of the pure (i.e., purely *absorbed* or purely *radiated* or purely *incident*) fields in V before going on with the description of the transformation between guided waves and these fields. The fields will be expressed in terms of equivalent surface currents on the surfaces S_1 and S_2[1] on the one hand and in terms of a spherical wave expansion[2]) on the other hand. Both descriptions are important for the upcoming analysis. Modal expansions or equivalent surface currents build the basis for most NFFFTs and many echo suppression techniques, and useful analogies will be found comparing the two formulations.

---

[1] In this case, the surfaces S_1 and S_2 may have arbitrary shapes as long as they are sufficiently smooth and do not intersect.

[2] In this case, the surfaces S_1 and S_2 should be spherical and concentric.

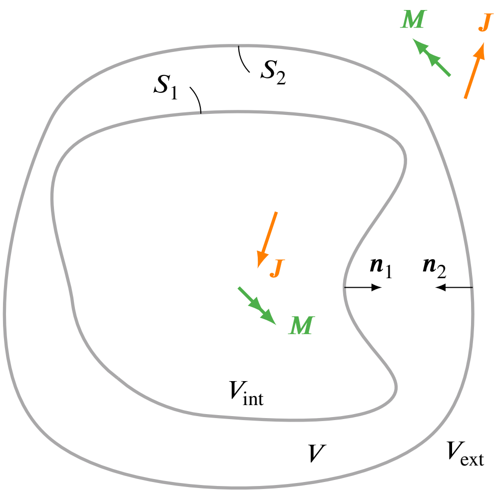

Fig. 3.1.: Considered situation for the fields in the vicinity of the antenna. The source free volume of interest V is located between two closed surfaces S_1 and S_2. Sources may be located in V_{int} and V_{ext}.

3.1. General Fields in Terms of Volume Current Densities

First, the aim is to find expressions for arbitrary fields in the source free and open volume V between two non-intersecting closed surfaces S_1 and S_2. A homogeneous background material with permeability μ and permittivity ε is assumed, in which the wavenumber k at the frequency ω can be given as $k = \omega\sqrt{\varepsilon\,\mu}$. Sources might be located in either V_{int} or V_{ext} or in both volumes simultaneously but not in V, such that the homogeneous curl-curl-equations

$$\nabla \times \nabla \times \boldsymbol{E}(\boldsymbol{r}) - k^2 \boldsymbol{E}(\boldsymbol{r}) = \boldsymbol{0} \tag{3.1}$$

and

$$\nabla \times \nabla \times \boldsymbol{H}(\boldsymbol{r}) - k^2 \boldsymbol{H}(\boldsymbol{r}) = \boldsymbol{0} \tag{3.2}$$

hold for all points $\boldsymbol{r} \in V$. The situation is depicted in Fig. 3.1.

As a starting point for the derivations, consider the dyadic Greens functions $\mathscr{G}_{JE}(\boldsymbol{r},\boldsymbol{r}')$, $\mathscr{G}_{JH}(\boldsymbol{r},\boldsymbol{r}')$, $\mathscr{G}_{ME}(\boldsymbol{r},\boldsymbol{r}')$, and $\mathscr{G}_{MH}(\boldsymbol{r},\boldsymbol{r}')$, which are subject to the defining equations [Tai 1994, p. 59]

$$\nabla \times \nabla \times \mathscr{G}_{JE}(\boldsymbol{r},\boldsymbol{r}') - k^2 \mathscr{G}_{JE}(\boldsymbol{r},\boldsymbol{r}') = -\mathrm{j}\omega\mu\,\mathbf{I}\,\delta(\boldsymbol{r}-\boldsymbol{r}')\ , \tag{3.3}$$

$$\nabla \times \nabla \times \mathscr{G}_{JH}(\boldsymbol{r},\boldsymbol{r}') - k^2 \mathscr{G}_{JH}(\boldsymbol{r},\boldsymbol{r}') = \nabla \times \mathbf{I}\,\delta(\boldsymbol{r}-\boldsymbol{r}')\ , \tag{3.4}$$

$$\nabla \times \nabla \times \mathscr{G}_{ME}(\boldsymbol{r},\boldsymbol{r}') - k^2 \mathscr{G}_{ME}(\boldsymbol{r},\boldsymbol{r}') = -\nabla \times \mathbf{I}\,\delta(\boldsymbol{r}-\boldsymbol{r}')\ , \tag{3.5}$$

and

$$\nabla \times \nabla \times \mathscr{G}_{MH}(\boldsymbol{r},\boldsymbol{r}') - k^2 \mathscr{G}_{MH}(\boldsymbol{r},\boldsymbol{r}') = -\mathrm{j}\omega\varepsilon\,\mathbf{I}\,\delta(\boldsymbol{r}-\boldsymbol{r}')\ , \tag{3.6}$$

where $\mathbf{I}$ denotes the unit dyadic. For the moment, no further assumption has to be made about the Green's functions except that (3.3) to (3.6) are fulfilled. For all points $\boldsymbol{r} \neq \boldsymbol{r}'$, all of the dyadic

Green's functions fulfill the homogeneous curl-curl-equation, such that the integrals

$$\boldsymbol{E}(\boldsymbol{r}) = \iiint\limits_{V_{\text{int}}} \left[\mathcal{G}_{JE}(\boldsymbol{r},\boldsymbol{r}') \cdot \boldsymbol{J}(\boldsymbol{r}') + \mathcal{G}_{ME}(\boldsymbol{r},\boldsymbol{r}') \cdot \boldsymbol{M}(\boldsymbol{r}')\right] \,\mathrm{d}a' + \iiint\limits_{V_{\text{ext}}} \left[\mathcal{G}_{JE}(\boldsymbol{r},\boldsymbol{r}') \cdot \boldsymbol{J}(\boldsymbol{r}') + \mathcal{G}_{ME}(\boldsymbol{r},\boldsymbol{r}') \cdot \boldsymbol{M}(\boldsymbol{r}')\right] \,\mathrm{d}a' \tag{3.7}$$

and

$$\boldsymbol{H}(\boldsymbol{r}) = \iiint\limits_{V_{\text{int}}} \left[\mathcal{G}_{JH}(\boldsymbol{r},\boldsymbol{r}') \cdot \boldsymbol{J}(\boldsymbol{r}') + \mathcal{G}_{MH}(\boldsymbol{r},\boldsymbol{r}') \cdot \boldsymbol{M}(\boldsymbol{r}')\right] \,\mathrm{d}a' + \iiint\limits_{V_{\text{ext}}} \left[\mathcal{G}_{JH}(\boldsymbol{r},\boldsymbol{r}') \cdot \boldsymbol{J}(\boldsymbol{r}') + \mathcal{G}_{MH}(\boldsymbol{r},\boldsymbol{r}') \cdot \boldsymbol{M}(\boldsymbol{r}')\right] \,\mathrm{d}a' \tag{3.8}$$

with arbitrary (integrable) electric and magnetic volume current densities $\boldsymbol{J}(\boldsymbol{r}')$ and $\boldsymbol{M}(\boldsymbol{r}')$ in the interior and exterior volumes V_{int} and V_{ext} lead to valid solutions of (3.1) and (3.2) at all points $\boldsymbol{r}$ in the source free volume V [Jin 2015, p. 67].

Analytic expressions for the dyadic Green's functions are found by [Tai 1994, p. 60], [Jin 2015, pp. 66f.], [Kong 1986, p. 376]

$$\mathcal{G}_{JE}(\boldsymbol{r},\boldsymbol{r}') = -\mathrm{j}\omega\mu \left[\left(\mathbf{I} + \frac{1}{k^2}\nabla\nabla\right) g_0(\boldsymbol{r},\boldsymbol{r}')\right] , \tag{3.9}$$

$$\mathcal{G}_{JH}(\boldsymbol{r},\boldsymbol{r}') = \nabla g_0(\boldsymbol{r},\boldsymbol{r}') \times \mathbf{I}, \tag{3.10}$$

$$\mathcal{G}_{ME}(\boldsymbol{r},\boldsymbol{r}') = -\nabla g_0(\boldsymbol{r},\boldsymbol{r}') \times \mathbf{I}, \tag{3.11}$$

and

$$\mathcal{G}_{MH}(\boldsymbol{r},\boldsymbol{r}') = -\mathrm{j}\omega\varepsilon \left[\left(\mathbf{I} + \frac{1}{k^2}\nabla\nabla\right) g_0(\boldsymbol{r},\boldsymbol{r}')\right] , \tag{3.12}$$

where the involved scalar Green's function $g_0(\boldsymbol{r},\boldsymbol{r}')$ is a fundamental solution for the Helmholtz operator, i.e., it solves the equation

$$\Delta g_0(\boldsymbol{r},\boldsymbol{r}') + k^2 g_0(\boldsymbol{r},\boldsymbol{r}') = -\delta(\boldsymbol{r}-\boldsymbol{r}') . \tag{3.13}$$

A set of fundamental solutions to (3.13) are well known to be [Sommerfeld 1912], [Stratton 1941, pp. 404ff.]

$$g_0(\boldsymbol{r},\boldsymbol{r}') = \frac{\mathrm{e}^{\pm\mathrm{j}k\,|\boldsymbol{r}-\boldsymbol{r}'|}}{4\pi|\boldsymbol{r}-\boldsymbol{r}'|} . \tag{3.14}$$

From a mathematical point of view, both solutions with "'+" or "−" in the exponent (or a suitable combination of them) are equally valid in the sense that either choice will lead to a valid solution of (3.13), however, subject to different boundary conditions[3].

---

[3] One can always add a function $\phi(\boldsymbol{r})$, which is a solution to the homogeneous Helmholtz equation $\Delta\phi(\boldsymbol{r}) + k^2\phi(\boldsymbol{r}) = 0$, to the fundamental solution without affecting the equality in (3.13).

Usually the scalar Green's function

$$g_0^-(\boldsymbol{r},\boldsymbol{r}') = \frac{\mathrm{e}^{-\mathrm{j}k\,|\boldsymbol{r}-\boldsymbol{r}'|}}{4\pi|\boldsymbol{r}-\boldsymbol{r}'|} \tag{3.15}$$

is preferred because it corresponds to outward-traveling waves propagating from a finite location to infinity[4]. Other choices lead to inward-traveling waves coming from infinity[5], i.e.,

$$g_0^+(\boldsymbol{r},\boldsymbol{r}') = \frac{\mathrm{e}^{+\mathrm{j}k\,|\boldsymbol{r}-\boldsymbol{r}'|}}{4\pi|\boldsymbol{r}-\boldsymbol{r}'|} \tag{3.16}$$

or standing waves [Helmholtz 1860], i.e.,

$$g_0^{(0)}(\boldsymbol{r},\boldsymbol{r}') = \frac{1}{2}\left(g_0^+(\boldsymbol{r},\boldsymbol{r}') + g_0^-(\boldsymbol{r},\boldsymbol{r}')\right) = \frac{\cos\left(k\,|\boldsymbol{r}-\boldsymbol{r}'|\right)}{4\pi|\boldsymbol{r}-\boldsymbol{r}'|}\,. \tag{3.17}$$

Although it would perhaps make sense intuitively, the function

$$g_0^{(\infty)}(\boldsymbol{r},\boldsymbol{r}') = \frac{1}{2}\left(g_0^+(\boldsymbol{r},\boldsymbol{r}') - g_0^-(\boldsymbol{r},\boldsymbol{r}')\right) = \frac{\mathrm{j}\,\sin\left(k\,|\boldsymbol{r}-\boldsymbol{r}'|\right)}{4\pi|\boldsymbol{r}-\boldsymbol{r}'|} \tag{3.18}$$

is not a valid Green's function of the Helmholtz operator but a source-free solution because

$$\Delta g_0^{(\infty)}(\boldsymbol{r},\boldsymbol{r}') + k^2 g_0^{(\infty)}(\boldsymbol{r},\boldsymbol{r}') = 0 \neq -\delta(\boldsymbol{r}-\boldsymbol{r}')\,. \tag{3.19}$$

To form valid Green's function by a linear combination from g_0^+ and g_0^-, the coefficients of the linear combination must add up to 1 (otherwise the right hand side of (3.13) is not the δ-distribution).

The different functions g_0^+, g_0^-, $g_0^{(0)}$ give rise to different dyadic Green's functions by replacing g_0 in (3.9) to (3.12) by g_0^+, g_0^-, $g_0^{(0)}$, respectively. The respective dyadic Green's functions are specified by the same exponent ("–", "+", or "(0)") as their scalar counterpart. If no superscript is specified, the expression is valid for all types of Green's functions. Notice that even though any kind of dyadic Greens function can be used to construct a valid solution of Maxwell's equation in V via (3.7) and (3.8), the solutions obtained with different Green's functions are not necessarily the same — they may obey different boundary conditions.

3.2. General Fields in Terms of Surface Current Densities

An important electromagnetic theorem — called the uniqueness theorem — states that the fields in the source free region V are uniquely defined by the tangential fields $\boldsymbol{n}_1 \times \boldsymbol{E}$, $\boldsymbol{n}_1 \times \boldsymbol{H}$ and $\boldsymbol{n}_2 \times \boldsymbol{E}$, $\boldsymbol{n}_2 \times \boldsymbol{H}$ on the surfaces S_1 and S_2 [Collin 1990, pp. 35f.], [Jin 2015, pp. 90f.], [Stratton

---

[4] The scalar Green's function g_0^- fulfills the Sommerfeld radiation condition $\lim_{|\boldsymbol{r}|\to\infty} |\boldsymbol{r}|[\partial g_0^-(\boldsymbol{r},\boldsymbol{r}')/\partial|\boldsymbol{r}| + \mathrm{j}kg_0^-(\boldsymbol{r},\boldsymbol{r}')] = 0$ for outgoing waves [Sommerfeld 1912; Schot 1992].

[5] The scalar Green's function g_0^+ fulfills the Sommerfeld radiation condition $\lim_{|\boldsymbol{r}|\to\infty} |\boldsymbol{r}|[\partial g_0^+(\boldsymbol{r},\boldsymbol{r}')/\partial|\boldsymbol{r}| - \mathrm{j}kg_0^+(\boldsymbol{r},\boldsymbol{r}')] = 0$ for incoming waves [Sommerfeld 1912].

1941, pp. 486ff.], [Harrington 1961, pp. 100ff.]. Following the derivation[6] in [Collin 1990, pp. 35f.] the desired field $\boldsymbol{E}(\boldsymbol{r})$ is scalar multiplied with (3.3) to obtain

$$\boldsymbol{E}(\boldsymbol{r}) \cdot \nabla \times \nabla \times \mathscr{G}_{JE}\left(\boldsymbol{r}, \boldsymbol{r}'\right) - k^2 \boldsymbol{E}(\boldsymbol{r}) \cdot \mathscr{G}_{JE}\left(\boldsymbol{r}, \boldsymbol{r}'\right) = -\mathrm{j}\omega\mu \boldsymbol{E}(\boldsymbol{r})\, \delta\left(\boldsymbol{r} - \boldsymbol{r}'\right) . \tag{3.20}$$

Using (3.1) one gets

$$\boldsymbol{E}(\boldsymbol{r}) \cdot \nabla \times \nabla \times \mathscr{G}_{JE}\left(\boldsymbol{r}, \boldsymbol{r}'\right) - \nabla \times \nabla \times \boldsymbol{E}(\boldsymbol{r}) \cdot \mathscr{G}_{JE}\left(\boldsymbol{r}, \boldsymbol{r}'\right) = -\mathrm{j}\omega\mu \boldsymbol{E}(\boldsymbol{r})\, \delta\left(\boldsymbol{r} - \boldsymbol{r}'\right) . \tag{3.21}$$

With the identity[7] $\nabla \cdot (\boldsymbol{F} \times \mathscr{D}) = (\nabla \times \boldsymbol{F}) \cdot \mathscr{D} - \boldsymbol{F} \cdot (\nabla \times \mathscr{D})$ valid for any vector $\boldsymbol{F}$ and any dyadic $\mathscr{D}$, one obtains

$$\boldsymbol{E}(\boldsymbol{r}) \cdot \nabla \times \nabla \times \mathscr{G}_{JE}\left(\boldsymbol{r}, \boldsymbol{r}'\right) = -\nabla \cdot \left[\boldsymbol{E}(\boldsymbol{r}) \times \nabla \times \mathscr{G}_{JE}\left(\boldsymbol{r}, \boldsymbol{r}'\right)\right] + [\nabla \times \boldsymbol{E}(\boldsymbol{r})] \times \nabla \times \mathscr{G}_{JE}\left(\boldsymbol{r}, \boldsymbol{r}'\right) \tag{3.22}$$

and

$$\nabla \times \nabla \times \boldsymbol{E}(\boldsymbol{r}) \cdot \mathscr{G}_{JE}\left(\boldsymbol{r}, \boldsymbol{r}'\right) = \nabla \times \boldsymbol{E}(\boldsymbol{r}) \cdot \left[\nabla \times \mathscr{G}_{JE}\left(\boldsymbol{r}, \boldsymbol{r}'\right)\right] + \nabla \cdot \left[\nabla \times \boldsymbol{E}(\boldsymbol{r})\, \mathscr{G}_{JE}\left(\boldsymbol{r}, \boldsymbol{r}'\right)\right] \tag{3.23}$$

for the two expressions on the left hand side of (3.21). Thus, (3.21) becomes

$$-\nabla \cdot \left[\boldsymbol{E}(\boldsymbol{r}) \times \nabla \times \mathscr{G}_{JE}\left(\boldsymbol{r}, \boldsymbol{r}'\right) + \nabla \times \boldsymbol{E}(\boldsymbol{r}) \times \mathscr{G}_{JE}\left(\boldsymbol{r}, \boldsymbol{r}'\right)\right] = -\mathrm{j}\omega\mu \boldsymbol{E}(\boldsymbol{r})\, \delta\left(\boldsymbol{r} - \boldsymbol{r}'\right) . \tag{3.24}$$

This expression integrated over the volume V leads to

$$\iiint\limits_V -\nabla \cdot \left[\boldsymbol{E}(\boldsymbol{r}) \times \nabla \times \mathscr{G}_{JE}\left(\boldsymbol{r}, \boldsymbol{r}'\right) + \nabla \times \boldsymbol{E}(\boldsymbol{r}) \times \mathscr{G}_{JE}\left(\boldsymbol{r}, \boldsymbol{r}'\right)\right] \mathrm{d}v = \iiint\limits_V -\mathrm{j}\omega\mu \boldsymbol{E}(\boldsymbol{r})\, \delta\left(\boldsymbol{r} - \boldsymbol{r}'\right) \mathrm{d}v , \tag{3.25}$$

which may be transformed into

$$\begin{aligned} &\oiint\limits_{S_1} \left[\boldsymbol{n}_1 \times \boldsymbol{E}(\boldsymbol{r}) \cdot \nabla \times \mathscr{G}_{JE}\left(\boldsymbol{r}, \boldsymbol{r}'\right) + \boldsymbol{n}_1 \times \nabla \times \boldsymbol{E}(\boldsymbol{r}) \cdot \mathscr{G}_{JE}\left(\boldsymbol{r}, \boldsymbol{r}'\right)\right] \mathrm{d}a \\ &+ \oiint\limits_{S_2} \left[\boldsymbol{n}_2 \times \boldsymbol{E}(\boldsymbol{r}) \cdot \nabla \times \mathscr{G}_{JE}\left(\boldsymbol{r}, \boldsymbol{r}'\right) + \boldsymbol{n}_2 \times \nabla \times \boldsymbol{E}(\boldsymbol{r}) \cdot \mathscr{G}_{JE}\left(\boldsymbol{r}, \boldsymbol{r}'\right)\right] \mathrm{d}a \\ &= \begin{cases} -\mathrm{j}\omega\mu\, \boldsymbol{E}\left(\boldsymbol{r}'\right) & \boldsymbol{r}' \in V \\ \boldsymbol{0} & \boldsymbol{r}' \notin V \end{cases} \end{aligned} \tag{3.26}$$

by using the divergence theorem and the filter property of the Dirac-Delta distribution. Finally, from [Tai 1994, p. 57], [Jin 2015, p. 69] $\nabla \times \mathscr{G}_{JE}\left(\boldsymbol{r}, \boldsymbol{r}'\right) = \mathrm{j}\omega\mu \mathscr{G}_{ME}\left(\boldsymbol{r}, \boldsymbol{r}'\right)$ and the Maxwell

---

[6] This well known derivation is repeated here to show that in fact either type of Green's functions (i.e., "–", "+", or "(0)") can be used in the surface equivalence principle.

[7] This identity can be found, e.g., in the very good appendix in [Bladel 2007].

equation $\nabla \times \boldsymbol{E}(\boldsymbol{r}) = -\mathrm{j}\omega\mu \boldsymbol{H}(\boldsymbol{r})$ one obtains

$$\begin{aligned}
&\oint\!\!\!\oint_{S_1} \left[\mathrm{j}\omega\mu\, \boldsymbol{n}_1 \times \boldsymbol{E}(\boldsymbol{r}) \cdot \mathcal{G}_{ME}(\boldsymbol{r}, \boldsymbol{r}') - \mathrm{j}\omega\mu\, \boldsymbol{n}_1 \times \boldsymbol{H}(\boldsymbol{r}) \cdot \mathcal{G}_{JE}(\boldsymbol{r}, \boldsymbol{r}')\right] \mathrm{d}a \\
&+ \oint\!\!\!\oint_{S_2} \left[\mathrm{j}\omega\mu\, \boldsymbol{n}_2 \times \boldsymbol{E}(\boldsymbol{r}) \cdot \mathcal{G}_{ME}(\boldsymbol{r}, \boldsymbol{r}') - \mathrm{j}\omega\mu\, \boldsymbol{n}_2 \times \boldsymbol{H}(\boldsymbol{r}) \cdot \mathcal{G}_{JE}(\boldsymbol{r}, \boldsymbol{r}')\right] \mathrm{d}a \\
&= \begin{cases} -\mathrm{j}\omega\mu\, \boldsymbol{E}(\boldsymbol{r}') & \boldsymbol{r}' \in V \\ \boldsymbol{0} & \boldsymbol{r}' \notin V \end{cases}.
\end{aligned} \tag{3.27}$$

Exchanging $\boldsymbol{r}$ and $\boldsymbol{r}'$ and exploiting the fact that $\mathcal{G}_{JE}(\boldsymbol{r}', \boldsymbol{r}) = \mathcal{G}_{JE}(\boldsymbol{r}, \boldsymbol{r}')$ and $\mathcal{G}_{ME}(\boldsymbol{r}', \boldsymbol{r}) = -\mathcal{G}_{ME}(\boldsymbol{r}, \boldsymbol{r}')$ are (anti-) symmetric dyadics [Tai 1994, p. 74] leads to the desired final result

$$\begin{aligned}
&\oint\!\!\!\oint_{S_1} \left[\mathcal{G}_{ME}(\boldsymbol{r}, \boldsymbol{r}') \cdot \left(\boldsymbol{E}(\boldsymbol{r}') \times \boldsymbol{n}_1\right) + \mathcal{G}_{JE}(\boldsymbol{r}, \boldsymbol{r}') \cdot \left(\boldsymbol{n}_1 \times \boldsymbol{H}(\boldsymbol{r}')\right)\right] \mathrm{d}a' \\
&+ \oint\!\!\!\oint_{S_2} \left[\mathcal{G}_{ME}(\boldsymbol{r}, \boldsymbol{r}') \cdot \left(\boldsymbol{E}(\boldsymbol{r}') \times \boldsymbol{n}_2\right) + \mathcal{G}_{JE}(\boldsymbol{r}, \boldsymbol{r}') \cdot \left(\boldsymbol{n}_2 \times \boldsymbol{H}(\boldsymbol{r}')\right)\right] \mathrm{d}a' = \begin{cases} \boldsymbol{E}(\boldsymbol{r}) & \boldsymbol{r} \in V \\ \boldsymbol{0} & \boldsymbol{r} \notin V \end{cases}.
\end{aligned} \tag{3.28}$$

An analogous derivation for the magnetic field leads to

$$\begin{aligned}
&\oint\!\!\!\oint_{S_1} \left[\mathcal{G}_{MH}(\boldsymbol{r}, \boldsymbol{r}') \cdot \left(\boldsymbol{E}(\boldsymbol{r}') \times \boldsymbol{n}_1\right) + \mathcal{G}_{JH}(\boldsymbol{r}, \boldsymbol{r}') \cdot \left(\boldsymbol{n}_1 \times \boldsymbol{H}(\boldsymbol{r}')\right)\right] \mathrm{d}a' \\
&+ \oint\!\!\!\oint_{S_2} \left[\mathcal{G}_{MH}(\boldsymbol{r}', \boldsymbol{r}) \cdot \left(\boldsymbol{E}(\boldsymbol{r}') \times \boldsymbol{n}_2\right) + \mathcal{G}_{JH}(\boldsymbol{r}', \boldsymbol{r}) \cdot \left(\boldsymbol{n}_2 \times \boldsymbol{H}(\boldsymbol{r}')\right)\right] \mathrm{d}a' = \begin{cases} \boldsymbol{H}(\boldsymbol{r}) & \boldsymbol{r} \in V \\ \boldsymbol{0} & \boldsymbol{r} \notin V \end{cases}.
\end{aligned} \tag{3.29}$$

Since the derivation is valid for general Green's functions, either the Green's functions of type "+", "−", or "(0)" can be used to evaluate (3.28) and (3.29) (as long as used consistently and Green's functions of different types are not mixed). The Green's functions for outward-traveling waves (type "−") are often considered to be the only sensible choice for unbounded regions. The fields tend toward zero at infinity under the assumption of arbitrarily small losses (other types of Green's functions lead to fields which increase toward infinity) [Harrington 1961, p. 78] and the "−"-type of Greens functions are the only type of Green's functions which do not require any sources in V_{ext} if S_2 is moved to infinity. In this work, V_{ext} is not necessarily source free and the region of interest V is not necessarily unbounded, thus, also other types of Green's functions are considered[8].

---

[8] The combined use of "advanced" and "retarded" Green's functions has been introduced in Quantum physics by Wheeler and Feynman in the so-called absorber theory [Wheeler 1945; Wheeler 1949]. Nevertheless, in classical electrodynamics, usually the advanced Green's functions are omitted due to causality arguments [Schwebel 1970].

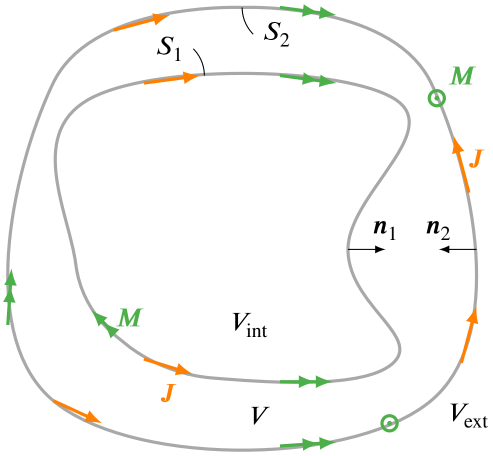

Fig. 3.2.: The source free volume of interest V is located between two closed surfaces S_1 and S_2. Source may be located on S_1 and S_2.

More generally, valid field solutions in V can be expressed by

$$\begin{aligned} \boldsymbol{E}(\boldsymbol{r}) = & \oiint_{S_1} \left[\mathcal{G}_{JE}(\boldsymbol{r},\boldsymbol{r}')\cdot\boldsymbol{J}(\boldsymbol{r}') + \mathcal{G}_{ME}(\boldsymbol{r},\boldsymbol{r}')\cdot\boldsymbol{M}(\boldsymbol{r}')\right]\,\mathrm{d}a' \\ & + \oiint_{S_2} \left[\mathcal{G}_{JE}(\boldsymbol{r},\boldsymbol{r}')\cdot\boldsymbol{J}(\boldsymbol{r}') + \mathcal{G}_{ME}(\boldsymbol{r},\boldsymbol{r}')\cdot\boldsymbol{M}(\boldsymbol{r}')\right]\,\mathrm{d}a' \end{aligned} \tag{3.30}$$

and

$$\begin{aligned} \boldsymbol{H}(\boldsymbol{r}) = & \oiint_{S_1} \left[\mathcal{G}_{JH}(\boldsymbol{r},\boldsymbol{r}')\cdot\boldsymbol{J}(\boldsymbol{r}') + \mathcal{G}_{MH}(\boldsymbol{r},\boldsymbol{r}')\cdot\boldsymbol{M}(\boldsymbol{r}')\right]\,\mathrm{d}a' \\ & + \oiint_{S_2} \left[\mathcal{G}_{JH}(\boldsymbol{r},\boldsymbol{r}')\cdot\boldsymbol{J}(\boldsymbol{r}') + \mathcal{G}_{MH}(\boldsymbol{r},\boldsymbol{r}')\cdot\boldsymbol{M}(\boldsymbol{r}')\right]\,\mathrm{d}a' \end{aligned} \tag{3.31}$$

with arbitrary (integrable) surface current densities[9] $\boldsymbol{J}(\boldsymbol{r}')$ and $\boldsymbol{M}(\boldsymbol{r}')$ on the surfaces S_1 and S_2 as denoted in Fig. 3.2. The statement that the fields in the source free region can be expressed by equivalent surface currents $\boldsymbol{J}$ and $\boldsymbol{M}$ is called *Huygens principle* (or sometimes just *surface equivalence principle*). The surfaces S_1, S_2 and the corresponding surface currents $\boldsymbol{J}$, $\boldsymbol{M}$ are accordingly named *Huygens surfaces* and *Huygens currents*.

The field solutions which are obtained by evaluating arbitrary Huygens currents on the surfaces S_1 and S_2 with different types of Green's functions differ from each other in general and we have

---

[9] If the context eliminates any possible confusion, the symbols $\boldsymbol{J}$ and $\boldsymbol{M}$ are used for either surface current densities or volume current densities, dependent on the integral type.

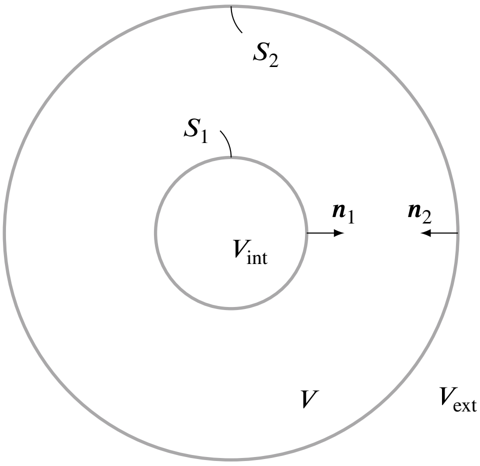

Fig. 3.3.: Considered situation for the spherical wave expansion: The volume V is enclosed by two concentric spherical surfaces surfaces S_1 and S_2.

in particular

$$\begin{aligned}
&\oiint_{S_1} \left[\boldsymbol{\mathscr{G}}^{-}_{JE}(\boldsymbol{r},\boldsymbol{r}') \cdot \boldsymbol{J}(\boldsymbol{r}') + \boldsymbol{\mathscr{G}}^{-}_{ME}(\boldsymbol{r},\boldsymbol{r}') \cdot \boldsymbol{M}(\boldsymbol{r}')\right] \mathrm{d}a' \\
&+ \oiint_{S_2} \left[\boldsymbol{\mathscr{G}}^{-}_{JE}(\boldsymbol{r},\boldsymbol{r}') \cdot \boldsymbol{J}(\boldsymbol{r}') + \boldsymbol{\mathscr{G}}^{-}_{ME}(\boldsymbol{r},\boldsymbol{r}') \cdot \boldsymbol{M}(\boldsymbol{r}')\right] \mathrm{d}a' \\
\neq &\oiint_{S_1} \left[\boldsymbol{\mathscr{G}}^{+}_{JE}(\boldsymbol{r},\boldsymbol{r}') \cdot \boldsymbol{J}(\boldsymbol{r}') + \boldsymbol{\mathscr{G}}^{+}_{ME}(\boldsymbol{r},\boldsymbol{r}') \cdot \boldsymbol{M}(\boldsymbol{r}')\right] \mathrm{d}a' \\
&+ \oiint_{S_2} \left[\boldsymbol{\mathscr{G}}^{+}_{JE}(\boldsymbol{r},\boldsymbol{r}') \cdot \boldsymbol{J}(\boldsymbol{r}') + \boldsymbol{\mathscr{G}}^{+}_{ME}(\boldsymbol{r},\boldsymbol{r}') \cdot \boldsymbol{M}(\boldsymbol{r}')\right] \mathrm{d}a' \qquad (3.32)
\end{aligned}$$

for general surface currents $\boldsymbol{J}$ and $\boldsymbol{M}$. Only if the currents $\boldsymbol{J}$ and $\boldsymbol{M}$ are directly related to the fields at the surface by $\boldsymbol{M} = -\boldsymbol{n} \times \boldsymbol{E}$ and $\boldsymbol{J} = \boldsymbol{n} \times \boldsymbol{H}$ — as was the case in (3.28) and (3.29) — the Green's functions from different types lead to the same fields in V. If the equivalent currents are related to the tangential components of the electric and magnetic fields via $\boldsymbol{M} = -\boldsymbol{n} \times \boldsymbol{E}$ and $\boldsymbol{J} = \boldsymbol{n} \times \boldsymbol{H}$ they are called *Love currents* [Love 1901].

3.3. General Fields in Terms of a Spherical Vector Wave Expansion

The spherical wave expansion of the fields in V exhibits some remarkable parallels with the already discussed formulation. For convenience with the spherical wave expansion, it is assumed that S_1 and S_2 are concentric spherical surfaces and the origin of the spherical wave expansion is set into the center of the two surfaces. The interest lies in the field solutions in the enclosed source free volume V, which has the form of a spherical shell in this case. The scenario is depicted in Fig. 3.3. The basis of the considered modal field transformations is an expansion of the electric field in eigensolutions of the curl-curl-equation

$$\nabla \times \nabla \times \boldsymbol{E} - k^2 \boldsymbol{E} = \boldsymbol{0} \tag{3.33}$$

in spherical coordinates. The solutions of this eigenvalue problem are well known and are derived in this section, mainly to clarify the notation and the sign and normalization conventions used in this work.

Solutions of (3.33) are given by[10] [Stratton 1941, p. 393]

$$\boldsymbol{M} = \nabla f \times \boldsymbol{e}_r \tag{3.34}$$

and

$$\boldsymbol{N} = \frac{1}{k} \nabla \times \boldsymbol{M}, \tag{3.35}$$

where $\boldsymbol{e}_r$ is the unit vector in radial direction and f is a solution to the homogeneous scalar Helmholtz equation

$$\Delta f + k^2 f = 0\,. \tag{3.36}$$

The general solution to (3.36) is a superposition of functions from the set[11] [Stratton 1941, pp. 398ff.], [Harrington 1963, pp. 264ff.]

$$\begin{Bmatrix} \mathrm{j}_n(kr) \\ \mathrm{n}_n(kr) \\ \mathrm{h}_n^{(1)}(kr) \\ \mathrm{h}_n^{(2)}(kr) \end{Bmatrix} \mathrm{P}_n^m(\cos\vartheta) \begin{Bmatrix} \sin(m\,\varphi) \\ \cos(m\,\varphi) \\ \mathrm{e}^{\mathrm{j}m\,\varphi} \\ \mathrm{e}^{-\mathrm{j}m\,\varphi} \end{Bmatrix}, \tag{3.37}$$

with $n = 1, 2, 3, \ldots$ and $m = 0, 1, 2, \ldots, n$ and where P_n^m are the associated Legendre functions [Abramowitz 1964, pp. 332ff.] of nth degree and mth order, j_n are the spherical Bessel functions, n_n are the spherical Neumann functions and $\mathrm{h}_n^{(1)} = \mathrm{j}_n + \mathrm{j}\,\mathrm{n}_n$, and $\mathrm{h}_n^{(2)} = \mathrm{j}_n - \mathrm{j}\,\mathrm{n}_n$ are the spherical Hankel functions of the first and second kind, respectively [Abramowitz 1964, pp. 437ff.]. For most antenna applications, the choice of the particular φ-dependence is not important (most of the time, periodic boundary conditions have to be considered, which are fulfilled by all of the functions presented here) and, thus, the considerations are limited to $\exp(\mathrm{j}\,m\,\varphi)$ and $\exp(-\mathrm{j}\,m\,\varphi)$. This choice leads to the well known spherical harmonics

$$Y_{nm}(\vartheta, \varphi) = \left(\frac{-m}{|m|}\right)^m \sqrt{\frac{(2n+1)}{4\pi} \frac{(n-m)!}{(n+m)!}}\, \mathrm{P}_n^{|m|}(\cos\vartheta)\, \mathrm{e}^{\mathrm{j}m\,\varphi} \tag{3.38}$$

---

[10] The vector function $\boldsymbol{M}$ must not be confused with a magnetic current density. After this section, the spherical vector function will always be accompanied with two indices and one superscript denoting the mode numbers, leading to an unambiguous notation.

[11] For every n either two of the radial functions j_n, n_n, $\mathrm{h}_n^{(1)}$, $\mathrm{h}_n^{(2)}$ are linearly independent, while the other two functions are linear combinations of the first two as is expected for a differential equation of second order. The same is true for every m for the φ-dependent functions $\sin(m\,\varphi)$, $\cos(m\,\varphi)$, $\exp(\mathrm{j}m\,\varphi)$, $\exp(-\mathrm{j}m\,\varphi)$. For the ϑ-dependency, there also exist linearly independent solutions $Q_n^m(\cos\vartheta)$ for every combination of indices n, m but this solutions are singular at $\cos\vartheta = \pm 1$, thus they are omitted for all physically relevant cases.

for the angular dependency of the solution set. The factor $\sqrt{(2n+1)\,(n-m)!/\,[4\pi\,(n+m)!]}$ ensures that the spherical harmonics are orthonormal, i.e.,

$$\int\limits_{\varphi=0}^{2\pi}\int\limits_{\vartheta=0}^{\pi} Y_{nm}(\vartheta,\varphi)\,Y^{*}_{n'm'}(\vartheta,\varphi)\,\sin\vartheta\,\mathrm{d}\vartheta\,\mathrm{d}\varphi = \delta_{mm'}\,\delta_{nn'}\,, \tag{3.39}$$

where $\delta_{mm'}$ is the Kronecker-Delta and the sign convention follows [Hansen 1988]. The starting point for the derivation of the corresponding (normalized) vector wave functions are the scalar solutions of the homogeneous Helmholtz equation

$$f^{(c)}_{mn} = \frac{z^{(c)}_n(kr)}{\sqrt{n\,(n+1)}} Y_{nm}(\vartheta,\varphi) \tag{3.40}$$

with $n = 1, 2, 3, \ldots$, and $m = -n, \ldots, n$, where the index $c \in \{1, 2, 3, 4\}$ is a short hand notation for choosing one of the radial functions with $z^{(1)}_n = \mathrm{j}_n$, $z^{(2)}_n = \mathrm{n}_n$, $z^{(3)}_n = \mathrm{h}^{(1)}_n$ and $z^{(4)}_n = \mathrm{h}^{(2)}_n$ for the field expansions. Letting the index m take on positive and negative numbers ensures to have the two independent types of φ-functions covered. An alternative form of the scalar solutions which makes use of the the normalized associated Legendre functions [Abramowitz 1964, p. 332]

$$\overline{\mathrm{P}}^{|m|}_n(\cos\vartheta) = \sqrt{\frac{2n+1}{2}\frac{(n-m)!}{(n+m)!}}\,\mathrm{P}^{|m|}_n(\cos\vartheta) \tag{3.41}$$

is given by [Hansen 1988, p. 13]

$$f^{(c)}_{mn} = \frac{1}{\sqrt{2\pi}}\frac{1}{\sqrt{n\,(n+1)}}\left(\frac{-m}{|m|}\right)^{m} z^{(c)}_n(kr)\,\overline{\mathrm{P}}^{|m|}_n(\cos\vartheta)\,\mathrm{e}^{\mathrm{j}m\varphi}\,. \tag{3.42}$$

The vector functions have the form [Hansen 1988, p. 13]

$$\begin{aligned}
\boldsymbol{M}^{(c)}_{mn} &= \nabla f^{(c)}_{mn} \times \left(r\,\boldsymbol{e}_r\right)\\
&= \frac{z^{(c)}_n(kr)}{\sqrt{n\,(n+1)}}\,\left(\nabla_{\mathrm{t}} Y_{nm}(\vartheta,\varphi)\right) \times \left(r\,\boldsymbol{e}_r\right)\\
&= \frac{z^{(c)}_n(kr)}{\sqrt{n\,(n+1)}}\left(\frac{1}{r}\frac{\partial Y_{nm}(\vartheta,\varphi)}{\partial\vartheta}\boldsymbol{e}_\vartheta + \frac{1}{r\,\sin\vartheta}\frac{\partial Y_{nm}(\vartheta,\varphi)}{\partial\varphi}\boldsymbol{e}_\varphi\right) \times \left(r\,\boldsymbol{e}_r\right)\\
&= \frac{1}{\sqrt{2\pi}}\,\frac{1}{\sqrt{n\,(n+1)}}\,\left(\frac{-m}{|m|}\right)^{m}\left(z^{(c)}_n(kr)\,\frac{\mathrm{j}m\,\overline{\mathrm{P}}^{|m|}_n(\cos\vartheta)}{\sin\vartheta}\mathrm{e}^{\mathrm{j}m\varphi}\boldsymbol{e}_\vartheta\right.\\
&\qquad\left. - z^{(c)}_n(kr)\,\frac{\mathrm{d}\,\overline{\mathrm{P}}^{|m|}_n(\cos\vartheta)}{\mathrm{d}\vartheta}\mathrm{e}^{\mathrm{j}m\varphi}\boldsymbol{e}_\varphi\right)\,,
\end{aligned} \tag{3.43}$$

where $\nabla_{\mathrm{t}} = \nabla - \frac{\partial}{\partial r}\boldsymbol{e}_r = 1/r\frac{\partial}{\partial\vartheta}\boldsymbol{e}_\vartheta + 1/(r\,\sin\vartheta)\frac{\partial}{\partial\varphi}\boldsymbol{e}_\varphi$ means the tangential part of the ∇-operator

and

$$\begin{aligned}\boldsymbol{N}_{mn}^{(c)} &= \frac{1}{k}\nabla\times\boldsymbol{M}_{mn}^{(c)}\\ &= \frac{1}{\sqrt{2\pi}}\frac{1}{\sqrt{n\,(n+1)}}\left(\frac{-m}{|m|}\right)^{m}\left(\frac{n\,(n+1)}{kr}z_n^{(c)}(kr)\,\overline{\mathrm{P}}_n^{|m|}(\cos\vartheta)\,\mathrm{e}^{\mathrm{j}m\varphi}\boldsymbol{e}_r\right.\\ &\qquad+\frac{1}{kr}\frac{\mathrm{d}}{\mathrm{d}\,kr}\left\{kr\,z_n^{(c)}(kr)\right\}\frac{\mathrm{d}\,\overline{\mathrm{P}}_n^{|m|}(\cos\vartheta)}{\mathrm{d}\vartheta}\mathrm{e}^{\mathrm{j}m\varphi}\boldsymbol{e}_\vartheta\\ &\qquad\left.+\frac{1}{kr}\frac{\mathrm{d}}{\mathrm{d}\,kr}\left\{kr\,z_n^{(c)}(kr)\right\}\frac{\mathrm{j}m\,\overline{\mathrm{P}}_n^{|m|}(\cos\vartheta)}{\sin\vartheta}\mathrm{e}^{\mathrm{j}m\varphi}\boldsymbol{e}_\varphi\right). \end{aligned} \tag{3.44}$$

For a condensed notation, this thesis follows the notation of [Hansen 1988], writing $\boldsymbol{F}_{1mn}^{(c)} = \boldsymbol{M}_{mn}^{(c)}$ and $\boldsymbol{F}_{2mn}^{(c)} = \boldsymbol{N}_{mn}^{(c)}$ to avoid having different symbols for the spherical vector wave functions. The fields in any source free region can be expanded into linear combinations[12] of $\boldsymbol{M}_{mn}^{(c)}$ and $\boldsymbol{N}_{mn}^{(c)}$. We have

$$\begin{aligned}\boldsymbol{E} &= k\sqrt{Z_\mathrm{F}}\sum_{c=3}^{4}\sum_{n=1}^{\infty}\sum_{m=-n}^{n}\left(\alpha_{1mn}^{(c)}\boldsymbol{M}_{mn}^{(c)}+\alpha_{2mn}^{(c)}\boldsymbol{N}_{mn}^{(c)}\right)\\ &= k\sqrt{Z_\mathrm{F}}\sum_{s=1}^{2}\sum_{c=3}^{4}\sum_{n=1}^{\infty}\sum_{m=-n}^{n}\alpha_{smn}^{(c)}\boldsymbol{F}_{smn}^{(c)}\end{aligned} \tag{3.45}$$

and

$$\begin{aligned}\boldsymbol{H} &= \mathrm{j}\frac{k}{\sqrt{Z_\mathrm{F}}}\sum_{c=3}^{4}\sum_{n=1}^{\infty}\sum_{m=-n}^{n}\left(\alpha_{1mn}^{(c)}\boldsymbol{N}_{mn}^{(c)}+\alpha_{2mn}^{(c)}\boldsymbol{M}_{mn}^{(c)}\right)\\ &= \mathrm{j}\frac{k}{\sqrt{Z_\mathrm{F}}}\sum_{s=1}^{2}\sum_{c=3}^{4}\sum_{n=1}^{\infty}\sum_{m=-n}^{n}\alpha_{smn}^{(c)}\boldsymbol{F}_{3-s,mn}^{(c)}\,,\end{aligned} \tag{3.46}$$

where $\alpha_{smn}^{(c)} \in \mathbb{C}\sqrt{\mathrm{W}}$ are the expansion coefficients. Inward- ($c = 3$) and outward-traveling ($c = 4$) waves are chosen for this expansion, but any two different values for c will lead to a valid field expansion (e.g., a linear combination of incident fields with $c = 1$ and outward-traveling waves with $c = 4$ is well suited to describe scattering). In certain special cases, only one type of radial functions may suffice to expand the fields.

In the remainder of this work, spherical wave expansions will be used side by side with field expressions based on equivalent spatial current distributions to analyze the field behavior. The formulation which is more appropriate to highlight the specific aspect of the current discussion will be used, having in mind that both formulations are representations of the very same fields. Any field properties which are easily found in one representation must also hold in the other representation (even if it is not obvious in there).

---

[12] The third type of vector wave functions $\boldsymbol{L} = \nabla f$ is only needed to express the fields in the source regions and not used in this work.

3.4. Purely Radiated Fields

Since it is known from the previous sections how arbitrary fields in the volume V can be expressed by either equivalent currents or a spherical mode expansion, the focus is now turned toward the characterization of some special fields with certain characteristic properties. The first type of interesting fields are *purely radiated fields*. As the name suggests, purely *radiated* fields transport power away from the interior volume V_{int} toward the exterior volume V_{ext}. Purely radiated fields consist only of outward-traveling waves. If the surface S_2 is moved to infinity, purely radiated fields fulfill the Silver-Müller radiation conditions [Silver 1949; Müller 1948]

$$\lim_{|\boldsymbol{r}|\to\infty} |\boldsymbol{r}| \left(\boldsymbol{E}_{\text{rad}} + \sqrt{\frac{\mu}{\varepsilon}} \boldsymbol{e}_r \times \boldsymbol{H}_{\text{rad}} \right) = \boldsymbol{0}\,, \tag{3.47}$$

$$\lim_{|\boldsymbol{r}|\to\infty} |\boldsymbol{r}| \left(\boldsymbol{H}_{\text{rad}} - \sqrt{\frac{\varepsilon}{\mu}} \boldsymbol{e}_r \times \boldsymbol{E}_{\text{rad}} \right) = \boldsymbol{0} \tag{3.48}$$

for outward-traveling waves. With the suitable choice of Greens functions $\boldsymbol{\mathcal{G}}_{JE}^{-}$, $\boldsymbol{\mathcal{G}}_{JH}^{-}$, $\boldsymbol{\mathcal{G}}_{ME}^{-}$, $\boldsymbol{\mathcal{G}}_{MH}^{-}$ the surface integral over the surface S_2 at infinity in (3.28) and (3.29) becomes zero. The integral at infinity vanishes only because the Greens functions of the "−"-type fulfill the same radiation conditions as the radiated fields at infinity [Collin 1990, pp.98f].

To see this more clearly, consider with the integral

$$\oiint\limits_{S_2} \left[\boldsymbol{n}_2 \times \boldsymbol{E}(\boldsymbol{r}) \cdot \nabla \times \boldsymbol{\mathcal{G}}_{JE}\left(\boldsymbol{r}, \boldsymbol{r}'\right) + \boldsymbol{n}_2 \times \nabla \times \boldsymbol{E}(\boldsymbol{r}) \cdot \boldsymbol{\mathcal{G}}_{JE}\left(\boldsymbol{r}, \boldsymbol{r}'\right) \right] \mathrm{d}a \tag{3.49}$$

which was used in (3.26) for the derivation of (3.28), where the surface S_2 has not yet been moved to infinity. Next, one can take the limiting process of this integral, such that S_2 is a spherical surface with radius approaching infinity. Making use of the Maxwell equation $\nabla \times \boldsymbol{E} = -\mathrm{j}\omega\mu\boldsymbol{H}$ the radiation condition (3.48) is restated for the electric field as [Collin 1990, p.98]

$$\lim_{r\to\infty} \nabla \times \boldsymbol{E} + \mathrm{j}k\boldsymbol{e}_r \times \boldsymbol{E} = \boldsymbol{F} \tag{3.50}$$

where $\lim\limits_{r\to\infty} r\,\boldsymbol{F} = \boldsymbol{0}$. Since the Green's function $\boldsymbol{\mathcal{G}}_{JE}^{-}$ was constructed from the scalar Green's function g_0^{-} fulfilling the Sommerfeld radiation condition

$$\lim_{|\boldsymbol{r}|\to\infty} |\boldsymbol{r}| \left(\frac{\partial g_0^{-}\left(\boldsymbol{r}, \boldsymbol{r}'\right)}{\partial|\boldsymbol{r}|} + \mathrm{j}k g_0^{-}\left(\boldsymbol{r}, \boldsymbol{r}'\right) \right) = 0\,, \tag{3.51}$$

it can be verified that $\boldsymbol{\mathcal{G}}_{JE}^{-}$ fulfills the radiation condition [Collin 1990, p. 99]

$$\lim_{r\to\infty} r \left(\nabla \times \boldsymbol{\mathcal{G}}_{JE}^{-} + \mathrm{j}k\boldsymbol{e}_r \times \boldsymbol{\mathcal{G}}_{JE}^{-} \right) = \boldsymbol{0} \tag{3.52}$$

or equivalently

$$\lim_{r\to\infty} \nabla \times \boldsymbol{\mathcal{G}}_{JE}^{-} + \mathrm{j}k\boldsymbol{e}_r \times \boldsymbol{\mathcal{G}}_{JE}^{-} = \boldsymbol{\mathcal{F}} \tag{3.53}$$

with $\lim\limits_{r\to\infty} r\boldsymbol{\mathscr{F}} = \mathbf{0}$. In the limiting process we have

$$\begin{aligned}
&\lim_{r\to\infty} \oiint\limits_{S_2} \left[\boldsymbol{n}_2 \times \boldsymbol{E}(\boldsymbol{r}) \cdot \nabla \times \boldsymbol{\mathscr{G}}_{JE}(\boldsymbol{r},\boldsymbol{r}') + \boldsymbol{n}_2 \times \nabla \times \boldsymbol{E}(\boldsymbol{r}) \cdot \boldsymbol{\mathscr{G}}_{JE}(\boldsymbol{r},\boldsymbol{r}')\right] \mathrm{d}a \\
&= \lim_{r\to\infty} \int\limits_0^\pi \int\limits_0^{2\pi} \left[-\boldsymbol{e}_r \times \boldsymbol{E}(\boldsymbol{r}) \cdot \nabla \times \boldsymbol{\mathscr{G}}_{JE}(\boldsymbol{r},\boldsymbol{r}') - \boldsymbol{e}_r \times \nabla \times \boldsymbol{E}(\boldsymbol{r}) \cdot \boldsymbol{\mathscr{G}}_{JE}(\boldsymbol{r},\boldsymbol{r}')\right] r\,\sin(\vartheta)\,\mathrm{d}\varphi\,\mathrm{d}\vartheta \\
&= \int\limits_0^\pi \int\limits_0^{2\pi} \lim_{r\to\infty} \left[-\boldsymbol{e}_r \times \boldsymbol{E}(\boldsymbol{r}) \cdot \nabla \times \boldsymbol{\mathscr{G}}_{JE}(\boldsymbol{r},\boldsymbol{r}') - \boldsymbol{e}_r \times \nabla \times \boldsymbol{E}(\boldsymbol{r}) \cdot \boldsymbol{\mathscr{G}}_{JE}(\boldsymbol{r},\boldsymbol{r}')\right] r\,\sin(\vartheta)\,\mathrm{d}\varphi\,\mathrm{d}\vartheta \\
&= \int\limits_0^\pi \int\limits_0^{2\pi} \lim_{r\to\infty} \Big[-\boldsymbol{e}_r \times \boldsymbol{E}(\boldsymbol{r}) \cdot \left(\boldsymbol{\mathscr{F}}(\boldsymbol{r},\boldsymbol{r}') - \mathrm{j}k\boldsymbol{e}_r \times \boldsymbol{\mathscr{G}}_{JE}(\boldsymbol{r},\boldsymbol{r}')\right) \\
&\qquad\qquad -\boldsymbol{e}_r \times \left(\boldsymbol{F}(\boldsymbol{r}) - \mathrm{j}k\boldsymbol{e}_r \times \boldsymbol{E}(\boldsymbol{r})\right) \cdot \boldsymbol{\mathscr{G}}_{JE}(\boldsymbol{r},\boldsymbol{r}')\Big] r\,\sin(\vartheta)\,\mathrm{d}\varphi\,\mathrm{d}\vartheta \\
&= \int\limits_0^\pi \int\limits_0^{2\pi} \lim_{r\to\infty} \left[-\boldsymbol{e}_r \times \boldsymbol{E}(\boldsymbol{r}) \cdot \boldsymbol{\mathscr{F}}(\boldsymbol{r},\boldsymbol{r}') - \boldsymbol{e}_r \times \boldsymbol{F}(\boldsymbol{r}) \cdot \boldsymbol{\mathscr{G}}_{JE}(\boldsymbol{r},\boldsymbol{r}')\right] r\,\sin(\vartheta)\,\mathrm{d}\varphi\,\mathrm{d}\vartheta \\
&= \mathbf{0}\,, \qquad (3.54)
\end{aligned}$$

since $\lim\limits_{r\to\infty} r\,\boldsymbol{F} = \mathbf{0}$ and $\lim\limits_{r\to\infty} r\,\boldsymbol{\mathscr{F}} = \mathbf{0}$.

The fields in $V = \mathbb{R}^3 \setminus V_\text{int}$ can therefore be expressed by outward-radiating Greens functions $\boldsymbol{\mathscr{G}}_{JE}^-$, $\boldsymbol{\mathscr{G}}_{JH}^-$, $\boldsymbol{\mathscr{G}}_{ME}^-$, $\boldsymbol{\mathscr{G}}_{MH}^-$ evaluating only the tangential fields on S_1. We have

$$\boldsymbol{E}_\text{rad} = \oiint\limits_{S_1} \left[\boldsymbol{\mathscr{G}}_{JE}^-(\boldsymbol{r},\boldsymbol{r}') \cdot \left(\boldsymbol{n}_1 \times \boldsymbol{H}_\text{rad}(\boldsymbol{r}')\right) + \boldsymbol{\mathscr{G}}_{ME}^-(\boldsymbol{r},\boldsymbol{r}') \cdot \left(\boldsymbol{E}_\text{rad}(\boldsymbol{r}') \times \boldsymbol{n}_1\right)\right] \mathrm{d}a' \qquad (3.55)$$

and

$$\boldsymbol{H}_\text{rad} = \oiint\limits_{S_1} \left[\boldsymbol{\mathscr{G}}_{JH}^-(\boldsymbol{r},\boldsymbol{r}') \cdot \left(\boldsymbol{n}_1 \times \boldsymbol{H}_\text{rad}(\boldsymbol{r}')\right) + \boldsymbol{\mathscr{G}}_{MH}^-(\boldsymbol{r},\boldsymbol{r}') \cdot \left(\boldsymbol{E}_\text{rad}(\boldsymbol{r}') \times \boldsymbol{n}_1\right)\right] \mathrm{d}a'\,. \qquad (3.56)$$

The fields in (3.55) and (3.56) are the unique fields with given boundary values $\boldsymbol{n}_1 \times \boldsymbol{E}_\text{rad}(\boldsymbol{r}')$ and $\boldsymbol{n}_1 \times \boldsymbol{H}_\text{rad}(\boldsymbol{r}')$ on S_1 and the radiating Silver-Müller conditions at infinity. The solution is valid in the complete unbounded region $V = \mathbb{R}^3 \setminus V_\text{int}$ no matter whether S_2 is located at infinity as assumed in the derivation or not. Thus, using the Green's functions of the "−"-type, one does not need to evaluate the tangential integrals on the outer surface S_2 to find the correct values for the outward-traveling fields in V even if S_2 is not located at infinity[13]. More generally, arbitrary

---

[13] In general, one needs to evaluate all integrals on S_1 and S_2 to find the correct fields in V. Only if the utilized Green's functions match with field properties of the fields in V—i.e., if the fields fulfill the same boundary conditions as the utilized Green's function on one of the surfaces—one can avoid having to evaluate the integrals on one of the surfaces. Thus, it can be seen as the defining property of purely *radiated* fields that they have to fulfill the same boundary conditions on $S_2 \to \infty$ as the corresponding Green's functions $\boldsymbol{\mathscr{G}}_{JE}^-$, $\boldsymbol{\mathscr{G}}_{JH}^-$, $\boldsymbol{\mathscr{G}}_{ME}^-$, $\boldsymbol{\mathscr{G}}_{MH}^-$.

radiated fields may be constructed by placing surface currents (not necessarily related to the tangential fields) $\boldsymbol{J}$ and $\boldsymbol{M}$ on the surface S_1 and evaluating them with the "−"-type Greens functions. We have

$$\boldsymbol{E}_{\mathrm{rad}} = \oiint\limits_{S_1} \left[\boldsymbol{\mathcal{G}}_{JE}^{-}(\boldsymbol{r},\boldsymbol{r}') \cdot \boldsymbol{J}(\boldsymbol{r}') + \boldsymbol{\mathcal{G}}_{ME}^{-}(\boldsymbol{r},\boldsymbol{r}') \cdot \boldsymbol{M}(\boldsymbol{r}')\right] \,\mathrm{d}a' \tag{3.57}$$

and analogously for the magnetic field. It is clear that by using the "−"-type Greens functions, all fields generated by currents on S_1 are purely outward-traveling.

In terms of a spherical wave expansion, the functions with $c = 4$ correspond to outward-traveling waves with the time convention $\mathrm{e}^{\mathrm{j}\omega t}$ used in this work. They fulfill the Silver-Müller radiation conditions (3.47) and (3.48) for outward-traveling waves. *Radiated fields* can be expressed purely in terms of $c = 4$ type functions and we have

$$\boldsymbol{E}_{\mathrm{rad}} = k\sqrt{Z_{\mathrm{F}}} \sum_{2=1}^{2} \sum_{n=1}^{\infty} \sum_{m=-n}^{n} \alpha_{smn}^{(4)} \boldsymbol{F}_{smn}^{(4)} \tag{3.58}$$

and

$$\boldsymbol{H}_{\mathrm{rad}} = \mathrm{j}\frac{k}{\sqrt{Z_{\mathrm{F}}}} \sum_{2=1}^{2} \sum_{n=1}^{\infty} \sum_{m=-n}^{n} \alpha_{smn}^{(4)} \boldsymbol{F}_{3-s,mn}^{(4)} \,. \tag{3.59}$$

3.5. Radiated Far-Fields

Antennas are devices which are often intended to radiate electromagnetic waves over large distances and, therefore, one is usually interested in how the radiated antenna fields look like at far distances. Arbitrary purely radiated fields are considered which can be expressed by (3.57). At far away distances with $r = |\boldsymbol{r}| \gg |\boldsymbol{r}'| = r'$, the term $R = |\boldsymbol{r} - \boldsymbol{r}'|$ can be approximated by [Collin 1990, p. 98]

$$\lim_{r\to\infty} |\boldsymbol{r} - \boldsymbol{r}'| = r - \boldsymbol{e}_r \cdot \boldsymbol{r}' \,, \tag{3.60}$$

where $\boldsymbol{e}_r = \boldsymbol{r}/r$ denotes the unit vector pointing into the direction of the FF observation location $\boldsymbol{r}$. For a condensed notation, often the vector $\boldsymbol{k} = k\,\boldsymbol{e}_r$ is used together with its normalized version $\hat{\boldsymbol{k}} = \boldsymbol{k}/k = \boldsymbol{e}_r$. The dyadic Green's functions for outward-traveling waves take the asymptotic forms [Collin 1990, pp. 98f], [Jin 2015, p. 74]

$$\lim_{r\to\infty} \boldsymbol{\mathcal{G}}_{JE}^{-}(\boldsymbol{r},\boldsymbol{r}') = -\mathrm{j}\omega\mu\frac{\mathrm{e}^{-\mathrm{j}k\,r}}{4\pi r}\left(\mathbf{I} - \boldsymbol{e}_r\boldsymbol{e}_r\right)\mathrm{e}^{\mathrm{j}\boldsymbol{e}_r\cdot\boldsymbol{r}'} = -\mathrm{j}\omega\mu\frac{\mathrm{e}^{-\mathrm{j}k\,r}}{4\pi r}\left(\mathbf{I} - \hat{\boldsymbol{k}}\hat{\boldsymbol{k}}\right)\mathrm{e}^{\mathrm{j}\boldsymbol{k}\cdot\boldsymbol{r}'} \,, \tag{3.61}$$

$$\lim_{r\to\infty} \boldsymbol{\mathcal{G}}_{JH}^{-}(\boldsymbol{r},\boldsymbol{r}') = -\mathrm{j}k\frac{\mathrm{e}^{-\mathrm{j}k\,r}}{4\pi r}\boldsymbol{e}_r \times \mathbf{I}\,\mathrm{e}^{\mathrm{j}k\,\boldsymbol{e}_r\cdot\boldsymbol{r}'} = -\mathrm{j}\frac{\mathrm{e}^{-\mathrm{j}k\,r}}{4\pi r}\boldsymbol{k} \times \mathbf{I}\,\mathrm{e}^{\mathrm{j}\boldsymbol{k}\cdot\boldsymbol{r}'} \,, \tag{3.62}$$

$$\lim_{r\to\infty} \boldsymbol{\mathcal{G}}_{ME}^{-}(\boldsymbol{r},\boldsymbol{r}') = \mathrm{j}k\frac{\mathrm{e}^{-\mathrm{j}k\,r}}{4\pi r}\boldsymbol{e}_r \times \mathbf{I}\,\mathrm{e}^{\mathrm{j}k\,\boldsymbol{e}_r\cdot\boldsymbol{r}'} = \mathrm{j}\frac{\mathrm{e}^{-\mathrm{j}k\,r}}{4\pi r}\boldsymbol{k} \times \mathbf{I}\,\mathrm{e}^{\mathrm{j}\boldsymbol{k}\cdot\boldsymbol{r}'} \,, \tag{3.63}$$

and

$$\lim_{r\to\infty} \boldsymbol{\mathcal{G}}_{MH}^{-}(\boldsymbol{r},\boldsymbol{r}') = -\mathrm{j}\omega\varepsilon\frac{\mathrm{e}^{-\mathrm{j}k\,r}}{4\pi r}\left(\mathbf{I} - \boldsymbol{e}_r\boldsymbol{e}_r\right)\mathrm{e}^{\mathrm{j}k\,\boldsymbol{e}_r\cdot\boldsymbol{r}'} = -\mathrm{j}\omega\varepsilon\frac{\mathrm{e}^{-\mathrm{j}k\,r}}{4\pi r}\left(\mathbf{I} - \hat{\boldsymbol{k}}\hat{\boldsymbol{k}}\right)\mathrm{e}^{\mathrm{j}\boldsymbol{k}\cdot\boldsymbol{r}'} \,. \tag{3.64}$$

The radiated fields asymptotically far away from the sources have no components in radial direction and depend on the radial variable r only by the term $\mathrm{e}^{-\mathrm{j}kr}/r$. We have

$$
\begin{aligned}
\lim_{r\to\infty} \boldsymbol{E}(r,\vartheta,\varphi) &= \lim_{r\to\infty} \oiint_{S_1} \left[\mathscr{G}^{-}_{JE}(\boldsymbol{r},\boldsymbol{r}') \cdot \boldsymbol{J}(\boldsymbol{r}') + \mathscr{G}^{-}_{ME}(\boldsymbol{r},\boldsymbol{r}') \cdot \boldsymbol{M}(\boldsymbol{r}')\right] \mathrm{d}a' \qquad (3.65)\\
&= \frac{\mathrm{e}^{-\mathrm{j}k\,r}}{4\pi r} \oiint_{S_1} \left[-\mathrm{j}\omega\mu \left(\mathrm{I} - \hat{\boldsymbol{k}}\hat{\boldsymbol{k}}\right) \mathrm{e}^{\mathrm{j}\boldsymbol{k}\cdot\boldsymbol{r}'} \cdot \boldsymbol{J}(\boldsymbol{r}') + \mathrm{j}\boldsymbol{k} \times \boldsymbol{M}(\boldsymbol{r}')\, \mathrm{e}^{\mathrm{j}\boldsymbol{k}\cdot\boldsymbol{r}'}\right] \mathrm{d}a' \qquad (3.66)\\
&= \frac{\mathrm{e}^{-\mathrm{j}k\,r}}{k\,r} \boldsymbol{E}_{\mathrm{FF}}(\vartheta,\varphi) \qquad (3.67)\\
&= \frac{\mathrm{e}^{-\mathrm{j}k\,r}}{k\,r} \boldsymbol{E}_{\mathrm{FF}}(\hat{\boldsymbol{k}}) \qquad (3.68)
\end{aligned}
$$

and

$$
\begin{aligned}
\lim_{r\to\infty} \boldsymbol{H}(r,\vartheta,\varphi) &= \lim_{r\to\infty} \oiint_{S_1} \left[\mathscr{G}^{-}_{JH}(\boldsymbol{r},\boldsymbol{r}') \cdot \boldsymbol{J}(\boldsymbol{r}') + \mathscr{G}^{-}_{MH}(\boldsymbol{r},\boldsymbol{r}') \cdot \boldsymbol{M}(\boldsymbol{r}')\right] \mathrm{d}a' \qquad (3.69)\\
&= \frac{\mathrm{e}^{-\mathrm{j}k\,r}}{4\pi r} \oiint_{S_1} \left[-\mathrm{j}\boldsymbol{k} \times \boldsymbol{J}(\boldsymbol{r}')\, \mathrm{e}^{\mathrm{j}\boldsymbol{k}\cdot\boldsymbol{r}'} - \mathrm{j}\omega\varepsilon \left(\mathrm{I} - \hat{\boldsymbol{k}}\hat{\boldsymbol{k}}\right) \mathrm{e}^{\mathrm{j}\boldsymbol{k}\cdot\boldsymbol{r}'} \cdot \boldsymbol{M}(\boldsymbol{r}')\right] \mathrm{d}a' \qquad (3.70)\\
&= \frac{\mathrm{e}^{-\mathrm{j}k\,r}}{k\,r} \boldsymbol{H}_{\mathrm{FF}}(\vartheta,\varphi) \qquad (3.71)\\
&= \frac{\mathrm{e}^{-\mathrm{j}k\,r}}{k\,r} \boldsymbol{H}_{\mathrm{FF}}(\hat{\boldsymbol{k}}) \qquad (3.72)
\end{aligned}
$$

where

$$
\boldsymbol{E}_{\mathrm{FF}}(\hat{\boldsymbol{k}}) = \frac{k}{4\pi} \oiint_{S_1} \left[-\mathrm{j}\omega\mu \left(\mathrm{I} - \hat{\boldsymbol{k}}\hat{\boldsymbol{k}}\right) \mathrm{e}^{\mathrm{j}\boldsymbol{k}\cdot\boldsymbol{r}'} \cdot \boldsymbol{J}(\boldsymbol{r}') + \mathrm{j}\boldsymbol{k} \times \boldsymbol{M}(\boldsymbol{r}')\, \mathrm{e}^{\mathrm{j}\boldsymbol{k}\cdot\boldsymbol{r}'}\right] \mathrm{d}a' \tag{3.73}
$$

and

$$
\boldsymbol{H}_{\mathrm{FF}}(\hat{\boldsymbol{k}}) = \frac{k}{4\pi} \oiint_{S_1} \left[-\mathrm{j}\boldsymbol{k} \times \boldsymbol{J}(\boldsymbol{r}')\, \mathrm{e}^{\mathrm{j}\boldsymbol{k}\cdot\boldsymbol{r}'} - \mathrm{j}\omega\varepsilon \left(\mathrm{I} - \hat{\boldsymbol{k}}\hat{\boldsymbol{k}}\right) \mathrm{e}^{\mathrm{j}\boldsymbol{k}\cdot\boldsymbol{r}'} \cdot \boldsymbol{M}(\boldsymbol{r}')\right] \mathrm{d}a' \tag{3.74}
$$

are the electric and magnetic FF patterns, respectively. Since the coordinates ϑ and φ are uniquely defined by the direction of the radial unit vector $\boldsymbol{e}_r = \hat{\boldsymbol{k}}$ one may use the compact notation $\boldsymbol{E}_{\mathrm{FF}}(\vartheta,\varphi) = \boldsymbol{E}_{\mathrm{FF}}(\hat{\boldsymbol{k}})$ and $\boldsymbol{H}_{\mathrm{FF}}(\vartheta,\varphi) = \boldsymbol{H}_{\mathrm{FF}}(\hat{\boldsymbol{k}})$. It is clear that the electric and the magnetic FFs are related by [Collin 1990, p. 98]

$$
Z_{\mathrm{F}}\, \boldsymbol{H}_{\mathrm{FF}}(\hat{\boldsymbol{k}}) = \hat{\boldsymbol{k}} \times \boldsymbol{E}_{\mathrm{FF}}(\hat{\boldsymbol{k}}) \;, \tag{3.75}
$$

where $Z_{\mathrm{F}} = \sqrt{\mu/\varepsilon}$ is the free-space wave impedance.

In terms of spherical waves, the FF patterns can easily be evaluated by using the asymptotic form of the spherical wave functions. We have

$$\begin{aligned}\boldsymbol{E}_{\mathrm{FF}}\big(\hat{\boldsymbol{k}}\big) &= \lim_{r\to\infty} \frac{k\,r}{\mathrm{e}^{-\mathrm{j}k\,r}} \boldsymbol{E}(r,\vartheta,\varphi) = k\sqrt{Z_{\mathrm{F}}} \sum_{s=1}^{2}\sum_{n=1}^{\infty}\sum_{m=-n}^{n} \alpha^{(4)}_{smn} \lim_{r\to\infty} \frac{k\,r}{\mathrm{e}^{-\mathrm{j}k\,r}} \boldsymbol{F}^{(4)}_{smn}(r,\vartheta,\varphi) \\ &= k\sqrt{Z_{\mathrm{F}}} \sum_{s=1}^{2}\sum_{n=1}^{\infty}\sum_{m=-n}^{n} \alpha^{(4)}_{smn}\, \boldsymbol{K}^{(4)}_{smn}\big(\hat{\boldsymbol{k}}\big)\end{aligned} \tag{3.76}$$

and

$$\begin{aligned}\boldsymbol{H}_{\mathrm{FF}}\big(\hat{\boldsymbol{k}}\big) &= \lim_{r\to\infty} \frac{k\,r}{\mathrm{e}^{-\mathrm{j}k\,r}} \boldsymbol{H}(r,\vartheta,\varphi) = \frac{\mathrm{j}\,k}{\sqrt{Z_{\mathrm{F}}}} \sum_{s=1}^{2}\sum_{n=1}^{\infty}\sum_{m=-n}^{n} \alpha^{(4)}_{smn} \lim_{r\to\infty} \frac{k\,r}{\mathrm{e}^{-\mathrm{j}k\,r}} \boldsymbol{F}^{(4)}_{3-s,mn}(r,\vartheta,\varphi) \\ &= \frac{\mathrm{j}\,k}{\sqrt{Z_{\mathrm{F}}}} \sum_{s=1}^{2}\sum_{n=1}^{\infty}\sum_{m=-n}^{n} \alpha^{(4)}_{smn}\, \boldsymbol{K}^{(4)}_{3-s,mn}\big(\hat{\boldsymbol{k}}\big) \\ &= \frac{\mathrm{j}\,k}{\sqrt{Z_{\mathrm{F}}}} \sum_{s=1}^{2}\sum_{n=1}^{\infty}\sum_{m=-n}^{n} \alpha^{(4)}_{smn} \left(\hat{\boldsymbol{k}} \times \boldsymbol{K}^{(4)}_{smn}\big(\hat{\boldsymbol{k}}\big)\right) .\end{aligned} \tag{3.77}$$

Formal expressions for the FF pattern functions $\boldsymbol{K}_{smn}$ are found by replacing the radial functions in (3.43) and (3.44) by their asymptotic behaviors [Hansen 1988, p. 315]

$$\lim_{kr\to\infty} z^{(4)}_n(kr) = \mathrm{j}^{n+1}\,\frac{\mathrm{e}^{-\mathrm{j}k\,r}}{k\,r} \tag{3.78}$$

and

$$\lim_{kr\to\infty} \frac{1}{kr}\frac{\mathrm{d}}{\mathrm{d}(kr)} \left(krz^{(4)}_n(kr)\right) = \mathrm{j}^{n}\,\frac{\mathrm{e}^{-\mathrm{j}k\,r}}{k\,r} . \tag{3.79}$$

This gives[14]

$$\begin{aligned}\boldsymbol{K}^{(4)}_{1mn}\big(\hat{\boldsymbol{k}}\big) &= \lim_{kr\to\infty} \frac{k\,r}{\mathrm{e}^{-\mathrm{j}k\,r}} \boldsymbol{F}^{(4)}_{1mn}(r,\vartheta,\varphi) \\ &= \lim_{kr\to\infty} \frac{k\,r}{\mathrm{e}^{-\mathrm{j}k\,r}} \frac{z^{(c)}_n(kr)}{\sqrt{n\,(n+1)}} \left(\nabla_{\mathrm{t}} Y_{nm}(\vartheta,\varphi)\right) \times \left(r\,\boldsymbol{e}_r\right) \\ &= \frac{\mathrm{j}^{n+1}}{\sqrt{n\,(n+1)}} \left(\nabla_{\mathrm{t}} Y_{nm}(\vartheta,\varphi)\right) \times \left(r\,\boldsymbol{e}_r\right) \\ &= \frac{\mathrm{j}^{n+1}}{\sqrt{n\,(n+1)}} \frac{1}{\sqrt{2\pi}} \left(\frac{-m}{|m|}\right)^{m} \mathrm{e}^{\mathrm{j}\,m\varphi} \left(\frac{\mathrm{j}m\,\overline{P}^{|m|}_n(\cos\vartheta)}{\sin\vartheta}\boldsymbol{e}_\vartheta - \frac{\mathrm{d}\,\overline{P}^{|m|}_n(\cos\vartheta)}{\mathrm{d}\vartheta}\boldsymbol{e}_\varphi \right)\end{aligned} \tag{3.80}$$

---

[14] The spherical FF functions $K^{(4)}_{smn}$ used in this work differ by a factor of $(-1)^{n+s}/\sqrt{4\pi}$ from the ones in [Hansen 1988] due to a different normalization and the different time convention.

and

$$\begin{aligned}\boldsymbol{K}^{(4)}_{2mn}\big(\hat{\boldsymbol{k}}\big) &= \lim_{kr\to\infty} \frac{k\,r}{\mathrm{e}^{-\mathrm{j}k\,r}} \boldsymbol{F}^{(4)}_{2mn}(r,\vartheta,\varphi) \\ &= \lim_{kr\to\infty} \frac{k\,r}{\mathrm{e}^{-\mathrm{j}k\,r}} \frac{1}{k} \nabla \times \boldsymbol{F}^{(4)}_{1mn}(r,\vartheta,\varphi) \\ &= -\mathrm{j}\,\hat{\boldsymbol{k}} \times \boldsymbol{K}^{(4)}_{1mn}\big(\hat{\boldsymbol{k}}\big) \\ &= \frac{\mathrm{j}^n}{\sqrt{n\,(n+1)}} \frac{1}{\sqrt{2\pi}} \left(\frac{-m}{|m|}\right)^m \mathrm{e}^{\mathrm{j}\,m\varphi} \left(\frac{\mathrm{d}\,\overline{P}_n^{|m|}(\cos\vartheta)}{\mathrm{d}\vartheta}\boldsymbol{e}_\vartheta + \frac{\mathrm{j}m\,\overline{P}_n^{|m|}(\cos\vartheta)}{\sin\vartheta}\boldsymbol{e}_\varphi\right). \end{aligned} \quad (3.81)$$

3.6. Purely Absorbed Fields

Similar to purely radiated fields, one can characterize *purely absorbed* fields by duality considerations. As the name suggests, fields which are *absorbed* in V_{int} transport power from V_{ext} to V_{int} [15]. If the surface S_2 is moved to infinity, *purely absorbed fields* fulfill the Silver-Müller radiation conditions [Silver 1949; Müller 1948]

$$\lim_{|\boldsymbol{r}|\to\infty} |\boldsymbol{r}| \left(\boldsymbol{E}_{\mathrm{ab}} - \sqrt{\frac{\mu}{\varepsilon}}\hat{\boldsymbol{r}} \times \boldsymbol{H}_{\mathrm{ab}}\right) = \boldsymbol{0} \quad (3.82)$$

and

$$\lim_{|\boldsymbol{r}|\to\infty} |\boldsymbol{r}| \left(\boldsymbol{H}_{\mathrm{ab}} + \sqrt{\frac{\varepsilon}{\mu}}\hat{\boldsymbol{r}} \times \boldsymbol{E}_{\mathrm{ab}}\right) = \boldsymbol{0} \quad (3.83)$$

for inward-traveling waves. In a fully analogous reasoning as for purely radiated waves, it may be found that purely *absorbed fields* can be expressed by evaluating only the tangential fields on S_1 using the inward-radiating Greens functions $\mathscr{G}^+_{JE}$, $\mathscr{G}^+_{ME}$, $\mathscr{G}^+_{JH}$, $\mathscr{G}^+_{MH}$. We have

$$\boldsymbol{E}_{\mathrm{ab}} = \oiint_{S_1} \left[\mathscr{G}^+_{JE}\big(\boldsymbol{r},\boldsymbol{r}'\big) \cdot \big(\boldsymbol{n}_1 \times \boldsymbol{H}_{\mathrm{ab}}\big(\boldsymbol{r}'\big)\big) + \mathscr{G}^+_{ME}\big(\boldsymbol{r},\boldsymbol{r}'\big) \cdot \big(\boldsymbol{E}_{\mathrm{ab}}\big(\boldsymbol{r}'\big) \times \boldsymbol{n}_1\big)\right] \mathrm{d}a' \quad (3.84)$$

and

$$\boldsymbol{H}_{\mathrm{ab}} = \oiint_{S_1} \left[\mathscr{G}^+_{JH}\big(\boldsymbol{r},\boldsymbol{r}'\big) \cdot \big(\boldsymbol{n}_1 \times \boldsymbol{H}_{\mathrm{ab}}\big(\boldsymbol{r}'\big)\big) + \mathscr{G}^+_{MH}\big(\boldsymbol{r},\boldsymbol{r}'\big) \cdot \big(\boldsymbol{E}_{\mathrm{ab}}\big(\boldsymbol{r}'\big) \times \boldsymbol{n}_1\big)\right] \mathrm{d}a'\,. \quad (3.85)$$

Using the Green's functions for inward-traveling waves, the tangential fields on S_2 are not needed for the evaluation of the absorbed fields in V[16]. More generally, arbitrary absorbed fields may be constructed by placing arbitrary surface currents (not necessarily related to the tangential fields) $\boldsymbol{J}$ and $\boldsymbol{M}$ on the surface S_1 and evaluating them with the "+"-type Greens functions. We have

$$\boldsymbol{E}_{\mathrm{ab}} = \oiint_{S_1} \left[\mathscr{G}^+_{JE}\big(\boldsymbol{r},\boldsymbol{r}'\big) \cdot \boldsymbol{J}\big(\boldsymbol{r}'\big) + \mathscr{G}^+_{ME}\big(\boldsymbol{r},\boldsymbol{r}'\big) \cdot \boldsymbol{M}\big(\boldsymbol{r}'\big)\right] \mathrm{d}a' \quad (3.86)$$

---

[15] The text does not differentiate between absorption due to losses and absorption due to, e.g., a receiving antenna placed in V_{int} at this point.

[16] This may be used as the defining property of purely *absorbed fields*.

and analogously for the magnetic field. It is clear that by using the "+"-type Greens functions, all fields generated by currents on S_1 are purely inward-traveling.

In the spherical wave expansion, the functions with $c = 3$ correspond to inward-traveling waves fulfilling the Silver-Müller radiation conditions (3.82) and (3.83) for inward-traveling waves. *Absorbed fields* can be expressed purely in terms of $c = 3$ type functions and we have

$$\boldsymbol{E}_{\mathrm{ab}} = k\sqrt{Z_{\mathrm{F}}} \sum_{2=1}^{2} \sum_{n=1}^{\infty} \sum_{m=-n}^{n} \alpha_{smn}^{(3)} \boldsymbol{F}_{smn}^{(3)} \tag{3.87}$$

and

$$\boldsymbol{H}_{\mathrm{ab}} = \mathrm{j}\frac{k}{\sqrt{Z_{\mathrm{F}}}} \sum_{2=1}^{2} \sum_{n=1}^{\infty} \sum_{m=-n}^{n} \alpha_{smn}^{(3)} \boldsymbol{F}_{3-s,mn}^{(3)} . \tag{3.88}$$

3.7. Purely Incident Fields

Purely *incident fields* are characterized by the fact that no sources (neither radiating sources, nor absorbing sources nor scattering sources) are present in V and V_{int}. All incident fields are due to sources in V_{ext} (thus the fields are *incident* on the volume V). The incident fields in V can be expressed by only evaluating the integrals on S_2. Additional evaluation of the integrals on S_1 only makes the volume V_{int} free of fields without affecting the fields in V. We have

$$\boldsymbol{E}_{\mathrm{inc}} = \oiint_{S_2} \left[\mathscr{G}_{JE}(\boldsymbol{r},\boldsymbol{r}') \cdot \left(\boldsymbol{n}_2 \times \boldsymbol{H}_{\mathrm{inc}}(\boldsymbol{r}')\right) + \mathscr{G}_{ME}(\boldsymbol{r},\boldsymbol{r}') \cdot \left(\boldsymbol{E}_{\mathrm{inc}}(\boldsymbol{r}') \times \boldsymbol{n}_2\right)\right] \mathrm{d}a' \tag{3.89}$$

and

$$\boldsymbol{H}_{\mathrm{inc}} = \oiint_{S_2} \left[\mathscr{G}_{JH}(\boldsymbol{r},\boldsymbol{r}') \cdot \left(\boldsymbol{n}_2 \times \boldsymbol{H}_{\mathrm{inc}}(\boldsymbol{r}')\right) + \mathscr{G}_{MH}(\boldsymbol{r},\boldsymbol{r}') \cdot \left(\boldsymbol{E}_{\mathrm{inc}}(\boldsymbol{r}') \times \boldsymbol{n}_2\right)\right] \mathrm{d}a' , \tag{3.90}$$

where any type of Green's function ("–", "+", or "(0)") can interchangeably be used to find the correct incident fields in V (but Green's functions of different type must not be mixed). The fields are finite in V, the net power absorption (or power generation) in V and V_{int} is zero and no distortion of the fields occurs in $\mathrm{V}_{\mathrm{int}}$.

Instead of expressing the incident fields by currents on S_2, one can also use arbitrary pseudo currents $\tilde{\boldsymbol{J}}$, $\tilde{\boldsymbol{M}}$ (not related to the tangential fields) on the surface S_1 which yield purely incident fields if evaluated with an appropriate convolution kernel. To this end, consider the pseudo Green's functions

$$\mathscr{G}_{JE}^{(\infty)}(\boldsymbol{r},\boldsymbol{r}') = \frac{1}{2}\left[\mathscr{G}_{JE}^{+}(\boldsymbol{r},\boldsymbol{r}') - \mathscr{G}_{JE}^{-}(\boldsymbol{r},\boldsymbol{r}')\right] = -\mathrm{j}\omega\mu\left[\left(\mathbf{I} + \frac{1}{k^2}\nabla\nabla\right)\frac{\mathrm{j}\,\sin\left(k\left|\boldsymbol{r}-\boldsymbol{r}'\right|\right)}{4\pi|\boldsymbol{r}-\boldsymbol{r}'|}\right] , \tag{3.91}$$

$$\mathscr{G}_{JH}^{(\infty)}(\boldsymbol{r},\boldsymbol{r}') = \frac{1}{2}\left[\mathscr{G}_{JH}^{+}(\boldsymbol{r},\boldsymbol{r}') - \mathscr{G}_{JH}^{-}(\boldsymbol{r},\boldsymbol{r}')\right] = \nabla\frac{\mathrm{j}\,\sin\left(k\left|\boldsymbol{r}-\boldsymbol{r}'\right|\right)}{4\pi|\boldsymbol{r}-\boldsymbol{r}'|} \times \mathbf{I} , \tag{3.92}$$

$$\mathscr{G}_{ME}^{(\infty)}(\boldsymbol{r},\boldsymbol{r}') = \frac{1}{2}\left[\mathscr{G}_{ME}^{+}(\boldsymbol{r},\boldsymbol{r}') - \mathscr{G}_{ME}^{-}(\boldsymbol{r},\boldsymbol{r}')\right] = -\nabla\frac{\mathrm{j}\,\sin\left(k\left|\boldsymbol{r}-\boldsymbol{r}'\right|\right)}{4\pi|\boldsymbol{r}-\boldsymbol{r}'|} \times \mathbf{I} , \tag{3.93}$$

and

$$\boldsymbol{\mathcal{G}}^{(\infty)}_{MH}\left(\boldsymbol{r},\boldsymbol{r}'\right) = \frac{1}{2}\left[\boldsymbol{\mathcal{G}}^{+}_{MH}\left(\boldsymbol{r},\boldsymbol{r}'\right) - \boldsymbol{\mathcal{G}}^{-}_{MH}\left(\boldsymbol{r},\boldsymbol{r}'\right)\right] = -\mathrm{j}\omega\varepsilon\left[\left(\mathbf{I}+\frac{1}{k^2}\nabla\nabla\right)\frac{\mathrm{j}\,\sin\left(k\left|\boldsymbol{r}-\boldsymbol{r}'\right|\right)}{4\pi\left|\boldsymbol{r}-\boldsymbol{r}'\right|}\right]. \tag{3.94}$$

Similar to the scalar Helmholtz equation, the pseudo Green's functions $\boldsymbol{\mathcal{G}}^{\infty}_{JE}$, $\boldsymbol{\mathcal{G}}^{(\infty)}_{JH}$, $\boldsymbol{\mathcal{G}}^{\infty}_{ME}$ and $\boldsymbol{\mathcal{G}}^{\infty}_{MH}$ are no Green's functions because they fulfill the homogeneous curl-curl equations (the right hand side is zero and not the Dirac-Delta distribution)

$$\nabla\times\nabla\times\boldsymbol{\mathcal{G}}^{(\infty)}_{JE}\left(\boldsymbol{r},\boldsymbol{r}'\right) - k^2\boldsymbol{\mathcal{G}}^{(\infty)}_{JE}\left(\boldsymbol{r},\boldsymbol{r}'\right) = \mathbf{0}\,, \tag{3.95}$$

$$\nabla\times\nabla\times\boldsymbol{\mathcal{G}}^{(\infty)}_{JH}\left(\boldsymbol{r},\boldsymbol{r}'\right) - k^2\boldsymbol{\mathcal{G}}^{(\infty)}_{JH}\left(\boldsymbol{r},\boldsymbol{r}'\right) = \mathbf{0}\,, \tag{3.96}$$

$$\nabla\times\nabla\times\boldsymbol{\mathcal{G}}^{(\infty)}_{ME}\left(\boldsymbol{r},\boldsymbol{r}'\right) - k^2\boldsymbol{\mathcal{G}}^{(\infty)}_{ME}\left(\boldsymbol{r},\boldsymbol{r}'\right) = \mathbf{0}\,, \tag{3.97}$$

and

$$\nabla\times\nabla\times\boldsymbol{\mathcal{G}}^{(\infty)}_{JE}\left(\boldsymbol{r},\boldsymbol{r}'\right) - k^2\boldsymbol{\mathcal{G}}^{(\infty)}_{JE}\left(\boldsymbol{r},\boldsymbol{r}'\right) = \mathbf{0} \tag{3.98}$$

everywhere, including the "source location" $\boldsymbol{r}'$. Due to the linearity of the curl-curl equation, a valid solution of

$$\nabla\times\nabla\times\boldsymbol{E}(\boldsymbol{r}) - k^2\boldsymbol{E}(\boldsymbol{r}) = \mathbf{0} \tag{3.99}$$

in the complete $\mathbb{R}^3$ can be constructed by

$$\boldsymbol{E}_{\mathrm{inc}} = \oiint\limits_{S_1}\left[\boldsymbol{\mathcal{G}}^{(\infty)}_{JE}\left(\boldsymbol{r},\boldsymbol{r}'\right)\cdot\tilde{\boldsymbol{J}}\left(\boldsymbol{r}'\right) + \boldsymbol{\mathcal{G}}^{(\infty)}_{ME}\left(\boldsymbol{r},\boldsymbol{r}'\right)\cdot\tilde{\boldsymbol{M}}\left(\boldsymbol{r}'\right)\right]\,\mathrm{d}a' \tag{3.100}$$

and analogously for the magnetic field. This might be surprising at first glance, because the incident field in the region V which is external to the surface S_1 can be expressed in terms of "sources" on the inner surface S_1. Since the incident fields in (3.100) are generated by subtracting a radiated field from an absorbed field with the same generating surface currents, the so found electromagnetic fields can be regarded as a superposition of an absorbed and a radiated field, which are carefully adjusted such that their generating currents cancel (thus the term *pseudo currents* for the "generating sources" $\tilde{\boldsymbol{J}}$ and $\tilde{\boldsymbol{M}}$). Using the "∞"-type pseudo Green's functions, it becomes obvious that all incident fields contain equal parts of absorbed and radiated fields. Furthermore, all types of source free fields in the source free volume V (i.e., absorbed, radiated or incident fields) can be expressed by a convolution integral over equivalent currents (or pseudo currents) on S_1 evaluated with convenient convolution kernels (i.e., Green's functions or pseudo Green's functions, respectively). This is a nice analogy to the corresponding spherical wave expansion of the fields in the source free region.

For the spherical wave expansion of *incident fields* it may be noted that the spherical Bessel function j_n is the only of the four $z_n^{(c)}$ functions which is finite at $r = 0$. This means that all *incident fields* can be expressed purely in terms of $c = 1$ type functions in a spherical wave expansion. If expressed in terms of inward- and outward-traveling waves, we can use the fact that $\mathrm{j}_n = (\mathrm{h}_n^{(1)} + \mathrm{h}_n^{(2)})/2$ to derive the fact that $\alpha_{smn}^{(3)} = \alpha_{smn}^{(4)}$ for incident waves. We have

$$\begin{aligned} \boldsymbol{E}_{\mathrm{inc}} &= k\sqrt{Z_{\mathrm{F}}} \sum_{2=1}^{2} \sum_{n=1}^{\infty} \sum_{m=-n}^{n} \alpha_{smn}^{(1)} \boldsymbol{F}_{smn}^{(1)} \\ &= \frac{1}{2} k\sqrt{Z_{\mathrm{F}}} \sum_{2=1}^{2} \sum_{n=1}^{\infty} \sum_{m=-n}^{n} \alpha_{smn}^{(1)} \left(\boldsymbol{F}_{smn}^{(3)} + \boldsymbol{F}_{smn}^{(4)} \right) \end{aligned} \tag{3.101}$$

and

$$\begin{aligned} \boldsymbol{H}_{\mathrm{inc}} &= \mathrm{j} \frac{k}{\sqrt{Z_{\mathrm{F}}}} \sum_{2=1}^{2} \sum_{n=1}^{\infty} \sum_{m=-n}^{n} \alpha_{smn}^{(1)} \boldsymbol{F}_{3-s,mn}^{(1)} \\ &= \frac{1}{2} \mathrm{j} \frac{k}{\sqrt{Z_{\mathrm{F}}}} \sum_{2=1}^{2} \sum_{n=1}^{\infty} \sum_{m=-n}^{n} \alpha_{smn}^{(1)} \left(\boldsymbol{F}_{3-s,mn}^{(3)} + \boldsymbol{F}_{3-s,mn}^{(4)} \right) . \end{aligned} \tag{3.102}$$

Using the spherical wave expansion of an arbitrary incident field $\boldsymbol{E}_{\mathrm{inc}}$, one can argue that the integral expression (3.100) must exist for every incident field which transports a finite amount of power. To this end, consider a purely radiated field $\boldsymbol{E}_{\mathrm{rad}}$ first, for which the spherical wave expansion

$$\boldsymbol{E}_{\mathrm{rad}} = k\sqrt{Z_{\mathrm{F}}} \sum_{2=1}^{2} \sum_{n=1}^{\infty} \sum_{m=-n}^{n} \alpha_{smn}^{(4)} \boldsymbol{F}_{smn}^{(4)} \tag{3.103}$$

converges everywhere in the volume of interest V (and analogously for the magnetic field). According to Section 3.4, the same field can be expressed in terms of an integral over the surface S_1 via

$$\boldsymbol{E}_{\mathrm{rad}} = \oiint_{S_1} \left[\mathscr{G}_{JE}^{-}(\boldsymbol{r}, \boldsymbol{r}') \cdot \boldsymbol{J}(\boldsymbol{r}') + \mathscr{G}_{ME}^{-}(\boldsymbol{r}, \boldsymbol{r}') \cdot \boldsymbol{M}(\boldsymbol{r}') \right] \mathrm{d}a' , \tag{3.104}$$

where

$$\boldsymbol{J}(\boldsymbol{r}) = k\sqrt{Z_{\mathrm{F}}}\, \boldsymbol{n}_1 \times \left(\sum_{2=1}^{2} \sum_{n=1}^{\infty} \sum_{m=-n}^{n} \alpha_{smn}^{(1)} \boldsymbol{F}_{smn}^{(4)}(\boldsymbol{r}) \right) \tag{3.105}$$

and

$$\boldsymbol{M}(\boldsymbol{r}) = \frac{-\mathrm{j}k}{\sqrt{Z_{\mathrm{F}}}} \boldsymbol{n}_1 \times \left(\sum_{2=1}^{2} \sum_{n=1}^{\infty} \sum_{m=-n}^{n} \alpha_{smn}^{(1)} \boldsymbol{F}_{smn}^{(4)}(\boldsymbol{r}) \right) . \tag{3.106}$$

There exists a unique purely *absorbed* field, which yields a purely *incident* field when added to the purely *radiated* field. To see this, consider the spherical wave expansion

$$\boldsymbol{E}_{\mathrm{ab}} = k\sqrt{Z_{\mathrm{F}}} \sum_{2=1}^{2} \sum_{n=1}^{\infty} \sum_{m=-n}^{n} \alpha_{smn}^{(3)} \boldsymbol{F}_{smn}^{(3)} \tag{3.107}$$

of an arbitrary purely absorbed field. In order for the sum $\boldsymbol{E}_{\mathrm{rad}} + \boldsymbol{E}_{\mathrm{ab}}$ to yield a purely incident field, we must have

$$\begin{aligned}\boldsymbol{E}_{\mathrm{rad}} + \boldsymbol{E}_{\mathrm{ab}} &= k\sqrt{Z_{\mathrm{F}}} \sum_{2=1}^{2} \sum_{n=1}^{\infty} \sum_{m=-n}^{n} \alpha_{smn}^{(4)} \boldsymbol{F}_{smn}^{(4)} + k\sqrt{Z_{\mathrm{F}}} \sum_{2=1}^{2} \sum_{n=1}^{\infty} \sum_{m=-n}^{n} \alpha_{smn}^{(3)} \boldsymbol{F}_{smn}^{(3)} \\ &= \frac{1}{2} k\sqrt{Z_{\mathrm{F}}} \sum_{2=1}^{2} \sum_{n=1}^{\infty} \sum_{m=-n}^{n} \alpha_{smn}^{(1)} \left(\boldsymbol{F}_{smn}^{(3)} + \boldsymbol{F}_{smn}^{(4)} \right) . \end{aligned} \tag{3.108}$$

Clearly, the only purely absorbed field which fulfills this requirement is characterized by the expansion coefficients $\alpha_{smn}^{(3)} = \alpha_{smn}^{(4)}$. In other words, there exists a unique purely absorbed field, which results in a purely incident field if added to the purely radiated field given in (3.104) and the integral representation of this absorbed field must have the form

$$\boldsymbol{E}_{\mathrm{ab}} = -\oiint_{S_1} \left[\mathscr{G}_{JE}^{+}(\boldsymbol{r}, \boldsymbol{r}') \cdot \boldsymbol{J}(\boldsymbol{r}') + \mathscr{G}_{ME}^{+}(\boldsymbol{r}, \boldsymbol{r}') \cdot \boldsymbol{M}(\boldsymbol{r}') \right] \mathrm{d}a' , \tag{3.109}$$

where the currents $\boldsymbol{J}$ and $\boldsymbol{M}$ are the same as for the corresponding radiated field. However, through the spherical wave expansion (3.101), every purely incident field is uniquely associated with a purely radiated field.

Therefore, one can find the integral representation (3.100) for an arbitrary incident field, as long as the associated radiated field does not become singular[17]. To represent an arbitrary incident field by (3.100), the key task is to identify the associated purely *radiated* field. The coefficients $\alpha_{smn}^{(4)}$ of the spherical wave expansion of the associated radiated field are related to the expansion coefficients $\alpha_{smn}^{(1)}$ of the incident field by $\alpha_{smn}^{(4)} = 1/2\, \alpha_{smn}^{(1)}$. Once the associated radiated fields $\boldsymbol{E}_{\mathrm{rad}}$, $\boldsymbol{H}_{\mathrm{rad}}$ are found, the pseudo currents $\tilde{\boldsymbol{J}}$, $\tilde{\boldsymbol{M}}$ for (3.100) are easily obtained — they correspond to any currents (e.g., the Love currents $\tilde{\boldsymbol{J}} = \boldsymbol{n}_1 \times \boldsymbol{H}_{\mathrm{rad}}$, $\tilde{\boldsymbol{M}} = -\boldsymbol{n}_1 \times \boldsymbol{E}_{\mathrm{rad}}$) which generate the radiated fields if evaluated with the "−"-type Green's functions.

3.8. Scattered Fields

The total fields in a scattering scenario are neither purely radiated fields nor purely absorbed fields nor purely incident fields, and, therefore, must be described by a combination of inward- and outward-traveling waves or a combination of incident fields and outward-traveling waves, respectively (the surface integrals on both surfaces S_1 and S_2 must be evaluated to find the correct total fields in V independent of which type of Green's functions ("−", "+", or "(0)") is used.). If the outward-traveling parts of the total fields depend linearly on the incident fields (or alternatively the inward-traveling fields) then the outward-traveling portion of the total field is called *scattered field*[18].

---

[17] Notice, that the associated purely radiated field of an incident plane wave does not have a convergent spherical wave expansion (the coefficients grow with increased mode number). However, an arbitrarily close approximation of the plane wave by finitely many spherical waves can be expressed by (3.100) in any finite observation volume.

[18] The term *scattered fields* is used in a really broad sense, here. It includes all scenarios, where the outward-traveling fields depend linearly on the incident fields. For example, this definition includes "active" scattered fields, where the total field has a time averaged power flow toward the external volume V_{ext}. If the inward- and outward-traveling fields are independent from each other, one would not speak of scattered fields, however.

Using the terminology of [Hansen 1988, pp. 46ff.], a description which splits the total fields as

$$\boldsymbol{E}_{\mathrm{tot}} = \boldsymbol{E}_{\mathrm{inc}} + \boldsymbol{E}_{\mathrm{sca}} \tag{3.110}$$

into an incident field $\boldsymbol{E}_{\mathrm{inc}}$ and a scattered field $\boldsymbol{E}_{\mathrm{sca}}$ is called *source scattering* description. The (purely radiating) scattered fields $\boldsymbol{E}_{\mathrm{sca}}$ are linearly related to the *incident* fields $\boldsymbol{E}_{\mathrm{inc}}$ in this description. Sometimes a different description is used relating the outward-traveling portion of the total fields to the inward-traveling portion $\boldsymbol{E}_{\mathrm{inw}}$ of the incident fields[19]. This description is called *classical scattering* description and it splits the total field according to

$$\boldsymbol{E}_{\mathrm{tot}} = \boldsymbol{E}_{\mathrm{inw}} + \boldsymbol{E}'_{\mathrm{sca}}\,. \tag{3.111}$$

The scattered fields $\boldsymbol{E}_{\mathrm{sca}}$ of the source scattering description differ from the scattered fields $\boldsymbol{E}'_{\mathrm{sca}}$ of the classical scattering description because the latter also includes the outward-traveling portion of the incident fields (this leads to the counter intuitive situation that one must include scattered fields for free-space in the classical scattering description).

3.8.1. Scattering Dyadics

For the formal analysis of the scattering scenario in terms of current representations of the fields, consider the scattering scenario in Fig. 3.4. Some incident field $\boldsymbol{E}_{\mathrm{inc}}$ impinges a scattering object which is totally enclosed by the surface S_1. Equivalent surface currents $\boldsymbol{J}_1$, $\boldsymbol{M}_1$ account for the scattered field. Any incident field can be expressed solely by equivalent surface currents $\boldsymbol{J}_2$, $\boldsymbol{M}_2$ on the outer surface S_2 (which may be moved to infinity, e.g., for a plane wave excitation), while the scattered fields are described by equivalent currents $\boldsymbol{J}_1$, $\boldsymbol{M}_1$ on the inner surface S_1. We thus have for the total electric field in V

$$\begin{aligned}\boldsymbol{E}_{\mathrm{tot}}(\boldsymbol{r}) =& \boldsymbol{E}_{\mathrm{sca}}(\boldsymbol{r}) + \boldsymbol{E}_{\mathrm{inc}}(\boldsymbol{r}) & (3.112)\\ =& \oiint\limits_{S_1} \left[\mathcal{G}^{-}_{ME}(\boldsymbol{r}',\boldsymbol{r}) \cdot \boldsymbol{M}_1(\boldsymbol{r}') + \mathcal{G}^{-}_{JE}(\boldsymbol{r}',\boldsymbol{r}) \cdot \boldsymbol{J}_1(\boldsymbol{r}')\right] \mathrm{d}a' \\ &+ \oiint\limits_{S_2} \left[\mathcal{G}^{-}_{ME}(\boldsymbol{r}',\boldsymbol{r}) \cdot \boldsymbol{M}_2(\boldsymbol{r}') + \mathcal{G}^{-}_{JE}(\boldsymbol{r}',\boldsymbol{r})\, \boldsymbol{J}_2(\boldsymbol{r}')\right] \mathrm{d}a'. & (3.113)\end{aligned}$$

According to their definition, the scattered fields must depend linearly on the incident fields (which are uniquely defined by the their tangential components on S_1). Consequently, the tangential fields $\boldsymbol{n} \times \boldsymbol{E}_{\mathrm{sca}}$ and $\boldsymbol{n} \times \boldsymbol{H}_{\mathrm{sca}}$ of the scattered fields depend linearly on the tangential fields $\boldsymbol{n} \times \boldsymbol{E}_{\mathrm{inc}}$ and $\boldsymbol{n} \times \boldsymbol{H}_{\mathrm{inc}}$ of the incident fields. Therefore, it is always possible to express the tangential components of the scattered fields with the help of scattering dyadics $\mathcal{S}_{EJ}(\boldsymbol{r},\boldsymbol{r}')$, $\mathcal{S}_{EM}(\boldsymbol{r},\boldsymbol{r}')$, $\mathcal{S}_{HJ}(\boldsymbol{r},\boldsymbol{r}')$, and $\mathcal{S}_{HM}(\boldsymbol{r},\boldsymbol{r}')$ in the manner of[20] [Saxon 1955; Martin 1995; Martin

---

[19] Notice the subtle difference between $\boldsymbol{E}_{\mathrm{inc}}$ and $\boldsymbol{E}_{\mathrm{inw}}$. While $\boldsymbol{E}_{\mathrm{inc}}$ denotes the complete incident field — including equal inwardly and outwardly traveling parts — the field $\boldsymbol{E}_{\mathrm{inw}}$ denotes only the inwardly traveling portion of the incident field.

[20] The here employed form of the scattering dyadics in terms of surface integrals is not commonly found in the literature. More common are scattering dyadics in volume integrals [Martin 1995; Martin 1998] or modal expansions of the scattering dyadic in form of spherical modes [Waterman 1965; Hansen 1988] or plane waves [Neitz 2020].

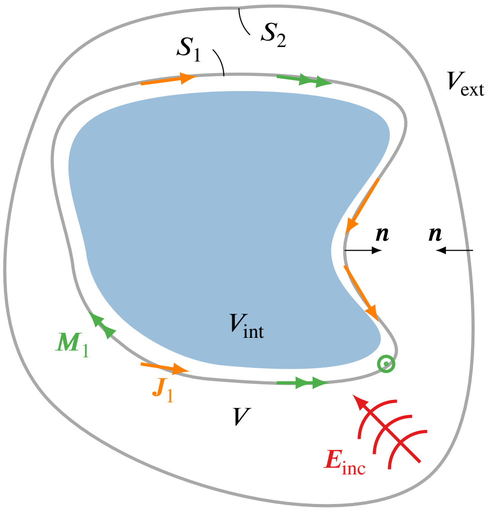

Fig. 3.4.: The scattered fields in V are expressed by the scattering currents $\boldsymbol{J}_1$ and $\boldsymbol{M}_1$ which depend linearly on the incident field.

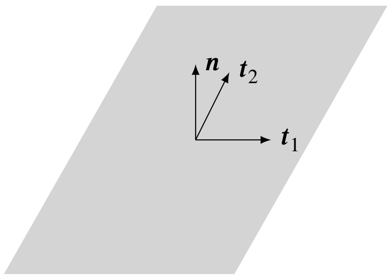

Fig. 3.5.: Small surface element with normal vector $\boldsymbol{n}$ and two orthogonal tangential vectors $\boldsymbol{t}_1$ ans $\boldsymbol{t}_2$.

1998; Korotkova 2007]

$$\boldsymbol{n} \times \boldsymbol{H}_{\mathrm{sca}}(\boldsymbol{r})\Big|_{\boldsymbol{r}\in S_1} = \oiint\limits_{S_1} \left[\mathcal{S}_{EJ}\left(\boldsymbol{r},\boldsymbol{r}'\right) \cdot \boldsymbol{E}_{\mathrm{inc}}\left(\vec{r}'\right) + \mathcal{S}_{HJ}\left(\boldsymbol{r},\boldsymbol{r}'\right) \cdot \boldsymbol{H}_{\mathrm{inc}}\left(\vec{r}'\right)\right] \mathrm{d}a' \tag{3.114}$$

and

$$-\boldsymbol{n} \times \boldsymbol{E}_{\mathrm{sca}}(\boldsymbol{r})\Big|_{\boldsymbol{r}\in S_1} = \oiint\limits_{S_1} \left[\mathcal{S}_{EM}\left(\boldsymbol{r},\boldsymbol{r}'\right) \cdot \boldsymbol{E}_{\mathrm{inc}}\left(\vec{r}'\right) + \mathcal{S}_{HM}\left(\boldsymbol{r},\boldsymbol{r}'\right) \cdot \boldsymbol{H}_{\mathrm{inc}}\left(\vec{r}'\right)\right] \mathrm{d}a' , \tag{3.115}$$

where the scattering dyadics $\mathcal{S}_{EJ}$, $\mathcal{S}_{HJ}$, $\mathcal{S}_{EM}$, and $\mathcal{S}_{HM}$ do not contain any components along the surface normal $\boldsymbol{n}$ but relate the tangential currents to tangential fields only. In general, the scattered field response $-\boldsymbol{n} \times \boldsymbol{E}_{\mathrm{sca}}(\boldsymbol{r})\big|_{\boldsymbol{r}\in S_1}$ and $\boldsymbol{n} \times \boldsymbol{H}_{\mathrm{sca}}(\boldsymbol{r})\big|_{\boldsymbol{r}\in S_1}$ at the location $\boldsymbol{r} \in S_1$ can depend on the incident field at all locations of the surface S_1 simultaneously and is not limited to depend on the incident field at the location $\boldsymbol{r}$, thus, the use of a second spatial variable $\boldsymbol{r}'$ for the incident fields in (3.114) and (3.115).

Referring to Fig. 3.5 for a clarification of the orientation of the respective vectors, the dyadics have the form

$$\mathcal{S}_{EJ}\left(\boldsymbol{r},\boldsymbol{r}'\right) = \sum_{k=1}^{2}\sum_{\ell=1}^{2} s_{k,\ell}^{(EJ)}\left(\boldsymbol{r},\boldsymbol{r}'\right)\, \boldsymbol{t}_k(\boldsymbol{r})\, \boldsymbol{t}_\ell\left(\boldsymbol{r}'\right) , \tag{3.116}$$

$$\mathcal{S}_{HJ}\left(\boldsymbol{r},\boldsymbol{r}'\right) = \sum_{k=1}^{2}\sum_{\ell=1}^{2} s_{k,\ell}^{(HJ)}\left(\boldsymbol{r},\boldsymbol{r}'\right)\, \boldsymbol{t}_k(\boldsymbol{r})\, \boldsymbol{t}_\ell\left(\boldsymbol{r}'\right) , \tag{3.117}$$

$$\mathcal{S}_{EM}\left(\boldsymbol{r},\boldsymbol{r}'\right) = \sum_{k=1}^{2}\sum_{\ell=1}^{2} s_{k,\ell}^{(EM)}\left(\boldsymbol{r},\boldsymbol{r}'\right)\, \boldsymbol{t}_k(\boldsymbol{r})\, \boldsymbol{t}_\ell\left(\boldsymbol{r}'\right) , \tag{3.118}$$

and

$$\boldsymbol{\mathcal{S}}_{HM}(\boldsymbol{r},\boldsymbol{r}') = \sum_{k=1}^{2}\sum_{\ell=1}^{2} s_{k,\ell}^{(HM)}(\boldsymbol{r},\boldsymbol{r}')\ \boldsymbol{t}_k(\boldsymbol{r})\,\boldsymbol{t}_\ell(\boldsymbol{r}')\ , \tag{3.119}$$

where $s_{k,\ell}^{(EJ)}(\boldsymbol{r},\boldsymbol{r}')$, $s_{k,\ell}^{(HJ)}(\boldsymbol{r},\boldsymbol{r}')$, $s_{k,\ell}^{(EM)}(\boldsymbol{r},\boldsymbol{r}')$, and $s_{k,\ell}^{(HM)}(\boldsymbol{r},\boldsymbol{r}')$ are scalar scattering functions relating the $\boldsymbol{t}_\ell$-field component at $\boldsymbol{r}'$ to the $\boldsymbol{t}_k$-current component at $\boldsymbol{r}$. As the tangential components of the scattered fields $\boldsymbol{n}\times\boldsymbol{H}_{\text{sca}} = \boldsymbol{J}_{\text{sca}}$ and $-\boldsymbol{n}\times\boldsymbol{E}_{\text{sca}} = \boldsymbol{M}_{\text{sca}}$ can be identified with the equivalent Love currents, the scattering dyadics express the linear relationship between the incident field and the scattering currents on the scatterer [21]. The scattering dyadics are analogous to the spherical wave source scattering matrices and completely characterize the scattering behavior of the object under consideration. However, they are usually not known explicitly for even moderately complicated scattering geometries but one can find some helpful properties from general considerations.

Reciprocity can be directly incorporated into the dyadics by assuming symmetry[22]. We have

$$s_{k,\ell}^{(AB)}(\boldsymbol{r},\boldsymbol{r}') = s_{\ell,k}^{(AB)}(\boldsymbol{r}',\boldsymbol{r}) \tag{3.120}$$

with indices $k,\ell \in \{1,2\}$, $A \in \{E,H\}$, and $B \in \{J,M\}$ — or in short

$$\boldsymbol{\mathcal{S}}_{AB}(\boldsymbol{r},\boldsymbol{r}') = \boldsymbol{\mathcal{S}}_{AB}^{\mathrm{T}}(\boldsymbol{r}',\boldsymbol{r}) \tag{3.121}$$

such that every dyad $\boldsymbol{\mathcal{S}}_{AB}$ is completely defined by three scalar functions $s_{1,1}^{(AB)}(\boldsymbol{r},\boldsymbol{r}')$, $s_{1,2}^{(AB)}(\boldsymbol{r},\boldsymbol{r}')$, $s_{2,2}^{(AB)}(\boldsymbol{r},\boldsymbol{r}')$, respectively. On a PEC scatterer $\boldsymbol{\mathcal{S}}_{EM} = \boldsymbol{\mathcal{S}}_{MH} = \boldsymbol{0}$ and analogously, $\boldsymbol{\mathcal{S}}_{EM} = \boldsymbol{\mathcal{S}}_{JH} = \boldsymbol{0}$ on a perfect magnetically conducting (PMC) scatterer.

3.8.2. Spherical Wave Scattering Matrix

The scattering dyadics can be expanded into spherical field modes. Often, the total electric field in the vicinity of a scatterer is then expressed by the classical scattering representation

$$\boldsymbol{E}_{\text{tot}} = k\sqrt{Z_{\mathrm{F}}}\sum_{s=1}^{2}\sum_{n=1}^{N}\sum_{m=-n}^{n}\left(\alpha_{smn}^{(3)}\boldsymbol{F}_{smn}^{(3)} + \alpha_{smn}^{(4)}\boldsymbol{F}_{smn}^{(4)}\right) \tag{3.122}$$

as the sum of inward- and outward-traveling waves[23] (as opposed to a sum of *incident* and outward-traveling waves).

---

[21] In this work, a form of the scattering dyadics is used which relates both types of incident fields (i.e., electric and magnetic) to both types of scattering currents (i.e., electric and magnetic). Note, however, that the incident magnetic field is the curl of the incident electric field, thus, it would also be possible to define scattering dyadics which only depend on the incident electric field (and its curl). Similarly, only equivalent electric currents are sufficient to represent all possible scattered fields such that in principle, the complete scattering can be characterized by a single scattering dyadic $\boldsymbol{\mathcal{S}}_{JE}$.

[22] If one works with all four types of scattering dyadics, symmetry is not required for the individual dyadics but can be ensured by suitable combinations of dyadics. It is, however, convenient (and necessary if only one type of dyadics is used in the formal description) to have symmetric scattering dyadics.

[23] Formally, this summation must be carried out over infinitely many modes ($N \to \infty$). However, for all practical purposes to represent the fields with any desired accuracy, the summation may be truncated at a finite N (this means that extremely superdirective effects are neglected). See Chapter 4 for details.

The linear relationship between the coefficients $\alpha_{smn}^{(4)}$ of the outward-traveling waves and the coefficients $\alpha_{smn}^{(3)}$ of the inward-traveling fields may be formally expressed by [Montgomery 1948, pp. 322ff.], [Hansen 1988, pp. 27 ff.]

$$\boldsymbol{\alpha}^{(4)} = \boldsymbol{S}\,\boldsymbol{\alpha}^{(3)}\,, \tag{3.123}$$

where $\boldsymbol{\alpha}^{(4)} \in \mathbb{C}^{2N(N+2)\times 1}\,\sqrt{\mathrm{W}}$ is the vector storing the coefficients of the outward-traveling waves, $\boldsymbol{\alpha}^{(3)} \in \mathbb{C}^{2N(N+2)\times 1}\,\sqrt{\mathrm{W}}$ is the vector storing the coefficients if the inward-traveling and $\boldsymbol{S} \in \mathbb{C}^{2N(N+2)\times 2N(N+2)}$ is the classical scattering matrix. The eigenvalues of the classical scattering matrix of a passive scatterer are always smaller or equal than one, such that the outward-traveling waves carry at most the same power as the inward traveling waves, i.e., $\|\boldsymbol{\alpha}^{(4)}\|_2^2 \leq \|\boldsymbol{\alpha}^{(3)}\|_2^2$ for a passive scatterer. Lossless scattering is characterized by a unitary scattering matrix, i.e., $\boldsymbol{S}^{\mathrm{H}}\boldsymbol{S} = \mathbf{1}$ with the unit matrix $\mathbf{1}$ [Montgomery 1948, pp. 323ff.]. No net power is generated or absorbed in either of the volumes V_{int} or V_{ext} in this case. purely incident fields consist of equal coefficients for inward-and outward-traveling waves (because of $\mathrm{z}_n^{(1)} = (\mathrm{z}_n^{(3)} + \mathrm{z}_n^{(4)})/2$), and we have $\boldsymbol{\alpha}^{(4)} = \boldsymbol{\alpha}^{(3)}$ for free-space and the "scattering" matrix of empty space (really denoting the absence of scattering here) is the unit matrix.

In the source scattering description (which is more closely related to the scattering dyadics from the previous section) the total electric field is expressed by [Yaghjian 1977], [Hansen 1988, pp. 46ff.]

$$\boldsymbol{E}_{\mathrm{tot}} = k\sqrt{Z_{\mathrm{F}}}\sum_{s=1}^{2}\sum_{n=1}^{N}\sum_{m=-n}^{n}\left(\alpha'^{(1)}_{smn}\boldsymbol{F}^{(1)}_{smn} + \alpha'^{(4)}_{smn}\boldsymbol{F}^{(4)}_{smn}\right) \tag{3.124}$$

as a linear combination of incident fields ($c = 1$) and outward-traveling fields ($c = 4$). Of course the coefficients $\alpha'^{(4)}_{smn}$ are different from the coefficients $\alpha^{(4)}_{smn}$ because the incident fields $\alpha'^{(1)}_{smn}$ in (3.124) also contain an outward-traveling part int contrast to the purely inward-traveling waves $\alpha^{(3)}_{smn}$ in (3.122). For (3.122) and (3.124) to be equal, one must have

$$\frac{1}{2}\alpha'^{(1)}_{smn} + \alpha'^{(4)}_{smn} = \alpha^{(4)}_{smn} \tag{3.125}$$

and

$$\frac{1}{2}\alpha'^{(1)}_{smn} = \alpha^{(3)}_{smn} \tag{3.126}$$

for all combinations of s, m, and n.

One can use the source scattering matrix[24] $\boldsymbol{S}' \in \mathbb{C}^{[2N(N+2)]\times[2N(N+2)]}$ to describe the linear relation [Yaghjian 1977]

$$\boldsymbol{\alpha}'^{(4)} = \boldsymbol{S}'\,\boldsymbol{\alpha}'^{(1)} \tag{3.127}$$

between the coefficients of the incident field stored in the vector $\boldsymbol{\alpha}'^{(1)} \in \mathbb{C}^{2N(N+2)\times 1}\,\sqrt{\mathrm{W}}$ and the coefficients of the outward-traveling waves stored in the vector $\boldsymbol{\alpha}'^{(4)} \in \mathbb{C}^{2N(N+2)\times 1}\,\sqrt{\mathrm{W}}$. The source scattering matrix is related to the classical scattering matrix by [Hansen 1988, p. 46]

$$\boldsymbol{S}' = \frac{1}{2}\left(\boldsymbol{S} - \mathbf{1}\right)\,. \tag{3.128}$$

---

[24] See [Hansen 1988, pp. 46ff.] for details about the differences between the descriptions involving $\boldsymbol{S}$ and $\boldsymbol{S}'$.

3.9. Chapter Summary

In this chapter, the fields in the environment of an antenna have been described in terms of spherical waves or alternatively by equivalent surface currents on the boundary of the observation volume V. By using different types of dyadic Green's functions — which are not commonly encountered in the literature about classical electrodynamics — one can characterize and express purely radiated, absorbed, or incident fields by equivalent sources only on the inner surface S_1 of the observation domain. Scattered fields have been described as a linear response to the incident fields in terms of scattering dyadics and spherical scattering matrices. The description of the fields in terms of spherical field modes is similar to the derivations which can be found in the corresponding textbooks [Hansen 1988]. The description of the fields in terms of equivalent current densities in this thesis is different from usual approaches. The general theorems have been adapted from existing literature [Collin 1990; Jin 2015] but Green's functions with an inward-traveling asymptotic boundary condition have not been ruled out in contrast to customary practice. In this way, purely radiated fields, purely absorbed fields, and even purely incident fields are described by sources only on the interior surface S_1 of the observation domain (and evaluated with the corresponding dyadic (pseudo) Green's functions). This completes the analogy between the field description in terms of equivalent surface currents and a spherical expansion (where purely absorbed and incident fields are prominently included by the corresponding field modes) of the field. The knowledge about the formal description of the various field types is needed for finding the characteristic transmit and receive fields of an antenna in later chapters.

4

Antennas

The transformation between guided waves and free-space fields taking place in an antenna is investigated in this chapter. Without loss of generality, the waveguide is oriented along the z-axis with guided waves propagating in positive z-direction exciting the antenna in transmit mode. The waveguide cross section at $z = 0$ is chosen as the reference plane. For simplicity, it is assumed that all but one waveguide modes (i.e., the fundamental mode) are evanescent and that the antenna and the excitation source are matched to the characteristic impedance of the fundamental waveguide mode[1]. This implies that for the transmitting antenna only the forward-propagating fundamental mode is present on the waveguide. For the receiving antenna all modes but the backward-traveling fundamental waveguide mode can be neglected at the reference plane if the waveguide length is long enough to sufficiently attenuate the evanescent modes before reaching the reference plane.

It will be shown that the *transmitted fields*[2] are essentially bandlimited (i.e., they consist of a limited number of spherical modes) dependent on the size of the antenna. An equivalent description of the antenna transmit behavior is obtained by equivalent surface currents on a Huygens surface enclosing the antenna.

For receiving antennas, one may be interested in one of two aspects. First and most important is the question of how to determine the received signal for an arbitrary incident field. To find the received signal, the same equivalent surface currents as for the transmit case can be used to test any given incident field. Second, one may be interested in how the total field outside the antenna volume is affected by the presence of the antenna. Most incident fields are only partially

---

[1] Most of the statements in this chapter would still be true for a mismatched antenna, if the source impedance was power-matched to the apparent input impedance at the reference plane such that all power provided by the source is accepted by the transmitting antenna. However, the description of the waveguide fields is more complicated in this case. For instance, the received signal is no longer directly proportional to the coefficient of the backward-traveling wave. Forward- and backward-traveling modes are present on the waveguide for mismatched transmitting and receiving antennas and the reflections at the source impedance have to be taken into account to correctly determine the total field on the waveguide.

[2] While the term *radiated fields* may be used for any outward-traveling field as defined in the previous chapter, the term *transmitted field* means the specific field distribution generated by a certain antenna in transmit mode.

transformed into guided waves by the receiving antenna, some parts of the incident fields may be scattered back toward the external volume V_{ext}. The scattered fields are hard to determine, since the full antenna geometry has to be taken into account, but some information can be deduced for the received portion of the incident field. It is useful to split the incident fields into two parts. One part — called the *characteristic incident field*[3] — is transformed into the received signal at the antenna port and another part — called the *residual incident field* — does not contribute at all to the received signal[4].

4.1. Transmitting Antennas

In order to obtain a characterization of the transmit behavior of the antenna, consider the problem depicted in Fig. 4.1. A well defined guided mode on the waveguide is excited by impressing the mode currents on the closed surface[5] S_0. The mode excitation currents

$$\boldsymbol{J}_0(x, y) = \boldsymbol{e}_z \times \boldsymbol{H}_{0\text{t}}(x, y, 0) \tag{4.1}$$

and

$$\boldsymbol{M}_0(x, y) = -\boldsymbol{e}_z \times \boldsymbol{E}_{0\text{t}}(x, y, 0) \tag{4.2}$$

correspond to the transversal fields $\boldsymbol{E}_{0\text{t}}(x, y, 0)$, $\boldsymbol{H}_{0\text{t}}(x, y, 0)$ of the fundamental waveguide mode discussed in Chapter 2. The guided wave is transformed into the transmitted fields $\boldsymbol{E}_{\text{tra}}$, $\boldsymbol{H}_{\text{tra}}$ in the volume V. The transmit fields consist only of pure radiated fields but the particular field distribution depends on the antenna geometry and it is inconvenient to solve Maxwell's equations for the complicated structure for every evaluation of the transmit fields.

4.1.1. Expressing the Transmit Fields by Currents on a Huygens Surface

It is more convenient to express the transmit fields in the volume V by equivalent free-space currents. Because every radiated field can be expressed by surface currents on S_1 alone — no currents are needed on S_2 when the fields are evaluated with the "–" type Green's functions (see Section 3.4) — it is clear that there exist some surface currents $\boldsymbol{J}_{\text{tra}}$, $\boldsymbol{M}_{\text{tra}}$ on the Huygens surfaces S_1 in Fig. 4.2 which generate exactly the transmitted fields of the antenna. One can see from (3.28) and (3.29) that for example the equivalent so-called Love currents $\boldsymbol{J}_{\text{tra}} = \boldsymbol{n} \times \boldsymbol{H}_{\text{tra}}$, $\boldsymbol{M}_{\text{tra}} = -\boldsymbol{n} \times \boldsymbol{E}_{\text{tra}}$ generate the desired transmit fields [Love 1901].

We have

$$\boldsymbol{E}_{\text{tra}} = \oiint\limits_{S_1} \left[\mathcal{G}_{JE}^{-}(\boldsymbol{r}, \boldsymbol{r}') \cdot \boldsymbol{J}_{\text{tra}}(\boldsymbol{r}') + \mathcal{G}_{ME}^{-}(\boldsymbol{r}, \boldsymbol{r}') \cdot \boldsymbol{M}_{\text{tra}}(\boldsymbol{r}')\right] \mathrm{d}a' \tag{4.3}$$

---

[3] The term *characteristic incident field* is used to denote the undistorted incident field. The total field in presence of the receiving antenna corresponding to the characteristic incident field is called *receive field*. The receive field is a purely absorbed field.

[4] The residual incident field can include an incident field portion which does not interact with the antenna at all.

[5] A closed surface S_0 is considered in order to have a well defined volume $V_{0,\text{int}}$ in which the power of the guided waves may be generated or consumed. Of course, the mode currents need only to be impressed in the reference plane at $z = 0$. No excitation currents are placed on other parts of S_0 which are located inside the PEC walls of the waveguide or in negative z-direction.

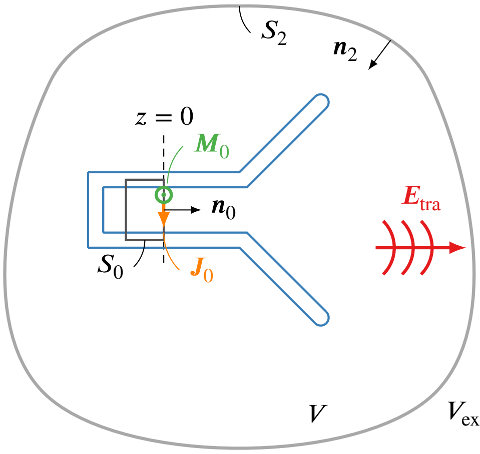

Fig. 4.1.: The transmitted fields in V are generated by impressing the modal currents $\boldsymbol{J}_0$ and $\boldsymbol{M}_0$ on S_0 for the fundamental guided mode. The whole antenna geometry must be considered.

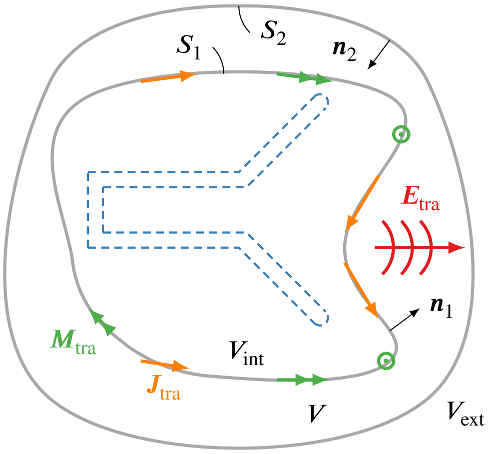

Fig. 4.2.: Equivalent problem with equivalent free-space currents impressed on S_1. No equivalent currents are needed on S_2 to evaluate the pure radiated fields with the "–"-type Green's functions.

and

$$\boldsymbol{H}_{\text{tra}} = \oiint_{S_1} \left[\mathcal{G}^{-}_{JH}(\boldsymbol{r}, \boldsymbol{r}') \cdot \boldsymbol{J}_{\text{tra}}(\boldsymbol{r}') + \mathcal{G}^{-}_{MH}(\boldsymbol{r}, \boldsymbol{r}') \cdot \boldsymbol{M}_{\text{tra}}(\boldsymbol{r}') \right] \mathrm{d}a' \,. \tag{4.4}$$

The complicated antenna geometry can be removed because the equivalent currents already define the fields in V appropriately, independent from the materials in V_{int}.

The equivalent surface currents are not unique, however. There exist infinitely many different distributions of electric and magnetic surface current densities $\boldsymbol{J}_{\text{tra}}$ and $\boldsymbol{M}_{\text{tra}}$ on the surface S_1, which produce the exact same fields $\boldsymbol{E}_{\text{tra}}$ and $\boldsymbol{H}_{\text{tra}}$ in V as the original sources [Rengarajan 2000; Yaghjian 2002], [Collin 1990, pp. 35ff.], [Jin 2015, p. 108], [Harrington 1961, pp. 106ff.]. Among these infinitely many surface current densities on S_1 which generate the same fields in V, there are surface current densities consisting of only electric currents or only magnetic currents [Martini 2008; Quijano 2010a; Schelkunoff 1936; Schelkunoff 1951] so the same fields can be expressed by electric or magnetic currents alone [Bladel 2007, pp. 320ff.]. This ambiguity immediately implies that there exist non-radiating surface current densities which do not generate any field in V. This non-uniqueness of the surface current representation of the fields in V does not impose a problem at the moment — any valid surface current density $\boldsymbol{J}_{\text{tra}}$ and $\boldsymbol{M}_{\text{tra}}$ may be used — but it will have implications for equivalent current based NFFFTs which will be discussed in Chapter 5.

Once suitable surface current densities $\boldsymbol{J}_{\text{tra}}$ and $\boldsymbol{M}_{\text{tra}}$ have been found, which represent the fields in V appropriately, many antenna characteristics can be readily derived from them. One may compute the FF radiation pattern, the radiated NF at any point of interest, the radiated power and so forth. The surface currents are particularly useful if they are normalized to the excitation power wave amplitude $a \in \sqrt{\mathrm{W}}$ at the antenna port. The normalized surface currents $\hat{\boldsymbol{J}}_{\text{tra}} = \boldsymbol{J}_{\text{tra}}/a$ and $\hat{\boldsymbol{M}}_{\text{tra}} = \boldsymbol{M}_{\text{tra}}/a$ can be used to determine the radiated fields per unit excitation, i.e., they may be used to determine the radiation efficiency or the gain of the antenna [Neitz 2017]. The unnormalized surface current densities $\boldsymbol{J}_{\mathrm{tra}}$ and $\boldsymbol{M}_{\mathrm{tra}}$ have units $[\boldsymbol{J}_{\mathrm{tra}}] = \mathrm{A/m}$ and $[\boldsymbol{M}_{\mathrm{tra}}] = \mathrm{V/m}$, respectively, and the units of the normalized surface currents are $[\hat{\boldsymbol{J}}_{\mathrm{tra}}] = 1/(\sqrt{\Omega}\,\mathrm{m})$ and $[\hat{\boldsymbol{M}}_{\mathrm{tra}}] = \sqrt{\Omega}/\mathrm{m}$.

4.1.2. Expressing the Transmit Fields by Spherical Vector Waves

The transmit behavior of the antenna can also be described in terms of a spherical wave expansion. The transmitted fields consist purely of outward-traveling waves and we have [Hansen 1988, p. 14]

$$\boldsymbol{E}_{\mathrm{tra}} = a\,k\sqrt{Z_0}\sum_{s=1}^{2}\sum_{n=1}^{\infty}\sum_{m=-n}^{n} \hat{\alpha}_{smn}^{(4),\mathrm{tra}} \boldsymbol{F}_{smn}^{(4)} \tag{4.5}$$

and

$$\boldsymbol{H}_{\mathrm{tra}} = a\,\mathrm{j}\,\frac{k}{\sqrt{Z_0}}\sum_{s=1}^{2}\sum_{n=1}^{\infty}\sum_{m=-n}^{n} \hat{\alpha}_{smn}^{(4),\mathrm{tra}} \boldsymbol{F}_{3-s,mn}^{(4)}\,, \tag{4.6}$$

where $a \in \mathbb{C}\sqrt{\mathrm{W}}$ is the excitation signal at the port and $\hat{\alpha}_{smn}^{(4),\mathrm{tra}} \in \mathbb{C}$ are the normalized expansion coefficients for the transmit fields outside the source volume V_{int} which is assumed to be a sphere for the spherical wave expansion.

The normalized expansion coefficients can be found from volume current densities $\boldsymbol{J}_{\mathrm{vol}}$ and $\boldsymbol{M}_{\mathrm{vol}}$ by [Hansen 1988, p. 333]

$$\hat{\alpha}_{smn}^{(4),\mathrm{tra}} = (-1)^{m+1} \iiint\limits_{V_1} \left[k\sqrt{Z_0}\,\boldsymbol{F}_{s,-m,n}^{(1)} \cdot \frac{\boldsymbol{J}_{\mathrm{vol}}}{a} - \mathrm{j}\frac{k}{\sqrt{Z_0}}\,\boldsymbol{F}_{3-s,-m,n}^{(1)} \cdot \frac{\boldsymbol{M}_{\mathrm{vol}}}{a} \right] \mathrm{d}a\,, \tag{4.7}$$

where a is the power wave amplitude which has been used to excite the currents in the volume. As the radiated fields in this thesis are usually expressed by equivalent surface current densities and not by volume current densities, it is intriguing to use the equation

$$\hat{\alpha}_{smn}^{(4),\mathrm{tra}} = (-1)^{m+1} \oint\!\!\!\oint\limits_{S_1} \left[k\sqrt{Z_0}\,\boldsymbol{F}_{s,-m,n}^{(1)} \cdot \hat{\boldsymbol{J}}_{\mathrm{tra}} - \mathrm{j}\frac{k}{\sqrt{Z_0}}\,\boldsymbol{F}_{3-s,-m,n}^{(1)} \cdot \hat{\boldsymbol{M}}_{\mathrm{tra}} \right] \mathrm{d}a \tag{4.8}$$

for calculating the coefficients from the normalized equivalent surface current densities $\hat{\boldsymbol{J}}_{\mathrm{tra}}$ and $\hat{\boldsymbol{M}}_{\mathrm{tra}}$. The surface current formulation (4.8) might be derived from (4.7) by considering a limiting process which confines the volume currents in a continuously decreasing volume, thus, approaching a surface current density in the limit. However, (4.8) can suffer from a resonance problem. The roots of $\boldsymbol{F}_{smn}^{(1)}$ lie on concentric spheres, due to the behavior of the spherical Bessel functions and its derivatives. The behavior of some spherical Bessel functions and their derivatives are depicted in Fig. 4.3 and Fig. 4.4. If the surface S_1 coincides with the spherical surface where a particular function $\boldsymbol{F}_{s,-m,n}^{(1)}$ is zero, then any finite and purely electric surface current density on S_1 leads to a zero coefficient $\hat{\alpha}_{smn}^{(4),\mathrm{tra}}$ according to (4.8) (and analogously for magnetic currents). Therefore, one cannot use (4.8) with arbitrary surface current densities on surfaces which show interior (electric or magnetic) resonances at the frequency of interest. The

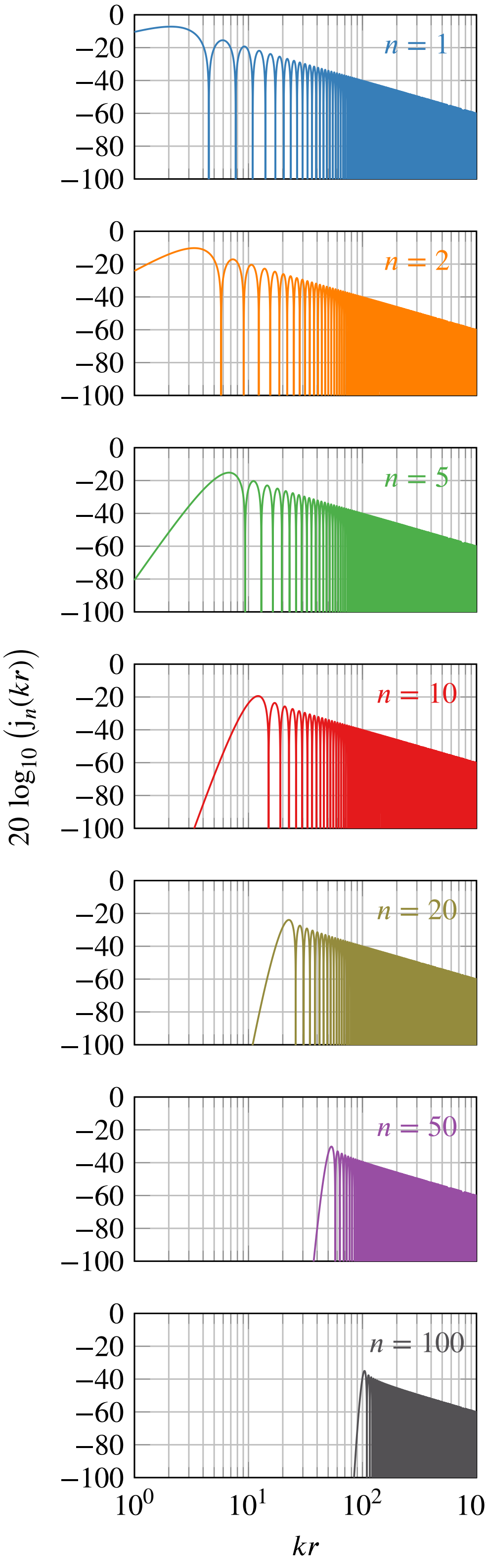

Fig. 4.3.: Behavior of the spherical Bessel functions of varying order.

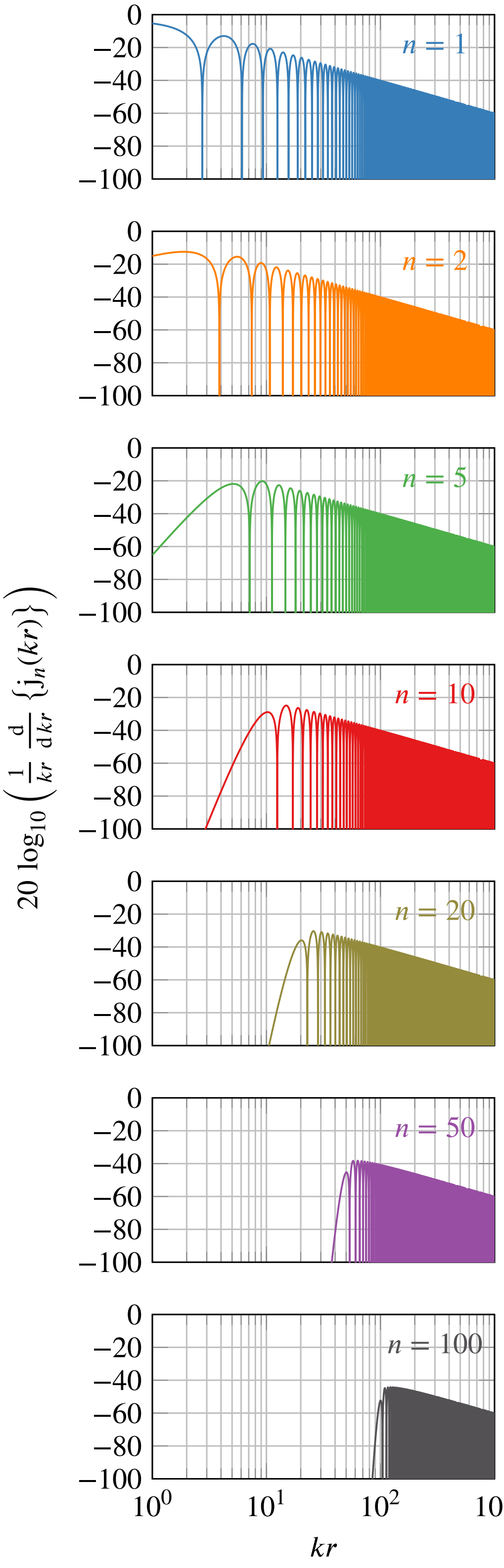

Fig. 4.4.: Behavior of the derivatives of spherical Bessel functions of varying order.

problem can be circumvented by using Love currents $\boldsymbol{J}_{\text{Love}} = \boldsymbol{n} \times \boldsymbol{H}_{\text{tra}}$ and $\boldsymbol{M}_{\text{Love}} = -\boldsymbol{n} \times \boldsymbol{E}_{\text{tra}}$ because either the magnetic or the electric part of the Love currents will always have a non-zero contribution to any given mode coefficient [Santiago 2019]. Alternatively, arbitrary (non-Love) surface current densities can still be used if the FFs

$$\hat{\boldsymbol{E}}_{\text{FF}}(\hat{\boldsymbol{k}}) = \frac{k}{4\pi} \oiint\limits_{S_1} \left[-\mathrm{j}\omega\mu \left(\mathbf{I} - \hat{\boldsymbol{k}}\hat{\boldsymbol{k}} \right) \mathrm{e}^{\mathrm{j}\boldsymbol{k}\cdot\boldsymbol{r}'} \cdot \hat{\boldsymbol{J}}_{\text{tra}}(\boldsymbol{r}') + \mathrm{j}\boldsymbol{k} \times \hat{\boldsymbol{M}}_{\text{tra}}(\boldsymbol{r}')\, \mathrm{e}^{\mathrm{j}\boldsymbol{k}\cdot\boldsymbol{r}'} \right] \mathrm{d}a' \tag{4.9}$$

from the equivalent surface currents are calculated first. The expansion coefficients

$$\hat{\alpha}_{smn}^{(4),\text{tra}} = (-1)^{s+m+n} \oiint \hat{\boldsymbol{E}}_{\text{FF}}(\hat{\boldsymbol{k}}) \cdot \boldsymbol{K}_{s,-m,n}^{(4)}(\hat{\boldsymbol{k}})\ \mathrm{d}\hat{\boldsymbol{k}} \tag{4.10}$$

are then found from the resulting FFs using convenient orthogonality relations[6].

Due to the orthogonality of the modes, the total power radiated by the transmit fields is the sum of the powers transported by each mode and we have $P_{\text{tra}} = 1/2 \sum_{smn} |a\, \hat{\alpha}_{smn}^{(4),\text{tra}}|^2$. Similar to the representation by surface current densities, the representation of the transmit fields by normalized expansion coefficients $\hat{\alpha}_{smn}^{(4),\text{tra}}$ contains all relevant information to determine relevant antenna parameters. The normalized fields (i.e., the fields per unit excitation) can readily be computed by setting $a = 1$ in (4.5) and (4.6). With the normalized expansion coefficients the radiation efficiency, the gain normalized FF pattern and so forth can easily be computed.

Apart from being useful as a characterization for the antenna parameters, the spherical wave expansion can be used as a powerful tool in the analysis of the transmitted fields. The spherical Bessel functions $\mathrm{j}_n(kr)$ and their derivatives $1/(kr)\,\mathrm{d}\left\{kr\,\mathrm{j}_n(kr)\right\}/(\mathrm{d}kr)$ appearing as radial dependencies of the spherical modes $\boldsymbol{F}_{smn}^{(1)}$ in (4.8) all show a characteristic behavior as can be seen in Fig. 4.3 and Fig. 4.4[7]. The values of the radial functions of different order n are negligible for small values of kr and become significant once kr reaches a critical value of about $kr \approx n$. With the $\boldsymbol{F}_{smn}^{(1)}$-functions having a low magnitude, the integral expressions in (4.8) become very small for current distributions $\hat{\boldsymbol{J}}_{\text{tra}}$, $\hat{\boldsymbol{M}}_{\text{tra}}$ with a bounded magnitude. Consequently, the $\hat{\alpha}_{smn}^{(4),\text{tra}}$ decrease rapidly for increasing mode orders.

The transmit fields of any finite sized antenna with minimum sphere radius r_0 can therefore effectively be expressed by a limited number of DoFs [Bucci 1987; Bucci 1989; Bucci 1991; Bucci 1998; Piestun 2000; Stupfel 2008; Hansen 2019]. Although formally, infinitely many field modes are needed for the field expansion in (4.5) and (4.6), it is sufficient in practice to limit the summation to mode indices $n = 1, \ldots, N$. Due to unavoidable measurement errors, e.g., by noise, the transmit fields can only be measured up to a certain accuracy. For all practical applications it is therefore sufficient to find an expression for the fields which is slightly more accurate than the measurements. In practice, the mode expansion of the radiated fields may be truncated at some $n = N$ with

$$N = \lfloor kr_0 \rfloor + n_{\text{buf}}, \tag{4.11}$$

---

[6] Inversely, the normalized transmit currents $\hat{\boldsymbol{J}}_{\text{tra}}$, $\hat{\boldsymbol{M}}_{\text{tra}}$ can always be found from known spherical expansion coefficients $\hat{\alpha}_{smn}^{(4),\text{tra}}$ by evaluating the fields on the hull surface S_1 (which is no longer required to be a sphere for the spatial equivalent current representation) via (4.5) and (4.6). The equivalent currents are then given by $\hat{\boldsymbol{J}}_{\text{tra}} = \boldsymbol{n}_1 \times \boldsymbol{H}_{\text{tra}}$ and $\hat{\boldsymbol{M}}_{\text{tra}} = \boldsymbol{E}_{\text{tra}} \times \boldsymbol{n}_1$.

[7] In this discussion, it is assumed that the surface S_1 does not lead to any resonance problems.

where r_0 is the radius of the minimum sphere around the antenna and some buffer n_{buf} may be chosen in the order of [Jensen 2004]

$$n_{\mathrm{buf}} = 0.045\, \sqrt[3]{kr_0}\, 10 \log_{10}\left(\frac{1}{\epsilon}\right) , \tag{4.12}$$

where

$$\epsilon = \frac{1}{2} \sum_{s=1}^{2} \sum_{n=N+1}^{\infty} \sum_{m=-n}^{n} \left| \hat{\alpha}_{smn}^{(4),\mathrm{tra}} \right|^2 \tag{4.13}$$

is the anticipated power of the neglected higher order modes (i.e., an estimate for the error of the truncated field expansion)[8].

4.1.3. Superdirectivity

The previous discussion may easily lead to the conclusion that the maximum directivity of an antenna pattern is directly limited by the antenna size and that higher directivities call for larger antennas [Chu 1948; Harrington 1960] , because the maximum directivity of an antenna is bound to the maximum mode number $n_{\max}$ by [Hansen 1988, pp. 55ff.]

$$D_{\max} = n_{\max}^2 + 2n_{\max} . \tag{4.14}$$

Theoretically, however, one can construct an antenna of finite size (minimum sphere radius r_0) which predominantly excites higher order modes with $n > r_0/k$ and arbitrary directivities can in principle be obtained with antennas of limited size [Oseen 1922; Schelkunoff 1943; Uzkov 1946; Harrington 1965; Salt 1977], [Hansen 2011a, pp. 181ff.]. To obtain this effect, the higher-order mode contribution in surface current densities must be several orders of magnitude larger than their lower-order counterparts to balance the effect of the vanishing magnitudes of $\boldsymbol{F}_{smn}^{(1)}$ for $n > r_0/k$ in (4.8). The higher-order mode currents generate large reactive fields in the direct proximity of the antenna which decay rapidly with increasing r until they reach the critical distance of around $kr \approx n$. The described behavior can be observed in Figs. 4.5 and 4.6, where the magnitudes of the functions $\mathrm{h}_n^{(2)}(kr)$ and $R_n = 1/(kr)\,\mathrm{d}\{kr\,\mathrm{h}_n^{(2)}(kr)\}/(\mathrm{d}kr)$ (i.e., the radial dependencies of the functions $\boldsymbol{F}_{smn}^{(4)}$) are plotted normalized to their value at $kr = 10$. It can be seen that the modes with $n \leq 10$ have approximately the same magnitude outside the distance $kr = 10$, while the higher order modes are further damped and result in several orders of magnitude weaker amplitudes at some distance away from the antenna.

Since the field patterns of such antennas exceeds the performance which is usually observed with an antenna of given size, these antennas are called *superdirective* antennas[9]. Strongly pronounced superdirective properties are rarely observed experimentally, however, because the

---

[8] Choosing the buffer in the order of $n_{\mathrm{buf}} = 10$ is good enough for an accuracy of better than −80 dB for the radiated fields of most antennas up to 100λ diameter [Hansen 1988, p. 21].

[9] If a strict distinction between superdirective and non-superdirective antennas is required, it can be found in terms of feasible modes per antenna radius r_0. For a given antenna with minimum sphere radius r_0, a spherical field mode may be called *feasible*, if its mode number $n \leq r_0/k$ and *unfeasible* otherwise. For a non-superdirective antenna, the fields in the region of interest can be expressed exclusively by feasible modes (up to the desired accuracy). If unfeasible modes are needed in the field expansion, the radiating antenna is superdirective. With this definition, a small amount of superdirectivity is allowed if the field expansion is truncated at a mode index $N = \lfloor kr_0 \rfloor + n_{\mathrm{buf}}$, slightly larger than the superdirectivity threshold $N = \lfloor kr_0 \rfloor$.

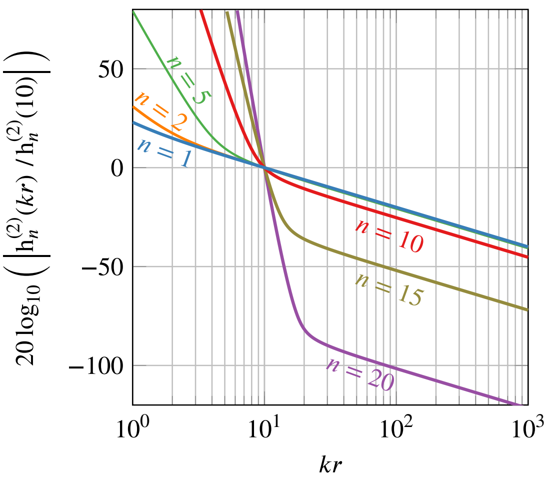

Fig. 4.5.: Radial dependence of the magnitude of the spherical Hankel functions of second kind of varying order normalized to their value at $kr = 10$. A similar plot can be found in [Hansen 1988, p. 18], but the graphs for the orders $n = 1$ and $n = 2$ have been added in this work.

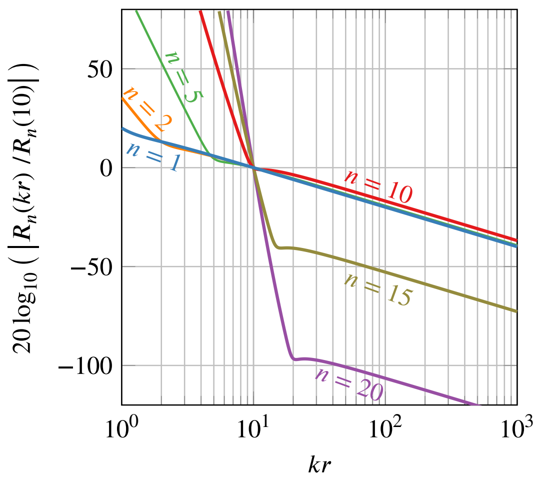

Fig. 4.6.: Radial dependence of the magnitude of the function $R_n = 1/(kr)\,\mathrm{d}\{kr\,\mathrm{h}_n^{(2)}(kr)\}/(\mathrm{d}kr)$ of varying order normalized to their value at $kr = 10$. A similar plot can be found in [Hansen 1988, p. 18], but the graphs for the orders $n = 1$ and $n = 2$ have been added in this work.

necessary current distributions in the antenna volume are extremely high in amplitude, very rapidly oscillating along the spatial coordinate, and extremely sensible to small variations [Yaru 1951; Hansen 1981; Cox 1986; Haskou 2017], [Hansen 2011a, p. 210]. The presence of losses or disturbances due to noise can easily break the strange but fragile superdirective behavior of the fields. Although playing a minor role in practical applications, superdirectivity effects are the cause of many problems in numerical algorithms.

Chapter 5 will reveal that superdirectivity effects can cause problems in NFFFTs because the reconstructed currents may have some contributions which barely generate observable fields on a measurement surface in some distance to the antenna.

4.2. Receiving Antennas

In the broad definition of Section 3.8, the term *scattering* applies to all changes of the incident field caused by induced currents in the antenna volume V_{int} or on its surface S_1. By this definition, also the receiving behavior of the antenna can be regarded as a form of (lossy) scattering. We have

$$\boldsymbol{E}_{\mathrm{tot}}(\boldsymbol{r}) = \boldsymbol{E}_{\mathrm{inc}}(\boldsymbol{r}) + \oiint\limits_{S_1} \left[\mathcal{G}_{JE}^{-}\left(\boldsymbol{r},\boldsymbol{r}'\right) \cdot \boldsymbol{J}_{\mathrm{sca}}\left(\boldsymbol{r}'\right) + \mathcal{G}_{ME}^{-}\left(\boldsymbol{r},\boldsymbol{r}'\right) \cdot \boldsymbol{M}_{\mathrm{sca}}\left(\boldsymbol{r}'\right)\right] \mathrm{d}a' \tag{4.15}$$

and analogous for the magnetic field. As discussed in Section 3.8, the scattering currents depend linearly on the incident field and can be expressed by

$$\boldsymbol{J}_{\mathrm{sca}}(\boldsymbol{r}) = \oiint\limits_{S_1} \left[\boldsymbol{\mathcal{S}}_{JE}(\boldsymbol{r},\boldsymbol{r}') \cdot \boldsymbol{E}_{\mathrm{inc}}(\boldsymbol{r}') + \boldsymbol{\mathcal{S}}_{JH}(\boldsymbol{r},\boldsymbol{r}') \cdot \boldsymbol{H}_{\mathrm{inc}}(\boldsymbol{r}')\right] \mathrm{d}a' \tag{4.16}$$

and

$$\boldsymbol{M}_{\mathrm{sca}}(\boldsymbol{r}) = \oiint\limits_{S_1} \left[\boldsymbol{\mathcal{S}}_{ME}(\boldsymbol{r},\boldsymbol{r}') \cdot \boldsymbol{E}_{\mathrm{inc}}(\boldsymbol{r}') + \boldsymbol{\mathcal{S}}_{MH}(\boldsymbol{r},\boldsymbol{r}') \cdot \boldsymbol{H}_{\mathrm{inc}}(\boldsymbol{r}')\right] \mathrm{d}a' \tag{4.17}$$

using the scattering dyadics $\boldsymbol{\mathcal{S}}_{JE}(\boldsymbol{r},\boldsymbol{r}')$, $\boldsymbol{\mathcal{S}}_{JH}(\boldsymbol{r},\boldsymbol{r}')$, $\boldsymbol{\mathcal{S}}_{ME}(\boldsymbol{r},\boldsymbol{r}')$, and $\boldsymbol{\mathcal{S}}_{MH}(\boldsymbol{r},\boldsymbol{r}')$, respectively. In the antenna receiving case, the incident fields $\boldsymbol{E}_{\mathrm{inc}}$, $\boldsymbol{H}_{\mathrm{inc}}$ are altered by the scattering currents $\boldsymbol{J}_{\mathrm{sca}}$, $\boldsymbol{M}_{\mathrm{sca}}$ such that a portion of the outward-traveling fields are canceled, leaving only their inward-traveling counterpart as a remainder (remember that pure incident fields contain equal parts of inward- and outward-traveling waves). As a result, the total fields $\boldsymbol{E}_{\mathrm{tot}}$, $\boldsymbol{H}_{\mathrm{tot}}$ produce a net power flow into the antenna volume V_{int}, which of course corresponds to the power of the received signal at the antenna port — parasitic losses are neglected at this point[10].

4.2.1. Calculating the Received Signal by Testing the Incident Field

Stressing the reciprocity relations, the received signal can be easily calculated if the transmit fields are known on a surface S_1 enclosing the antenna[11]. The starting point of the discussion is the equivalence between the situations depicted in Fig. 4.7 and Fig. 4.8. In Fig. 4.7, the (normalized) surface current densities $\hat{\boldsymbol{J}}_0$ and $\hat{\boldsymbol{M}}_0$ on the waveguide (corresponding to the wave traveling in positive z-direction, would generate the (normalized) transmit fields $\hat{\boldsymbol{E}}_{\mathrm{tra}}$ and $\hat{\boldsymbol{H}}_{\mathrm{tra}}$ see Section 4.1) on the one hand and the total fields $\boldsymbol{E}_{\mathrm{tot}}$ and $\boldsymbol{H}_{\mathrm{tot}}$ (with the scattering effects of the receiving antenna included) are generated by the (equivalent) volume current densities $\boldsymbol{J}_{\mathrm{ext}}$, $\boldsymbol{M}_{\mathrm{ext}}$ in the volume V_{ext} on the other hand. If no antenna would be present, the volume current densities $\boldsymbol{J}_{\mathrm{ext}}$, $\boldsymbol{M}_{\mathrm{ext}}$ would generate a purely incident field in the volume V. However, with the antenna being present, scattering at the antenna will change the field distribution in V. The whole antenna geometry is taken into account for the calculation of either the transmit fields $\hat{\boldsymbol{E}}_{\mathrm{tra}}$, $\hat{\boldsymbol{H}}_{\mathrm{tra}}$ from the currents $\hat{\boldsymbol{J}}_0$, $\hat{\boldsymbol{M}}_0$ or the total fields $\boldsymbol{E}_{\mathrm{tot}}$, $\boldsymbol{H}_{\mathrm{tot}}$ due to the currents $\boldsymbol{J}_{\mathrm{ext}}$, $\boldsymbol{M}_{\mathrm{ext}}$. We have the reciprocity relation [Jin 2015, pp. 101ff.], [Collin 1990, pp. 49f.], [Bladel 2007, p. 407]

$$\iint\limits_{S} \left(\hat{\boldsymbol{J}}_0 \cdot \boldsymbol{E}_{\mathrm{tot}} - \hat{\boldsymbol{M}}_0 \cdot \boldsymbol{H}_{\mathrm{tot}}\right) \mathrm{d}a = \iiint\limits_{V_{\mathrm{ext}}} \left(\boldsymbol{J}_{\mathrm{ext}} \cdot \hat{\boldsymbol{E}}_{\mathrm{tra}} - \boldsymbol{M}_{\mathrm{ext}} \cdot \hat{\boldsymbol{H}}_{\mathrm{tra}}\right) \mathrm{d}v\,, \tag{4.18}$$

where S is the cross section of the waveguide at $z = 0$ serving as reference plane for the waveguide modes.

---

[10] In general, the scattering at the antenna may be divided into structural scattering and reradiation. Reradiation happens, because of a mismatched load ($\Gamma \neq 0$). The received waveguide mode is partially reflected at the mismatched load, giving rise to a waveguide mode traveling in positive z-direction. This waveguide mode traveling in positive z-direction is transformed into a transmitted field by the antenna. Reradiation does not contribute to the received signal. Since only matched antennas ($\Gamma = 0$) are considered in this work, only structural scattering is of interest. In the following, if not stated otherwise, it is assumed that no forward-traveling wave exists on the antenna waveguide in receiving mode.

[11] This is true even if losses are considered.

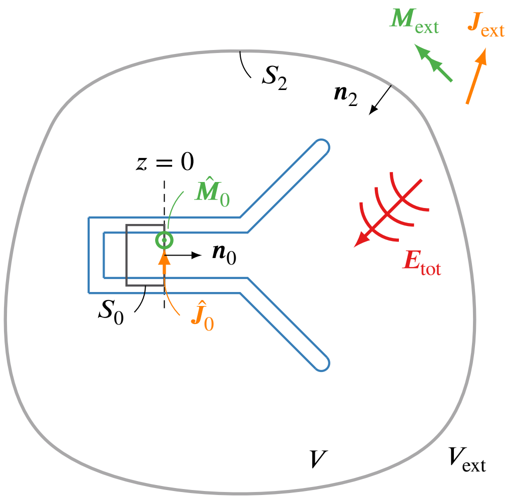

Fig. 4.7.: The total fields $\boldsymbol{E}_{\mathrm{tot}}$ generated by the currents $\boldsymbol{J}_{\mathrm{ext}}$ and $\boldsymbol{M}_{\mathrm{ext}}$ in presence of the complicated antenna geometry are tested with the normalized modal currents $\hat{\boldsymbol{J}}_0$, $\hat{\boldsymbol{M}}_0$ to find the received signal b.

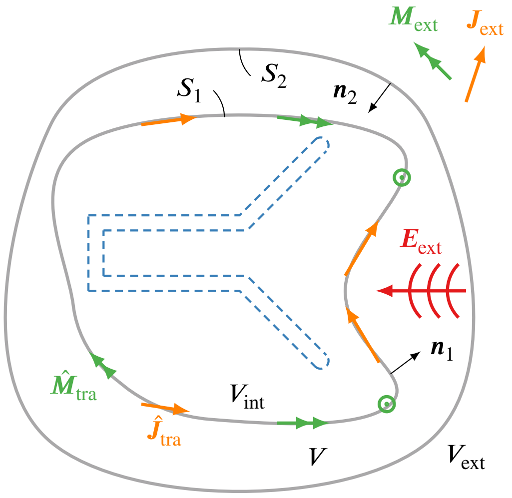

Fig. 4.8.: Equivalent problem with normalized equivalent free-space currents $\hat{\boldsymbol{J}}_{\mathrm{tra}}$ and $\hat{\boldsymbol{M}}_{\mathrm{tra}}$ testing the undistorted incident fields $\boldsymbol{E}_{\mathrm{ext}}$ on S_1. The antenna geometry is removed.

Due to the equivalence of the configurations in Fig. 4.7 and Fig. 4.8, the expression in (4.18) can be written as

$$\oiint_{S_1} \left(\hat{\boldsymbol{J}}_{\mathrm{tra}} \cdot \boldsymbol{E}_{\mathrm{ext}} - \hat{\boldsymbol{M}}_{\mathrm{tra}} \cdot \boldsymbol{H}_{\mathrm{ext}}\right) \mathrm{d}a = \iiint_{V_{\mathrm{ext}}} \left(\boldsymbol{J}_{\mathrm{ext}} \cdot \hat{\boldsymbol{E}}_{\mathrm{tra}} - \boldsymbol{M}_{\mathrm{ext}} \cdot \hat{\boldsymbol{H}}_{\mathrm{tra}}\right) \mathrm{d}v\,, \tag{4.19}$$

where $\boldsymbol{E}_{\mathrm{ext}}$, $\boldsymbol{H}_{\mathrm{ext}}$ are the undistorted free-space incident fields generated by $\boldsymbol{J}_{\mathrm{ext}}$ and $\boldsymbol{M}_{\mathrm{ext}}$.

From (2.42) it is known that the desired received signal b is obtained by testing[12] the total fields in a cross section S of the waveguide in the manner of

$$b = \frac{1}{2} \underbrace{\frac{1}{\iint_S \boldsymbol{e}_z \cdot \left(\hat{\boldsymbol{J}}_0 \times \hat{\boldsymbol{M}}_0\right) \mathrm{d}a}}_{c_{\mathrm{aut}}} \left[\iint_S \left(\hat{\boldsymbol{J}}_0 \cdot \boldsymbol{E}_{\mathrm{tot}} - \hat{\boldsymbol{M}}_0 \cdot \boldsymbol{H}_{\mathrm{tot}}\right) \mathrm{d}a\right], \tag{4.20}$$

where $\hat{\boldsymbol{J}}_0$, $\hat{\boldsymbol{M}}_0$ are the normalized mode excitation currents for the fundamental mode traveling in positive (!) z-direction and $\boldsymbol{E}_{\mathrm{tot}}$ and $\boldsymbol{H}_{\mathrm{tot}}$ are the total fields in the waveguide. The constant

$$c_{\mathrm{aut}} = \frac{1}{\iint_S \boldsymbol{e}_z \cdot \left(\hat{\boldsymbol{M}}_0 \times \hat{\boldsymbol{J}}_0\right) \mathrm{d}a} \tag{4.21}$$

---

[12] The procedure of generating a scalar quantity from a continuously distributed field by taking a weighted mean over the field in a certain domain is called *testing*, borrowing the terminology from the method of moments [Jin 2015, pp. 505ff.].

is independent of the incident field and can be regarded as an antenna gain calibration factor.

Since the right hand sides of (4.18) and (4.19) are identical, one finds that the received signal can also be computed by the much more convenient expression

$$b = \frac{c_{\text{aut}}}{2} \oiint\limits_{S_1} \left(\hat{\boldsymbol{J}}_{\text{tra}} \cdot \boldsymbol{E}_{\text{ext}} - \hat{\boldsymbol{M}}_{\text{tra}} \cdot \boldsymbol{H}_{\text{ext}} \right) \, \mathrm{d}a \,, \tag{4.22}$$

where the incident fields $\boldsymbol{E}_{\text{ext}}$, $\boldsymbol{H}_{\text{ext}}$ are tested with the normalized free-space surface currents $\hat{\boldsymbol{J}}_{\text{tra}}$ and $\hat{\boldsymbol{M}}_{\text{tra}}$. These are the same currents which are also used to characterize the transmit properties of the antenna.

All relevant properties of the receiving antenna required for determining the received signal can be found from the transmitting antenna by using reciprocity considerations[13].

However, the testing currents $\hat{\boldsymbol{J}}_{\text{tra}}$ and $\hat{\boldsymbol{M}}_{\text{tra}}$ must not be mistaken to account for the scattered fields in the vicinity of the antenna. In particular the total fields are not the sum of the incident fields $\boldsymbol{E}_{\text{ext}}$, $\boldsymbol{H}_{\text{ext}}$ and the fields $\hat{\boldsymbol{E}}_{\text{tra}}$, $\hat{\boldsymbol{H}}_{\text{tra}}$[14]. Determining the total field in the vicinity of the antenna is more complicated and the normalized currents $\hat{\boldsymbol{J}}_{\text{tra}}$ and $\hat{\boldsymbol{M}}_{\text{tra}}$ serve only as a calculation tool for the receive signal at this point but cannot be used to determine the resulting fields in the vicinity of the antenna.

4.2.2. Calculating the Received Signal in Terms of Spherical Wave Receiving Coefficients

A complete description of the total fields in the vicinity of a receiving antenna and on the waveguide connected to it may be given by extending the spherical source scattering description (3.124) to also include the waveguide modes [Hansen 1988, pp. 27ff.], [Yaghjian 1977]. We have

$$\begin{bmatrix} b \\ \boldsymbol{\alpha}'^{(4)} \end{bmatrix} = \begin{bmatrix} \Gamma & \left(\hat{\boldsymbol{\beta}}^{(1),\text{rec}}\right)^{\mathrm{T}} \\ \hat{\boldsymbol{\alpha}}^{(4),\text{tra}} & \boldsymbol{S}' \end{bmatrix} \begin{bmatrix} a \\ \boldsymbol{\alpha}'^{(1),\text{ext}} \end{bmatrix} . \tag{4.23}$$

The vectors $\boldsymbol{\alpha}'^{(1),\text{ext}}$ and $\boldsymbol{\alpha}'^{(4)}$ are the known vectors from Section 3.8 describing the total fields in the vicinity of the antenna and the vector $\hat{\boldsymbol{\alpha}}^{(4),\text{tra}} \in \mathbb{C}^{2N(N+2)\times 1}$ contains the normalized transmit coefficients known from Section 4.1. The reflection coefficient $\Gamma \in \mathbb{C}$ relates the backward-traveling wave on the waveguide to the forward-traveling wave. In this thesis, all antennas are assumed to be matched, i.e., $\Gamma = 0$. Finally, the vector $\hat{\boldsymbol{\beta}}^{(1),\text{rec}} \in \mathbb{C}^{2N(N+2)\times 1}$ contains the receiving coefficients $\hat{\beta}^{(1),\text{rec}}_{smn} \in \mathbb{C}$ relating the received signal b to the coefficients $\alpha'^{(1)}_{smn}$ of the incident field such that[15]

$$b = (\hat{\boldsymbol{\beta}}^{(1),\text{rec}})^{\mathrm{T}} \, \boldsymbol{\alpha}'^{(1),\text{ext}} = \sum_{s=1}^{2} \sum_{n=1}^{N} \sum_{m=-n}^{n} \hat{\beta}^{(1),\text{rec}}_{smn} \, \alpha'^{(1),\text{ext}}_{smn} \,. \tag{4.24}$$

---

[13] Since there is no incident field in the analysis of a transmitting antenna, the antenna scattering properties do not play any role for the transmitting case. Naturally, not all aspects of the receiving behavior of the antenna can be found from reciprocity considerations alone. No information about the residual scattering can be obtained from the transmitting case.

[14] Such a sum would be meaningless since the different terms of the sum have different units due to the normalization of $\hat{\boldsymbol{E}}_{\text{tra}}$ and $\hat{\boldsymbol{H}}_{\text{tra}}$.

[15] Formally, this summation must be carried out over infinitely many modes ($N \to \infty$). However,to represent the fields with any desired accuracy, the summation may be truncated at a finite N for all practical purposes (this means that extreme supergain effects are neglected).

The characteristic incident field is therefore characterized by the portion of the vector $\boldsymbol{\alpha}'^{(1),\mathrm{ext}}$, which is parallel to the receiving coefficient vector $\hat{\boldsymbol{\beta}}^{(1),\mathrm{rec}}$ (i.e., parallel with respect to the product $(\hat{\boldsymbol{\beta}}^{(1),\mathrm{rec}})^{\mathrm{T}}\,\boldsymbol{\alpha}'^{(1),\mathrm{ext}}$). The portion of $\boldsymbol{\alpha}'^{(1),\mathrm{ext}}$ which is orthogonal to $\hat{\boldsymbol{\beta}}^{(1),\mathrm{rec}}$ leads to residual scattering, not contributing to the received signal[16].

The receiving coefficients $\hat{\beta}_{smn}^{(1),\mathrm{rec}}$ are directly related to the transmit coefficients $\hat{\alpha}_{smn}^{(4),\mathrm{tra}}$. Using reciprocity on (4.22), it may be shown that testing the incident fields with the normalized currents $\hat{\boldsymbol{J}}_{\mathrm{tra}}$, $\hat{\boldsymbol{M}}_{\mathrm{tra}}$ on S_1 can be replaced by testing the incident fields with the normalized fields $\hat{\boldsymbol{E}}_{\mathrm{tra}}$, $\hat{\boldsymbol{H}}_{\mathrm{tra}}$ on a second surface S_2, where the surface S_2 is assumed to be spherical with radius r_2, such that the surface S_1 is completely enclosed by S_2 with inward-directed normal vector $\boldsymbol{n}_2$ (see Fig. 4.8). We have

$$\begin{aligned} b &= \frac{c_{\mathrm{aut}}}{2} \oiint\limits_{S_1} \left[\hat{\boldsymbol{J}}_{\mathrm{tra}} \cdot \boldsymbol{E}_{\mathrm{ext}} - \hat{\boldsymbol{M}}_{\mathrm{tra}} \cdot \boldsymbol{H}_{\mathrm{ext}}\right] \mathrm{d}a \\ &= \frac{c_{\mathrm{aut}}}{2} \oiint\limits_{S_2} \left[\hat{\boldsymbol{E}}_{\mathrm{tra}} \times \boldsymbol{H}_{\mathrm{ext}} - \boldsymbol{E}_{\mathrm{ext}} \times \hat{\boldsymbol{H}}_{\mathrm{tra}}\right] \cdot \boldsymbol{n}_2 \,\mathrm{d}a\,. \end{aligned} \tag{4.25}$$

Expanding the fields in (4.25) into spherical field modes leads to (see Appendix A)

$$b = \frac{c_{\mathrm{aut}}}{2} \sum_{s=1}^{2} \sum_{n=1}^{N} \sum_{m=-n}^{n} (-1)^m \,\hat{\alpha}_{s,-m,n}^{(4),\mathrm{tra}}\, \alpha'^{(1),\mathrm{ext}}_{smn}\,. \tag{4.26}$$

Due to the orthogonality of the incident field modes, the receiving coefficients $\hat{\beta}_{smn}^{(1),\mathrm{rec}}$ can by found by a term-by-term comparison of (4.24) with (4.26) and we have[17]

$$\hat{\beta}_{smn}^{(1),\mathrm{rec}} = \frac{c_{\mathrm{aut}}}{2} (-1)^m \,\hat{\alpha}_{s,-m,n}^{(4),\mathrm{tra}}\,. \tag{4.27}$$

4.2.3. Receive Scattering and the Characteristic Incident Fields

For a more detailed analysis of the total fields in the vicinity of the receiving antenna, it makes sense to separate the receive scattering from the other parts of the scattering, which might be called residual scattering. The scattering description with spherical waves in (4.23) suggests that only the portion of the incident field which has a coefficient vector $\boldsymbol{\alpha}'^{(1)}_{\parallel}$ parallel to $\hat{\boldsymbol{\beta}}^{(1),\mathrm{rec}}$ (with respect to the scalar product $(\hat{\boldsymbol{\beta}}^{(1),\mathrm{rec}})^{\mathrm{T}}\boldsymbol{\alpha}'^{(1),\mathrm{ext}}$) is responsible for the received signal, while the remaining portion of the incident field has a coefficient vector $\boldsymbol{\alpha}'^{(1)}_{\perp}$, which is perpendicular to the receiving vector $\hat{\boldsymbol{\beta}}^{(1),\mathrm{rec}}$ and does not contribute to the received signal.

It is therefore convenient, to split the incident field into two parts as (analogously for the magnetic field)

$$\boldsymbol{E}_{\mathrm{inc}} = b\,\hat{\boldsymbol{E}}_{\mathrm{cha}} + \boldsymbol{E}_{\mathrm{res}}\,, \tag{4.28}$$

where $b \in \mathbb{C}\sqrt{\mathrm{W}}$ is the received signal at the waveguide port of the antenna, $\hat{\boldsymbol{E}}_{\mathrm{cha}}$ is the normalized characteristic incident field responsible for the received signal, and $\boldsymbol{E}_{\mathrm{res}}$ is the residual incident

---

[16] Residual scattering may include incident fields which are not affected by the presence of the receiving antenna.

[17] The receiving coefficients differ from [Hansen 1988] by a factor of 1/2. This is because [Hansen 1988] uses the receiving coefficients with respect to inward-traveling waves ($c = 3$), while in this work the receiving coefficients are defined with respect to incident fields ($c = 1$).

field which has no influence at all on the received signal. The characteristic incident fields $\boldsymbol{E}_{\text{cha}}$, $\boldsymbol{H}_{\text{cha}}$ have a spherical wave expansion with the coefficients $\alpha'^{(1)}_{smn,\|}$ contained in the portion of the coefficient vector for the incident field which is parallel to the vector $\hat{\boldsymbol{\beta}}^{(1),\text{rec}}$. They are transformed into purely absorbed fields through scattering at the matched receiving antenna[18] [Montgomery 1948, p. 326]. If the antenna is lossless, the perfect receive fields are the only possible incident fields which are transformed into purely absorbed fields as the only absorption of a lossless antenna is due to reception. If the appropriately scaled characteristic fields are subtracted from an arbitrary incident field, the remaining residual fields $\boldsymbol{E}_{\text{res}}$, $\boldsymbol{H}_{\text{res}}$ are such that they will not produce any received signal when the receiving antenna is placed into them[19].

The scattering currents $\boldsymbol{J}_{\text{sca}}$, $\boldsymbol{M}_{\text{sca}}$ are split in the same manner into

$$\boldsymbol{J}_{\text{sca}} = b\,\hat{\boldsymbol{J}}_{\text{cha}} + \boldsymbol{J}_{\text{res}} \tag{4.29}$$

and

$$\boldsymbol{M}_{\text{sca}} = b\,\hat{\boldsymbol{M}}_{\text{cha}} + \boldsymbol{M}_{\text{res}}\,, \tag{4.30}$$

where the corresponding characteristic and residual scattering currents are given by

$$\hat{\boldsymbol{J}}_{\text{cha}}(\boldsymbol{r}) = \oiint\limits_{S_1} \left[\boldsymbol{\mathcal{S}}_{EJ}\left(\boldsymbol{r},\boldsymbol{r}'\right)\cdot\hat{\boldsymbol{E}}_{\text{cha}}\left(\boldsymbol{r}'\right) + \boldsymbol{\mathcal{S}}_{HJ}\left(\boldsymbol{r},\boldsymbol{r}'\right)\cdot\hat{\boldsymbol{H}}_{\text{cha}}\left(\boldsymbol{r}'\right)\right]\mathrm{d}a' \tag{4.31}$$

and

$$\boldsymbol{J}_{\text{res}}(\boldsymbol{r}) = \oiint\limits_{S_1} \left[\boldsymbol{\mathcal{S}}_{EJ}\left(\boldsymbol{r},\boldsymbol{r}'\right)\cdot\boldsymbol{E}_{\text{res}}\left(\boldsymbol{r}'\right) + \boldsymbol{\mathcal{S}}_{HJ}\left(\boldsymbol{r},\boldsymbol{r}'\right)\cdot\boldsymbol{H}_{\text{res}}\left(\boldsymbol{r}'\right)\right]\mathrm{d}a'\,, \tag{4.32}$$

respectively (analogous for the magnetic currents). The complete information about the changes of the field distribution in the proximity of the receiving antenna due to scattering for every given incident field is contained in the scattering dyadics $\boldsymbol{\mathcal{S}}_{EJ}\left(\boldsymbol{r},\boldsymbol{r}'\right)$, $\boldsymbol{\mathcal{S}}_{HJ}\left(\boldsymbol{r},\boldsymbol{r}'\right)$, $\boldsymbol{\mathcal{S}}_{EM}\left(\boldsymbol{r},\boldsymbol{r}'\right)$, and $\boldsymbol{\mathcal{S}}_{HM}\left(\boldsymbol{r},\boldsymbol{r}'\right)$. While all receiving antennas must produce some scattering currents $\hat{\boldsymbol{J}}_{\text{cha}}(\boldsymbol{r})$ for the characteristic incident field — the field must be altered such that a certain amount of power flows into the antenna — it is possible that certain residual incident fields do not cause any scattering currents at all. The antenna is practically invisible for these fields.

If no scattering currents appear on the antenna for all possible residual incident fields (i.e., incident fields, which produce a zero received signal at the receiving antenna port, do not produce any scattering currents on the antenna), the antenna is called a *minimum scattering* antenna [Montgomery 1948, pp. 329ff.]. The only possible scattering currents of a minimum scattering antenna are scaled versions of the characteristic receiving currents $\hat{\boldsymbol{J}}_{\text{rec}}$, $\hat{\boldsymbol{M}}_{\text{rec}}$.

Since the residual scattering does not contribute to the received signal, it is often neglected when receiving antennas are analyzed [20]. This does not lead to any problems in most cases, as

---

[18] If a mismatched load is connected to the waveguide at the reference plane, some portion of the backward-traveling fundamental mode will be reflected, which leads to reradiation.

[19] The residual fields do not cause any wave traveling on the waveguide attached to the antenna. For this reason, the residual fields do not cause any reradiation, even for a mismatched antenna.

[20] This can lead to unfortunate misconceptions such as the assumption that half of the incident power must be scattered by a receiving antenna [Balanis 2005, p.85]. This misconception has been the center of heated arguments in the past [Green 1966; de Hoop 1974; Van Bladel 2002; Collin 2003a; Andersen 2003; Love 2003; Collin 2003b; Su 2003; Pozar 2004; Geyi 2004; Van Bladel 2007; Best 2009; Kwon 2009; Alu 2010; Steyskal 2010; Schejbal 2011; Gustafsson 2012; Hoop 2013; Socher 2013; Socher 2015; Socher 2014; Štumpf 2016].

one is often not interested in the total fields in the environment of the receiving antenna but only in the signal which is received at the antenna port.

The remainder of this section covers the problem of finding the (normalized) characteristic incident fields $\hat{\boldsymbol{E}}_{\text{cha}}$, $\hat{\boldsymbol{H}}_{\text{cha}}$ and the corresponding receiving scattering currents $\hat{\boldsymbol{J}}_{\text{cha}}$, $\hat{\boldsymbol{M}}_{\text{cha}}$ for a given antenna[21]. Of course, the received fields are proportional to the received signal b and for convenience in the remainder of this section, all fields and currents are normalized to the wave amplitude $b \in \mathbb{C}\sqrt{\text{W}}$ of the backward-traveling field mode. The normalization will be denoted by a hat over the corresponding quantity. To avoid confusion, the resulting purely absorbed fields (i.e., the resulting fields with the receiving antenna present) will be denoted by $\hat{\boldsymbol{E}}_{\text{rec}}$, $\hat{\boldsymbol{H}}_{\text{rec}}$ (receive fields), whereas the corresponding characteristic incident fields (i.e., the unperturbed free-space fields without the antenna being present) are denoted by $\hat{\boldsymbol{E}}_{\text{cha}}$, $\hat{\boldsymbol{H}}_{\text{cha}}$.

The (normalized) characteristic incident fields $\hat{\boldsymbol{E}}_{\text{cha}}$, $\hat{\boldsymbol{H}}_{\text{cha}}$ and the corresponding (normalized) characteristic scattering currents $\hat{\boldsymbol{J}}_{\text{cha}}$, $\hat{\boldsymbol{M}}_{\text{cha}}$, which transform the incident fields into purely absorbed fields, are found in a two step procedure. In a first step, the resulting purely absorbed receive fields $\hat{\boldsymbol{E}}_{\text{rec}}$, $\hat{\boldsymbol{H}}_{\text{rec}}$ are found by solving Maxwell's equations for the situation depicted in Fig. 4.9. In a second step, the receive fields $\hat{\boldsymbol{E}}_{\text{rec}}$, $\hat{\boldsymbol{H}}_{\text{rec}}$ are represented by equivalent currents on the surfaces S_1 and S_2 as depicted in Fig. 4.10. In the representation using the conventional "$-$"-type Green's functions, the scattered fields are expressed only by the currents $\boldsymbol{J}_1$, $\boldsymbol{M}_1$ on S_1 (they correspond to the desired characteristic scattering currents), while the incident fields are due to the currents $\boldsymbol{J}_2$, $\boldsymbol{M}_2$ on S_2 (the fields generated by $\boldsymbol{J}_2$, $\boldsymbol{M}_2$ correspond to $\hat{\boldsymbol{E}}_{\text{rec}}$, $\hat{\boldsymbol{H}}_{\text{rec}}$, i.e., the characteristic incident fields of interest).

The desired solution for the purely absorbed receive fields $\hat{\boldsymbol{E}}_{\text{rec}}$, $\hat{\boldsymbol{H}}_{\text{rec}}$ can be found from the arrangement in Fig. 4.9 by enforcing the following boundary conditions on the surfaces S_0 and S_2. The tangential fields on S_0 must correspond to the tangential fields of the waveguide mode traveling in negative z-direction. They are denoted by their equivalent Love currents $-\hat{\boldsymbol{J}}_0 = \boldsymbol{n}_0 \times (-\hat{\boldsymbol{H}}_0)$ (the tangential magnetic field of the backward-traveling mode is the negative of the corresponding forward-traveling mode) and $\hat{\boldsymbol{M}}_0 = -\boldsymbol{n}_0 \times \hat{\boldsymbol{E}}_0$ (the tangential electric field of the backward-traveling mode is equal to the corresponding forward-traveling mode). The correct tangential fields on S_2 are not known in advance, but the Silver-Müller conditions

$$\lim_{|\boldsymbol{r}|\to\infty} |\boldsymbol{r}| \left(\hat{\boldsymbol{E}} - \sqrt{\frac{\mu}{\varepsilon}} \hat{\boldsymbol{r}} \times \hat{\boldsymbol{H}} \right) = \boldsymbol{0}\,, \tag{4.33}$$

and

$$\lim_{|\boldsymbol{r}|\to\infty} |\boldsymbol{r}| \left(\hat{\boldsymbol{H}} + \sqrt{\frac{\varepsilon}{\mu}} \hat{\boldsymbol{r}} \times \hat{\boldsymbol{E}} \right) = \boldsymbol{0}\,, \tag{4.34}$$

for inward-traveling waves must be fulfilled if S_2 is moved toward infinity. The situation is analogous to the radiating case, but instead of radiating power away from the antenna volume, all power flows into V_{int}. The asymptotic boundary condition is readily fulfilled by the inward-traveling Green's functions $\mathscr{G}^{+}_{JE}$, $\mathscr{G}^{+}_{ME}$, $\mathscr{G}^{+}_{JH}$, $\mathscr{G}^{+}_{MH}$ and, therefore, the characteristic received fields can be calculated in a manner perfectly dual to the calculation of the transmit fields in Section 4.1. The duality transformation between the transmitted fields and the received fields involves

---

[21] The characteristic incident fields are already determined by the coefficient vector $\boldsymbol{\alpha}'^{(1)}_{\parallel}$ but they can also be determined without the help of the spherical wave expansion.

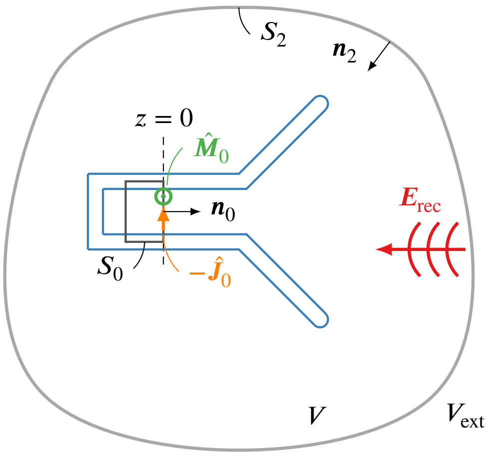

Fig. 4.9.: Boundary conditions for finding the perfectly absorbed receive fields.

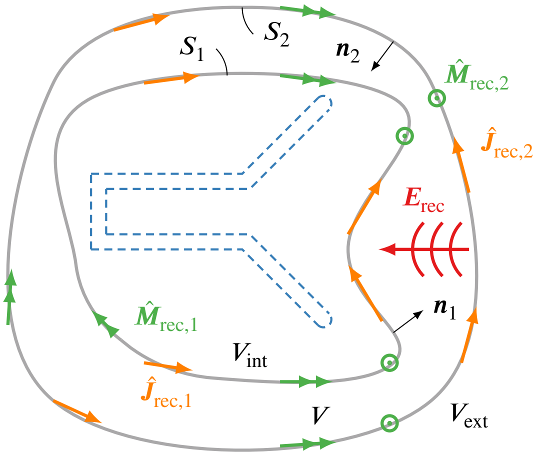

Fig. 4.10.: Equivalent currents on S_1 and S_2 are used to represent the receive field.

exchanging the "−"-type Green's functions with the "+"-type Green's functions and exchanging the tangential fields in the waveguide to account for the wave traveling into the opposite direction ($\hat{\boldsymbol{E}}_0 \to \hat{\boldsymbol{E}}_0$, $\hat{\boldsymbol{H}}_0 \to -\hat{\boldsymbol{H}}_0$ or $\hat{\boldsymbol{M}}_0 \to \hat{\boldsymbol{M}}_0$, $\hat{\boldsymbol{J}}_0 \to -\hat{\boldsymbol{J}}_0$, respectively).

Once the receive fields $\hat{\boldsymbol{E}}_{\text{rec}}$, $\hat{\boldsymbol{H}}_{\text{rec}}$ are known, one may use the tangential fields (or equivalently the corresponding Love currents $\hat{\boldsymbol{J}}_{\text{rec},1/2} = \boldsymbol{n}_{1/2} \times \hat{\boldsymbol{H}}_{\text{rec}}$, $\hat{\boldsymbol{M}}_{\text{rec},1/2} = -\boldsymbol{n}_{1/2} \times \hat{\boldsymbol{E}}_{\text{rec}}$) on two surfaces S_1 and S_2 to represent the fields in V uniquely as depicted in Fig. 4.10. Using the equivalent currents $\hat{\boldsymbol{J}}_{1/2} = \boldsymbol{n}_{1/2} \times \hat{\boldsymbol{H}}_{\text{rec}}$ and $\hat{\boldsymbol{M}}_{1/2} = -\boldsymbol{n}_{1/2} \times \hat{\boldsymbol{E}}_{\text{rec}}$, we have

$$\hat{\boldsymbol{E}}_{\text{rec}} = \oiint_{S_1} \left[\mathcal{G}^{+}_{JE}(\boldsymbol{r},\boldsymbol{r}') \cdot \hat{\boldsymbol{J}}_1(\boldsymbol{r}') + \mathcal{G}^{+}_{ME}(\boldsymbol{r},\boldsymbol{r}') \cdot \hat{\boldsymbol{M}}_1(\boldsymbol{r}')\right] \mathrm{d}a' \tag{4.35}$$

and

$$\hat{\boldsymbol{H}}_{\text{rec}} = \oiint_{S_1} \left[\mathcal{G}^{+}_{JH}(\boldsymbol{r},\boldsymbol{r}') \cdot \hat{\boldsymbol{J}}_1(\boldsymbol{r}') + \mathcal{G}^{+}_{MH}(\boldsymbol{r},\boldsymbol{r}') \cdot \hat{\boldsymbol{M}}_1(\boldsymbol{r}')\right] \mathrm{d}a' \tag{4.36}$$

using the "+"-type Greens functions or

$$\begin{aligned}\hat{\boldsymbol{E}}_{\text{rec}} = &\oiint_{S_1} \left[\mathcal{G}^{-}_{JE}(\boldsymbol{r},\boldsymbol{r}') \cdot \hat{\boldsymbol{J}}_1(\boldsymbol{r}') + \mathcal{G}^{-}_{ME}(\boldsymbol{r},\boldsymbol{r}') \cdot \hat{\boldsymbol{M}}_1(\boldsymbol{r}')\right] \mathrm{d}a' \\ &+ \oiint_{S_2} \left[\mathcal{G}^{-}_{JE}(\boldsymbol{r},\boldsymbol{r}') \cdot \hat{\boldsymbol{J}}_2(\boldsymbol{r}') + \mathcal{G}^{-}_{ME}(\boldsymbol{r},\boldsymbol{r}') \cdot \hat{\boldsymbol{M}}_2(\boldsymbol{r}')\right] \mathrm{d}a'\end{aligned} \tag{4.37}$$

and

$$\begin{aligned}\hat{\boldsymbol{H}}_{\text{rec}} = &\oiint_{S_1} \left[\mathcal{G}^{-}_{JH}(\boldsymbol{r},\boldsymbol{r}') \cdot \hat{\boldsymbol{J}}_1(\boldsymbol{r}') + \mathcal{G}^{-}_{MH}(\boldsymbol{r},\boldsymbol{r}') \cdot \hat{\boldsymbol{M}}_1(\boldsymbol{r}')\right] \mathrm{d}a' \\ &+ \oiint_{S_2} \left[\mathcal{G}^{-}_{JH}(\boldsymbol{r},\boldsymbol{r}') \cdot \hat{\boldsymbol{J}}_2(\boldsymbol{r}') + \mathcal{G}^{-}_{MH}(\boldsymbol{r},\boldsymbol{r}') \cdot \hat{\boldsymbol{M}}_2(\boldsymbol{r}')\right] \mathrm{d}a'\end{aligned} \tag{4.38}$$

using the "–"-type Greens functions[22]. With the insights from Section 3.8, the currents $\hat{\boldsymbol{J}}_2(\boldsymbol{r}')$, $\hat{\boldsymbol{M}}_2(\boldsymbol{r}')$ on S_2 in (4.37) and (4.38) are responsible for the incident fields and the currents $\hat{\boldsymbol{J}}_1(\boldsymbol{r}')$, $\hat{\boldsymbol{M}}_1(\boldsymbol{r}')$ on S_1 are responsible for the purely outward-traveling scattered fields.

The characteristic incident fields $\hat{\boldsymbol{E}}_{\text{cha}}$, $\hat{\boldsymbol{H}}_{\text{cha}}$ are found by subtracting the scattered fields, i.e.,

$$\hat{\boldsymbol{E}}_{\text{cha}} = \hat{\boldsymbol{E}}_{\text{rec}} - \oiint_{S_1} \left[\mathscr{G}^{-}_{JE}(\boldsymbol{r},\boldsymbol{r}') \cdot \hat{\boldsymbol{J}}_1(\boldsymbol{r}') + \mathscr{G}^{-}_{ME}(\boldsymbol{r},\boldsymbol{r}') \cdot \hat{\boldsymbol{M}}_1(\boldsymbol{r}')\right] \mathrm{d}a' \tag{4.39}$$

and

$$\hat{\boldsymbol{H}}_{\text{cha}} = \hat{\boldsymbol{H}}_{\text{rec}} - \oiint_{S_1} \left[\mathscr{G}^{-}_{JH}(\boldsymbol{r},\boldsymbol{r}') \cdot \hat{\boldsymbol{J}}_1(\boldsymbol{r}') + \mathscr{G}^{-}_{MH}(\boldsymbol{r},\boldsymbol{r}') \cdot \hat{\boldsymbol{M}}_1(\boldsymbol{r}')\right] \mathrm{d}a' . \tag{4.40}$$

These are the fields, which are transformed into purely absorbed fields when scattered at the antenna.

With (4.37) and (4.38) we have

$$\hat{\boldsymbol{E}}_{\text{cha}} = \oiint_{S_2} \left[\mathscr{G}^{-}_{JE}(\boldsymbol{r},\boldsymbol{r}') \cdot \hat{\boldsymbol{J}}_2(\boldsymbol{r}') + \mathscr{G}^{-}_{ME}(\boldsymbol{r},\boldsymbol{r}') \cdot \hat{\boldsymbol{M}}_2(\boldsymbol{r}')\right] \mathrm{d}a' \tag{4.41}$$

and

$$\hat{\boldsymbol{H}}_{\text{cha}} = \oiint_{S_2} \left[\mathscr{G}^{-}_{JH}(\boldsymbol{r},\boldsymbol{r}') \cdot \hat{\boldsymbol{J}}_2(\boldsymbol{r}') + \mathscr{G}^{-}_{MH}(\boldsymbol{r},\boldsymbol{r}') \cdot \hat{\boldsymbol{M}}_2(\boldsymbol{r}')\right] \mathrm{d}a' \tag{4.42}$$

using the "–"-type Green's functions. Equations (4.35) and (4.36) substituted into (4.39) and (4.40) lead to

$$\begin{aligned}\hat{\boldsymbol{E}}_{\text{cha}} = & \oiint_{S_1} \left[\mathscr{G}^{+}_{JE}(\boldsymbol{r},\boldsymbol{r}') \cdot \hat{\boldsymbol{J}}_1(\boldsymbol{r}') + \mathscr{G}^{+}_{ME}(\boldsymbol{r},\boldsymbol{r}') \cdot \hat{\boldsymbol{M}}_1(\boldsymbol{r}')\right] \mathrm{d}a' \\ & - \oiint_{S_1} \left[\mathscr{G}^{-}_{JE}(\boldsymbol{r},\boldsymbol{r}') \cdot \hat{\boldsymbol{J}}_1(\boldsymbol{r}') + \mathscr{G}^{-}_{ME}(\boldsymbol{r},\boldsymbol{r}') \cdot \hat{\boldsymbol{M}}_1(\boldsymbol{r}')\right] \mathrm{d}a' \qquad (4.43) \\ =& 2 \oiint_{S_1} \left[\mathscr{G}^{(\infty)}_{JE}(\boldsymbol{r},\boldsymbol{r}') \cdot \hat{\boldsymbol{J}}_1(\boldsymbol{r}') + \mathscr{G}^{(\infty)}_{ME}(\boldsymbol{r},\boldsymbol{r}') \cdot \hat{\boldsymbol{M}}_1(\boldsymbol{r}')\right] \mathrm{d}a' \qquad (4.44)\end{aligned}$$

---

[22] Since the total fields are purely absorbed fields, they can be expressed by only evaluating the surface currents on S_1 with the "+"-type Green's functions. The description with the "+"-type Green's functions is useful because it leads to a condensed representation of the fields. Note that only the usage of the "–"-type Green's functions gives rise to a simple interpretation of the fields associated with currents on S_1 in terms of purely outward-traveling fields. When other types of Green's functions are used, the currents on S_1 do not generate purely outward-traveling waves.

and

$$\begin{aligned}\hat{\boldsymbol{H}}_{\mathrm{cha}} = & \oiint_{S_1} \left[\boldsymbol{\mathscr{G}}_{JH}^{+}(\boldsymbol{r},\boldsymbol{r}') \cdot \hat{\boldsymbol{J}}_1(\boldsymbol{r}') + \boldsymbol{\mathscr{G}}_{MH}^{+}(\boldsymbol{r},\boldsymbol{r}') \cdot \hat{\boldsymbol{M}}_1(\boldsymbol{r}')\right] \mathrm{d}a' \\ & - \oiint_{S_1} \left[\boldsymbol{\mathscr{G}}_{JH}^{-}(\boldsymbol{r},\boldsymbol{r}') \cdot \hat{\boldsymbol{J}}_1(\boldsymbol{r}') + \boldsymbol{\mathscr{G}}_{MH}^{-}(\boldsymbol{r},\boldsymbol{r}') \cdot \hat{\boldsymbol{M}}_1(\boldsymbol{r}')\right] \mathrm{d}a' \qquad (4.45) \\ = & 2 \oiint_{S_1} \left[\boldsymbol{\mathscr{G}}_{JH}^{(\infty)}(\boldsymbol{r},\boldsymbol{r}') \cdot \hat{\boldsymbol{J}}_1(\boldsymbol{r}') + \boldsymbol{\mathscr{G}}_{MH}^{(\infty)}(\boldsymbol{r},\boldsymbol{r}') \cdot \hat{\boldsymbol{M}}_1(\boldsymbol{r}')\right] \mathrm{d}a' \,, \qquad (4.46)\end{aligned}$$

respectively, where the shorthand notations

$$\boldsymbol{\mathscr{G}}_{JE}^{(\infty)}(\boldsymbol{r},\boldsymbol{r}') = \frac{1}{2}\left[\boldsymbol{\mathscr{G}}_{JE}^{+}(\boldsymbol{r},\boldsymbol{r}') - \boldsymbol{\mathscr{G}}_{JE}^{-}(\boldsymbol{r},\boldsymbol{r}')\right] = -\mathrm{j}\omega\mu \left[\left(\mathbf{I} + \frac{1}{k^2}\nabla\nabla\right)\frac{\mathrm{j}\,\sin(k|\boldsymbol{r}-\boldsymbol{r}'|)}{4\pi\,|\boldsymbol{r}-\boldsymbol{r}'|}\right] , \qquad (4.47)$$

$$\boldsymbol{\mathscr{G}}_{ME}^{(\infty)}(\boldsymbol{r},\boldsymbol{r}') = \frac{1}{2}\left[\boldsymbol{\mathscr{G}}_{ME}^{+}(\boldsymbol{r},\boldsymbol{r}') - \boldsymbol{\mathscr{G}}_{ME}^{-}(\boldsymbol{r},\boldsymbol{r}')\right] = -\nabla\left(\frac{\mathrm{j}\,\sin(k|\boldsymbol{r}-\boldsymbol{r}'|)}{4\pi\,|\boldsymbol{r}-\boldsymbol{r}'|}\right)\times\mathbf{I}\,, \qquad (4.48)$$

$$\boldsymbol{\mathscr{G}}_{JH}^{(\infty)}(\boldsymbol{r},\boldsymbol{r}') = \frac{1}{2}\left[\boldsymbol{\mathscr{G}}_{JH}^{+}(\boldsymbol{r},\boldsymbol{r}') - \boldsymbol{\mathscr{G}}_{JH}^{-}(\boldsymbol{r},\boldsymbol{r}')\right] = \nabla\left(\frac{\mathrm{j}\,\sin(k|\boldsymbol{r}-\boldsymbol{r}'|)}{4\pi\,|\boldsymbol{r}-\boldsymbol{r}'|}\right)\times\mathbf{I}\,, \qquad (4.49)$$

and

$$\boldsymbol{\mathscr{G}}_{JE}^{(\infty)}(\boldsymbol{r},\boldsymbol{r}') = \frac{1}{2}\left[\boldsymbol{\mathscr{G}}_{JE}^{+}(\boldsymbol{r},\boldsymbol{r}') - \boldsymbol{\mathscr{G}}_{JE}^{-}(\boldsymbol{r},\boldsymbol{r}')\right] = -\mathrm{j}\omega\varepsilon \left[\left(\mathbf{I} + \frac{1}{k^2}\nabla\nabla\right)\frac{\mathrm{j}\,\sin(k|\boldsymbol{r}-\boldsymbol{r}'|)}{4\pi\,|\boldsymbol{r}-\boldsymbol{r}'|}\right] \qquad (4.50)$$

have been used[23]. This is a remarkable result. In order to calculate the characteristic incident fields $\hat{\boldsymbol{E}}_{\mathrm{cha}}$, $\hat{\boldsymbol{H}}_{\mathrm{cha}}$ for a receiving antenna, one only needs to know the tangential fields of the resulting absorbed fields $\hat{\boldsymbol{E}}_{\mathrm{rec}}$, $\hat{\boldsymbol{H}}_{\mathrm{rec}}$ (or equivalently the corresponding Love currents $\boldsymbol{J}_1$, $\boldsymbol{M}_1$) on the surface S_1. The problem of finding the tangential fields of $\hat{\boldsymbol{E}}_{\mathrm{rec}}$, $\hat{\boldsymbol{H}}_{\mathrm{rec}}$ becomes particularly simple in the lossless case.

For a lossless antenna in a lossless environment ($\varepsilon = \varepsilon^*$, $\mu = \mu^*$), the receive fields $\hat{\boldsymbol{E}}_{\mathrm{rec}}$, $\hat{\boldsymbol{H}}_{\mathrm{rec}}$ are the perfectly time reversed copies of the transmitted fields. The Green's functions fulfill the relations

$$\boldsymbol{\mathscr{G}}_{JE}^{+} = -\left(\boldsymbol{\mathscr{G}}_{JE}^{-}\right)^* \qquad (4.51)$$

$$\boldsymbol{\mathscr{G}}_{ME}^{+} = \left(\boldsymbol{\mathscr{G}}_{ME}^{-}\right)^* \qquad (4.52)$$

$$\boldsymbol{\mathscr{G}}_{JH}^{+} = \left(\boldsymbol{\mathscr{G}}_{JH}^{-}\right)^* \qquad (4.53)$$

and

$$\boldsymbol{\mathscr{G}}_{MH}^{+} = -\left(\boldsymbol{\mathscr{G}}_{MH}^{-}\right)^* \,. \qquad (4.54)$$

---

[23] Despite the fact that the scalar function $g_0^{(\infty)}$ is not a fundamental solution of the Helmholtz equation (see Section 3.2) it is still useful for some calculations.

The received fields are directly related to the transmit fields of the antenna by

$$\hat{\boldsymbol{E}}_{\mathrm{rec}} = \hat{\boldsymbol{E}}^{*}_{\mathrm{tra}}\,, \tag{4.55}$$

$$\hat{\boldsymbol{H}}_{\mathrm{rec}} = -\hat{\boldsymbol{H}}^{*}_{\mathrm{tra}}\,. \tag{4.56}$$

In this case, the transmit fields of the antenna can directly be used to determine the receive scattering of the antenna (but not the residual scattering).

4.3. Chapter Summary

In this chapter the bridge between guided waves and free-space fields has been built with the formal description of the antenna behavior in terms of spherical waves and equivalent surface currents. In transmit mode, the radiated fields can be expressed by equivalent free-space surface currents, scaled by the excitation $a \in \mathbb{C}\sqrt{\mathrm{W}}$. The same free-space current distribution can be used to find the coefficient of the backward-traveling waveguide mode in the receiving case. Similarly, the radiated fields can be expressed by spherical modes. In the receiving case, the incident field must be weighted by a vector of receiving coefficients, related to the transmit coefficients via a reciprocity relation. The receiving antennas have been treated in greater detail than in most textbooks [Balanis 2005], where the receiving case is covered by just referring to reciprocity and where the received signal is often only reduced to a description of voltages and currents in a infinitesimally small gap. In contrast to this, in this thesis, all interactions between the antenna and its environment are expressed in terms of waveguide modes — a description which is much more suitable for radio frequency devices. Furthermore, the characteristic incident fields, which are completely transformed into purely absorbed fields by the receiving antenna, have been also described in terms of equivalent surface currents as opposed to existing literature [Montgomery 1948; Hansen 1988], where only the mode expansions of these special fields are discussed. The formal description of the transmitted fields and the received signal from an arbitrary incident field are the basis for the derivation of a transmission equation between two antennas, which will finally lead to the desired field transformation algorithms in the following.

5

Antenna Near-Field Measurements

In order to characterize or to verify the performance of an AUT, relevant antenna properties are determined by measurements. Mostly, one is interested in the antenna performance in the FF. However, often the measurement setups are easier to realize in the NF because of limited space requirements. For the determination of the desired FF quantities, the measured fields are then processed in an NFFFT.

This chapter describes how a model of the AUT fields is obtained from field samples in the NF of the AUT[1]. Based on a formal description of the measured S_{21}- or S_{12}-parameter between an AUT and a probe antenna in terms of equivalent surface current densities or a spherical wave expansion, a linear system of equations is derived to find the equivalent sources modeling the AUT radiation. The derived AUT model can be used to calculate the NF and the FF at arbitrary locations outside of the AUT volume.

5.1. Interaction Between Antennas

The basis of source reconstruction methods applicable for NF measurements is a formal description of the interaction between two arbitrary antennas. In the context of antenna measurements, one of the antennas is a known probe antenna while the derived description can be used to characterize the unknown AUT.

5.1.1. Interaction Between Antennas in Terms of Equivalent Surface Currents

The radiated fields and the receiving behavior of an antenna can be characterized by the same equivalent surface current distributions on a Huygens surface enclosing the antenna. For calculating the transmitted signal of one of two arbitrary antennas enclosed by the Huygens surfaces S_1 and S_2, respectively, it is thus sufficient to know the characteristic equivalent surface current

---

[1] The interaction between two antennas is more complicated in the NF. In principle, the same formulations are also valid in the FF, but the description can often be simplified by FF approximations. The NF description is more general.

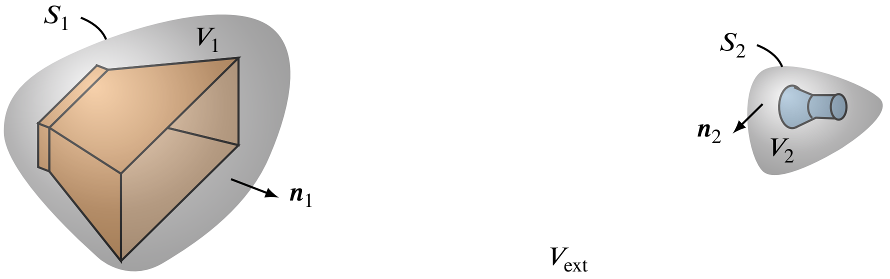

Fig. 5.1.: Two antennas enclosed by individual Huygens surfaces S_1 and S_2.

distributions on the respective Huygens surface of each antenna, if mutual interactions between the two antennas can be neglected. An exemplary situation is depicted in Fig. 5.1. Here, the normalized equivalent currents accounting for the free-space radiation of antenna 1 are denoted by $\hat{\boldsymbol{J}}_1$, $\hat{\boldsymbol{M}}_1$ and the normalized equivalent currents accounting for the free-space radiation of antenna 2 by $\hat{\boldsymbol{J}}_2$, $\hat{\boldsymbol{M}}_2$. Of course, the currents $\hat{\boldsymbol{J}}_1$, $\hat{\boldsymbol{M}}_1$ are located on S_1 and the currents $\hat{\boldsymbol{J}}_2$, $\hat{\boldsymbol{M}}_2$ are located on S_2.

The transmitted fields $\boldsymbol{E}_1,\boldsymbol{H}_1$ of antenna 1 in any observation location $\boldsymbol{r}$ outside the volume V_1 can be expressed by

$$\boldsymbol{E}_1(\boldsymbol{r}) = a_1 \oiint_{S_1} \left[\mathscr{G}^{-}_{JE}(\boldsymbol{r},\boldsymbol{r}')\cdot\hat{\boldsymbol{J}}_1(\boldsymbol{r}') + \mathscr{G}^{-}_{ME}(\boldsymbol{r},\boldsymbol{r}')\cdot\hat{\boldsymbol{M}}_1(\boldsymbol{r}')\right]\,\mathrm{d}a' \tag{5.1}$$

and

$$\boldsymbol{H}_1(\boldsymbol{r}) = a_1 \oiint_{S_1} \left[\mathscr{G}^{-}_{JH}(\boldsymbol{r},\boldsymbol{r}')\cdot\hat{\boldsymbol{J}}_1(\boldsymbol{r}') + \mathscr{G}^{-}_{MH}(\boldsymbol{r},\boldsymbol{r}')\cdot\hat{\boldsymbol{M}}_1(\boldsymbol{r}')\right]\,\mathrm{d}a'\,, \tag{5.2}$$

where $a_1 \in \mathbb{C}\,\sqrt{\mathrm{W}}$ is the power wave amplitude of the excitation at the port of antenna 1.

According to (4.22), the power wave amplitude b_2 of the receive signal at the port of antenna 2 due to the incident fields generated by antenna 1 is given by[2]

$$b_2 = \frac{1}{2} \oiint_{S_2} \left[\boldsymbol{E}_1(\boldsymbol{r})\cdot\hat{\boldsymbol{J}}_2(\boldsymbol{r}) - \boldsymbol{H}_1(\boldsymbol{r})\cdot\hat{\boldsymbol{M}}_2(\boldsymbol{r})\right]\,\mathrm{d}a\,. \tag{5.3}$$

Expanding the terms for $\boldsymbol{E}_1$ and $\boldsymbol{H}_1$ yields

$$\begin{aligned} b_2 = \frac{a_1}{2} \oiint_{S_2} \Bigg[& \oiint_{S_1} \left[\mathscr{G}^{-}_{JE}(\boldsymbol{r},\boldsymbol{r}')\cdot\hat{\boldsymbol{J}}_1(\boldsymbol{r}') + \mathscr{G}^{-}_{ME}(\boldsymbol{r},\boldsymbol{r}')\cdot\hat{\boldsymbol{M}}_1(\boldsymbol{r}')\right]\,\mathrm{d}a'\cdot\hat{\boldsymbol{J}}_2(\boldsymbol{r}) \\ & - \oiint_{S_1} \left[\mathscr{G}^{-}_{JH}(\boldsymbol{r},\boldsymbol{r}')\cdot\hat{\boldsymbol{J}}_1(\boldsymbol{r}') + \mathscr{G}^{-}_{MH}(\boldsymbol{r},\boldsymbol{r}')\cdot\hat{\boldsymbol{M}}_1(\boldsymbol{r}')\right]\,\mathrm{d}a'\cdot\hat{\boldsymbol{M}}_2(\boldsymbol{r})\Bigg]\,\mathrm{d}a\,. \end{aligned} \tag{5.4}$$

---

[2] The antenna constants c_{aut} are assumed to be equal to 1.

The S_{21}-parameter which is given by the ratio $S_{21} = b_2/a_1$ is therefore given by

$$S_{21} = \frac{1}{2} \oiint\limits_{S_2} \oiint\limits_{S_1} \Big[\hat{\boldsymbol{J}}_2(\boldsymbol{r}) \cdot \boldsymbol{\mathcal{G}}^{-}_{JE}\big(\boldsymbol{r}, \boldsymbol{r}'\big) \cdot \hat{\boldsymbol{J}}_1\big(\boldsymbol{r}'\big) + \hat{\boldsymbol{J}}_2(\boldsymbol{r}) \cdot \boldsymbol{\mathcal{G}}^{-}_{ME}\big(\boldsymbol{r}, \boldsymbol{r}'\big) \cdot \hat{\boldsymbol{M}}_1\big(\boldsymbol{r}'\big)$$
$$- \hat{\boldsymbol{M}}_2(\boldsymbol{r}) \cdot \boldsymbol{\mathcal{G}}^{-}_{JH}\big(\boldsymbol{r}, \boldsymbol{r}'\big) \cdot \hat{\boldsymbol{J}}_1\big(\boldsymbol{r}'\big) - \hat{\boldsymbol{M}}_2(\boldsymbol{r}) \cdot \boldsymbol{\mathcal{G}}^{-}_{MH}\big(\boldsymbol{r}, \boldsymbol{r}'\big) \cdot \hat{\boldsymbol{M}}_1\big(\boldsymbol{r}'\big) \Big] \, \mathrm{d}a' \, \mathrm{d}a \,. \tag{5.5}$$

An analogous derivation yields for the S_{12}-parameter

$$S_{12} = \frac{1}{2} \oiint\limits_{S_1} \oiint\limits_{S_2} \Big[\hat{\boldsymbol{J}}_1(\boldsymbol{r}) \cdot \boldsymbol{\mathcal{G}}^{-}_{JE}\big(\boldsymbol{r}, \boldsymbol{r}'\big) \cdot \hat{\boldsymbol{J}}_2\big(\boldsymbol{r}'\big) + \hat{\boldsymbol{J}}_1(\boldsymbol{r}) \cdot \boldsymbol{\mathcal{G}}^{-}_{ME}\big(\boldsymbol{r}, \boldsymbol{r}'\big) \cdot \hat{\boldsymbol{M}}_2\big(\boldsymbol{r}'\big)$$
$$- \hat{\boldsymbol{M}}_1(\boldsymbol{r}) \cdot \boldsymbol{\mathcal{G}}^{-}_{JH}\big(\boldsymbol{r}, \boldsymbol{r}'\big) \cdot \hat{\boldsymbol{J}}_2\big(\boldsymbol{r}'\big) - \hat{\boldsymbol{M}}_1(\boldsymbol{r}) \cdot \boldsymbol{\mathcal{G}}^{-}_{MH}\big(\boldsymbol{r}, \boldsymbol{r}'\big) \cdot \hat{\boldsymbol{M}}_2\big(\boldsymbol{r}'\big) \Big] \, \mathrm{d}a' \, \mathrm{d}a \,. \tag{5.6}$$

Since the reciprocity relations

$$\boldsymbol{\mathcal{G}}^{-}_{JE}\big(\boldsymbol{r}, \boldsymbol{r}'\big) = \big(\boldsymbol{\mathcal{G}}^{-}_{JE}\big(\boldsymbol{r}', \boldsymbol{r}\big)\big)^{\mathrm{T}} \tag{5.7}$$

$$\boldsymbol{\mathcal{G}}^{-}_{JH}\big(\boldsymbol{r}, \boldsymbol{r}'\big) = -\big(\boldsymbol{\mathcal{G}}^{-}_{ME}\big(\boldsymbol{r}', \boldsymbol{r}\big)\big)^{\mathrm{T}} \tag{5.8}$$

and

$$\boldsymbol{\mathcal{G}}^{-}_{MH}\big(\boldsymbol{r}, \boldsymbol{r}'\big) = \big(\boldsymbol{\mathcal{G}}^{-}_{MH}\big(\boldsymbol{r}', \boldsymbol{r}\big)\big)^{\mathrm{T}} \tag{5.9}$$

hold for the Green's functions [Tai 1994, p. 77], the expressions for S_{12} and S_{21} are identical.

5.1.2. Interaction Between Antennas in Terms of Spherical Wave Expansions

One can also describe the interaction between the two antennas in term of spherical modes. The two volumes V_1 and V_2 are assumed to be spherical for a description of the antenna transmission in terms of a spherical wave expansion. The two spherical volumes have centers $\boldsymbol{r}_{01}$ and $\boldsymbol{r}_{02}$, respectively. The geometric situation is clarified in Fig. 5.2. The transmitted fields $\boldsymbol{E}_1, \boldsymbol{H}_1$ of antenna 1 outside V_1 can be expressed purely in terms of outward-traveling waves ($c = 4$) and we have

$$\boldsymbol{E}_1(\boldsymbol{r})\Big|_{\boldsymbol{r} \notin V_1} = a_1 \, k \sqrt{Z_{\mathrm{F}}} \sum_{s=1}^{2} \sum_{n=1}^{N_1} \sum_{m=-n}^{n} \hat{\alpha}^{(4),\,\mathrm{ant1}}_{smn} \, \boldsymbol{F}^{(4)}_{smn}(r, \vartheta, \varphi) \tag{5.10}$$

and

$$\boldsymbol{H}_1(\boldsymbol{r})\Big|_{\boldsymbol{r} \notin V_1} = a_1 \, \mathrm{j} \frac{k}{\sqrt{Z_{\mathrm{F}}}} \sum_{s=1}^{2} \sum_{n=1}^{N_1} \sum_{m=-n}^{n} \hat{\alpha}^{(4),\,\mathrm{ant1}}_{smn} \, \boldsymbol{F}^{(4)}_{3-s,mn}(r, \vartheta, \varphi) \;, \tag{5.11}$$

where the spherical wave expansion is given with respect to the origin of the primary coordinate system at $\boldsymbol{r}_{01}$.

In the secondary coordinate system with origin $\boldsymbol{r}_{02}$, only the fields inside the volume V_2 are of interest. They can be expressed purely in terms of incident fields ($c = 1$) and we have

$$\boldsymbol{E}_1\big(\boldsymbol{r}'\big)\Big|_{\boldsymbol{r} \in V_2} = a_1 \, k \sqrt{Z_{\mathrm{F}}} \sum_{s=1}^{2} \sum_{n=1}^{N_2} \sum_{m=-n}^{n} \hat{\alpha}'^{(1),\,\mathrm{ant1}}_{smn} \, \boldsymbol{F}^{(1)}_{smn}\big(r', \vartheta', \varphi'\big) \tag{5.12}$$

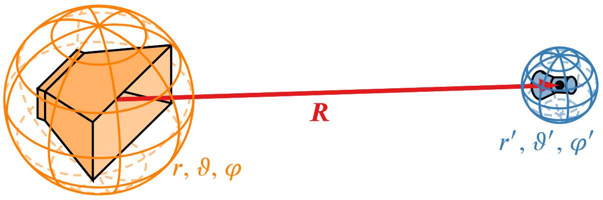

Fig. 5.2.: Two antennas enclosed by their respective minimum spheres. The coordinates r, ϑ, φ and r', ϑ', φ' are defined with respect to the center of the respective minimum sphere.

and

$$\boldsymbol{H}_1\left(\boldsymbol{r}'\right)\Big|_{\boldsymbol{r}\in V_2} = a_1\,\mathrm{j}\frac{k}{\sqrt{Z_\mathrm{F}}}\sum_{s=1}^{2}\sum_{n=1}^{N_2}\sum_{m=-n}^{n}\hat{\alpha}'^{(1),\,\mathrm{ant1}}_{smn}\,\boldsymbol{F}^{(1)}_{3-s,mn}\left(r',\vartheta',\varphi'\right)\,, \tag{5.13}$$

where the primed indices, primed coefficients, and primed location vectors denote the fact that the spherical wave expansion is obtained with respect to spherical coordinates (r', ϑ', and φ') with the origin at $\boldsymbol{r}_{02}$.

The primed coefficients $\hat{\alpha}'^{\,\mathrm{ant1}}_{\sigma\mu\nu}$ in the secondary coordinate system are found from the transmit coefficients $\hat{\alpha}^{\mathrm{ant1}}_{smn}$ in the primary coordinate system by

$$\hat{\alpha}'^{(1),\,\mathrm{ant1}}_{smn} = \sum_{\sigma=1}^{2}\sum_{\nu=1}^{N_1}\sum_{\mu=-\nu}^{\nu}\mathscr{T}^{\sigma\mu\nu}_{smn}\left(\boldsymbol{r}_{02}-\boldsymbol{r}_{01}\right)\hat{\alpha}^{(4),\,\mathrm{ant1}}_{\sigma\mu\nu}\,, \tag{5.14}$$

making use of the spherical wave translation coefficients $\mathscr{T}^{\sigma\mu\nu}_{smn}(\boldsymbol{R})$, for which several expressions have been derived [Cruzan 1962; Stein 1961; Danos 1965; Borghese 1980; Felderhof 1987; Wittmann 1988; Chew 1995; Chew 2001; Chew 1993; Chew 2007; Haynes 2011; Kim 1996; He 2008; Chew 2008; Dufva 2008], e.g., in the spectral form[3]

$$\begin{aligned}
&\mathscr{T}^{\sigma\mu\nu}_{smn}(\boldsymbol{R})\\
&= (-1)^{s+m+n}\sum_{\ell=0}^{\infty}\sum_{q=-\ell}^{\ell}4\pi\,(-\mathrm{j})^{\ell}\,\mathrm{h}^{(2)}_{\ell}(k|\boldsymbol{R}|)\oint\!\!\!\oint\boldsymbol{K}^{(4)}_{\sigma\mu\nu}\left(\hat{\boldsymbol{k}}\right)\cdot\boldsymbol{K}^{(4)}_{s,-m,n}\left(\hat{\boldsymbol{k}}\right)\mathrm{Y}^{*}_{\ell,q}\left(\hat{\boldsymbol{R}}\right)\mathrm{Y}_{\ell,q}\left(\hat{\boldsymbol{k}}\right)\,\mathrm{d}\hat{\boldsymbol{k}}\\
&= (-1)^{s+m+n}\oint\!\!\!\oint\boldsymbol{K}^{(4)}_{\sigma\mu\nu}\left(\hat{\boldsymbol{k}}\right)\cdot\boldsymbol{K}^{(4)}_{s,-m,n}\left(\hat{\boldsymbol{k}}\right)\left(\sum_{\ell=0}^{\infty}(-\mathrm{j})^{\ell}\,(2\ell+1)\,\mathrm{h}^{(2)}_{\ell}(k|\boldsymbol{R}|)\,\mathrm{P}_{\ell}\left(\hat{\boldsymbol{k}}\cdot\hat{\boldsymbol{R}}\right)\right)\mathrm{d}\hat{\boldsymbol{k}}
\end{aligned} \tag{5.15}$$

based on [Chew 2008; He 2008; Dufva 2008], where

$$\boldsymbol{K}^{(4)}_{smn}\left(\hat{\boldsymbol{k}}\right) = \lim_{kr\to\infty}\frac{kr}{\mathrm{e}^{-\mathrm{j}kr}}\boldsymbol{F}^{(4)}_{smn}(r,\vartheta,\varphi) \tag{5.16}$$

are the spherical vector mode far-field functions and the integration is performed over the complete Ewald sphere. A derivation of the expressions for the translation coefficients $\mathscr{T}^{\sigma\mu\nu}_{smn}(\boldsymbol{R})$ can be

---

[3] In slight abuse of notation, the surface element of the integration over all directions the complete Ewald sphere is denoted by $\mathrm{d}\hat{\boldsymbol{k}}$. The symbol $\mathrm{d}\hat{\boldsymbol{k}}$ should be understood as a shorthand notation for the spherical surface element $\sin\vartheta\,\mathrm{d}\vartheta\,\mathrm{d}\varphi$. The integration domain is implied to be over the complete sphere with $0 \leq \vartheta \leq \pi$ and $0 \leq \varphi \leq 2\pi$.

found in Appendix B. Strictly speaking, exchanging the order of integration and summation in (5.15) is not valid since the series

$$\sum_{\ell=0}^{\infty} (-\mathrm{j})^{\ell}\,(2\ell+1)\,\mathrm{h}_{\ell}^{(2)}(k|\boldsymbol{R}|)\,\mathrm{P}_{\ell}\big(\hat{\boldsymbol{k}}\cdot\hat{\boldsymbol{R}}\big) \tag{5.17}$$

diverges, but if the sum is understood in a distributional sense and appears only under an integral together with suitable functions, the integral value is well defined [Chew 2008]. In a numerical implementation, the summation will be truncated after a finite number of terms and the question about the convergence of the series is circumvented.

Combining (5.14) with (4.24), we have

$$\begin{aligned} b_2 &= a_1 \sum_{s=1}^{2}\sum_{n=1}^{N_2}\sum_{m=-n}^{n} \hat{\beta}'^{(1),\mathrm{ant2}}_{smn}\,\hat{\alpha}'^{(1),\mathrm{ant1}}_{smn} \\ &= a_1 \sum_{s=1}^{2}\sum_{n=1}^{N_2}\sum_{m=-n}^{n} \hat{\beta}'^{(1),\mathrm{ant2}}_{smn} \sum_{\sigma=1}^{2}\sum_{\nu=1}^{N_1}\sum_{\mu=-\nu}^{\nu} \mathcal{T}^{\sigma\mu\nu}_{smn}\big(\boldsymbol{r}_{02}-\boldsymbol{r}_{01}\big)\,\hat{\alpha}^{(4),\,\mathrm{ant1}}_{\sigma\mu\nu}\,, \end{aligned} \tag{5.18}$$

where the receiving coefficients $\hat{\beta}'^{(1),\mathrm{ant2}}_{smn}$ of antenna 2 are expressed in terms of the spherical wave expansion with origin at $\boldsymbol{r}_{02}$ (denoted by the primed coefficients). The S_{21}-parameter therefore is given by

$$S_{21} = \sum_{s=1}^{2}\sum_{n=1}^{N_2}\sum_{m=-n}^{n} \hat{\beta}'^{(1),\mathrm{ant2}}_{smn} \sum_{\sigma=1}^{2}\sum_{\nu=1}^{N_1}\sum_{\mu=-\nu}^{\nu} \mathcal{T}^{\sigma\mu\nu}_{smn}\big(\boldsymbol{r}_{02}-\boldsymbol{r}_{01}\big)\,\hat{\alpha}^{(4),\,\mathrm{ant1}}_{\sigma\mu\nu}\,, \tag{5.19}$$

since $S_{21} = b_2/a_1$. This equation corresponds to the commonly encountered spherical wave transmission formula [Hansen 1988, pp. 62ff.].

A similar derivation for the S_{12}-parameter results in

$$S_{12} = \sum_{s=1}^{2}\sum_{n=1}^{N_1}\sum_{m=-n}^{n} \hat{\beta}^{(1),\mathrm{ant1}}_{smn} \sum_{\sigma=1}^{2}\sum_{\nu=1}^{N_2}\sum_{\mu=-\nu}^{\nu} \mathcal{T}^{\sigma\mu\nu}_{smn}\big(\boldsymbol{r}_{01}-\boldsymbol{r}_{02}\big)\,\hat{\alpha}'^{(4),\,\mathrm{ant2}}_{\sigma\mu\nu} \tag{5.20}$$

and the reciprocity relation $S_{12} = S_{21}$ can be verified using the identity[4]

$$\boldsymbol{K}^{(4)}_{smn}\big(-\hat{\boldsymbol{k}}\big) = (-1)^{s+n}\,\boldsymbol{K}^{(4)}_{s,-m,n}\big(\hat{\boldsymbol{k}}\big) \tag{5.21}$$

---

[4] It is straightforward to verify that $\boldsymbol{K}^{(4)}_{smn}\big(-\hat{\boldsymbol{k}}\big) = (-1)^{s+n}\,\boldsymbol{K}^{(4)}_{s,-m,n}\big(\hat{\boldsymbol{k}}\big)$ by using the definitions (3.80) and (3.81) and basic properties of the associated Legendre polynomials.

together with the reciprocity relations from (4.27). From (5.15) we have

$$\begin{aligned}
&\mathscr{T}_{smn}^{\sigma\mu\nu}(-\boldsymbol{R}) \\
&= (-1)^{s+m+n} \oiint \boldsymbol{K}_{\sigma\mu\nu}^{(4)}\big(\hat{\boldsymbol{k}}\big) \cdot \boldsymbol{K}_{s,-m,n}^{(4)}\big(\hat{\boldsymbol{k}}\big) \left(\sum_{\ell=0}^{\infty} (-\mathrm{j})^{\ell}\, (2\ell+1)\, \mathrm{h}_{\ell}^{(2)}(k|\boldsymbol{R}|)\, \mathrm{P}_{\ell}\big(-\hat{\boldsymbol{k}} \cdot \hat{\boldsymbol{R}}\big) \right) \mathrm{d}\hat{\boldsymbol{k}} \\
&= (-1)^{s+m+n} \oiint \boldsymbol{K}_{\sigma\mu\nu}^{(4)}\big(-\hat{\boldsymbol{k}}\big) \cdot \boldsymbol{K}_{s,-m,n}^{(4)}\big(-\hat{\boldsymbol{k}}\big) \left(\sum_{\ell=0}^{\infty} (-\mathrm{j})^{\ell}\, (2\ell+1)\, \mathrm{h}_{\ell}^{(2)}(k|\boldsymbol{R}|)\, \mathrm{P}_{\ell}\big(\hat{\boldsymbol{k}} \cdot \hat{\boldsymbol{R}}\big) \right) \mathrm{d}\hat{\boldsymbol{k}} \\
&= (-1)^{m} \oiint (-1)^{\sigma+\nu}\, \boldsymbol{K}_{\sigma,-\mu,\nu}^{(4)}\big(\hat{\boldsymbol{k}}\big) \cdot \boldsymbol{K}_{s,m,n}^{(4)}\big(\hat{\boldsymbol{k}}\big) \left(\sum_{\ell=0}^{\infty} (-\mathrm{j})^{\ell}\, (2\ell+1)\, \mathrm{h}_{\ell}^{(2)}(k|\boldsymbol{R}|)\, \mathrm{P}_{\ell}\big(\hat{\boldsymbol{k}} \cdot \hat{\boldsymbol{R}}\big) \right) \mathrm{d}\hat{\boldsymbol{k}} \\
&= (-1)^{\mu+m}\, \mathscr{T}_{\sigma\mu\nu}^{smn}(\boldsymbol{R})
\end{aligned} \tag{5.22}$$

and therefore

$$\begin{aligned}
S_{12} &= \sum_{s=1}^{2} \sum_{n=1}^{N_1} \sum_{m=-n}^{n} \hat{\beta}_{smn}^{(1),\mathrm{ant1}} \sum_{\sigma=1}^{2} \sum_{\nu=1}^{N_2} \sum_{\mu=-\nu}^{\nu} \mathscr{T}_{smn}^{\sigma\mu\nu}\big(\boldsymbol{r}_{01} - \boldsymbol{r}_{02}\big)\, \hat{\alpha}'^{(4),\,\mathrm{ant2}}_{\sigma\mu\nu} \\
&= \sum_{s=1}^{2} \sum_{n=1}^{N_1} \sum_{m=-n}^{n} \sum_{\sigma=1}^{2} \sum_{\nu=1}^{N_2} \sum_{\mu=-\nu}^{\nu} \hat{\alpha}_{smn}^{(4),\mathrm{ant1}}\, \mathscr{T}_{\sigma\mu\nu}^{smn}\big(\boldsymbol{r}_{02} - \boldsymbol{r}_{01}\big)\, \hat{\beta}'^{(1),\,\mathrm{ant2}}_{\sigma\mu\nu} \\
&= S_{12}\,.
\end{aligned} \tag{5.23}$$

5.2. Near-Field Far-Field Transformations

In contrast to FF measurements, the output signal of a field probe in the NF is not directly proportional to the electric field at a single point in space, but the probe antenna performs a weighting of the NFs in a certain volume (or equivalently over a certain surface, see Section 4.2). Therefore, the Huygens principle is not directly applicable and the NFFFT must take the probe influences into account. This so-called *probe correction* is especially important if the incident field at the probe antenna is composed from components coming from different directions, as it is the case in the echoic environments which will be discussed later in this thesis.

The general idea behind (most) NFFFTs lies in the fact that the DoFs for the radiated fields of an antenna with a certain size are essentially limited. Thus, an unambiguous description of the radiated fields in the whole region of interest, including the NF and the FF region, may be obtained from a finite number of measurement samples.

5.2.1. Field Transformation Based on Spatial Current Distributions

The transmit and receive behavior of an antenna can both be characterized by an equivalent surface current description on a closed Huygens surface enclosing the antenna. A logical approach to characterize an antenna is therefore to obtain an equivalent current distribution for the antenna. The fields at any location in space in the NF as well as in the FF can be computed from the retrieved sources in these so-called current reconstruction methods [Petre 1992; Petre 1996; Taaghol 1996; Sarkar 1999; Persson 2005; Las-Heras 2002; Álvarez 2006; Schmidt 2008b;

Eibert 2010; Foged 2012]. Due to their great flexibility in the placement of the source and measurement locations, surface current reconstruction based methods are ideal for processing irregularly sampled NF measurements, e.g., with unmanned aerial vehicles [Knapp 2018d]. The surface currents have to be discretized and the unknown coefficients of the discretized currents have to be determined by relating them to the measurement samples.

An arbitrary Huygens surface can be discretized by triangles with readily available meshing software. Rao-Wilton-Glisson (RWG)-basis functions can be used to discretize either electric or magnetic currents[5] [Rao 1982; Caorsi 1993]. The RWG-basis functions are defined on any pair of adjacent triangles to discretize the surface currents, so there is one current unknown per current type associated with every edge of the mesh (provided one has a closed mesh, containing only internal edges). Of course, if both current types (electric and magnetic) are used together, one has two unknowns associated with every edge of the mesh — one for each current type. The size of the triangles must be chosen small enough to be able to represent the spatial variations of the expected surface currents. Since highly oscillating currents do not contribute much to the radiated fields (see Section 4.1.3), it is usually sufficient to have triangles with an edge length of about $\lambda/4$ depending on the wavelength of the monofrequent signal under consideration, in particular if the Huygens surface has a certain separation from the actual AUT.

Let N_{edg} be the number of internal edges of the mesh used to discretize the Huygens surface. For the electric and magnetic currents together, one has $N = 2\,N_{\mathrm{edg}}$ unknowns in total. For the discretized and normalized electric and magnetic surface current densities we have

$$\hat{\boldsymbol{J}}(\boldsymbol{r}) = \mathrm{A}/\left(\sqrt{\mathrm{W}}\mathrm{m}\right) \sum_{n=1}^{N/2} x_n\, \boldsymbol{\beta}_n(\boldsymbol{r}) \tag{5.24}$$

and

$$\hat{\boldsymbol{M}}(\boldsymbol{r}) = \mathrm{V}/\left(\sqrt{\mathrm{W}}\mathrm{m}\right) \sum_{n=1+N/2}^{N} x_n\, \boldsymbol{\beta}_{n-N/2}(\boldsymbol{r})\ , \tag{5.25}$$

where $\boldsymbol{\beta}_n(\boldsymbol{r})$ is the RWG-basis function associated with the nth edge of the mesh and $x_n \in \mathbb{C}$ is the expansion coefficient for the corresponding electric or magnetic current element, respectively.

The goal of the NFFFT is to find the unknown coefficients x_n such that the resulting equivalent currents generate the same fields as the AUT. To this end, the interaction between the current elements and a measurement probe with known equivalent currents $\hat{\boldsymbol{J}}_{\mathrm{pro}}(\boldsymbol{r})$, $\hat{\boldsymbol{M}}_{\mathrm{pro}}(\boldsymbol{r})$ is expressed by

$$\begin{aligned} S_{21} = \oiint\limits_{S_{\mathrm{pro}}} \oiint\limits_{S_{\mathrm{aut}}} \Big[&\hat{\boldsymbol{J}}_{\mathrm{pro}}(\boldsymbol{r}) \cdot \mathscr{G}^{-}_{JE}\left(\boldsymbol{r},\boldsymbol{r}'\right) \cdot \hat{\boldsymbol{J}}\left(\boldsymbol{r}'\right) + \hat{\boldsymbol{J}}_{\mathrm{pro}}(\boldsymbol{r}) \cdot \mathscr{G}^{-}_{ME}\left(\boldsymbol{r},\boldsymbol{r}'\right) \cdot \hat{\boldsymbol{M}}\left(\boldsymbol{r}'\right) \\ &- \hat{\boldsymbol{M}}_{\mathrm{pro}}(\boldsymbol{r}) \cdot \mathscr{G}^{-}_{JH}\left(\boldsymbol{r},\boldsymbol{r}'\right) \cdot \hat{\boldsymbol{J}}\left(\boldsymbol{r}'\right) - \hat{\boldsymbol{M}}_{\mathrm{pro}}(\boldsymbol{r}) \cdot \mathscr{G}^{-}_{MH}\left(\boldsymbol{r},\boldsymbol{r}'\right) \cdot \hat{\boldsymbol{M}}\left(\boldsymbol{r}'\right)\Big]\, \mathrm{d}a'\, \mathrm{d}a\,, \end{aligned} \tag{5.26}$$

where S_{pro} is a Huygens surface around the probe and S_{aut} is the discretized Huygens surface

---

[5] The described procedure is the same for other discretizations of the equivalent surface currents, e.g., electric and magnetic dipoles [Paulus 2018b].

around the AUT. Substituting (5.24) and (5.25) into (5.26), we have

$$
\begin{aligned}
S_{21}
&= \frac{\mathrm{A}}{\sqrt{\mathrm{Wm}}} \sum_{n=1}^{N/2} x_n \oiint_{S_{\mathrm{pro}}} \oiint_{S_{\mathrm{aut}}} \left[\hat{\boldsymbol{J}}_{\mathrm{pro}}(\boldsymbol{r}) \cdot \boldsymbol{\mathcal{G}}^{-}_{JE}\left(\boldsymbol{r}, \boldsymbol{r}'\right) - \hat{\boldsymbol{M}}_{\mathrm{pro}}(\boldsymbol{r}) \cdot \boldsymbol{\mathcal{G}}^{-}_{JH}\left(\boldsymbol{r}, \boldsymbol{r}'\right)\right] \cdot \boldsymbol{\beta}_n\left(\boldsymbol{r}'\right) \,\mathrm{d}a' \,\mathrm{d}a \\
&+ \frac{\mathrm{V}}{\sqrt{\mathrm{Wm}}} \sum_{n=1+\frac{N}{2}}^{N} x_n \oiint_{S_{\mathrm{pro}}} \oiint_{S_{\mathrm{aut}}} \left[\hat{\boldsymbol{J}}_{\mathrm{pro}}(\boldsymbol{r}) \cdot \boldsymbol{\mathcal{G}}^{-}_{ME}\left(\boldsymbol{r}, \boldsymbol{r}'\right) - \hat{\boldsymbol{M}}_{\mathrm{pro}}(\boldsymbol{r}) \cdot \boldsymbol{\mathcal{G}}^{-}_{MH}\left(\boldsymbol{r}, \boldsymbol{r}'\right)\right] \cdot \boldsymbol{\beta}_{n-\frac{N}{2}}\left(\boldsymbol{r}'\right) \,\mathrm{d}a' \,\mathrm{d}a \,.
\end{aligned}
\tag{5.27}
$$

When the field is sampled with different probes or the same probe at different measurement locations, the interaction between the mth probe (or the probe at the mth measurement location) and the basis functions is given by

$$
S_{21,m} = \sum_{n=1}^{N} A_{mn} \, x_n \,, \tag{5.28}
$$

with

$$
A_{mn} = \frac{\mathrm{A}}{\sqrt{\mathrm{Wm}}} \oiint_{S_{\mathrm{pro},m}} \oiint_{S_{\mathrm{aut}}} \left[\hat{\boldsymbol{J}}_{\mathrm{pro},m}(\boldsymbol{r}) \cdot \boldsymbol{\mathcal{G}}^{-}_{JE}\left(\boldsymbol{r}, \boldsymbol{r}'\right) - \hat{\boldsymbol{M}}_{\mathrm{pro},m}(\boldsymbol{r}) \cdot \boldsymbol{\mathcal{G}}^{-}_{JH}\left(\boldsymbol{r}, \boldsymbol{r}'\right)\right] \cdot \boldsymbol{\beta}_n\left(\boldsymbol{r}'\right) \,\mathrm{d}a' \,\mathrm{d}a \tag{5.29}
$$

for the electric current elements stored at the indices $n \leq N/2$ and

$$
A_{mn} = \frac{\mathrm{V}}{\sqrt{\mathrm{Wm}}} \oiint_{S_{\mathrm{pro},m}} \oiint_{S_{\mathrm{aut}}} \left[\hat{\boldsymbol{J}}_{\mathrm{pro},m}(\boldsymbol{r}) \cdot \boldsymbol{\mathcal{G}}^{-}_{ME}\left(\boldsymbol{r}, \boldsymbol{r}'\right) - \hat{\boldsymbol{M}}_{\mathrm{pro},m}(\boldsymbol{r}) \cdot \boldsymbol{\mathcal{G}}^{-}_{MH}\left(\boldsymbol{r}, \boldsymbol{r}'\right)\right] \cdot \boldsymbol{\beta}_{n-\frac{N}{2}}\left(\boldsymbol{r}'\right) \,\mathrm{d}a' \,\mathrm{d}a \tag{5.30}
$$

for the magnetic current elements stored at the indices $n > N/2$. Here, $S_{\mathrm{pro},m}$ is the Huygens surface around the mth probe and $\hat{\boldsymbol{J}}_{\mathrm{pro},m}$, $\hat{\boldsymbol{M}}_{\mathrm{pro},m}$ are the normalized equivalent surface currents on $S_{\mathrm{pro},m}$ for that probe.

Naturally, one ends up with a linear system of equations of the form

$$
\boldsymbol{b} = \boldsymbol{A}\boldsymbol{x} \,, \tag{5.31}
$$

where the vector $\boldsymbol{b} \in \mathbb{C}^{M \times 1}$ stores the measured S_{21}-values for the M different probes (or the probe at the M different locations), the vector $\boldsymbol{x} \in \mathbb{C}^{N \times 1}$ stores the expansion coefficients x_n and the matrix $\boldsymbol{A} \in \mathbb{C}^{M \times N}$ describes the linear relationship between the source coefficients and the measured signals with the elements of $\boldsymbol{A}$ being defined by (5.29) and (5.30).

Generally, the DoFs for the radiated antenna fields are basically limited by the antenna size and the number N_{DoF} of practically relevant DoFs for the radiated fields. The number N_{DoF} depends on the desired accuracy of the field description (see Section 4.1) which should always be better than the measurement accuracy due to the noise floor to avoid significant additional errors being introduced by the field transformations. The number N_{DoF} may be estimated by counting the relevant spherical vector wave modes of the antenna with given size. From (4.11) in Section 4.1.2 it is known that the summation over radiating modes can be truncated at some $N_{\max} = \lfloor kr_0 \rfloor + n_{\mathrm{buffer}}$, where r_0 is the minimum sphere around the AUT and n_{buffer} is a small buffer to allow for moderate superdirectivity effects (see Section 4.1.3) leading to a total count of $2N_{\max}\left(N_{\max}+2\right)$ possible spherical modes [Hansen 1988, p. 128]. This estimation is an upper limit for the DoFs and the bound is only tight for antennas which fill the complete spherical volume. For non-spherical antennas, more accurate bounds have been derived [Toraldo di Francia 1969; Gori 1973; Bucci 1989; Bucci 1996; Bucci 1998; Piestun 2000; Bucci 2012; D'Agostino 2011; Fischer 2011] but in in the following spherical modes are used to estimate the DoFs due to their simplicity. The number of measurement samples M must of course be at least as large as N_{DoF} to be able to resolve all DoFs of the field[6]. Usually one has a certain degree of redundancy in the sampling (i.e., $M > N_{\mathrm{DoF}}$), which helps to diminish the influence of measurement noise, therefore, the overestimation of N_{DoF} by the spherical mode expansion does not hurt. Apart from the required number of measurement samples also their spatial distribution and the choice of the measurement probe matters. A lot of research has been put into optimizing the location of the measurement samples [Bucci 1998; Qureshi 2013b; Qureshi 2013c; Qureshi 2013a; Solimene 2013; D'Agostino 2013; Giordanengo 2014; Khare 2007; Solimene 2019]. As a rule of thumb, the fields are sufficiently sampled if — when projected to the smallest possible convex hull enclosing the AUT — there is a measurement sample approximately every $\lambda/2$ (in every direction on the hull) for the two linearly independent polarizations [Bucci 1998]. The number of singular values of the matrix $\boldsymbol{A}$ which have a magnitude above a certain accuracy threshold coincides well with the DoFs in the field, as long as enough measurement samples are obtained and the discretization of the surface currents is fine enough to allow for all relevant fields modes to be radiated [Peterson 1988; Stupfel 2008; Stupfel 2004; Vipiana 2007; Hansen 2019; Kornprobst 2019c; Kornprobst 2021a; Kornprobst 2019b]. To support well-conditioned systems of linear equations, it is beneficial to use a measurement probe which illuminates the probe with a homogeneous field. Successful transformations of measurement signals from probes without a main beam toward the AUT or even probes with a null toward the AUT have been demonstrated [Knapp 2018b] but the conditioning of the system matrix suffers from using inconvenient probes.

Assuming that the equivalent sources and the measurement samples were picked appropriately to represent all relevant DoFs of the radiated fields, solving (5.31) is still not straightforward. First of all, the matrix $\boldsymbol{A} \in \mathbb{C}^{M\times N}$ is not square, in general and therefore, a direct inverse $\boldsymbol{A}^{-1}$ does not exist. Often the normal-residual system of equations

$$\boldsymbol{A}^{\mathrm{H}}\boldsymbol{A}\boldsymbol{x} = \boldsymbol{A}^{\mathrm{H}}\boldsymbol{b} \tag{5.32}$$

is solved if $\boldsymbol{A}$ is overdetermined ($N > M$) [Saad 2003, p. 259] or the normal-error system of equations

$$\boldsymbol{A}\boldsymbol{A}^{\mathrm{H}}\boldsymbol{y} = \boldsymbol{b} \tag{5.33}$$

is used if $\boldsymbol{A}$ is underdetermined ($N < M$, the desired $\boldsymbol{x}$ can be found by $\boldsymbol{x} = \boldsymbol{A}^{\mathrm{H}}\boldsymbol{y}$) [Saad 2003, p. 259]. If the matrix $\boldsymbol{A}$ is overdetermined but has full column rank ($\mathrm{rank}(\boldsymbol{A}) = M$) the inverse

---

[6] If $M < N_{\mathrm{DoF}}$, one must rely on additional assumptions on the radiated field such as that the field representation in terms of spherical modes is sparse [Hofmann 2019].

of the normal-residual matrix $\boldsymbol{A}^{\mathrm{H}}\boldsymbol{A}$ exists and $\boldsymbol{x}$ is found by multiplying both sides of (5.32) with $\left(\boldsymbol{A}^{\mathrm{H}}\boldsymbol{A}\right)^{-1}$. If the matrix $\boldsymbol{A}$ is underdetermined but has full row rank ($\operatorname{rank}(\boldsymbol{A}) = N$) the inverse of the normal-error matrix $\boldsymbol{A}\boldsymbol{A}^{\mathrm{H}}$ exists and $\boldsymbol{y}$ is found by multiplying both sides of (5.32) with $\left(\boldsymbol{A}\boldsymbol{A}^{\mathrm{H}}\right)^{-1}$.

Unfortunately, the NF matrices $\boldsymbol{A}$ describing the NF measurement scenario do neither have full column rank nor full row rank (i.e., $\operatorname{rank}(\boldsymbol{A}) < M$ and $\operatorname{rank}(\boldsymbol{A}) < N$)[7]. This happens because usually the number of measurement samples exceeds the DoFs of the radiated fields and the equivalent sources have non-radiating and weakly radiating contributions. As discussed in Section 4.1.1, the representation of radiated fields by equivalent electric and magnetic currents is not unique, implying that there exist some current distributions, which do not generate any fields outside the Huygens surface. In addition to the non-radiating currents, some current distributions radiate a field which becomes negligibly small already at small distances to the AUT. The fields of these weakly radiating currents correspond to higher-order spherical modes and are associated with the superdirectivity effects discussed in Section 4.1.3. The singular values in $\boldsymbol{A}$ corresponding to non-radiating currents or weakly radiating currents are zero or at least very small.

The ambiguity in the currents associated to the strictly non-radiating portions can be overcome by using only one type of currents (only electric or only magnetic) [Petre 1992; Quijano 2010b] or by enforcing a fixed relation between both types. In the context of field transformations the most notably current constraints are combined source formulations [Mautz 1979; Harrington 1989; Kornprobst 2018] enforcing a fixed ratio between electric and magnetic currents and Love current formulations which force the fields on the inside of the Huygens surface to zero[8] [Quijano 2009; Quijano 2010a; Jørgensen 2010]. Although the ambiguities due to non-radiating currents are eliminated by imposing constraints on the currents, the problem associated with the superdirectivity effects of weakly radiating currents persists. The matrix $\boldsymbol{A}$ is similarly ill-conditioned for all constraint or unconstrained current types [Kornprobst 2021a]. The weakly radiating currents can not be reconstructed consistently with either method and the additional effort or the slowed convergence behavior associated with the constraints on the currents is often not justified [Kornprobst 2021a; Kornprobst 2019c]. The accuracy of the reconstructed fields depends more crucially on the method used to invert (5.32) or (5.33).

In principle, a truncated singular value decomposition (SVD) [Hansen 1990; Li 2011] of the matrix $\boldsymbol{A}$ can be used to eliminate all singular vectors associated with non-radiating or weakly radiating currents. All singular values below a certain accuracy threshold associated with the measurement error are neglected and the inversion of the resulting matrix only includes the relevant singular vectors [Sarkar 1999]. The high computational burden associated with an SVD prevents to use it directly for larger problems but iterative solvers such as the Generalized Minimal Residual (GMRES) [Saad 1986], [Saad 2003, pp. 171 ff.] algorithm show similar regularization properties if the iteration process is stopped at the right time [Calvetti 2002; Elden 2012]. To this end, using the normal-error system (5.33) is to be preferred over the normal-

---

[7] Technically, the singular values will not exactly be equal to zero, but the numerical rank is defined as the number of singular values above a certain accuracy threshold.

[8] The combined source constraints do not increase the computational and implementation effort for the source reconstruction whereas the implementation of the Love constraint can require to implement a singularity cancellation method or to invert a Gram matrix [Kornprobst 2021a; Kornprobst 2019a].

residual formulation (5.32), because it minimizes the the error $\|\boldsymbol{b} - \tilde{\boldsymbol{b}}\|$ directly linked to the observation vector $\boldsymbol{b}$ rather than the artificial residual $\|\boldsymbol{A}^{\mathrm{H}}\boldsymbol{b} - \boldsymbol{A}^{\mathrm{H}}\tilde{\boldsymbol{b}}\|$ ($\tilde{\boldsymbol{b}}$ denotes the estimate for the measurement vector in each iteration). The reconstructed solution after a fixed number of iterations is almost identical for both formulations but the correct stopping criterion is not clear for an iterative solver if the normal-residual equation (5.32) is used. With the normal-error equation (5.33), however, the iteration process can be stopped once the residual reaches a level comparable to the measurement error [Kornprobst 2019b; Kornprobst 2019c; Kornprobst 2019d; Kornprobst 2021a].

5.2.2. Field Transformation Based on Spherical Wave Expansions

The basic idea behind the field transformation based on spherical wave expansions is similar to the field transformation based on spatial current distributions. A linear model of the form $\boldsymbol{b} = \boldsymbol{A}\boldsymbol{x}$ is established to find the unknowns — here the AUT receive coefficients (which are of course directly related to the expansion coefficients of the radiated field) — from measured S_{12}-values. The expression in (5.20) may in principle be used to determine the elements of the system matrix $\boldsymbol{A}$. The coefficients in $\boldsymbol{x}$ could be found by inverting the system of equations in the same manner as for the spatial currents based transformation and, thus, the spherical wave expansion transformation could be used for arbitrary measurement setups, but the field transformation becomes particularly efficient when the measurements are obtained on a canonical measurement surface. First of all, it is desirable to sample the fields on a spherical measurement surface with constant radius R such that the same incident field coefficients $\tilde{\alpha}'^{(1),\mathrm{pro}}_{s\tilde{\mu}n}(\boldsymbol{R})$ can be used for all measurement samples. Second, a probe with rotationally symmetric pattern around the main beam direction is preferable, such that it is sufficient to consider the $m' = \pm 1$ probe modes, simplifying the translation of the probe fields into the AUT region. Probes which meet this requirement are sometimes called first-order probes[9]. Finally, having the probe positions at equiangular sampling steps in ϑ- and φ-direction is extremely useful to decrease the computational complexity of the NFFFT algorithm. To make full use of the efficient spherical transformation, it is assumed here that the AUT (antenna 1) is rotated around the rotation center $\boldsymbol{r}_{01}$ and the probe antenna (antenna 2, centered at $\boldsymbol{r}_{02}$) is positioned at a fixed distance $R = \|\boldsymbol{r}_{01} - \boldsymbol{r}_{02}\|$ from the AUT rotation center.

The unknown AUT receive coefficients are expressed in a local coordinate system fixed to the AUT and the known probe transmit coefficients are expressed in another local coordinate system fixed to the probe antenna. The probe coordinate system is parallel to the global coordinate system but shifted by an amount $\boldsymbol{R} = \boldsymbol{r}_{01} - \boldsymbol{r}_{02}$ in positive direction along the z-axis. Several S_{12} measurement samples are obtained with the AUT rotated against the global coordinate system. The position of the M measurement samples is defined by the Euler angles φ_m, ϑ_m, and χ_m with $m = 1, \ldots, M$. In order to find an expression for the S_{12} in dependency of the unknown AUT coefficients, one must transform the AUT receive coefficients and the probe transmit coefficients into a common coordinate system. To this end, in a first step, the test zone field which is created by the probe antenna is found by translating the radiated probe fields into

---

[9] Conical horn antennas can be considered as first-order probes. Rectangular horn antennas are not perfect first-order probes but they approximate a $\mu' = \pm 1$ probe with good accuracy as long as the measurement location is not too close to the AUT [Hansen 1988, p. 107].

incident field modes centered at $\boldsymbol{r}_{01}$. The S_{12}-parameter for every AUT rotation angle is then found by testing the incident field modes with the rotated AUT receive coefficients. Substituting rotated AUT receiving coefficients and translated probe field coefficients into (5.23), we have

$$
\begin{aligned}
&S_{12}\big(\vartheta_m, \varphi_m, \chi_m\big) \\
&= \sum_{s=1}^{2} \sum_{n=1}^{N_{\text{aut}}} \sum_{\tilde{\mu}=-n}^{n} \left[\underbrace{\sum_{\mu=-n}^{n} \left(\hat{\beta}_{s\mu n}^{(1),\text{aut}} \, \mathrm{e}^{\mathrm{j}\mu\varphi_m} \, \mathrm{d}_{\tilde{\mu}\mu}^{n}\big(\vartheta_m\big) \, \mathrm{e}^{\mathrm{j}\tilde{\mu}\chi_m} \right)}_{\text{rotated AUT receiving coefficients}} \underbrace{\sum_{\sigma=1}^{2} \sum_{\nu=1}^{N_{\text{pro}}} \sum_{\mu'=-\nu}^{\nu} \mathscr{T}_{s\tilde{\mu}n}^{\sigma\mu'\nu}(\boldsymbol{R}) \, \hat{\alpha}_{\sigma\mu'\nu}^{(4),\,\text{pro}}}_{\text{translated probe field coefficients}} \right] \\
&= \sum_{s=1}^{2} \sum_{n=1}^{N_{\text{aut}}} \sum_{\tilde{\mu}=-n}^{n} \sum_{\mu=-n}^{n} \hat{\beta}_{s\mu n}^{(1),\text{aut}} \, \mathrm{e}^{\mathrm{j}\mu\varphi_m} \, \mathrm{d}_{\tilde{\mu},\mu}^{n}\big(\vartheta_m\big) \, \mathrm{e}^{\mathrm{j}\tilde{\mu}\chi_m} \, \tilde{\alpha}_{s\tilde{\mu}n}^{\prime(1),\,\text{pro}}(\boldsymbol{R}) \,, \qquad (5.34)
\end{aligned}
$$

where

$$
\tilde{\alpha}_{s\tilde{\mu}n}^{\prime(1),\,\text{pro}}(\boldsymbol{R}) = \sum_{\sigma=1}^{2} \sum_{\nu=1}^{N_{\text{pro}}} \sum_{\mu'=-\nu}^{\nu} \mathscr{T}_{s\tilde{\mu}n}^{\sigma\mu'\nu}(\boldsymbol{R}) \, \hat{\alpha}_{\sigma\mu'\nu}^{(4),\,\text{pro}} \qquad (5.35)
$$

are the (normalized) expansion coefficients of the (normalized) incident fields in the AUT region (i.e., the translated probe field coefficients), which can be precomputed as they are the same for all measurement positions (as long as the measurement distance R does not change)[10]. Expressions for the translation coefficients $\mathscr{T}_{s\tilde{\mu}n}^{\sigma\mu'\nu}(\boldsymbol{R})$, which translate the outgoing $c = 4$-type transmit coefficients into incident $c = 1$-type coefficients, can be found in Appendix B. The Wigner-d-function $\mathrm{d}_{\tilde{\mu},\mu}^{n}(\vartheta)$ involved in the rotation is defined by [Wigner 1931, pp. 179ff.], [Hansen 1988, p. 345]

$$
\begin{aligned}
\mathrm{d}_{\tilde{\mu},\mu}^{n}(\vartheta) =& \sqrt{\frac{(n+\tilde{\mu})!\,(n-\tilde{\mu})!}{(n+\mu)!\,(n-\mu)!}} \\
&\times \sum_{p=0}^{n-\tilde{\mu}} \binom{n+\mu}{n-\tilde{\mu}-p} \binom{n-\mu}{p} (-1)^{n-\tilde{\mu}-p} \left(\cos\frac{\vartheta}{2}\right)^{2p+\tilde{\mu}+\mu} \left(\sin\frac{\vartheta}{2}\right)^{2n-2p-\tilde{\mu}-\mu} \qquad (5.36)
\end{aligned}
$$

where the symbol

$$
\binom{i}{j} = \frac{i!}{(i-j)!j!} \qquad (5.37)
$$

is the binomial coefficient. Notably, the Wigner-d-functions have a finite Fourier series expansion of the form [Hansen 1988, p. 346]

$$
\mathrm{d}_{\tilde{\mu},\mu}^{n}(\vartheta) = \mathrm{j}^{\tilde{\mu}-\mu} \sum_{\mu'=-n}^{n} \Delta_{\mu',\tilde{\mu}}^{n} \, \Delta_{\mu',\mu}^{n} \, \mathrm{e}^{-\mathrm{j}\mu'\vartheta} \,, \qquad (5.38)
$$

---

[10] Because the translation direction $\boldsymbol{R}$ is parallel to the z-axis, all translation coefficients with $\tilde{\mu} \neq \mu'$ are equal to zero and we have $\tilde{\alpha}_{s\tilde{\mu}n}^{\prime(1),\,\text{pro}}(\boldsymbol{R}) = \sum_{\sigma=1}^{2} \sum_{\substack{\nu=|\tilde{\mu}| \\ \nu\neq 0}}^{N_{\text{pro}}} \mathscr{T}_{s\tilde{\mu}n}^{\sigma\tilde{\mu}\nu}(\boldsymbol{R}) \, \hat{\alpha}_{\sigma\tilde{\mu}\nu}^{(4),\,\text{pro}}$. There exist efficient formulations for the translation coefficients if the translation is parallel to the z-axis [Hansen 1988, pp. 356ff.], [Stein 1961; Cruzan 1962].

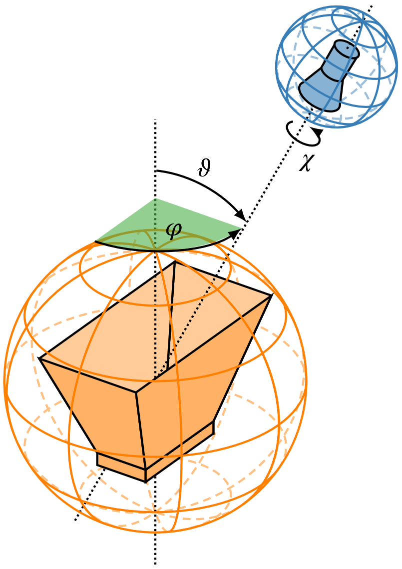

Fig. 5.3.: The probe is moved toward a certain ϑ- and φ-position, and rotated around its own axis by the angle χ.

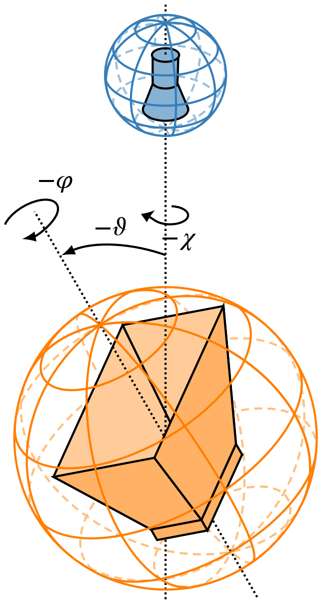

Fig. 5.4.: The AUT is rotated in reverse direction around the ϑ- and φ-axes. Thereafter, the AUT is rotated by $-\chi$ around the global z-axis.

where the $\Delta^n_{\mu',\tilde\mu}$ are given by [Hansen 1988, p. 346]

$$\Delta^n_{\mu',\tilde\mu} = \mathrm{d}^n_{\mu',\tilde\mu}\left(\frac{\pi}{2}\right) \tag{5.39}$$

as the Wigner-d-function with argument π/2.

The rotations around ϑ_m, φ_m, and χ_m can theoretically be achieved by either rotating the AUT or moving the probe as can be seen in the two equivalent scenarios depicted in Figs. 5.3 and 5.4, respectively. In many measurement setups, the probe will perform only the χ_m-rotation, whereas the AUT performs the ϑ- and φ-rotations. In anechoic measurement environments it is irrelevant for the formal description which antenna performs the rotations — e.g., the factor $\mathrm{e}^{\mathrm{j}\mu\chi_m}$ can easily be shifted from the AUT coefficients to the probe coefficients — but it will make a difference when echoes are considered in the formal description.

The total of $2N(N+2)$ unknowns $\hat\beta^{(1),\mathrm{aut}}_{smn}$ are stored in the vector $\boldsymbol{x} \in \mathbb{C}^{2N(N+2)}$. Having M measurements of the S_{12}-parameter obtained with the kth probe position defined by ϑ_m, φ_m, and χ_m we have

$$S_{12,m} = \sum_{\ell=1}^{2N(N+2)} A_{m\ell}x_\ell \,, \tag{5.40}$$

with

$$A_{m\ell} = \sum_{\tilde\mu=-n}^{n} \left(\mathrm{e}^{-\mathrm{j}\tilde\mu\varphi_m}\, \mathrm{d}^n_{\tilde\mu,\mu}\left(-\vartheta_m\right)\, \mathrm{e}^{-\mathrm{j}\mu\chi_m} \right)\, \tilde\alpha'^{(1),\,\mathrm{pro}}_{s\mu n}(\boldsymbol{R}) \,, \tag{5.41}$$

where the triple sum $\sum_{s=1}^{2}\sum_{n=1}^{N}\sum_{\mu=-n}^{n}$ is replaced by a single index summation $\sum_{\ell=1}^{2N(N+2)}$. The triple (s,μ,n) is found from ℓ as follows [Hansen 1988, p. 314]: $s=1$ for odd ℓ and $s=2$ for even ℓ, n is the integer part of $\sqrt{(\ell-s)/2+1}$, and μ is then given by $\mu=(j-s)/2+1-n\,(n+1)$. Naturally, one ends up with a system of equations of the form

$$\boldsymbol{b}=\boldsymbol{A}\boldsymbol{x}\,, \tag{5.42}$$

where the vector $\boldsymbol{b}\in\mathbb{C}^{M\times 1}$ stores the measured S_{12}-values for the M different probes positions, the vector $\boldsymbol{x}\in\mathbb{C}^{2N(N+2)\times 1}$ stores the receive coefficients $\hat{\beta}^{(1),\mathrm{aut}}_{s\tilde{\mu}n}$, and the matrix $\boldsymbol{A}\in\mathbb{C}^{M\times 2N(N+2)}$ describes the linear relationship between the receive coefficients and the measured signals with the elements of $\boldsymbol{A}$ being defined by (5.41). Of course, the expansion coefficients $\hat{\alpha}^{(4),\mathrm{aut}}_{s\tilde{\mu}n}$ for describing the transmit behavior of the AUT can be obtained by the reciprocity relationship (4.27). In fact, the same formulas can be directly used with S_{21}-parameter measurements by simply exchanging the AUT receiving coefficients $\hat{\beta}^{(1),\mathrm{aut}}_{s\mu n}$ with the corresponding transmit coefficients $\hat{\alpha}^{(4),\mathrm{aut}}_{s\mu n}$ and exchanging the probe transmit coefficients $\hat{\alpha}^{(4),\,\mathrm{pro}}_{\sigma\mu'\nu}$ with their corresponding receiving coefficients $\hat{\beta}^{(1),\,\mathrm{pro}}_{\sigma\mu'\nu}$.

In principle, the system of equations (5.42) can be readily solved for $\boldsymbol{x}$ with any of the methods described in Section 5.2.1, but particularly efficient implementations of the inversion of the system of equations (5.42) are based on the orthogonality relations [Hansen 1988, p. 111]

$$\int_0^{\pi} \mathrm{d}^{n}_{\tilde{\mu},\mu}(\vartheta)\;\mathrm{d}^{n'}_{\tilde{\mu},\mu}(\vartheta)\;\sin(\vartheta)\;\mathrm{d}\vartheta=\frac{2}{2n+1}\,\delta_{nn'} \tag{5.43}$$

for the Wigner-d-functions and

$$\int_0^{2\pi} \mathrm{e}^{\mathrm{j}\,(\mu-\mu')\,\varphi}\,\mathrm{d}\varphi=2\pi\,\delta_{\mu,\mu'} \tag{5.44}$$

for the exponential functions. Regarding the S_{12}-parameter from (5.34) as continuous function of the variables ϑ, φ, and χ, one obtains [Laitinen 2005, p. 25]

$$\frac{1}{4\pi^2}\,\frac{2n+1}{2}\int_0^{\pi}\int_0^{2\pi}\int_0^{2\pi}\mathrm{e}^{-\mathrm{j}\mu\varphi}\,\mathrm{e}^{-\mathrm{j}\tilde{\mu}\chi}\,\mathrm{d}^{n}_{\tilde{\mu},\mu}(\vartheta)\;S_{12}(\vartheta,\varphi,\chi)\;\mathrm{d}\chi\,\mathrm{d}\varphi\,\mathrm{d}\vartheta=\sum_{s=1}^{2}\;\hat{\beta}^{(1),\mathrm{aut}}_{s\mu n}\;\tilde{\alpha}'^{(1),\,\mathrm{pro}}_{s\tilde{\mu}n}(\boldsymbol{R}) \tag{5.45}$$

by applying the corresponding orthogonality integrals to (5.34). Each mode number $\tilde{\mu}$, for which the corresponding incident probe field coefficients $\tilde{\alpha}'^{(1),\,\mathrm{pro}}_{s\tilde{\mu}n}$ are non-zero, constitutes a new equation for the pair of unknowns $\hat{\beta}^{(1),\mathrm{aut}}_{1\mu n}$ and $\hat{\beta}^{(1),\mathrm{aut}}_{2\mu n}$ [Hansen 1988, p. 107]. Usually, one will use two arbitrary values for $\tilde{\mu}$ ($\tilde{\mu}=\pm 1$ is common as these are the only two non-zero choices for a first-order probe) to obtain a 2×2 matrix equation for the two unknowns $\hat{\beta}^{(1),\mathrm{aut}}_{1\mu n}$ and $\hat{\beta}^{(1),\mathrm{aut}}_{2\mu n}$.

The integrals in (5.45) are Fourier-type integrals which can be solved with an IFFT from a finite number of samples due to the band limitation of the involved angular dependencies[11].

---

[11] The IFFT can be directly applied for the φ- and χ-dependencies but the dependencies in ϑ-direction have to be extended into the domain $\pi<\vartheta<2\pi$ first [Hansen 1988, pp. 111ff.]. A detailed description of all steps involved in the efficient evaluation of the integrals can be found in [Hansen 1988].

The reduction of the computational cost comes along with an increased amount of measurement samples. The required number of sampling points in ϑ and φ can be derived from the Nyquist sampling theorem [Hansen 1988, pp. 128f.]. Since the modal expansion is truncated at the mode number $N = kr_0 + n_{\text{buffer}}$, the φ-dependency of the S_{12}-parameter includes harmonics from $\mathrm{e}^{-\mathrm{j}N\varphi}$ to $\mathrm{e}^{+\mathrm{j}N\varphi}$, a total of $2N + 1$ measurement samples must be obtained for every value of χ along every ring with constant ϑ such that the data can be processed with an FFT. The equiangular sampling step is $\Delta\varphi = \Delta\vartheta = 2\pi/(2N)$ which leads to a maximum distance of $\lambda/2$ if the sampling points are projected to the minimum sphere. In ϑ-direction, one must have $N + 1$ sampling locations. In general, $2N_{\text{pro}} + 1$ different samples for χ are required to evaluate the integral along χ exactly, since in principle $\tilde{\mu}$ may have any value between $-N_{\text{pro}}$ and N_{pro}. Only for first-order probes for which all probe coefficients with $\tilde{\mu} \neq \pm 1 = 0$, the integral can be evaluated with only two χ-samples (usually $\chi = 0$ and $\chi = \pi/2$) [Hansen 1988, pp. 108ff.]. This is the reason, why first-order probes are very popular for spherical measurement setups despite having a small bandwidth. For a first-order probe measurement setup, thus, the total number of measurement samples is $M = 2\,(2N + 1)\,(N + 1)$ [Hansen 1988, p. 129]. Obviously, the number of measurements M is about twice the number of unknown mode coefficients which is given by $2N\,(N + 2)$. The redundancy comes from the high sampling density near the poles. Alternative sampling schemes with $M \approx 2N\,(N + 2)$ can be used on spherical surfaces, for example by thinning the samples near the poles with a $\sin\vartheta$-taper. However, to be able to use the efficient FFT implementation, the samples on the equiangular grid have to be interpolated in an intermediate processing step [Hansen 1988, p. 129].

In contrast to equivalent surface current based approaches, the NFFFT based on spherical vector wave expansions does not suffer from the same source ambiguities (if the mode expansions are truncated appropriately). There are no non-radiating sources and the weakly radiating currents are strictly separated from the source coefficients of interest. This comes with a reduced flexibility in the placement of equivalent currents. The effective reconstruction surface in the spherical vector wave expansion is always a sphere while surface current based approaches can distribute the sources on an arbitrarily shaped Huygens surface. Thus, the possible radiated fields can be constrained more tightly by the surface current approach. Due to the larger source domain for the equivalent sources, a larger portion of the observation error may be mapped to the source coefficients in spherical-expansion based reconstruction methods than in equivalent current based reconstructions with a tight Huygens surface.

All spherical wave based based algorithms have been implemented in this thesis with a direct implementation (without FFT acceleration) of the matrix vector product (and its Hermitian transpose) in (5.42) to avoid any implementation artifacts as the spherical wave expansions are considered as a reference for the analysis of frequency domain echo suppression algorithms in this thesis. The inversion was performed using the iterative GMRES method with comparable stopping criteria as for the equivalent current based transformation algorithms.

5.2.3. Fast Multipole Method and Fully Probe Corrected Fast Irregular Antenna Field Transformation Algorithm

When the probe locations are not distributed on a spherical surface, but arbitrarily irregularly distributed, it is advisable to reduce the number of required operations which involve the translation operator $\mathscr{T}_{smn}^{\sigma\mu\nu}(\boldsymbol{R})$ from (5.35). This can be accomplished by performing translations from the

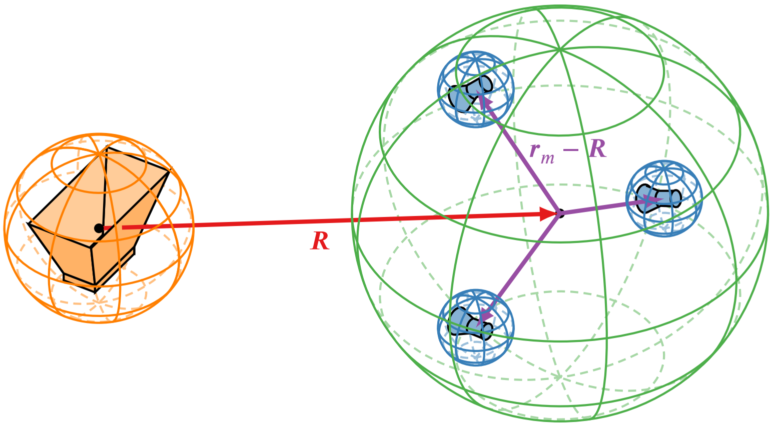

Fig. 5.5.: The centers of the AUT volume and of the observation volume are separated by $\boldsymbol{R}$. The locations of the probe centers can be expressed as $\boldsymbol{r}_m$. The arrows indicate the respective translations for the spherical coefficients.

AUT volume into a spherical observation volume which contains multiple probe locations (here it is customary to describe the scenario with a radiating AUT) and thereafter perform a secondary translation from the center of the observation region into the probe centers. The situation is depicted in Fig. 5.5.

The translation between the AUT center and the center of the spherical observation volume — separated by the translation vector $\boldsymbol{R}$ — transforming outward-traveling AUT coefficients $\hat{\alpha}^{(4),\mathrm{aut}}_{smn}$ into incident spherical wave coefficients $\hat{\alpha}^{(1),\mathrm{obs}}_{\sigma\mu\nu}$ in the observation volume is accomplished by a translation using the translation coefficients (see Appendix B)

$$\begin{aligned}&\mathscr{T}^{\sigma\mu\nu}_{smn}(\boldsymbol{R})\\&= -4\pi \sum_{\ell=0}^{\infty} (-1)^{\sigma+\mu+\nu} \oint\!\!\!\oint (-\mathrm{j})^{\ell}\, (2\ell+1)\, \mathrm{h}^{(2)}_{\ell}(k\,|\boldsymbol{R}|)\, \mathrm{P}_{\ell}\big(\hat{\boldsymbol{k}}\cdot\hat{\boldsymbol{R}}\big)\, \boldsymbol{K}^{(4)}_{smn}\big(\hat{\boldsymbol{k}}\big)\cdot \boldsymbol{K}^{(4)}_{\sigma,-\mu,\nu}\big(\hat{\boldsymbol{k}}\big)\, \mathrm{d}\hat{\boldsymbol{k}}\,.\end{aligned} \tag{5.46}$$

In a numerical implementation, the sum over ℓ is truncated at a finite index $\ell = L$, allowing to switch the order of the sum and the integral in (5.46). The translation coefficient can then be expressed in a compact notation as

$$\mathscr{T}^{\sigma\mu\nu}_{smn}(\boldsymbol{R}) \approx -4\pi\,(-1)^{\sigma+\mu+\nu} \oint\!\!\!\oint T_L\big(kR, \hat{\boldsymbol{k}}\cdot\hat{\boldsymbol{R}}\big)\, \boldsymbol{K}^{(4)}_{smn}\big(\hat{\boldsymbol{k}}\big)\cdot \boldsymbol{K}^{(4)}_{\sigma,-\mu,\nu}\big(\hat{\boldsymbol{k}}\big)\, \mathrm{d}\hat{\boldsymbol{k}} \tag{5.47}$$

with the the so-called propagating plane-wave translation operator

$$T_L\big(kR, \hat{\boldsymbol{k}}\cdot\hat{\boldsymbol{R}}\big) = \sum_{\ell=0}^{L} (-\mathrm{j})^{\ell}\, (2\ell+1)\, \mathrm{h}^{(2)}_{\ell}(k\,|\boldsymbol{R}|)\, \mathrm{P}_{\ell}\big(\hat{\boldsymbol{k}}\cdot\hat{\boldsymbol{R}}\big)\ , \tag{5.48}$$

which is known from the MLFMM and related methods. The approximation in (5.47) becomes exact in the limiting case of[12] $L \to \infty$.

---

[12] The diverging series for T_∞ is still well defined if the resulting expression is interpreted in a distributional sense [Chew 2007].

The coefficients $\hat{\alpha}^{(1),\mathrm{inc,pro}}_{\sigma'\mu'\nu'}$ of the incident fields in the probe centered coordinate systems can be found by a secondary translation involving the translation coefficients (see Appendix B and [Chew 2007].)

$$T^{\sigma'\mu'\nu'}_{\sigma\mu\nu}\big(\boldsymbol{r}_m - \boldsymbol{R}\big) = (-1)^{\sigma'+\mu'+\nu'} \oiint \boldsymbol{K}^{(4)}_{\sigma\mu\nu}\big(\hat{\boldsymbol{k}}\big)\, \mathrm{e}^{-\mathrm{j}\boldsymbol{k}\cdot(\boldsymbol{r}_m-\boldsymbol{R})} \cdot \boldsymbol{K}^{(4)}_{\sigma',-\mu',\nu'}\big(\hat{\boldsymbol{k}}\big)\, \mathrm{d}\hat{\boldsymbol{k}}\,. \tag{5.49}$$

Analogous to (5.20), the received probe signal (i.e., the S_{21}-parameter, as the description deals with normalized expansion coefficients) can be computed by weighting the incident field coefficients $\hat{\alpha}^{(1),\mathrm{inc,pro}}_{\sigma'\mu'\nu'}$ expressed in the probe centered coordinate system by the probe receive coefficients $\hat{\beta}^{(1),\mathrm{pro}}_{\sigma'\mu'\nu'}$ and one obtains[13]

$$\begin{aligned}
S_{21} &= \sum_{\sigma'=1}^{2}\sum_{\nu'=1}^{N_\mathrm{pro}}\sum_{\mu'=-\nu'}^{\nu'} \hat{\beta}^{(1),\mathrm{pro}}_{\sigma'\mu'\nu'}\,\hat{\alpha}^{(1),\mathrm{inc,pro}}_{\sigma'\mu'\nu'}\\
&= \sum_{\sigma'=1}^{2}\sum_{\nu'=1}^{N_\mathrm{pro}}\sum_{\mu'=-\nu'}^{\nu'} \hat{\beta}^{(1),\mathrm{pro}}_{\sigma'\mu'\nu'} \left(\sum_{\sigma=1}^{2}\sum_{\nu=1}^{N_\mathrm{obs}}\sum_{\mu=-\nu}^{\nu} T^{\sigma'\mu'\nu'}_{\sigma\mu\nu}\big(\boldsymbol{r}_m - \boldsymbol{R}\big)\,\hat{\alpha}^{(1),\mathrm{obs}}_{\sigma\mu\nu}\right)\\
&= \sum_{\sigma'=1}^{2}\sum_{\nu'=1}^{N_\mathrm{pro}}\sum_{\mu'=-\nu'}^{\nu'} \hat{\beta}^{(1),\mathrm{pro}}_{\sigma'\mu'\nu'}\\
&\qquad\qquad \times \left[\sum_{\sigma=1}^{2}\sum_{\nu=1}^{N_\mathrm{obs}}\sum_{\mu=-\nu}^{\nu} T^{\sigma'\mu'\nu'}_{\sigma\mu\nu}\big(\boldsymbol{r}_m - \boldsymbol{R}\big)\left(\sum_{s=1}^{2}\sum_{n=1}^{N_\mathrm{aut}}\sum_{m=-n}^{n} \mathcal{T}^{\sigma\mu\nu}_{smn}(\boldsymbol{R})\,\hat{\alpha}^{(4),\mathrm{aut}}_{smn}\right)\right]\\
&= \frac{1}{2}\sum_{\sigma'=1}^{2}\sum_{\nu'=1}^{N_\mathrm{pro}}\sum_{\mu'=-\nu'}^{\nu'} (-1)^{\mu'}\,\hat{\alpha}^{(4),\mathrm{pro}}_{\sigma',-\mu',\nu'}\\
&\qquad\qquad \times \left[\sum_{\sigma=1}^{2}\sum_{\nu=1}^{N_\mathrm{obs}}\sum_{\mu=-\nu}^{\nu} T^{\sigma'\mu'\nu'}_{\sigma\mu\nu}\big(\boldsymbol{r}_m - \boldsymbol{R}\big)\left(\sum_{s=1}^{2}\sum_{n=1}^{N_\mathrm{aut}}\sum_{m=-n}^{n} \mathcal{T}^{\sigma\mu\nu}_{smn}(\boldsymbol{R})\,\hat{\alpha}^{(4),\mathrm{aut}}_{smn}\right)\right],
\end{aligned} \tag{5.50}$$

where the reciprocity relation (4.27) was used. Inserting (5.47) and (5.49) into (5.50) one ends up with the equation

$$\begin{aligned}
&S_{21}\\
&= -2\pi \sum_{\sigma'\mu'\nu'} (-1)^{\mu'}\,\hat{\alpha}^{(4),\mathrm{pro}}_{\sigma',-\mu',\nu'} \oiint \left[\sum_{\sigma\mu\nu} (-1)^{\sigma'+\mu'+\nu'}\,\boldsymbol{K}^{(4)}_{\sigma\mu\nu}\big(\hat{\boldsymbol{k}}'\big)\,\mathrm{e}^{-\mathrm{j}\boldsymbol{k}'\cdot(\boldsymbol{r}_m-\boldsymbol{R})} \cdot \boldsymbol{K}^{(4)}_{\sigma',-\mu',\nu'}\big(\hat{\boldsymbol{k}}'\big)\right.\\
&\qquad \left. \times \left(\oiint \sum_{smn} \hat{\alpha}^{(4),\mathrm{aut}}_{smn}\,(-1)^{\sigma+\mu+\nu}\,T_L\big(kR, \hat{\boldsymbol{k}}\cdot\hat{\boldsymbol{R}}\big)\,\boldsymbol{K}^{(4)}_{smn}\big(\hat{\boldsymbol{k}}\big)\cdot\boldsymbol{K}^{(4)}_{\sigma,-\mu,\nu}\big(\hat{\boldsymbol{k}}\big)\right)\mathrm{d}\hat{\boldsymbol{k}}\right]\mathrm{d}\hat{\boldsymbol{k}}'\,,
\end{aligned} \tag{5.51}$$

---

[13] It is understood that the probe location and rotation is different for every sample of the S_{21}-parameter. This dependency is implicitly incorporated into the probe receive coefficients. The index m of the probe location $\boldsymbol{r}_m$ must not be confused with a mode order m of the spherical expansion.

which can be further simplified by

$$\sum_{\sigma\mu\nu} \boldsymbol{K}^{(4)}_{\sigma\mu\nu}\big(\hat{\boldsymbol{k}}'\big)\ (-1)^{\sigma+\mu+\nu} \oiint \boldsymbol{K}^{(4)}_{\sigma,-\mu,\nu}\big(\hat{\boldsymbol{k}}\big) \cdot \boldsymbol{E}_{\mathrm{FF}}\big(\hat{\boldsymbol{k}}\big)\ \mathrm{d}\hat{\boldsymbol{k}} = \boldsymbol{E}_{\mathrm{FF}}\big(\hat{\boldsymbol{k}}'\big)\ , \tag{5.52}$$

which holds for an arbitrary FF pattern function[14] $\boldsymbol{E}_{\mathrm{FF}}\big(\hat{\boldsymbol{k}}\big)$. One obtains

$$\begin{aligned} S_{21} = -2\pi \sum_{\sigma'=1}^{2} \sum_{\nu'=1}^{N_{\mathrm{pro}}} \sum_{\mu'=-\nu'}^{\nu'} (-1)^{\mu'}\, \hat{\alpha}^{(4),\mathrm{pro}}_{\sigma',-\mu',\nu'} \oiint \Bigg[&(-1)^{\sigma'+\mu'+\nu'}\, \mathrm{e}^{-\mathrm{j}\boldsymbol{k}'\cdot(\boldsymbol{r}_m-\boldsymbol{R})}\, \boldsymbol{K}^{(4)}_{\sigma',-\mu',\nu'}\big(\hat{\boldsymbol{k}}'\big) \\ &\times \left(\sum_{s'=1}^{2} \sum_{n=1}^{N_{\mathrm{aut}}} \sum_{m=-n}^{n} \hat{\alpha}^{(4),\mathrm{aut}}_{smn}\, T_L\big(kR, \hat{\boldsymbol{k}}' \cdot \hat{\boldsymbol{R}}\big)\, \boldsymbol{K}^{(4)}_{smn}\big(\hat{\boldsymbol{k}}'\big) \right) \Bigg] \mathrm{d}\hat{\boldsymbol{k}}'\ , \end{aligned} \tag{5.53}$$

The final expression is obtained by substituting the FF pattern of the AUT

$$\hat{\boldsymbol{E}}^{(4),\mathrm{aut}}_{\mathrm{FF}}\big(\hat{\boldsymbol{k}}\big) = \sum_{s=1}^{2} \sum_{n=1}^{N_{\mathrm{aut}}} \sum_{m=-n}^{n} \hat{\alpha}^{(4),\mathrm{aut}}_{smn} \boldsymbol{K}^{(4)}_{smn}\big(\hat{\boldsymbol{k}}\big) \tag{5.54}$$

and the inverted FF pattern ($-\hat{\boldsymbol{k}}$ instead of $\hat{\boldsymbol{k}}$) of the equivalent probe sources[15]

$$\hat{\boldsymbol{E}}^{(4),\mathrm{pro}}_{\mathrm{FF}}\big(-\hat{\boldsymbol{k}}\big) = \sum_{\sigma'=1}^{2} \sum_{\nu'=1}^{N_{\mathrm{pro}}} \sum_{\mu'=-\nu'}^{\nu'} (-1)^{\sigma'+\nu'}\, \hat{\alpha}^{(4),\mathrm{pro}}_{\sigma',-\mu',\nu'} \boldsymbol{K}^{(4)}_{\sigma',-\mu',\nu'}\big(\hat{\boldsymbol{k}}\big)\ . \tag{5.55}$$

into (5.53) to find the spectral domain transmission equation

$$S_{21} = -2\pi \oiint \hat{\boldsymbol{E}}^{(4),\mathrm{pro}}_{\mathrm{FF}}\big(-\hat{\boldsymbol{k}}\big)\ \mathrm{e}^{-\mathrm{j}\boldsymbol{k}'\cdot(\boldsymbol{r}_m-\boldsymbol{R})}\ T_L\big(kR, \hat{\boldsymbol{k}}' \cdot \hat{\boldsymbol{R}}\big) \cdot \hat{\boldsymbol{E}}^{(4),\mathrm{aut}}_{\mathrm{FF}}\big(\hat{\boldsymbol{k}}\big)\, \mathrm{d}\hat{\boldsymbol{k}}\,, \tag{5.56}$$

which coincides with the gain normalized transmission equations in [Neitz 2017; Neitz 2020] if one considers the differently scaled definitions of FF patterns in this thesis. This transmission equation is the key for the efficient evaluation of the interaction between an AUT and arbitrarily located probes. It is closely related to the fast multipole method (FMM) [Rokhlin 1993; Darve 2000; Coifman 1993] but has full probe correction incorporated.

Noticeably, only the FF patterns of the AUT and the probe are needed to be able to evaluate the transmission equation (5.56), even if the probes are located in the NF. The only limitation comes from the fact that the spherical observation volume must not interfere with the minimum sphere around the AUT. The transmission equation (5.56) unifies the different descriptions of the AUT

---

[14] The term $\alpha_{\sigma,\mu,\nu} = (-1)^{\sigma'+\mu'+\nu'} \oiint \boldsymbol{K}^{(4)}_{\sigma,-\mu,\nu}\big(\hat{\boldsymbol{k}}\big)\, \boldsymbol{E}_{\mathrm{FF}}\big(\hat{\boldsymbol{k}}\big)\ \mathrm{d}\hat{\boldsymbol{k}}$ can be easily identified as the spherical wave expansion for $\boldsymbol{E}_{\mathrm{FF}}\big(\hat{\boldsymbol{k}}\big)$, thus, the summation in (5.52) yields $\sum_{\sigma\mu\nu} \alpha_{\sigma,\mu,\nu} \boldsymbol{K}^{(4)}_{\sigma\mu\nu}\big(\hat{\boldsymbol{k}}'\big) = \boldsymbol{E}_{\mathrm{FF}}\big(\hat{\boldsymbol{k}}'\big)$. If the summation of ν is truncated at some finite value N_{obs}, only the low-order modes (up to the mode order $\nu = N_{\mathrm{obs}}$) of the resulting $\boldsymbol{E}_{\mathrm{FF}}\big(\hat{\boldsymbol{k}}'\big)$ will agree with the original function $\boldsymbol{E}_{\mathrm{FF}}\big(\hat{\boldsymbol{k}}\big)$, but this is sufficient for the current discussion because the low-order modes suffice to accurately describe the field in the complete observation volume.

[15] The same identity for the spherical expansion of the inverted FF pattern has already been used in (5.21) to derive reciprocity.

fields by either equivalent currents or spherical waves, as it is in principle irrelevant by which kind of equivalent source description the AUT and probe FF patterns $\hat{\boldsymbol{E}}_{\mathrm{FF}}^{(4),\mathrm{aut}}$ and $\hat{\boldsymbol{E}}_{\mathrm{FF}}^{(4),\mathrm{pro}}$ are obtained. As long as an FF pattern can be computed from the sources, it can be used with (5.56).

Adapting the ideas from the MLFMM [Song 1995; Song 1997] and refining the evaluation of the spectral domain integrals and translations [Eibert 2016b; Eibert 2004; Eibert 2005; Eibert 2016a] has led to a very powerful algorithm called FIAFTA. A detailed discussion of FIAFTA is out of the scope of this thesis and the interested reader may refer to, for instance, [Schmidt 2011b; Schmidt 2008a; Schmidt 2008b; Schmidt 2007] for details. The AUT FF pattern which is translated toward the observation volume can efficiently be calculated in a hierarchical manner from a domain decomposition of the AUT volume. The AUT is decomposed in many small, non-intersecting source domains and the equivalent FF patterns are calculated for each small source domain separately, requiring only a small computational effort for every domain as few FF samples are sufficient to represent the fields accurately [Chew 2001]. The FF spectra of neighboring source domains are then subsequently combined in a hierarchical scheme until one finds the FF pattern of the complete source domain before it is translated toward the observation volume[16]. This procedure is called *aggregation*. An analogous procedure (in reverse order of the operations) distributes the incident field in the observation region from a large observation region to smaller and smaller observation volumes until each observation volume only contains a single probe. This procedure is called *disaggregation*. The hierarchical aggregation and disaggregation allows to evaluate the matrix vector product $\boldsymbol{Ax}$ and its Hermitian transpose with a complexity of $N\log(N)$, where N is the number of unknowns for the equivalent AUT description. This allows to use iterative equation solvers such as GMRES to invert the arising systems of equations in inverse source problems even for large problems.

FIAFTA has been used in this thesis to evaluate the interactions between the AUT and the probe for all current-based AUT representations. Due to its beneficial regularization properties, the GMRES solver is used whenever an NFFFT related system of equations is to be solved in this work (including all transformations with FIAFTA and the spherical expansion based methods). The normal-error equation (5.33) is preferred when an a priori estimate for the reconstruction deviation (e.g., based on the noise level) exists. If no estimate for the reconstruction deviation can be used as a stopping criterion (e.g., when it is known that the chosen source model is not sufficient to recreate the measurements), the normal-residual equation (5.32) is used with a stopping criterion for the residual in the order of 10^{-6}, which has shown to be a good choice in many practical situations.

5.2.4. A Note on Phaseless Field Transformation Algorithms

In general, fully coherent (i.e., magnitude and phase) measurement samples have to be collected at sufficiently many sampling locations on a closed measurement surface around the AUT in order to be able to transform the NF measurements into the FF. The requirement for measuring the phase can be relaxed, if the phase information can be reconstructed from the available measurement samples [Yaccarino 1999; Isernia 1994a; Migliore 2000; Schnattinger 2014; Schmidt 2009; Schmidt 2010; Razavi 2006; Candes 2013]. Naturally, additional information (as compared to

---

[16] The translations can also be performed on lower source box levels. Then multiple translations must be performed before the complete incident field in the observation volume is obtained.

a coherent measurement) is required for the phase reconstruction [Knapp 2019b] which may be provided by field measurements on multiple measurement surfaces [Bucci 1990], by using multiple or specialized probes [Pierri 1999; Costanzo 2002; Costanzo 2005; Paulus 2017a], by increased sampling rates [Álvarez 2018; Álvarez 2015], by using local coherence [Knapp 2017b; Paulus 2017c; Kornprobst 2021b; Paulus 2021] or by combining the measurements at different frequencies [Paulus 2020b; Paulus 2020a; Knapp 2021]. For most phase reconstruction methods, the success of the reconstruction depends on the measurement data, as usually an underlying non-convex minimization problem must be solved [Balan 2015; Isernia 1994b; Isernia 1995; Candes 2015; Knapp 2017a; Paulus 2018a; Paulus 2017b; Paulus 2016; Paulus 2018c]. Convex formulations of the phase retrieval problem require the measurement data to be obtained in a special form [Kornprobst 2021b], have a high computational complexity [Candes 2013], or rely on very high numbers of measurement samples (around the square of the number which is required in fully coherent measurements) [Knapp 2018c; Knapp 2019d].

Phase reconstruction methods require redundancy in the data to be able to determine the missing phase of the measurement samples. Echo suppression methods — which are subject of this thesis — require redundancy in the data to be able to separate the undesired echo influences from the free-space AUT signals. Consequently, there is a conflict of interest about the usage of the redundant data if the post-processing has to perform echo suppression as well as phase reconstruction. The optimal trade-off in this regard is subject of future research and phaseless NFFFT algorithms are not further investigated in this thesis.

5.3. Chapter Summary

In this chapter, NFFFTs have been revisited. Their formal description has been based on the transmission equation for a transmitted signal between two antennas in terms of spherical waves or equivalent surface currents. The spherical-wave based NFFFT is particularly efficient for a spherical measurement surface with a first-order probe, whereas the equivalent current based approach is much more flexible with the location of the equivalent sources which can be placed on an arbitrarily shaped Huygens surface. The FMM-inspired FIAFTA has been shown to unify the different approaches and yields an efficient NFFFT algorithm for arbitrary probes with possibly irregular locations. FIAFTA is used for all current based NFFFTs in this thesis, whereas a naive implementation of the direct matrix inversion is used for all spherical expansion based transformations. The NFFFTs presented in this thesis can already be found in the literature [Hansen 1988; Álvarez 2006; Schmidt 2008b]. The spectral domain transmission equation (5.56) has been derived slightly differently in this thesis (starting from the spherical wave expansion) than for example in [Neitz 2017]. Spherical and current based NFFFTs are the core of the frequency domain echo suppression techniques discussed in this thesis.

6

Antenna Measurements in Echoic Environments

This chapter presents the formal description of the interaction between two antennas in presence of echo objects. The situation is depicted in Fig. 6.1. The echo object alters the total field distribution by scattering or absorption. The influence of the echo object on the total field can be represented by equivalent surface currents on the surface S_{ech} enclosing the echo object and by commonly less important additional equivalent surface currents at the probe or AUT to account for mutual interactions between the antennas and the echo object.

The scattered fields generated by the equivalent currents on S_{ech} depend only (ignoring multiple reflections) on the incident fields around the echo object. Different incident fields cause different scattered fields and, therefore, the equivalent currents on S_{ech} differ if antenna 1 or antenna 2 is transmitting. Reciprocity between antenna 1 and antenna 2 still holds ($S_{12} = S_{21}$) and one can use either by the S_{12}- or the S_{21}-parameter depending on which one is more convenient.

The receiving antenna (either the AUT or the probe may be receiving) alters the total field distribution by absorbing some of the incident fields and by structural scattering (a perfectly matched antenna is assumed such that no reradiation occurs). Theoretically, the changed total fields may have an influence on the equivalent currents on the radiating antenna and the echo object. The effect of these distortions of equivalent current distributions on the S_{21}- or the S_{12}-parameter is neglected in this section.

6.1. Transmitting Antenna Under Test

First, consider a radiating AUT (antenna 1). The radiating AUT model is convenient for all situations, in which the relative position of the echo object with respect to the AUT does not change[1]. Neglecting the probe antenna, the radiated fields of the AUT (normalized to the

---

[1] This situation may occur if the echo is due to scattering at AUT mounting structures which are fixed to the AUT or if the AUT is stationary in an echoic environment while the probe antenna is moved to different locations to

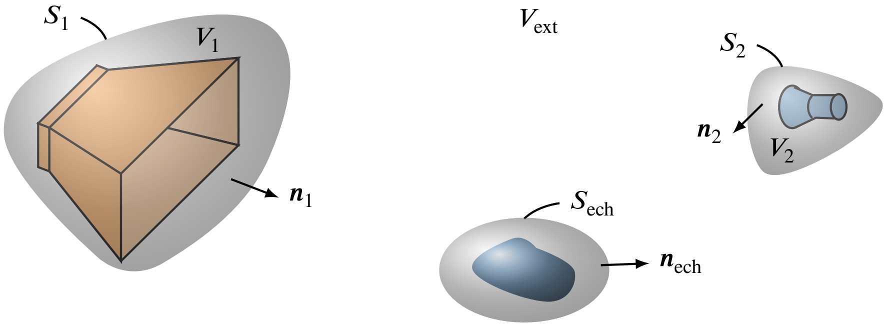

Fig. 6.1.: Two antennas enclosed by two Huygens surfaces S_1 and S_2 in proximity of an echo object.

excitation a_1) in presence of the echo object may be expressed by

$$\begin{aligned}\frac{\boldsymbol{E}(\boldsymbol{r})}{a_1} = &\oiint\limits_{S_1} \left[\boldsymbol{\mathcal{G}}^{-}_{JE}(\boldsymbol{r},\boldsymbol{r}')\cdot\hat{\boldsymbol{J}}_{\tilde{1}}(\boldsymbol{r}') + \boldsymbol{\mathcal{G}}^{-}_{ME}(\boldsymbol{r},\boldsymbol{r}')\cdot\hat{\boldsymbol{M}}_{\tilde{1}}(\boldsymbol{r}')\right]\,\mathrm{d}a' \\ &+ \oiint\limits_{S_{\text{ech}}} \left[\boldsymbol{\mathcal{G}}^{-}_{JE}(\boldsymbol{r},\boldsymbol{r}')\cdot\hat{\boldsymbol{J}}_{\text{ech1}}(\boldsymbol{r}') + \boldsymbol{\mathcal{G}}^{-}_{ME}(\boldsymbol{r},\boldsymbol{r}')\cdot\hat{\boldsymbol{M}}_{\text{ech1}}(\boldsymbol{r}')\right]\,\mathrm{d}a'\,, \end{aligned} \tag{6.1}$$

$$\begin{aligned}\frac{\boldsymbol{H}(\boldsymbol{r})}{a_1} = &\oiint\limits_{S_1} \left[\boldsymbol{\mathcal{G}}^{-}_{JH}(\boldsymbol{r},\boldsymbol{r}')\cdot\hat{\boldsymbol{J}}_{\tilde{1}}(\boldsymbol{r}') + \boldsymbol{\mathcal{G}}^{-}_{MH}(\boldsymbol{r},\boldsymbol{r}')\cdot\hat{\boldsymbol{M}}_{\tilde{1}}(\boldsymbol{r}')\right]\,\mathrm{d}a' \\ &+ \oiint\limits_{S_{\text{ech}}} \left[\boldsymbol{\mathcal{G}}^{-}_{JH}(\boldsymbol{r},\boldsymbol{r}')\cdot\hat{\boldsymbol{J}}_{\text{ech1}}(\boldsymbol{r}') + \boldsymbol{\mathcal{G}}^{-}_{MH}(\boldsymbol{r},\boldsymbol{r}')\cdot\hat{\boldsymbol{M}}_{\text{ech1}}(\boldsymbol{r}')\right]\,\mathrm{d}a'\,, \end{aligned} \tag{6.2}$$

where $\hat{\boldsymbol{J}}_{\text{ech1}}$, $\hat{\boldsymbol{M}}_{\text{ech1}}$ are the (normalized) equivalent currents expressing the field scattered by the echo object due to the incident field generated by the transmitting antenna 1. Notice that the equivalent currents

$$\hat{\boldsymbol{J}}_{\tilde{1}} = \hat{\boldsymbol{J}}_1 + \hat{\boldsymbol{J}}_{1,\text{dis}}\,, \tag{6.3}$$

$$\hat{\boldsymbol{M}}_{\tilde{1}} = \hat{\boldsymbol{M}}_1 + \hat{\boldsymbol{M}}_{1,\text{dis}}\,, \tag{6.4}$$

differ from the undistorted AUT currents $\hat{\boldsymbol{J}}_1$, $\hat{\boldsymbol{M}}_1$ by a distortion $\hat{\boldsymbol{J}}_{1,\text{dis}}$, $\hat{\boldsymbol{M}}_{1,\text{dis}}$ because some portion of the scattered field is incident on the AUT, causing a distortion in the current distribution. The equivalent currents $\hat{\boldsymbol{J}}_{\tilde{1}}$, $\hat{\boldsymbol{M}}_{\tilde{1}}$ not only account for the AUT radiation but also for the scattering at the AUT. Finally the currents on the AUT and the scattering object represent the steady state with all multiple interactions included.

Under the assumption that the presence of a probe antenna (antenna 2) does not alter the total

---

sample the radiated field (e.g., in a planar measurement setup or when the AUT is measured in-situ).

field distribution decisively[2], the S_{21}-parameter between the AUT and the probe is given by

$$\begin{aligned} S_{21} = \oiint\limits_{S_2} \oiint\limits_{S_1} & \Big[\hat{\boldsymbol{J}}_2(\boldsymbol{r}) \cdot \boldsymbol{\mathcal{G}}^-_{JE}(\boldsymbol{r},\boldsymbol{r}') \cdot \hat{\boldsymbol{J}}_{\tilde{1}}(\boldsymbol{r}') + \hat{\boldsymbol{J}}_2(\boldsymbol{r}) \cdot \boldsymbol{\mathcal{G}}^-_{ME}(\boldsymbol{r},\boldsymbol{r}') \cdot \hat{\boldsymbol{M}}_{\tilde{1}}(\boldsymbol{r}') \\ & - \hat{\boldsymbol{M}}_2(\boldsymbol{r}) \cdot \boldsymbol{\mathcal{G}}^-_{JH}(\boldsymbol{r},\boldsymbol{r}') \cdot \hat{\boldsymbol{J}}_{\tilde{1}}(\boldsymbol{r}') - \hat{\boldsymbol{M}}_2(\boldsymbol{r}) \cdot \boldsymbol{\mathcal{G}}^-_{MH}(\boldsymbol{r},\boldsymbol{r}') \cdot \hat{\boldsymbol{M}}_{\tilde{1}}(\boldsymbol{r}')\Big] \,\mathrm{d}a'\,\mathrm{d}a \\ + \oiint\limits_{S_2} \oiint\limits_{S_{\mathrm{ech}}} & \Big[\hat{\boldsymbol{J}}_2(\boldsymbol{r}) \cdot \boldsymbol{\mathcal{G}}^-_{JE}(\boldsymbol{r},\boldsymbol{r}') \cdot \hat{\boldsymbol{J}}_{\mathrm{ech1}}(\boldsymbol{r}') + \hat{\boldsymbol{J}}_2(\boldsymbol{r}) \cdot \boldsymbol{\mathcal{G}}^-_{ME}(\boldsymbol{r},\boldsymbol{r}') \cdot \hat{\boldsymbol{M}}_{\mathrm{ech1}}(\boldsymbol{r}') \\ & - \hat{\boldsymbol{M}}_2(\boldsymbol{r}) \cdot \boldsymbol{\mathcal{G}}^-_{JH}(\boldsymbol{r},\boldsymbol{r}') \cdot \hat{\boldsymbol{J}}_{\mathrm{ech1}}(\boldsymbol{r}') - \hat{\boldsymbol{M}}_2(\boldsymbol{r}) \cdot \boldsymbol{\mathcal{G}}^-_{MH}(\boldsymbol{r},\boldsymbol{r}') \cdot \hat{\boldsymbol{M}}_{\mathrm{ech1}}(\boldsymbol{r}')\Big] \,\mathrm{d}a'\,\mathrm{d}a\,. \end{aligned} \tag{6.5}$$

To highlight the deviation to the anechoic case, one substitutes (6.3) and (6.4) into (6.5) to get

$$\begin{aligned} S_{21} = \oiint\limits_{S_2} \oiint\limits_{S_1} & \Big[\hat{\boldsymbol{J}}_2(\boldsymbol{r}) \cdot \boldsymbol{\mathcal{G}}^-_{JE}(\boldsymbol{r},\boldsymbol{r}') \cdot \hat{\boldsymbol{J}}_1(\boldsymbol{r}') + \hat{\boldsymbol{J}}_2(\boldsymbol{r}) \cdot \boldsymbol{\mathcal{G}}^-_{ME}(\boldsymbol{r},\boldsymbol{r}') \cdot \hat{\boldsymbol{M}}_1(\boldsymbol{r}') \\ & - \hat{\boldsymbol{M}}_2(\boldsymbol{r}) \cdot \boldsymbol{\mathcal{G}}^-_{JH}(\boldsymbol{r},\boldsymbol{r}') \cdot \hat{\boldsymbol{J}}_1(\boldsymbol{r}') - \hat{\boldsymbol{M}}_2(\boldsymbol{r}) \cdot \boldsymbol{\mathcal{G}}^-_{MH}(\boldsymbol{r},\boldsymbol{r}') \cdot \hat{\boldsymbol{M}}_1(\boldsymbol{r}')\Big] \,\mathrm{d}a'\,\mathrm{d}a \\ + \oiint\limits_{S_2} \oiint\limits_{S_1} & \Big[\hat{\boldsymbol{J}}_2(\boldsymbol{r}) \cdot \boldsymbol{\mathcal{G}}^-_{JE}(\boldsymbol{r},\boldsymbol{r}') \cdot \hat{\boldsymbol{J}}_{1,\mathrm{dis}}(\boldsymbol{r}') + \hat{\boldsymbol{J}}_2(\boldsymbol{r}) \cdot \boldsymbol{\mathcal{G}}^-_{ME}(\boldsymbol{r},\boldsymbol{r}') \cdot \hat{\boldsymbol{M}}_{1,\mathrm{dis}}(\boldsymbol{r}') \\ & - \hat{\boldsymbol{M}}_2(\boldsymbol{r}) \cdot \boldsymbol{\mathcal{G}}^-_{JH}(\boldsymbol{r},\boldsymbol{r}') \cdot \hat{\boldsymbol{J}}_{1,\mathrm{dis}}(\boldsymbol{r}') - \hat{\boldsymbol{M}}_2(\boldsymbol{r}) \cdot \boldsymbol{\mathcal{G}}^-_{MH}(\boldsymbol{r},\boldsymbol{r}') \cdot \hat{\boldsymbol{M}}_{1,\mathrm{dis}}(\boldsymbol{r}')\Big] \,\mathrm{d}a'\,\mathrm{d}a \\ + \oiint\limits_{S_2} \oiint\limits_{S_{\mathrm{ech}}} & \Big[\hat{\boldsymbol{J}}_2(\boldsymbol{r}) \cdot \boldsymbol{\mathcal{G}}^-_{JE}(\boldsymbol{r},\boldsymbol{r}') \cdot \hat{\boldsymbol{J}}_{\mathrm{ech1}}(\boldsymbol{r}') + \hat{\boldsymbol{J}}_2(\boldsymbol{r}) \cdot \boldsymbol{\mathcal{G}}^-_{ME}(\boldsymbol{r},\boldsymbol{r}') \cdot \hat{\boldsymbol{M}}_{\mathrm{ech1}}(\boldsymbol{r}') \\ & - \hat{\boldsymbol{M}}_2(\boldsymbol{r}) \cdot \boldsymbol{\mathcal{G}}^-_{JH}(\boldsymbol{r},\boldsymbol{r}') \cdot \hat{\boldsymbol{J}}_{\mathrm{ech1}}(\boldsymbol{r}') - \hat{\boldsymbol{M}}_2(\boldsymbol{r}) \cdot \boldsymbol{\mathcal{G}}^-_{MH}(\boldsymbol{r},\boldsymbol{r}') \cdot \hat{\boldsymbol{M}}_{\mathrm{ech1}}(\boldsymbol{r}')\Big] \,\mathrm{d}a'\,\mathrm{d}a\,. \end{aligned} \tag{6.6}$$

The expression (6.6) for the S_{21}-parameter in presence of an echo object differs from the free-space radiation in two additive integral terms. The term

$$\begin{aligned} \oiint\limits_{S_2} \oiint\limits_{S_1} & \Big[\hat{\boldsymbol{J}}_2(\boldsymbol{r}) \cdot \boldsymbol{\mathcal{G}}^-_{JE}(\boldsymbol{r},\boldsymbol{r}') \cdot \hat{\boldsymbol{J}}_{1,\mathrm{dis}}(\boldsymbol{r}') + \hat{\boldsymbol{J}}_2(\boldsymbol{r}) \cdot \boldsymbol{\mathcal{G}}^-_{ME}(\boldsymbol{r},\boldsymbol{r}') \cdot \hat{\boldsymbol{M}}_{1,\mathrm{dis}}(\boldsymbol{r}') \\ & - \hat{\boldsymbol{M}}_2(\boldsymbol{r}) \cdot \boldsymbol{\mathcal{G}}^-_{JH}(\boldsymbol{r},\boldsymbol{r}') \cdot \hat{\boldsymbol{J}}_{1,\mathrm{dis}}(\boldsymbol{r}') - \hat{\boldsymbol{M}}_2(\boldsymbol{r}) \cdot \boldsymbol{\mathcal{G}}^-_{MH}(\boldsymbol{r},\boldsymbol{r}') \cdot \hat{\boldsymbol{M}}_{1,\mathrm{dis}}(\boldsymbol{r}')\Big] \,\mathrm{d}a'\,\mathrm{d}a \end{aligned} \tag{6.7}$$

accounts for deviations of the current distribution of the AUT in presence of echoes and

$$\begin{aligned} \oiint\limits_{S_2} \oiint\limits_{S_{\mathrm{ech}}} & \Big[\hat{\boldsymbol{J}}_2(\boldsymbol{r}) \cdot \boldsymbol{\mathcal{G}}^-_{JE}(\boldsymbol{r},\boldsymbol{r}') \cdot \hat{\boldsymbol{J}}_{\mathrm{ech1}}(\boldsymbol{r}') + \hat{\boldsymbol{J}}_2(\boldsymbol{r}) \cdot \boldsymbol{\mathcal{G}}^-_{ME}(\boldsymbol{r},\boldsymbol{r}') \cdot \hat{\boldsymbol{M}}_{\mathrm{ech1}}(\boldsymbol{r}') \\ & - \hat{\boldsymbol{M}}_2(\boldsymbol{r}) \cdot \boldsymbol{\mathcal{G}}^-_{JH}(\boldsymbol{r},\boldsymbol{r}') \cdot \hat{\boldsymbol{J}}_{\mathrm{ech1}}(\boldsymbol{r}') - \hat{\boldsymbol{M}}_2(\boldsymbol{r}) \cdot \boldsymbol{\mathcal{G}}^-_{MH}(\boldsymbol{r},\boldsymbol{r}') \cdot \hat{\boldsymbol{M}}_{\mathrm{ech1}}(\boldsymbol{r}')\Big] \,\mathrm{d}a'\,\mathrm{d}a \end{aligned} \tag{6.8}$$

---

[2] That means that the absorption and the scattering at the probe changes the total field distribution only in a way such that the subsequent changes of the equivalent current distributions at the AUT and the scattering object do not lead to a significant change of the incident fields in the probe volume.

accounts for the influence of the echo object currents on the receive signal. Very conveniently, all currents accounting for the distortions in the field (i.e., $\hat{\boldsymbol{J}}_{1,\mathrm{dis}}$, $\hat{\boldsymbol{M}}_{1,\mathrm{dis}}$ and $\hat{\boldsymbol{J}}_{\mathrm{ech1}}$, $\hat{\boldsymbol{M}}_{\mathrm{ech1}}$) are independent of the probe position and the probe receive currents $\hat{\boldsymbol{J}}_2$, $\hat{\boldsymbol{M}}_2$ are identical to the free-space receive currents (i.e., they are known).

Thus, if the echo object position is fixed with respect to the AUT, the echo influence can be expressed by additional equivalent AUT currents — not only present in the original AUT volume V_1 but also on the surface of the echo object. The probe is treated as in free-space.

6.2. Transmitting Probe

An expression for the S_{12}-parameter for a radiating probe analogous to (6.6) is also possible. We have

$$
\begin{aligned}
S_{12} = \oiint_{S_1} \oiint_{S_2} & \Big[\hat{\boldsymbol{J}}_1(\boldsymbol{r}) \cdot \mathscr{G}^{-}_{JE}(\boldsymbol{r},\boldsymbol{r}') \cdot \hat{\boldsymbol{J}}_2(\boldsymbol{r}') + \hat{\boldsymbol{J}}_1(\boldsymbol{r}) \cdot \mathscr{G}^{-}_{ME}(\boldsymbol{r},\boldsymbol{r}') \cdot \hat{\boldsymbol{M}}_2(\boldsymbol{r}') \\
& - \hat{\boldsymbol{M}}_1(\boldsymbol{r}) \cdot \mathscr{G}^{-}_{JH}(\boldsymbol{r},\boldsymbol{r}') \cdot \hat{\boldsymbol{J}}_2(\boldsymbol{r}') - \hat{\boldsymbol{M}}_1(\boldsymbol{r}) \cdot \mathscr{G}^{-}_{MH}(\boldsymbol{r},\boldsymbol{r}') \cdot \hat{\boldsymbol{M}}_2(\boldsymbol{r}')\Big] \, \mathrm{d}a' \, \mathrm{d}a \\
+ \oiint_{S_1} \oiint_{S_2} & \Big[\hat{\boldsymbol{J}}_1(\boldsymbol{r}) \cdot \mathscr{G}^{-}_{JE}(\boldsymbol{r},\boldsymbol{r}') \cdot \hat{\boldsymbol{J}}_{2,\mathrm{dis}}(\boldsymbol{r}') + \hat{\boldsymbol{J}}_1(\boldsymbol{r}) \cdot \mathscr{G}^{-}_{ME}(\boldsymbol{r},\boldsymbol{r}') \cdot \hat{\boldsymbol{M}}_{2,\mathrm{dis}}(\boldsymbol{r}') \\
& - \hat{\boldsymbol{M}}_1(\boldsymbol{r}) \cdot \mathscr{G}^{-}_{JH}(\boldsymbol{r},\boldsymbol{r}') \cdot \hat{\boldsymbol{J}}_{2,\mathrm{dis}}(\boldsymbol{r}') - \hat{\boldsymbol{M}}_1(\boldsymbol{r}) \cdot \mathscr{G}^{-}_{MH}(\boldsymbol{r},\boldsymbol{r}') \cdot \hat{\boldsymbol{M}}_{2,\mathrm{dis}}(\boldsymbol{r}')\Big] \, \mathrm{d}a' \, \mathrm{d}a \\
+ \oiint_{S_1} \oiint_{S_\mathrm{ech}} & \Big[\hat{\boldsymbol{J}}_1(\boldsymbol{r}) \cdot \mathscr{G}^{-}_{JE}(\boldsymbol{r},\boldsymbol{r}') \cdot \hat{\boldsymbol{J}}_{\mathrm{ech2}}(\boldsymbol{r}') + \hat{\boldsymbol{J}}_1(\boldsymbol{r}) \cdot \mathscr{G}^{-}_{ME}(\boldsymbol{r},\boldsymbol{r}') \cdot \hat{\boldsymbol{M}}_{\mathrm{ech2}}(\boldsymbol{r}') \\
& - \hat{\boldsymbol{M}}_1(\boldsymbol{r}) \cdot \mathscr{G}^{-}_{JH}(\boldsymbol{r},\boldsymbol{r}') \cdot \hat{\boldsymbol{J}}_{\mathrm{ech2}}(\boldsymbol{r}') - \hat{\boldsymbol{M}}_1(\boldsymbol{r}) \cdot \mathscr{G}^{-}_{MH}(\boldsymbol{r},\boldsymbol{r}') \cdot \hat{\boldsymbol{M}}_{\mathrm{ech2}}(\boldsymbol{r}')\Big] \, \mathrm{d}a' \, \mathrm{d}a \,.
\end{aligned}
\tag{6.9}
$$

Here, the equivalent currents in the probe region may differ from the free-space probe currents (this difference is accounted for by $\hat{\boldsymbol{J}}_{2,\mathrm{dis}}$ and $\hat{\boldsymbol{M}}_{2,\mathrm{dis}}$) and the currents $\hat{\boldsymbol{J}}_{\mathrm{ech2}}$, $\hat{\boldsymbol{M}}_{\mathrm{ech2}}$ on the echo object account for the scattering due to the illumination by the probe. All echo influences are expressed by additional equivalent probe currents — not only present in the original probe volume V_2 but also on the surface of the echo object. The AUT is treated as in free-space.

The echo currents on the echo object differ dependent on whether the AUT or the probe is illuminating the object, but for reciprocal antennas in reciprocal media we have $S_{12} = S_{21}$ and the expressions (6.6) and (6.9) may be used interchangeably. The expression in (6.9) has advantages over (6.6) in a moving AUT scenario, where the position of the echo object is fixed to the probe.

6.3. Chapter Summary

The transmission equation has been extended to account for the influence of an echo object in this chapter. Additional currents were introduced at the echo and antenna locations. The additional echo currents differ dependent on which antenna radiates but the interaction described by either the S_{12}- or the S_{21}-parameter remains the same. The more convenient formulation can be used to describe the interaction but different scenarios call for different representations.

7

Echo Suppression Methods in Time Domain

Echo suppression techniques based on the time-domain representation of a signal[1] exploit the fact that in conventional measurement setups, the direct AUT contributions[2] usually have shorter path lengths than the scattered contributions, as can be seen in Fig. 7.1 [Henderson 1989; Waiyapattanakorn 1993; Jough 1997; Hsiao 2003; Mauermayer 2016; Mauermayer 2017; De Porrata-Doria i Yague 1998; Lestari 2005; Levitas 1996; Blech 2010a; Tian 2008; Young 1973]. The signal of interest[3] may therefore be truncated before the influences of the scattered paths become visible in the signal. Of course, to end up with a useful signal after truncation, it is desirable to keep the portion of the signal belonging to the LOS part of the signal unaltered.

In theory, a viable method to measure the signal would be to feed antenna 1 with a short impulse and record the received signal in time-domain at antenna 2. If everything works as planned, one can see distinct maxima in the signal for the desired LOS paths and for the scattered paths. By choosing a suitable truncation window, one can get rid of the undesired signal contributions occurring at later times. Filtering signal portions based on their occurrence in time is called *time gating*, but the term *time gating* is used rather broadly in this work and includes the process of deducing the time-domain signal from frequency samples as well as windowing the reconstructed time-domain signal appropriately. Hardware time gating — i.e., measuring and truncating the signal directly in time-domain — requires specialized hardware and is rarely encountered in practice [Blech 2010a; Blech 2010b; Hartmann 1998]. The discussion of time gating is therefore

---

[1] Here, the term *signal* represents a certain scalar quantity of interest, which may vary in time and/or frequency. Time-varying signals have a representation in frequency-domain, related by the Fourier transform. A typical *signal* is the output of a probe (i.e., the voltage or the wave amplitude of the guided mode at the probe antenna port). However, one can also apply time-gating to other signals such as the source coefficients of the AUT.

[2] The term LOS path will be used in the following for the direct AUT contributions, in the style of FF scenarios although it is clear that in NF scenarios the image of a single path connecting the AUT to the probe is not accurate.

[3] In this chapter the signal of interest is the output signal of the probe, other signals are time gated in later chapters.

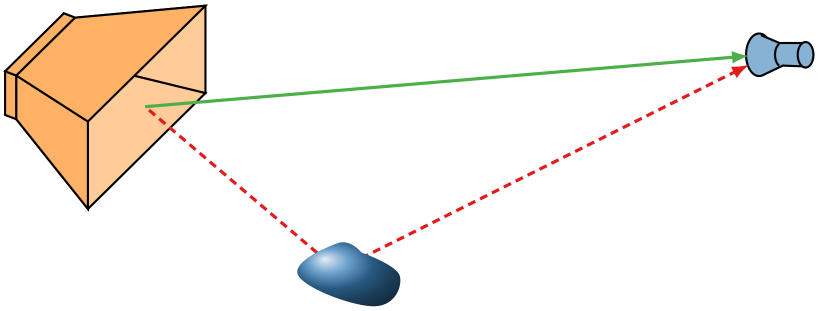

Fig. 7.1.: Line of sight path (green, solid line) and scattered path (red, dashed line) between antenna 1 and antenna 2.

limited to software time gating in this thesis — i.e., measuring the signal at discrete frequencies in the frequency-domain and deducing and windowing a time-domain signal from there. The truncated time-domain signal is then transformed into frequency-domain, where all further processing (e.g., an NFFFT) takes place.

In practice, several difficulties complicate the situation. The signal is distorted on its way "over the air". The transmit channel between the antenna ports has a frequency dependency and also depends on the relative position of the two antennas to each other (after all, this frequency dependent behavior of the transmission channel is what one wants to measure). Even though the excitation signal may have been a sharply time limited impulse, the measurement signal to be time gated can span over a much longer duration. It is therefore hard to guarantee in practice that the time signal of the desired signal contribution does not interfere with the time signal corresponding to the scattered paths. Finding a suitable time-domain representation and choosing an effective gating window which suppresses as much as possible of the echo contributions and preserves as much as possible of the desired portion is a delicate task.

Commonly, a (sampled) time-domain signal is obtained by directly applying the inverse discrete Fourier transform to the measured frequency-domain signal components. Possible interpretations of the resulting time-domain sequences are discussed first, before the impact of altering the time-domain sequence — e.g., by windowing or frequency-domain extrapolation — is investigated in this chapter.

7.1. Estimating the Time-Domain Signal From Frequency-Domain Measurements

Since often, the signal is measured at discrete samples in frequency-domain, a corresponding time signal must be estimated. To this end, the measured samples at different frequencies are interpreted as samples of the frequency response $H(\omega)$ of a transfer function of a linear, time-invariant system.

The time-domain impulse response $h(t)$ of a linear, time-invariant system is related to its spectral representation $H(\omega)$ via the Fourier transformation

$$H(\omega) = \mathcal{F}\{h(t)\} = \frac{1}{\sqrt{2\pi}} \int_{-\infty}^{\infty} h(t)\ \mathrm{e}^{-\mathrm{j}\omega t}\,\mathrm{d}t \tag{7.1}$$

and the inverse Fourier transformation

$$h(t) = \mathcal{F}^{-1}\{H(\omega)\} = \frac{1}{\sqrt{2\pi}} \int_{-\infty}^{\infty} H(\omega)\ \mathrm{e}^{\mathrm{j}\omega t}\,\mathrm{d}\omega\,. \tag{7.2}$$

Of course, the spectrum $H(\omega)$ is only known at several discrete measurement frequencies ω_k, $k = 0, \dots, N-1$. The time-domain signal $h(t)$ is not uniquely defined by the few measurement samples in frequency-domain. In principle infinitely many time-domain signals $h_{\mathrm{est}}(t)$ can have the measured spectral components at the measured frequencies but different spectral components at frequencies which have not been measured. Formally, different estimates

$$h_{\mathrm{est}}(t) = \frac{1}{\sqrt{2\pi}} \int_{-\infty}^{\infty} H_{\mathrm{est}}(\omega)\ \mathrm{e}^{\mathrm{j}\omega t}\,\mathrm{d}\omega \tag{7.3}$$

of the time-domain function can be obtained by using different estimates $H_{\mathrm{est}}(\omega)$ for the frequency-domain functions. The frequency-domain estimates solely have to agree with the measured spectral components at the measured frequencies, i.e., $H_{\mathrm{est}}\big(\omega_k\big) \overset{!}{=} H\big(\omega_k\big)$ for all $k \in \{0, \dots, N-1\}$. It is therefore in general not possible to reconstruct the *true* time-domain signal $h(t)$ from measurements of a finite number of spectral component samples at discrete frequencies.

Since the *true* time-domain signal cannot be found with certainty from the finite number of measurement samples, the question arises, how one can at least recover a *reasonable* or *helpful* time-domain signal from the limited spectral information. Certain useful assumptions on reasonable time-domain signals are helpful to find a useful time-domain signal which may be used for time gating. The time-domain impulse response signal should be causal and time limited, i.e., $h_{\mathrm{est}}(t) = 0$ for $t < 0$ and $t > T$ for some finite duration T. For practical purposes, it is sufficient that the signal has decayed to a small enough value below the noise limit of the measurement hardware after the duration T.

To simplify the upcoming discussion, it is assumed that the spectrum $H(\omega)$ is known at N equispaced frequencies $\omega_k = \omega_{\min} + k\,\Delta\omega$, $k = 0, \dots, N-1$ with a constant frequency step $\Delta\omega = \omega_{k+1} - \omega_k$. The samples of the spectrum $H(\omega)$ at the discrete frequencies ω_k are denoted by $H[k] = H\big(\omega_k\big)$, where the square brackets indicate that $H[k]$ corresponds to a frequency-discrete function.

7.1.1. Estimating the Time-Domain Signal as a Periodic Function with the Inverse Fast Fourier Transform

A straightforward way to generate a time-domain signal in accordance with the measured frequency-domain samples is to assign an exponential time dependency of the form $\mathrm{e}^{\mathrm{j}\omega_k t}$ to every measured spectral component ω_k.

This is equivalent to estimating the spectrum as $H_{\mathrm{est}}(\omega) = \sum_{k=0}^{N-1} \delta\big(\omega - \omega_k\big)\ H[k]$ — not a very realistic estimate, as one would expect a continuous spectrum, but it can serve as a starting point for the analysis. The corresponding time-domain signal can be found as [Oppenheim 2010]

$$h_{\mathrm{est}}(t) = \frac{1}{\sqrt{2\pi}} \sum_{k=0}^{N-1} H[k]\, \mathrm{e}^{\mathrm{j}\omega_k t} = \frac{1}{\sqrt{2\pi}} \mathrm{e}^{\mathrm{j}t\,\omega_{\mathrm{min}}} \sum_{k=0}^{N-1} H[k]\, \mathrm{e}^{\mathrm{j}k\,\Delta\omega\, t}\,. \tag{7.4}$$

The estimated time-domain function h_{est} is periodic with periodicity $T = 2\pi/\Delta\omega$. This means that the estimated time-domain function $h_{\mathrm{est}}(t)$ is strictly band limited ($H_{\mathrm{est}}(\omega) = 0$ for $\omega < \omega_{\mathrm{min}}$ and for $\omega > \omega_{\mathrm{min}} + (N-1)\,\Delta\omega$) and, thus, not time limited. This time-domain signal does not meet the criteria of a reasonable time-domain estimate, but it serves as a starting point for the discussion. The inverse discrete Fourier transform $\mathscr{F}^{-1}[\cdot]$ defined as[4]

$$f[n] = \mathscr{F}^{-1}\left[F[k]\right] = \frac{1}{N} \sum_{k=0}^{N-1} F[k]\, \mathrm{e}^{\mathrm{j}\frac{2\pi}{N}kn} \tag{7.5}$$

between a time-discrete function $f[n]$ and a frequency-discrete function $F[n]$ can be used to calculate the value of the estimated time-domain signal at the discrete times $t_n = 2\pi\, n/(\Delta\omega N) = n\,\Delta t$, spaced with a regular time step $\Delta t = 2\pi/(N\,\Delta\omega)$. We have

$$\begin{aligned} h_{\mathrm{est}}[n] &= \frac{1}{\sqrt{2\pi}} \mathrm{e}^{\mathrm{j}t_n\,\omega_{\mathrm{min}}} \sum_{k=0}^{N-1} H[k]\, \mathrm{e}^{\mathrm{j}k\,\Delta\omega\, t_n} \\ &= \frac{N}{\sqrt{2\pi}} \mathrm{e}^{\mathrm{j}2\pi\frac{\omega_{\mathrm{min}} n}{\Delta\omega\, N}}\, \mathscr{F}^{-1}\left[H[k]\right] \\ &= \frac{N}{\sqrt{2\pi}} \mathrm{e}^{\mathrm{j}\Delta t\,\omega_{\mathrm{min}} n}\, \mathscr{F}^{-1}\left[H[k]\right]\,, \end{aligned} \tag{7.6}$$

where $h_{\mathrm{est}}[n] = h_{\mathrm{est}}\big(t_n\big)$ is the estimated time-domain signal sampled at the discrete times t_n. Since the time-domain signal is known to be periodic, one only needs to know the values of $h_{\mathrm{est}}[n]$ in the interval $n = 1, \ldots, N-1$ to be able to deduce $h_{\mathrm{est}}[n]$ for all integers n.

Efficient implementations of the discrete Fourier transform and the inverse discrete Fourier transform are provided by the FFT and IFFT, respectively[5]. Often it is useful to consider the corresponding baseband signal

$$h_{\mathrm{est,BB}}[n] = h_{\mathrm{est}}[n] \frac{\sqrt{2\pi}}{N} \mathrm{e}^{-\mathrm{j}2\pi\frac{\omega_{\mathrm{min}} n}{\Delta\omega\, N}} = \mathscr{F}^{-1}\left[H[k]\right] \tag{7.7}$$

and its continuous counterpart

$$h_{\mathrm{est,BB}}(t) = \mathrm{e}^{-\mathrm{j}\omega_{\mathrm{min}} t} h_{\mathrm{est}}(t) \tag{7.8}$$

---

[4] The discrete Fourier transform $\mathscr{F}[\cdot]$ and its inverse $\mathscr{F}^{-1}[\cdot]$ can be distinguished from their continuous counterparts $\mathscr{F}\{\cdot\}$ and $\mathscr{F}^{-1}\{\cdot\}$ by the square brackets instead of the curly brackets.

[5] As all discrete Fourier transforms (and their inverses) have been evaluated by means of FFTs and IFFTs, the term "FFT" is used synonymously with "discrete Fourier transform" in this work (analogous for the IFFT).

to simplify some calculations. The information in the (downconverted) complex base band signal $h_{\mathrm{est,BB}}(t)$ is equivalent to the information in the original time-domain sequence $h_{\mathrm{est}}(t)$ and one expression can easily be obtained from the other. Therefore, in the following the text will switch between the expressions whenever convenient.

Dealing with a properly sampled, strictly band limited signal, one can exactly interpolate the continuous base band signal $h_{\mathrm{est,BB}}(t)$ from its samples at the discrete times by[6] [Oppenheim 2010, pp. 192ff.]

$$h_{\mathrm{est,BB}}(t) = \sum_{n=-\infty}^{\infty} h_{\mathrm{est,BB}}[n] \operatorname{sinc}\left(\frac{t - n\Delta t}{\Delta t}\right) \tag{7.10}$$

with the sinc-function $\operatorname{sinc}(x) = \sin(\pi x)/(\pi x)$. In practice, the interpolation of the time-domain data can be performed by "zero padding" the frequency-domain data [Smith 2010]. By attending zeros to the frequency-domain sequence $H[k]$, the effective length of the sequence is increased from N to N_{pad} and, consequently, the time-domain samples

$$h_{\mathrm{est,padded}}[n] = \frac{N_{\mathrm{pad}}}{\sqrt{2\pi}} \mathrm{e}^{\mathrm{j}2\pi \frac{\omega_{\mathrm{min}} n}{\Delta\omega N_{\mathrm{pad}}}} \mathscr{F}^{-1}\left[H_{\mathrm{pad}}[k]\right] \tag{7.11}$$

are now sampled at the discrete times $t_n = 2\pi n / \left(\Delta\omega N_{\mathrm{pad}}\right) = n\,\Delta t_{\mathrm{pad}}$. By changing the number of zeros which are appended to the frequency-domain sequence, one can generate time-domain samples which are arbitrarily close to any desired time t. One should remember that zero padding in the frequency domain corresponds to the cyclic (the underlying time-domain signal is assumed to be periodic) interpolation (7.10) of the corresponding time-domain signal when the domains are related by an IFFT. Also the "true" resolution of the time-domain signal (i.e., the capabilty of separating two peaks) is not affected by zero padding. Zero padding is only a method to re-sample the same slowly varying time-domain signal $h_{\mathrm{est}}(t)$.

The spectral samples $H[k]$ at the discrete frequencies ω_k can be obtained from the sampled time-domain signal $h_{\mathrm{est}}[n]$ with the help of the discrete Fourier transform $\mathscr{F}[\cdot]$ (or the FFT), defined as

$$F[k] = \mathscr{F}[f[n]] = \sum_{k=0}^{N-1} f[n]\,\mathrm{e}^{-\mathrm{j}\frac{2\pi}{N}kn}\,. \tag{7.12}$$

We have

$$H[k] = \frac{\sqrt{2\pi}}{N} \mathscr{F}\left[h_{\mathrm{est}}[n]\,\mathrm{e}^{-\mathrm{j}2\pi\frac{\omega_{\mathrm{min}} n}{\Delta\omega N}}\right] \tag{7.13}$$

or in terms of the corresponding base band signal

$$H[k] = \mathscr{F}\left[h_{\mathrm{est,BB}}[n]\right]\,. \tag{7.14}$$

---

[6] Luckily, the infinite sum can be exactly evaluated by the finite sum [Schanze 1995]

$$h_{\mathrm{est,BB}}(t) = \frac{\sin(\pi t)}{2N} \sum_{n=-L}^{M-1} h_{\mathrm{est}}[n](-1)^n \left[(-1)^{N+1} \tan\left(\pi\frac{t-n}{2N}\right) + \cot\left(\pi\frac{t-n}{2N}\right)\right]\,, \tag{7.9}$$

where $L + M = N$ because the discrete signal $h_{\mathrm{est}}[n]$ is N-periodic. For a detailed discussion and derivation see [Schanze 1995; Cavicchi 1992; Yaroslavsky 1996; Candocia 1998; Dooley 2000] and references therein.

7.1.2. Estimation of the Time-Domain Signal as a Time-Limited Function with the Inverse Fast Fourier Transform

As mentioned previously, the time-domain impulse response should fulfill certain causality and energy conservation properties and thus it is inconvenient to estimate $h(t)$ as a periodic function (periodic functions in time-domain are neither causal nor finite in their energy content). Thus, a causal and time limited estimate

$$\overline{h}_{\mathrm{est}}(t) = \mathrm{rect}\left(\frac{t}{T} - \frac{T}{2}\right)\, h_{\mathrm{est}}(t) \tag{7.15}$$

for the time-domain signal can be obtained by windowing the periodic estimate $h_{\mathrm{est}}(t)$ from the previous section with a properly scaled and shifted rectangular function

$$\mathrm{rect}(t) = \begin{cases} 0 & \text{for } |t| > 1/2 \\ 1 & \text{for } |t| < 1/2 \\ 1/2 & \text{for } |t| = 1/2 \end{cases} . \tag{7.16}$$

For $0 < t < T$, the functions $h_{\mathrm{est}}(t)$ and $\overline{h}_{\mathrm{est}}(t)$ are identical but $\overline{h}_{\mathrm{est}}(t)$ is zero outside this interval. As for the periodic time-domain estimate we must have (since the time-domain estimates are identical in the interval $0 < t < T$)

$$\overline{h}_{\mathrm{est}}[n] = \frac{N}{\sqrt{2\pi}} \mathrm{e}^{\mathrm{j}2\pi\frac{\omega_{\mathrm{min}} n}{\Delta\omega N}}\, \mathscr{F}^{-1}\left[H[k]\right] , \tag{7.17}$$

where $\overline{h}_{\mathrm{est}}[n]$ is the estimated time-domain signal at the discrete times $t_n = 2\pi\, n/(\Delta\omega N)$, with $n = 0, \dots, N-1$. Correspondingly, we have for the discrete base band signal

$$\overline{h}_{\mathrm{est,BB}}[n] = \mathscr{F}^{-1}\left[H[k]\right] . \tag{7.18}$$

Since the two time-domain signals $\overline{h}_{\mathrm{est}}(t)$ and $h_{\mathrm{est}}(t)$ are identical in the interval $0 < t < T$, one can use the identical methods to find and interpolate the time-domain signals in this interval.

However, the estimates for the corresponding frequency-domain signals differ. While in the previous section the frequency-domain signal was discontinuous, the frequency-domain signal $\overline{H}_{\mathrm{est}}(\omega)$ corresponding to the time limited time-domain estimate $\overline{h}_{\mathrm{est}}(t)$ is a continuous function in ω. Since the Fourier transform of the involved rectangular window is given by

$$\mathscr{F}\left\{\mathrm{rect}\left(\frac{t}{T} - \frac{T}{2}\right)\right\} = \mathrm{e}^{-\mathrm{j}\frac{\omega T}{2}}\, \frac{T}{\sqrt{2\pi}}\, \mathrm{sinc}\left(\frac{\omega T}{2\pi}\right) , \tag{7.19}$$

with the sinc-function $\mathrm{sinc}(x) = \sin(\pi\, x)/(\pi\, x)$, the frequency-domain function corresponding to $\overline{h}_{\mathrm{est}}(t)$ is given by

$$\begin{aligned} \overline{H}_{\mathrm{est}}(\omega) &= \mathscr{F}\left\{\overline{h}_{\mathrm{est}}(t)\right\} \\ &= \frac{T}{\sqrt{2\pi}} \int_{-\infty}^{\infty} H_{\mathrm{est}}(\nu)\, \mathrm{e}^{-\mathrm{j}\frac{T(\omega-\nu)}{2}}\, \mathrm{sinc}\left(\frac{T}{2\pi}(\omega-\nu)\right) \mathrm{d}\nu \\ &= \frac{T}{\sqrt{2\pi}} \sum_{k=0}^{N-1} H[k]\, \mathrm{e}^{-\mathrm{j}\frac{T(\omega-\omega_k)}{2}}\, \mathrm{sinc}\left(\frac{T}{2\pi}\left(\omega-\omega_k\right)\right) . \end{aligned} \tag{7.20}$$

By analogy to the Whittaker-Shannon interpolation [Shannon 1998; Marks 1991] of a time-domain signal, it is clear that $\overline{H}_{\mathrm{est}}(\omega_k)$ agrees with the spectral components $H(\omega_k)$ at the measured frequencies, i.e., $\overline{H}_{\mathrm{est}}(\omega_k) = H[k] = H(\omega_k)$. We therefore have

$$H[k] = \frac{\sqrt{2\pi}}{N}\,\mathscr{F}\left[\overline{h}_{\mathrm{est}}[n]\,\mathrm{e}^{-\mathrm{j}2\pi\frac{\omega_{\min} n}{\Delta\omega\, N}}\right] \tag{7.21}$$

or in terms of the corresponding base band signal

$$H[k] = \mathscr{F}\left[\overline{h}_{\mathrm{est,BB}}[n]\right] . \tag{7.22}$$

This means that not only the (periodic) time-periodic estimate $h_{\mathrm{est}}(t)$ from the previous section is identical to the time limited estimate $\overline{h}_{\mathrm{est}}(t)$ in the interval $0 < t < T$ but also their corresponding spectral components are identical and equal to the measured spectral components $H_{\mathrm{est}}(\omega_k) = \overline{H}_{\mathrm{est}}(\omega_k) = H(\omega_k)$. The discretized versions $h_{\mathrm{est}}[n] = \overline{h}_{\mathrm{est}}[n]$ and $H_{\mathrm{est}}[k] = \overline{H}_{\mathrm{est}}[k]$ are identical for $n = 0, \ldots, N-1$ and $k = 0, \ldots, N-1$. One can interpret either of the two time-domain functions $h_{\mathrm{est}}(t)$ or $\overline{h}_{\mathrm{est}}(t)$ as the result obtained from applying the IFFT directly to the measured frequency-domain sequence $H[k]$.

For the practical application of the FFT (and its inverse) in time gating, one should have the following relations in mind. The duration T of the time-domain sequence (or the periodicity if the time-domain sequence is interpreted as part of a periodic signal) — sometimes called the unambiguous interval — is governed by the spacing $\Delta\omega$ of the spectral sampling points of the originally measured frequency-domain $H[k]$ sequence by

$$T = \frac{2\pi}{\Delta\omega} . \tag{7.23}$$

To avoid aliasing errors, the true time-domain impulse response $h(t)$ should have decayed to a sufficiently small value within the duration T. Longer impulse responses require a longer unambiguous interval and consequently a smaller spectral step width $\Delta\omega$. The temporal resolution Δt of the resulting time-domain signal using an IFFT is determined by the bandwidth $B = N\Delta\omega$ of the originally measured frequency-domain sequence $H[k]$ via

$$\Delta t = \frac{2\pi}{B} . \tag{7.24}$$

If one wants to separate two peaks which follow shortly after each other in time-domain, a large measurement bandwidth B is required. If the two peaks overlap in the true time-domain signal $h(t)$, they are fundamentally inseparable in time-domain.

Another important property inherited by using the FFT and its inverse to relate the frequency-domain sequence $H_{\mathrm{est}}[k]$ with the time-domain sequence $h_{\mathrm{est}}[n]$ is the inherent (implicitly assumed) periodicity of both sequences [Oppenheim 2010, p. 669]. Because the representation is discrete in each domain, it must be periodic in the respective other domain. A periodic impulse train in frequency-domain is related to a periodic impulse train in time-domain by the FFT and IFFT. The impulse train representation in both domains is only useful because under certain assumptions there exist continuous time- or frequency-domain signals which coincide with the impulse trains at the sampled points. However, when the discrete data is altered by processing the data it is important to keep in mind that all alterations are effectively performed periodically on the infinitely long impulse trains, and operations such as convolutions must be interpreted in cyclic manner.

7.2. Time Windowing and Alternative Time-Domain Signals by Frequency-Domain Extrapolation

In this work, the purpose of finding the time-domain representation of the measured signal is to identify and remove the echoic contribution which ideally manifests itself as a second peak (or multiple peaks) after the direct AUT contribution in the time-domain signal. If the (first) echo peak follows shortly after the LOS signal it is desirable to be able to effectively truncate the time-domain function in a fine temporal resolution.

Zero padding the discretized frequency-domain signal (i.e., appending a sequence of zeroes to $H[k]$ or adding a zero sequence between the two spectral components in the center of the measured frequency band) can increase the number of samples N and lead to a denser sampling of the sampled time-domain signal $h_{\text{est}}[n]$ computed by the IFFT. The true resolution of the time-domain signal (i.e., the separability of two peaks) is, however, governed by the respective continuous time-domain signal $h_{\text{est}}(t)$ [Luo 2016]. If the time-domain signal is windowed between two samples of the non-zero-padded time-domain representation $h_{\text{est}}[n]$ for example, this has the same effect on the measured frequency components as windowing $h_{\text{est}}[n]$ exactly on the nearest sampling point of the non-zero-padded time-domain representation (only the unimportant frequency samples which were added by zero padding are affected in this case).

This means that zero padding does not help with increasing the time-domain resolution for time gating. Also repeating the measured spectral sequence several times does not help as this only introduces additional zero samples between the original time-domain samples $h_{\text{est}}[n]$. The thereby constructed base band signal $h_{\text{est,BB}}[n]$ is not continuous and does not adequately recreate the expected physics for an impulse response (one would expect a single more or less continuous impulse). To find a more useful time-domain signal with a high temporal resolution, a more meaningful way to extrapolate the frequency-domain sequence $H[k]$ is needed.

It has to be stressed here that one cannot expect that "guessing" additional frequency samples can be rigorously justified from a theoretical point of view. For all extrapolation methods, additional assumptions about the signals are (at least implicitly) incorporated in the extrapolation process. Rigorous time gating is only possible if the frequency-domain sequence $H[k]$ contains enough samples that the spectral sequence as well as the corresponding time-domain sequence can be regarded to be zero outside the observed interval[7]. Such a strict requirement exceeds the feasibility of most measurement setups.

7.2.1. Parametric Signal Representation

In the decades around the year 2000 it was en vogue to extrapolate time and frequency-domain signals using parametric models of either the time-domain or the frequency-domain signal [Adve 1997; J. 2007; Rao 1999; Adve 1998; Sarkar 1995; Fernández del Río 1996; Fourestie 2001]. Here, the matrix pencil method [Hua 1989; Hua 1990a; Sarkar 1995; Fernández del Río 1996] is described as an example of a parametric representation of the frequency-domain sequence. Although a detailed examination of parametric extrapolations is out of the scope of this thesis,

---

[7] Of course a strictly band limited signal cannot be strictly time limited and vice versa. However, a signal can be *approximately* time and band limited simultaneously. The value of the signal in both domains should reach a value below the noise level at the ends of the sampling intervals in both domains.

the matrix pencil method has a certain importance in this respect because it was used at several occasions for echo suppression in the available literature [Leon Fernandez 2009; Fourestie 1999].

In the matrix pencil method the assumed base band frequency-domain signal $H_{\text{est,BB}}(\omega)$ takes the form

$$H_{\text{est,BB}}(\omega) = \sum_{i=1}^{M} c_i \mathrm{e}^{-\gamma_i \omega} u(\omega) \tag{7.25}$$

of a sum of M exponentials limited to positive frequencies by the Heaviside unit step function

$$u(x) = \begin{cases} 0 & \text{for } x < 0 \\ \frac{1}{2} & \text{for } x = 0 \\ 1 & \text{for } x > 0 \end{cases} . \tag{7.26}$$

The parameters $c_i \in \mathbb{C}$, $\gamma_i \in \mathbb{C}$ (and sometimes also the number M of exponentials) have to be estimated to fit the measured spectral components. The assumed number M of exponentials should match the number of expected impulses due to scattering. The truncation of $H_{\text{est}}(\omega)$ to positive frequencies with the step function $u(\omega)$ has no influence on the measured spectral components ω_k (and is often neglected in the literature) but is required to be able to compute the corresponding estimated time-domain signal given by

$$h_{\text{est,BB}}(t) = \mathscr{F}^{-1}\left\{H_{\text{est,BB}}(\omega)\right\} = \sum_{i=1}^{M} \frac{c_i}{\alpha_i - \mathrm{j}\left(t - \beta_i\right)} , \tag{7.27}$$

where $\alpha_i > 0$ is the real part of γ_i and $\beta_i \in \mathbb{R}$ is the imaginary part. It can be argued if such a signal model represents the physics of the real signal accurately but the the above model has been successfully applied in several cases [Fourestie 1999].

Using this signal model, the base band frequency-domain sequence $H[k]$ can be expressed as [Fourestie 1999]

$$H[k] = \sum_{i=1}^{M} c_i \mathrm{e}^{-\gamma_i (k-1)\Delta\omega} . \tag{7.28}$$

The spectral sequence $H[k]$ is split into several vectors y_0, y_1, ..., y_L of length L according to [Hua 1989]

$$\boldsymbol{y}_i = \begin{bmatrix} H[i] \\ H[i+1] \\ \vdots \\ H[i+N-L-1] \end{bmatrix} \tag{7.29}$$

to build the two matrices

$$\boldsymbol{Y}_1 = \begin{bmatrix} \boldsymbol{y}_0 & \boldsymbol{y}_1 & \cdots & \boldsymbol{y}_{L-1} \end{bmatrix} \tag{7.30}$$

and

$$\boldsymbol{Y}_2 = \begin{bmatrix} \boldsymbol{y}_1 & \boldsymbol{y}_2 & \cdots & \boldsymbol{y}_L \end{bmatrix} . \tag{7.31}$$

For noisy data, the value for L should be chosen as $L = n/2$ [Hua 1989].

Finally, when the complex numbers $\lambda_i = \mathrm{e}^{-\gamma_i \omega}$ are introduced for the exponential terms, the problem of estimating the parameters γ_i can be recast into a generalized eigenvalue problem [Hua 1989]

$$\left(\boldsymbol{Y}_2 - \lambda_i \boldsymbol{Y}_1\right) \boldsymbol{v}_i = \boldsymbol{0}\,. \tag{7.32}$$

The complex numbers λ_i are called eigenvalues of the matrix pencil $\left(\boldsymbol{Y}_2, \boldsymbol{Y}_1\right)$, hence the name for the reconstruction method. Once the λ_i (and thereby the γ_i) are known, the c_i can be found by solving a linear system of equations.

The parametric representation of $H_{\mathrm{est,BB}}(\omega)$ can be used to extrapolate the spectral sequence $H[k]$ to generate a highly resolved time-domain sequence $h[n]$ via an IFFT for time gating. Alternatively, the parametric representation can directly be used to truncate the data by removing all exponential terms except the one with the largest magnitude (thereby fitting a simple exponential model to the measured data).

Compared to the direct FFT method, the matrix pencil method needs less measured bandwidth for a comparable temporal resolution and seems to be more accurate at the edges of the measured frequency band [Leon Fernandez 2009; Fourestie 1999]. This comes at the cost of an increased processing effort (an eigendecomposition is required). If the procedure must be repeated multiple times for many signals, this can be problematic, in particular if many echo sources can lead to a large number M of required exponentials.

7.2.2. Sparsity Based Time-Domain Reconstruction

Another approach to reconstruct a time-domain sequence with increased resolution from the frequency-domain sequence $H[k]$ data is based on a sparsity assumption for the time-domain sequence. The sparsity based reconstruction of the time-domain signal for time gating was introduced in [Mauermayer 2016; Mauermayer 2017] and also used in [Knapp 2020] for time gating of reconstructed currents as described later in Section 9.1.

Samples for the estimated (base band) time-domain sequence $h_{\mathrm{est,BB}}$ are assumed at the times $n\Delta\tilde{t}$, where $\Delta\tilde{t} = \Delta t / L$ with $L \in \mathbb{N}$ is an integer fraction of the time step Δt which would result by applying the IFFT directly to the measured spectral sequence. Consequently, the time-domain sequence $h_{\mathrm{est,BB}}[n]$, $n = 0, \ldots, L\,N - 1$ has the length $L\,N$, with N being the length of the original frequency-domain sequence. The corresponding frequency-domain sequence

$$H_{\mathrm{est,BB}}[k] = \mathscr{F}\left[h_{\mathrm{est,BB}}[n]\right] \qquad \text{with } k = 0, \ldots, L\,N - 1 \tag{7.33}$$

is related to the time-domain sequence by an FFT and is extended by the same factor L as compared to the original frequency-domain sequence. Formally this can be expressed as

$$\begin{bmatrix} H_{\mathrm{est,BB}}[0] \\ H_{\mathrm{est,BB}}[1] \\ \vdots \\ H_{\mathrm{est,BB}}[N-1] \\ \vdots \\ H_{\mathrm{est,BB}}[L\,N-1] \end{bmatrix} = \underbrace{\begin{bmatrix} 1 & 1 & 1 & \cdots & 1 \\ 1 & \Omega & \Omega^2 & \cdots & \Omega^{LN-1} \\ \vdots & \vdots & \vdots & \ddots & \vdots \\ 1 & \Omega^{N-1} & \Omega^{2(N-1)} & \cdots & \Omega^{(LN-1)(N-1)} \\ \vdots & \vdots & \vdots & \ddots & \vdots \\ 1 & \Omega^{LN-1} & \Omega^{2(LN-1)} & \cdots & \Omega^{(LN-1)(LN-1)} \end{bmatrix}}_{\boldsymbol{D}} \begin{bmatrix} h_{\mathrm{est,BB}}[0] \\ h_{\mathrm{est,BB}}[1] \\ \vdots \\ h_{\mathrm{est,BB}}[N-1] \\ \vdots \\ h_{\mathrm{est,BB}}[L\,N-1] \end{bmatrix} \tag{7.34}$$

with the help of the FFT matrix $\boldsymbol{D} \in \mathbb{C}^{L\,N \times L\,N}$, where $\Omega = \mathrm{e}^{-\mathrm{j}2\pi/(LN)}$.

Only the first N values of the frequency-domain sequence $H_{\mathrm{est,BB}}[k]$ must agree with the measured spectral components, i.e.,

$$H_{\mathrm{est,BB}}[k] \overset{!}{=} H[k] \qquad \text{for } k = 0, \dots N-1\,, \tag{7.35}$$

whereas the remaining values of $H_{\mathrm{est,BB}}[k]$ are unrestricted. This leads to a highly underdetermined system

$$\underbrace{\begin{bmatrix} H_{\mathrm{est,BB}}[0] \\ H_{\mathrm{est,BB}}[1] \\ \vdots \\ H_{\mathrm{est,BB}}[N-1] \end{bmatrix}}_{\boldsymbol{h}_{\mathrm{freq}} \in \mathbb{C}^{N \times 1}} = \underbrace{\begin{bmatrix} 1 & 1 & 1 & \cdots & 1 \\ 1 & \Omega & \Omega^2 & \cdots & \Omega^{LN-1} \\ \vdots & \vdots & \vdots & \ddots & \vdots \\ 1 & \Omega^{N-1} & \Omega^{2(N-1)} & \dots & \Omega^{(LN-1)(N-1)} \end{bmatrix}}_{\boldsymbol{D}' \in \mathbb{C}^{N \times L\,N}} \underbrace{\begin{bmatrix} h_{\mathrm{est,BB}}[0] \\ h_{\mathrm{est,BB}}[1] \\ \vdots \\ h_{\mathrm{est,BB}}[N-1] \\ \vdots \\ h_{\mathrm{est,BB}}[L\,N-1] \end{bmatrix}}_{\boldsymbol{h}_{\mathrm{time}} \in \mathbb{C}^{L\,N \times 1}} \tag{7.36}$$

with a broad matrix $\boldsymbol{D}' \in \mathbb{C}^{N \times L\,N}$. Out of the infinitely many possible solutions for the time-domain sequence, the sparsest (i.e., with the lowest amount of non-zero entries) is desired as the assumption is that the time-domain sequence can be expressed as a sum of few impulses corresponding to the direct AUT contribution and few scattered paths. Formally, one tries to solve the minimization problem

$$\min_{\boldsymbol{h}_{\mathrm{time}} \in \mathbb{C}^{LN \times 1}} \left\| \boldsymbol{h}_{\mathrm{time}} \right\|_1 \quad \text{s.t. } \left\| \boldsymbol{D}' \boldsymbol{h}_{\mathrm{time}} - \boldsymbol{h}_{\mathrm{freq}} \right\|_2^2 \le \sigma\,, \tag{7.37}$$

known from compressive sensing as the so-called basis pursuit denoising method where σ is a relaxation parameter which should be chosen in the order of the noise level. The solution of the basis pursuit denoising problem is computationally tractable — e.g., by the readily available SPGL1 solver [Friedlander 2008] — and leads to an approximately sparse solution, where only few elements are significantly larger than zero.

Because the thereby found time-domain sequence contains $L\,N$ samples and is related to $L\,N$ spectral components via the FFT, the sparsity based reconstruction of a highly resolved time-domain sequence can be interpreted as a frequency-domain extrapolation method. The highly resolved time-domain sequence can be used for time gating, where the effective temporal resolution is increased compared to the direct IFFT approach.

7.3. Chapter Summary

In this chapter, existing time-domain echo suppression methods have been revisited. Only the interpretation of the time-domain reconstruction methods in terms of frequency-domain signal extrapolation and the explicit derivation of an expression for the time-domain signal (7.27) for the matrix pencil method can be regarded as original contributions of this thesis. All time-domain methods consist of a two step procedure (hardware time gating has not been considered). In the first step, the time-domain signal is reconstructed from the measured spectral components, and in the second step, the time-domain signal is truncated to exclude the undesired echo influences and transformed back into frequency-domain. The direct FFT based reconstruction of the time-domain signal has the disadvantage of requiring a large bandwidth for a certain temporal resolution of the time-domain signal, thus frequency-domain extrapolation methods have been presented. In this thesis, the FFT-based and the sparsity-based time-domain reconstruction methods have been adapted for time gating, whereas the remaining methods have been described only to deliver a comprehensive picture of the available methods.

8

Echo Suppression Methods in Frequency Domain

In this chapter, echo suppression methods are investigated which work with single-frequency measurements to separate the undesired echo contributions from the desired free-space AUT contributions in a quantity of interest (usually the AUT-FF pattern or an equivalent AUT source model). Fields generated by sources in different source regions have distinct features in their spatial distribution allowing to differentiate the source location of different field contributions. The spatial analysis can be applied to measurements at a single frequency, thus, giving rise to frequency domain echo suppression methods. The drawback is, however, that more measurement samples in spatial domain — meaning more AUT or more probe positions — are needed.

The particular measurement setup determines how effectively the undesired echo contributions can be separated from the AUT sources. In general, the scenario is characteristically different for the echo being stationary with respect to the AUT or the probe.

8.1. Stationary Antenna Under Test

Consider the case of a stationary AUT first[1]. The AUT is enclosed by a minimum sphere (surface S_{aut}, radius r_{aut}) centered at $\boldsymbol{r}_{0,\text{a}}$. The measurement probe moves to different locations around the AUT. All measurement locations lie in the volume V between the two spherical surfaces S_1 with radius r_1 and S_2 with radius r_2. The AUT center does not necessarily coincide with the center of the measurement surface. Figures 8.1 and 8.2 depict the stationary AUT measurement scenario with an echo object placed inside or outside the measurement region, respectively.

With a stationary AUT, the situation is described best by letting the AUT radiate and the probe receive[2]. The AUT radiation is described by equivalent currents in the AUT region and the echo

---

[1] The term “stationary” means that the AUT is stationary with respect to the scattering environment, i.e., the relative position between the echo objects and the AUT does not change throughout the whole measurement.

[2] Due to reciprocity,one can always consider the more convenient case for the analysis.

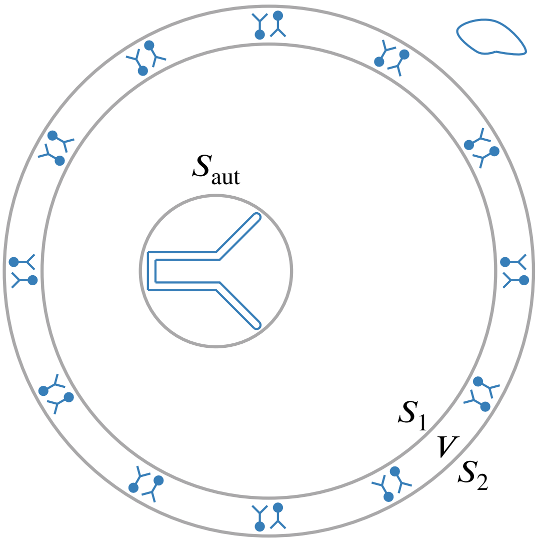

Fig. 8.1.: Echoic measurement scenario with moving probe and a scatterer outside the measurement sphere. Inward and outward directed probes are depicted at different measurement positions. The AUT is not required to sit in the center of the measurement surfaces.

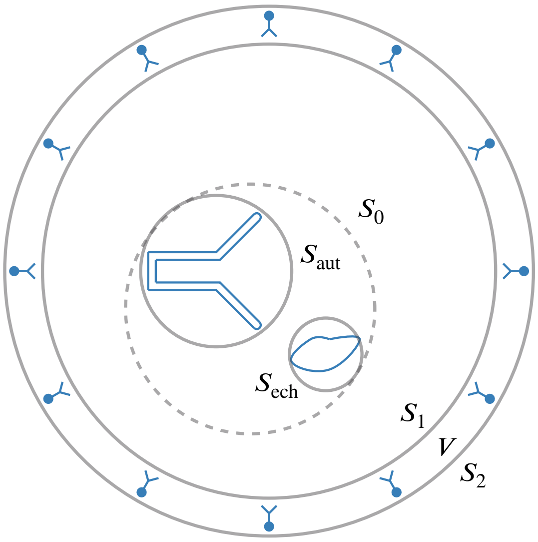

Fig. 8.2.: Echoic measurement scenario with moving probe and a scatterer within the measurement sphere. The inward directed probe is depicted at different measurement positions. The AUT is not required to sit in the center of the measurement surfaces.

is described by equivalent scattering currents in the echo region[3]. Due to the stationary AUT, the relative position between the echo object and the AUT never changes. The success of frequency domain echo suppression technique with a stationary AUT is related to the question whether it is possible to unambiguously separate the total field $\boldsymbol{E}(\boldsymbol{r}) = \boldsymbol{E}_{\mathrm{aut}}(\boldsymbol{r}) + \boldsymbol{E}_{\mathrm{ech}}(\boldsymbol{r})$ into two parts $\boldsymbol{E}_{\mathrm{aut}}(\boldsymbol{r})$ and $\boldsymbol{E}_{\mathrm{ech}}(\boldsymbol{r})$ with different source regions.

8.1.1. Echoes From Outside the Measurement Surface

If the echo object is located outside of S_2, as shown in Fig. 8.1, it is in theory straightforward to separate the AUT fields from the echo fields. The total fields in V can be expressed as a superposition of outward-traveling waves of the $c = 4$ type and incident waves of the $c = 1$ type. Placing the origin for the spherical wave expansion into the center of the measurement sphere, we have

$$\begin{aligned}\boldsymbol{E}(\boldsymbol{r})\Big|_{\boldsymbol{r}\in V} =& k\sqrt{Z_{\mathrm{F}}}\sum_{s=1}^{2}\sum_{n=1}^{N_{\mathrm{max}}}\sum_{m=-n}^{n}\left(\alpha_{smn}^{(4),\mathrm{aut}}\,\boldsymbol{F}_{smn}^{(4)}(r,\vartheta,\varphi)\right)\\ &+ k\sqrt{Z_{\mathrm{F}}}\sum_{\sigma=1}^{2}\sum_{\nu=1}^{N'_{\mathrm{max}}}\sum_{\mu=-\nu}^{\nu}\left(\alpha_{\sigma\mu\nu}^{(1),\mathrm{ech}}\,\boldsymbol{F}_{\sigma\mu\nu}^{(1)}(r,\vartheta,\varphi)\right),\end{aligned} \tag{8.1}$$

---

[3] Because of mutual interactions with the echo object, the equivalent currents in the AUT region may differ from the free-space case. These distortions cannot be removed by frequency domain echo suppression techniques with a stationary AUT.

where the coefficients $\alpha_{smn}^{(4),\mathrm{aut}}$ of the outward-traveling waves belong to the AUT and the coefficients $\alpha_{\sigma\mu\nu}^{(1),\mathrm{ech}}$ of the incident fields must be attributed to the echoes. The expansion of the total fields into outward-traveling fields and incident fields is uniquely defined, once the coordinate origin is fixed. Accordingly, the expansion coefficients $\alpha_{smn}^{(4),\mathrm{aut}}$ and $\alpha_{\sigma\mu\nu}^{(1),\mathrm{ech}}$ are also uniquely defined by the total fields and can be found if enough field samples are obtained in the observation volume V. To be able to separate the incident waves from the outward-traveling waves, it is no longer sufficient to sample the field with one probe type oriented toward the antenna. Either the electric and magnetic field have to be sampled independently, or inward and outward oriented probes must be used to obtain the required information about the total fields in V [Yinusa 2013; Yinusa 2015]. Heuristically, on can understand that the additional measurements are required because the total fields are no longer uniquely defined by the tangential electric fields on the surface S_1 alone (as would be the case for purely outward-traveling fields). Different total fields are possible with the same tangential electric fields on S_1 and varying tangential electric fields on S_2. Thus, the tangential electric field on both surfaces (S_1 and S_2) must be known to uniquely define the total fields in V (up to internal resonances which are neglected in this heuristic explanation).

The maximum mode index $N_{\max} = k\,r_{\mathrm{aut}} + n_{\mathrm{buf}}$ only depends on the AUT size, while the maximum mode index $N'_{\max} = k\,r_2 + n_{\mathrm{buf}}$ for the incident fields depends on the size of the measurement surface S_2. Without a more precise knowledge of the echo location, the number of measurement samples in the volume V must be sufficient to resolve all outward-traveling modes up to the mode number $N_{\max}$ and all incident modes up to the mode number $N'_{\max}$. If the echo location is approximately known, this knowledge can be used by restricting those fields which might be incident on V, e.g., by expressing the echo fields in terms of a spherical wave expansion with its origin in the center of an echo object (if several echo objects are present, one might use a linear combination of several spherical mode expansions with different origins).

In principle, perfect[4] echo suppression is possible if the echo is completely outside the measurement surface. However, if the echo location is not known — not even approximately — a huge number $N'_{\max}$ of incident field modes must be assumed. If the number of measurement samples is not sufficient to resolve all field modes, it is possible that the reconstructed AUT coefficients still contain some echo contributions due to aliasing.

It is not sufficient to assume only AUT sources $\alpha_{smn}^{(4),\mathrm{aut}}$ and neglect the echo coefficients $\alpha'^{(1),\mathrm{ech}}_{\sigma\mu\nu}$. It may happen that some echo contributions in the observations may actually be mapped to the source coefficients in the reconstruction process. The relation between source models with and without assumed echo sources is analogous to the problem in the next section, where the situation is analyzed in greater detail.

8.1.2. Echoes From Inside the Measurement Surface

The situation is more complicated if the AUT and all echo objects are placed inside S_1. The total fields in the measurement volume V consist only of outward-traveling waves of the $c = 4$ type. This obstructs the distinction between echo fields and AUT fields, as both contributions consist of the same field type. It is unclear at this point of the current discussion if it is always possible to separate the echo influences from the AUT influences. To illustrate the complications, consider

---

[4] The field reconstruction is exact except for the effects of evanescent field portions and mutual coupling, which are neglected.

the situation depicted in Fig. 8.2. The AUT sources are enclosed by a sphere S_{aut} centered at $\boldsymbol{r}_{0,\text{a}}$, the echo sources are enclosed by a sphere S_{ech} centered at $\boldsymbol{r}_{0,\text{e}}$, and both spheres are again enclosed by a third sphere S_0 centered at $\boldsymbol{r}_0$. For the moment, S_0 can be an arbitrary sphere enclosing both the AUT and the echo sources.

The total fields at the observation locations can be expressed by[5]

$$\boldsymbol{E}_{\text{tot}}(\boldsymbol{r})\Big|_{\boldsymbol{r}\in V} = \boldsymbol{E}_{\text{aut}}(\boldsymbol{r}) + \boldsymbol{E}_{\text{ech}}(\boldsymbol{r}) \;, \tag{8.2}$$

where

$$\boldsymbol{E}_{\text{aut}}(\boldsymbol{r}) = k\sqrt{Z_{\text{F}}} \sum_{s=1}^{2} \sum_{n=1}^{N_{\text{aut}}} \sum_{m=-n}^{n} \alpha'^{(4),\text{aut}\star}_{smn}\, \boldsymbol{F}^{(4)}_{smn}\big(r',\vartheta',\varphi'\big) \tag{8.3}$$

is the expansion of the fields generated by the sources[6] inside S_{aut}, expressed in an AUT centered coordinate system (denoted by the primed coordinates r',ϑ', and φ') and

$$\boldsymbol{E}_{\text{ech}}(\boldsymbol{r}) = k\sqrt{Z_{\text{F}}} \sum_{\sigma=1}^{2} \sum_{\nu=1}^{N_{\text{ech}}} \sum_{\mu=-\nu}^{\nu} \alpha''^{(4),\text{ech}\star}_{\sigma\mu\nu}\, \boldsymbol{F}^{(4)}_{\sigma\mu\nu}\big(r'',\vartheta'',\varphi''\big) \tag{8.4}$$

is the expansion of the echo fields originating from the sources inside S_{ech}, expressed in an echo centered coordinate system (denoted by the doubly-primed coordinates r'',ϑ'', and φ''). Since the individual expansions are intended to represent only the AUT fields or the echo fields respectively, the truncation indices $N_{\text{aut}} = kr_{\text{aut}} + n_{\text{buf}}$ and $N_{\text{ech}} = kr_{\text{ech}} + n_{\text{buf}}$ depend only on the radii r_{aut} and r_{ech} of the corresponding spheres S_{aut} and S_{ech} (see Fig. 8.2).

8.1.3. Source Reconstruction and Source Separation

How well can the echo influences in the measured fields be separated from the true AUT fields? The objective of this section is an analysis of the performance of different reconstruction schemes concerning their capabilities to find the true AUT expansion coefficients $\alpha'^{(4),\text{aut}\star}_{smn}$. The general analysis will be based on spherical wave expansions whereas similar conclusions are drawn for equivalent current based field reconstruction methods by analogy. The analysis revolves around the situation depicted in Fig. 8.3. Two distinct source regions — the AUT source region and the echo source region — are enclosed by their respective minimum spheres S_{aut} and S_{ech}. The centers of the minimum spheres are denoted by $\boldsymbol{r}_{0,\text{a}}$ and $\boldsymbol{r}_{0,\text{e}}$, respectively. The smallest sphere enclosing all AUT and echo sources simultaneously is called S_0 and its center $\boldsymbol{r}_0$. In the following, different spherical expansions are investigated, with their coordinate origins at $\boldsymbol{r}_{0,\text{a}}$, $\boldsymbol{r}_{0,\text{e}}$, and $\boldsymbol{r}_0$. The respective spherical expansions include either only one source region (i.e., only the AUT sources or only the echo sources) or both source regions simultaneously. The overall goal is to extract the “true” AUT coefficients $\alpha'^{(4),\text{aut}\star}_{smn}$ from the measured echo distorted S_{21}-values.

---

[5] Here and in the following, the ⋆-symbol denotes the “true” solution. Alternative expansions are also possible but the “true” AUT contribution can not always easily be extracted from them.

[6] The AUT sources can differ from the purely anechoic case due to mutual interactions with the environment. These distortions cannot be cured by pure frequency domain methods and for the moment it is assumed that the source distortions due to environmental interactions are negligible in the AUT volume.

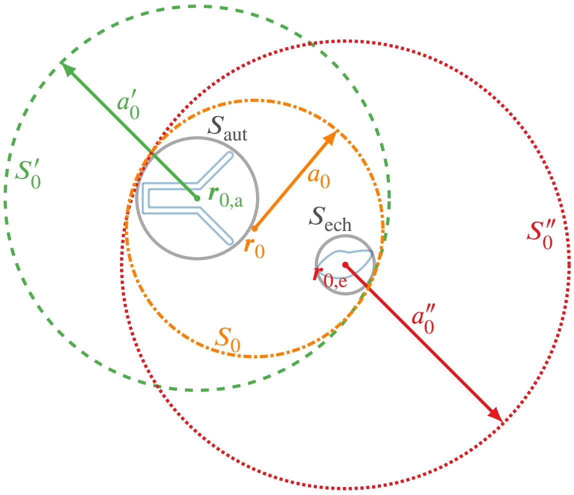

Fig. 8.3.: Minimum spheres with different centers enclosing all sources. The radiated fields expressed by a spherical wave expansion with its origin in either center are practically the same.

Choosing $\boldsymbol{r}_0$ as the origin for the spherical wave expansion, we have

$$\boldsymbol{E}_{\text{tot}}(\boldsymbol{r})\Big|_{\boldsymbol{r}\in V} = k\sqrt{Z_{\text{F}}}\sum_{s=1}^{2}\sum_{n=1}^{N_{\text{tot}}}\sum_{m=-n}^{n} \alpha_{smn}^{(4),\,\text{tot}}\,\boldsymbol{F}_{smn}^{(4)}(r,\vartheta,\varphi) \tag{8.5}$$

for the total fields in V. Here, $N_{\text{tot}} = k_0\,a_0 + n_{\text{buf}}$ denotes the largest mode number which is generated either by the AUT or the echo, with a_0 being the radius of the sphere S_0 enclosing all sources.

Alternatively, the total fields in V can be expressed as[7]

$$\boldsymbol{E}_{\text{tot}}(\boldsymbol{r})\Big|_{\boldsymbol{r}\in V} = k\sqrt{Z_{\text{F}}}\sum_{s=1}^{2}\sum_{n=1}^{N'_{\text{tot}}}\sum_{m=-n}^{n} \alpha'^{(4),\text{aut}}_{smn}\,\boldsymbol{F}_{smn}^{(4)}\left(r',\vartheta',\varphi'\right) \tag{8.6}$$

in terms of a single mode expansion with respect to the coordinate origin at $\boldsymbol{r}_{0,\text{a}}$. Because the expansion (8.6) considers AUT sources and echo sources simultaneously, the highest mode order N'_{tot} in the expansion (8.6) exceeds the highest mode order N_{aut} which is required to represent only the *true* AUT fields in (8.3). Finally, it is also possible to represent the total fields as

$$\boldsymbol{E}_{\text{tot}}(\boldsymbol{r})\Big|_{\boldsymbol{r}\in V} = k\sqrt{Z_{\text{F}}}\sum_{s=1}^{2}\sum_{n=1}^{N''_{\text{tot}}}\sum_{m=-n}^{n} \alpha''^{(4),\text{ech}}_{smn}\,\boldsymbol{F}_{smn}^{(4)}\left(r'',\vartheta'',\varphi''\right) \tag{8.7}$$

in terms of a single mode expansion with respect to the coordinate origin at $\boldsymbol{r}_{0,\text{e}}$.

---

[7] The symbol $\boldsymbol{r}$ is a coordinate-free description of a location in space. The vector $\boldsymbol{r}$ can have several different coordinate representations and can thus either be described by the triple (r,ϑ,φ) or by the triple (r',ϑ',φ'), depending on the respective coordinate system in use. Here, it is understood that the primed coordinates (and also the primed expansion coefficients) correspond to the coordinate system with origin $\boldsymbol{r}_{0,\text{a}}$

In the region outside of all minimum spheres, the fields of expansion in (8.5), (8.6), or (8.7) are practically the same[8]. In principle, the fields could be generated by sources either in the echo volume or the AUT volume[9]. Consequently, one cannot uniquely identify the source location of the fields by (noisy) observations at some distance to the sources. Many expansions of the form

$$\begin{aligned} \boldsymbol{E}_{\text{tot}}(\boldsymbol{r})\Big|_{\boldsymbol{r}\in V} &= \underbrace{k\sqrt{Z_{\text{F}}}\sum_{s=1}^{2}\sum_{n=1}^{N'_{\text{tot}}}\sum_{m=-n}^{n} \alpha'^{(4),\text{aut}}_{smn}\,\boldsymbol{F}^{(4)}_{smn}(r',\vartheta',\varphi')}_{\text{expansion centered at } \boldsymbol{r}_{0,\text{a}}} \\ &+ \underbrace{k\sqrt{Z_{\text{F}}}\sum_{\sigma=1}^{2}\sum_{\nu=1}^{N''_{\text{tot}}}\sum_{\mu=-\nu}^{\nu} \alpha''^{(4),\text{ech}}_{\sigma\mu\nu}\,\boldsymbol{F}^{(4)}_{\sigma\mu\nu}(r'',\vartheta'',\varphi'')}_{\text{expansion centered at } \boldsymbol{r}_{0,\text{e}}} \\ &+ \underbrace{k\sqrt{Z_{\text{F}}}\sum_{s=1}^{2}\sum_{n=1}^{N_{\text{tot}}}\sum_{m=-n}^{n} \alpha^{(4),\text{ tot}}_{smn}\,\boldsymbol{F}^{(4)}_{smn}(r,\vartheta,\varphi)}_{\text{expansion centered at } \boldsymbol{r}_{0}} \end{aligned} \tag{8.8}$$

are possible as a sum of expansions with coordinate origin at $\boldsymbol{r}_{0,\text{a}}$, $\boldsymbol{r}_{0,\text{e}}$, or $\boldsymbol{r}_{0}$, respectively[10].

As detailed in Chapter 5, the S_{21}-parameter can be expressed by testing the total field $\hat{\boldsymbol{E}}_{\text{tot}}$ (normalized to the AUT excitation $a_1 \in \mathbb{C}\sqrt{\text{W}}$) with the normalized probe currents. Thus, the measured S_{21}-parameter for the ℓth probe position can be modeled by

$$\begin{aligned} S_{21,\ell} = \oiint\limits_{S_{\text{pro},\ell}} \hat{\boldsymbol{J}}_{\text{pro},\ell}\cdot\hat{\boldsymbol{E}}_{\text{tot}}\,\mathrm{d}a &= k\sqrt{Z_{\text{F}}}\sum_{j'=1}^{J'_{\text{tot}}} \hat{\alpha}'^{(4),\text{aut}}_{j'} \oiint\limits_{S_{\text{pro},\ell}} \hat{\boldsymbol{J}}_{\text{pro},\ell}\cdot\boldsymbol{F}^{(4)}_{j'}\left(r',\vartheta',\varphi'\right)\,\mathrm{d}v\,, \\ &+ k\sqrt{Z_{\text{F}}}\sum_{j''=1}^{J''_{\text{tot}}} \hat{\alpha}''^{(4),\text{ech}}_{j''} \oiint\limits_{S_{\text{pro},\ell}} \hat{\boldsymbol{J}}_{\text{pro},\ell}\cdot\boldsymbol{F}^{(4)}_{j''}\left(r'',\vartheta'',\varphi''\right)\,\mathrm{d}a\,, \\ &+ k\sqrt{Z_{\text{F}}}\sum_{j=1}^{J_{\text{tot}}} \hat{\alpha}^{(4),\text{ tot}}_{j} \oiint\limits_{S_{\text{pro},\ell}} \hat{\boldsymbol{J}}_{\text{pro},\ell}\cdot\boldsymbol{F}^{(4)}_{j}(r,\vartheta,\varphi)\,\mathrm{d}a\,, \end{aligned} \tag{8.9}$$

---

[8] This is only exactly true, when N_{tot}, N'_{tot} and N''_{tot} go to infinity, allowing superdirective effects. This may lead to pointwise divergence (in particular inside the source region) [Yaghjian 2000]. If one truncates the expansions, the external fields will differ by higher-order modes which are negligible at some distance to the sources.

[9] This statement holds true if the fields can be measured with a finite accuracy only. For every arbitrary finite $\varepsilon > 0$, one can find finite summation indices $N'_{\text{aut}} < \infty$ and $N''_{\text{ech}} < \infty$ such that

$$\iiint\limits_{V} \left| k\sqrt{Z_{\text{F}}}\sum_{s=1}^{2}\sum_{n=1}^{N''_{\text{ech}}}\sum_{m=-n}^{n} \alpha''^{(4),\text{ tot}}_{smn}\,\boldsymbol{F}^{(4)}_{smn}\left(r'',\vartheta'',\varphi''\right) - k\sqrt{Z_{\text{F}}}\sum_{s=1}^{2}\sum_{n=1}^{N'_{\text{aut}}}\sum_{m=-n}^{n} \alpha'^{(4),\text{ au}}_{smn}\,\boldsymbol{F}^{(4)}_{smn}\left(r',\vartheta',\varphi'\right)\right|^2 \mathrm{d}v < \epsilon\,.$$

With infinite measurement accuracy, it should be possible to uniquely determine the source locations [Klinkenbusch 2008; Klinkenbusch 2009].

[10] Many expansions with different coordinate origins could be considered, but the presented ones suffice for the following discussion. With more than one echo object being present, one may use additional expansions.

where $\hat{\boldsymbol{J}}_{\mathrm{pro},\ell}$ are the normalized equivalent probe surface currents for the ℓth probe position and $\hat{\alpha}'^{(4),\mathrm{aut}}_{j'}$, $\hat{\alpha}''^{(4),\mathrm{ech}}_{j''}$, and $\hat{\alpha}^{(4),\,\mathrm{tot}}_{j}$ are the normalized (normalized to the AUT excitation a_1) expansion coefficients of the respective mode expansions centered at $\boldsymbol{r}_{0,\mathrm{a}}$, $\boldsymbol{r}_{0,\mathrm{e}}$, and $\boldsymbol{r}_0$, with the multi index $j = \{smn\}$ which uniquely maps every j to a triplet $\{smn\}$ by the indexing rule [Hansen 1988, p. 313] $j = 2\,[n\,(n+1) + m - 1] + s$. The maximum summation indices $J_{\mathrm{tot}} = 2N_{\mathrm{tot}}\left(N_{\mathrm{tot}} + 2\right)$, $J'_{\mathrm{tot}} = 2N'_{\mathrm{tot}}\left(N'_{\mathrm{tot}} + 2\right)$, and $J''_{\mathrm{tot}} = 2N''_{\mathrm{tot}}\left(N''_{\mathrm{tot}} + 2\right)$ depend on the maximum mode numbers N_{tot}, N'_{tot}, N''_{tot} of the respective modal expansions. Equation (8.9) leads to a matrix equation of the form[11]

$$\boldsymbol{b} = \boldsymbol{A}\boldsymbol{x}'_{\mathrm{aut}} + \boldsymbol{B}\boldsymbol{x}''_{\mathrm{ech}} + \boldsymbol{C}\boldsymbol{x}_{\mathrm{tot}}\,, \tag{8.10}$$

where $\boldsymbol{b} \in \mathbb{C}^{M\times 1}$ is the vector storing the measured S_{21}-samples, $\boldsymbol{x}'_{\mathrm{aut}} \in \mathbb{C}^{J'_{\mathrm{tot}}\times 1}$ is the vector of normal expansion coefficients $\hat{\alpha}'^{(4),\mathrm{aut}}_{j'}$ of the AUT centered modal expansion, $\boldsymbol{x}''_{\mathrm{ech}} \in \mathbb{C}^{J''_{\mathrm{tot}}\times 1}$ is the vector of normalized expansion coefficients $\hat{\alpha}''^{(4),\mathrm{ech}}_{j'}$ of the echo centered modal expansion, and $\boldsymbol{x}_{\mathrm{tot}} \in \mathbb{C}^{J_{\mathrm{tot}}\times 1}$ stores the normalized coefficients $\hat{\alpha}^{(4),\,\mathrm{tot}}_{j}$ of the expansion with origin $\boldsymbol{r}_0$. The elements[12] of the matrix $\boldsymbol{A} \in \mathbb{C}^{M\times J'_{\mathrm{tot}}}$ are given by

$$A_{\ell j'} = \frac{k}{\sqrt{Z_{\mathrm{F}}}} \oiint\limits_{S_{\mathrm{pro},\ell}} \hat{\boldsymbol{J}}_{\mathrm{pro},\ell} \cdot \boldsymbol{F}^{(4)}_{j'}\big(r', \vartheta', \varphi'\big)\ \mathrm{d}a\,, \tag{8.11}$$

the elements of the matrix $\boldsymbol{B} \in \mathbb{C}^{M\times J''_{\mathrm{tot}}}$ are given by

$$B_{\ell j''} = \frac{k}{\sqrt{Z_{\mathrm{F}}}} \oiint\limits_{S_{\mathrm{pro},\ell}} \hat{\boldsymbol{J}}_{\mathrm{pro},\ell} \cdot \boldsymbol{F}^{(4)}_{j''}\big(r'', \vartheta'', \varphi''\big)\ \mathrm{d}a\,, \tag{8.12}$$

and the elements of the matrix $\boldsymbol{C} \in \mathbb{C}^{M\times J_{\mathrm{tot}}}$ are given by

$$C_{\ell j} = \frac{k}{\sqrt{Z_{\mathrm{F}}}} \oiint\limits_{S_{\mathrm{pro},\ell}} \hat{\boldsymbol{J}}_{\mathrm{pro},\ell} \cdot \boldsymbol{F}^{(4)}_{j}(r, \vartheta, \varphi)\ \mathrm{d}a\,. \tag{8.13}$$

Notice that the “true” expansion (8.2) has a maximum mode index of N_{aut} for the AUT centered expansion and a maximum mode index N_{ech} as opposed to $N'_{\mathrm{tot}} > N_{\mathrm{aut}}$ and $N''_{\mathrm{tot}} > N_{\mathrm{ech}}$ in (8.9). Consequently, the first $J_{\mathrm{aut}} = 2N_{\mathrm{aut}}\left(N_{\mathrm{aut}} + 2\right)$ entries of the vector $\boldsymbol{x}'_{\mathrm{aut}}$ and the first $J_{\mathrm{ech}} = 2N_{\mathrm{ech}}\left(N_{\mathrm{ech}} + 2\right)$ entries of the vector $\boldsymbol{x}''_{\mathrm{ech}}$ play a special role and it makes sense to split these vectors according to

$$\boldsymbol{x}'_{\mathrm{aut}} = \begin{bmatrix} \boldsymbol{x}'_{\mathrm{aut,low}} \\ \boldsymbol{x}'_{\mathrm{aut,high}} \end{bmatrix} \qquad \boldsymbol{x}''_{\mathrm{ech}} = \begin{bmatrix} \boldsymbol{x}'_{\mathrm{ech,low}} \\ \boldsymbol{x}'_{\mathrm{ech,high}} \end{bmatrix} \tag{8.14}$$

---

[11] The primed and double primed vectors remind us that the corresponding coefficients belong to modal expansions centered at $\boldsymbol{r}_{0,\mathrm{a}}$ and $\boldsymbol{r}_{0,\mathrm{e}}$, respectively.

[12] While it is formally possible to express the matrix elements with the spatial weighting by a normalized current as shown here, an actual implementation will more likely utilize equivalent expressions similar to those found in Section 5.2.2. Since it is more tedious to express the matrix elements in this way, the spatial weighting is used here, keeping in mind that the expression is not necessarily implemented in the given form in an actual algorithm.

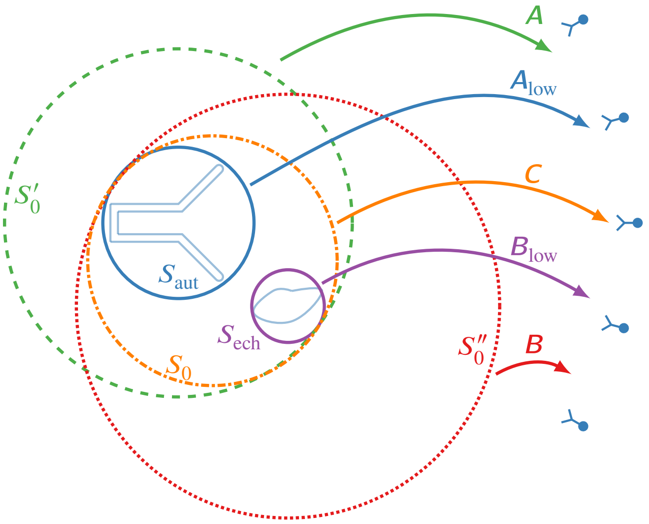

Fig. 8.4.: Different source regions denoted by the spheres S_aut, S_ech, S_0, S_0', and S_0'' and corresponding forward operators $\boldsymbol{A}$, $\boldsymbol{B}$, $\boldsymbol{C}$, $\boldsymbol{A}_\mathrm{low}$, $\boldsymbol{B}_\mathrm{low}$.

into low-order parts $\boldsymbol{x}'_\mathrm{aut,low} \in \mathbb{C}^{J_\mathrm{aut}\times 1}$, $\boldsymbol{x}''_\mathrm{ech,low} \in \mathbb{C}^{J_\mathrm{ech}\times 1}$ and high-order parts $\boldsymbol{x}'_\mathrm{aut,high} \in \mathbb{C}^{(J'_\mathrm{tot}-J_\mathrm{aut})\times 1}$, $\boldsymbol{x}''_\mathrm{ech,low} \in \mathbb{C}^{(J''_\mathrm{tot}-J_\mathrm{ech})\times 1}$. Accordingly, the matrices $\boldsymbol{A}$ and $\boldsymbol{B}$ are as well split into low-order parts $\boldsymbol{A}_\mathrm{low} \in \mathbb{C}^{M\times J_\mathrm{aut}}$, $\boldsymbol{B}_\mathrm{low} \in \mathbb{C}^{M\times J_\mathrm{ech}1}$ and high-order parts $\boldsymbol{A}_\mathrm{high} \in \mathbb{C}^{M\times(J'_\mathrm{tot}-J_\mathrm{aut})}$, $\boldsymbol{B}_\mathrm{high} \in \mathbb{C}^{M\times(J''_\mathrm{tot}-J_\mathrm{ech})}$ according to

$$\boldsymbol{A} = \begin{bmatrix}\boldsymbol{A}_\mathrm{low} & \boldsymbol{A}_\mathrm{high}\end{bmatrix} \qquad \boldsymbol{B} = \begin{bmatrix}\boldsymbol{B}_\mathrm{low} & \boldsymbol{B}_\mathrm{high}\end{bmatrix} . \tag{8.15}$$

The meaning of the matrices $\boldsymbol{A}$, $\boldsymbol{B}$, $\boldsymbol{C}$, $\boldsymbol{A}_\mathrm{low}$, $\boldsymbol{B}_\mathrm{low}$ is summarized in Fig. 8.4. They represent the linear operators between the sources of the different source regions — defined by the surfaces S_aut, S_ech, S_0, S_0', and S_0'' — to the measurement samples.

Different reconstruction methods are compared in the following, which all attempt to find the “true” AUT coefficients $\alpha'^{(4),\mathrm{aut}\star}_{smn}$ appearing in (8.2). The vector containing the “true” AUT coefficients is denoted by $\boldsymbol{x}'_{\mathrm{aut}\star} \in \mathbb{C}^{J_\mathrm{aut}\times 1}$ and the vector containing the “true” echo coefficients is denoted by $\boldsymbol{x}''_{\mathrm{ech}\star} \in \mathbb{C}^{J_\mathrm{ech}\times 1}$. The different algorithms can be easily expressed in terms of the matrices $\boldsymbol{A}$ and $\boldsymbol{B}$ whereas the matrix $\boldsymbol{C}$ is only needed in an intermediate step in some cases. The reconstruction methods are based on different models of the total fields, where the AUT is modeled alone or together with some echo sources.

A close analogy can be drawn to a representation of radiated fields by equivalent surface currents instead of spherical wave expansions. If discretized surface currents are placed on the surfaces S_aut, S_ech, S_0, S_0', or S_0'' (for the equivalent currents the surface are not bound to be spherical), the linear relationships between the current coefficients and the measured samples are expressed by the matrices $\boldsymbol{A}_\mathrm{cur}$, $\boldsymbol{B}_\mathrm{cur}$, $\boldsymbol{C}_\mathrm{cur}$, $\boldsymbol{A}_\mathrm{cur,low}$, $\boldsymbol{B}_\mathrm{cur,low}$ (see Section 5.2). The following discussion of reconstruction methods is in essence also true for equivalent currents, where in particular a direct analogy is used between the matrices $\boldsymbol{A}_\mathrm{cur,low} \hat{=} \boldsymbol{A}_\mathrm{low}$ and $\boldsymbol{B}_\mathrm{cur,low} \hat{=} \boldsymbol{B}_\mathrm{low}$. It is therefore expected that equivalent current based methods perform similar as spherical expansion based methods concerning their echo suppression capabilities — with the major difference coming from the fact that the radiated fields can be more accurately constrained to the actual (possibly not spherically shaped) source regions of the AUT and the echo object.

Reconstructing Sources Only for the Antenna Under Test

A direct approach to reconstruct the AUT sources is to find the vector of AUT coefficients $\boldsymbol{x}'_{\text{aut}}$ which solves the minimization problem

$$\min_{\boldsymbol{x}'_{\text{aut}} \in \mathbb{C}^{J'_{\text{tot}} \times 1}} \left\| \boldsymbol{b} - \boldsymbol{A}\, \boldsymbol{x}'_{\text{aut}} \right\| , \tag{8.16}$$

formally expressed as

$$\boldsymbol{x}'_{\text{aut}} = \boldsymbol{A}^{\dagger}\, \boldsymbol{b} , \tag{8.17}$$

with the pseudo inverse $\boldsymbol{A}^{\dagger}$. The echoes are accounted for by the higher-order mode coefficients, which would not be needed if only the AUT radiation was considered. The reconstructed solution for the free-space AUT radiation consists of the low-order part $\boldsymbol{x}'_{\text{aut,low}}$ of $\boldsymbol{x}'_{\text{aut}}$, i.e., its first J_{aut} entries. This may be expressed as

$$\begin{aligned} \boldsymbol{x}'_{\text{aut,low}} &= \begin{bmatrix} \mathbf{1}_{J_{\text{aut}}} & \mathbf{0}_{J'_{\text{tot}} - J_{\text{aut}}} \end{bmatrix} \boldsymbol{x}'_{\text{aut}} \\ &= \begin{bmatrix} \mathbf{1}_{J_{\text{aut}}} & \mathbf{0}_{J'_{\text{tot}} - J_{\text{aut}}} \end{bmatrix} \boldsymbol{A}^{\dagger}\, \boldsymbol{b} , \end{aligned} \tag{8.18}$$

where $\mathbf{1}_{J_{\text{aut}}}$ is the $J_{\text{aut}} \times J_{\text{aut}}$ unit matrix and $\mathbf{0}_{J'_{\text{tot}} - J_{\text{aut}}}$ is the $\left(J'_{\text{tot}} - J_{\text{aut}}\right) \times \left(J'_{\text{tot}} - J_{\text{aut}}\right)$ zero matrix. The pseudo inverse of a (full rank) block matrix can be expressed as [Cline 1964; Baksalary 2007]

$$\begin{bmatrix} \boldsymbol{A}_{\text{low}} & \boldsymbol{A}_{\text{high}} \end{bmatrix}^{\dagger} = \begin{bmatrix} \left(P_{\text{high},\perp}\, \boldsymbol{A}_{\text{low}}\right)^{\dagger} \\ \left(P_{\text{low},\perp}\, \boldsymbol{A}_{\text{high}}\right)^{\dagger} \end{bmatrix} , \tag{8.19}$$

where $P_{\text{low},\perp}$ and $P_{\text{high},\perp}$ are the projection matrices in the orthogonal complements of the column spaces of $\boldsymbol{A}_{\text{low}}$ and $\boldsymbol{A}_{\text{high}}$, respectively. Using the matrix separation into low-order and high-order parts the reconstructed vector $\boldsymbol{x}'_{\text{aut,low}}$ can, thus, formally be expressed as

$$\boldsymbol{x}'_{\text{aut,low}} = \left(P_{\text{high},\perp}\, \boldsymbol{A}_{\text{low}}\right)^{\dagger}\, \boldsymbol{b} \tag{8.20}$$

where $P_{\text{high},\perp} = \mathbf{1}_M - \left(\boldsymbol{A}_{\text{high}}\, \boldsymbol{A}_{\text{high}}{}^{\dagger}\right)$ is the projection matrix into the orthogonal complement of the column space of the higher-order matrix $\boldsymbol{A}_{\text{high}}$. This fact will be useful when comparing (8.18) to other implementations of the reconstruction method.

The solution vector $\boldsymbol{x}'_{\text{aut,low}}$ not only contains the desired coefficients $\hat{\alpha}'^{(4),\text{aut}\star}_{smn}$ but also the echo contribution which is mapped onto the AUT coefficients. Using the translation coefficients

$$T^{\sigma\mu\nu}_{smn}(\boldsymbol{R}) = (-1)^{m+n+s} \oiint \boldsymbol{K}_{\sigma\mu\nu}\big(\hat{\boldsymbol{k}}\big) \cdot \boldsymbol{K}_{s,-m,n}\big(\hat{\boldsymbol{k}}\big)\, \mathrm{e}^{-\mathrm{j}\boldsymbol{k}\cdot\boldsymbol{R}}\, \mathrm{d}\hat{\boldsymbol{k}} , \tag{8.21}$$

which are derived in Appendix B, the relation between the reconstructed coefficients $\hat{\alpha}'^{(4),\text{aut}}_{smn}$ and the desired true AUT coefficients $\hat{\alpha}'^{(4),\text{aut}\star}_{smn}$ can be found to be

$$\hat{\alpha}'^{(4),\text{aut}}_{smn} = \hat{\alpha}'^{(4),\text{aut}\star}_{smn} + \sum_{\sigma=1}^{2} \sum_{\nu=1}^{N_{\text{ech}}} \sum_{\mu=-\nu}^{\nu} \hat{\alpha}''^{(4),\text{ech}\star}_{\sigma\mu\nu}\, T^{smn}_{\sigma\mu\nu}\big(\boldsymbol{r}_{0,\text{a}} - \boldsymbol{r}_{0,\text{e}}\big) , \tag{8.22}$$

where the additional sum in the right hand side of (8.22) is the portion of the echo contribution which is mapped onto the AUT coefficient $\hat{\alpha}'^{(4),\mathrm{aut}}_{smn}$. The coefficients of the echo fields — originally expressed by low-order modes in the echo centered coordinate system — are mapped to AUT coefficients of varying orders, dependent on the translation distance $\|\boldsymbol{R}\|$. The complete[13], echo influence is distributed over the AUT modes which correspond to a non-negligible magnitude of the translation operator. For small translation distances, the translation operator is significant only for the low-order AUT modes, consequently the low-order echo contributions from the echo-centered coordinate system are translated toward only low-order coefficients in the AUT-centered coordinate system. This leads to a significant distortion in the reconstructed AUT coefficients (which consist of only the low-order AUT modes). The magnitude of the translation operator $T^{\sigma\mu\nu}_{smn}(\boldsymbol{R})$ can be found in Fig. 8.5 for varying translation distances for modes up to the mode number $n = 14$. For short translation distances $\|\boldsymbol{R}\| \leq 0.5\lambda$ (see Fig. 8.5 (a) and (b)), the low-order coefficients $\hat{\alpha}''^{(4),\mathrm{ech}\star}_{\sigma\mu\nu}$ in the echo centered coordinate system only influence the AUT coefficients $\hat{\alpha}'^{(4),\mathrm{aut}}_{smn}$ of relatively low orders (e.g., the echo coefficients of orders $\nu \leq 4$ only have a significant influence on the AUT coefficients up to a mode order of $n \leq 10$ in Fig. 8.5 (a) and (b)).

With increasing translation distance $\|\boldsymbol{R}\|$, the echo influence is distributed over a larger number of AUT coefficients and — assuming that the echo influence is more or less evenly distributed over all coefficients — the amount of echo distortions which is mapped into the critical range of low-order mode indices $n \leq N_{\mathrm{aut}}$ in the AUT-centered coordinate system decreases. The echo distortion which is still contained in the reconstructed solution can be quantified by (8.22). The (squared) deviation $\|\boldsymbol{x}'_{\mathrm{aut,low}} - \boldsymbol{x}'_{\mathrm{aut}\star}\|^2$ between the reconstructed vector $\boldsymbol{x}'_{\mathrm{aut,low}}$ and the vector $\boldsymbol{x}'_{\mathrm{aut}\star} \in \mathbb{C}^{J_{\mathrm{aut}}\times 1}$ containing the true AUT coefficients $\alpha'^{(4),\mathrm{aut}\star}_{smn}$ is given by [14]

$$\begin{aligned}\left\|\boldsymbol{x}'_{\mathrm{aut,low}} - \boldsymbol{x}'_{\mathrm{aut}\star}\right\|^2 &= \sum_{s=1}^{2}\sum_{n=1}^{N_{\mathrm{aut}}}\sum_{m=-n}^{n}\left|\hat{\alpha}'^{(4),\mathrm{aut}}_{smn} - \hat{\alpha}'^{(4),\mathrm{aut}\star}_{smn}\right|^2 \\ &= \sum_{s=1}^{2}\sum_{n=1}^{N_{\mathrm{aut}}}\sum_{m=-n}^{n}\left|\sum_{\sigma=1}^{2}\sum_{\nu=1}^{N_{\mathrm{ech}}}\sum_{\mu=-\nu}^{\nu}\hat{\alpha}''^{(4),\mathrm{ech}\star}_{\sigma\mu\nu}\, T^{smn}_{\sigma\mu\nu}\left(\boldsymbol{r}_{0,\mathrm{a}} - \boldsymbol{r}_{0,\mathrm{e}}\right)\right|^2 .\end{aligned} \tag{8.23}$$

Other implementations based on modeling only the AUT sources lead to arguably very similar results. Instead of reconstructing the complete $\boldsymbol{x}'_{\mathrm{aut}}$ in (8.18) and truncating it afterwards, one can directly solve the minimization problem

$$\min_{\tilde{\boldsymbol{x}}'_{\mathrm{aut,low}} \in \mathbb{C}^{J_{\mathrm{aut}}\times 1}} \left\|\boldsymbol{b} - \boldsymbol{A}_{\mathrm{low}}\, \tilde{\boldsymbol{x}}'_{\mathrm{aut,low}}\right\|, \tag{8.24}$$

only involving the low-order contributions in the first place. This can be formally expressed as

$$\tilde{\boldsymbol{x}}'_{\mathrm{aut,low}} = \boldsymbol{A}^{\dagger}_{\mathrm{low}}\, \boldsymbol{b}, \tag{8.25}$$

---

[13] One must say *all but a negligible small portion of the echo contributions*, because the translation operator is only *approximately unitary* if only finitely many modes are considered.

[14] This way of quantifying the echo distortion is essentially equal to determining the scattered pseudo-power, i.e., determining the hypothetical power which is radiated toward infinity by the field distortion alone.

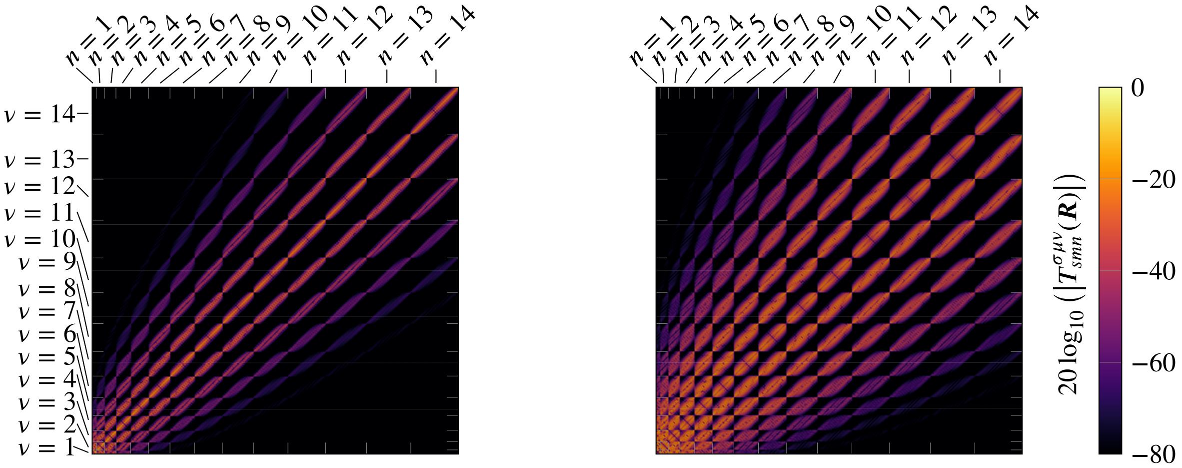

(a) $\boldsymbol{R} = 0.2\,\lambda\,\left(\boldsymbol{e}_x + \boldsymbol{e}_y + \boldsymbol{e}_z\right)/\sqrt{3}$

(b) $\boldsymbol{R} = 0.5\,\lambda\,\left(\boldsymbol{e}_x + \boldsymbol{e}_y + \boldsymbol{e}_z\right)/\sqrt{3}$

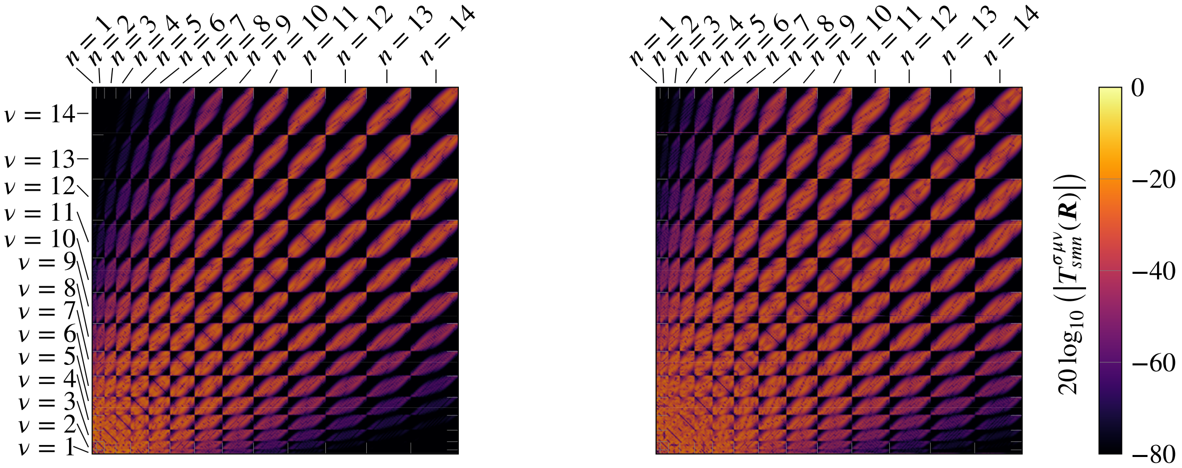

(c) $\boldsymbol{R} = 0.8\,\lambda\,\left(\boldsymbol{e}_x + \boldsymbol{e}_y + \boldsymbol{e}_z\right)/\sqrt{3}$

(d) $\boldsymbol{R} = 1.0\,\lambda\,\left(\boldsymbol{e}_x + \boldsymbol{e}_y + \boldsymbol{e}_z\right)/\sqrt{3}$

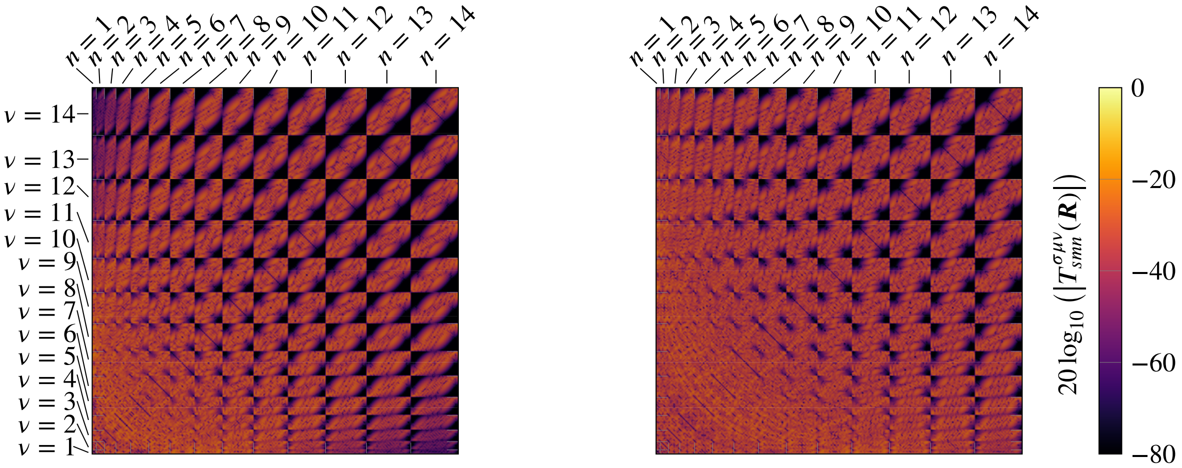

(e) $\boldsymbol{R} = 1.5\,\lambda\,\left(\boldsymbol{e}_x + \boldsymbol{e}_y + \boldsymbol{e}_z\right)/\sqrt{3}$

(f) $\boldsymbol{R} = 2.0\,\lambda\,\left(\boldsymbol{e}_x + \boldsymbol{e}_y + \boldsymbol{e}_z\right)/\sqrt{3}$

Fig. 8.5.: Magnitude of the translation operator $T_{smn}^{\sigma\mu\nu}(\boldsymbol{R})$ with varying translation distance. With growing distance, a certain coefficient $\alpha_{smn}^{(4)}$ from the original coordinate system is distributed over more coefficients $\alpha_{\sigma\mu\nu}^{(4)}$ in the translated coordinate system.

with the pseudo inverse $\boldsymbol{A}_{\mathrm{low}}^{\dagger}$. A comparison with (8.20) reveals that the result of (8.25) is very similar and provides identical results if the columns of $\boldsymbol{A}_{\mathrm{low}}$ are orthogonal to the columns of $\boldsymbol{A}_{\mathrm{high}}$. Since the columns of $\boldsymbol{A}_{\mathrm{low}}$ and $\boldsymbol{A}_{\mathrm{high}}$ correspond to the (sampled) fields of orthogonal field modes, they can indeed be expected to be nearly orthogonal in many cases.

Another implementation variant which is important to discuss due to its widespread use in literature [Gregson 2010a; Gregson 2011b; Gregson 2013; Gregson 2010b; Gregson 2012a; Gregson 2012b; Gregson 2010c; Gregson 2009; Gregson 2017a; Gregson 2017b; Newell 2008; Hess 2010b; Hess 2008; Hess 2006; Hess 2011] computes the AUT coefficients via a detour involving the matrix $\boldsymbol{C}$. First, the expansion coefficients $\hat{\alpha}_j^{(4),\,\mathrm{tot}}$ of the total field — stored in the vector $\boldsymbol{x}_{\mathrm{tot}} \in \mathbb{C}^{J_{\mathrm{tot}} \times 1}$ — are reconstructed in a coordinate system centered at $\boldsymbol{r}_0$ by solving the minimization problem

$$\min_{\boldsymbol{x}_{\mathrm{tot}} \in \mathbb{C}^{J_{\mathrm{tot}} \times 1}} \left\| \boldsymbol{b} - \boldsymbol{C}\, \boldsymbol{x}_{\mathrm{tot}} \right\|, \tag{8.26}$$

which can be alternatively expressed as

$$\boldsymbol{x}_{\mathrm{tot}} = \boldsymbol{C}^{\dagger}\, \boldsymbol{b}, \tag{8.27}$$

with the pseudo inverse $\boldsymbol{C}^{\dagger}$. Using the translation operator $T_{smn}^{\sigma\mu\nu}\left(\boldsymbol{r}_{0,\mathrm{a}} - \boldsymbol{r}_0\right)$, the expansion coefficients $\hat{\alpha}'^{(4),\mathrm{aut}}_j$ of the total field — stored in the vector $\tilde{\boldsymbol{x}}'_{\mathrm{aut}}$ — in terms of a single expansion with coordinate origin $\boldsymbol{r}_{0,\mathrm{a}}$ are found from there. This procedure is totally analogous to the well known modal echo suppression methods known under the names Mathematical Absorber Reflection Suppression (MARS) [Gregson 2010a; Gregson 2011b; Gregson 2013; Gregson 2010b; Gregson 2012a; Gregson 2012b; Gregson 2010c; Gregson 2009; Gregson 2017a; Gregson 2017b] or IsoFilter™ [Hess 2006; Hess 2010a; Hess 2011; Hess 2010b], which can be regarded as state of the art frequency domain echo suppression algorithms.

Since the expansion of total fields in terms of a single spherical mode expansion centered at $\boldsymbol{r}_{0,\mathrm{a}}$ is unique, the reconstructed vector $\tilde{\boldsymbol{x}}'_{\mathrm{aut}}$ should in theory be identical to the vector $\boldsymbol{x}'_{\mathrm{aut}}$ obtained in (8.18). Deviations may only come from aliasing errors if the number of modes J_{tot} was chosen too small to represent the total fields correctly or due to truncation errors introduced with the numerical implementation of the translation operator $T_{smn}^{\sigma\mu\nu}\left(\boldsymbol{r}_{0,\mathrm{a}} - \boldsymbol{r}_0\right)$. The reason why (8.27) with a subsequent translation of spherical modes to the coordinate origin in the center of the AUT can be found in literature rather than the direct evaluation of (8.18) lies in the fact that the pseudo inverse $\boldsymbol{C}^{\dagger}$ can be computed efficiently if $\boldsymbol{r}_0$ is located in the center of a spherical measurement surface which does often not coincide with the center of the AUT. Placing the AUT outside of the center of the measurement sphere has benefits in the stationary probe scenario (as discussed later) whereas the placement of the AUT is irrelevant in the stationary AUT case — only the relative separation between the AUT and the echo object matters here.

Reconstructing AUT and Echo Sources Simultaneously

So far the echo has been neglected in modeling the total fields leading to suboptimal solutions as shown by the error estimate (8.23). The solution can be improved by assuming echo sources simultaneously to the AUT sources. In agreement with (8.2), only low-order modes have to be considered for both, the AUT and the echo yielding the minimization problem

$$\min_{\substack{\overline{\boldsymbol{x}}'_{\mathrm{aut,low}} \in \mathbb{C}^{J_{\mathrm{aut}}\times 1} \\ \overline{\boldsymbol{x}}''_{\mathrm{ech,low}} \in \mathbb{C}^{J_{\mathrm{ech}}\times 1}}} \left\| \boldsymbol{b} - \left(\boldsymbol{A}_{\mathrm{low}}\, \overline{\boldsymbol{x}}'_{\mathrm{aut,low}} + \boldsymbol{B}_{\mathrm{low}}\, \overline{\boldsymbol{x}}''_{\mathrm{ech,low}} \right) \right\| , \tag{8.28}$$

which can be formally expressed as

$$\begin{bmatrix} \overline{\boldsymbol{x}}'_{\mathrm{aut,low}} \\ \overline{\boldsymbol{x}}''_{\mathrm{ech,low}} \end{bmatrix} = \begin{bmatrix} \boldsymbol{A}_{\mathrm{low}} & \boldsymbol{B}_{\mathrm{low}} \end{bmatrix}^{\dagger} \boldsymbol{b} . \tag{8.29}$$

By the same token as for (8.20), one can express the reconstructed AUT coefficients as

$$\overline{\boldsymbol{x}}'_{\mathrm{aut,low}} = \left(\boldsymbol{P}_{\mathrm{ech,low}\perp} \boldsymbol{A}_{\mathrm{low}} \right)^{\dagger} , \tag{8.30}$$

where $\boldsymbol{P}_{\mathrm{ech,low}\perp} = \mathbf{1}_M - \boldsymbol{B}_{\mathrm{low}} \boldsymbol{B}_{\mathrm{low}}^{\dagger}$ is the projection into the orthogonal complement of the column space of $\boldsymbol{B}_{\mathrm{low}}$.

Of course, taking echo sources into account can only improve the reconstruction of the AUT coefficients, but it is not necessarily perfect. The solution of (8.29) is unique, if the echo fields are unambiguously distinguishable from the AUT fields, i.e., if the columns of the combined matrix $\begin{bmatrix} \boldsymbol{A}_{\mathrm{low}} & \boldsymbol{B}_{\mathrm{low}} \end{bmatrix}$ are linearly independent, i.e., if the columns of the matrix $\boldsymbol{B}_{\mathrm{low}}$ are linearly independent from the columns of $\boldsymbol{A}_{\mathrm{low}}$ (i.e., if the fields from the different source regions are linearly independent).

8.1.4. A Minimum Surface Argument

To reveal possible undesired ambiguities in (8.2) (and related to that: in the reconstruction (8.29)), it is necessary to answer the question under which circumstances it is possible to find a combination of non-zero spherical mode coefficients $\alpha'^{(4),\mathrm{aut}}_{smn}$ and $\alpha''^{(4),\mathrm{ech}}_{smn}$ for the AUT and the echo, respectively, such that the resulting total field is zero at the sampling locations. Possible non-trivial zero fields in the region external to the common enclosure S_0 of AUT and echo sources are problematic as they can be superimposed to any retrieved solution for the $\alpha'^{(4),\mathrm{aut}}_{smn}$ and $\alpha''^{(4),\mathrm{ech}}_{\sigma\mu\nu}$ coefficients without changing the fields at the observation locations. If non-trivial zero fields exist, it is impossible to unambiguously determine the desired isolated AUT fields from measurements of the total fields. The situation of interest is depicted in Fig. 8.6. AUT and echo sources are located in two well separated regions enclosed by the two spheres S_{aut} and S_{ech}, respectively.

Non-trivial AUT and echo sources can cancel identical to zero in the exterior region outside S_0 only, if the fields are zero everywhere in the source free region [Klinkenbusch 2008; Klinkenbusch 2009] — including the source free-space inside S_0. This follows directly from the unique continuation property, which holds for the scalar Helmholtz equation. If a solution $\varphi(\boldsymbol{r})$ to the homogeneous Helmholtz equation

$$\Delta\varphi(\boldsymbol{r}) + k^2\varphi(\boldsymbol{r}) = 0 \quad \boldsymbol{r} \in \Omega \tag{8.31}$$

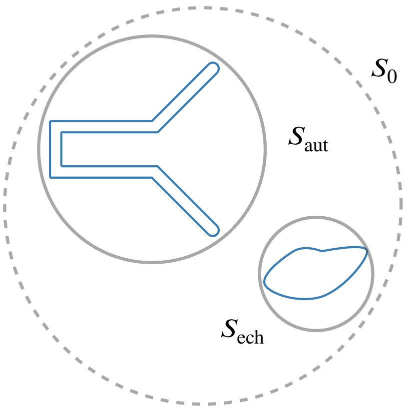

Fig. 8.6.: AUT and echo sources enclosed by two well separated spheres S_{aut} and S_{ech}, respectively. Can there be a zero field outside S_0 for non-zero echo and AUT sources?

is identical to zero in a finite open subdomain $V \subset \Omega$, it must be identical to zero in the complete region Ω, as long as V and Ω are sufficiently regular domains (i.e., connected, with sufficiently continuous borders, etc.)[15] [Müller 1954; Kenig 1989].

Non-trivial non-radiating fields which cancel identical to zero in the exterior region are therefore impossible and with infinite measurement accuracy it should always be possible to distinguish the echo fields from the AUT fields. This finding holds not only true for spherical surfaces as depicted in Fig. 8.6 but also for more general enclosing surfaces. This does not resolve the issue in practical terms, however, because weakly radiating fields which decay rapidly on their way from the source region toward the measurement locations pose similar problems to any practically relevant measurement setup as strictly non-radiating currents because of unavoidable accuracy limitations of real measurements.

The original question must therefore be modified to take a limited measurement accuracy into account: under which circumstances is it possible to find a combination of non-zero (low-order) spherical mode coefficients $\alpha'^{(4),\mathrm{aut}}_{smn}$ and $\alpha''^{(4),\mathrm{ech}}_{\sigma\mu\nu}$ for the AUT and the echo, respectively, such

---

[15] Every cartesian component of the electric field $\boldsymbol{E}$ must necessarily fulfill the Helmholtz equation. This is a necessary but not sufficient condition for the electric field in the source free region to fulfill Maxwell's equations. To be a correct solution to Maxwell's equations, the electric field must also have a zero divergence $\nabla \cdot \boldsymbol{E} = 0$ in the source free region. This result is not a contradiction to the fact that the external field outside of S_0 can also exactly be expressed by two different series expansions (with infinitely many terms)

$$\boldsymbol{E}_{\mathrm{tot}}(\boldsymbol{r})\Big|_{\boldsymbol{r}\in V} = k\sqrt{Z_{\mathrm{F}}}\sum_{s=1}^{2}\sum_{n=1}^{\infty}\sum_{m=-n}^{n} \alpha'^{(4),\mathrm{aut}}_{smn}\, \boldsymbol{F}^{(4)}_{smn}\left(r', \vartheta', \varphi'\right)$$

in terms of a mode expansion with respect to the coordinate origin at $\boldsymbol{r}_{0,\mathrm{a}}$ or

$$\boldsymbol{E}_{\mathrm{tot}}(\boldsymbol{r})\Big|_{\boldsymbol{r}\in V} = k\sqrt{Z_{\mathrm{F}}}\sum_{s=1}^{2}\sum_{n=1}^{\infty}\sum_{m=-n}^{n} \alpha''^{(4),\mathrm{ech}}_{smn}\, \boldsymbol{F}^{(4)}_{smn}\left(r'', \vartheta'', \varphi''\right)$$

in terms of a mode expansion with respect to the coordinate origin at $\boldsymbol{r}_{0,\mathrm{e}}$, respectively. Outside their respective convergence radius, both expansions converge exactly to the correct field but inside the convergence radius, the expansions show a singular behavior and cannot be used to express the field correctly [Bleistein 1977; Bates 1975; Yaghjian 1997; Yaghjian 2000].

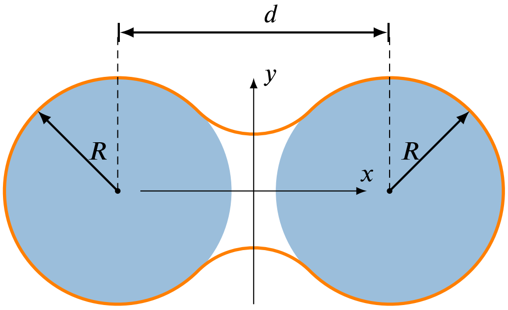

Fig. 8.7.: Minimum area surface enclosing two separated spherical source regions of identical shape.

that the resulting total field is *negligibly small* at the sampling locations? The effective DoFs of the total source distributions would be less than the sum of DoFs for each individual source distribution.

A plausible way to estimate an upper bound for the DoFs which can be radiated by a certain source distribution is to consider the surface area of an enclosing Huygens surface[16] (i.e., the DoFs appear to be more closely related to the surface area of a source region than to the volume [Bucci 1998]). If one can find a surface enclosing both source regions simultaneously with a total surface area less than the sum of the surface areas enclosing each source domain separately, it is expected that also the DoFs of the total field are less than the sum of DoFs for each separate source region.

Consider the two identical separated spherical source regions depicted in Fig. 8.7 as an illustrative example. Both spheres have the radius R and the sphere centers are separated by the distance d. The geometry is rotationally symmetric around the x-axis. This symmetry can be exploited to simplify the computation of surface areas. A surface of revolution is created by rotating a curve $f(x)$ around the x-axis. The surface area A of such a surface of revolution is readily found by

$$A = 2\pi \int_a^b f(x) \sqrt{1 + \left(\frac{\mathrm{d}f(x)}{\mathrm{d}x}\right)^2} \,\mathrm{d}x \,. \tag{8.32}$$

If the two spheres are not too far separated, it is possible to find a surface connecting both spheres which has a total surface area less than the sum of the two spherical surface areas. Finding the minimum area surface enclosing the two spheres can be expressed as a variational calculus problem, minimizing the quantity in (8.32). If the two spheres are not too far apart, the minimum enclosing hull takes the shape of a catenoid between the two spheres. The curve forming the catenoid surface between the spheres for this symmetric configuration is given by [Arfken 2005, pp. 931ff.], [Goldstein 1980, p.42], [Isenberg 1992]

$$f(x) = a \cosh\left(\frac{x}{a}\right) \,, \tag{8.33}$$

---

[16] All possibly radiated fields can be expressed by equivalent surface currents on the Huygens surface. The DoFs can be estimated by the number of surface current elements which are necessary to represent the equivalent currents accordingly. Experience has shown that for reasonably smooth surfaces, surface currents can be appropriately discretized by triangular elements of approximately constant shape. One can therefore expect an upper bound for the DoFs which is approximately proportional to the surface area of the smallest hull enclosing all sources.

where $a > 0$ is a real valued parameter which has to be adjusted such that the catenoid touches the spheres but does not intersect them.

With a positive parameter a (such that the catenoid surface does not intersect itself) it is easy to verify that $a \cosh(x/a) > c\,x$, with a constant $c \approx 1.508880$. A catenary solution to the surface minimization problem thus only exists if the tangent on the sphere through the coordinate origin has a slope which is at least c. The slope of this tangent is given by the expression $\tan(\sin(2R/d))$ and if the distance between the two spheres increases such that $2R/d < \sin\big(\tan^{-1}(c)\big) \approx 0.833557$, no catenary solution exists anymore and the smallest enclosing hull of the sources consists just of the two separate spherical surfaces.

This means that the total fields of the two source regions have less DoFs than the sum of the DoFs of the individual source regions if the distance between the spheres $d < 2.399357R$ — i.e., if the minimum distance between the two spheres is smaller than $0.399357R$. In this case one can expect that some non-observable fields — these are fields which have a large magnitude in the source free region between the individual source regions but a weak magnitude at the observation locations outside a common enclosure — exist and an accurate source localization for the observed fields is not possible.

Similar considerations hold also for different source geometries as for example two cubical source regions. It should be understood that the minimum surface argument presented in this section can be used to justify the existence of fields with an evanescent behavior if two source regions are located too close together. However, the estimate for the total DoFs derived from the surface area of the enclosure is a heuristic, approximate upper bound. It cannot be used to predict exactly at which separation distance the radiated fields from the two source regions can be clearly distinguished — the argument from this section gives a *qualitative* not a *quantitative* explanation of the situation.

8.1.5. Numerical Investigations with Stationary Antennas Under Test

In this section, numerical experiments are carried out to support the claims which have been made in the previous sections. More specifically, the following five statements are confirmed

- The reconstruction methods from (8.20), (8.25), and (8.27) are practically equivalent concerning their echo suppression.
- Reconstructing only AUT sources is inferior to reconstructing AUT and echo sources simultaneously.
- Equivalent current based methods behave similar to spherical expansion based methods concerning their capability to separate AUT fields from echo fields but may have benefits because the source regions can be confined more precisely according to the true source geometries.
- When two source regions are well separated (i.e., not intersecting) but too close to each other, they can excite evanescent waves despite each source region only radiating low-order modes.
- In a stationary AUT scenario, the absolute position of the AUT is irrelevant — only the relative position with respect to the echo is important.

The numerical experiments have been carried out at a symbolic frequency of 1 GHz, but due to the scale invariance of Maxwell's equations the results are generally valid for all frequencies and all dimensions are given in terms of wavelengths to reflect this fact. Two identical source regions are considered — representing the AUT region and the echo region, respectively — each with two square shaped current sheets placed in front of each other with a separation in x-direction of $0.25\,\lambda$. Two simulation campaigns have been carried out with two different sizes for the current sheets. In the first campaign, every current sheet had the dimensions $1.403\,122\,\lambda \times 1.403\,122\,\lambda$ in the y-z-plane such that all AUT sources and all echo sources were confined in a minimum sphere of radius $r_{\mathrm{aut}} = r_{\mathrm{ech}} = 1.0\lambda$, respectively. In the second campaign, every current sheet had the dimensions $2.822\,897\,\lambda \times 2.822\,897\,\lambda$ in the y-z-plane such that all AUT sources and all echo sources were confined in a minimum sphere of radius $r_{\mathrm{aut}} = r_{\mathrm{ech}} = 2.0\lambda$, respectively. Hertzian dipoles were regularly distributed on the current sheets with a separation of 0.1λ in y- and z-direction. The dipole excitation is constant along the z-direction, follows a half-wave of a sine curve along the y-direction, and has a phase shift according to $\mathrm{e}^{\mathrm{j}k_0x}$ to form a main beam into the positive x-direction, following the procedure described in [Schmidt 2011a].

The considered situation is depicted in Fig. 8.8. The two source regions were placed with a varying separation (in $0.2\,\lambda$ steps) from $d = 0.0\lambda$ to $d = 10.0\,\lambda$(such that the same scenarios can be simulated later with the AUT in the center of the measurement sphere without letting the echo sources collide with the measurement sphere) in y-direction to each other. Their separation is quantified by the minimum distance d between the two enclosing minimum spheres (see Fig. 8.8). The tangential components of the total field radiated by all sources were sampled on a measurement sphere with radius $r_{\mathrm{meas}} = 14.0\,\lambda$ ($r_{\mathrm{meas}} = 16.0\,\lambda$ for the larger scenario) centered in the common center of the AUT and the echo sources. The measurement sphere has been sampled with equiangular step sizes of $\Delta\vartheta = \Delta\varphi = 2.5°$.

For every measurement constellation, the AUT fields have been reconstructed with the different modal and current based reconstruction methods discussed previously. Eight different reconstruction methods are considered — four modal methods and four surface current based methods — leading to the following reconstructed AUT fields

- The field $\boldsymbol{E}_{\mathrm{a}}$ is the reconstructed AUT field according to (8.20) where spherical coefficients (high-order and low-order according to the measurement sphere enclosing all sources) were reconstructed only for the AUT but the reconstructed higher-order modes were discarded for finding the AUT fields. The reconstructed (truncated to low-order) AUT coefficients are stored in the vector $\boldsymbol{x}'_{\mathrm{a}}$.

- The field $\boldsymbol{E}_{\mathrm{a,low}}$ is the reconstructed AUT field according to (8.25), where only low-order spherical coefficients (according to the measurement sphere enclosing only AUT sources) were reconstructed for the AUT. The reconstructed AUT coefficients are stored in the vector $\boldsymbol{x}'_{\mathrm{a,low}}$. The difference to $\boldsymbol{x}'_{\mathrm{a}}$ is that no high-order AUT coefficients were involved in the reconstruction process.

- The field $\boldsymbol{E}_{\mathrm{MARS}}$ is the reconstructed AUT field according to (8.27), where — as in the MARS procedure — spherical coefficients were reconstructed in the center of the measurement sphere and thereafter translated to the AUT center. The reconstructed higher-order modes were discarded before computing the AUT fields. The reconstructed AUT coefficients are stored in the vector $\boldsymbol{x}'_{\mathrm{MARS}}$.

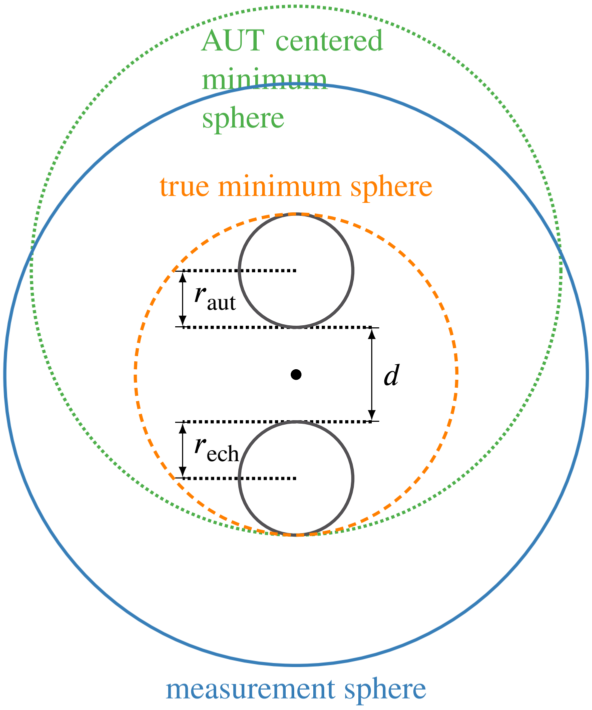

Fig. 8.8.: Echoic measurement scenario with a stationary probe and echo object. The rotating AUT is depicted at different measurement positions. With the AUT placed at the rotation center, the size of the test zone is equal to the minimum sphere around the AUT.

- The field $\boldsymbol{E}_{\mathrm{a+e}}$ is the reconstructed AUT field according to (8.30), where low-order spherical coefficients were reconstructed for the AUT and the echo, simultaneously. The reconstructed echo modes were discarded for finding the AUT fields. The reconstructed AUT coefficients are stored in the vector $\boldsymbol{x}'_{\mathrm{a+e}}$.
- The field $\boldsymbol{E}_{\mathrm{sph}}$ is the reconstructed AUT obtained by reconstructing surface currents on a Huygens surface. The Huygens surface for the reconstruction was a single spherical surface (radius r_{aut}) enclosing only the AUT sources.
- The field $\boldsymbol{E}_{\mathrm{2sph}}$ is the reconstructed AUT obtained by reconstructing surface currents on two Huygens surfaces. The Huygens surfaces for the reconstruction were two spherical surfaces (radii r_{aut} and r_{ech}) enclosing the AUT sources and the echo sources, respectively. The reconstructed currents on the echo surface were discarded before computing the AUT fields.
- The field $\boldsymbol{E}_{\mathrm{box}}$ is the reconstructed AUT obtained by reconstructing surface currents on a Huygens surface. The Huygens surface for the reconstruction was a single cuboid surface ($1.5\,\lambda \times 1.5\,\lambda \times 0.3\,\lambda$ for the first scenario and $2.9\,\lambda \times 2.9\,\lambda \times 0.3\,\lambda$ for the second scenario) enclosing only the AUT sources.
- The field $\boldsymbol{E}_{\mathrm{2box}}$ is the reconstructed AUT obtained by reconstructing surface currents on two Huygens surfaces. The Huygens surfaces for the reconstruction were two cuboid

surfaces ($1.5\,\lambda \times 1.5\,\lambda \times 0.3\,\lambda$ for the first scenario and $2.9\,\lambda \times 2.9\,\lambda \times 0.3\,\lambda$ for the second scenario) enclosing the AUT sources and the echo sources, respectively. The reconstructed currents on the echo surface were discarded for finding the AUT fields.

The reconstructed AUT fields are compared to the true AUT field generated by the AUT dipoles. The reconstruction error ϵ is quantified as

$$\epsilon = \sqrt{\frac{\oiint \left[\left|E_{\mathrm{FF},\vartheta}(\vartheta,\varphi) - E_{\mathrm{FF},\vartheta,\mathrm{ref}}(\vartheta,\varphi)\right|^2 + \left|E_{\mathrm{FF},\varphi}(\vartheta,\varphi) - E_{\mathrm{FF},\varphi,\mathrm{ref}}(\vartheta,\varphi)\right|^2\right] \mathrm{d}\hat{\boldsymbol{k}}}{\oiint \left[\left|E_{\mathrm{FF},\vartheta,\mathrm{ref}}(\vartheta,\varphi)\right|^2 + \left|E_{\mathrm{FF},\varphi,\mathrm{ref}}(\vartheta,\varphi)\right|^2\right] \mathrm{d}\hat{\boldsymbol{k}}}}\,, \tag{8.34}$$

i.e., the root mean square error between the reference FF and the reconstructed FF. For the coefficients of a spherical wave expansion, this is equivalent to

$$\begin{aligned}\epsilon &= \sqrt{\frac{\sum\limits_{s=1}^{2}\sum\limits_{n=1}^{\infty}\sum\limits_{m=-n}^{n}\left|\alpha'^{(4),\mathrm{aut}}_{smn} - \alpha'^{(4),\mathrm{aut}\star}_{smn}\right|^2}{\sum\limits_{s=1}^{2}\sum\limits_{n=1}^{\infty}\sum\limits_{m=-n}^{n}\left|\alpha'^{(4),\mathrm{aut}\star}_{smn}\right|^2}}\\ &= \frac{\left\|x'_{\mathrm{rec}} - x'_{\mathrm{aut}\star}\right\|}{\left\|x'_{\mathrm{aut}\star}\right\|}\,,\end{aligned} \tag{8.35}$$

where $\alpha'^{(4),\mathrm{aut}\star}_{smn}$ are the true spherical coefficients of the radiated AUT field stored in the vector $x'_{\mathrm{aut}\star}$ and $\alpha'^{(4),\mathrm{aut}}_{smn}$ are the reconstructed coefficients stored in the vector x'_{rec} (the vector x'_{rec} can represent either x'_{a}, $x'_{\mathrm{a,low}}$, x'_{MARS}, or $x'_{\mathrm{a+e}}$). This corresponds to the relative L_2-error of the reconstructed coefficient vector. As no spherical coefficients are available for the surface current based reconstruction methods, one must rely on (8.34).

The retrieved errors for the different reconstruction methods can be seen in Fig. 8.9 for the source size $r_{\mathrm{aut}} = r_{\mathrm{ech}} = 1\,\lambda$ and in Fig. 8.10 for the source size $r_{\mathrm{aut}} = r_{\mathrm{ech}} = 2\,\lambda$. The truncation indices for all spherical mode expansions are based on the minimum sphere around the sources with a small mode buffer of $n_{\mathrm{buf}} = 2$, thus, the reconstruction accuracy of the reconstructed fields are limited by the truncation of higher-order modes in favor of a more localized source model.

As can be expected from the analysis in Section 8.1.3, all methods which only reconstruct AUT sources without considering echo sources (i.e., ϵ_{a}, $\epsilon_{\mathrm{a,low}}$, ϵ_{MARS}, ϵ_{sph}, and ϵ_{box}) show a very similar performance as long as they do not face numerical stability problems. Such numerical problems arise for the reconstruction of x'_{a} once the distance d becomes large enough that the AUT centered minimum sphere enclosing all AUT and echo sources interferes with the measurement sphere. In this case, some of the considered high-order mode fields have an extensively large magnitude at some of the measurement locations, concealing the influence of the other modes to the total fields. As a consequence, the mode coefficients can no longer be reconstructed accurately, once the minimum sphere around the sources interferes with the measurement sphere. These interference problems occur for the reconstruction of x'_{a} at a distance of $d \approx 7\,\lambda$ for the scenario with the smaller source radii $r_{\mathrm{aut}} = r_{\mathrm{ech}} = 1\,\lambda$ and at a distance of $d \approx 5\,\lambda$ for the larger source radii $r_{\mathrm{aut}} = r_{\mathrm{ech}} = 2\,\lambda$. Apart from this numerical instability, the reconstruction error curve for ϵ_{a} is very similar to $\epsilon_{\mathrm{a,low}}$, ϵ_{MARS}, ϵ_{sph}, and ϵ_{box}, verifying the first of the five statements from

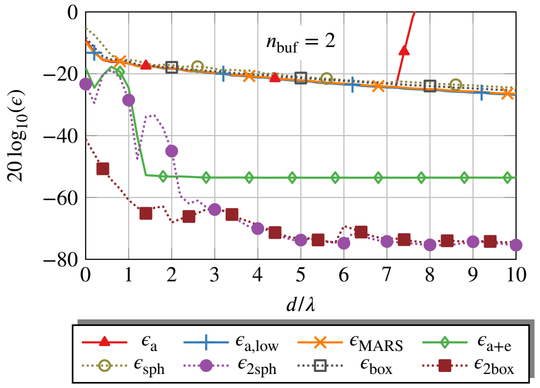

Fig. 8.9.: Reconstruction error of different reconstruction methods dependent on the distance d between echo and AUT with source radii $r_{\text{aut}} = r_{\text{ech}} = 1\,\lambda$.

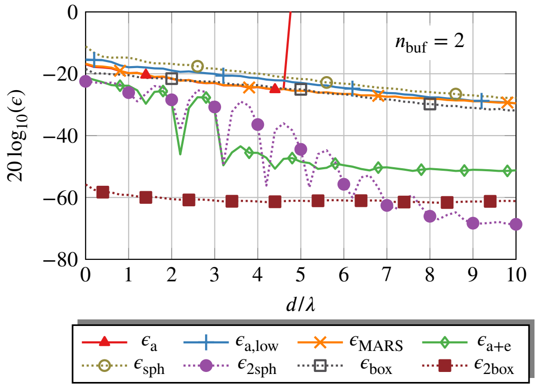

Fig. 8.10.: Reconstruction error of different reconstruction methods dependent on the distance d between echo and AUT with source radii $r_{\text{aut}} = r_{\text{ech}} = 2\,\lambda$.

the beginning of this section. The slow but steady decrease of the reconstruction error is in agreement with the prediction from (8.23) where it was claimed that with increasing distance between the AUT and the echo a larger portion of the echo distortion is mapped onto higher-order modes in the AUT centered coordinate system, thus, being removed by modal filtering.

Reconstructing AUT sources simultaneously with echo sources drastically improves the reconstruction quality compared to only reconstructing the AUT sources. After the separation between AUT and the echo exceeds a critical distance — around $d = 2\,\lambda$ for the $1\,\lambda$-sized sources and around $d = 3\,\lambda$ for the $2\,\lambda$-sized sources — the reconstruction of the AUT sources is successful up to the maximum achievable accuracy (see the curves for $\epsilon_{\text{a+e}}$ in Figs. 8.9 and 8.10). This confirms the second of the five statements from the beginning of this section. The achievable accuracy of around −55 dB for the truncated spherical wave expansion is due to the source model. The truncated modal expansion ($n_{\text{buf}} = 2$) is only capable to represent the true AUT field up to −52 dB, which was independently verified by a direct calculation of the spherical wave coefficients for the AUT from the source distribution via

$$\hat{\alpha}_{smn}^{(4),\text{tra}} = (-1)^{m+1} \iiint\limits_{V_{\text{aut}}} k\sqrt{Z_0}\, \boldsymbol{F}^{(1)}_{s,-m,n} \cdot \hat{\boldsymbol{J}}_{\text{tra}} \mathrm{d}v \,. \tag{8.36}$$

When the spherical wave expansion is truncated at a larger mode index (e.g., $n_{\text{buf}} = 3, 4, \ldots$), the AUT can be more accurately represented and error levels in the order of the current based methods are reached. This comes with the drawback that ambiguities due to evanescent waves persist for larger distances, as will become clear from the discussion below.

For all reconstructions, the results of the spherical expansion based methods are comparable to the corresponding results obtained with surface currents, as long as the reconstruction surface for the currents is comparable to the spherical equivalent source region for the modal expansion. With no echo sources considered in the reconstruction, the error curves of the spherical expansion methods (see the curves for ϵ_{a}, $\epsilon_{\text{a,low}}$, and ϵ_{MARS} in Figs. 8.9 and 8.10) are very similar to the corresponding error curves for the current based methods with only one Huygens surface (see

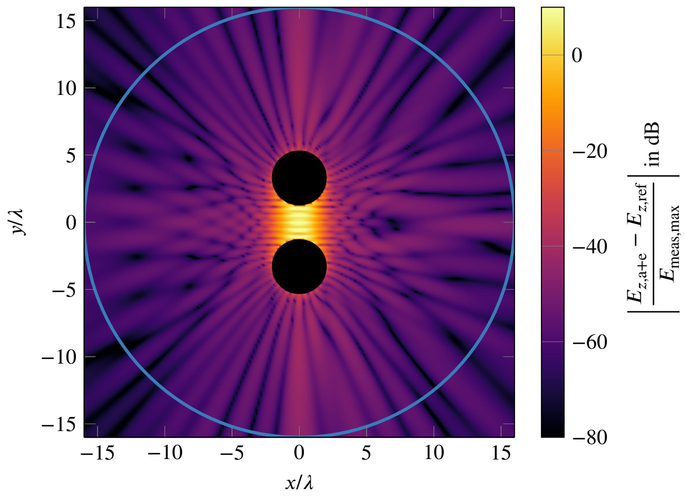

Fig. 8.11.: Difference between the z-component of the reference field and the reconstructed field using spherical wave expansions for the AUT and echo simultaneously ($r_{\mathrm{aut}} = r_{\mathrm{ech}} = 2\,\lambda$ and $d = 2.6\,\lambda$).

the curves for ϵ_{sph} and ϵ_{box} in Figs. 8.9 and 8.10). The error curve for the reconstruction of spherical mode coefficients with two expansion centers (ϵ_{a}) resembles the error curve for the current reconstruction on two spherical surfaces ($\epsilon_{\mathrm{a+e}}$). The higher achievable accuracy of around −70 dB for the surface currents is determined by the stopping criterion of the solver for the linear system of equations (and no hard mode threshold limits the accuracy of the reconstructed fields).

The tight box-shaped Huygens surface does not bring any clear advantages as compared to the spherical surface if the echo is excluded from the reconstruction. The error curve for ϵ_{sph} is similar to the error curve for ϵ_{box} for both source sizes. In contrast to this, the tight Huygens surface shows clear benefits when echo sources are reconstructed simultaneously with the AUT sources. Restricting the AUT and echo sources to a tightly confined surface can help with avoiding ambiguities due to evanescent fields. Consequently, the reconstruction error ϵ_{2box} is below −40 dB even for small separation distances d. The separation parameter d is related to the minimum spheres around the sources, thus, the box-shaped Huygens surfaces do not touch even for $d = 0$. More important is, however, that the cross sections of the the opposing faces of the AUT box and the echo box are rather flat and no standing waves can be generated between them. Since no evanescent waves obscure the reconstruction process, the reconstructed AUT fields agree well with the true AUT fields even for small separation distances d. This confirms the third of the five initial statements from the beginning of this section, which stated that equivalent current based reconstruction methods perform similar as spherical expansion based methods, but the current based methods may be able to confine the reconstructed currents more precisely.

When the separation between the echo and the AUT is below the critical distance, the AUT fields are reconstructed with the same (insufficient) accuracy for the methods involving the additional echo sources as for the MARS-like reconstruction methods (despite the total fields were excellently reconstructed in the methods which considered the echo sources). The reconstruction deviation $\tilde{\epsilon} = \left\|\boldsymbol{b} - \boldsymbol{b}_{\mathrm{rec}}\right\| / \|\boldsymbol{b}\|$ was below $\tilde{\epsilon} < 0.0002$ for all separation distances d for all reconstruction methods which included the echo in the source model. This leads to the conclusion, that different source distributions (i.e., the true and the reconstructed ones) can lead to practically the same fields at the measurement sphere. This conclusion is further confirmed in Fig. 8.11, showing the

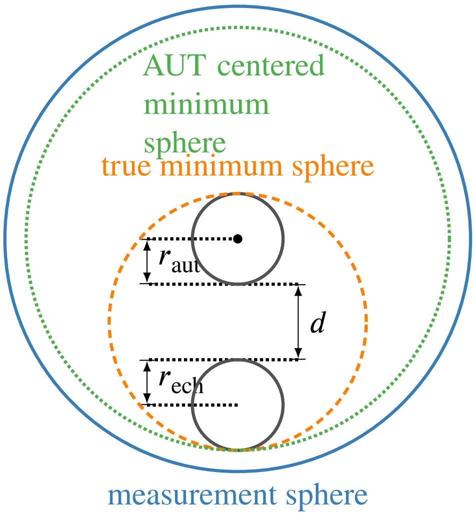

Fig. 8.12.: Echoic measurement scenario with a stationary probe and echo object. The rotating AUT is depicted at different measurement positions. With the AUT placed outside the rotation center.

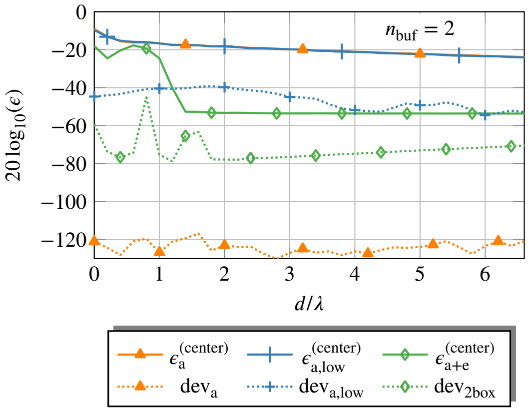

Fig. 8.13.: Reconstruction error of spherical AUT coefficients dependent on the distance d between echo and AUT with source radii $r_{\text{aut}} = r_{\text{ech}} = 1\,\lambda$, with the AUT in the center of the measurement sphere. The deviations from the previous scenario are shown with dotted lines.

difference between the dominant z-component of the reference field and the reconstructed field, where spherical wave expansions for the AUT and echo were used simultaneously for the source radii $r_{\text{aut}} = r_{\text{ech}} = 2\,\lambda$ with distance $d = 2.6\,\lambda$. The depicted difference is normalized to the maximum measured field value on the measurement sphere (i.e., normalized to the maximum field value on the measurement sphere generated by the original sources) to verify that this difference is negligible at the measurement distance (denoted by the blue circle). Reconstructing the total fields simultaneously with AUT and echo sources yields practically ambiguous results — the total fields of different source distributions, i.e., the true source distribution and the reconstructed one, have negligibly small deviation at the observation surface. One can observe the behavior which has been predicted in Section 8.1.4. Evanescent modes are generated despite only low-order field modes were reconstructed for the AUT and echo centered spherical expansions, respectively. This confirms the fourth of the five statements from the beginning of this section.

Finally, the simulations were repeated for the configuration shown in Fig. 8.12 and compared to the results from the previous scenario from Fig. 8.8. In contrast to the previous case, the AUT was fixed to the center of the measurement sphere, while the echo was moved in y-direction to obtain varying separation distances d between the AUT and the probe. This way, the distance can only be increased until $d = 6.6666\,\lambda$ before the echo minimum sphere interferes with the measurement surface. The retrieved errors for the spherical expansion based methods can be seen in Fig. 8.13. Since the AUT center coincides with the center of the measurement sphere, no translation of the retrieved coefficients is required in the MARS procedure and the reconstructed coefficients x'_{MARS} are therefore identical to x'_{a} and, thus, not shown in the figure.

The error curves (denoted with a superscript “(center)” to highlight that here the AUT was

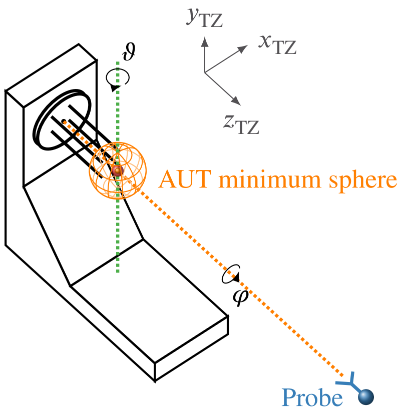

Fig. 8.14.: Schematic drawing of a spherical measurement range with an AUT rotation stage. The probe position is fixed.

in the center of the measurement surface) for the spherical coefficients in Fig. 8.13 are almost identical to the ones in Fig. 8.9. The relative L_2-norm deviations between the coefficient vectors are given by the dotted lines. The deviations between the corresponding reconstructed coefficient vectors is well below their deviation from the true AUT fields and one can certainly say that the absolute AUT position does not matter in the reconstruction of the AUT fields — only the distance between the AUT and the echo object is important in stationary AUT scenarios. This confirms the last of the five statements from the beginning of this section.

8.2. Stationary Probe

Now the situation with a stationary probe is analyzed. The echo object has a fixed position relative to the probe and the AUT is rotated such that the AUT field can be observed from different angles. Such scenarios are encountered in many spherical measurement ranges as depicted in Fig. 8.14.

The whole AUT positioner rotates around the global y-axis. The global stationary coordinate system denoted by x_{TZ}, y_{TZ}, z_{TZ} is also depicted in Fig. 8.14. The index “TZ” stands for *test zone* as it is convenient to consider the situation from the point of view of a radiating probe creating a certain incident field in the so-called test zone around the AUT. The receiving AUT is then rotated through this field. The rotation around χ is performed by the probe rotating around the global z-axis. In theory, the χ-rotation can also be performed by the AUT, e.g., with the help of a robotic arm. The following description is general enough to include the case where the χ-rotation is performed by the AUT as a special case.

The test zone is a spherical volume V_1 enclosed by the surface S_1. The center of the test zone coincides with the rotation center of the AUT and the radius of the test zone is determined by the maximum distance of any AUT part to the rotation center. The test zone may coincide with the AUT minimum sphere if the AUT is centered at the rotation center as depicted in Fig. 8.14. When the AUT is displaced from the rotation center, in general the test zone will be increased as the AUT traverses a larger volume when being rotated. The scenario is depicted in Fig. 8.15 for an AUT placed at the rotation center and in Fig. 8.16 for an AUT placed away from the rotation center. The AUT is depicted with a solid line in its original position and with a dashed line in a

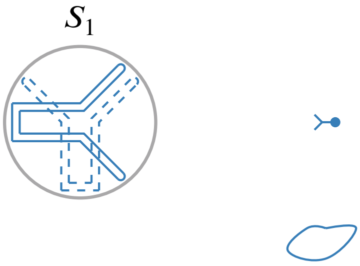

Fig. 8.15.: Echoic measurement scenario with a stationary probe and echo object. The rotating AUT is depicted for different measurement positions. With the AUT placed at the rotation center, the size of the test zone is equal to the minimum sphere around the AUT.

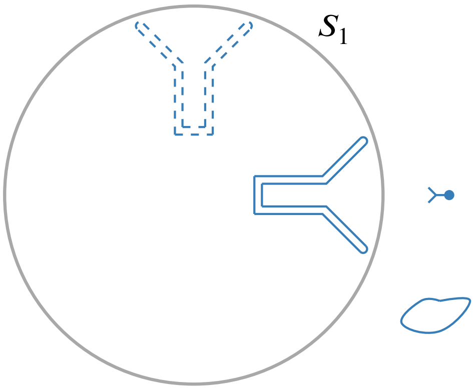

Fig. 8.16.: Echoic measurement scenario with a stationary probe and echo object. The rotating AUT is depicted for different measurement positions. With the AUT placed outside the rotation center, the size of the test zone is larger than the minimum sphere around the AUT.

rotated position.

The test zone field, consists of two parts. One part of the test zone field is generated by the radiating probe as if it was in free space. This part is known due to the known probe characteristics. The second part of the test zone field is due to the echoes. This part is generally not known. The test zone field may, thus, be expressed as

$$\boldsymbol{E}_{\mathrm{TZ}}(\boldsymbol{r}) = k\sqrt{Z_{\mathrm{F}}}\sum_{s=1}^{2}\sum_{n=1}^{N_{\mathrm{TZ}}}\sum_{\mu'=-n}^{n}\left(\alpha^{(1),\mathrm{pro}}_{s\mu' n} + \alpha^{(1),\mathrm{ech}}_{s\mu' n}\right)\boldsymbol{F}^{(1)}_{s\mu' n}(\boldsymbol{r}) \ , \tag{8.37}$$

where $\alpha^{(1),\mathrm{pro}}_{s\mu' n}$ are the known expansion coefficients of the probe portion of the test zone field and $\alpha^{(1),\mathrm{ech}}_{s\mu' n}$ are the unknown expansion coefficients of the echo portion of the test zone fields. The limit for the summation is as usual given by $N_{\mathrm{TZ}} = k_0\, r_1 + n_{\mathrm{buf}}$, where r_1 denotes the radius of the test zone field.

When the probe is rotated around its axis to perform the χ-rotation, the coefficients of the incident probe field are transformed according to $\alpha^{(1),\mathrm{pro}}_{s\mu' n} \rightarrow \mathrm{e}^{\mathrm{j}\mu'\chi}\alpha^{(1),\mathrm{pro}}_{s\mu' n}$, but the echo coefficients $\alpha^{(1),\mathrm{ech}}_{s\mu' n}$ transform in a rather unpredictable manner because the rotated probe illuminates the echo objects differently. It is, therefore, convenient to describe the incident echo field by varying expansion coefficients $\alpha^{(1),\mathrm{ech}}_{s\mu' n}(\chi)$ which depend on χ [Pogorzelski 2009; Pogorzelski 2010].

A convenient description of the S_{12}-parameter for the AUT rotated to different positions described by the angles ϑ_m, φ_m, χ_m, $m = 1, \ldots, M$ is given by

$$S_{12}\left(\vartheta_m, \varphi_m, \chi_m\right) = \sum_{s=1}^{2}\sum_{n=1}^{N_{\mathrm{TZ}}}\sum_{\mu=-n}^{n}\sum_{\mu'=-n}^{n}\beta^{(1),\mathrm{aut}}_{s\mu n}\,\mathrm{e}^{\mathrm{j}\mu\varphi_m}\,\mathrm{d}^{n}_{\mu'\mu}\left(\vartheta_m\right)\left(\alpha^{(1),\mathrm{pro}}_{s\mu' n}\mathrm{e}^{\mathrm{j}\mu'\chi_m} + \alpha^{(1),\mathrm{ech}}_{s\mu' n}\left(\chi_m\right)\right) , \tag{8.38}$$

where $\beta^{(1),\mathrm{aut}}_{s\mu,n}$ are the unknown AUT receiving coefficients of the unrotated AUT with respect to the center of the test zone field and $\mathrm{d}^{n}_{\mu'\mu}\left(\vartheta_m\right)$ is the Wigner-d-function.

8.2.1. Extended Probe Calibration and Test Zone Field Compensation

Having an appropriate formal description of the $S_{12}\left(\vartheta_m, \varphi_m, \chi_m\right)$, one can attempt to account for the undesired echo influences. The unknown incident echo field coefficients $\alpha^{(1),\mathrm{ech}}_{s\mu'n}(0^\circ)$ and $\alpha^{(1),\mathrm{ech}}_{s\mu'n}(90^\circ)$ for $\chi = 0^\circ$ and $\chi = 90^\circ$ can be determined in preliminary measurements with two known test antennas[17] [Pogorzelski 2009; Pogorzelski 2010]. The corresponding method was named *extended probe instrument calibration*. The measured S_{12}-parameters for the two test antennas in different orientations have the form

$$S^{\mathrm{aut1}}_{12}\left(\vartheta_m, \varphi_m, 0^\circ\right) = \sum_{s=1}^{2}\sum_{n=1}^{N_{\mathrm{TZ}}}\sum_{\mu=-n}^{n}\sum_{\mu'=-n}^{n} \beta^{(1),\mathrm{aut1}}_{s\mu n}\mathrm{e}^{\mathrm{j}\mu\varphi_m}\,\mathrm{d}^{n}_{\mu'\mu}\left(\vartheta_m\right)\,\left(\alpha^{(1),\mathrm{pro}}_{s\mu'n} + \alpha^{(1),\mathrm{ech}}_{s\mu'n}(0^\circ)\right), \tag{8.39}$$

$$S^{\mathrm{aut2}}_{12}\left(\vartheta_m, \varphi_m, 0^\circ\right) = \sum_{s=1}^{2}\sum_{n=1}^{N_{\mathrm{TZ}}}\sum_{\mu=-n}^{n}\sum_{\mu'=-n}^{n} \beta^{(1),\mathrm{aut2}}_{s\mu n}\mathrm{e}^{\mathrm{j}\mu\varphi_m}\,\mathrm{d}^{n}_{\mu'\mu}\left(\vartheta_m\right)\,\left(\alpha^{(1),\mathrm{pro}}_{s\mu'n} + \alpha^{(1),\mathrm{ech}}_{s\mu'n}(0^\circ)\right), \tag{8.40}$$

$$S^{\mathrm{aut1}}_{12}\left(\vartheta_m, \varphi_m, 90^\circ\right) = \sum_{s=1}^{2}\sum_{n=1}^{N_{\mathrm{TZ}}}\sum_{\mu=-n}^{n}\sum_{\mu'=-n}^{n} \beta^{(1),\mathrm{aut1}}_{s\mu,n}\mathrm{e}^{\mathrm{j}\mu\varphi_m}\,\mathrm{d}^{n}_{\mu'\mu}\left(\vartheta_m\right)\,\left(\mathrm{j}^{\mu'}\,\alpha^{(1),\mathrm{pro}}_{s\mu'n} + \alpha^{(1),\mathrm{ech}}_{s\mu'n}(90^\circ)\right), \tag{8.41}$$

and

$$S^{\mathrm{aut2}}_{12}\left(\vartheta_m, \varphi_m, 90^\circ\right) = \sum_{s=1}^{2}\sum_{n=1}^{N_{\mathrm{TZ}}}\sum_{\mu=-n}^{n}\sum_{\mu'=-n}^{n} \beta^{(1),\mathrm{aut2}}_{s\mu,n}\mathrm{e}^{\mathrm{j}\mu\varphi_m}\,\mathrm{d}^{n}_{\mu'\mu}\left(\vartheta_m\right)\,\left(\mathrm{j}^{\mu'}\,\alpha^{(1),\mathrm{pro}}_{s\mu'n} + \alpha^{(1),\mathrm{ech}}_{s\mu'n}(90^\circ)\right). \tag{8.42}$$

The only unknowns in these equations are the incident echo field coefficients $\alpha^{(1),\mathrm{ech}}_{s\mu'n}(0^\circ)$ and $\alpha^{(1),\mathrm{ech}}_{s\mu'n}(90^\circ)$ and they can be found by solving the system of equations defined by (8.39) to (8.42) in a least squares manner.

After the incident echo field coefficients are known, they can be used in a subsequent measurement to find the coefficients $\beta^{(1),\mathrm{aut}}_{s\mu,n}$ of an unknown AUT by solving another linear system of equations defined by (8.38) for different measurement angles ϑ_m, φ_m and $\chi_m \in \{0^\circ, 90^\circ\}$. Note that although the equations obtained from the S_{12}-measurements at the different angles suffice to form a non-singular system of equations for the $\beta^{(1),\mathrm{aut}}_{s\mu,n}$ coefficients in general, the efficient FFT-based method cannot be used for the inversion of this system because the χ-dependency of the fields does not meet the requirements of a first-order probe and, thus, the orthogonality integral for the χ-dependency cannot be calculated from the discrete samples.

A similar idea is followed in the so-called test zone field compensation method [Black 1995], where also spherical expansion coefficients of the incident field have to be determined in a

---

[17] The two test antennas are not required to be physically different antennas but the same antenna mounted in different orientations to the AUT rotation stage may also suffice.

preliminary step. The difference to the previously described method lies in the reconstruction for the unknown AUT coefficients. While in [Pogorzelski 2009; Pogorzelski 2010] the system of equations is solved taking full probe correction into account (and, therefore, loosing the efficiency of the spherical setup), in [Black 1995] the system of equations is repeatedly solved with only a first-order probe correction. By iteratively removing all portions in the reconstructed S_{12}-parameter, which do not match the low-order probe model, acceptable accuracy levels are reported.

Related algorithms have been formulated by expressing the previously measured total incident fields in terms of plane waves instead of spherical modes [Koh 2011], but all these methods have in common that the complete incident field must be characterized with the use of known test antennas. This procedure must be repeated, whenever the probe antenna or its position is changed or when any significant change happens in the echoic environment. Thus, the chamber calibration methods requiring a preliminary measurement of the echo influence are not treated in further detail in this thesis.

8.2.2. Accounting for the Echo Distortion by Unphysical Auxiliary Sources

When the echoic environment is not characterized in a preliminary measurement, one can account for the echo by additional unknowns. The correct physical description would consist of assigning unknowns for the AUT receive coefficients as well as for the incident field but this is not very convenient.

If possible, it would be much more convenient, to just work with unknowns for the AUT. This idea is at the core of modal echo suppression algorithms [Hess 2006; Hess 2010a; Hess 2011; Hess 2010b; Gregson 2009; Gregson 2010a; Gregson 2011a; Gregson 2011b; Gregson 2011d; Gregson 2011c; Gregson 2013; Gregson 2010b; Gregson 2012a; Gregson 2012b; Gregson 2010c; Gregson 2017a; Gregson 2017b; Tian 2019], but it is clear from the discussion of the previous section, that current reconstruction methods behave in a similar manner[18] [Quijano 2011a; Quijano 2011b; Quijano 2011b; Cano 2010; Cano-Facila 2011; Garcia-Gonzalez 2011]. At this point of the current discussion, it is unclear if it is possible to find an equivalent source model for the AUT, which can account for the echo influences. Furthermore, if the AUT model shall be extended to account for the echo influences one should have an understanding of where to locate these additional sources.

To this end, assume an AUT model consisting of spherical receiving coefficients $\tilde{\beta}_{s\mu n} = \beta^{\mathrm{aut}}_{s\mu' n} + \beta^{\mathrm{gho}}_{s\mu n}$, where $\beta^{\mathrm{gho}}_{s\mu n}$ are additional AUT receiving coefficients (they will be called *ghost* coefficients) which are intended to account for the echo contributions. With the additional receiving coefficients, the S_{12}-parameter from (8.38) can be modeled as

$$\begin{aligned} S'_{12}\big(\vartheta_m, \varphi_m, \chi_m\big) &= \sum_{s=1}^{2} \sum_{n=1}^{N_{\mathrm{TZ}}} \sum_{\mu=-n}^{n} \sum_{\mu'=-n}^{n} \tilde{\beta}_{s\mu n}\, \mathrm{e}^{\mathrm{j}\mu\varphi_m}\, \mathrm{d}^{n}_{\mu'\mu}\big(\vartheta_m\big)\, \mathrm{e}^{\mathrm{j}\mu'\chi_m}\, \alpha^{(1),\mathrm{pro}}_{s\mu' n} \\ &= \sum_{s=1}^{2} \sum_{n=1}^{N_{\mathrm{TZ}}} \sum_{\mu=-n}^{n} \sum_{\mu'=-n}^{n} \Big(\beta^{\mathrm{aut}}_{s\mu n} + \beta^{\mathrm{gho}}_{s\mu n}\Big)\, \mathrm{e}^{\mathrm{j}\mu\varphi_m}\, \mathrm{d}^{n}_{\mu'\mu}\big(\vartheta_m\big)\, \mathrm{e}^{\mathrm{j}\mu'\chi_m}\, \alpha^{(1),\mathrm{pro}}_{s\mu' n}\,, \end{aligned} \tag{8.43}$$

---

[18] Differences may occur because higher-order modes are not as stringently suppressed in current reconstruction methods as in spherical wave expansions and since the reconstruction surfaces can be non-spherical in current reconstruction methods.

where now all the echo influences shall be expressed by the additional ghost AUT coefficients $\beta_{s\mu n}^{\text{gho}}$. Notice, that the expressions (8.38) and (8.43) agree with their description of the direct contribution

$$S_{12}^{\text{direct}}(\vartheta_m, \varphi_m, \chi_m) = \sum_{s=1}^{2} \sum_{n=1}^{N_{\text{TZ}}} \sum_{\mu=-n}^{n} \sum_{\mu'=-n}^{n} \beta_{s\mu n}^{\text{aut}}\, \mathrm{e}^{\mathrm{j}\mu\varphi_m}\, \mathrm{d}_{\mu'\mu}^{n}(\vartheta_m)\, \mathrm{e}^{\mathrm{j}\mu'\chi_m}\, \alpha_{s\mu' n}^{(1),\text{pro}} \tag{8.44}$$

between the AUT and the probe, but the description of the echo influence differs in both expressions — in (8.38) the echo influences are (correctly) modeled by additional incident fields in the test zone, whereas in (8.43) the echoes are modeled by additional (unphysical) AUT receive coefficients. The echoic part of (8.38) is given by[19]

$$S_{12}^{\text{ech}}(\vartheta_m, \varphi_m, \chi_m) = \sum_{s=1}^{2} \sum_{n=1}^{N_{\text{TZ}}} \sum_{\mu=-n}^{n} \sum_{\mu'=-n}^{n} \beta_{s\mu n}^{\text{aut}}\, \mathrm{e}^{\mathrm{j}\mu\varphi_m}\, \mathrm{d}_{\mu'\mu}^{n}(\vartheta_m)\, \alpha_{s\mu' n}^{(1),\text{ech}}(\chi_m)\,, \tag{8.45}$$

whereas the echoic part in (8.43) is expressed by

$$S'^{\text{ech}}_{12}(\vartheta_m, \varphi_m, \chi_m) = \sum_{s=1}^{2} \sum_{n=1}^{N_{\text{TZ}}} \sum_{\mu=-n}^{n} \sum_{\mu'=-n}^{n} \beta_{s\mu n}^{\text{gho}}\, \mathrm{e}^{\mathrm{j}\mu\varphi_m}\, \mathrm{d}_{\mu'\mu}^{n}(\vartheta_m)\, \mathrm{e}^{\mathrm{j}\mu'\chi_m}\, \alpha_{s\mu' n}^{(1),\text{pro}}\,. \tag{8.46}$$

When the AUT coefficients are determined via an inverse problem, one can regard any deviations from the true solution to be concentrated in the ghost coefficients $\beta_{s\mu n}^{\text{gho}}$.

The first question is now, whether the ghost coefficients $\beta_{s\mu n}^{\text{gho}}$ can account for the echo influences in such a way that the S_{12}-parameter in (8.38) is equal to the S'_{12}-parameter in (8.43) for all measurement positions $m = 1, \dots, M$. Obviously, this implies to make (8.46) equal to (8.45). The second question is whether it is possible to find appropriate locations of the equivalent ghost sources corresponding to the $\beta_{s\mu n}^{\text{gho}}$ coefficients. The latter question of defining a restricted source region for the ghost contributions is relevant for the investigation of the separability of AUT and ghost contributions, similar to the discussion for a stationary AUT from the previous sections.

Echo Influences Along a Latitude Circle (constant ϑ)

Is it possible to find some ghost coefficients $\beta_{s\mu n}^{(1),\text{gho}}$ which establish the equality between (8.45) and (8.46) for all angles ϑ_m, φ_m, and χ_m? The answer to this question depends on the properties of the echo contribution in the truly measured S_{21}-parameters and the echo contribution which can be reconstructed by the unphysical additional ghost coefficients in (8.46). At any arbitrary fixed ϑ_m and for a fixed χ_m, the φ-dependency of the echo influence in the physically correct description of the S_{21}-parameter in (8.45) is given by the finite Fourier series

$$S_{12}^{\text{ech}}(\vartheta_m, \varphi, \chi_m) = \sum_{\mu=-N_{\text{TZ}}}^{N_{\text{TZ}}} \gamma_\mu(\theta_m, \chi_m)\, \mathrm{e}^{\mathrm{j}\mu\varphi}\,, \tag{8.47}$$

---

[19] The echo contribution of the incident field can have a complicated dependency on rotations about χ if the probe performs the χ rotations. When the probe is rotated, the environment is illuminated differently, and the echoes can change. However, if the AUT performs the χ- rotation, we have $\alpha_{s\mu n}^{(1),\text{ech}}(\chi_m) = \mathrm{e}^{\mathrm{j}\mu'\chi_m}\, \alpha_{s\mu n}^{(1),\text{ech}}(0^\circ)$.

with the Fourier coefficients

$$\gamma_\mu\big(\theta_m, \chi_m\big) = \sum_{s=1}^{2} \sum_{\substack{n=|\mu| \\ n\neq 0}}^{N_{\mathrm{TZ}}} \sum_{\mu'=-n}^{n} \beta^{\mathrm{aut}}_{s\mu n}\, \mathrm{d}^n_{\mu'\mu}\big(\vartheta_m\big)\; \alpha^{(1),\mathrm{ech}}_{s\mu' n}\big(\chi_m\big)\ . \tag{8.48}$$

Note that $\gamma_\mu\big(\theta_m, \chi_m\big)$ will generally be non-zero for $|\mu| \leq N_{\mathrm{TZ}}$ independent of the values of the fixed angles ϑ_m and χ_m, because the $\alpha^{(1),\mathrm{ech}}_{s\mu' n}\big(\chi_m\big)$ are generally non-zero for all $|\mu'| \leq N_{\mathrm{TZ}}$

The echo contribution which is modeled by (8.46) for the same φ-circle at a fixed ϑ_m and for a fixed χ_m is given by the finite Fourier series

$$S'^{\mathrm{ech}}_{12}\big(\vartheta_m, \varphi, \chi_m\big) = \sum_{\mu=-N_{\vartheta_m}}^{N_{\vartheta_m}} \gamma'_\mu\big(\theta_m, \chi_m\big)\; \mathrm{e}^{\mathrm{j}\mu\varphi}\,, \tag{8.49}$$

with the Fourier coefficients

$$\gamma'_\mu\big(\theta_m, \chi_m\big) = \sum_{s=1}^{2} \sum_{\substack{n=|\mu| \\ n\neq 0}}^{N_{\mathrm{TZ}}} \sum_{\mu'=-n}^{n} \beta^{\mathrm{gho}}_{s\mu n}\, \mathrm{d}^n_{\mu'\mu}\big(\vartheta_m\big)\; \mathrm{e}^{\mathrm{j}\mu'\chi_m}\, \alpha^{\mathrm{pro}}_{s\mu' n}\,. \tag{8.50}$$

The largest mode number N_{ϑ_m} which must be considered in the Fourier series (8.49) depends on ϑ_m and can be estimated by $N_{\vartheta_m} \approx \big\lceil N_{\mathrm{TZ}}\, \sin\big(\vartheta_m\big)\big\rceil$ for first-order probes, where $\lceil\cdot\rceil$ denotes the rounding operation to the next higher integer [Hansen 1988, p. 23 and p.129]. For higher-order probes, N_{ϑ_m} will be slightly larger in the order of $\big\lceil N_{\mathrm{TZ}}\, \sin\big(\vartheta_m\big) + N_{\mathrm{pro}}\big\rceil$, where N_{pro} is the largest non-zero mode order $|\mu'|$ for the direct probe contribution to the incident field. The reason for this can be found in the behavior of the Wigner-d-functions $\mathrm{d}^n_{\mu'\mu}\big(\vartheta_m\big)$, which tend toward [Hansen 1988, p. 346]

$$\mathrm{d}^n_{\mu'\mu}(0^\circ) = \delta_{\mu\mu'} \tag{8.51}$$

and

$$\mathrm{d}^n_{\mu'\mu}(180^\circ) = (-1)^{n+\mu}\, \delta_{-\mu,\mu'} \tag{8.52}$$

at $\vartheta_m = 0^\circ$ and $\vartheta_m = 180^\circ$. This means that while the echo contribution at $\vartheta = 90^\circ$ can be completely represented by the unphysical model (8.46) (at $\vartheta = 90^\circ$ we have $N_{\vartheta_m} \approx N_{\mathrm{TZ}}$ in (8.49)), only a small portion of the echo contribution can be represented at $\vartheta = 0^\circ$ by the model (8.46). Only the lowest order modes of the corresponding Fourier expansion (8.47) can be represented toward $\vartheta = 0^\circ$ and $\vartheta = 90^\circ$ (at $\vartheta = 0^\circ$ and $\vartheta = 90^\circ$ we have $N_{\vartheta_m} \approx N_{\mathrm{pro}}$).

This shows that the formulation (8.43) cannot reproduce all of the echo influences. This can be a desired effect because it means that some portions of the undesired echoes are removed automatically if AUT sources are reconstructed from the measurements without caring for echoes.

Recommendations for Antenna Mounting

While it is hard to predict which percentage of the echo is removed by the formulation (8.43) (this depends on the unknown AUT radiation pattern and the unknown characteristics of the echo), the insights from the previous discussion can be used to formulate specific recommendations for the measurement setup concerning the location and orientation in which the AUT should be mounted to the AUT rotation stage.

Concerning the AUT location, it is recommended that the AUT is moved as far away from the z-axis as possible. If the AUT is rotated by a full circle along the φ-coordinate, it is irrelevant if the translation is performed along the x- or the y-axis. The further the AUT is mounted away from the rotation center, a larger portion of the echo influences is mapped toward higher-order mode contributions which cannot be recreated by additional ghost sources. Furthermore, a larger portion of echo influences is mapped toward ghost sources, which are not compatible with a localized AUT model.

Concerning the AUT orientation, it is if course advisable to orient the AUT in such a way that it does not point directly into the direction of the echo, if possible. For example, if the echo object is located along the y-axis of the test zone coordinate system, aligning the AUT parallel to the z-axis ensures that the AUT does not point directly toward the echo (see Fig. 8.14). If the echo object is located along the x-axis, then the direction of the ϑ-rotation of the AUT positioner matters (assuming that only the range $0 \leq \vartheta \leq \pi$ is sampled). Dependent on the rotation direction, the AUT will point only in one of the half spaces with $x \leq 0$ or $x \geq 0$. If it cannot be avoided that the AUT eventually points into the direction of the echo, one should mount the AUT such that it points directly toward the echo when the AUT rotation stage is in the position $\vartheta = 0$, $\varphi = 0$. It may appear counter intuitive to mount the AUT such that it points toward the echo but (8.50) shows that the largest echo suppression capabilities are given for $\vartheta = 0$. Therefore, one should aim for a measurement setup in which the maximum of the echo influence is expected for polar angles around $\vartheta = 0$.

8.2.3. Numerical Investigations for the Reconstruction of Spherical Coefficients for the Antenna Under Test

In this section, numerical experiments are carried out to support the recommendations for antenna mounting. Ideally the AUT never points toward the echo. If the measurement setup cannot avoid that the AUT eventually points into the direction of the echo, it is beneficial if this undesired case happens for $\vartheta = \varphi = 0°$. The numerical experiments have been carried out at a symbolic frequency of 1 GHz, but due to the scale invariance of Maxwell's equations the results are generally valid for all frequencies and all dimensions are given in terms of wavelengths to reflect this fact.

The simulated measurement setup is depicted in Fig. 8.17 along with the directions of the unit vectors in the test zone coordinates (the origin lies in the AUT rotation center). The AUT is rotated through the test zone by the AUT rotation stage, which is indicated in the figure but was not part of the simulations. The incident field in the test zone is composed of the probe field plus an echo field from one of the five depicted echo locations. All echoes were located at $32\,\lambda$ distance from the AUT rotation stage. The echo locations 1 and 2 are on the x-axis, whereas the echo locations 3 and 4 are rotated 30° away from the x-axis toward the z-axis. The echo location 5 lies on the y-axis. The probe location is at $16\,\lambda$ away from the AUT rotation center. The AUT is translated away from the rotation center along the positive x-axis by a translation distance d which has been varied from 0 to $8\,\lambda$. The χ-rotation is assumed to be performed by the probe. This was accomplished by considering two Hertzian dipole probes along the positive y- and negative x-direction indicated by the two perpendicular arrows. The echo fields are simulated

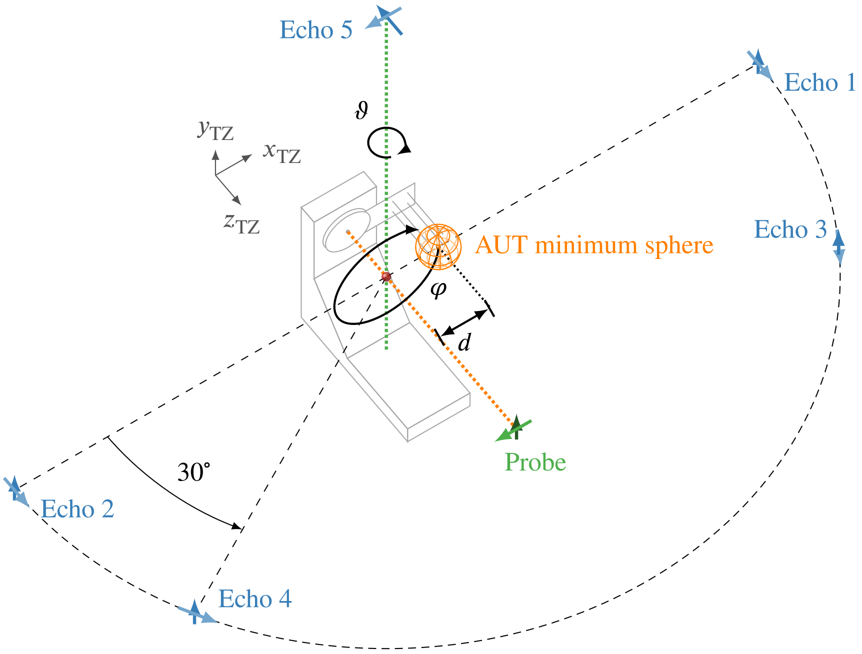

Fig. 8.17.: Simulated stationary probe scenario (not to scale). The incident field in the test zone is composed of the probe field plus an echo field from one of the five depicted echo locations.

by Hertzian dipoles as well, all with unit excitation. To simulate the varying echo influence dependent on the probe orientation χ, also two polarizations have been considered for the echoes, dependent on which of the two probe dipoles was active.

The same AUT with a $2\,\lambda$ minimum sphere as in Section 8.1.5 was considered. Two square shaped current sheets are placed in front of each other with a separation in z-direction of $0.25\,\lambda$. Every current sheet had the dimensions $2.822\,897\,\lambda \times 2.822\,897\,\lambda$ in the x-plane such that all AUT sources were confined in a minimum sphere of radius $r_{\mathrm{aut}} = 2.0\,\lambda$, respectively. Hertzian dipoles were regularly distributed on the current sheets with a separation of $0.1\,\lambda$ in x- and y-direction. The dipole excitation is constant along the y-direction, follows a half-wave of a sine curve along the x-direction, and has a phase shift according to $\mathrm{e}^{\mathrm{j}k_0 z}$ to form a main beam toward the positive z-direction, following the procedure described in [Schmidt 2011a].

For every scenario, two measurements were simulated, with the AUT in one of two orientations, pointing either in z-direction or toward the echo in the initial position at $\vartheta = \varphi = 0$. This means that for every translation distance d, a total of ten spherical measurements were obtained — in every measurement, only the echoes at one of the five locations were active, yielding five different echo scenarios and for each echo scenario two AUT orientations were considered.

The spherical measurements were obtained by rotating the AUT around ϑ and φ along the directions indicated in Fig. 8.17. The rotation along φ was performed in the range $0 \leq \varphi < 360°$ and a measurement sample was obtained every $\Delta\varphi = 2°$. The rotation along ϑ was performed in the range $0 \leq \vartheta \leq 180°$ and a measurement sample was obtained every $\Delta\vartheta = 2°$. This means that the AUT rotation stage did never point toward the echo locations 1, 3, and 5. Thus the AUT orientation along the z-direction should be beneficial for the scenarios involving these echoes, according to the recommendations from above.

In contrast to this, the AUT rotation stage does eventually point toward the echo positions 2 and 4 and if the AUT is mounted pointing in z-direction it will, thus, also eventually point toward the echo locations. In the echo scenarios 2 and 4 it is, therefore, recommended to mount the AUT with its orientation toward the probes, according to the discussion above.

Two sets of spherical wave coefficients are independently reconstructed from each echoic measurement: The spherical wave coefficients $\tilde{\beta}^{(1),\mathrm{TZ}}_{s\mu n}$ corresponding to a large spherical wave expansion in a coordinate system centered at the AUT rotation center (i.e., the center of the test zone) — these coefficients will hereafter be referred to as the *test zone field coefficients* — and the spherical wave coefficients $\tilde{\beta}^{(1),\mathrm{aut}}_{s\mu n}$ which correspond to a smaller spherical wave expansion centered at the center of the AUT minimum sphere[20] — these coefficients will be called *AUT field coefficients*. The tilde over the coefficients hints to the fact that both sets of retrieved coefficients are potentially distorted by the echo influences.

For the test zone field coefficients, mode orders with $n \leq N_{\mathrm{TZ}} = r_{\mathrm{TZ}}\, k_0 + n_{\mathrm{buf}}$ are considered, where r_1 is the radius of the test zone and $n_{\mathrm{buf}} = 2$ has been chosen in this simulation campaign. The test zone field coefficients correspond to a very large source region. They are intended to include the true AUT contributions as well as all possible ghost contributions. Furthermore, the deviation of the reconstructed test zone field coefficients from the ideal test zone field coefficients (i.e., the free-space AUT coefficients translated into a spherical wave expansion centered at the rotation center) can be regarded as a measure of the total distortion caused by the echoes in the complete spherical measurement.

For the AUT field coefficients, only mode orders with $n \leq N_{\mathrm{aut}} = r_{\mathrm{aut}}\, k_0 + n_{\mathrm{buf}}$ are considered, based on the radius r_{aut} of the minimum sphere around the AUT sources. The retrieved AUT field coefficients are an approximation to the free-space AUT coefficients. Notice that retrieving the AUT field coefficients is exactly equivalent to the MARS technique (e.g., [Gregson 2010b])[21].

In the following, the AUT reconstruction error will be quantified by the mean square deviation

$$\epsilon_{\mathrm{aut}} = \sqrt{\frac{\sum\limits_{s=1}^{2}\sum\limits_{n=1}^{\infty}\sum\limits_{\mu=-n}^{n}\left|\tilde{\beta}^{(1),\mathrm{aut}}_{s\mu n} - \beta^{(1),\mathrm{aut}\star}_{s\mu n}\right|^2}{\sum\limits_{s=1}^{2}\sum\limits_{n=1}^{\infty}\sum\limits_{\mu=-n}^{n}\left|\beta^{(1),\mathrm{aut}\star}_{s\mu n}\right|^2}} \tag{8.53}$$

of the reconstructed coefficients $\tilde{\beta}^{(1),\mathrm{aut}}_{s\mu n}$ from the true free-space coefficients $\beta^{(1),\mathrm{aut}\star}_{s\mu n}$. This is equivalent to the root mean square deviation

$$\epsilon_{\mathrm{aut}} = \sqrt{\frac{\oiint \left[\left|E_{\vartheta,\mathrm{aut}}(\vartheta,\varphi) - E_{\vartheta,\mathrm{ref}}(\vartheta,\varphi)\right|^2 + \left|E_{\varphi,\mathrm{aut}}(\vartheta,\varphi) - E_{\varphi,\mathrm{ref}}(\vartheta,\varphi)\right|^2\right] \mathrm{d}\hat{\boldsymbol{k}}}{\oiint \left[\left|E_{\vartheta,\mathrm{ref}}(\vartheta,\varphi)\right|^2 + \left|E_{\varphi,\mathrm{ref}}(\vartheta,\varphi)\right|^2\right] \mathrm{d}\hat{\boldsymbol{k}}}} \tag{8.54}$$

---

[20] In the actual implementation, the corresponding transmit coefficients $\tilde{\alpha}^{(4),\mathrm{TZ}}_{s\mu n}$ and $\tilde{\alpha}^{(4),\mathrm{aut}}_{s\mu n}$ were reconstructed, but it is clear that these relate to the receiving coefficients by a simple reciprocity relationship.

[21] The AUT field coefficients can as well be found from the test zone field coefficients by performing a translation between the coordinate origins and truncating the resulting mode expansion at N_{aut} (This is the reconstruction procedure of MARS). The equivalence between directly reconstructing the AUT field coefficients and taking the detour via the test zone field coefficients was discussed at length in Section 8.1.3.

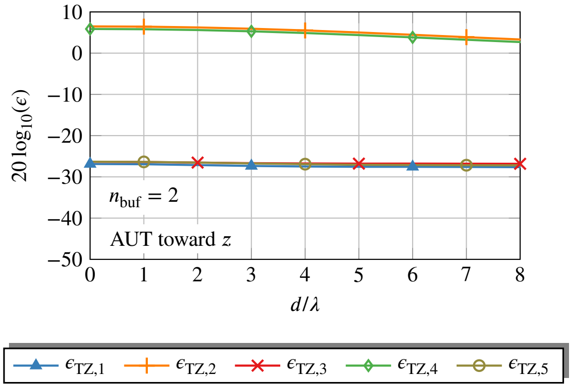

Fig. 8.18.: Reconstruction error for $\tilde{\beta}^{(1),\mathrm{TZ}}_{s\mu n}$ dependent on the AUT translation distance d with the AUT pointing toward the z-direction.

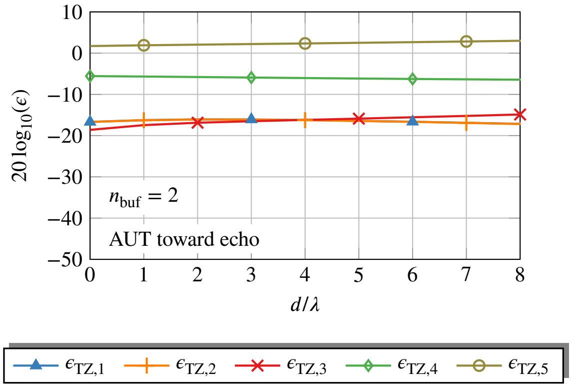

Fig. 8.19.: Reconstruction error for $\tilde{\beta}^{(1),\mathrm{TZ}}_{s\mu n}$ dependent on the AUT translation distance d with the AUT pointing toward the echo.

of the reconstructed FF pattern $\boldsymbol{E}_{\mathrm{FF,aut}}(\vartheta,\varphi)$ from the true AUT FF $\boldsymbol{E}_{\mathrm{FF,ref}}(\vartheta,\varphi)$. The reconstructed FF is obtained from the AUT transmission coefficients $\tilde{\alpha}^{(1),\mathrm{aut}}_{s\mu n} = 2\,(-1)^{\mu}\,\tilde{\beta}^{(1),\mathrm{aut}}_{s,-\mu,n}$, which are reciprocal to the receiving coefficients (see (4.27)).

Analogously, the error in the test zone field coefficients is quantified by the deviation

$$\epsilon_{\mathrm{TZ}} = \sqrt{\frac{\sum\limits_{s=1}^{2}\sum\limits_{n=1}^{\infty}\sum\limits_{\mu=-n}^{n}\left|\tilde{\beta}^{(1),\,\mathrm{TZ}}_{s\mu n} - \beta^{(1),\,\mathrm{TZ}\star}_{s\mu n}\right|^{2}}{\sum\limits_{s=1}^{2}\sum\limits_{n=1}^{\infty}\sum\limits_{\mu=-n}^{n}\left|\beta^{(1),\,\mathrm{TZ}\star}_{s\mu n}\right|^{2}}} \tag{8.55}$$

of the reconstructed coefficients $\tilde{\beta}^{(1),\,\mathrm{TZ}}_{s\mu n}$ from the true free-space coefficients $\beta^{(1),\,\mathrm{TZ}\star}_{s\mu n}$.

The resulting reconstruction errors for the test zone field coefficients in the different echo scenarios (denoted by $\epsilon_{\mathrm{TZ},1}$ to $\epsilon_{\mathrm{TZ},5}$) are shown in Fig. 8.18 for the AUT being mounted pointing into the z-direction (i.e., for $\vartheta = \varphi = 0°$, the AUT points in z-direction) and in Fig. 8.19 for the AUT being mounted pointing toward the echo (i.e., for $\vartheta = \varphi = 0°$, the AUT points toward the echo object). The reconstruction deviation of the test zone field coefficients $\tilde{\beta}^{(1),\mathrm{aut}}_{s\mu n}$ is dominated by the echo perturbation collected by the AUT traversing through the test zone. It can be seen that the total influence of the echo on the test zone field coefficients is approximately constant with respect to the translation distance d of the AUT (which should not be surprising given the approximately homogeneous echo field in the test zone and thus the same echo influences are collected by the AUT). The scenarios 1, 3, and 5 with the AUT mounted in z-direction show the lowest reconstruction error for the test zone coefficients. These are the scenarios, where the AUT never points directly toward the echo and thereby collects the least amount of echo signals. In all other scenarios, the AUT is eventually oriented directly toward the echo for some positions of the AUT rotation stage. The total echo influence in the scenarios 2 and 4 is smaller when the AUT was initially pointing directly into the echo direction (Fig. 8.19) than for the corresponding

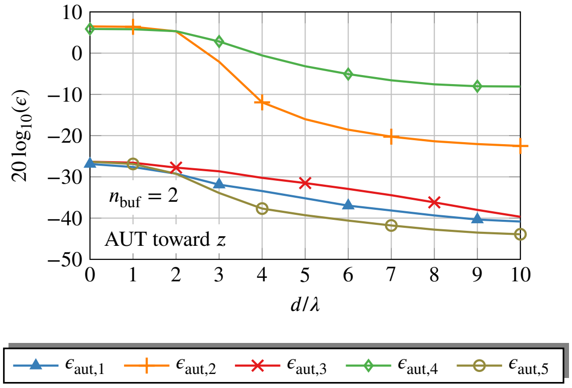

Fig. 8.20.: Reconstruction error for $\tilde{\beta}_{s\mu n}^{(1),\mathrm{aut}}$ dependent on the AUT translation distance d with the AUT pointing toward the z-direction.

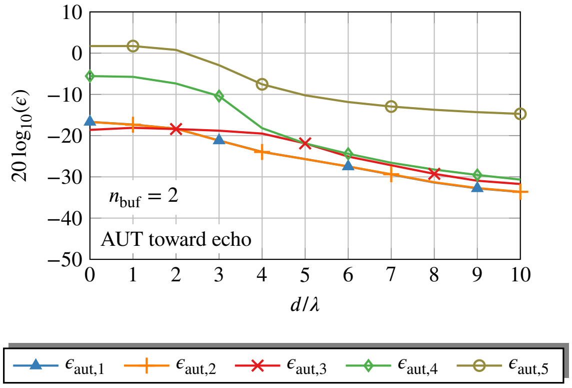

Fig. 8.21.: Reconstruction error for $\tilde{\beta}_{s\mu n}^{(1),\mathrm{aut}}$ dependent on the AUT translation distance d with the AUT pointing toward the echo.

scenario when the AUT was initially pointing in z-direction (Fig. 8.18), showing the importance of orienting the AUT optimally. If it cannot be avoided that the AUT eventually points to the echo during the measurement, it is beneficial to let this happen for $\vartheta = \varphi = 0°$.

The reconstruction error for the AUT field coefficients is shown in Fig. 8.20 for the AUT being mounted pointing in z-direction and in Fig. 8.21 for the AUT being mounted pointing toward the echo. In contrast to the test zone field coefficients, the AUT coefficients are more accurately reconstructed the further the AUT is translated from the rotation center. This implies that the equivalent sources which correspond to the additional ghost coefficients $\beta_{s\mu n}^{\mathrm{gho}}$ move away from the location of the true AUT sources the further the AUT is dislocated from the rotation center. With increasing separation between the ghost sources and the true AUT sources, the portion of the ghost sources which is mapped onto the real AUT sources decreases. This effect has been investigated in detail in Section 8.1.3.

In the scenarios 1, 3, and 5, the AUT does never point toward the echo when it is originally oriented toward the z-axis (Fig. 8.20). Naturally, this way of mounting the AUT is preferred over orienting it toward the echoes (Fig. 8.21), because less echo influences are overall collected while traversing the test zone if the AUT does never point toward the echo. In the scenarios 2 and 4, it cannot be avoided that the AUT eventually points toward the echo. As predicted, it is beneficial to mount the AUT pointing toward the echo in these cases.

The results support the recommendations for antenna mounting. The reconstruction errors are at a minimum for those measurement scenarios, where the AUT does never point directly into the echo direction (scenarios 1,3, and 5 in Figs. 8.18 and 8.20). If it cannot be avoided that the AUT points eventually into the direction of the echo, it is beneficial to let this happen at the measurement angle $\vartheta = 0$ (The error curves in Figs. 8.19 and 8.21 for scenarios 2 and 4, where the AUT points toward the echo in the measurement position $\vartheta = 0$ are below the corresponding error curves in Figs. 8.18 and 8.20, where the AUT points toward the echo for some other ϑ-angle). Mounting the AUT further away from the rotation center leads to less echo contributions being mapped to the reconstructed AUT coefficients.

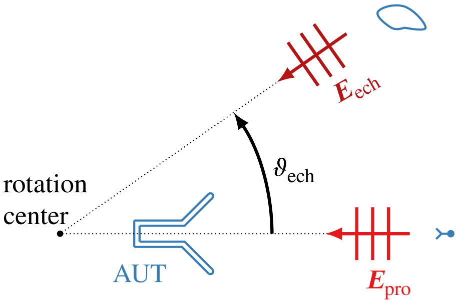

Fig. 8.22.: Incident field on the AUT consisting of two plane waves from the probe and echo direction, respectively. The total received signal is the sum of the received signals from each plane wave.

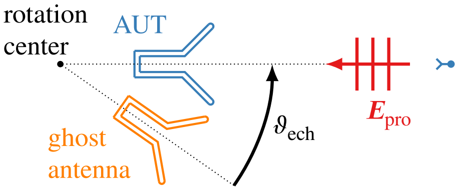

Fig. 8.23.: Equivalent model with incident field being a single plane wave from the probe direction. The total received signal is the sum of the signals from the true AUT and the ghost antenna.

8.2.4. Spatial Distribution of the Ghost Sources

Is it possible to find a suitable source region for the equivalent currents corresponding to the additional ghost coefficients $\beta_{s\mu n}^{\text{gho}}$? Identifying the source region for the additional sources could be beneficial for two reasons. First of all, knowledge about the spatial distribution of the equivalent sources can lead to valuable insights about the echo scenario. Second, echo suppression can be more effective in some cases, if equivalent sources for the echo are considered simultaneously with the AUT sources in the source reconstruction process, as was shown in section 8.1. In this section it is argued that a suitable source region for the additional ghost sources corresponding to $\beta_{s\mu n}^{\text{gho}}$ is a certain torus-shaped region. Two arguments are made to support this statement. First, a heuristic explanation is given why the equivalent sources may be found in a torus shaped region. Thereafter, numerical experiments show that the reconstructed fields by the equivalent sources in the torus together with the AUT currents are the same fields as the reconstructed fields from sources which are located on a large sphere enclosing the complete test zone (and also the same fields as the reconstructed fields using a spherical wave expansion for the complete test zone).

Heuristic Argument about the Location of the Additional Ghost Sources

To build an intuition about why a torus-shaped region is a good candidate for a possible spatial support for the additional ghost sources, consider the following situation. Both, the probe antenna and the echo object, are located in FF distance from the AUT such that the incident field can be regarded as a superposition of two plane waves from different directions spanning the angle ϑ_{ech} as depicted in Fig. 8.22 (the same argument would apply as long as the echo fields can be regarded as a scaled and rotated version of the probe fields in the complete test zone region). The aim is to find an equivalent scenario without the echo portion of the incident field (i.e., only the unperturbed probe field is incident on the AUT). In the equivalent scenario, the echo influence is accounted for by adding the received signal of an additional ghost antenna to the received signal of the AUT. To correctly account for the echo influence in the measured S_{12}-parameter in the equivalent scenario, the ghost antenna must be a (scaled and) rotated version of the true AUT. This scenario is depicted in Fig. 8.23. Knowing the echo rotation angle ϑ_{ech}, one can rotate the

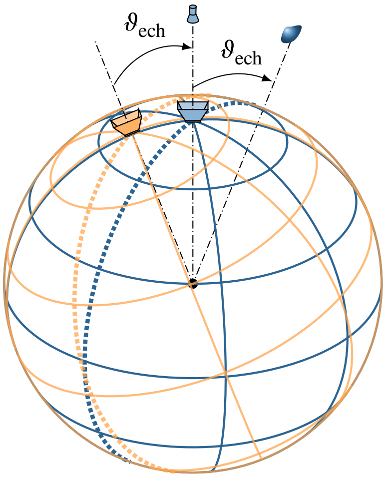

Fig. 8.24.: When the true AUT moves along the surface of the test zone (blue coordinate system), the ghost antenna performs the corresponding movement in the rotated (orange) coordinate system.

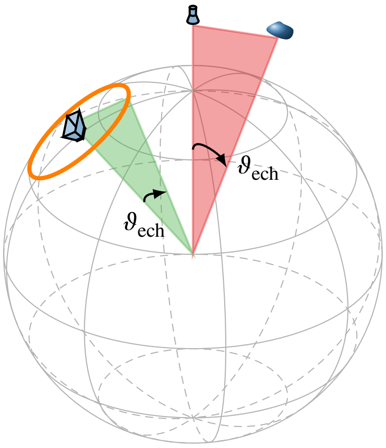

Fig. 8.25.: The spherical surface denotes the surface of the test zone. The probe and the echo object remain at their respective position. The circle around the AUT clarifies possible locations of the center of the ghost antenna for the given AUT position.

ghost antenna into the appropriate position for any AUT position.

When the AUT moves to different positions on the surface of the test zone sphere, the ghost antenna must appear at different positions relative to the AUT to ensure that the relative position between the ghost antenna and the incident probe field remains equal to the relative position between the true AUT and the incident echo field in the original scenario. In fact, for every movement of the AUT, the ghost antenna has to perform a corresponding movement in a rotated coordinate system as depicted in Fig. 8.24. The angle between corresponding points in the blue and orange coordinate systems in Fig. 8.24 is always ϑ_{ech}.

This means that for all AUT positions, the ghost antenna can be found somewhere on a well defined circle around the AUT, such that it spans the angle ϑ_{ech} to the AUT (measured from the AUT rotation center), ensuring that the S_{12}-parameter of the equivalent scenario is the same as in the original scenario. The constellation is depicted in Fig. 8.25 for an AUT which is mounted outside the rotation center and rotates through the test zone. The gray sphere in Fig. 8.25 denotes the surface of the test zone, which may be traversed by the AUT (the AUT does not always traverse the complete test zone surface in a complete spherical measurement, dependent on the mounting of the AUT). The orange circle on the surface of the sphere denotes the possible center locations for the ghost antenna. No matter, where the AUT is rotated on the gray sphere, the ghost antenna is found on the indicated circle (which moves along with the AUT).

It is plausible that the combined influence of all ghost antennas for the different AUT positions can be represented by some current distribution performing a weighted mean of the corresponding ghost antennas. This leads to the conclusion that the suitable region for the ghost sources is a torus around the orange circle in Fig. 8.25 (the orange circle in Fig. 8.25 denotes the major radius of the torus). Since the ghost AUT in this scenario consists of a rotated version of the true AUT, the minor radius of the torus must be large enough to fit around the complete AUT, thus, the

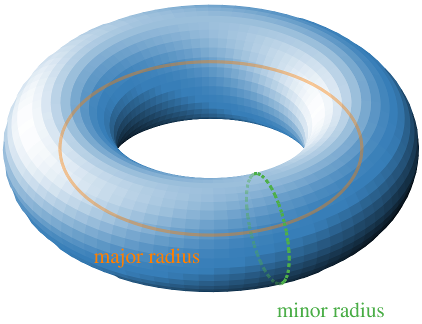

Fig. 8.26.: A torus with indicated major radius as the distance between the center of mass and the central ring of the torus and the minor radius as the “thickness of the tube”.

minor radius is equal to the radius of the minimum sphere around the AUT. See Fig. 8.26 for a clarification of the terms *major radius* and *minor radius*.

All points on the major radius of the torus must enclose the fixed angle ϑ_{ech} with the rotation center and the AUT center. Therefore, the major radius of the torus is larger, the further the AUT is mounted outside the rotation center. As a consequence, the separation between the actual AUT sources and the unphysical ghost contributions is increased for an AUT which is placed further away from the rotation center. If the antenna is placed exactly in the rotation center, the locations of the AUT sources and the unphysical ghost sources coincide. For small translation distances, the torus will still intersect the AUT region, but if the AUT translation becomes large enough, the ghost torus is well separated from the AUT sources.

This argument for the locations of the ghost sources is based on assumption that the incident echo field can be approximately regarded as as scaled and rotated version of the incident probe fields. For more complicated echo scenarios, one must consider a torus with a larger minor and major radius because the ghost sources must be distributed over a larger region, dependent on the minimal and maximal angular ϑ-separation between the echo and the probe, and consequently the source region for the ghost sources gets “smeared” in a larger region.

Certainly, the presented argument for the location of the ghost sources is not very rigorous. The argument itself cannot be used to convincingly prove that sources can be found in the described toroidal region which are equivalent to the ghost coefficients of the spherical wave expansion.

Numerical Investigations for the Reconstruction of Surface Currents for the Antenna Under Test

Numerical simulations have been performed in order to support the suspicion that one can find the ghost sources from Section 8.2.3 in a toroidal source region. The same simulated data as in Section 8.2.3 has been used in this section, but the reconstruction of the AUT fields is carried out with equivalent surface current based methods instead of spherical wave expansions. Equivalent currents were reconstructed on three different Huygens surfaces from the simulated S_{12}-values with the AUT at the translation distances $d = 4\,\lambda$, $d = 8\,\lambda$, and $d = 10\lambda$ (see Fig. 8.17). The three different Huygens surfaces are

- a spherical surface S_{aut} with radius $r_{\mathrm{aut}} = 2\,\lambda$ centered at the AUT center for each AUT

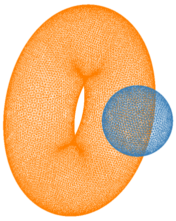

(a) $\vartheta_{\mathrm{ech}} = 90°$

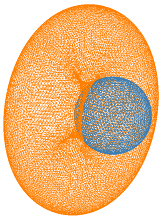

(b) $\vartheta_{\mathrm{ech}} = 60°$

Fig. 8.27.: Huygens surface for the AUT (blue) and ghost (orange) sources for the translation distance 4 λ.

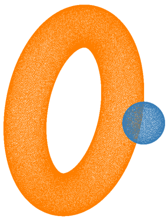

(a) $\vartheta_{\mathrm{ech}} = 90°$

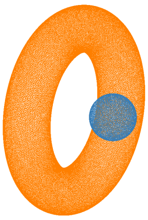

(b) $\vartheta_{\mathrm{ech}} = 60°$

Fig. 8.28.: Huygens surface for the AUT (blue) and ghost (orange) sources for the translation distance 8 λ.

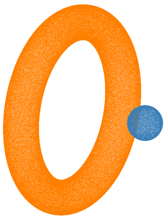

(a) $\vartheta_{\mathrm{ech}} = 90°$

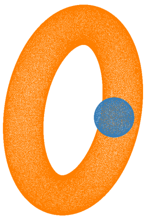

(b) $\vartheta_{\mathrm{ech}} = 60°$

Fig. 8.29.: Huygens surface for the AUT (blue) and ghost (orange) sources for the translation distance 10 λ.

translation distance, respectively. The reconstructed FFs from this reconstruction surface are indicated by an index “A”.

- a composed surface $S_{\mathrm{com}} = S_{\mathrm{aut}} \cup S_{\mathrm{gho}}$ consisting of the combination of two parts — the AUT surface S_{aut} and a toroidal surface S_{gho} with its major radius spanning an angle of either 90° or 60° to the AUT (as seen from the center of the test zone, i.e., the rotation center of the AUT) to account for the echoes coming from different directions. The reconstructed FFs obtained by only considering the reconstructed currents on the AUT surface from this two-part surface (the reconstructed currents on the torus are neglected for the FF calculation) are indicated by an index “B” in the following. The complete FFs obtained from the currents on both reconstruction surfaces are denoted by an index “C”.

- a spherical surface S_{TZ} with radius $r_{\mathrm{TZ}} = 12\,\lambda$ centered at the AUT rotation center (i.e., the stationary center of the test zone). The FFs are obtained from this large spherical surface and are denoted by the index “D”.

The aim is to show that the reconstructed fields from case “C” are practically the same as the reconstructed fields from case “D”. The fields from case “D” should be equivalent to the fields from the spherical test zone coefficients $\tilde{\beta}_{s\mu n}^{(1),\,\mathrm{TZ}}$. The results obtained in the case “A” are expected to be very similar to the results from the spherical-mode based reconstruction and the results of case “B” are used to investigate if the explicit consideration of the ghost sources brings any advantages for the source reconstruction.

The meshed surfaces for the AUT and the ghost sources (serving as reconstruction surface for the FFs $\boldsymbol{E}_{\mathrm{FF,B}}$ and $\boldsymbol{E}_{\mathrm{FF,C}}$) are depicted in Figs. 8.27 to 8.29 for the AUT translation distances

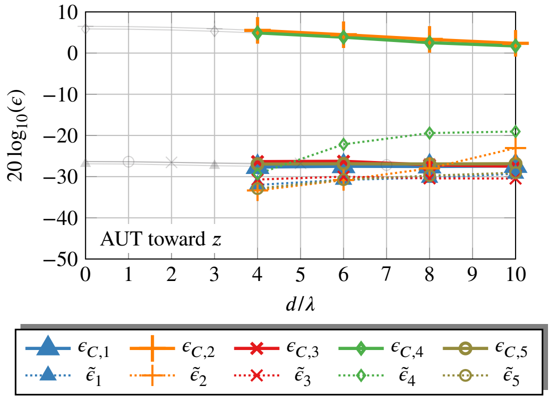

Fig. 8.30.: Error $\boldsymbol{E}_{\mathrm{FF,C}} - \boldsymbol{E}_{\mathrm{FF,ref}}$ with the AUT pointing into z-direction. Dashed lines denote the deviation $\boldsymbol{E}_{\mathrm{FF,C}} - \boldsymbol{E}_{\mathrm{FF,D}}$. Background lines are from Fig. 8.18 for comparison.

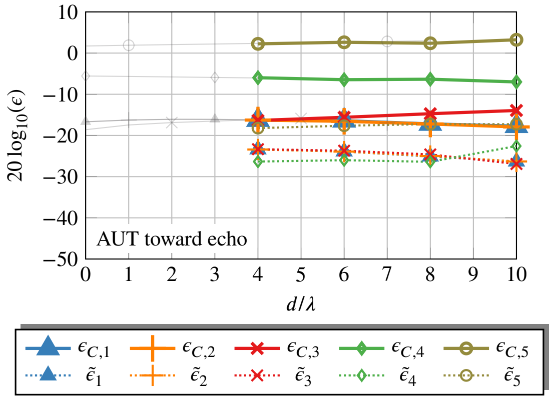

Fig. 8.31.: Error $\boldsymbol{E}_{\mathrm{FF,C}} - \boldsymbol{E}_{\mathrm{FF,ref}}$ with the AUT pointing toward the echo. Dashed lines denote the deviation $\boldsymbol{E}_{\mathrm{FF,C}} - \boldsymbol{E}_{\mathrm{FF,D}}$. Background lines are from Fig. 8.19 for comparison.

$d = 4\,\lambda$, $d = 8\,\lambda$, and $d = 10\lambda$, respectively. Each AUT sphere has the radius $r_{\mathrm{aut}} = 2\,\lambda$ which is also the minor radius of the torus. It can be clearly seen how a larger AUT translation distance d leads to a larger separation between the AUT and the ghost torus.

The solid lines in Fig. 8.30 show the root mean square error $\epsilon_{C,1}$ (i.e., the deviation from the ideal free-space AUT fields, see (8.54)) of the retrieved FFs from reconstructed surface currents on $S_{\mathrm{com}} = S_{\mathrm{aut}} \cup S_{\mathrm{gho}}$ (index "C") for the different echo scenarios with the AUT mounted to initially point in z-direction. The faint lines in the background show the corresponding error curves of the spherical test zone coefficients $\tilde{\beta}_{s\mu n}^{(1),\,\mathrm{TZ}}$ from Fig. 8.18, where a spherical expansion with a large minimum sphere was used. The error curves for the equivalent current based reconstruction of the case "C" show a good agreement with the results for the test zone field coefficients $\tilde{\beta}_{s\mu n}^{(1),\,\mathrm{TZ}}$ obtained in the spherical expansion. The error curves are shown in Fig. 8.31 for the same configurations but the AUT mounted toward the echoes. Again, the curves show a good agreement with the results obtained from the spherical expansion. This indicates that the reconstructed currents on the ghost and AUT surfaces (case "C") generate the same fields as the reconstructed spherical test zone coefficients $\beta_{s\mu n}^{\mathrm{gho}}$ because the error curves are the same for both cases (compare the solid lines in Figs. 8.30 and 8.31 to their respective counterparts in Figs. 8.18 and 8.19, which are also shown as gray lines in the background.)

The dotted lines show the root mean square deviation $\tilde{\epsilon}_k$ between the retrieved FFs from the reconstructed surface currents on the surface S_{com} (case "C") and the retrieved FFs from the reconstructed surface currents on the large surface S_{TZ} (case "D") for the kth echo position. The deviation between the reconstructed fields from case "C" and case "D" is well below their individual deviations from the actual reference[22]. These results show, that practically the same fields are generated by the reconstructed currents on the large sphere (case "D") and the

---

[22] The root mean square error curves for case "D" are, thus, not depicted because the curves are not visibly distinguishable from the already plotted lines for the case "C".

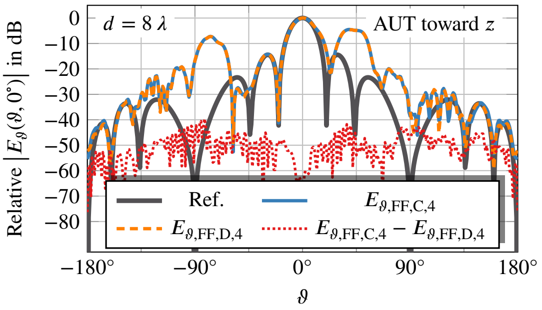

Fig. 8.32.: Co-polar pattern of $\boldsymbol{E}_{\mathrm{FF,C}}$ and $\boldsymbol{E}_{\mathrm{FF,D}}$ in the $\varphi = 0°$-cut for the echo in position 4. The AUT was 8 λ away from the z-axis and mounted toward the z-direction.

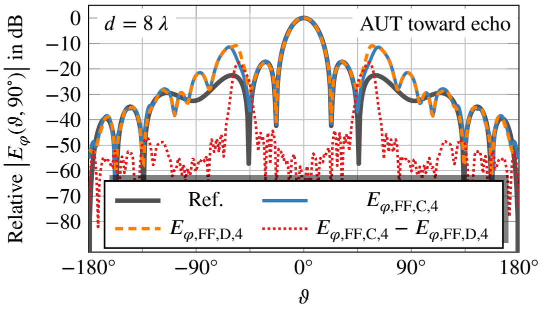

Fig. 8.33.: Co-polar pattern of $\boldsymbol{E}_{\mathrm{FF,C}}$ and $\boldsymbol{E}_{\mathrm{FF,D}}$ in the $\varphi = 90°$-cut for the echo in position 4. The AUT was 8 λ away from the z-axis and mounted toward the echo direction.

reconstructed currents on the torus and the AUT surface (case “C”)[23].

The error curves alone are not well suited to support the statement that the fields generated by the reconstructed currents on the torus and the AUT surface (case “C”) are the same as the fields generated by the reconstructed currents on a Huygens surface enclosing the complete test zone (case “D”). To further supplement the idea that the ghost sources are located in the torus, Fig. 8.32 shows the $\varphi = 0°$-cut of the co-polar component of the reconstructed FF from either the sources on the combined surface S_{com} (index “C”), or the sources on the large spherical surface S_{TZ} (index “D”) for the exemplary case of the echo scenario 4 with the AUT translated 8 λ away from the rotation center and mounted toward the z-axis[24]. The gray curve in the background denotes the ideal free-space AUT fields for comparison. The corresponding $\varphi = 90°$-cuts are shown in Fig. 8.33. Apart from a small angular region around $\vartheta = \pm 60°$ in Fig. 8.33, a very good agreement[25] is found between the reconstructed fields from the equivalent surface currents on the torus together with the sources on the AUT (index “C”) and the sources on a large spherical surface (index “D”). The depicted FFs correspond to the (worst case) scenario 4, where according to Fig. 8.30 the largest deviations occur between the fields of case “C” and the fields of case “D” (compare the dotted lines in Fig. 8.30). The agreement between the reconstructed fields of case “C” and the reconstructed fields of case “D” is even better in the other scenarios. The fields generated by the surface currents on the large spherical surface (case “D”) are very similar to the corresponding fields from the reconstructed test zone field coefficients $\tilde{\beta}_{s\mu n}^{(1),\,\mathrm{TZ}}$ (maximum FF deviation $< -40\,\mathrm{dB}$ for all cases, but the spherical coefficients $\tilde{\beta}_{s\mu n}^{(1),\,\mathrm{TZ}}$ were only reconstructed up to a maximum AUT translation distance of $d = 8\,\lambda$), thus, the comparison to the spherical expansion is not shown here to avoid unnecessary repetition. The results support the suspicion

---

[23] A possible explanation for the larger deviation for the echo positions 2 and 4 in Fig. 8.18 is that the echo fields are not exactly a rotated version of the probe fields in the test zone and therefore the argument about the torus shaped ghost source region is not exactly accurate. These unideal influences are more prominent in cases 2 and 4, where the echo distortions are strongest.

[24] The situation is very similar for all other cases.

[25] The echo fields are not exactly a rotated version of the probe fields in the test zone. The argument about the torus shaped ghost source region is not exactly accurate. This may explain the deviations in the small angular region around $\vartheta = \pm 60°$ in Fig. 8.33.

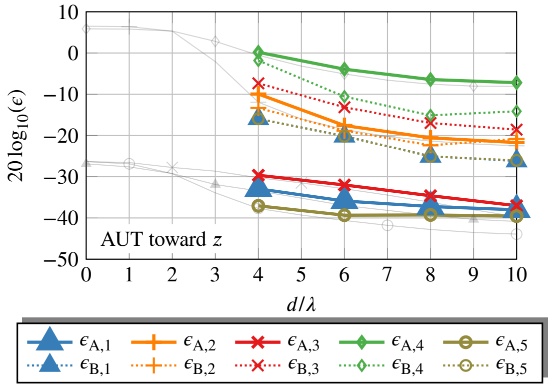

Fig. 8.34.: Error $\boldsymbol{E}_{\mathrm{FF,A/B}} - \boldsymbol{E}_{\mathrm{FF,ref}}$ with the AUT pointing toward the echo. Background lines are from Fig. 8.20 for comparison.

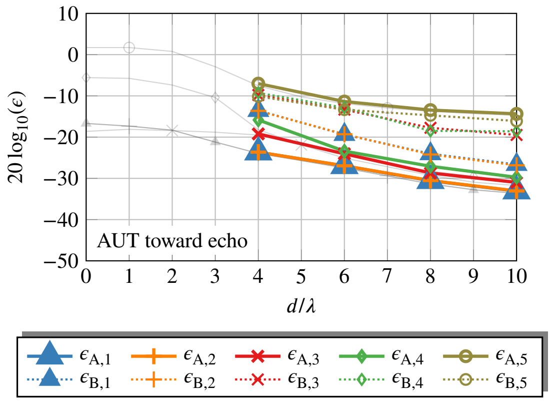

Fig. 8.35.: Error $\boldsymbol{E}_{\mathrm{FF,A/B}} - \boldsymbol{E}_{\mathrm{FF,ref}}$ with the AUT pointing toward the echo. Background lines are from Fig. 8.21 for comparison.

that all ghost fields do in fact correspond to fields generated in the proposed torus.

Can this knowledge about the location of the ghost sources be utilized to separate them better from the desired AUT contributions as was the case for a static AUT? This question can be answered by neglecting the reconstructed sources on the torus for the FF calculation (case “B”) and comparing the results to the case, where no torus shaped ghost source region is considered for the reconstruction (case “A”). The root mean square errors of the relevant reconstruction scenarios are found in Fig. 8.34 for the echoic measurement scenarios with the AUT mounted in z-direction and in Fig. 8.35 for the AUT mounted toward the echo. The solid lines denote the errors in the reconstructed FFs when currents are only reconstructed on the AUT surface (case “A”). These lines are again in good agreement with the lines from Figs. 8.20 and 8.21, which are shown faintly in the background, indicating that the surface current based methods perform similar to the spherical wave based methods, if no additional sources for the echo are considered. The dotted lines denote the error corresponding to the retrieved FFs from the currents on the AUT surface, where for the reconstruction also currents on the torus were assumed (index “B”, the currents on the torus were discarded for the FF calculation). Some scenarios benefit from modeling the ghost sources simultaneously with the AUT sources (the dotted lines are below the corresponding solid lines), but a beneficial behavior cannot be claimed in general. For many scenarios the achieved mean square error is lower for case “A”, where only AUT sources have been modeled without the ghost sources. Apparently, the mutual coupling effects between the AUT sphere and the torus which have been described qualitatively in Section 8.1 cannot be avoided in the reconstruction case “B”, even for large separation distances d of the AUT. The problem is that even though the absolute separation between the AUT and the torus increases, also the size of the torus increases with the same rate. The AUT radiation into the direction of the torus cannot be reconstructed with certainty, as the radiated field portions into this direction cannot unambiguously be assigned to either source region.

8.3. Directive Probes and Virtual Probe Arrays

Getting rid of the echo influence in measurement scenarios with a static probe is particularly challenging. Perfectly removing the echoes in post-processing is often not possible even if the locations of the equivalent sources accounting for the distortion are known. Therefore, the goal must be to obtain measurement samples, which have as little echo contamination as possible. A simple, yet effective method to avoid the negative influence of echoes in stationary probe as well as in stationary AUT measurement scenarios is to use directive probes. If the probe does not illuminate the echoes in the first place, no echo currents are induced and the incident fields on the AUT are the same as in a completely anechoic environment. More precisely, according to (6.5), the S_{21}-parameter between the radiating AUT (antenna 1) and the receiving probe (antenna 2) can be expressed by

$$\begin{aligned} S_{21} = \oiint\limits_{S_2} \oiint\limits_{S_1} \Big[& \hat{\boldsymbol{J}}_2(\boldsymbol{r}) \cdot \boldsymbol{\mathcal{G}}^{-}_{JE}(\boldsymbol{r},\boldsymbol{r}') \cdot \hat{\boldsymbol{J}}_{\tilde{1}}(\boldsymbol{r}') + \hat{\boldsymbol{J}}_2(\boldsymbol{r}) \cdot \boldsymbol{\mathcal{G}}^{-}_{ME}(\boldsymbol{r},\boldsymbol{r}') \cdot \hat{\boldsymbol{M}}_{\tilde{1}}(\boldsymbol{r}') \\ & - \hat{\boldsymbol{M}}_2(\boldsymbol{r}) \cdot \boldsymbol{\mathcal{G}}^{-}_{JH}(\boldsymbol{r},\boldsymbol{r}') \cdot \hat{\boldsymbol{J}}_{\tilde{1}}(\boldsymbol{r}') - \hat{\boldsymbol{M}}_2(\boldsymbol{r}) \cdot \boldsymbol{\mathcal{G}}^{-}_{MH}(\boldsymbol{r},\boldsymbol{r}') \cdot \hat{\boldsymbol{M}}_{\tilde{1}}(\boldsymbol{r}') \Big] \, \mathrm{d}a' \, \mathrm{d}a \\ + \oiint\limits_{S_2} \oiint\limits_{S_\mathrm{ech}} \Big[& \hat{\boldsymbol{J}}_2(\boldsymbol{r}) \cdot \boldsymbol{\mathcal{G}}^{-}_{JE}(\boldsymbol{r},\boldsymbol{r}') \cdot \hat{\boldsymbol{J}}_{\mathrm{ech},1}(\boldsymbol{r}') + \hat{\boldsymbol{J}}_2(\boldsymbol{r}) \cdot \boldsymbol{\mathcal{G}}^{-}_{ME}(\boldsymbol{r},\boldsymbol{r}') \cdot \hat{\boldsymbol{M}}_{\mathrm{ech},1}(\boldsymbol{r}') \\ & - \hat{\boldsymbol{M}}_2(\boldsymbol{r}) \cdot \boldsymbol{\mathcal{G}}^{-}_{JH}(\boldsymbol{r},\boldsymbol{r}') \cdot \hat{\boldsymbol{J}}_{\mathrm{ech},1}(\boldsymbol{r}') - \hat{\boldsymbol{M}}_2(\boldsymbol{r}) \cdot \boldsymbol{\mathcal{G}}^{-}_{MH}(\boldsymbol{r},\boldsymbol{r}') \cdot \hat{\boldsymbol{M}}_{\mathrm{ech},1}(\boldsymbol{r}') \Big] \, \mathrm{d}a' \, \mathrm{d}a \,, \end{aligned} \tag{8.56}$$

where $\hat{\boldsymbol{J}}_2$, $\hat{\boldsymbol{M}}_2$ are the normalized equivalent probe currents, $\hat{\boldsymbol{J}}_{\mathrm{ech},1}$, $\hat{\boldsymbol{M}}_{\mathrm{ech},1}$ are the scattering currents induced on the echo object due to the AUT fields and $\hat{\boldsymbol{J}}_{\tilde{1}}$, $\hat{\boldsymbol{M}}_{\tilde{1}}$ are the equivalent currents on the AUT, which contain the distortions from multiple interactions between the AUT and the probe but distortions due to multiple interactions between the AUT and the echo object are neglected for the moment. With the identity (compare (3.10) to (3.11))

$$\boldsymbol{\mathcal{G}}^{-}_{JH}(\boldsymbol{r},\boldsymbol{r}') = -\boldsymbol{\mathcal{G}}^{-}_{ME}(\boldsymbol{r},\boldsymbol{r}') \tag{8.57}$$

for the dyadic Green's functions and by observing that the normalized probe fields are found by

$$\hat{\boldsymbol{E}}_2(\boldsymbol{r}') = \oiint\limits_{S_2} \Big[\hat{\boldsymbol{J}}_2(\boldsymbol{r}) \cdot \boldsymbol{\mathcal{G}}^{-}_{JE}(\boldsymbol{r},\boldsymbol{r}') + \hat{\boldsymbol{M}}_2(\boldsymbol{r}) \cdot \boldsymbol{\mathcal{G}}^{-}_{ME}(\boldsymbol{r},\boldsymbol{r}') \Big] \, \mathrm{d}a \tag{8.58}$$

and

$$\hat{\boldsymbol{H}}_2(\boldsymbol{r}') = \oiint\limits_{S_2} \Big[\hat{\boldsymbol{J}}_2(\boldsymbol{r}) \cdot \boldsymbol{\mathcal{G}}^{-}_{JH}(\boldsymbol{r},\boldsymbol{r}') + \hat{\boldsymbol{M}}_2(\boldsymbol{r}) \cdot \boldsymbol{\mathcal{G}}^{-}_{MH}(\boldsymbol{r},\boldsymbol{r}') \Big] \, \mathrm{d}a \tag{8.59}$$

one finds for the S_{21}-parameter

$$\begin{aligned} S_{21} = & \oiint\limits_{S_1} \Big[\hat{\boldsymbol{E}}_2(\boldsymbol{r}') \cdot \hat{\boldsymbol{J}}_{\tilde{1}}(\boldsymbol{r}') - \hat{\boldsymbol{H}}_2(\boldsymbol{r}') \cdot \hat{\boldsymbol{M}}_{\tilde{1}}(\boldsymbol{r}') \Big] \, \mathrm{d}a' \\ & + \oiint\limits_{S_1} \Big[\hat{\boldsymbol{E}}_2(\boldsymbol{r}') \cdot \hat{\boldsymbol{J}}_{\mathrm{ech},1}(\boldsymbol{r}') - \hat{\boldsymbol{H}}_2(\boldsymbol{r}') \cdot \hat{\boldsymbol{M}}_{\mathrm{ech},1}(\boldsymbol{r}') \Big] \, \mathrm{d}a' \,, \end{aligned} \tag{8.60}$$

i.e., the S_{21}-parameter is obtained by weighting the equivalent AUT and echo currents by the incident probe fields and adding both contributions. The magnitude of the probe fields at the location of the corresponding equivalent currents can be interpreted as the probe sensitivity of the corresponding currents [Jin 2015, p. 103]. If the probe fields have a much lower magnitude at the echo location than the AUT location, the measured S_{21}-parameter is much more sensitive for the AUT currents than for the echo currents. Due to antenna reciprocity, it is irrelevant whether the probe antenna was radiating or receiving in the actual measurement. The echo distortions do not influence the S_{21}-parameter measurement (or the S_{12}-parameter measurement) if the probe does not illuminate the echo, thus, directive probes are desired to suppress the echo influences.

However, (highly) directive probes bring certain disadvantages with them. In order to shape the directive beam, they are electrically large and thus prone to multiple interactions with the AUT. These drawbacks can be mitigated to some extend if virtual probe arrays [Yinusa 2014; Dohler 2002; Dohler 2004; Dohler 2009] are used. The received signal of a probe array consisting of several antenna elements can be synthesized by a coherent linear combination of measured samples from different probe positions. In this way the beneficial effects of a highly directive probe can be achieved also with probes of smaller size. In particular if the individual probe positions used to form the virtual array vary their distance to the AUT, one can increase the directivity toward the AUT while simultaneously decreasing the influence of multiple interactions. Simply speaking, the reason for this can be found in the fact that the path length of the first-order scattered field (i.e., the field distortion caused by a scatterer at the receiving antenna, which is again scattered at the transmitting antenna) is three times the path length of the direct LOS contribution. Thus the phase of the direct LOS signal varies approximately by $\mathrm{e}^{-\mathrm{j}k_0 r}$ with the distance r between the AUT and the probe while the the phase of the nth order multiple scattering (i.e., the signal contribution which is characterized by bouncing n times back and forth between the AUT and the probe) varies approximately by $\mathrm{e}^{-\mathrm{j}(1+2n)k_0 r}$. Consequently, multiple scattering leads to variations in the measurement signal dependent on the distance between the AUT and the probe with a period of $\lambda/(2n)$ [Hansen 1988, p.208]. While the coherent sum of the measurement signal with the correct phase leads to constructive interference of the desired LOS contribution, the contribution from multiple scattering is mitigated by destructive interference.

The principle of virtual array measurements is explained for a specific measurement example in the following.

8.3.1. Measurement with a Virtual Array

To investigate the effectiveness of synthesizing virtual probe arrays for echo suppression, measurements have been obtained in the anechoic antenna measurement chamber of the Chair of High-Frequency Engineering at TUM. Preliminary results from this measurement set have been presented at conferences [Knapp 2016; Knapp 2017c]. Spherical measurements have been conducted with a dual-ridged horn DRH400 as an AUT and a dual-ridged horn DRH18 as a probe at 2.5 GHz. An echo influence was created by putting a metal plate into the chamber. The size of the plate was 80 cm × 55 cm with about 5 mm thickness. The plate was mounted on a tripod and placed into the chamber with an approximate distance between the plate center to the probe center of 1.20 m in x-direction, 1.88 m in y-direction and 0.04 m in z-direction.

The AUT was rotated and the S_{12}-parameter was sampled every 1.5° in ϑ- and φ-direction with two orthogonal probe polarizations, yielding a total of $241 \cdot 121 \cdot 2 = 58\,322$ measurement

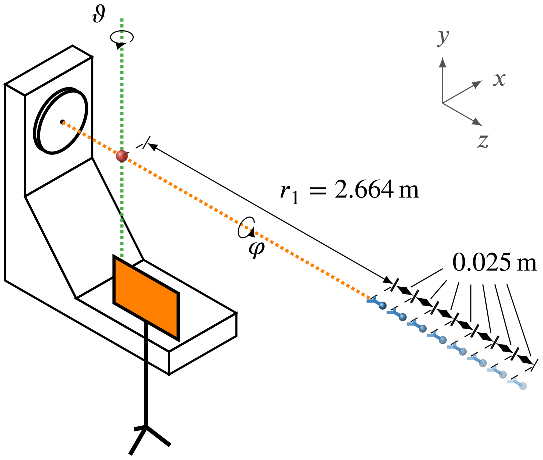

Fig. 8.36.: Schematic drawing of the measurement setup for the virtual array measurements (not to scale).

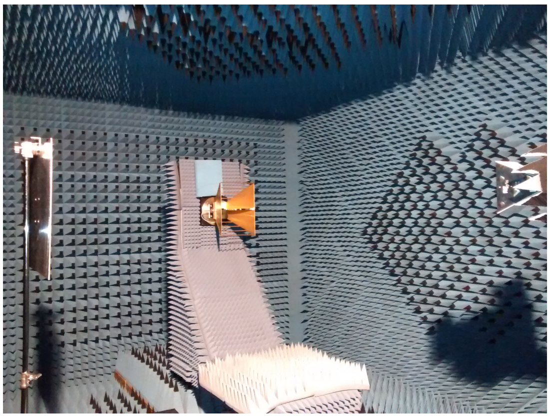

Fig. 8.37.: Photo of the measurement setup for the virtual array measurements.

samples per spherical measurement. The distance between the AUT rotation center was varied from $r_1 = 2.664\,\mathrm{m}$ to $r_8 = 2.839\,\mathrm{m}$ in steps of 0.025 m and a complete spherical measurement was obtained with every probe distance such that in the end eight spherical measurements with identical AUT angles were available. A schematic drawing and a photo of the measurement setup are depicted in Fig. 8.36 and Fig. 8.37, respectively.

To get an idea of the impact of the echo on NF measurements, first, the NF data from each measurement surface is transformed into the FF by FIAFTA, where in an intermediate step the equivalent surface currents on an enclosing hull were reconstructed for the AUT. The echo object has a considerable impact and the retrieved FFs from the perturbed measurements deviate from the reference FF which are obtained from an anechoic NF measurement. The co-polar component of the reconstructed FF from the spherical measurements at the closest of the eight measurement distances $r_1 = 2.664\,\mathrm{m}$ is shown in Fig. 8.38 for the $\varphi = 0°$-cut and in Fig. 8.39 for the $\varphi = 90°$-cut. All FFs are normalized to their respective co-polar component in main beam direction and the logarithmic deviation is calculated component wise as

$$\epsilon_{\vartheta/\varphi,\mathrm{dB}}(\vartheta,\varphi) = 20\,\log_{10}\left(\left|\frac{E_{\mathrm{FF},\vartheta/\varphi}(\vartheta,\varphi)}{E_{\mathrm{FF,max}}} - \frac{E_{\mathrm{refFF},\vartheta/\varphi}(\vartheta,\varphi)}{E_{\mathrm{refFF,max}}}\right|\right)\,, \tag{8.61}$$

where $E_{\mathrm{FF},\vartheta}$ is the ϑ-component of the echo contaminated retrieved FF with $E_{\mathrm{FF,max}}$ its co-polar component in main beam direction and $E_{\mathrm{FF},\varphi}$ the corresponding φ-component. Correspondingly, $E_{\mathrm{refFF},\vartheta}$ and $E_{\mathrm{refFF},\varphi}$ are the ϑ- and φ-components of the reference FF with $E_{\mathrm{refFF,max}}$ being the co-polar component in main beam direction. The maximum deviation of the echoic FF from the reference is larger than −20 dB showing a clear impact of the echo object. In fact, the influence of the echo perturbation varies with different probe positions (because the total incident field on the AUT consisting of the LOS probe field plus the reflected field at the echo changes when the probe illuminates the echo differently) and the retrieved FF looks different when retrieved from echo perturbed NF measurements with a different measurement distance.

The varying influence of the echo for different measurement distances is shown exemplarily in

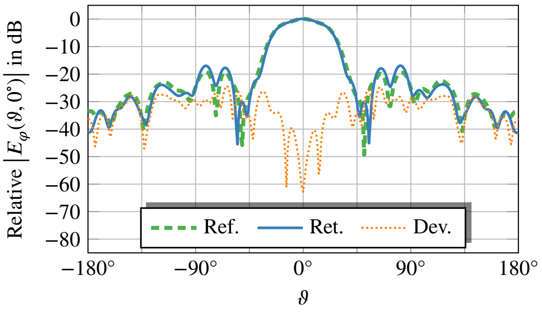

Fig. 8.38.: Co-polar component in the $\varphi = 0^\circ$-cut of the retrieved FF from NF measurements at $r_1 = 2.664\,\mathrm{m}$.

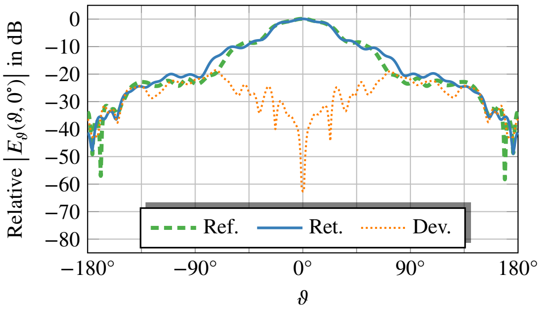

Fig. 8.39.: Co-polar component in the $\varphi = 90^\circ$-cut of the retrieved FF from NF measurements at $r_1 = 2.664\,\mathrm{m}$.

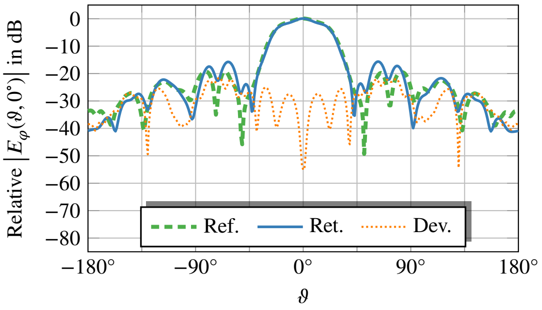

Fig. 8.40.: Co-polar component in the $\varphi = 0^\circ$-cut of the retrieved FF from NF measurements at $r_8 = 2.839\,\mathrm{m}$.

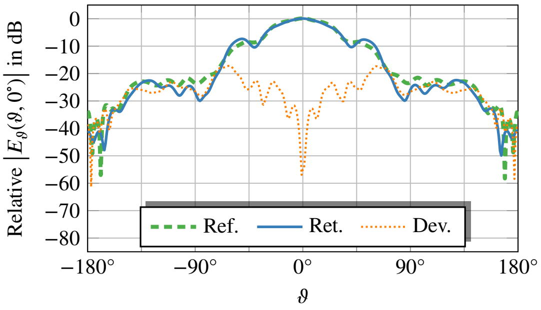

Fig. 8.41.: Co-polar component in the $\varphi = 90^\circ$-cut of the retrieved FF from NF measurements at $r_8 = 2.839\,\mathrm{m}$.

Figs. 8.40 and 8.41, where the co-polar components of the retrieved FF from measurements at the furthest distance $r_8 = 3.299\,\mathrm{m}$ are shown for comparison. The maximum deviation from the reference FF pattern is larger than −20 dB — just as it was the case for the retrieved FF from the closer NF distance — but the shapes of the retrrieved FFs from different measurement distances differ. It can be concluded that the NF measurements from all eight distances (only the furthest and closest distance are shown here, but similar deviations can be observed for all other distances) are contaminated by undesired echo influences which results in considerable deviations from the anechoic reference when the FF pattern is computed from the distorted NF measurements.

In order to mitigate the undesired echo influences, hypothetically measured S_{12}-values of a virtual probe array — called $S_{12,\mathrm{arr}}$ — were synthesized by forming a linear combination of the different measured S_{12}-values with different probe positions according to

$$S_{12,\mathrm{arr}}\left(\vartheta, \varphi, r_0\right) = \sum_{k=1}^{N_\mathrm{arr}} \alpha_k S_{12}\left(\vartheta, \varphi, r_k\right) \tag{8.62}$$

where the angles ϑ and φ denote the AUT position and $r_k = 2.664\,\mathrm{m} + (k-1)\,0.025\,\mathrm{m}$ is the radius of the kth measurement sphere — the number of array elements is $N_\mathrm{arr} = 8$ in the considered example. The distance r_0 denotes an arbitrary reference distance for the virtual array, which should be chosen between r_1 and r_8. The significance of the reference distance r_0 is that it specifies the reference point $\boldsymbol{r}_0 \hat{=} \left(r_0, \vartheta, \varphi\right)$ for the virtual array which is used for probe correction. The FF pattern $\boldsymbol{E}_{\mathrm{arrFF}}(\hat{\boldsymbol{k}})$ of the virtual array can be computed from the known FF pattern $\boldsymbol{E}_{\mathrm{DRH18,FF}}(\hat{\boldsymbol{k}})$ of the DRH18 probe via [Balanis 2005, pp. 283ff.]

$$\boldsymbol{E}_{\mathrm{arrFF}}(\hat{\boldsymbol{k}}) = \sum_{k=1}^{N_{\mathrm{arr}}} \alpha_k \boldsymbol{E}_{\mathrm{DRH18,FF}}(\hat{\boldsymbol{k}})\, \mathrm{e}^{-\mathrm{j}k_0\, \hat{\boldsymbol{k}}\cdot(\boldsymbol{r}_k-\boldsymbol{r}_0)} \tag{8.63}$$

as the weighted sum of the individual element patterns with respect to the reference point at r_0. In this way, synthetic measurement samples are obtained for the virtual array as if they were measured by an antenna with the synthesized FF pattern in the first place. The NF measurements from the virtual array probe were then transformed into the FF via FIAFTA, in a similar manner as for the previous case, with the only difference being the pattern used for probe compensation — instead of the DRH18 pattern, the pattern of the virtual array is used.

A large variety of different array patterns can be synthesized in principle by adjusting the $\alpha_k \in \mathbb{C}$. The overall goal is to synthesize an array field which has much larger magnitude at the AUT location than at the echo location, such that the virtual array is much less sensitive for the echo contribution than for the AUT contribution. A very general but laborious method to find appropriate coefficients α_k for the linear combination of N_{arr} array elements is to solve a field synthesis problem [Dohler 2002; Dohler 2004; Dohler 2009; Clauzier 2015; Bucci 2013; Ford 2013; Laitinen 2010; Hill 1988; Haupt 2003b; Haupt 2003a; Mauermayer 2015; Knapp 2019c]

$$\min_{\alpha_k} \gamma \iint\limits_{S_{\mathrm{aut}}} \left\| \left(\boldsymbol{E}_{\mathrm{tar}} - \sum_{k=1}^{N_{\mathrm{arr}}} \alpha_k \boldsymbol{E}_{\mathrm{pro},k} \right) \Big|_{\mathrm{tan}} \right\|^2 \mathrm{d}a + (1-\gamma) \iint\limits_{S_{\mathrm{ech}}} \left\| \sum_{k=1}^{N_{\mathrm{arr}}} \alpha_k \boldsymbol{E}_{\mathrm{pro},k} \Big|_{\mathrm{tan}} \right\|^2 \mathrm{d}a\,, \tag{8.64}$$

where $\gamma \in [0;1]$ is a weighting factor, $\boldsymbol{E}_{\mathrm{pro},k}$ denotes the radiated field from the probe at the kth position, $\boldsymbol{E}_{\mathrm{tar}}$ is the target field distribution one wants to synthesize — e.g., a plane wave — and S_{aut} and S_{ech} are surfaces denoting the AUT and echo location, respectively.

In contrast to this, a relatively simple method to achieve an increased focus toward the AUT without explicitly taking any a priori knowledge about the echo into account is to adjust the array coefficients α_k in a way such that the fields of the individual array elements interfere constructively toward the AUT. The virtual array becomes more directive than its single elements and therefore less sensitive for fields coming from other directions than the AUT. Consequently, the array coefficients are chosen as

$$\alpha_k = \mathrm{e}^{\mathrm{j}k_0\,(r_k - r_0)}\,. \tag{8.65}$$

This choice of array coefficients will be referred to as *conventional beamforming*. The co-polar components of the FF patterns for the single DRH18 probe and the virtual array with two, five, and eight elements is shown in Fig. 8.42 for the $\varphi = 0°$-cut and in Fig. 8.43 for the $\vartheta = 90°$-cut, respectively. The echo object appears in the approximate angular range[26] of $45° \leq \varphi \leq 90°$ in the probe centered coordinate system (with the main beam of the probe in positive x-direction) in the considered measurement setup. With increasing number of array elements, the array pattern becomes more directive and thus less sensitive to the echo object in general but in the particular example it can be noted that the five-element array and the eight-element array radiate a field with similar magnitude toward the echo (i.e., $45° \leq \varphi \leq 90°$, see Fig. 8.43).

---

[26] The exact view angle spanned by the echo object depends on the exact location in the virtual array.

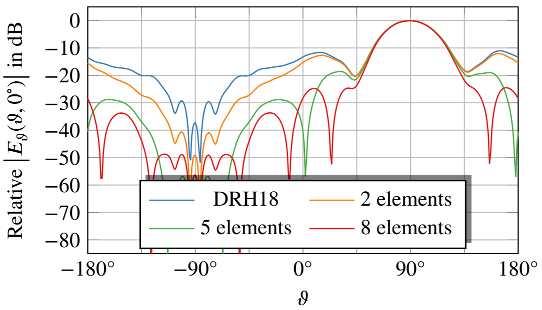

Fig. 8.42.: Co-polar component in the $\varphi = 0°$-cut of the DRH18 probe pattern and the virtual array pattern with two, five, and eight elements, respectively.

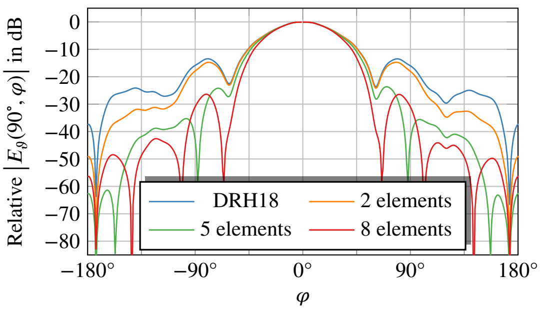

Fig. 8.43.: Co-polar component in the $\vartheta = 90°$-cut of the DRH18 probe pattern and the virtual array pattern with two, five, and eight elements, respectively.

The reconstructed FFs corresponding to the probe array with varying number of array elements can be found in Figs. 8.44 to 8.49. Fig. 8.44 and Fig. 8.45 show the co-polar component of the retrieved FF from NF measurements with a two-element virtual array in the $\varphi = 0°$-cut and the $\varphi = 90°$-cut, respectively. The deviation from the reference pattern is — if at all — only slightly smaller than for the retrieved FFs obtained from NF measurements with a single DRH18 probe (see Figs. 8.38 and 8.39), with a maximum deviation from the reference of about −20 dB, while the typical deviation is well above the −30 dB line for most angles. The two-element array pattern is only slightly more directive than the single DRH18 pattern (see Figs. 8.42 and 8.43) and, thus, it is understandable that the two-element array is similarly sensitive for echo influences as the single probe.

The co-polar components in the $\varphi = 0°$ and $\varphi = 90°$-cuts of the retrieved FFs can be seen in Figs. 8.46 and 8.47 for the five-element array, and Figs. 8.48 and 8.49 for the eight-element array. With the virtual array having more elements, the influence of the echo gradually decreases. The maximum deviation from the reference is about −22 dB with a typical deviation varying around the −28 dB line for the five-element array. For the eight-element array, the maximum deviation from the reference case is about −25 dB while for most angles, the deviation is well below −30 dB. Apparently, doubling the number of array elements brings about 3 dB increase in the dynamic range of the reconstructed FF pattern in this experiment. One would expect the same accuracy improvement if the oversampling factor is doubled in a noise contaminated signal. Certainly there exists a similarity between noise (and echo) filtering capabilities of oversampled measurements and the echo suppression of the presented virtual beamforming method.

8.3.2. Similarity Between Conventional Beamforming and Processing of Oversampled Measurements

From the observations in the previously described measurement, a close similarity between forming a virtual array and processing all measurement samples simultaneously is expected. In fact, the resulting FF patterns from the virtual arrays with conventional beamforming element weights are almost identical to the FF patterns obtained by using a single DRH18 probe and processing all measurement samples with the corresponding measurement distances simultaneously. The maximum deviation between the FF from the two-element virtual array measurement and the

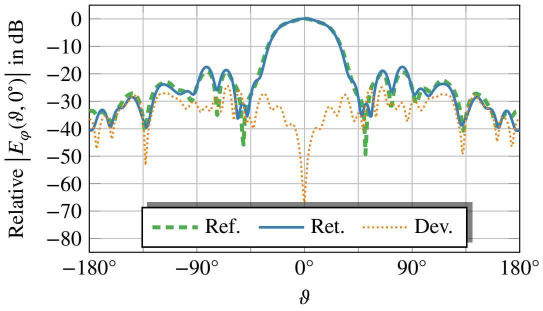

Fig. 8.44.: Co-polar component in the $\varphi = 0°$-cut of the retrieved FF from NF measurements with a virtual array consisting of two elements.

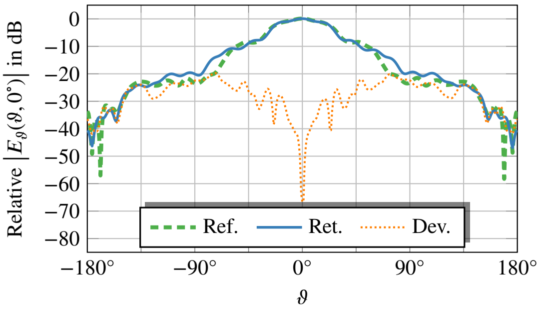

Fig. 8.45.: Co-polar component in the $\varphi = 90°$-cut of the retrieved FF from NF measurements with a virtual array consisting of two elements.

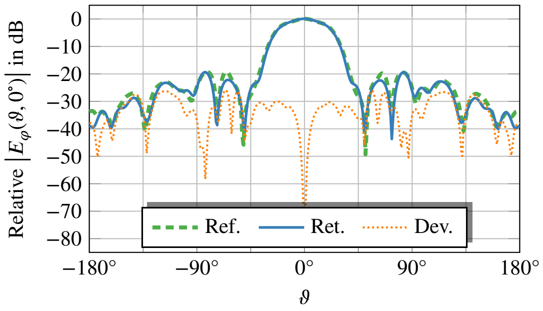

Fig. 8.46.: Co-polar component in the $\varphi = 0°$-cut of the retrieved FF from NF measurements with a virtual array consisting of five elements.

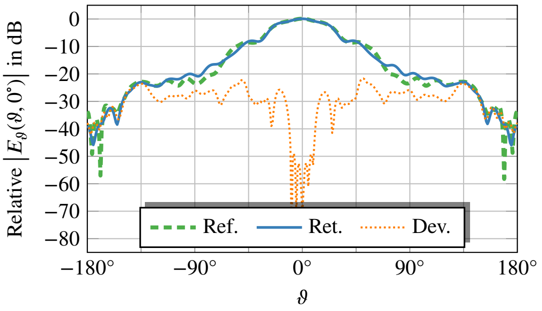

Fig. 8.47.: Co-polar component in the $\varphi = 90°$-cut of the retrieved FF from NF measurements with a virtual array consisting of five elements.

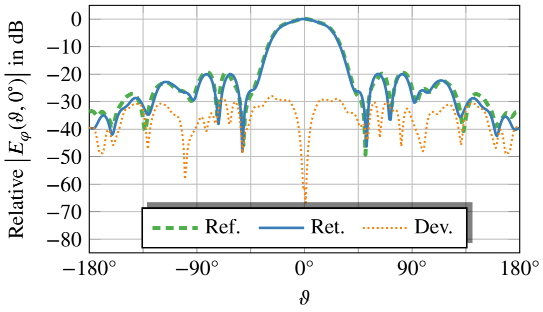

Fig. 8.48.: Co-polar component in the $\varphi = 0°$-cut of the retrieved FF from NF measurements with a virtual array consisting of eight elements.

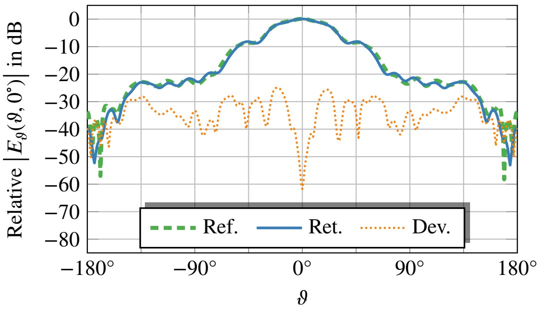

Fig. 8.49.: Co-polar component in the $\varphi = 90°$-cut of the retrieved FF from NF measurements with a virtual array consisting of eight elements.

FF obtained from processing the measurement samples of the corresponding two measurement spheres with radii r_1 and r_2 is below −74 dB. The maximum deviation between the FF from the five-element virtual array measurement and the FF obtained from processing the measurement samples of the corresponding five measurement spheres with radii r_1 to r_5 is below −58 dB. The maximum deviation between the FF from the eight-element virtual array measurement and the FF obtained from processing the measurement samples of the corresponding eight measurement spheres with radii r_1 to r_8 is below −53 dB. In all cases, the deviation between the FFs of the virtual array and of the oversampled measurements of a single DRH18 is well below the echo contribution[27]. This can be explained by the following observation. Let $\boldsymbol{b}_k \in \mathbb{C}^{58322\times 1}$ be the vector storing the measured S_{12}-samples measured with the DRH18 probe at the kth measurement distance $\boldsymbol{r}_k$ and $\boldsymbol{A}_k \in \mathbb{C}^{58322\times N}$ the discretized forward operator relating the N AUT source coefficients to the measurement samples. Using a single DRH18 as a probe and processing the measurement samples from the first K measurement distances simultaneously, the linear system of equations to solve is given by

$$\begin{bmatrix} \boldsymbol{A}_1 \\ \vdots \\ \boldsymbol{A}_K \end{bmatrix} \boldsymbol{x} = \begin{bmatrix} \boldsymbol{b}_1 \\ \vdots \\ \boldsymbol{b}_K \end{bmatrix}. \tag{8.66}$$

Since the radiated fields from the AUT propagate approximately as spherical waves with a radial dependency of $\mathrm{e}^{-\mathrm{j}k_0 r}/r$ we have $\boldsymbol{A}_\ell \approx \boldsymbol{A}_k \mathrm{e}^{-\mathrm{j}k_0(r_\ell - r_k)}\, r_\ell / r_k$. If $\left(r_\ell - r_k\right) \ll r_\ell$, then $r_\ell / r_k \approx 1$ and $\boldsymbol{A}_\ell \approx \boldsymbol{A}_k \mathrm{e}^{-\mathrm{j}k_0(r_\ell - r_k)}$. This approximation becomes exact if all measurement radii are in FF distance of the AUT. Applying these approximations to (8.66) gives

$$\begin{bmatrix} \mathbf{1} & & \\ & \ddots & \\ & & \mathrm{e}^{-\mathrm{j}k_0(r_K - r_1)}\mathbf{1} \end{bmatrix} \begin{bmatrix} \boldsymbol{A}_1 \\ \vdots \\ \boldsymbol{A}_1 \end{bmatrix} \boldsymbol{x} = \begin{bmatrix} \boldsymbol{b}_1 \\ \vdots \\ \boldsymbol{b}_K \end{bmatrix} \quad \Rightarrow \quad \begin{bmatrix} \boldsymbol{A}_1 \\ \vdots \\ \boldsymbol{A}_1 \end{bmatrix} \boldsymbol{x} = \begin{bmatrix} \boldsymbol{b}_1 \\ \vdots \\ \mathrm{e}^{\mathrm{j}k_0(r_K - r_1)}\, \boldsymbol{b}_K \end{bmatrix}, \tag{8.67}$$

where $\mathbf{1} \in \mathbb{C}^{58322\times 58322}$ is the identity matrix.

Compare the result from (8.67) to the processing with a virtual array. Choosing the measurement distance r_1 of the first element for the array reference distance, i.e., $r_0 = r_1$, the linear system of equations for the measurement with the K element virtual array with conventional beamforming is given by

$$\left(\boldsymbol{A}_1 + \ldots + \mathrm{e}^{\mathrm{j}k_0(r_K - r_1)}\, \boldsymbol{A}_K\right) \boldsymbol{x} = \boldsymbol{b}_1 + \ldots + \mathrm{e}^{\mathrm{j}k_0(r_K - r_1)}\, \boldsymbol{b}_K. \tag{8.68}$$

Using the approximation $\boldsymbol{A}_\ell \approx \boldsymbol{A}_k \mathrm{e}^{-\mathrm{j}k_0(r_\ell - r_k)}$, the linear system (8.68) for the virtual array measurement simplifies to

$$K \boldsymbol{A}_1 \boldsymbol{x} = \boldsymbol{b}_1 + \ldots + \mathrm{e}^{\mathrm{j}k_0(r_K - r_1)}\, \boldsymbol{b}_K. \tag{8.69}$$

The normal residual equations are identical for (8.67) and (8.69) and it can be concluded that the measurement with the conventional beamforming virtual array leads to very similar results as processing all measurement distances with a single probe at once if the approximation $\boldsymbol{A}_\ell \approx \boldsymbol{A}_k \mathrm{e}^{-\mathrm{j}k_0(r_\ell - r_k)}$ holds between the forward operator at different measurement radii.

---

[27] For the sake of avoiding unnecessary repetition, no plots are shown here, because the curves would not be distinguishable from the curves in Figs. 8.48 and 8.49.

	$\epsilon_{\mathrm{DRH18}}$	ϵ_{arr}
two distances	0.0664	0.0544
five distances	0.1045	0.0541
eight distances	0.1299	0.0539

Tab. 8.1.: Reconstruction deviation for a single probe processing multiple positions or a virtual array.

Nevertheless, using the virtual array has benefits over processing all measurements at once with a single probe. The processing effort is reduced. The forward operator for the virtual array has essentially the same computational cost as the forward operator for a single probe at a single measurement distance — much less than the added computational cost for the K distances. Since the measurement samples of the virtual array do not contain a strong echo influence, the reconstruction deviation is in the order of an anechoic measurement and can, thus, be used effectively as a stopping criterion for iterative solvers. The reconstruction deviations for a single DRH18 probe processing multiple distances at once and the reconstruction deviation for the corresponding virtual array are shown in Tab 8.1.

8.4. Chapter Summary

This chapter has presented an extensive analysis of frequency domain echo suppression algorithms. First, echo scenarios with a stationary AUT have been investigated. The echo suppression capability is linked to be able to separate the fields from sources in different source domains. It has been found that it depends only on the relative separation between the source domains, how well the corresponding fields can be separated in this scenario. Ambiguities can persist even for well separated source domains because of evanescent fields which are excited by standing waves between the source domains. Once the separation between the source domains becomes large enough that the standing waves can be ruled out, the fields can be unambiguously assigned to the correct source domain and the echoes influence can be removed, if the echo sources are modeled simultaneously with the AUT sources. If only the AUT sources are modeled, some part of the echo influence is mapped to the AUT sources, leaving a remaining echo distortion in the reconstructed sources. This analysis has been presented for the first time in this thesis.

Second, echo suppression algorithms with a stationary probe have been analyzed. As a formal analysis of the chamber calibration methods in the literature revealed, the echo influence can be described correctly by additional sources assigned to the probe (as opposed to the sources assigned to the AUT). If the echo influence is nevertheless accounted for by (unphysical) additional AUT sources, it has been found that not all echo influences on the measured S-parameters can be reproduced by the extended model (at least for low-order probes). This consideration has given an illustrative insight why the translation of the AUT away from the rotation center leads to an increased separation between the echo sources and the AUT sources, but due to the large size of the torus, mutual interactions can persist and distort the reconstructed sources. While modal suppression methods such as MARS are well known in the literature, the rigorous analysis which has been presented in this chapter explains the success in echo suppression for the first time by identifying the source location of the additionally reconstructed ghost sources.

To overcome the limits of the echo suppression in stationary probe scenarios, virtual beam forming has been proposed as a solution. Virtual beam forming has been used for echo suppression before [Yinusa 2014], but in this thesis, the crucial distinction between stationary echo and stationary AUT scenarios has been introduced first. It is an important realization that these virtual beam forming algorithms are particularly well suited to serve in stationary echo suppression scenarios (where under certain circumstances they are equivalent to a more cumbersome simultaneous consideration of all probe positions in the NFFFT).

9

Hybrid Echo Suppression Methods for Strongly Echoic Environments

The most effective echo suppression methods are obtained when frequency domain and time domain methods are combined and tailored to the requirements of the situation at hand. Echoes behave differently when either the AUT or the probe moves and so should the echo suppression methods. In this chapter several examples are presented in which the previously discussed echo suppression methods were combined to achieve unprecedented echo suppression in antenna measurements — even in challenging echoic environments.

9.1. Time Gating of Reconstructed Currents

In scenarios with a stationary AUT[1], conventional time gating of the measured signal is often not feasible because for some measurement positions the probe is in the shadow region of the echo object. For these measurement positions, there is no noticeable path length difference between the LOS path and the first reflected path which can be exploited in time gating. Frequency domain methods can to a certain extent separate the source locations of the AUT and the echo objects (if they are well separated) but the distortions of the AUT currents due to multiple reflections remain in this case. In this section, frequency domain source reconstruction is combined with time gating where time gating is not applied to the measured signals but to the reconstructed source coefficients at several frequencies with the goal of mitigating the mutual coupling influences, which remain after the spatial separation of the AUT sources from the echo sources. The results of the Feko [Altair 2021] simulations of the horn antenna in this Section 9.1.1 were first presented in [Knapp 2019e] with FFT-based time gating and in [Knapp 2020] with sparsity based time gating.

---

[1] I.e., the AUT is stationary with respect to the echo objects. If the echo is mounted in a fixed relative position with respect to a rotating AUT, it is still referred to as a scenario with a *stationary* AUT.

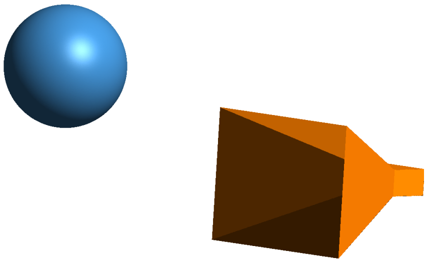

Fig. 9.1.: AUT configuration simulated in Feko [Altair 2021].

The measurement results in Section 9.1.2 were first presented in the conference presentation of [Knapp 2020]. They appear for the first time in printed form, here.

9.1.1. Simulation Result

Before coming to actual measurements, simulated results for a horn antenna with a PEC sphere in close proximity are considered first. The scenario depicted in Fig. 9.1 has been simulated in Feko [Altair 2021]. The sphere was placed in approximately 0.3 m distance to the AUT aperture, asymmetrically offset from the x-axis. The fields generated by the currents on the AUT and the scattering sphere have been evaluated on a spherical surface with distance 1.5 m to the coordinate origin in the AUT center in a frequency range from 1.7 GHz – 5.7 GHz with a frequency step of $\Delta f = 50\,\mathrm{MHz}$ to form the synthetic measurements. The radiated fields are reconstructed in a two-step process. First equivalent electric and magnetic surface currents (coupled with a combined source condition to yield an unambiguous solution) are reconstructed for every frequency by FIAFTA on two Huygens surfaces enclosing the AUT and the echo, respectively. The Huygens surface for the source reconstruction was larger than the mesh from the Feko simulation with about 1 cm space between the original Feko mesh and the new Huygens surface. In a second step the electric and magnetic current coefficients were time gated to remove the undesired mutual coupling effects. Note that due to the stationary AUT scenario, a direct time gating of the measurement samples is not feasible for all measurement positions because for some of the measurement samples the probe is located in the shadow region of the echo object. After the time-gating step, the radiated fields are calculated thereafter from the reconstructed and time gated sources only on the AUT (any reconstructed currents on the echo sphere are neglected for the FF calculation) and compared to the reference generated by Feko without the PEC sphere.

Two cases are considered for the source reconstruction step. The equivalent currents are either reconstructed on a Huygens surface only enclosing the AUT or on two separate Huygens surfaces, enclosing the AUT and the echo sphere, respectively. The corresponding AUT FFs are calculated using only the reconstructed currents on the AUT in both cases. The co-polar ϑ-component of the reconstructed FF at the center frequency of 3.7 GHz can be seen in Fig. 9.2 for the $\varphi = 0°$-cut and in Fig. 9.3 for the $\vartheta = 90°$-cut, respectively, where during the reconstruction equivalent sources were reconstructed only on the Huygens surface enclosing the AUT. In this case the spatial filtering is not very successful and a part of the echo contribution is mapped onto the reconstructed AUT sources, leading to a maximum deviation of about $-10\,\mathrm{dB}$ between the reconstructed FF and the reference.

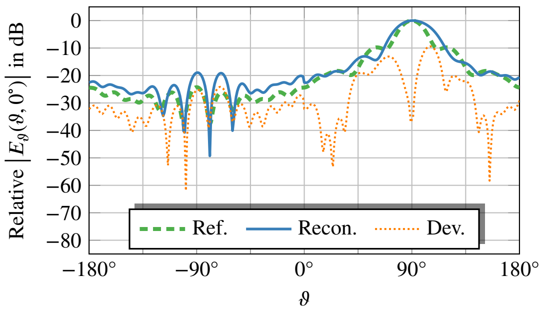

Fig. 9.2.: Co-polar component in the $\varphi = 0^\circ$-cut of the reconstructed AUT pattern at 3.7 GHz. Only the AUT Huygens surface was used for the source reconstruction.

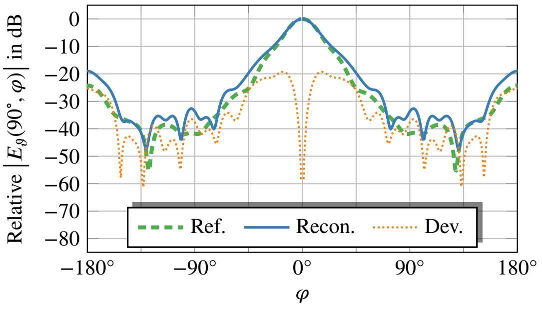

Fig. 9.3.: Co-polar component in the $\vartheta = 90^\circ$-cut of the reconstructed AUT pattern at 3.7 GHz. Only the AUT Huygens surface was used for the source reconstruction.

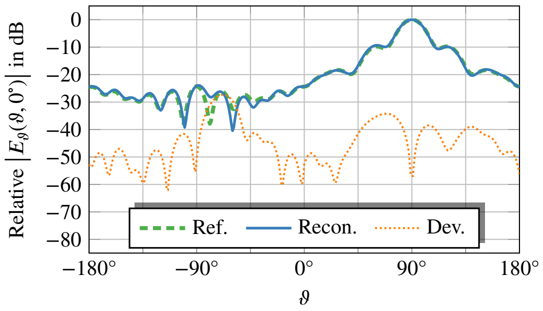

Fig. 9.4.: Co-polar component in the $\varphi = 0^\circ$-cut of the reconstructed AUT pattern at 3.7 GHz. Huygens surfaces around the AUT and the echo were used for the source reconstruction. Figure adapted from [Knapp 2020].

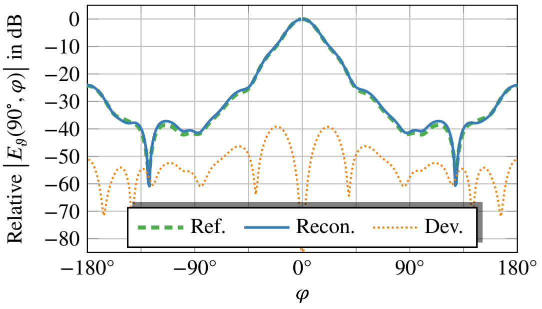

Fig. 9.5.: Co-polar component in the $\vartheta = 90^\circ$-cut of the reconstructed AUT pattern at 3.7 GHz. Huygens surfaces around the AUT and the echo were used for the source reconstruction.

In contrast to this, the co-polar ϑ-component of the reconstructed FF at the center frequency of 3.7 GHz can be seen in Fig. 9.4 for the $\varphi = 0^\circ$-cut and in Fig. 9.5 for the $\vartheta = 90^\circ$-cut, respectively, where during the reconstruction the equivalent sources were reconstructed on the AUT and on the echo hull simultaneously, while the echo currents were discarded for the FF calculation. The spatial echo filtering process is very successful in this case as a maximum deviation between the reconstructed FF and the reference is approximately −28 dB near the backlobe (around $\vartheta = -80^\circ$) in the $\varphi = 0^\circ$-cut. For most other directions the deviation is less than −40 dB. The remaining distortions must be due to mutual interactions between the AUT and the echo object. The current density on the AUT is distorted as the scattered wave from the PEC sphere is incident on the AUT causing scattering currents on its surface which superimpose with the original AUT radiation currents. The FF deviations in Fig. 9.4 appearing in the backlobe of the AUT (around $\vartheta = -80^\circ$) agree well with a distortion caused by a scattered wave from the sphere.

The mutual interactions are even more evident in a time domain representation of the currents. The source coefficients which are retrieved by FIAFTA on the discretized Huygens surface at all

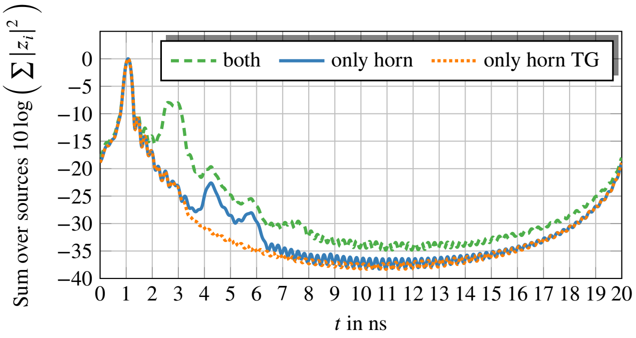

Fig. 9.6.: Sum over source coefficients in time domain. The different curves denote the source coefficients present on both objects — echo and AUT — or the AUT alone.

simulated frequencies are transformed into the time domain with an FFT. The (squared) sum of all resulting source coefficients at every time step can be seen in Fig. 9.6, where the different curves denote the sum of all coefficients — on the AUT and on the echo — or the sum of only the AUT coefficients, respectively. The peak at 1.0 ns corresponds to the free-space currents on the AUT. At around 2.5 ns to 3.0 ns, some currents appear on the echo sphere. These echo currents are only visible as a peak in the curve for both objects, visualizing the spatial filtering effect of the source reconstruction on separate surfaces. Further peaks between 4.0 ns and 6.5 ns correspond to currents appearing on the AUT. These peaks correspond to the undesired mutual interactions which change the current distribution on the AUT. These distortions of the current distribution on the AUT are responsible for the deviations between the reconstructed FF and the reference FF in Fig. 9.4. For a more accurate reconstruction of the free-space AUT currents, this mutual interaction contribution must be eliminated by time gating. To this end, a rectangular time-gating window was applied to force the value of all time samples later than 3.1 ns (i.e., 2.0 ns after the peak) to zero. The gated time sequences were transformed back into frequency domain with an FFT to the corresponding frequencies, before the FF was computed from the time gated frequency domain source coefficients. The time gated time-domain signal is also depicted in Fig. 9.6. Its value is not exactly zero at times $t > 3.1$ ns, because the resolution of the time-domain signal used for time gating was much higher than what can be obtained from the frequency samples directly (the time-domain signal was interpolated, by appending flipped versions of the frequency domain data multiple times and time shifted before being gated). When the frequency samples are recovered from the oversampled time domain data, all frequency points which do not match a measured frequency were discarded. The visualized time domain representation of the gated signal was obtained from the gated frequency samples at only the measured frequencies, explaining the slight discrepancy between the originally gated time domain data and the shown curve.

The reconstructed FF from the time gated source coefficients at 3.7 GHz are shown in Fig. 9.7 for the $\varphi = 0°$-cut and in Fig. 9.8 for the $\vartheta = 90°$-cut, respectively. The final reconstructed FF has a good agreement with the reference. The maximum deviation is well below −40 dB, while the typical deviation is well below −50 dB for most directions, often even below −60 dB. A key for the success of echo suppression in this example has been the well separated nature of the AUT and the echo volume such that the spatial filtering of the reconstructed currents was very

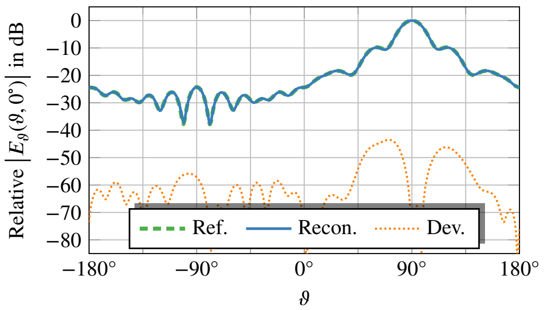

Fig. 9.7.: Co-polar component in the $\varphi = 0°$-cut of the reconstructed AUT pattern at 3.7 GHz. Time gated versions of the source coefficients on the AUT Huygens surface were used for the FF calculation.

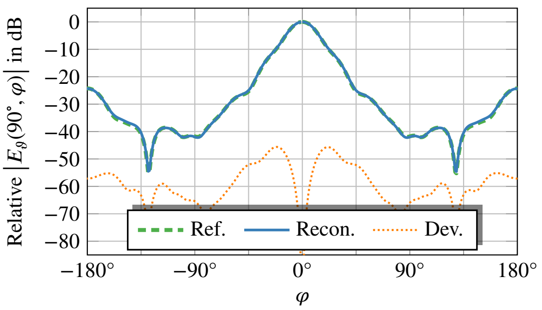

Fig. 9.8.: Co-polar component in the $\vartheta = 90°$-cut of the reconstructed AUT pattern at 3.7 GHz. Time gated versions of the source coefficients on the AUT Huygens surface were used for the FF calculation.

effective, before the remaining distortions could be filtered in time domain.

9.1.2. Measurement Results

The same post processing as in the numerical example has been applied to a measurement setup where an obstacle has been mounted in proximity to the AUT. The measurement setup is depicted in Fig. 9.9. A DRH18 horn antenna served as an AUT and an open ended WR-187 waveguide served as a probe. The AUT was mounted with a vertical offset to the rotation center (as depicted in Fig. 9.9 for the AUT position at $\varphi = 0°$, $\vartheta = 0°$). With the same vertical offset in opposite direction, a metallic plate is mounted to the same base plate as the AUT with the help of three metallic rods such that the metal plate is positioned in front of the AUT with a fixed relative position to the AUT. Although not clearly visible in the photo, the metal plate is rotated by about 20°around its own axis and the complete setup of AUT and obstacle does not have a symmetry plane. Since the echo obstacle position is fixed with respect to the AUT, the measurement scenario is considered to have a *stationary* AUT. Spherical NF measurements at a distance of 2.651 m with equiangular sampling ($\Delta\vartheta = \Delta\varphi = 0.5°$ stepsize) in ϑ- and φ-direction have been obtained in this constellation from 3.95 GHz to 5.85 GHz in $\Delta f = 50$ MHz steps. The Huygens surfaces for the reconstruction of AUT and echo currents are depicted in Fig. 9.10. A trade-off had to be made between an accurate modelling of the echo sources (which would include also the metal rods in the model) and an unambiguous solution for the reconstructed currents (only if the Huygens surfaces for AUT and echo are well separated, one can distinguish the source locations by their respective radiated currents).

The co-polar ϑ-component of the reconstructed FF after the source reconstruction step at the center frequency of 5.0 GHz can be seen in Fig. 9.11 for the $\varphi = 0°$-cut and in Fig. 9.12 for the $\varphi = 90°$-cut, respectively. No time gating has been applied to the source coefficients, yet. In the $\varphi = 90°$-cut, i.e., the cut in which the echo obstacle is located, large deviations can be observed between the reconstructed FF and the reference. In this cut, the $\vartheta = 45°$ and $\vartheta = -135°$ directions are influenced by the echo most. These are the directions toward the echo plate and opposite of it. It can be assumed that in particular the deviation in the direction opposite to the

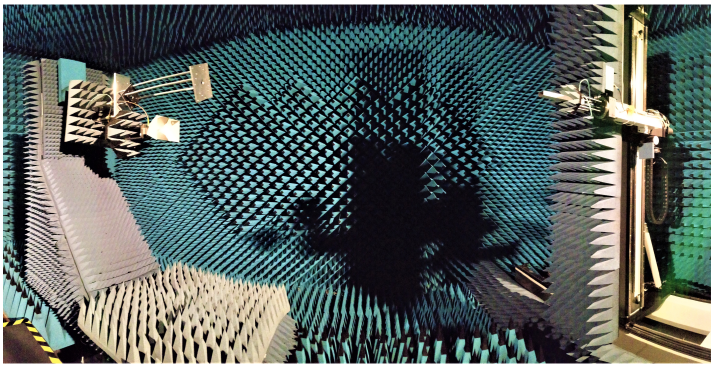

Fig. 9.9.: Photo of the measurement setup between the DRH18 horn antenna as an AUT and an open ended waveguide probe with a metallic obstacle fixed to the rotating AUT.

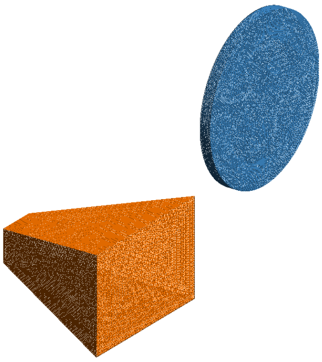

Fig. 9.10.: Huygens surfaces around the AUT and the echo objects in the source reconstruction.

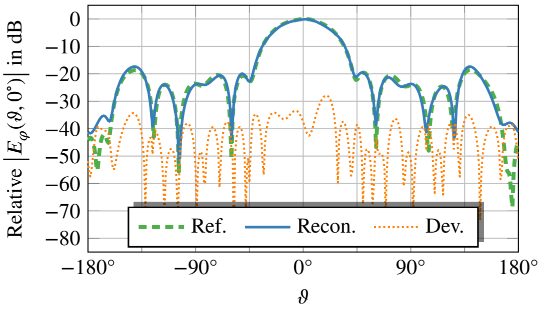

Fig. 9.11.: Co-polar component in the $\varphi = 0°$-cut of the reconstructed AUT pattern at 5.0 GHz. Only the reconstructed source coefficients on the AUT Huygens surface were used for the FF calculation.

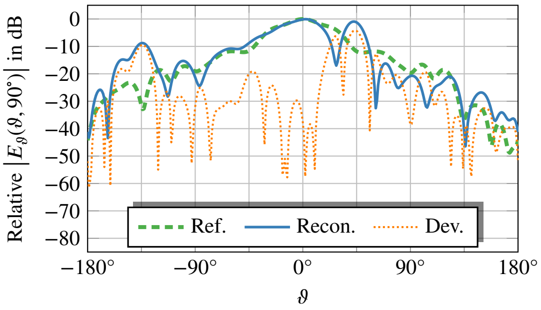

Fig. 9.12.: Co-polar component in the $\varphi = 90°$-cut of the reconstructed AUT pattern at 5.0 GHz. Only the reconstructed source coefficients on the AUT Huygens surface were used for the FF calculation.

echo is due to mutual interactions changing the true current distribution on the AUT.

The co-polar ϑ-component of the reconstructed FF at the center frequency of 5.0 GHz after the time gating step can be seen in Fig. 9.13 for the $\varphi = 0°$-cut and in Fig. 9.14 for the $\varphi = 90°$-cut, respectively. For all directions where no obstacle is located, the reconstructed FF deviates less than −30 dB from the reference. Only those directions, in which the echo was present remain distorted even after time gating the sources. A probable cause for this is the fact that the spatial filtering (i.e., the source reconstruction step) was not successful for the currents which are responsible for radiation toward these directions. The relevant AUT currents on the top of the AUT are not properly illuminated by the probe in this measurement setup and the close proximity to the echo object makes it impossible to differentiate between echo or AUT source location for the radiated fields. Time gating can only cure the current mutual coupling distortions for the currents which are already correctly reconstructed in the AUT volume. The deviations of the reconstructed pattern in the direction opposite to the echo obstacle are therefore successfully removed and the AUT radiation is correctly determined for all directions other than those directly

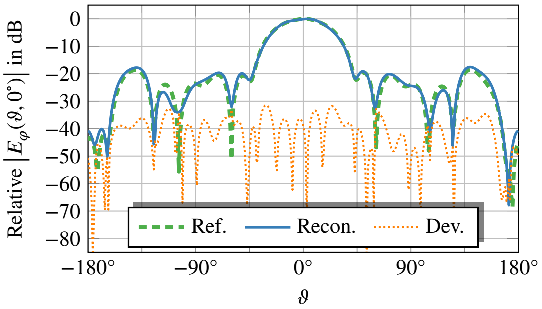

Fig. 9.13.: Co-polar component in the $\varphi = 0°$-cut of the reconstructed AUT pattern at 5.0 GHz. Time gated versions of the source coefficients on the AUT Huygens surface were used for the FF calculation.

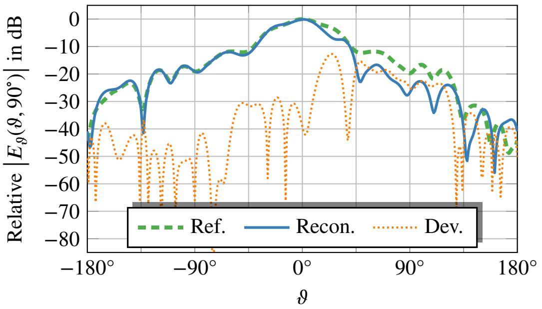

Fig. 9.14.: Co-polar component in the $\varphi = 90°$-cut of the reconstructed AUT pattern at 5.0 GHz. Time gated versions of the source coefficients on the AUT Huygens surface were used for the FF calculation.

covered by the echo object. This example shows the capabilities but also the limitation of echo suppression methods which combine frequency- and time-domain methods. To be successful, the spatial filtering step must succeed to separate the source locations for the AUT and echo contributions of the total field. After successful spatial filtering, the remaining distortions due to mutual coupling can be effectively removed by echo suppression.

9.2. The Mosquito Chamber: Processing Data from Strongly Reflective Environments

When frequency domain and time domain methods are combined, the resulting processing methods can provide excellent echo suppression capabilities. The measurement samples must in principle suffice to characterize the unknown echoes simultaneously with the unknown AUT. The more echo sources are contaminating the measurement samples, the more “redundant” (with respect to the free-space AUT) measurements have to be collected and processed as a consequence if one wants to succeed in removing the undesired distortions. To demonstrate that antenna pattern measurements can be reasonably successful even in strongly reflective environments if only enough measurement samples are collected, a laborious measurement campaign has been carried out in the antenna measurement chamber at TUM involving three different AUTs covering different frequency bands. The measurement results shown in this section involving the DRH400 AUT were first presented in [Knapp 2018a], and more thoroughly analyzed in in [Knapp 2019a] concerning the influence of time gating and usage of various probe configurations for virtual beam forming. The measurement results shown in this section, involving a RUAG S-band antenna and a RUAG Ku-band antenna as AUT, were first presented in [Knapp 2019c].

The previously anechoic chamber was transformed into a strongly reflective measurement environment. To this end, the four walls, the floor, and the ceiling were covered with an aluminum net mounted on a wooden frame of size 7.5 m × 4.0 m × 3.5 m. Due to its visual appearance, the resulting strongly echoic environment is called *Mosquito chamber*. The moving parts inside the chamber, i.e., the AUT and probe positioners were covered with absorbers whereas all other absorbing materials were removed from the Mosquito chamber. The moving rail on which the

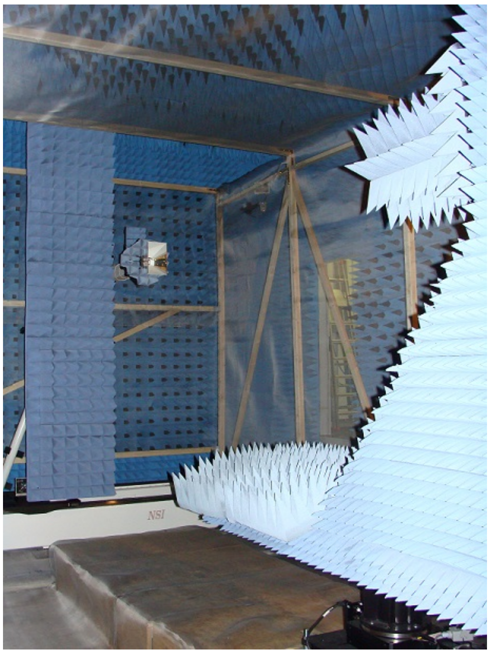

Fig. 9.15.: Photograph of the assembled Mosquito chamber inside the anechoic chamber at TUM [Knapp 2019c]. ©2019, IEEE

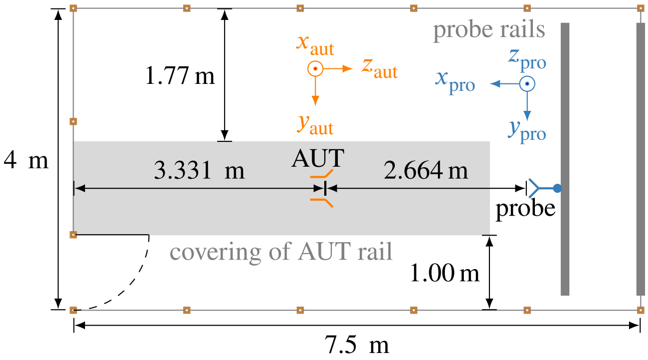

(a) Dimensions

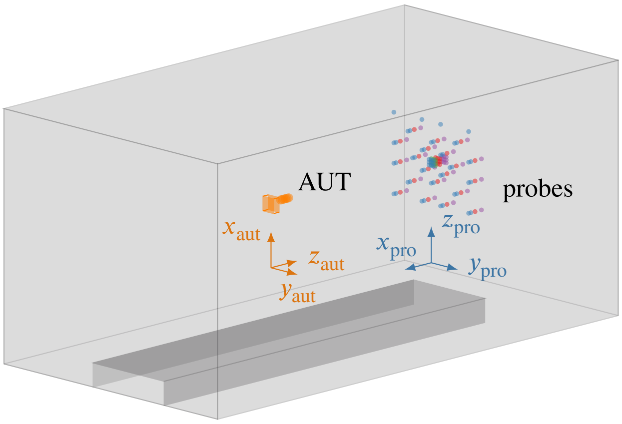

(b) Antenna positions

Fig. 9.16.: Layout of the Mosquito chamber assembly [Knapp 2019c]. ©2019, IEEE

AUT positioner is mounted to be able to adjust the distance between AUT and the probe was not used in this measurement campaign and consequently covered by 0.33 m high wooden boxes with the metallic mesh on top. To allow a free movement of the probe positioning system, only two openings in the metallic mesh — about 1 m broad — had to be left open at the back and the ceiling of the back wall behind the probe. A photograph of the Mosquito chamber setup can be seen in Fig. 9.15. The schematic layout of the Mosquito chamber and the locations of AUT and probe are shown in Fig. 9.16, including the probe coordinate system x_{pro}, y_{pro}, z_{pro} and the AUT coordinate system x_{aut}, y_{aut}, z_{aut} for the reference position $\vartheta = \varphi = 0°$.

The AUT is placed approximately in the middle of the chamber. Full spherical measurements can be obtained by rotating the two axes of the AUT. The probe can be moved along the x-, y-, and z-axis which is useful for building virtual arrays. All measurements in this section were obtained with a DRH18 probe. Its usable frequency easily covers all frequencies between the S-band and the Ku-band but its pattern varies with frequency. Consequently, an accurate probe correction is required, in particular when signals from different probe positions are combined in a virtual array.

An a priori simulation of the aluminum net led to the conclusion that the reflection coefficient for incident plane waves is larger than 0.99 for all frequencies up to 15 GHz. The chamber

Q-factor and the corresponding time constant τ were determined by fitting an exponential model

$$x(t) = x_{\max} \mathrm{e}^{-t/\tau} \tag{9.1}$$

to the measured impulse response between two antennas mounted inside the chamber, where the Q-factor can be estimated from the recovered τ by [Hill 2009, p. 11]

$$Q = \omega\tau . \tag{9.2}$$

The resulting value of $\tau = 0.1116\,\mu\mathrm{s}$ suggests a chamber Q-factor of $Q = 1402$ at 2 GHz or $Q = 9116$ at 13 GHz. It is important to know the chamber time constant because it determines the maximum frequency step Δf which can be used for sampling the signal such that no aliasing effects occur in time gating. To avoid aliasing, the impulse response corresponding to the IFFT of the measured frequency sequence should have decayed to a value below −40 dB. A smaller frequency step Δf yields a longer time sequence in the corresponding impulse response, leading to more decay. The spacing of the frequency samples has been set to $\Delta f = 2\,\mathrm{MHz}$ for all measurements in this section.

9.2.1. Measurements with the RUAG S-Band Antenna

In [Knapp 2019c], measurements were considered for the circularly polarized RUAG S-band helix antenna in the Mosquito Chamber. For the RUAG S-band antenna, full spherical measurements with equiangular sampling steps of $\Delta\vartheta = \Delta\varphi = 3^\circ$ were obtained with 120 probe locations distributed in four planes with distances $z_1 = 2.664\,\mathrm{m}$, $z_2 = 2.704\,\mathrm{m}$, $z_3 = 2.784\,\mathrm{m}$, and $z_4 = 2.914\,\mathrm{m}$ to the AUT rotation center. The exact probe positions in the respective planes are depicted in Fig. 9.17. The top four probe locations (labeled “30”, “31”, “32”, and “33”) were obtained only in the first measurement plane with distance z_1, whereas in the remaining three planes only the first 29 probe positions were used. Overall, 120 full spherical measurements were performed. The S_{12}-parameter between the probe and the AUT was measured for all combinations of probe and AUT positions in the frequency range from 1.5 GHz to 3.5 GHz.

Processing of the measured signals involves several steps. First, the signals at each measurement position[2] are time gated. The time gated signals of the 120 different probe positions are then combined to synthesize a virtual probe array. As the virtual array signal is thereby determined for every AUT position, a conventional NFFFT is carried out as if the measurements had been obtained with the virtual array probe in the first place.

For time gating, the standard FFT based method was used here for simplicity because a large number of measurement samples — each featuring 1001 frequency samples — had to be processed. The time-domain signal was obtained by directly applying the IFFT to the measured frequency sequence for every measurement position. The time domain sequence was then truncated using a Hamming window. The truncation times were chosen according to the distance d of the probe from the AUT rotation center to acknowledge that the traveling times of the signal varies when the probe is further away from the AUT. Four probe regions were introduced based on the distances $d_1 = 2.7030\,\mathrm{m}$, $d_2 = 2.7815\,\mathrm{m}$, $d_3 = 2.899\,\mathrm{m}$. The signals of all probes in the first region defined by $d < d_1$ were truncated at $t_1 = 34\,\mathrm{ns}$, the signals of the second region with $d_1 < d < d_2$ were

---

[2] The term *measurement position* here denotes a certain combination of a fixed AUT position and a fixed probe position. If either the AUT position or the probe position is changed, it counts as a new *measurement position*.

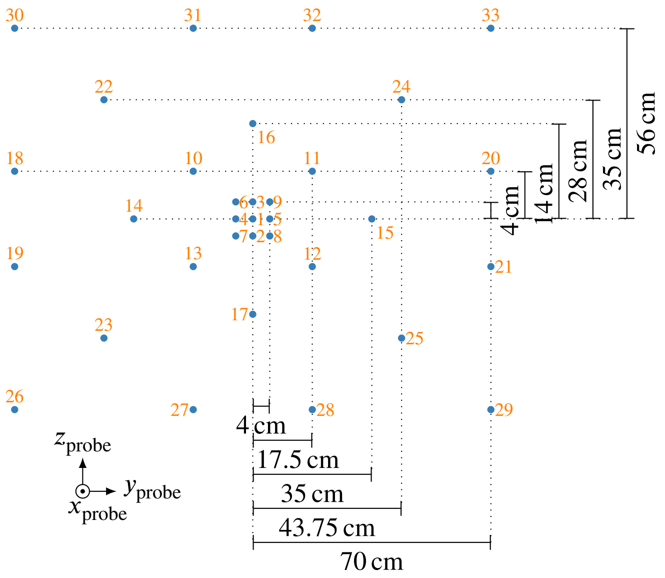

Fig. 9.17.: Positions of the probes in the four measurement planes of the RUAG S-band measurements [Knapp 2019c].

truncated at $t_1 = 35\,\text{ns}$, signals in the third region with $d_2 < d < d_3$ were truncated at $t_3 = 36\,\text{ns}$, and the remaining signals with $d > d_3$ were truncated at $t_1 = 38\,\text{ns}$.

The virtual array signal was synthesized according to

$$S_{12,\text{array}} = \sum_{k=1}^{120} \alpha_k S_{12,k}\,, \tag{9.3}$$

where $S_{12,k}$ is the measured signal of the probe at the kth probe position. The linear coefficients $\alpha_k \in \mathbb{C}$ were found by solving the minimization problem [Mauermayer 2015]

$$\min_{\alpha_k} \frac{1}{2} \iint\limits_{S_{\text{aut}}} \left\| \left(\boldsymbol{E}_{\text{tar}} - \sum_{k=1}^{120} \alpha_k \boldsymbol{E}_{\text{pro},k} \right) \Big|_{\text{tan}} \right\|^2 \mathrm{d}a + \frac{1}{2} \iint\limits_{S_{\text{ech}}} \left\| \sum_{k=1}^{120} \alpha_k \boldsymbol{E}_{\text{pro},k} \Big|_{\text{tan}} \right\|^2 \mathrm{d}a\,, \tag{9.4}$$

where $\boldsymbol{E}_{\text{pro},k}$ denotes the radiated field from the probe at the kth position, $\boldsymbol{E}_{\text{tar}}$ is the target field distribution one wants to synthesize and S_{aut} and S_{ech} are surfaces denoting the AUT and echo location, respectively. The target field at the AUT resembles a plane wave incident from the central probe position. At the echo location, the magnitude of the target field is set to zero. The resulting array field pattern is shown in Fig 9.18 and compared to a single DRH18 probe and a virtual array resulting from a “matched filter” choice of coefficients according to

$$\alpha_k = \frac{\mathrm{e}^{\mathrm{j}k_0 d_k}}{d_k}\,, \tag{9.5}$$

where d_k is the distance of the kth probe position to the measurement sphere center. The matched filter coefficients are very similar to the standard beam forming coefficients from Section 8.3.

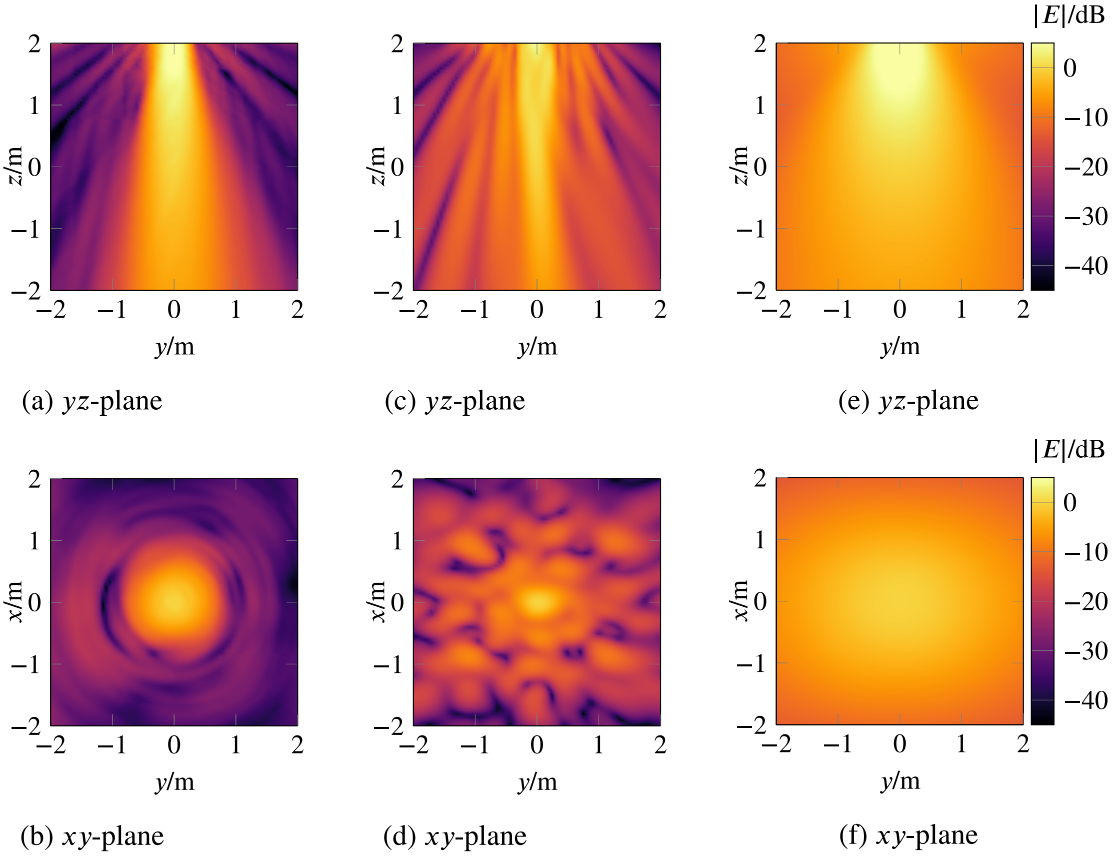

(a) *yz*-plane (c) *yz*-plane (e) *yz*-plane

(b) *xy*-plane (d) *xy*-plane (f) *xy*-plane

Fig. 9.18.: Synthesized virtual array field in the AUT coordinate system in (a) and (b) compared to the array field with matched filter coefficients in (c) and (d) and the single DRH18 pattern in (e) and (f). The AUT is positioned around the coordinate origin. [Knapp 2019c]. ©2019, IEEE

It can be seen that the synthesized virtual array has a well focused beam toward the AUT volume and the metallic walls located at the borders of the depicted spatial region are not illuminated much. In contrast to this, the single DRH18 probe illuminates the AUT as well as the echoes and the matched filter virtual array shows a directive beam toward the AUT but has many side lobes.

Figures 9.19 and 9.20 show the retrieved co- and cross-polar circular polarizations of the retrieved FF magnitude pattern of the RUAG S-band antenna in the $\varphi = 0^\circ$-cut at 2.3 GHz after all processing steps compared to a reference measurement obtained in the anechoic chamber after the Mosquito chamber had been disassembled. The componentwise magnitude deviation

$$\epsilon(\vartheta, \varphi) = \left| \frac{\left|E_{\text{ret.}}(\vartheta, \varphi)\right|}{\left|E_{\text{ret.,max}}\right|} - \frac{\left|E_{\text{ref.}}(\vartheta, \varphi)\right|}{\left|E_{\text{ref.,max}}\right|} \right| \tag{9.6}$$

does not exceed −25 dB and is below −30 dB for most directions in the co-polar as well as the cross-polar component, showing that the FF pattern can be reconstructed reasonably well given the harsh measurement conditions in the strongly reflective environment.

In comparison, Figs. 9.21 and 9.22 show the retrieved (circular) co- and cross-polar FF magnitude patterns of the RUAG S-band antenna in the $\varphi = 0^\circ$-cut at 2.3 GHz after time gating only (single probe in the center of the first measurement plane) and Figs. 9.23 and 9.24 show

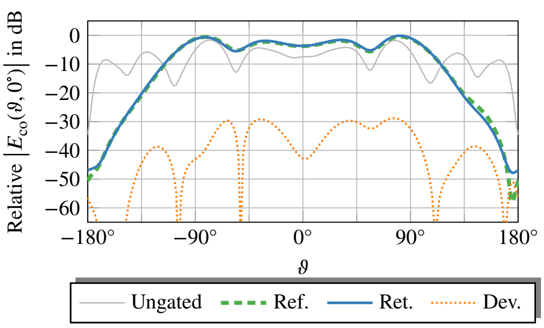

Fig. 9.19.: Co-polar component in the $\varphi = 0°$-cut retrieved FF of the RUAG S-band antenna after time gating and virtual array beam forming [Knapp 2019c]. ©2019, IEEE

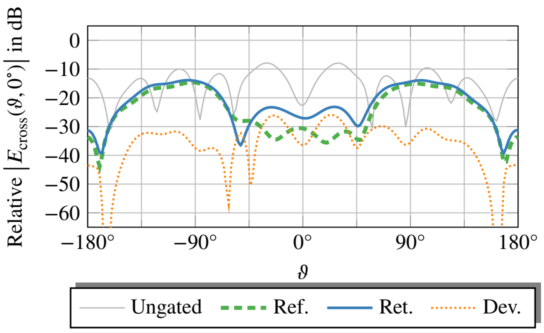

Fig. 9.20.: Cross-polar component in the $\varphi = 0°$-cut retrieved FF of the RUAG S-band antenna after time gating and virtual array beam forming [Knapp 2019c]. ©2019, IEEE

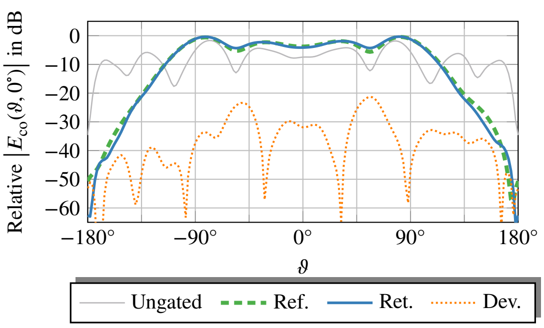

Fig. 9.21.: Co-polar component in the $\varphi = 0°$-cut retrieved FF of the RUAG S-band antenna after time gating [Knapp 2019c]. ©2019, IEEE

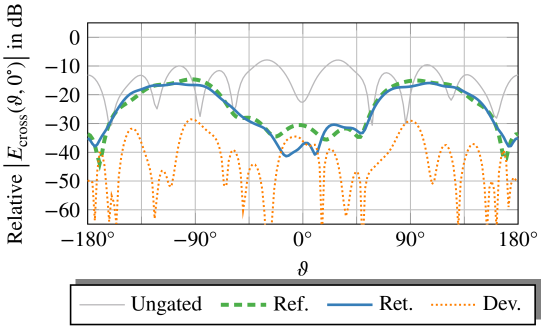

Fig. 9.22.: Cross-polar component in the $\varphi = 0°$-cut retrieved FF of the RUAG S-band antenna after time gating [Knapp 2019c]. ©2019, IEEE

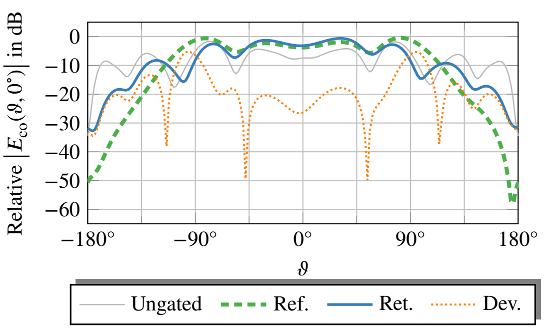

Fig. 9.23.: Co-polar component in the $\varphi = 0°$-cut retrieved FF of the RUAG S-band antenna after virtual array beam forming [Knapp 2019c]. ©2019, IEEE

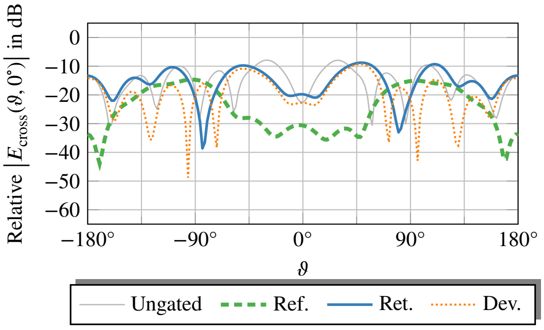

Fig. 9.24.: Cross-polar component in the $\varphi = 0°$-cut retrieved FF of the RUAG S-band antenna after virtual array beam forming [Knapp 2019c]. ©2019, IEEE

the retrieved co- and cross-polar circular polarizations of the retrieved FF magnitude pattern in the $\varphi = 0^{\circ}$-cut at 2.3 GHz after virtual array beam forming only (the measured S_{12}-parameters were utilized directly without the time gating step). Both methods show a clear improvement in the accuracy of the retrieved patterns as compared to the case without any particular echo suppression[3]. Time gating only yields better results than virtual array beam forming only. This is no surprise, as 1001 frequency samples were used for time gating, as compared to only 120 different probe positions for building the virtual array. Nevertheless, if only time gating is used, the deviation between the retrieved FF magnitude and the reference is up to −20 dB – i.e., approximately 10 dB worse than the largest deviation for the retrieved FFs when time gating was combined with virtual array beam forming in Figs. 9.19 and 9.20. The best results are only obtained, when time gating of the measured signals is combined with virtual array beam forming.

9.2.2. Measurements with the DRH400 Antenna

The reconstruction process turns out to be very sensitive to the exact choices of the parameters for beam forming or time gating. The problem with beam forming in this strongly reflective environment is that the location of the echo sources which contribute the most to the distortions are not known and can in principle be arbitrarily located over the metallic walls. Thus, it is not easily possible to predict where it is best to enforce deep nulls in the shaped beam of the synthesized array. Forcing the pattern to zero everywhere on the wall is not exactly possible and modest adjustments of the pattern can lead to several dB difference in the deviation of the reconstructed patterns from the reference.

The problem with time gating is to delicately balancing the truncation of useful and undesired signal components. If the signal is truncated too early, useful signal components which belong to the desired free-space impulse response may be removed. When the truncation time is too late, the signal is already distorted by the echoes. For every probe position, the traveling time of the LOS signal between the AUT and the probe varies as well as the arrival time of the first echo contribution. The path length difference between the useful and the scattered signals depends on the probe position, making the determination of the best time gate a hard task.

For an investigation of the influences of different virtual arrays and different time gates on the reconstructed pattern, measurements with a DRH400 horn antenna were carried out in the Mosquito chamber and reported in [Knapp 2019a]. The measurements were obtained in the same frequency band — from 1.5 GHz to 3.5 GHz — as the RUAG S-band measurements.

Influence of Different Time Gates

First, the influence of different time gates was investigated. To this end, a full spherical measurement with an equiangular sampling step of $\Delta\vartheta = \Delta\varphi = 2.5^{\circ}$ was obtained with the probe at a distance $z_1 = 2.664\,\mathrm{m}$ from the AUT rotation center. The measured S_{12}-parameter at all measurement positions was time gated before the data was further processed. The time gating method used for the processing of the DRH400 measurements is a slightly modified version of

---

[3] Of course, even if no particular echo suppression method is applied, echo contributions are effectively filtered by the localized source model of the AUT. Only fields which are in agreement with currents on the conformal Huygens surface around the AUT are reconstructed.

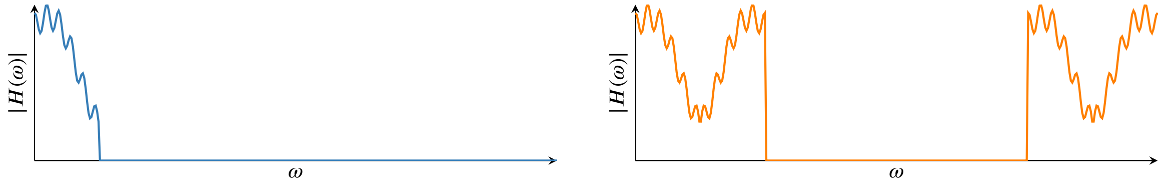

(a) Conventional zero padding (b) Appended in reversed order and repeated at end

Fig. 9.25.: Comparison between conventional zero padded frequency domain signal and the altered frequency domain signal used in this measurement [Knapp 2019a]. ©2019, IET

the direct IFFT-based method and was heuristically motivated[4].

Before the frequency-domain sequence for every measurement point was transformed into time domain, a linear phase term of the form $e^{j\omega t_{\text{shift}}}$ was multiplied to the measured frequency-domain samples, leading to an effective time shift of the resulting time domain sequence. The shift time t_{shift} was determined in a preliminary step from a highly oversampled time-domain sequence (obtained by a zero-padded frequency domain sequence, where the zero sequence was 49 times longer than the originally measured spectral sequence), such that the maximum peak of the time domain sequence appears at $t = 0$. The same time shift was thereafter used for all measurement positions with the same probe position. Furthermore, the frequency sequence was appended to itself in reversed order, before it was zero padded and repeated in the end. The relation between a conventional zero padding of the frequency domain data and the altered frequency domain signal which was used for this measurement is shown in Fig. 9.25.

After the reconstructed time-domain signal was truncated after the truncation time t_{stop}, the spectral samples at the measured frequencies were retrieved, using an FFT and the phase shift was reversed. The resulting frequency domain data for the measurement position $\vartheta = \varphi = 0^\circ$ before and after time gating with the conventional and the altered time gating method can be seen in Fig. 9.26 for an exemplary rectangular time gate which was non-zero for times between 17 ns to 38 ns. Away from the band edges, both time gating methods yield very similar results, while the conventional time gating method shows ringing effects at the band edges. The corresponding time-domain signal (related to the frequency domain data by an IFFT) is shown in Fig. 9.27, where it can be seen that both time gating methods lead to a similar time domain sequence, in particular in the neighborhood of the first peak. The time domain sequence from both time gating methods is not exactly zero outside the gating window because the sampling rate for the gating was different as the sampling in Fig. 9.27 and in the process, the data at the uninteresting frequencies was discarded. The alternative time gating does not suppress the signal outside the time window as much as the conventional time gating, but the ringing effects at the band edges are not as prominent.

The stop time t_{stop} of the time gate was varied from 41 ns to 47 ns, while the start time was kept at 17 ns (i.e., 15.5 ns before the signal peak at 32.5 ns). The influence of the time gate was quantified by reconstructing equivalent AUT currents on a conformal Huygens surface from the

---

[4] The resulting time gated version of the samples did not show a prominent ringing effect at the band edges for these particular data and was, thus, preferred over conventional time gating for this measurement. Apart from the differences at the band edges, the altered and the conventional time gating methods perform very similar.

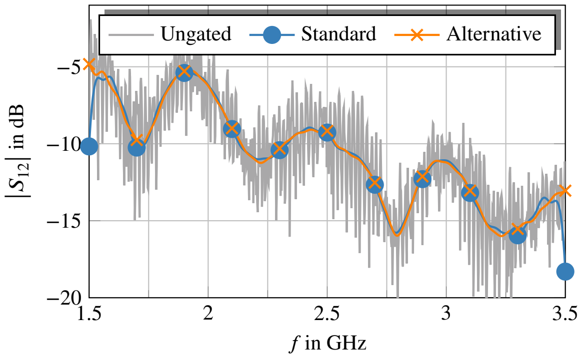

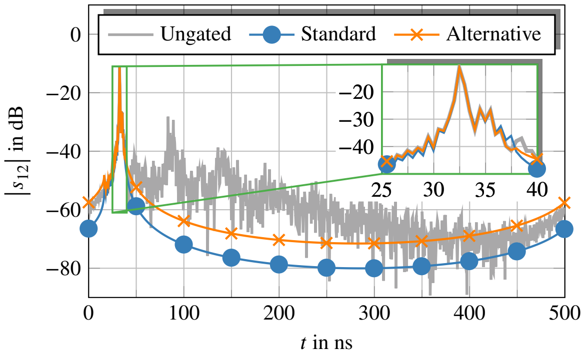

Fig. 9.26.: Comparison between the ungated S_{12}-parameter in frequency domain and the time gated versions from the conventional and alternative time gating methods [Knapp 2019a]. ©2019, IET

Fig. 9.27.: Comparison between the ungated s_{12}-parameter in time domain and the time gated versions from the conventional and alternative time gating methods [Knapp 2019a]. ©2019, IET

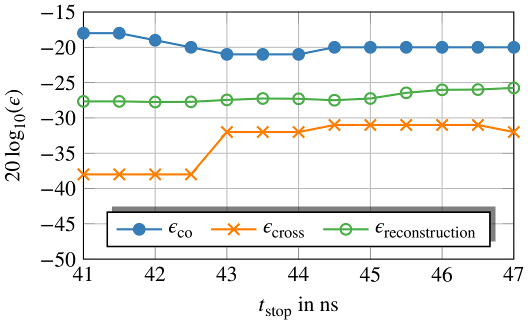

Fig. 9.28.: Maximum FF magnitude deviation and reconstruction deviation dependent on the truncation time of the time gate. The plot is based on the data of Table 1 in [Knapp 2019a].

time gated signals at 3.4 GHz, which is relatively close to the largest measured frequency (i.e., 3.5 GHz) and comparing the resulting FFs to a reference obtained in an anechoic environment. The frequency of 3.4 GHz is close to the edge of the measured frequency band and can be regarded as a particularly tough challenge for time gating. The maximum magnitude deviation according to (9.6) for the co-polarized (ϵ_{co}) and cross-polarized ($\epsilon_{\mathrm{cross}}$) component for the different time gates can be seen in Fig. 9.28 along with the reconstruction deviation $\|\boldsymbol{b} - \boldsymbol{A}\boldsymbol{x}\|/\|\boldsymbol{b}\|$ of the GMRES solver after 50 iterations. Since no good estimate for the expected error level is known a priori due to the unknown echo influence, a suitable stopping criterion cannot be based on the reconstruction deviation alone. A stopping criterion based on the residual $\left\|\boldsymbol{A}^{\mathrm{H}}\boldsymbol{b} - \boldsymbol{A}^{\mathrm{H}}\boldsymbol{A}\boldsymbol{x}\right\|$ often leads to unnecessary many iterations. A fixed number of 50 iterations is therefore reasonable and usually more than sufficient for measurements of an AUT of this size. The curves in Fig. 9.28 show the trade-off which has to be made with time gating. On the one hand, when the time sequence is truncated too late — the effect is particularly visible for truncation times later than 45 ns in this example — echo influences distort the measurements leading to signal contributions which cannot

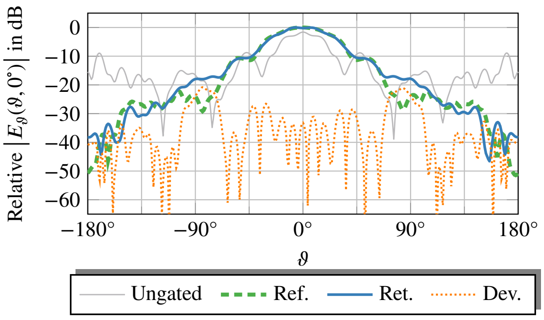

Fig. 9.29.: Co-polar component in the $\varphi = 0°$-cut of the retrieved FF of the DRH400 antenna after time gating [Knapp 2019a]. ©2019, IET

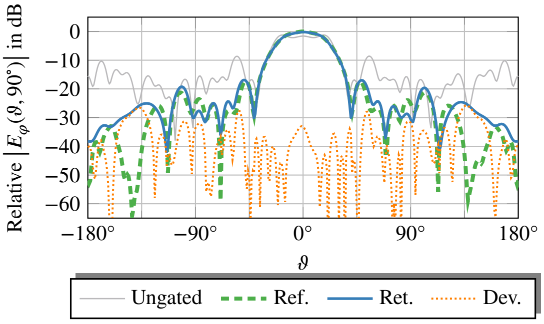

Fig. 9.30.: Co-polar component in the $\varphi = 90°$-cut of the retrieved FF of the DRH400 antenna after time gating [Knapp 2019a]. ©2019, IET

be reconstructed by the sources in the limited AUT volume. Consequently, the reconstruction deviation ϵ_{rec} increases for later truncation times. On the other hand, when the truncation time is too early, the reconstruction deviation ϵ_{rec} is lower, indicating that the measurements can be more accurately expressed by currents in the AUT volume, but the deviations ϵ_{co} to the anechoic case in the co-polar FF components are larger for too early truncation times ($t_{\text{stop}} < 43\,\text{ns}$), indicating that significant portions of the free-space impulse response of the AUT were discarded. Similar trends can be found at the other frequencies more in the center of the measured frequency band, where also the conventional time gating method leads to comparable results.

The resulting co-polar components of the retrieved FF at 3.4 GHz in the $\varphi = 0°$- and $\varphi = 90°$-cuts are compared to the reference in Figs. 9.29 and 9.30 after time gating with a stop time $t_{\text{stop}} = 43.5\,\text{ns}$, which led to the smallest maximum deviation. Compared to the ungated reconstruction, where the measured data at 3.4 GHz was directly fed into FIAFTA, the reconstruction of the radiated fields after time gating is relatively successful with a maximum deviation of around −21 dB in the regions of $\vartheta = \pm 90°$ in the $\varphi = 0°$-cut. In particular the obvious deviations at $\vartheta = \pm 90°$ in the $\varphi = 0°$ cut were successfully removed by the virtual array spatial filtering.

Influence of Different Virtual Arrays

In Section 9.2.1, it has already been shown that combining time gating with virtual beam forming from Section 8.3 can lead to acceptable reconstruction results, even in strongly reflective environments such as the Mosquito chamber. In this section, the role of the number of array elements for the virtual beam forming is investigated. This investigation has first been presented in [Knapp 2019a].

To be able to form virtual receiving arrays for every measurement position, full spherical measurements were obtained not only with the probe in its central position but with a total of different 110 probe positions distributed over four measurement planes with distances $z_1 = 2.664\,\text{m}$, $z_2 = 2.704\,\text{m}$, $z_3 = 2.784\,\text{m}$, and $z_4 = 2.914\,\text{m}$ to the AUT rotation center. The 35 different probe positions in the first plane with $z_1 = 2.664\,\text{m}$ were differently distributed than the 25 different probe positions in the remaining three planes. The probe positions in the first plane at $z_1 = 2.664\,\text{m}$ are depicted in Fig. 9.31 and the probe positions in the remaining three

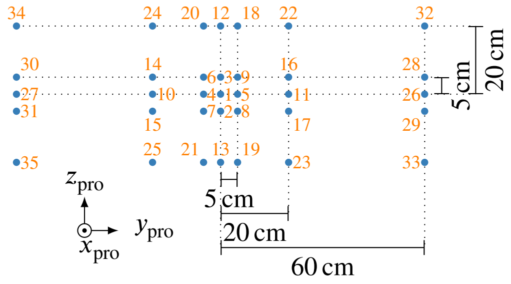

Fig. 9.31.: Positions of the probes in the first measurement plane of the DRH400 measurements [Knapp 2019a]. ©2019, IET

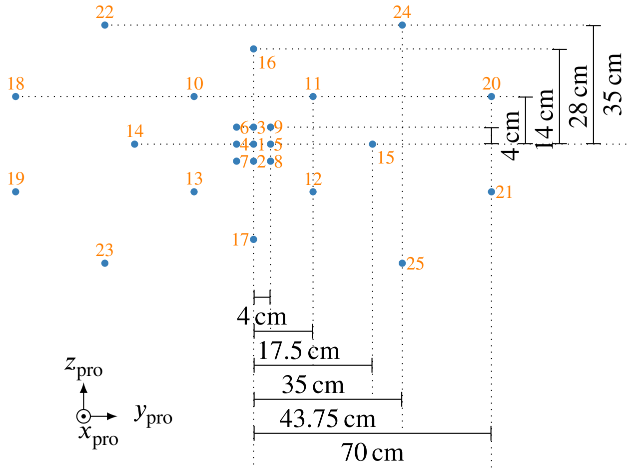

Fig. 9.32.: Positions of the probes in the last three measurement planes of the DRH400 measurements [Knapp 2019a] ©2019, IET.

planes are depicted in Fig. 9.32, where the probe position number 1 lies on the z-axis of the AUT coordinate system for the reference position $\vartheta = \varphi = 0°$ in every plane.

For every probe position, the S_{12}-parameter was sampled with an equiangular sampling step of $\varDelta\vartheta = \varDelta\varphi = 2.5°$. The measured S_{12} were time gated with a gating window dependent on the probe position. The gating window was chosen with respect to the AUT reference position at $\vartheta = \varphi = 0°$ for every probe position such that the time-domain signal was set to zero for times earlier than 10 ns before the strongest peak or later than 15 ns after the strongest peak in the time-domain signal of the co-polar component. The same time gate was used for all measurement positions with the same probe location. The time gate was deliberately chosen to be non-zero for a longer duration than in the previous case to collect more of the useful AUT free-space response (but also more undesired echo contributions). Ideally, the additional undesired echo influences can be cured with the additional help of spatial filtering being supported by virtual array beam forming.

Different collections of probes from the four planes were used to form a virtual array with matched filter coefficients

$$\alpha_k = \frac{\mathrm{e}^{\mathrm{j}k_0 d_k}}{d_k} \tag{9.7}$$

for the synthesis of the virtual array. Table 9.1 summarizes the residual of the iterative solver and the achieved deviations from the reference with the different probe configurations, where the numbers denote, how many probes were used from each plane, respectively (e.g., “17/9/5/1” means that 17 probes were used in plane z_1, nine probes were used in plane z_1, five probes were used in plane z_3, and one probe was used in plane z_4.). In every plane, the probe positions closer to the center position were considered first, according to the numbering scheme in Figs. 9.31 and 9.32. The data from Tab. 9.1 is also visualized in Fig. 9.33. The reconstruction accuracy does not always benefit from a larger number of probe locations. While the “25/17/17/17”-configuration (76 probe locations) shows the smallest maximum error in the co-polar component, the accuracy

Measurement configuration	Number of probes	Maximum co-polar FF deviation ϵ_{FF}	Maximum cross-polar FF deviation ϵ_{FF}	Reconstruction deviation $\|\boldsymbol{b} - \boldsymbol{A}\boldsymbol{x}\|/\|\boldsymbol{b}\|$
1/0/0/0	1	−20 dB	−31 dB	0.0520
5/0/0/0	5	−25 dB	−34 dB	0.0320
9/0/0/0	9	−26 dB	−37 dB	0.0267
17/0/0/0	17	−26 dB	−36 dB	0.0263
25/0/0/0	25	−25 dB	−30 dB	0.0342
31/0/0/0	31	−23 dB	−31 dB	0.0299
35/0/0/0	35	−24 dB	−30 dB	0.0312
1/1/1/1	4	−26 dB	−38 dB	0.0288
5/5/0/0	10	−25 dB	−34 dB	0.0331
5/5/5/5	20	−25 dB	−39 dB	0.0246
9/1/1/1	12	−26 dB	−38 dB	0.0254
9/5/0/0	14	−26 dB	−36 dB	0.0289
9/5/1/0	15	−26 dB	−34 dB	0.0280
9/5/5/5	24	−24 dB	−40 dB	0.0242
9/9/9/9	36	−25 dB	−39 dB	0.0243
17/9/5/1	34	−26 dB	−39 dB	0.0270
17/9/9/9	46	−26 dB	−36 dB	0.0258
25/17/17/17	76	−28 dB	−36 dB	0.0294
35/25/25/25	110	−23 dB	−34 dB	0.0259

Tab. 9.1.: Reconstruction deviation for different probe configurations [Knapp 2019a].

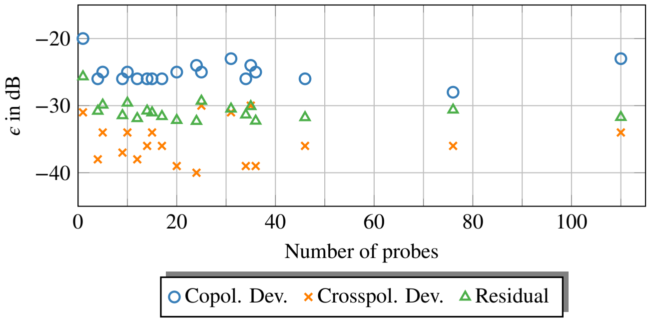

Fig. 9.33.: Reconstruction deviation for different probe configurations dependent on the number of probes [Knapp 2019a].

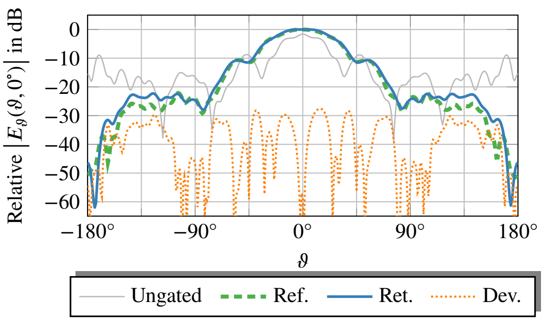

Fig. 9.34.: Co-polar component in the $\varphi = 0°$-cut of the retrieved FF of the DRH400 antenna after time gating and virtual array beam forming [Knapp 2019a]. ©2019, IET

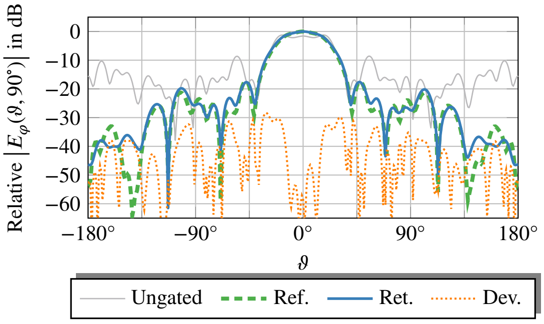

Fig. 9.35.: Co-polar component in the $\varphi = 90°$-cut of the retrieved FF of the DRH400 antenna after time gatingand virtual array beam forming [Knapp 2019a]. ©2019, IET

of the "35/25/25/25" (110 probe locations) is among the worst. Also the reconstruction deviation $\|\boldsymbol{b} - \boldsymbol{A}\boldsymbol{x}\|/\|\boldsymbol{b}\|$ is not a reliable indicator for an accurate reconstruction of the AUT radiation. The reconstruction deviation is around −30 dB for all probe configurations, independent of the achieved FF reconstruction. The overall lower reconstruction deviation indicates that the signal to echo ratio is increased in the measurement samples of the virtual array as compared to the only time gated case but the lower reconstruction deviation does not automatically translate into a better agreement of the reconstructed AUT fields and the reference. Using more probes for building a virtual array requires a better precision in the measurement setup as, e.g., the influence of positioning errors can increase with more probe positions. Furthermore, the more probes are used, the closer some of the probes come to the reflective chamber walls, making time gating less effective. Furthermore it has to be mentioned that neither the time gate nor the virtual array coefficients were optimally chosen. The chamber walls are inhomogeneously illuminated by the virtual array, similar to Figs. 9.20 (c) and (d). Using varying numbers of probes for the virtual array, it is hard to predict, where local intensity maxima of the array radiation coincide with locations of significant echo currents, thus, the influence of the echoes can vary in unpredictable manner.

The resulting co-polar components of the retrieved FF at 3.4 GHz in the $\varphi = 0°$- and $\varphi = 90°$-cuts are compared to the reference in Figs. 9.34 and 9.35 after time gating and virtual array beam forming with the "25/17/17/17"-configuration, which led to the smallest maximum deviation.

9.2.3. Measurements with the RUAG Ku-Band Antenna

Reconstructing the correct AUT pattern from measurements in the Mosquito chamber (or any comparable strongly reflective environment) becomes easier with increasing frequency (but obtaining accurate measurement samples and positioning data becomes more challenging). The reason for this can be found in the facts that antennas working in higher frequency bands usually have a larger absolute operational bandwidth and the separation between the AUT and the chamber walls in terms of wavelengths is larger. Furthermore, if two antennas have a comparable size, the antenna operating at the higher frequency usually has a more directive pattern.

To verify this intuition, spherical measurements of the RUAG Ku-Band antenna were obtained

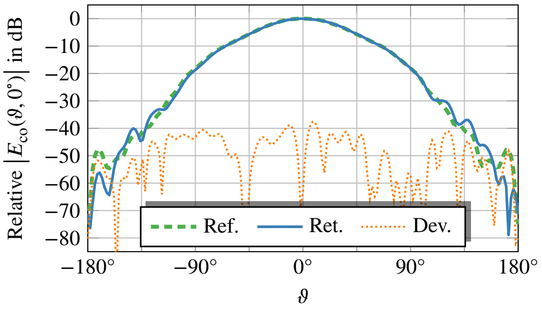

Fig. 9.36.: Co-polar component in the $\varphi = 0°$-cut retrieved FF of the RUAG Ku-band antenna after time gating and virtual beam forming [Knapp 2019c]. ©2019, IEEE

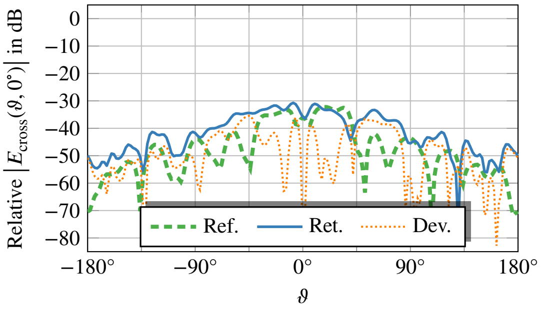

Fig. 9.37.: Cross-polar component in the $\varphi = 0°$-cut retrieved FF of the RUAG Ku-band antenna after time gating and virtual beam forming [Knapp 2019c]. ©2019, IEEE

in the Mosquito chamber from 11 GHz to 13 GHz with an equiangular sampling step of $\Delta\vartheta = \Delta\varphi = 3°$ [Knapp 2019c]. The probe locations were located in four planes with distances $z_1 = 2.664$ m, $z_2 = 2.670$ m, $z_3 = 2.714$ m, and $z_4 = 2.814$ m. In every plane, nine probe locations were used with an equidistant spacing of $\Delta x = \Delta y = 0.025$ m around the probe center position.

First, time gating was applied to the measurement data at every measurement position by truncating the time-domain signal which was obtained directly with an IFFT from the frequency sequence at 32.5 ns for probe locations with a distance $d < 2.72$ m to the AUT rotation center and at 33 ns for probe locations with $d > 2.72$ m.

A virtual probe array was formed at using the time gated S_{12}-parameters at 12.75 GHz with matched filter coefficients

$$\alpha_k = \frac{e^{jk_0 d_k}}{d_k} . \tag{9.8}$$

Due to the small number of probe coefficients, there was no considerable benefit of solving the minimization problem (9.4) because the resulting pattern was similar to the pattern obtained with the matched filtering coefficients. The measurement data of the virtual array was subsequently transformed into the FF. The resulting co-polar and cross-polar components for the $\varphi = 0°$ FF cuts can be seen in the Figs. 9.36 and 9.37, respectively.

The magnitude deviation does not much exceed −40 dB for the co-polar component and −35 dB for the cross-polar component despite the relatively small number (36) of utilized probe positions. This supports the intuition that the the separation of the desired AUT sources is simpler at higher frequencies.

9.3. Chapter Summary

In this chapter, time gating and frequency domain echo suppression capabilities have been combined in hybrid procedures to suppress the echo influences in challenging environments. First, time gating has been applied to the reconstructed AUT currents in a stationary AUT scenario to tackle mutual coupling effects between the AUT and the echo object. Conventional time gating of measured probe signals is not directly feasible in stationary AUT scenarios. Second, laborious measurement campaigns have been carried out in the anechoic chamber at TUM, which was transformed into the strongly reflective Mosquito chamber. It has been shown that the free-space radiation pattern of the AUT can be obtained with a reasonable accuracy if high effort is put into the collection and processing of large amounts of measurement data. The performed measurement campaign shows the possibilities of specialized echo suppression algorithms but also the price one has to pay in terms of measurement and processing effort.

10

Conclusion

Antenna measurements in echoic environments need a careful consideration of the specific characteristics of the scenario. In ideal anechoic measurement scenarios it makes no difference whether the individual measurement positions are reached by rotating the AUT or moving the probe whereas such a subtle difference has significant impact on measurements with echoes being present in the environment. The various scattering scenarios encountered in antenna NF measurements have been formally described in terms of spherical vector expansions and equivalent surface current formulations. A close analogy between both types of formulations for the fields in the antenna environment could be established which was essential for the unified discussion of the manifold echo suppression algorithms.

Based on the formal understanding of the underlying physics, it was shown that the echo influence differs in antenna measurement scenarios with either a stationary AUT or a stationary probe. In antenna measurements with a stationary AUT, the separability of the echo contributions from the desired AUT fields is determined mainly by the separation between the AUT and the echo volume. The dislocation of the AUT from the center of the measurement sphere does not influence the obtained results. Modal reconstruction methods are in many regards equivalent to current based approaches, but the current based approaches are much more flexible concerning the definition of the source geometry. Providing good a priori information about the AUT in form of a Huygens surface can help to filter all field contributions which are not in agreement with the limited source volume. Explicitly modeling the echo sources by introducing further source locations is almost always a good idea as long as no evanescent fields are generated by mutual interactions between the source domains (this implies a large enough separation between the respective source domains).

If the additional sources are assumed to be fixed to the AUT, the echo distortion in antenna measurement scenarios with a stationary probe can only partially be accounted for by additional sources[1]. The portion of the echo influence which can be accounted for by additional sources was called ghost contribution as it leads to additional unphysical sources being reconstructed (similar

---

[1] In chamber calibration techniques the additional echo influences are correctly and completely accounted for by additional sources for the probe.

to ghost targets in imaging applications). The ghost contributions can be unambiguously localized inside a certain torus spanning the same angle form the test zone center to the AUT as the probe spans to the echo location. If these ghost sources are explicitly reconstructed simultaneously with the AUT sources, improvements can be found in some cases but the reconstructed AUT fields into the direction of the torus may remain highly distorted due to unavoidable mutual interactions between the torus currents and the AUT currents. Moving the AUT further away from the rotation center leads to a larger separation between the AUT volume and the ghost torus and consequently to a (slow) decrease of the echo influences when the AUT is further dislocated from the rotation center. The orientation of the AUT plays an important role and sometimes the best way to mount an antenna is to point it directly toward the echo object.

Echo suppression algorithms must be carefully adapted to the situation at hand to be effective. The theoretical analysis culminated in the investigation of time and frequency domain echo suppression techniques, which were effectively combined to complement each other in order to enable antenna measurements even in challenging scattering scenarios. The developed methods are very flexible as they can efficiently handle irregularly distributed measurement samples and full probe correction thanks to the underlying equivalent current reconstruction based on FIAFTA. However, the main focus of this thesis was not laid on computational efficiency but on bringing the echo suppression capabilities to their limits. Aside from many numerical and real measurement examples which illustrate the theoretical analysis throughout the thesis, in particular the measurement campaign inside the Mosquito chamber — a purposefully challenging measurement — is of interest for the evaluation of the capabilities of post processing echo suppression methods. It was shown that under enormous measurement and post processing effort one can reconstruct the free-space radiated fields of an AUT from measurements in an essentially metallic chamber to accuracy levels which are almost comparable with anechoic measurements. This delicate reconstruction task was only possible by combining time gating and frequency-domain echo suppression methods.

This thesis can serve as the theoretical foundation for antenna measurements in almost arbitrary echoic measurement scenarios. It is now understood and has been demonstrated on examples how the different scenarios with either a stationary AUT or a stationary probe can be correctly modeled and how the undesired echo influences can be removed in rather general circumstances. Certainly, the field of echo suppression will see further advancements in the future, enabling a variety of new applications. For instance the possibility of combining phaseless antenna measurement techniques with echo suppression algorithms [Loredo 2011] can possibly lead to an even greater flexibility for antenna measurement applications. In any case, the powerful and flexible echo suppression methods come at the right time to supplement newly emerging measurement techniques such as unmanned aerial vehicle based antenna measurements, where the AUT fields are measured in-situ in the real working environment of the AUT, where echo suppression techniques are necessary to be able to translate the measured NFs into the desired FF distance.

A

Reciprocity Relation for the Antenna Receive Coefficient

In this Appendix, it is shown that the receive signal b of an antenna can be expressed as

$$b = \frac{c_{\text{aut}}}{2} \sum_{s=1}^{2} \sum_{n=1}^{N} \sum_{m=-n}^{n} (-1)^m \; \hat{\alpha}_{s,-m,n}^{(4),\text{tra}} \, {\alpha'}_{smn}^{(1)} \,, \tag{A.1}$$

where ${\alpha'}_{smn}^{(1)}$ are the expansion coefficients for the incident field and $\hat{\alpha}_{s,-m,n}^{(4),\text{tra}}$ are the normalized transmission coefficients for the transmitting antenna[1].

The starting point is the relation

$$b = \frac{c_{\text{aut}}}{2} \oiint_{S_1} \left(\hat{\boldsymbol{J}}_{\text{tra}} \cdot \boldsymbol{E}_{\text{ext}} - \hat{\boldsymbol{M}}_{\text{tra}} \cdot \boldsymbol{H}_{\text{ext}} \right) \mathrm{d}a = \frac{c_{\text{aut}}}{2} \oiint_{S_2} \left(\hat{\boldsymbol{E}}_{\text{tra}} \times \boldsymbol{H}_{\text{ext}} - \boldsymbol{E}_{\text{ext}} \times \hat{\boldsymbol{H}}_{\text{tra}} \right) \cdot \boldsymbol{n}_2 \, \mathrm{d}a \,, \tag{A.2}$$

with a spherical surface S_2 with radius r_2 and the normal vector $\boldsymbol{n}_2$ is pointing inwards (see Fig. 4.8.). The fields in the integral may be expanded using their spherical wave expansion leading to

$$\begin{aligned} b = & \frac{c_{\text{aut}}}{2} \oiint_{S_2} \Bigg[\left(k\sqrt{Z_0} \sum_{s=1}^{2} \sum_{n=1}^{N} \sum_{m=-n}^{n} \hat{\alpha}_{smn}^{(4),\text{tra}} \boldsymbol{F}_{smn}^{(4)} \right) \times \left(\mathrm{j} \frac{k}{\sqrt{Z_0}} \sum_{\sigma=1}^{2} \sum_{\nu=1}^{N} \sum_{\mu=-\nu}^{\nu} {\alpha'}_{\sigma\mu\nu}^{(1)} \boldsymbol{F}_{3-\sigma,\mu\nu}^{(1)} \right) \\ & - \left(k\sqrt{Z_0} \sum_{\sigma=1}^{2} \sum_{\nu=1}^{N} \sum_{\mu=-\nu}^{\nu} {\alpha'}_{\sigma\mu\nu}^{(1)} \boldsymbol{F}_{\sigma\mu\nu}^{(1)} \right) \times \left(\mathrm{j} \frac{k}{\sqrt{Z_0}} \sum_{s=1}^{2} \sum_{n=1}^{N} \sum_{m=-n}^{n} \hat{\alpha}_{smn}^{(4),\text{tra}} \boldsymbol{F}_{3-s,mn}^{(4)} \right) \Bigg] \cdot \boldsymbol{n}_2 \, \mathrm{d}a \end{aligned} \tag{A.3}$$

---

[1] Even though a similar derivation can be found in [Hansen 1988], it is worth to go through the derivation because of the different time convention which was used in this work.

$$
\begin{aligned}
&= \mathrm{j}k^2\,\frac{c_{\mathrm{aut}}}{2}\sum_{s=1}^{2}\sum_{n=1}^{N}\sum_{m=-n}^{n}\;\sum_{\sigma=1}^{2}\sum_{\nu=1}^{N}\sum_{\mu=-\nu}^{\nu}\hat{\alpha}^{(4),\mathrm{tra}}_{smn}\,{\alpha'}^{(1)}_{\sigma\mu\nu} \\
&\qquad\qquad \times \oiint_{S_2}\left[\boldsymbol{F}^{(4)}_{smn}\times\boldsymbol{F}^{(1)}_{3-\sigma,\mu\nu}-\boldsymbol{F}^{(1)}_{\sigma\mu\nu}\times\boldsymbol{F}^{(4)}_{3-s,mn}\right]\cdot\boldsymbol{n}_2\,\mathrm{d}a \\
&= \mathrm{j}k^2\,\frac{c_{\mathrm{aut}}}{2}\sum_{s=1}^{2}\sum_{n=1}^{N}\sum_{m=-n}^{n}\;\sum_{\sigma=1}^{2}\sum_{\nu=1}^{N}\sum_{\mu=-\nu}^{\nu}\hat{\alpha}^{(4),\mathrm{tra}}_{smn}\,{\alpha'}^{(1)}_{\sigma\mu\nu} \\
&\qquad\qquad \times\int_{\varphi=0}^{2\pi}\int_{\vartheta=0}^{\pi}\left[\boldsymbol{F}^{(4)}_{smn}\times\boldsymbol{F}^{(1)}_{3-\sigma,\mu\nu}-\boldsymbol{F}^{(1)}_{\sigma\mu\nu}\times\boldsymbol{F}^{(4)}_{3-s,mn}\right]\cdot\boldsymbol{n}_2\,\left(r_2\right)^2\,\sin\vartheta\,\mathrm{d}\vartheta\,\mathrm{d}\varphi\,.
\end{aligned}
\tag{A.4}
$$

Using the identity [Hansen 1988, p. 331]

$$
\begin{aligned}
&\int_{\varphi=0}^{2\pi}\int_{\vartheta=0}^{\pi}\left[\boldsymbol{F}^{(c)}_{smn}(r,\vartheta,\varphi)\times\boldsymbol{F}^{(\gamma)}_{3-\sigma,\mu\nu}(r,\vartheta,\varphi)\right]\cdot\boldsymbol{e}_r\,\sin\vartheta\,\mathrm{d}\vartheta,\mathrm{d}\varphi \\
&=\begin{cases}\delta_{s\sigma}\,\delta_{m,-\mu}\,\delta_{n\nu}\,(-1)^m\,z^{(c)}(kr)\,\dfrac{1}{kr}\dfrac{\mathrm{d}}{\mathrm{d}\,(kr)}\left(kr\,z^{(\gamma)}_n(kr)\right) & \text{if } s=1\\[2ex] -\delta_{s\sigma}\,\delta_{m,-\mu}\,\delta_{n\nu}\,(-1)^m\,z^{(\gamma)}(kr)\,\dfrac{1}{kr}\dfrac{\mathrm{d}}{\mathrm{d}\,(kr)}\left(kr\,z^{(c)}_n(kr)\right) & \text{if } s=2\end{cases}
\end{aligned}
\tag{A.5}
$$

one obtains

$$
\begin{aligned}
b = -\mathrm{j}k^2\frac{c_{\mathrm{aut}}}{2}&\sum_{s=1}^{2}\sum_{n=1}^{N}\hat{\alpha}^{(4),\mathrm{tra}}_{s,-m,n}{\alpha'}^{(1)}_{smn}\,(-1)^m\,\left(r_2\right)^2 \\
&\times\left[z^{(1)}_n(kr)\,\frac{1}{kr}\frac{\mathrm{d}}{\mathrm{d}\,(kr)}\left(kr\,z^{(4)}_n(kr)\right)-z^{(4)}_n(kr)\,\frac{1}{kr}\frac{\mathrm{d}}{\mathrm{d}\,(kr)}\left(kr\,z^{(1)}_n(kr)\right)\right]\Bigg|_{r=r_2}
\end{aligned}
\tag{A.6}
$$

where the Wronskian is given as [Abramowitz 1964, p. 437] [Hansen 1988, p. 316]

$$
\begin{aligned}
\left[\frac{z^{(1)}_n(kr)}{kr}\frac{\mathrm{d}\left(kr\,z^{(4)}_n(kr)\right)}{\mathrm{d}\,(kr)}-\frac{z^{(4)}_n(kr)}{kr}\frac{\mathrm{d}\left(kr\,z^{(1)}_n(kr)\right)}{\mathrm{d}\,(kr)}\right] &= \left[\mathrm{j}_n(kr)\,\frac{\mathrm{dh}^{(2)}_n(kr)}{\mathrm{d}\,(kr)}-\mathrm{h}^{(2)}_n(kr)\,\frac{\mathrm{d}\,\mathrm{j}_n(kr)}{\mathrm{d}\,(kr)}\right] \\
&= (-\mathrm{j})\left[\mathrm{j}_n(kr)\,\frac{\mathrm{dn}_n(kr)}{\mathrm{d}\,(kr)}-\mathrm{n}_n(kr)\,\frac{\mathrm{dj}_n(kr)}{\mathrm{d}\,(kr)}\right] \\
&= \frac{-\mathrm{j}}{(kr)^2}\,.
\end{aligned}
\tag{A.7}
$$

Finally, we have

$$
b=\frac{c_{\mathrm{aut}}}{2}\sum_{s=1}^{2}\sum_{n=1}^{N}\sum_{m=-n}^{n}(-1)^m\,\hat{\alpha}^{(4),\mathrm{tra}}_{s,-m,n}\,{\alpha'}^{(1)}_{smn}\,. \tag{A.8}
$$

B

Translation Coefficients for the Spherical Wave Expansion

In this appendix, diagonalized spectral expressions for the spherical translation coefficients $T_{smn}^{\sigma\mu\nu}(\boldsymbol{R})$ and $\mathscr{T}_{smn}^{\sigma\mu\nu}(\boldsymbol{R})$ are derived which provide the relationships between the spherical wave coefficients of an electromagnetic field in two coordinate systems, centered at $\boldsymbol{r}_{01}$ and $\boldsymbol{r}_{02}$, respectively. The coordinate system centered at $\boldsymbol{r}_{01}$ is denoted as the primary coordinate system and the spherical expansion coefficients are assumed to be known in this coordinate system in the first place. The secondary coordinate system is shifted by $\boldsymbol{R}$ against the primary coordinate system, i.e., $\boldsymbol{R} = \boldsymbol{r}_{02} - \boldsymbol{r}_{01}$ and the spherical expansion coefficients in this secondary coordinate system shall be determined from the primary coefficients with the help of the translation operators.

Such expressions have been derived multiple times [Chew 2007; Wittmann 1988; Stein 1961; Kim 1996; Cruzan 1962; Dufva 2008; Chew 1993; Borghese 1980; Felderhof 1987; Danos 1965; He 2008; Chew 2008; Devaney 1974] and although the derivation shown here may be less rigorous than for example in [Chew 2008; He 2008; Dufva 2008], it is hopefully more approachable.

Two different cases depicted in Fig. B.1 and Fig. B.2 must be distinguished. In the first case depicted in Fig. B.1, the coordinate origins $\boldsymbol{r}_{01}$ and $\boldsymbol{r}_{02}$ of the primary and the secondary coordinate system are both located in the same spherical volume V_1 and the sources are either completely inside or outside of V_1. If the sources are all inside V_1, than the spherical expansion of the radiated fields is valid only in the source free region external to V_1 and will consist of purely outwards traveling waves (of type $c = 4$). We have

$$\boldsymbol{E}(\boldsymbol{r})\Big|_{\boldsymbol{r}\notin V_1} = k\sqrt{Z_\mathrm{F}}\sum_{s=1}^{2}\sum_{n=1}^{N}\sum_{m=-n}^{n}\alpha_{smn}^{(4)}\,\boldsymbol{F}_{smn}^{(4)}(\boldsymbol{r}) \tag{B.1}$$

for the primary expansion and

$$\boldsymbol{E}(\boldsymbol{r})\Big|_{\boldsymbol{r}\notin V_1} = k\sqrt{Z_\mathrm{F}}\sum_{\sigma=1}^{2}\sum_{\nu=1}^{\tilde{N}}\sum_{\mu=-\nu}^{\nu}\tilde{\alpha}_{\sigma\mu\nu}^{(4)}\,\boldsymbol{F}_{\sigma\mu\nu}^{(4)}(\boldsymbol{r}-\boldsymbol{R}) \tag{B.2}$$

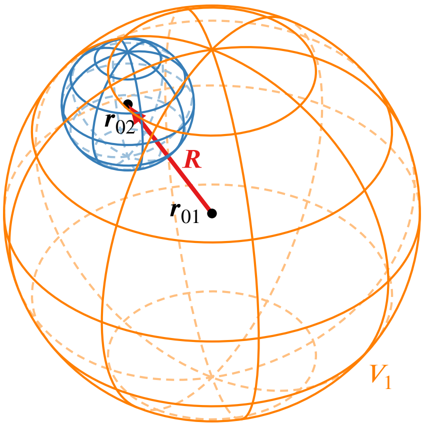

Fig. B.1.: The coordinate origins $\boldsymbol{r}_{01}$ and $\boldsymbol{r}_{02}$ of the primary and the secondary coordinate system are both located int the same spherical volume V_1. The sources for the considered fields are either completely inside or outside V_1.

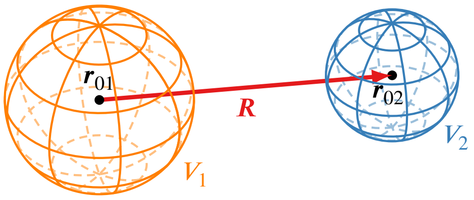

Fig. B.2.: The coordinate origins $\boldsymbol{r}_{01}$ and $\boldsymbol{r}_{02}$ of the primary and secondary coordinate system are the centers of two non-interacting spherical volumes V_1 and V_1. The sources for the considered fields are completely inside V_1.

for the secondary expansion. Naturally, both expansions are exactly true only if $N \to \infty$ and $\tilde{N} \to \infty$, but for all practically relevant cases, the mode expansions can be truncated at finite values. The expansion coefficients in (B.1) and (B.2) are related by

$$\tilde{\alpha}^{(4)}_{\sigma\mu\nu} = \sum_{s=1}^{2} \sum_{n=1}^{N} \sum_{m=-n}^{n} \alpha^{(4)}_{smn} \, T^{\sigma\mu\nu}_{smn}(\boldsymbol{R}) \tag{B.3}$$

and consequently

$$\boldsymbol{F}^{(4)}_{smn}(\boldsymbol{r}) = \sum_{\sigma=1}^{2} \sum_{\nu=1}^{\tilde{N}} \sum_{\mu=-\nu}^{\nu} T^{\sigma\mu\nu}_{smn}(\boldsymbol{R}) \; \boldsymbol{F}^{(4)}_{\sigma\mu\nu}(\boldsymbol{r} - \boldsymbol{R}) \; . \tag{B.4}$$

If all sources are located outside V_1 then the field expansion is only valid in the source free region V_1 and consists of purely incident fields (of type $c = 1$), i.e.,

$$\boldsymbol{E}(\boldsymbol{r})\Big|_{\boldsymbol{r}\in V_1} = k\sqrt{Z_\mathrm{F}} \sum_{s=1}^{2} \sum_{n=1}^{N} \sum_{m=-n}^{n} \alpha^{(1)}_{smn} \, \boldsymbol{F}^{(1)}_{smn}(\boldsymbol{r}) \tag{B.5}$$

or

$$\boldsymbol{E}(\boldsymbol{r})\Big|_{\boldsymbol{r}\in V_1} = k\sqrt{Z_\mathrm{F}} \sum_{\sigma=1}^{2} \sum_{\nu=1}^{\tilde{N}} \sum_{\mu=-\nu}^{\nu} \tilde{\alpha}^{(1)}_{\sigma\mu\nu} \, \boldsymbol{F}^{(1)}_{\sigma\mu\nu}(\boldsymbol{r} - \boldsymbol{R}) \; . \tag{B.6}$$

The expansion coefficients in (B.5) and (B.6) are related by

$$\tilde{\alpha}^{(1)}_{\sigma\mu\nu} = \sum_{s=1}^{2} \sum_{n=1}^{N} \sum_{m=-n}^{n} \alpha^{(1)}_{smn} \, T^{\sigma\mu\nu}_{smn}(\boldsymbol{R}) \tag{B.7}$$

and consequently

$$\boldsymbol{F}^{(1)}_{smn}(\boldsymbol{r}) = \sum_{\sigma=1}^{2} \sum_{\nu=1}^{\tilde{N}} \sum_{\mu=-\nu}^{\nu} T^{\sigma\mu\nu}_{smn}(\boldsymbol{R})\ \boldsymbol{F}^{(1)}_{\sigma\mu\nu}(\boldsymbol{r} - \boldsymbol{R})\ . \tag{B.8}$$

In both of the previous cases, the translation operator to translate the expansion coefficients from the primary to the secondary coordinate system (both have their origin in V_1) is given by the same expression $T^{\sigma\mu\nu}_{smn}(\boldsymbol{R})$.

If the coordinate origins $\boldsymbol{r}_{01}$ and $\boldsymbol{r}_{02}$ of the primary and the secondary coordinate system are the centers of two different non-intersecting spherical volumes V_1 and V_2 as depicted in Fig. B.2, the translation operator has a different form. Sources are assumed only in V_1. In this case, the field expansion in the primary coordinate system consists of only outwards traveling waves (type $c = 4$) and is valid only in the region external to V_1. The field expansion in the secondary coordinate system consists of only incident fields (type $c = 1$) and is valid only inside the source free volume V_2. We have

$$\boldsymbol{E}(\boldsymbol{r})\Big|_{\boldsymbol{r}\notin V_1} = k\sqrt{Z_\mathrm{F}} \sum_{s=1}^{2} \sum_{n=1}^{N} \sum_{m=-n}^{n} \alpha^{(4)}_{smn}\, \boldsymbol{F}^{(4)}_{smn}(\boldsymbol{r}) \tag{B.9}$$

and

$$\boldsymbol{E}(\boldsymbol{r})\Big|_{\boldsymbol{r}\in V_2} = k\sqrt{Z_\mathrm{F}} \sum_{\sigma=1}^{2} \sum_{\nu=1}^{\tilde{N}} \sum_{\mu=-\nu}^{\nu} \tilde{\alpha}^{(1)}_{\sigma\mu\nu}\, \boldsymbol{F}^{(1)}_{\sigma\mu\nu}(\boldsymbol{r} - \boldsymbol{R}) \tag{B.10}$$

for the expansions in the primary and secondary coordinate systems, respectively.

The translation operator between the spherical expansion coefficients in both coordinate system takes the form

$$\alpha^{(1)}_{\sigma\mu\nu} = \sum_{s=1}^{2} \sum_{n=1}^{N} \sum_{m=-n}^{n} \alpha^{(4)}_{smn}\, \mathscr{T}^{\sigma\mu\nu}_{smn}(\boldsymbol{R}) \tag{B.11}$$

in this case, where $\alpha^{(4)}_{smn}$ are the expansion coefficient of the radiated field in the primary coordinate system — centered at $\boldsymbol{r}_{01}$ — and $\alpha^{(1)}_{\sigma\mu\nu}$ are the expansion coefficients of the incident field in V_2 with respect to the coordinate origin at $\boldsymbol{r}_{02}$. Consequently tho field modes in the primary and secondary coordinate system are related by

$$\boldsymbol{F}^{(4)}_{smn}(\boldsymbol{r}) = \sum_{\sigma=1}^{2} \sum_{\nu=1}^{\tilde{N}} \sum_{\mu=-\nu}^{\nu} \mathscr{T}^{\sigma\mu\nu}_{smn}(\boldsymbol{R})\ \boldsymbol{F}^{(1)}_{\sigma\mu\nu}(\boldsymbol{r} - \boldsymbol{R})\ . \tag{B.12}$$

B.1. Preliminaries

Before going into the derivations for the formal expressions of $T^{\sigma\mu\nu}_{smn}(\boldsymbol{R})$ and $\mathscr{T}^{\sigma\mu\nu}_{smn}(\boldsymbol{R})$, some preparation is needed. First, it is noted that any incident field can be represented in terms of an incident plane wave spectrum by

$$\boldsymbol{E}(\boldsymbol{r}) = \oiint \tilde{\boldsymbol{E}}_\mathrm{in}\big(\hat{\boldsymbol{k}}\big)\, \mathrm{e}^{-\mathrm{j}\boldsymbol{k}\cdot\boldsymbol{r}}\, \mathrm{d}\hat{\boldsymbol{k}}\,, \tag{B.13}$$

or by an expansion into incident spherical waves [Devaney 1974] [Hansen 1988, p. 341]

$$\boldsymbol{E}(\boldsymbol{r}) = k\sqrt{Z_\mathrm{F}} \sum_{s=1}^{2} \sum_{n=1}^{N_\mathrm{obs}} \sum_{m=-n}^{n} \alpha_{smn}^{(1)} \boldsymbol{F}_{smn}^{(1)}(r,\vartheta,\varphi) \;. \tag{B.14}$$

The spherical wave expansion coefficients $\alpha_{\sigma\mu\nu}^{(1)}$ can be directly computed from the plane wave spectrum $\tilde{\boldsymbol{E}}_\mathrm{in}(\hat{\boldsymbol{k}})$ of the incident fields by

$$\alpha_{\sigma\mu\nu}^{(1)} = \frac{\mathrm{j}\,4\pi}{\sqrt{Z_\mathrm{F}}\,k} (-1)^{\sigma+\mu+\nu} \oiint \tilde{\boldsymbol{E}}_\mathrm{in}(\hat{\boldsymbol{k}}) \cdot \boldsymbol{K}_{\sigma,-\mu,\nu}^{(4)}(\hat{\boldsymbol{k}}) \;\mathrm{d}\hat{\boldsymbol{k}} \tag{B.15}$$

and conversely, the plane wave spectrum $\tilde{\boldsymbol{E}}_\mathrm{in}(\hat{\boldsymbol{k}})$ is obtained from the spherical wave expansion by

$$\tilde{\boldsymbol{E}}_\mathrm{in}(\hat{\boldsymbol{k}}) = \frac{k\sqrt{Z_\mathrm{F}}}{\mathrm{j}\,4\pi} \sum_{s=1}^{2} \sum_{n=1}^{N_\mathrm{obs}} \sum_{m=-n}^{m} \alpha_{smn}^{(1)} \boldsymbol{K}_{smn}^{(4)}(\hat{\boldsymbol{k}}) \;. \tag{B.16}$$

The transformation between the spherical wave expansion and the plane wave spectral domain will be the core of the derivations in the subsequent subsections.

In addition to the transformation between spherical and plane wave domain, the derivations will make use of the fact that

$$\nabla\nabla \frac{\mathrm{e}^{-\mathrm{j}k\,|\boldsymbol{r}-\boldsymbol{r}'|}}{4\pi\,|\boldsymbol{r}-\boldsymbol{r}'|} = \nabla'\nabla' \frac{\mathrm{e}^{-\mathrm{j}k\,|\boldsymbol{r}-\boldsymbol{r}'|}}{4\pi\,|\boldsymbol{r}-\boldsymbol{r}'|} \qquad \forall \boldsymbol{r} \neq \boldsymbol{r}' \;. \tag{B.17}$$

The validity of this identity will be shown in the following by explicitly working out the analytical expressions for the two expressions in (B.17). The derivation starts in a coordinate system where $\boldsymbol{r}' = \boldsymbol{0}$ and the general solution is obtained by shifting the derived solution along the vector $\boldsymbol{r}'$ afterwards. We have

$$\begin{aligned}
\nabla\nabla \frac{\mathrm{e}^{-\mathrm{j}k\,|\boldsymbol{r}-\boldsymbol{r}'|}}{4\pi\,|\boldsymbol{r}-\boldsymbol{r}'|}\bigg|_{\boldsymbol{r}'=\boldsymbol{0}} &= \nabla\nabla \left(\frac{\mathrm{e}^{-\mathrm{j}k\,|\boldsymbol{r}|}}{4\pi\,|\boldsymbol{r}|} \right) \\
&= \nabla\nabla \frac{\mathrm{e}^{-\mathrm{j}k\,r}}{4\pi\,r} \\
&= \nabla \left[\left(-\mathrm{j}k - \frac{1}{r} \right) \frac{\mathrm{e}^{-\mathrm{j}k\,r}}{4\pi\,r}\, \boldsymbol{e}_r \right] \\
&= \nabla \left[\left(-\mathrm{j}k - \frac{1}{r} \right) \frac{\mathrm{e}^{-\mathrm{j}k\,r}}{4\pi\,r} \right] \boldsymbol{e}_r + \left[\left(-\mathrm{j}k - \frac{1}{r} \right) \frac{\mathrm{e}^{-\mathrm{j}k\,r}}{4\pi\,r} \right] \nabla\boldsymbol{e}_r \\
&= \left(\frac{2}{r^2} + \frac{2\mathrm{j}k}{r} - k^2 \right) \frac{\mathrm{e}^{-\mathrm{j}k\,r}}{4\pi\,r}\, \boldsymbol{e}_r\boldsymbol{e}_r - \left[\left(\mathrm{j}k + \frac{1}{r} \right) \frac{\mathrm{e}^{-\mathrm{j}k\,r}}{4\pi\,r} \right] \frac{1}{r} \left(\mathbf{I} - \boldsymbol{e}_r\boldsymbol{e}_r \right) \\
&= \left(\frac{3}{r^2} + \frac{3\mathrm{j}k}{r} - k^2 \right) \frac{\mathrm{e}^{-\mathrm{j}k\,r}}{4\pi\,r}\, \boldsymbol{e}_r\boldsymbol{e}_r - \left(\frac{\mathrm{j}k}{r} + \frac{1}{r^2} \right) \frac{\mathrm{e}^{-\mathrm{j}k\,r}}{4\pi\,r}\, \mathbf{I} \,,
\end{aligned} \tag{B.18}$$

for the special case $\boldsymbol{r}' = \boldsymbol{0}$. In the derivation above, the identity $\nabla\boldsymbol{e}_r = \left(\mathbf{I} - \boldsymbol{e}_r\boldsymbol{e}_r \right)/r$ has been used[1]. The general solution is obtained from this special case by a translation along $\boldsymbol{r}'$. To this end, one has to perform the substitutions $r \rightarrow \left|\boldsymbol{r}-\boldsymbol{r}'\right|$ and $\boldsymbol{e}_r \rightarrow \left(\boldsymbol{r}-\boldsymbol{r}'\right) / \left(\left|\boldsymbol{r}-\boldsymbol{r}'\right|\right)$. Using the shorthand notations $\boldsymbol{R} = \boldsymbol{r}-\boldsymbol{r}'$ and $R = |\boldsymbol{R}|$, one obtains

$$\nabla\nabla \frac{\mathrm{e}^{-\mathrm{j}k\,|\boldsymbol{r}-\boldsymbol{r}'|}}{4\pi\,|\boldsymbol{r}-\boldsymbol{r}'|} = \left(\frac{3}{R^2} + \frac{3\,\mathrm{j}k}{R} - k^2\right) \frac{\mathrm{e}^{-\mathrm{j}kR}}{4\pi\,R}\,\frac{\boldsymbol{R}\boldsymbol{R}}{R^2} - \left(\frac{\mathrm{j}k}{R} + \frac{1}{R^2}\right) \frac{\mathrm{e}^{-\mathrm{j}kR}}{4\pi\,R}\,\mathbf{I}\,. \tag{B.19}$$

An almost identical derivation leads to

$$\nabla'\nabla' \left.\frac{\mathrm{e}^{-\mathrm{j}k\,|\boldsymbol{r}'-\boldsymbol{r}|}}{4\pi\,|\boldsymbol{r}'-\boldsymbol{r}|}\right|_{\boldsymbol{r}=\mathbf{0}} = \left(\frac{3}{r'^2} + \frac{3\,\mathrm{j}k}{r'} - k^2\right) \frac{\mathrm{e}^{-\mathrm{j}k\,r'}}{4\pi\,r'}\,\boldsymbol{e}_{r'}\boldsymbol{e}_{r'} - \left(\frac{\mathrm{j}k}{r'} + \frac{1}{r'^2}\right) \frac{\mathrm{e}^{-\mathrm{j}k\,r'}}{4\pi\,r'}\,\mathbf{I}\,, \tag{B.20}$$

for the special case $\boldsymbol{r} = \mathbf{0}$. The general solution is again obtained by a translation along the vector $\boldsymbol{r}$. One has to perform the substitutions[2] $r \rightarrow \left|\boldsymbol{r}'-\boldsymbol{r}\right|$ and $\boldsymbol{e}_r' \rightarrow \left(\boldsymbol{r}'-\boldsymbol{r}\right) / \left(\left|\boldsymbol{r}'-\boldsymbol{r}\right|\right) = -\boldsymbol{R}/R$. Thus, we have for the general solution

$$\nabla'\nabla' \frac{\mathrm{e}^{-\mathrm{j}k\,|\boldsymbol{r}-\boldsymbol{r}'|}}{4\pi\,|\boldsymbol{r}-\boldsymbol{r}'|} = \left(\frac{3}{R^2} + \frac{3\,\mathrm{j}k}{R} - k^2\right) \frac{\mathrm{e}^{-\mathrm{j}kR}}{4\pi\,R}\,\frac{\boldsymbol{R}\boldsymbol{R}}{R^2} - \left(\frac{\mathrm{j}k}{R} + \frac{1}{R^2}\right) \frac{\mathrm{e}^{-\mathrm{j}kR}}{4\pi\,R}\,\mathbf{I}\,, \tag{B.21}$$

establishing the equality in (B.17) at least for all observation points $\boldsymbol{r}$ which are well separated[3] from the source locations $\boldsymbol{r}'$ (this limitation is irrelevant in the current discussion as the interest lies in expressing the fields outside the source volume V_1).

Next, the scalar Green's function $\dfrac{\mathrm{e}^{-\mathrm{j}k\,|\boldsymbol{r}-\boldsymbol{r}'|}}{4\pi\,|\boldsymbol{r}-\boldsymbol{r}'|}$ in (B.42) is replaced by its well known spherical expansion[4] [Stratton 1941, p.414], [Abramowitz 1964, p.440], [Jin 2015, p.362], [Wittmann 1988]

$$\frac{\mathrm{e}^{-\mathrm{j}k\,|\boldsymbol{r}-\boldsymbol{r}'|}}{4\pi\,|\boldsymbol{r}-\boldsymbol{r}'|} = \begin{cases} -\mathrm{j}k \displaystyle\sum_{\ell=0}^{\infty} \frac{2\ell+1}{4\pi} \mathrm{j}_\ell\!\left(k\left|\boldsymbol{r}'\right|\right) \mathrm{h}_\ell(k\,|\boldsymbol{r}|)\, \mathrm{P}_\ell\!\left(\hat{\boldsymbol{r}}'\cdot\hat{\boldsymbol{r}}\right) & \text{for } \left|\boldsymbol{r}'\right| < |\boldsymbol{r}| \\ -\mathrm{j}k \displaystyle\sum_{\ell=0}^{\infty} \frac{2\ell+1}{4\pi} \mathrm{j}_\ell(k\,|\boldsymbol{r}|)\, \mathrm{h}_\ell\!\left(k\left|\boldsymbol{r}'\right|\right) \mathrm{P}_\ell\!\left(\hat{\boldsymbol{r}}'\cdot\hat{\boldsymbol{r}}\right) & \text{for } |\boldsymbol{r}| < \left|\boldsymbol{r}'\right| \end{cases} \tag{B.22}$$

---

[1] In spherical coordinates we have for the gradient of a vector field [Reddy 2013, p. 52] $\nabla\boldsymbol{F} = \dfrac{\partial F_r}{\partial r}\boldsymbol{e}_r\boldsymbol{e}_r + \dfrac{\partial F_\vartheta}{\partial r}\boldsymbol{e}_r\boldsymbol{e}_\vartheta + \dfrac{\partial F_\varphi}{\partial r}\boldsymbol{e}_r\boldsymbol{e}_\varphi + \dfrac{1}{r}\left(\dfrac{\partial F_r}{\partial\vartheta} - F_\vartheta\right)\boldsymbol{e}_\vartheta\boldsymbol{e}_r + \dfrac{1}{r}\left(F_r + \dfrac{\partial F_\vartheta}{\partial\vartheta}\right)\boldsymbol{e}_\vartheta\boldsymbol{e}_\vartheta + \dfrac{1}{r}\dfrac{\partial F_\varphi}{\partial\vartheta}\boldsymbol{e}_\vartheta\boldsymbol{e}_\varphi + \dfrac{1}{r\sin\vartheta}\left(\dfrac{\partial F_r}{\partial\varphi} - F_\varphi\sin\vartheta\right)\boldsymbol{e}_\varphi\,\boldsymbol{e}_r + \dfrac{1}{r\sin\vartheta}\left(\dfrac{\partial F_\vartheta}{\partial\varphi} - F_\varphi\cos\vartheta\right)\boldsymbol{e}_\varphi\,\boldsymbol{e}_\vartheta + \dfrac{1}{r\sin\vartheta}\left(F_r\sin\vartheta + F_\vartheta\cos\vartheta + \dfrac{\partial F_\varphi}{\partial\varphi}\right)\boldsymbol{e}_\varphi\,\boldsymbol{e}_\varphi\,.$

[2] Notice the subtle difference in the substitutions for $\boldsymbol{e}_r \rightarrow \boldsymbol{R}/R$ and $\boldsymbol{e}_{r'} \rightarrow -\boldsymbol{R}/R$. Therefore, while $\nabla\dfrac{\mathrm{e}^{-\mathrm{j}k\,|\boldsymbol{r}'-\boldsymbol{r}|}}{4\pi\,|\boldsymbol{r}'-\boldsymbol{r}|} \neq \nabla'\dfrac{\mathrm{e}^{-\mathrm{j}k\,|\boldsymbol{r}'-\boldsymbol{r}|}}{4\pi\,|\boldsymbol{r}'-\boldsymbol{r}|}$ it is nevertheless true that $\nabla\nabla\dfrac{\mathrm{e}^{-\mathrm{j}k\,|\boldsymbol{r}'-\boldsymbol{r}|}}{4\pi\,|\boldsymbol{r}'-\boldsymbol{r}|} = \nabla'\nabla'\dfrac{\mathrm{e}^{-\mathrm{j}k\,|\boldsymbol{r}'-\boldsymbol{r}|}}{4\pi\,|\boldsymbol{r}'-\boldsymbol{r}|}$.

[3] Since the $\boldsymbol{e}_r$ vector is not well defined at the origin, the derivation breaks down if $\boldsymbol{r} = \boldsymbol{r}'$.

[4] With $\displaystyle\sum_{p=-\ell}^{\ell} \mathrm{Y}^*_{\ell p}\!\left(\vartheta',\varphi'\right)\mathrm{Y}_{\ell p}(\vartheta,\varphi) = \frac{2\ell+1}{4\pi}\mathrm{P}_\ell\!\left(\hat{\boldsymbol{r}}'\cdot\hat{\boldsymbol{r}}\right)$ one can also find the alternative representation

$$\frac{\mathrm{e}^{-\mathrm{j}k\,|\boldsymbol{r}-\boldsymbol{r}'|}}{4\pi\,|\boldsymbol{r}-\boldsymbol{r}'|} = \begin{cases} -\mathrm{j}k \displaystyle\sum_{\ell=0}^{\infty}\sum_{p=-\ell}^{\ell} \mathrm{j}_\ell\!\left(k\left|\boldsymbol{r}'\right|\right) \mathrm{h}^{(2)}_\ell(k\,|\boldsymbol{r}|)\, \mathrm{Y}^*_{\ell p}\!\left(\vartheta',\varphi'\right)\mathrm{Y}_{\ell p}(\vartheta,\varphi) & \text{for } \left|\boldsymbol{r}'\right| < |\boldsymbol{r}| \\ -\mathrm{j}k \displaystyle\sum_{\ell=0}^{\infty}\sum_{p=-\ell}^{\ell} \mathrm{j}_\ell(k\,|\boldsymbol{r}|)\, \mathrm{h}^{(2)}_\ell\!\left(k\left|\boldsymbol{r}'\right|\right) \mathrm{Y}^*_{\ell p}\!\left(\vartheta',\varphi'\right)\mathrm{Y}_{\ell p}(\vartheta,\varphi) & \text{for } |\boldsymbol{r}| < \left|\boldsymbol{r}'\right| \end{cases}.$$

With [Stratton 1941, p. 410], [Rahola 1996]

$$\mathrm{j}_\ell(k\,|\boldsymbol{r}|)\,\mathrm{P}_\ell\big(\hat{\boldsymbol{r}}'\cdot\hat{\boldsymbol{r}}\big) = \frac{-1}{4\pi}\,(-\mathrm{j})^n \oiint \mathrm{e}^{\mathrm{j}\boldsymbol{k}\cdot\boldsymbol{r}}\mathrm{P}_\ell\big(\hat{\boldsymbol{k}}\cdot\hat{\boldsymbol{r}}'\big)\;\mathrm{d}\hat{\boldsymbol{k}} \tag{B.23}$$

one obtains the useful identity

$$\frac{\mathrm{e}^{-\mathrm{j}k\,|\boldsymbol{r}-\boldsymbol{r}'|}}{4\pi\,|\boldsymbol{r}-\boldsymbol{r}'|} = \begin{cases} \dfrac{\mathrm{j}k}{4\pi}\sum\limits_{\ell=0}^{\infty}(-\mathrm{j})^\ell\;(2\ell+1)\;\mathrm{h}_\ell^{(2)}(k\,|\boldsymbol{r}|)\oiint \mathrm{e}^{\mathrm{j}\boldsymbol{k}\cdot\boldsymbol{r}'}\;\mathrm{P}_\ell\big(\hat{\boldsymbol{k}}\cdot\hat{\boldsymbol{r}}\big)\;\mathrm{d}\hat{\boldsymbol{k}} & \text{for } |\boldsymbol{r}'|<|\boldsymbol{r}| \\ \dfrac{\mathrm{j}k}{4\pi}\sum\limits_{\ell=0}^{\infty}(-\mathrm{j})^\ell\;(2\ell+1)\;\mathrm{h}_\ell^{(2)}\big(k\,|\boldsymbol{r}'|\big)\oiint \mathrm{e}^{\mathrm{j}\boldsymbol{k}\cdot\boldsymbol{r}}\;\mathrm{P}_\ell\big(\hat{\boldsymbol{k}}\cdot\hat{\boldsymbol{r}}'\big)\;\mathrm{d}\hat{\boldsymbol{k}} & \text{for } |\boldsymbol{r}'|>|\boldsymbol{r}| \end{cases}, \tag{B.24}$$

which is sometimes called Gegenbauer addition theorem[5].

B.2. Translations Between Coordinate Origins in the Same Volume

Next, a diagonal spectral representation of the $T_{smn}^{\sigma\mu\nu}(\boldsymbol{R})$ translation coefficient will be derived corresponding to a translation of coordinate systems depicted in Fig. B.1, where the origins $\boldsymbol{r}_{01}$ and $\boldsymbol{r}_{02}$ of the primary and secondary coordinate system are both located in the same spherical volume V_1. First, the expression will be derived with sources being exclusively outside of V_1, such that the spherical wave expansions in both coordinate systems involve only incident field modes (type $c = 1$). Second, the expression for the translation coefficients will be derived for the radiated fields with all sources being located in V_1. The spherical wave expansion will only need outwards traveling waves (type $c = 4$) in both coordinate systems and although it turns out that the expression is the same as in the previous case, the derivation is considerably different.

B.2.1. Transformation of Incident Fields

Consider an incident field $\boldsymbol{E}$ in volume V_1 with a spherical wave expansion given by

$$\boldsymbol{E}(\boldsymbol{r}) = k\,\sqrt{Z_\mathrm{F}}\sum_{s=1}^{2}\sum_{n=1}^{N_\mathrm{obs}}\sum_{m=-n}^{n}\alpha_{smn}^{(1)}\boldsymbol{F}_{smn}^{(1)}(r,\vartheta,\varphi)\;, \tag{B.25}$$

where $\alpha_{smn}^{(1)}$ are the known expansion coefficients of the spherical wave expansion in the primary coordinate system centered at $\boldsymbol{r}_{01}$. Using a propagating plane wave expansion, the same incident field is expressed by

$$\boldsymbol{E}(\boldsymbol{r}) = \oiint \tilde{\boldsymbol{E}}_{\mathrm{in},01}\big(\hat{\boldsymbol{k}}\big)\,\mathrm{e}^{-\mathrm{j}\boldsymbol{k}\cdot(\boldsymbol{r}-\boldsymbol{r}_{01})}\,\mathrm{d}\hat{\boldsymbol{k}}\,, \tag{B.26}$$

where

$$\tilde{\boldsymbol{E}}_{\mathrm{in},01}\big(\hat{\boldsymbol{k}}\big) = \frac{k\,\sqrt{Z_\mathrm{F}}}{\mathrm{j}\,4\pi}\sum_{s=1}^{2}\sum_{n=1}^{N_\mathrm{obs}}\sum_{m=-n}^{m}\alpha_{smn}^{(1)}\boldsymbol{K}_{smn}^{(4)}\big(\hat{\boldsymbol{k}}\big) \tag{B.27}$$

---

[5] The name appears to originate from the fact that the Legendre polynomials are closely related to the Gegenbauer polynomials such that the addition theorem can be equivalently stated in terms of Gegenbauer polynomials.

is the plane wave spectrum of the incident field with respect to the origin at $\boldsymbol{r}_{01}$ (this is indicated by the subscript "01"). An alternative plane wave representation of the incident field can be given by

$$\boldsymbol{E}(\boldsymbol{r}) = \oiint \tilde{\boldsymbol{E}}_{\mathrm{in},02}\big(\hat{\boldsymbol{k}}\big)\, \mathrm{e}^{-\mathrm{j}\boldsymbol{k}\cdot(\boldsymbol{r}-\boldsymbol{r}_{02})}\, \mathrm{d}\hat{\boldsymbol{k}}\,, \tag{B.28}$$

where the plane wave spectrum $\tilde{\boldsymbol{E}}_{\mathrm{in},02}$ is now expressed with respect to the origin at $\boldsymbol{r}_{02}$ (this is indicated by the subscript "02"). The two alternative plane wave representations yield the same result for

$$\tilde{\boldsymbol{E}}_{\mathrm{in},02} = \tilde{\boldsymbol{E}}_{\mathrm{in},01}\, \mathrm{e}^{-\mathrm{j}\boldsymbol{k}\cdot(\boldsymbol{r}_{02}-\boldsymbol{r}_{01})} = \tilde{\boldsymbol{E}}_{\mathrm{in},01}\, \mathrm{e}^{-\mathrm{j}\boldsymbol{k}\cdot\boldsymbol{R}}\,, \tag{B.29}$$

such that a translational shift of the coordinate system along $\boldsymbol{r}_{02} - \boldsymbol{r}_{01} = \boldsymbol{R}$ is established by multiplying the spectral components of the incident plane wave spectrum with $\mathrm{e}^{-\mathrm{j}\boldsymbol{k}\cdot\boldsymbol{R}}$.

Finally, the plane wave representation of the incident field in the secondary coordinate system can be transformed into a spherical wave expansion having its origin at $\boldsymbol{r}_{02}$. The spherical expansion coefficients in the secondary coordinate system are given by

$$\begin{aligned}
\alpha^{(1)}_{\sigma\mu\nu} &= \frac{\mathrm{j}\,4\pi}{\sqrt{Z_\mathrm{F}}\,k}\,(-1)^{\sigma+\mu+\nu} \oiint \tilde{\boldsymbol{E}}_{\mathrm{in},02}\big(\hat{\boldsymbol{k}}\big) \cdot \boldsymbol{K}^{(4)}_{\sigma,-\mu,\nu}\big(\hat{\boldsymbol{k}}\big)\, \mathrm{d}\hat{\boldsymbol{k}} \\
&= \frac{\mathrm{j}\,4\pi}{\sqrt{Z_\mathrm{F}}\,k}\,(-1)^{\sigma+\mu+\nu} \oiint \tilde{\boldsymbol{E}}_{\mathrm{in},01}\big(\hat{\boldsymbol{k}}\big)\, \mathrm{e}^{-\mathrm{j}\boldsymbol{k}\cdot\boldsymbol{R}} \cdot \boldsymbol{K}^{(4)}_{\sigma,-\mu,\nu}\big(\hat{\boldsymbol{k}}\big)\, \mathrm{d}\hat{\boldsymbol{k}} \\
&= \frac{\mathrm{j}\,4\pi}{\sqrt{Z_\mathrm{F}}\,k}\,(-1)^{\sigma+\mu+\nu} \oiint \frac{k\sqrt{Z_\mathrm{F}}}{\mathrm{j}\,4\pi} \sum_{s=1}^{2}\sum_{n=1}^{N_\mathrm{obs}}\sum_{m=-n}^{m} \alpha^{(1)}_{smn}\boldsymbol{K}^{(4)}_{smn}\big(\hat{\boldsymbol{k}}\big)\, \mathrm{e}^{-\mathrm{j}\boldsymbol{k}\cdot\boldsymbol{R}} \cdot \boldsymbol{K}^{(4)}_{\sigma,-\mu,\nu}\big(\hat{\boldsymbol{k}}\big)\, \mathrm{d}\hat{\boldsymbol{k}} \\
&= \sum_{s=1}^{2}\sum_{n=1}^{N_\mathrm{obs}}\sum_{m=-n}^{m} \alpha^{(1)}_{smn}\,(-1)^{\sigma+\mu+\nu} \oiint \boldsymbol{K}^{(4)}_{smn}\big(\hat{\boldsymbol{k}}\big)\, \mathrm{e}^{-\mathrm{j}\boldsymbol{k}\cdot\boldsymbol{R}} \cdot \boldsymbol{K}^{(4)}_{\sigma,-\mu,\nu}\big(\hat{\boldsymbol{k}}\big)\, \mathrm{d}\hat{\boldsymbol{k}} \\
&= \sum_{s=1}^{2}\sum_{n=1}^{N_\mathrm{obs}}\sum_{m=-n}^{m} \alpha^{(1)}_{smn} T^{\sigma\mu\nu}_{smn}(\boldsymbol{R})\,.
\end{aligned} \tag{B.30}$$

Therefore, the translation coefficient from the primary to the secondary coordinate system is given by

$$T^{\sigma\mu\nu}_{smn}(\boldsymbol{R}) = (-1)^{\sigma+\mu+\nu} \oiint \boldsymbol{K}^{(4)}_{smn}\big(\hat{\boldsymbol{k}}\big)\, \mathrm{e}^{-\mathrm{j}\boldsymbol{k}\cdot\boldsymbol{R}} \cdot \boldsymbol{K}^{(4)}_{\sigma,-\mu,\nu}\big(\hat{\boldsymbol{k}}\big)\, \mathrm{d}\hat{\boldsymbol{k}} \tag{B.31}$$

for the two coordinate origins placed in the same source free volume V_1.

B.2.2. Transformation of Radiated Fields

Consider a field radiated by an arbitrary electric volume current density $\boldsymbol{J}$, which is completely inside V_1. The electric FF pattern of this current distribution with respect to the coordinate center at $\boldsymbol{r}_{01}$ is given by (see Section 3.5)

$$\boldsymbol{E}_{\mathrm{FF},01}\big(\hat{\boldsymbol{k}}\big) = \frac{-\mathrm{j}\omega\mu k}{4\pi}\,\big(\mathbf{I} - \hat{\boldsymbol{k}}\hat{\boldsymbol{k}}\big) \iiint\limits_{V_1} \mathrm{e}^{\mathrm{j}\boldsymbol{k}\cdot(\boldsymbol{r}'-\boldsymbol{r}_{01})} \cdot \boldsymbol{J}\big(\boldsymbol{r}'\big)\, \mathrm{d}v'\,. \tag{B.32}$$

In the secondary coordinate system, with origin at $\boldsymbol{r}_{02}$, the electric FF pattern is given by

$$\boldsymbol{E}_{\mathrm{FF},02}\left(\hat{\boldsymbol{k}}\right) = \frac{-\mathrm{j}\omega\mu k}{4\pi}\left(\mathbf{I}-\hat{\boldsymbol{k}}\hat{\boldsymbol{k}}\right)\iiint\limits_{V_1} \mathrm{e}^{\mathrm{j}\boldsymbol{k}\cdot\left(\boldsymbol{r}'-\boldsymbol{r}_{02}\right)}\cdot\boldsymbol{J}\left(\boldsymbol{r}'\right)\,\mathrm{d}v' . \tag{B.33}$$

and clearly

$$\boldsymbol{E}_{\mathrm{FF},02}\left(\hat{\boldsymbol{k}}\right) = \boldsymbol{E}_{\mathrm{FF},01}\left(\hat{\boldsymbol{k}}\right)\,\mathrm{e}^{\mathrm{j}\left(\boldsymbol{r}_{01}-\boldsymbol{r}_{02}\right)} = \boldsymbol{E}_{\mathrm{FF},01}\left(\hat{\boldsymbol{k}}\right)\,\mathrm{e}^{-\mathrm{j}\,\boldsymbol{k}\cdot\boldsymbol{R}} . \tag{B.34}$$

Both FF functions may alternatively expressed by their spherical wave expansions. We have

$$\boldsymbol{E}_{\mathrm{FF},01}\left(\hat{\boldsymbol{k}}\right) = k\sqrt{Z_{\mathrm{F}}}\sum_{s=1}^{2}\sum_{n=1}^{N}\sum_{m=-n}^{n}\alpha_{smn}^{(4)}\,\boldsymbol{K}_{smn}^{(4)}\left(\hat{\boldsymbol{k}}\right) , \tag{B.35}$$

where $\alpha_{smn}^{(4)}$ are the expansion coefficients of the radiated fields in the primary coordinate system and

$$\boldsymbol{E}_{\mathrm{FF},02}\left(\hat{\boldsymbol{k}}\right) = k\sqrt{Z_{\mathrm{F}}}\sum_{\sigma=1}^{2}\sum_{\nu=1}^{N'_{\mathrm{aut}}}\sum_{\mu=-\nu}^{\nu}\alpha_{\sigma\mu\nu}^{(4)}\,\boldsymbol{K}_{\sigma\mu\nu}^{(4)}\left(\hat{\boldsymbol{k}}\right) , \tag{B.36}$$

where $\alpha_{\sigma\mu\nu}^{(4)}$ are the expansion coefficients of the radiated fields in the primary coordinate system. From (B.34) it follows that

$$\sum_{\sigma=1}^{2}\sum_{\nu=1}^{N'_{\mathrm{aut}}}\sum_{\mu=-\nu}^{\nu}\alpha_{\sigma\mu\nu}^{(4)}\,\boldsymbol{K}_{\sigma\mu\nu}^{(4)}\left(\hat{\boldsymbol{k}}\right) = \mathrm{e}^{-\mathrm{j}\,\boldsymbol{k}\cdot\boldsymbol{R}}\sum_{s=1}^{2}\sum_{n=1}^{N}\sum_{m=-n}^{n}\alpha_{smn}^{(4)}\,\boldsymbol{K}_{smn}^{(4)}\left(\hat{\boldsymbol{k}}\right) . \tag{B.37}$$

Applying the orthogonality relation [Hansen 1988, p. 330]

$$\oiint \boldsymbol{K}_{smn}^{(4)}\left(\hat{\boldsymbol{k}}\right)\cdot\boldsymbol{K}_{\sigma\mu\nu}^{(4)}\left(\hat{\boldsymbol{k}}\right)\,\mathrm{d}\hat{\boldsymbol{k}} = (-1)^{\sigma+\mu+\nu}\,\delta_{s\sigma}\delta_{m,-\mu}\delta_{n\nu} \tag{B.38}$$

leads to the final result

$$\begin{aligned}\alpha_{\sigma\mu\nu}^{(4)} &= \sum_{s=1}^{2}\sum_{n=1}^{N_{\mathrm{obs}}}\sum_{m=-n}^{m}\alpha_{smn}^{(4)}\,(-1)^{\sigma+\mu+\nu}\oiint \boldsymbol{K}_{smn}^{(4)}\left(\hat{\boldsymbol{k}}\right)\,\mathrm{e}^{-\mathrm{j}\boldsymbol{k}\cdot\boldsymbol{R}}\cdot\boldsymbol{K}_{\sigma,-\mu,\nu}^{(4)}\left(\hat{\boldsymbol{k}}\right)\,\mathrm{d}\hat{\boldsymbol{k}}\\ &= \sum_{s=1}^{2}\sum_{n=1}^{N_{\mathrm{obs}}}\sum_{m=-n}^{m}\alpha_{smn}^{(4)}\,T_{smn}^{\sigma\mu\nu}(\boldsymbol{R}) ,\end{aligned} \tag{B.39}$$

with the translation coefficient from the primary to the secondary coordinate system being given by

$$T_{smn}^{\sigma\mu\nu}(\boldsymbol{R}) = (-1)^{\sigma+\mu+\nu}\oiint \boldsymbol{K}_{smn}^{(4)}\left(\hat{\boldsymbol{k}}\right)\,\mathrm{e}^{-\mathrm{j}\boldsymbol{k}\cdot\boldsymbol{R}}\cdot\boldsymbol{K}_{\sigma,-\mu,\nu}^{(4)}\left(\hat{\boldsymbol{k}}\right)\,\mathrm{d}\hat{\boldsymbol{k}} \tag{B.40}$$

for the two coordinate origins placed in the same source volume V_1.

B.3. Translations Between Coordinate Origins in Different Volumes

Now, the situation of Fig. B.2 is considered, featuring the spherical source volume V_1 and a second spherical source free volume V_2. The volume V_1 has its center at $\boldsymbol{r}_{01}$ and the volume V_2 has its center at $\boldsymbol{r}_{02}$. The two centers are separated by the vector $\boldsymbol{R} = \boldsymbol{r}_{02} - \boldsymbol{r}_{01}$. An electric volume current density $\boldsymbol{J}$ in the source volume V_1 generates radiated fields which are incident on the source free observation volume V_2.

Employing (B.17), the fields in the source free region external to V_1 are given by

$$\begin{aligned}
\boldsymbol{E}(\boldsymbol{r}) &= \iiint\limits_{V_1} \mathscr{G}_{JE}^{-}\big(\boldsymbol{r}, \boldsymbol{r}'\big) \cdot \boldsymbol{J}\big(\boldsymbol{r}'\big)\, \mathrm{d}v' \\
&= -\mathrm{j}\omega\mu \iiint\limits_{V_1} \Big(\mathbf{I} + \frac{1}{k^2}\nabla\nabla\Big) \frac{\mathrm{e}^{-\mathrm{j}k\,|\boldsymbol{r}-\boldsymbol{r}'|}}{4\pi\,|\boldsymbol{r}-\boldsymbol{r}'|} \cdot \boldsymbol{J}\big(\boldsymbol{r}'\big)\, \mathrm{d}v' \\
&= -\mathrm{j}\omega\mu \iiint\limits_{V_1} \Big(\mathbf{I} + \frac{1}{k^2}\nabla'\nabla'\Big) \frac{\mathrm{e}^{-\mathrm{j}k\,|\boldsymbol{r}-\boldsymbol{r}'|}}{4\pi\,|\boldsymbol{r}-\boldsymbol{r}'|} \cdot \boldsymbol{J}\big(\boldsymbol{r}'\big)\, \mathrm{d}v' &\text{(B.41)} \\
&= -\mathrm{j}\omega\mu \iiint\limits_{V_1} \frac{\mathrm{e}^{-\mathrm{j}k\,|\boldsymbol{r}-\boldsymbol{r}'|}}{4\pi\,|\boldsymbol{r}-\boldsymbol{r}'|} \Big(\mathbf{I} + \frac{1}{k^2}\nabla'\nabla'\Big) \cdot \boldsymbol{J}\big(\boldsymbol{r}'\big)\, \mathrm{d}v'\,. &\text{(B.42)}
\end{aligned}$$

If the current functions are not sufficiently regular such that differentiation on them is not well defined, the differential operators have to be interpreted in in a distributional sense [Jin 2015, p. 65] (i.e., by using (B.41) instead of (B.42)). The shift of the differential operators from the unprimed to the primed coordinates is valid in this particular case since

$$\nabla\nabla \frac{\mathrm{e}^{-\mathrm{j}k\,|\boldsymbol{r}-\boldsymbol{r}'|}}{4\pi\,|\boldsymbol{r}-\boldsymbol{r}'|} = \nabla'\nabla' \frac{\mathrm{e}^{-\mathrm{j}k\,|\boldsymbol{r}-\boldsymbol{r}'|}}{4\pi\,|\boldsymbol{r}-\boldsymbol{r}'|} \qquad \forall \boldsymbol{r} \neq \boldsymbol{r}'\,. \tag{B.43}$$

The substitutions $\boldsymbol{r} \to \boldsymbol{r}_{02} - \boldsymbol{r}_{01} = \boldsymbol{R}$ and $\boldsymbol{r}' \to \big(\boldsymbol{r}' - \boldsymbol{r}_{01}\big) - \big(\boldsymbol{r} - \boldsymbol{r}_{02}\big)$ in the branch of the Gegenbauer addition theorem (B.24) for $\big|\boldsymbol{r}'\big| < |\boldsymbol{r}|$ lead to the well known identity [Coifman 1993]

$$\frac{\mathrm{e}^{-\mathrm{j}k\,|\boldsymbol{r}-\boldsymbol{r}'|}}{4\pi\,|\boldsymbol{r}-\boldsymbol{r}'|} = \frac{\mathrm{j}k}{4\pi} \sum_{\ell=0}^{\infty} (-\mathrm{j})^{\ell}\, (2\ell+1)\, \mathrm{h}_{\ell}^{(2)}(k\,|\boldsymbol{R}|) \oiint \mathrm{e}^{-\mathrm{j}\boldsymbol{k}\cdot(\boldsymbol{r}-\boldsymbol{r}_{02})}\, \mathrm{e}^{\mathrm{j}\boldsymbol{k}\cdot(\boldsymbol{r}'-\boldsymbol{r}_{01})}\, \mathrm{P}_{\ell}\big(\hat{\boldsymbol{k}} \cdot \hat{\boldsymbol{R}}\big)\, \mathrm{d}\hat{\boldsymbol{k}}\,, \tag{B.44}$$

valid for $\big|\big(\boldsymbol{r}' - \boldsymbol{r}_{01}\big) - \big(\boldsymbol{r} - \boldsymbol{r}_{02}\big)\big| < |\boldsymbol{R}|$. Plugging this identity into (B.42), one obtains

$$\begin{aligned}
\boldsymbol{E}(\boldsymbol{r}) = \frac{\omega\mu k}{4\pi} \sum_{\ell=0}^{\infty} \oiint (-\mathrm{j})^{\ell}\, (2\ell+1)\, \mathrm{h}_{\ell}^{(2)}(k\,|\boldsymbol{R}|)\, \mathrm{e}^{-\mathrm{j}\boldsymbol{k}\cdot(\boldsymbol{r}-\boldsymbol{r}_{02})}\, \mathrm{P}_{\ell}\big(\hat{\boldsymbol{k}} \cdot \hat{\boldsymbol{R}}\big) \\
\times \iiint\limits_{V_1} \mathrm{e}^{\mathrm{j}\boldsymbol{k}\cdot(\boldsymbol{r}'-\boldsymbol{r}_{01})} \Big(\mathbf{I} + \frac{1}{k^2}\nabla'\nabla'\Big) \cdot \boldsymbol{J}\big(\boldsymbol{r}'\big)\, \mathrm{d}v'\, \mathrm{d}\hat{\boldsymbol{k}}\,. \qquad \text{(B.45)}
\end{aligned}$$

Using partial integration, the term

$$\begin{aligned}\boldsymbol{E}_{\mathrm{FF}}\big(\hat{\boldsymbol{k}}\big) &= \frac{-\mathrm{j}\omega\mu k}{4\pi}\iiint\limits_{V_1} \mathrm{e}^{\mathrm{j}\boldsymbol{k}\cdot(\boldsymbol{r}'-\boldsymbol{r}_{01})}\left(\mathbf{I}+\frac{1}{k^2}\nabla'\nabla'\right)\cdot\boldsymbol{J}\big(\boldsymbol{r}'\big)\,\mathrm{d}v' \\ &= \frac{-\mathrm{j}\omega\mu k}{4\pi}\iiint\limits_{V_1}\left(\mathbf{I}+\frac{1}{k^2}\nabla'\nabla'\right)\mathrm{e}^{\mathrm{j}\boldsymbol{k}\cdot(\boldsymbol{r}'-\boldsymbol{r}_{01})}\cdot\boldsymbol{J}\big(\boldsymbol{r}'\big)\,\mathrm{d}v' \\ &= \frac{-\mathrm{j}\omega\mu k}{4\pi}\left(\mathbf{I}-\frac{1}{k^2}\boldsymbol{k}\boldsymbol{k}\right)\iiint\limits_{V_1}\mathrm{e}^{\mathrm{j}\boldsymbol{k}\cdot(\boldsymbol{r}'-\boldsymbol{r}_{01})}\cdot\boldsymbol{J}\big(\boldsymbol{r}'\big)\,\mathrm{d}v' \end{aligned}\tag{B.46}$$

can be easily identified as the FF pattern of the current distribution $\boldsymbol{J}$ with respect to the coordinate origin at $\boldsymbol{r}_{01}$ (see Section 3.5) and we have

$$\boldsymbol{E}(\boldsymbol{r}) = \mathrm{j}\sum_{\ell=0}^{\infty}\oiint(-\mathrm{j})^{\ell}\,(2\ell+1)\,\mathrm{h}_{\ell}^{(2)}(k\,|\boldsymbol{R}|)\,\mathrm{e}^{-\mathrm{j}\boldsymbol{k}\cdot(\boldsymbol{r}-\boldsymbol{r}_{02})}\,\mathrm{P}_{\ell}\big(\hat{\boldsymbol{k}}\cdot\hat{\boldsymbol{R}}\big)\,\boldsymbol{E}_{\mathrm{FF}}\big(\hat{\boldsymbol{k}}\big)\,\mathrm{d}\hat{\boldsymbol{k}}\,. \tag{B.47}$$

The FF pattern of the source distribution can alternatively be expressed in terms of its spherical wave expansion by

$$\boldsymbol{E}_{\mathrm{FF}}\big(\hat{\boldsymbol{k}}\big) = k\sqrt{Z_{\mathrm{F}}}\sum_{s=1}^{2}\sum_{n=1}^{N}\sum_{m=-n}^{n}\alpha_{smn}^{(4)}\boldsymbol{K}_{smn}^{(4)}\big(\hat{\boldsymbol{k}}\big)\,, \tag{B.48}$$

where $\alpha_{smn}^{(4)}$ are the expansion coefficients of the radiated fields in the primary coordinate system (centered at $\boldsymbol{r}_{01}$). This leads to

$$\begin{aligned}\boldsymbol{E}(\boldsymbol{r}) = \mathrm{j}k\sqrt{Z_{\mathrm{F}}}\sum_{\ell=0}^{\infty}\oiint(-\mathrm{j})^{\ell}\,(2\ell+1)\,\mathrm{h}_{\ell}^{(2)}(k\,|\boldsymbol{R}|)\,\mathrm{e}^{-\mathrm{j}\boldsymbol{k}\cdot(\boldsymbol{r}-\boldsymbol{r}_{02})}\,\mathrm{P}_{\ell}\big(\hat{\boldsymbol{k}}\cdot\hat{\boldsymbol{R}}\big) \\ \times\left(\sum_{s=1}^{2}\sum_{n=1}^{N}\sum_{m=-n}^{n}\alpha_{smn}^{(4)}\boldsymbol{K}_{smn}^{(4)}\big(\hat{\boldsymbol{k}}\big)\right)\mathrm{d}\hat{\boldsymbol{k}}\,.\end{aligned}\tag{B.49}$$

Notice that (B.49) takes the form of a summation partial incident fields $\boldsymbol{E}_{\ell}$, i.e.,

$$\boldsymbol{E}(\boldsymbol{r}) = \sum_{\ell=0}^{\infty}\boldsymbol{E}_{\ell}(\boldsymbol{r})\,. \tag{B.50}$$

Each individual partial incident field $\boldsymbol{E}_{\ell}$ is given in terms of a plane wave representation with respect to a coordinate origin at $\boldsymbol{r}_{02}$ by

$$\boldsymbol{E}_{\ell}(\boldsymbol{r}) = \oiint\tilde{\boldsymbol{E}}_{\mathrm{in},\ell}\big(\hat{\boldsymbol{k}}\big)\,\mathrm{e}^{-\mathrm{j}\boldsymbol{k}\cdot\mathrm{e}^{-\mathrm{j}\boldsymbol{k}\cdot(\boldsymbol{r}-\boldsymbol{r}_{02})}}\,\mathrm{d}\hat{\boldsymbol{k}}\,, \tag{B.51}$$

where the plane wave spectra $\tilde{\boldsymbol{E}}_{\mathrm{in},\ell}\big(\hat{\boldsymbol{k}}\big)$ are given by

$$\tilde{\boldsymbol{E}}_{\mathrm{in},\ell}\big(\hat{\boldsymbol{k}}\big) = \mathrm{j}\,(-\mathrm{j})^{\ell}\,(2\ell+1)\,\mathrm{h}_{\ell}^{(2)}(k\,|\boldsymbol{R}|)\,\mathrm{P}_{\ell}\big(\hat{\boldsymbol{k}}\cdot\hat{\boldsymbol{R}}\big)\,\boldsymbol{E}_{\mathrm{FF}}\big(\hat{\boldsymbol{k}}\big)\,. \tag{B.52}$$

The partial incident fields $\boldsymbol{E}_\ell$ each have a spherical wave expansion

$$\boldsymbol{E}_\ell(\boldsymbol{r}) = k\sqrt{Z_\mathrm{F}} \sum_{\sigma=1}^{2} \sum_{\nu=1}^{N_\mathrm{obs}} \sum_{\mu=-\nu}^{\nu} \alpha^{(1)}_{\sigma\mu\nu,\ell} \boldsymbol{F}^{(1)}_{\sigma\mu\nu}(\tilde{r}, \tilde{\vartheta}, \tilde{\varphi}) \ , \tag{B.53}$$

of which the expansion coefficients can be computed according to (B.15) by

$$\begin{aligned}\alpha^{(1)}_{\sigma\mu\nu,\ell} &= \frac{\mathrm{j}\,4\pi}{\sqrt{Z_\mathrm{F}}\,k} (-1)^{\sigma+\mu+\nu} \oiint \tilde{\boldsymbol{E}}_{\mathrm{in}}, \ell(\hat{\boldsymbol{k}}) \cdot \boldsymbol{K}^{(4)}_{\sigma,-\mu,\nu}(\hat{\boldsymbol{k}})\ \mathrm{d}\hat{\boldsymbol{k}} \\ &= -4\pi\,(-1)^{\sigma+\mu+\nu} \oiint \sum_{s=1}^{2} \sum_{n=1}^{N} \sum_{m=-n}^{n} \alpha^{(4)}_{smn}\,(-\mathrm{j})^\ell\,(2\ell+1)\,\mathrm{h}^{(2)}_\ell(k\,|\boldsymbol{R}|)\,\mathrm{P}_\ell(\hat{\boldsymbol{k}} \cdot \hat{\boldsymbol{R}}) \\ &\qquad \times \boldsymbol{K}^{(4)}_{smn}(\hat{\boldsymbol{k}}) \cdot \boldsymbol{K}^{(4)}_{\sigma,-\mu,\nu}(\hat{\boldsymbol{k}})\ \mathrm{d}\hat{\boldsymbol{k}} \,. \end{aligned} \tag{B.54}$$

The final result is obtained by summing over all partial expansion coefficients. We have

$$\begin{aligned}\alpha^{(1)}_{\sigma\mu\nu} = -4\pi \sum_{s=1}^{2} \sum_{n=1}^{N} \sum_{m=-n}^{n} \alpha^{(4)}_{smn} \sum_{\ell=0}^{\infty} (-1)^{\sigma+\mu+\nu} \oiint (-\mathrm{j})^\ell\,(2\ell+1)\,\mathrm{h}^{(2)}_\ell(k\,|\boldsymbol{R}|)\,\mathrm{P}_\ell(\hat{\boldsymbol{k}} \cdot \hat{\boldsymbol{R}}) \\ \times \boldsymbol{K}^{(4)}_{smn}(\hat{\boldsymbol{k}}) \cdot \boldsymbol{K}^{(4)}_{\sigma,-\mu,\nu}(\hat{\boldsymbol{k}})\ \mathrm{d}\hat{\boldsymbol{k}} \,. \end{aligned} \tag{B.55}$$

This equation must be equal to

$$\alpha^{(1)}_{\sigma\mu\nu} = \sum_{s=1}^{2} \sum_{n=1}^{N} \sum_{m=-n}^{n} \alpha^{(4)}_{smn}\,\mathscr{T}^{\sigma\mu\nu}_{smn}(\boldsymbol{R}) \tag{B.56}$$

and by a term-by-term comparison one obtains

$$\begin{aligned}&\mathscr{T}^{\sigma\mu\nu}_{smn}(\boldsymbol{R}) \\ &= -4\pi \sum_{\ell=0}^{\infty} (-1)^{\sigma+\mu+\nu} \oiint (-\mathrm{j})^\ell\,(2\ell+1)\,\mathrm{h}^{(2)}_\ell(k\,|\boldsymbol{R}|)\,\mathrm{P}_\ell(\hat{\boldsymbol{k}} \cdot \hat{\boldsymbol{R}})\,\boldsymbol{K}^{(4)}_{smn}(\hat{\boldsymbol{k}}) \cdot \boldsymbol{K}^{(4)}_{\sigma,-\mu,\nu}(\hat{\boldsymbol{k}})\ \mathrm{d}\hat{\boldsymbol{k}} \,. \end{aligned} \tag{B.57}$$

The order of the summation and integration must not be changed (i.e., the infinte series must not be evaluated before the integration over the plane wave spectra), because the series

$$\sum_{\ell=0}^{\infty} (-\mathrm{j})^\ell\,(2\ell+1)\,\mathrm{h}^{(2)}_\ell(k\,|\boldsymbol{R}|)\,\mathrm{P}_\ell(\hat{\boldsymbol{k}} \cdot \hat{\boldsymbol{R}}) \tag{B.58}$$

diverges — the expression $\sum_{\ell=0}^{\infty} (-\mathrm{j})^\ell\,(2\ell+1)\,\mathrm{h}^{(2)}_\ell(k\,|\boldsymbol{R}|)\,\mathrm{P}_\ell(\hat{\boldsymbol{k}} \cdot \hat{\boldsymbol{R}})$ is no proper function but a distribution. The series must be interpreted in a distributional sense, having in mind that it is only well defined under an integral together with a sufficiently smooth function f [Chew 2007]. Formally, one can write the symbolic integral

$$\oiint \sum_{\ell=0}^{\infty} (-\mathrm{j})^\ell\,(2\ell+1)\,\mathrm{h}^{(2)}_\ell(k\,|\boldsymbol{R}|)\,\mathrm{P}_\ell(\hat{\boldsymbol{k}} \cdot \hat{\boldsymbol{R}})\,f(\hat{\boldsymbol{k}})\ \mathrm{d}\hat{\boldsymbol{k}} \tag{B.59}$$

remembering that this is not an integral which can be evaluated in the conventional (i.e., Riemann or Lebesgue) sense. Instead, one falls back to defining this symbolic (distributional) integral as[6]

$$\begin{aligned}&\oiint \sum_{\ell=0}^{\infty} (-\mathrm{j})^{\ell}\ (2\ell+1)\ \mathrm{h}_{\ell}^{(2)}(k\,|\boldsymbol{R}|)\,\mathrm{P}_{\ell}\big(\hat{\boldsymbol{k}}\cdot\hat{\boldsymbol{R}}\big)\ f\big(\hat{\boldsymbol{k}}\big)\ \mathrm{d}\hat{\boldsymbol{k}} \\ &:= \sum_{\ell=0}^{\infty} \oiint (-\mathrm{j})^{\ell}\ (2\ell+1)\ \mathrm{h}_{\ell}^{(2)}(k\,|\boldsymbol{R}|)\,\mathrm{P}_{\ell}\big(\hat{\boldsymbol{k}}\cdot\hat{\boldsymbol{R}}\big)\ f\big(\hat{\boldsymbol{k}}\big)\ \mathrm{d}\hat{\boldsymbol{k}}\,. \qquad \text{(B.60)}\end{aligned}$$

These problems are of course avoided in any numerical implementation because the series is truncated after a finite number of terms and the finite sum is guaranteed to converge.

An empirical rule for choosing the truncation index L of the summation in the so-called propagating plane-wave translation operator

$$T_L\big(kR, \hat{\boldsymbol{k}}\cdot\hat{\boldsymbol{R}}\big) = \sum_{\ell=0}^{L} (-\mathrm{j})^{\ell}\ (2\ell+1)\ \mathrm{h}_{\ell}^{(2)}(k\,|\boldsymbol{R}|)\,\mathrm{P}_{\ell}\big(\hat{\boldsymbol{k}}\cdot\hat{\boldsymbol{R}}\big) \qquad \text{(B.61)}$$

is given by [Song 2001]

$$L = kr_0 + 1.8\ \left(\log_{10}\left(\frac{1}{\epsilon}\right)\right)^{\frac{2}{3}}\ \sqrt[3]{kr_0}\,, \qquad \text{(B.62)}$$

where r_0 is the radius of the minimum sphere enclosing all sources and $\log_{10}(1/\epsilon)$ is the number of desired decimal digits of accuracy. Naturally, the rule (B.62) for choosing a sensible truncation index in the translation of spherical waves has striking similarities to the rule in (4.12) for choosing a sensible truncation index for the spherical expansion of a radiated field.

---

[6] This is similar to how integrals involving the Dirac-Delta distribution cannot be evaluated in the conventional sense but must be interpreted as symbolic integrals which get their meaning only through a separate definition.

Bibliography

Abramowitz, M. and I. A. Stegun (1964). *Handbook of Mathematical Functions with Formulas, Graphs, and Mathematical Tables*. 1st ed. National Bureau of Standards Applied Mathematics series 55.

Adve, R. S., T. K. Sarkar, S. M. Rao, E. K. Miller, and D. R. Pflug (1997). "Application of the Cauchy method for extrapolating/interpolating narrowband system responses". In: *IEEE Transactions on Microwave Theory and Techniques* 45.5, pp. 837–845.

Adve, R. S. and T. K. Sarkar (1998). "Simultaneous time- and frequency-domain extrapolation". In: *IEEE Transactions on Antennas and Propagation* 46.4, pp. 484–493.

Altair (2021). *Feko: https://altairhyperworks.com/ (Accessed May., 1, 2021)*.

Alu, A. and S. Maslovski (2010). "Power relations and a consistent analytical model for receiving wire antennas". In: *IEEE Transactions on Antennas and Propagation* 58.5, pp. 1436–1448.

Álvarez, J. F., S. Pivnenko, and O. Breinbjerg (2015). "Probe-corrected phaseless planar near-field antenna measurements at 60 GHz". In: *Antenna Measurement Techniques Association Symposium (AMTA)*. Long Beach, CA.

Álvarez, J. F. and O. Breinbjerg (2018). "A computational and experimental investigation of λ/2 and λ/4 sampling step in phaseless planar near-field measurements at 60 GHz". In: *European Conference on Antennas and Propagation (EuCAP)*. London, UK.

Álvarez, Y. and F. Las-Heras (2006). "Integral equation algorithms for the reconstruction of the equivalent currents distribution over arbitrary three-dimensional surfaces". In: *IEEE Antennas and Propagation Society International Symposium APSURSI*. Albuquerque, NM.

Álvarez, Y., F. Las-Heras, and M. R. Pino (2007). "Reconstruction of equivalent currents distributionover arbitrary three-diemnsional surfaces based on integral equation algorithms". In: *IEEE Transactions on Antennas and Propagation* 55.12, pp. 3460–3468.

Álvarez, Y., F. Las-Heras, and M. R. Pino (2008). "On the comparison between the spherical wave expansion and the sources reconstruction method". In: *IEEE Transactions on Antennas and Propagation* 56.10, pp. 3337–3341.

Andersen, J. B. and R. G. Vaughan (2003). "Transmitting, receiving, and scattering properties of antennas". In: *IEEE Antennas and Propagation Magazine* 45.4, pp. 93–98.

Arfken, G. B. and H.-J. Weber (2005). *Mathematical Methods for Physicists*. 6th ed. Boston: Elsevier.

Baksalary, J. K. and O. M. Baksalary (2007). “Particular formulae for the Moore–Penrose inverse of a columnwise partitioned matrix”. In: *Linear Algebra and its Applications* 421.1, pp. 16–23.

Balan, R. and Y. Wang (2015). “Invertibility and robustness of phaseless reconstruction”. In: *Applied and Computational Harmonic Analysis* 38.3, pp. 469–488.

Balanis, C. A. (2005). *Antenna Theory: Analysis and Design*. 2nd ed. New Jersey: John Wiley & Sons.

Bates, R. H. T. (1975). “Analytic constraints on electromagnetic field computations”. In: *IEEE Transactions on Microwave Theory and Techniques* 23.8, pp. 605–623.

Best, S. R. and B. C. Kaanta (2009). “A tutorial on the receiving and scattering properties of antennas”. In: *IEEE Antennas and Propagation Magazine* 51.5, pp. 26–37.

Black D. N., J. and E. B. Joy (1995). “Test zone field compensation”. In: *IEEE Transactions on Antennas and Propagation* 43.4, pp. 362–368.

Bladel, J. v. (2007). *Electromagnetic FIELDS*. 2nd ed. IEEE Press series on electromagnetic wave theory. Hoboken, N.J: IEEE/Wiley-Interscience.

Blech, M. D. and T. F. Eibert (2008). “A time domain spherical antenna near field measurement facility for UWB antennas employing a hardware gating technique”. In: *Kleinheubacher Tagung*. Miltenberg, Germany.

Blech, M. D., M. M. Leibfritz, R. Hellinger, D. Geier, F. A. Maier, A. M. Pietsch, and T. F. Eibert (2010a). “A time domain spherical near-field measurement facility for UWB antennas employing a hardware gating technique”. In: *Advances in Radio Science*, pp. 243–250.

Blech, M. D., M. M. Leibfritz, R. Hellinger, D. Geier, F. A. Maier, A. M. Pietsch, and T. F. Eibert (2010b). “Time-domain spherical near-field antenna measurement system employing a switched continuous-wave hardware gating technique”. In: *IEEE Transactions on Instrumentation and Measurement* 59.2, pp. 387–395.

Bleistein, N. and J. K. Cohen (1977). “Nonuniqueness in the inverse source problem in acoustics and electromagnetics”. In: *Journal of Mathematical Physics* 18.2, p. 194.

Borghese, F., P. Denti, G. Toscano, and O. I. Sindoni (1980). “An addition theorem for vector Helmholtz harmonics”. In: *Journal of Mathematical Physics* 21.12, pp. 2754–2755.

Bucci, O. M. and G. Franceschetti (1989). “On the degrees of freedom of scattered fields”. In: *IEEE Transactions on Antennas and Propagation* 37.7, pp. 918–926.

Bucci, O. M., C. Gennarelli, and C. Savarese (1991). “Optimal interpolation of radiated fields over a sphere”. In: *IEEE Transactions on Antennas and Propagation* 39.11, pp. 1633–1643.

Bucci, O. M., G. D’Elia, G. Leone, and R. Pierri (1990). “Far-field pattern determination from the near-field amplitude on two surfaces”. In: *IEEE Transactions on Antennas and Propagation* 38.11, pp. 1772–1779.

Bucci, O. M. and G. Franceschetti (1987). “On the spatial bandwidth of scattered fields”. In: *IEEE Transactions on Antennas and Propagation* 35.12, pp. 1445–1455.

Bucci, O. M., C. Gennarelli, G. Riccio, V. Speranza, and C. Savarese (1996). “Nonredundant representations of the electromagnetic fields over a cylinder with application to the near-field far-field transformation”. In: *Electromagnetics* 16.3, pp. 273–290.

Bucci, O. M., C. Gennarelli, and C. Savarese (1998). “Representation of electromagnetic fields over arbitrary surfaces by a finite and nonredundant number of samples”. In: *IEEE Transactions on Antennas and Propagation* 46.3, pp. 351–359.

Bucci, O. M. and C. Gennarelli (2012). “Application of nonredundant sampling representation of electromagnetic fields to NF-FF transformation techniques”. In: *International Journal of Antennas and Propagation* 2012, e319856.

Bucci, O. M., M. D. Migliore, G. Panariello, and D. Pinchera (2013). “Plane-wave generators: Design guidelines, achievable performances and effective synthesis”. In: *IEEE Transactions on Antennas and Propagation* 61.4, pp. 2005–2018.

Burrell, G. and A. Jamieson (1973). “Antenna radiation pattern measurement using time-to-frequency transformation (TFT) techniques”. In: *IEEE Transactions on Antennas and Propagation* 21.5, pp. 702–704.

Calvetti, D., B. Lewis, and L. Reichel (2002). “On the regularizing properties of the GMRES method”. In: *Springer, Numerische Mathematik* 91.4, pp. 605–625.

Candes, E. J., T. Strohmer, and V. Voroninski (2013). “Phaselift: Exact and stable signal recovery from magnitude measurements via convex programming”. In: *Communications on Pure and Applied Mathematics* 66.8, pp. 1241–1274.

Candes, E. J., X. Li, and M. Soltanolkotabi (2015). “Phase retrieval via Wirtinger flow: Theory and algorithms”. In: *IEEE Transactions on Information Theory* 61.4, pp. 1985–2007.

Candocia, F. and J. C. Principe (1998). “Comments on ”Sinc interpolation of discrete periodic signals”. In: *IEEE Transactions on Signal Processing* 46.7, pp. 2044–2047.

Cano, F., M. Sierra-Castañer, S. Burgos, and J. L. Besada (2010). “Applications of sources reconstruction techniques: Theory and practical results”. In: *European Conference on Antennas and Propagation (EuCAP)*. Barcelona, Spain.

Cano-Facila, F., S. Burgos, F. Martin, and M. Sierra-Castaner (2011). “New reflection suppression method in antenna measurement systems based on diagnostic techniques”. In: *IEEE Transactions on Antennas and Propagation* 59.3, pp. 941–949.

Caorsi, S., D. Moreno, and F. Sidoti (1993). “Theoretical and numerical treatment of surface integrals involving the free-space Green’s function”. In: *IEEE Transactions on Antennas and Propagation* 41.9, pp. 1296–1301.

Cavicchi, T. J. (1992). “DFT time-domain interpolation”. In: *IEE Proceedings F Radar and Signal Processing* 139.3, p. 207.

Chew, W. C. and Y. M. Wang (1993). “Efficient ways to compute the vector addition theorem”. In: *Journal of Electromagnetic Waves and Applications* 7.5, pp. 651–665.

Chew, W. C. (2007). “Diagonalization of the vector addition theorem”. In: *IEEE Antennas and Propagation Society International Symposium (APSURSI)*. Honolulu, HI.

Chew, W. C. (1995). *Waves and Fields in Inhomogeneous Media*. 1st ed. OCLC: 31169540. New York: IEEE Press.

– ed. (2001). *Fast and efficient algorithms in computational electromagnetics*. 1st ed. Artech House antennas and propagation library. Boston: Artech House.

– (2008). “Vector addition theorem and its diagonalization”. In: *Global Science Press, Communications in Computational Physics* 3.2, pp. 330–341.

Chu, L. J. (1948). “Physical limitations of omni-directional antennas”. In: *Journal of applied physics, American Institute of Physics* 19.12, pp. 1163–1175.

Clauzier, S., S. M. Mikki, and Y. M. M. Antar (2015). “Design of near-field synthesis arrays through global optimization”. In: *IEEE Transactions on Antennas and Propagation* 63.1, pp. 151–165.

Cline, R. E. (1964). “Representations for the generalized inverse of a partitioned matrix”. In: *Journal of the Society for Industrial and Applied Mathematics (SIAM)* 12.3, pp. 588–600.

Coifman, R., V. Rokhlin, and S. Wandzura (1993). “The fast multipole method for the wave equation: A pedestrian prescription”. In: *IEEE Antennas and Propagation Magazine* 35.3, pp. 7–12.

Collin, R. E. (2003a). “Limitations of the Thevenin and Norton equivalent circuits for a receiving antenna”. In: *IEEE Antennas and Propagation Magazine* 45.2, pp. 119–124.

– (2003b). “Remarks on ”Comments on the limitations of the Thevenin and Norton equivalent circuits for a receiving antenna””. In: *IEEE Antennas and Propagation Magazine* 45.4, pp. 99–100.

Collin, R. E. (1990). *Field Theory of Guided Waves*. 1st ed. Vol. 5. John Wiley & Sons.

Costanzo, S., G. Di Massa, and M. D. Migliore (2005). “A novel hybrid approach for far-field characterization from near-field amplitude-only measurements on arbitrary scanning surfaces”. In: *IEEE Transactions on Antennas and Propagation* 53.6, pp. 1866–1874.

Costanzo, S. and G. Di Massa (2002). “An integrated probe for phaseless near-field measurements”. In: *Measurement* 31.2, pp. 123–129.

Cox, H., R. Zeskind, and T. Kooij (1986). “Practical supergain”. In: *IEEE Transactions on Acoustics, Speech, and Signal Processing* 34.3, pp. 393–398.

Cruzan, O. R. (1962). “Translational addition theorems for spherical vector wave functions”. In: *Quarterly of Applied Mathematics* 20.1, pp. 33–40.

D’Agostino, F., F. Ferrara, C. Gennarelli, R. Guerriero, and M. Migliozzi (2016). “Far-field pattern reconstruction from a nonredundant plane-polar near-field sampling arrangement: experimental testing”. In: *IEEE Antennas and Wireless Propagation Letters* 15, pp. 1345–1348.

D’Agostino, F., F. Ferrara, C. Gennarelli, R. Guerriero, and M. Migliozzi (2011). “Effective antenna modellings for NF-FF transformations with spherical scanning using the minimum number of data”. In: *International Journal of Antennas and Propagation* 2011.

– (2013). “Non-redundant spherical NF - FF transformations using ellipsoidal antenna modeling: Experimental assessments [Measurements corner]”. In: *IEEE Antennas and Propagation Magazine* 55.4, pp. 166–175.

Danos, M. and L. C. Maximon (1965). “Multipole matrix elements of the translation operator”. In: *Journal of Mathematical Physics* 6.5, pp. 766–778.

Darve, E. (2000). “The Fast Multipole Method: Numerical Implementation”. In: *Journal of Computational Physics* 160.1, pp. 195–240.

de Hoop, A. T. and G. de Jong (1974). “Power reciprocity in antenna theory”. In: *Proceedings of the Institution of Electrical Engineers* 121.10, p. 1051.

De Porrata-Doria i Yague, R., A. B. Ibars, and L. F. Martinez (1998). “Analysis and reduction of the distortions induced by time-domain filtering techniques in network analyzers”. In: *IEEE Transactions on Instrumentation and Measurement* 47.4, pp. 930–934.

Devaney, A. J. and E. Wolf (1974). “Multipole expansions and plane wave representations of the electromagnetic field”. In: *Journal of Mathematical Physics* 15.2, pp. 234–244.

Dohler, M. (2004). “Virtual antenna arrays”. PhD thesis.

Dohler, M., E. Lefranc, and H. Aghvami (2002). “Virtual antenna arrays for future wireless mobile communication systems”. In: *IEEE ICT*.

Dohler, M., A. H. Aghvami, F. Said, and S. A. Ghorashi (2009). *Virtual antenna array*. 1st ed. Google Patents.

Dooley, S. R. and A. K. Nandi (2000). “Notes on the interpolation of discrete periodic signals using sinc function related approaches”. In: *IEEE Transactions on Signal Processing* 48.4, pp. 1201–1203.

Dufva, T. J., J. Sarvas, and J. C.-E. Sten (2008). “Unified derivation of the translational addition theorems for the spherical scalar and vector wave functions”. In: *Progress In Electromagnetics Research B* 4, pp. 79–99.

Eibert, T., D. Vojvodic, and T. Hansen (2016a). “Fast inverse equivalent source solutions with directive sources”. In: *IEEE Transactions on Antennas and Propagation* PP.99, pp. 1–1.

Eibert, T. F. (2005). “A diagonalized multilevel fast multipole method with spherical harmonics expansion of the k-space integrals”. In: *IEEE Transactions on Antennas and Propagation* 53.2, pp. 814–817.

Eibert, T. F. and C. H. Schmidt (2009). “Multilevel fast multipole accelerated inverse equivalent current method employing Rao-Wilton-Glisson discretization of electric and magnetic surface currents”. In: *IEEE Transactions on Antennas and Propagation* 57.4, pp. 1178–1185.

Eibert, T. F. (2004). “A multilevel fast multipole method with spherical harmonics expansion of the k-space integrals”. In: *URSI International Symposium on Electromagnetic Theory*. Pisa, Italy.

Eibert, T. F., E. Kaliyaperumal, C. H. Schmidt, (2010). “Inverse equivalent surface current method with hierarchical higher order basis functions, full probe correction and multilevel fast multipole acceleration”. In: *Progress In Electromagnetics Research* 106, pp. 377–394.

Eibert, T. F., R. A. M. Mauermayer, and G. Schnattinger (2014). “Fast irregular electromagnetic field transformation utilizing spatial or spectral equivalent sources representations together with hierarchical radiation operator evaluation”. In: *URSI General Assembly and Scientific Symposium*. Beijing, China.

Eibert, T. F., E. Kilic, C. Lopez, R. A. M. Mauermayer, O. Neitz, and G. Schnattinger (2015). “Electromagnetic field transformations for measurments and simulations (Invited Paper)”. In: *Progress In Electromagnetics Research* 151, pp. 127–150.

Eibert, T. F., C. Lopez, and T. B. Hansen (2016b). “Irregular probe corrected antenna field transformations utilizing Gaussian beam based fast multipole translation operators”. In: *European Conference on Antennas and Propagation (EuCAP)*. Davos, Switzerland.

Elden, L. and V. Simoncini (2012). “Solving ill-posed linear systems with GMRES and a singular preconditioner”. In: *SIAM Journal on Matrix Analysis and Applications* 33.4, pp. 1369–1394.

Felderhof, B. U. and R. B. Jones (1987). “Addition theorems for spherical wave solutions of the vector Helmholtz equation”. In: *Journal of Mathematical Physics* 28.4, pp. 836–839.

Fernández del Río, J. E. and T. K. Sarkar (1996). “Comparison between the matrix pencil method and the Fourier transform technique for high-resolution spectral estimation”. In: *Digital Signal Processing* 6.2, pp. 108–125.

Fischer, D. G., R. A. Frazin, M. Asipauskas, and P. S. Carney (2011). “Information content of the near field: three-dimensional samples”. In: *Journal of the Optical Society of America A* 28.3, p. 296.

Foged, L. J., L. Scialacqua, F. Saccardi, J. L. A. Quijano, M. Sabbadini, and G. Vecchi (2012). “Equivalent current approach as an advanced field interpolation technique”. In: *IEEE Antennas and Propagation Society International Symposium (APSURSI)*. Chicago, IL.

Foged, L., L. Scialacqua, F. Saccardi, F. Mioc, P. O. Iversen, L. Shmidov, R. Braun, J. L. Araque Quijano, and G. Vecchi (2013). "Comparison of echo suppression techniques in near field antenna measurement applications". In: *European Conference on Antennas and Propagation (EuCAP).* Gothenburg, Sweden.

Ford, K. L., J. C. Bennett, and D. G. Holtby (2013). "Use of a plane-wave synthesis technique to obtain target RCS from near-field measurements, with selective feature extraction capability". In: *IEEE Transactions on Antennas and Propagation* 61.4, pp. 2051–2057.

Fourestie, B., Z. Altman, J. Wiart, and A. Azoulay (1999). "Correlate measurements at different test sites". In: *IEEE Transactions on Antennas and Propagation* 47.10, pp. 1569–1573.

Fourestie, B. and Z. Altman (2001). "Gabor schemes for analyzing antenna measurements". In: *IEEE Transactions on Antennas and Propagation* 49.9, pp. 1245–1253.

Friedlander, M. and E. Van den Berg (2008). "SPGL1: A solver for large-scale sparse reconstruction". In: *SIAM Journal on Scientific Computing* 31.2, pp. 890–912.

Garcia-Gonzalez, C., Y. Alvarez-Lopez, A. D. Casas, and F. Las Heras Andres (2011). "Characterization of antenna interaction with scatterers by means of equivalent currents". In: *Progress In Electromagnetics Research* 116, pp. 185–202.

Geyi, W. (2004). "Derivation of equivalent circuits for receiving antenna". In: *IEEE Transactions on Antennas and Propagation* 52.6, pp. 1620–1623.

Giordanengo, G., M. Righero, F. Vipiana, G. Vecchi, and M. Sabbadini (2014). "Fast antenna testing with reduced near field sampling". In: *IEEE Transactions on Antennas and Propagation* 62.5, pp. 2501–2513.

Goldstein, H. (1980). *Classical Mechanics*. 2nd ed. Addison-Wesley series in physics. Reading, Mass: Addison-Wesley Pub. Co.

Gori, F. and G. Guattari (1973). "Shannon number and degrees of freedom of an image". In: *Optics Communications* 7.2, pp. 163–165.

Green, R. (1966). "Scattering from conjugate-matched antennas". In: *IEEE Transactions on Antennas and Propagation* 14.1, pp. 17–21.

Gregson, S. F., A. C. Newell, and G. E. Hindman (2009). "Reflection suppression in cylindrical near-field antenna measurement systems–cylindrical MARS". In: *Antenna Measurement Techniques Association Symposium (AMTA).* Salt Lake City, UT.

Gregson, S. F., A. C. Newell, G. E. Hindman, and M. J. Carey (2010a). "Advances in cylindrical mathematical absorber reflection suppression". In: *European Conference on Antennas and Propagation (EuCAP).* Barcelona, Spain, pp. 1–5.

– (2010b). "Comparison of cylindrical and spherical Mathematical Absorber Reflection Suppression". In: *Loughborough Antennas & Propagation Conference (LAPC).* Loughborough, UK, pp. 181–184.

– (2010c). "Extension of the mathematical absorber reflection suppression technique to the planar near-field geometry". In: *Antenna Measurement Techniques Association Symposium (AMTA).* Atlanta, GA.

Gregson, S. F., A. C. Newell, and G. E. Hindman (2011a). "Advances in planar Mathematical Absorber Reflection Suppression". In: *Antenna Measurement Techniques Association Symposium (AMTA).* Denver, CO.

Gregson, S. F., B. M. Williams, G. F. Masters, A. C. Newell, and G. E. Hindman (2011b). "Application of mathematical absorber reflection suppression to direct far-field antenna range measurements". In: *Antenna Measurement Techniques Association Symposium (AMTA)*. Denver, CO.

Gregson, S. F., J. Dupuy, C. G. Parini, A. C. Newell, and G. E. Hindman (2011c). "Application of mathematical absorber reflection suppression to far-field antenna testing". In: *Loughborough Antennas & Propagation Conference (LAPC)*.

Gregson, S. F., A. C. Newell, G. E. Hindman, and M. J. Carey (2011d). "Application of mathematical absorber reflection suppression to planar near-field antenna measurements". In: *European Conference on Antennas and Propagation (EuCAP)*. Rome, Italy.

Gregson, S. F., J. McCormick, B. J. Kerse, A. C. Newell, and G. E. Hindman (2012a). "Computational and experimental verification of far-field mathematical absorber reflection suppression". In: *European Conference on Antennas and Propagation (EuCAP)*. Prague, Czech Republic.

Gregson, S. F., A. C. Newell, and G. E. Hindman (2012b). "Examination of far-field mathematical absorber reflection suppression through computational electromagnetic simulation". In: *International Journal of Antennas and Propagation* 2012, pp. 1–10.

– (2013). "Behaviour of orthogonal wave functions and the correction of antenna measurements taken in non-anechoic environments". In: *Antennas and Propagation Conference (LAPC)*. Loughborough.

Gregson, S. F., C. G. Parini, A. C. Newell, and P. N. Betjes (2017a). "Using Mathematical Absorber Reflection Suppression (MARS) to partially correct for the non-uniformity of a CATR quiet zone". In: *ESA Workshop on Antenna Measurements, ESA ESTEC*. Nordwijk, the Netherlends.

Gregson, S. F., A. C. Newell, and C. G. Parini (2017b). "Verification of feed spillover reduction using FF-MARS in a CATR using computational electromagnetic simulation". In: *IEEE Antennas and Propagation Society International Symposium (APSURSI)*. San Diego, CA.

Gruber, M. E., J. Knapp, T. M. Dengler, A. Knaak, and T. F. Eibert (2015). "Analysis of a simultaneous clockwise and counterclockwise rotated stirrer in a reverberation chamber". In: *EMC Europe*. Dresden, Germany.

Gustafsson, M., J. B. Andersen, G. Kristensson, and G. F. Pedersen (2012). "Forward scattering of loaded and unloaded antennas". In: *IEEE Transactions on Antennas and Propagation* 60.12, pp. 5663–5668.

Hansen, J. E. (1988). *Spherical Near-Field Antenna Measurements*. 1st ed. London, UK: Peter Pelegrinus Ltd.

Hansen, P. and F. Larsen (1984). "Suppression of reflections by directive probes in spherical near-field measurements". In: *IEEE Transactions on Antennas and Propagation* 32.2, pp. 119–125.

Hansen, P. C. (1990). "Truncated singular value decomposition solutions to discrete ill-posed problems with ill-determined numerical rank". In: *SIAM Journal on Scientific and Statistical Computing* 11.3, pp. 503–518.

Hansen, R. C. (1981). "Fundamental limitations in antennas". In: *Proceedings of the IEEE* 69.2, pp. 170–182.

Hansen, R. C. and R. E. Collin (2011a). *Small Antenna Handbook*. 1st ed. John Wiley & Sons.

Hansen, T. B. (2011b). "Spherical near-field scanning with higher-order probes". In: *IEEE Transactions on Antennas and Propagation* 59.11, pp. 4049–4059.

Hansen, T. B., A. Paulus, and T. F. Eibert (2019). “On the Condition Number of a Normal Matrix in Near-Field to Far-Field Transformations”. In: *IEEE Transactions on Antennas and Propagation* 67.3, pp. 2028–2033.

Harrington, R. (1963). “Electromagnetic scattering by antennas”. In: *IEEE Transactions on Antennas and Propagation* 11.5, pp. 595–596.

– (1965). “Antenna excitation for maximum gain”. In: *IEEE Transactions on Antennas and Propagation* 13.6, pp. 896–903.

Harrington, R. F. (1960). “Effect of antenna size on gain, bandwidth, and efficiency”. In: *Journal of Research of the National Institute of Standards and Technology* 64.1, pp. 1–12.

– (1989). “Boundary integraö formulations for homogenious material bodies”. In: *Journal of Electromagnetic Waves and Applications* 3.1, pp. 1–15.

Harrington, R. F. (1961). *Time-Harmonic Electromagnetic Fields*. 1st ed. McGraw-Hill texts in electrical engineering. OCLC: 832821052. New York: McGraw-Hill.

Hartmann, J. and D. Fasold (1998). “A flexible hardgating system as a diagnostic tool in single and double reflector compact ranges”. In: *Antenna Measurement Techniques Association Symposium (AMTA)*. Montreal, Canada.

Haskou, A., A. Sharaiha, and S. Collardey (2017). “Theoretical and practical limits of superdirective antenna arrays”. In: *Elsevier Comptes Rendus Physique* 18.2, pp. 118–124.

Haupt, R. (2003a). “Synthesis of a plane wave in the near field with a planar phased array”. In: *IEEE Antennas and Propagation Society International Symposium (APSURSI)*. Vol. 1. Columbus, OH.

Haupt, R. (2003b). “Generating a plane wave in the near field with a planar array antenna”. In: *Microwave Journal* 46.9, pp. 152–154.

Haynes, M. and M. Moghaddam (2011). “Multipole and S-parameter antenna and propagation modell”. In: *IEEE Transactions on Antennas and Propagation* 59.1, pp. 225–235.

He, B. and W. C. Chew (2008). “Diagonalizations of vector and tensor addition theorems”. In: *Global Science Press, Communications in Computational Physics* 4.4, pp. 797–819.

Helmholtz, H. v. (1860). “Theorie der Luftschwingungen in Röhren mit offenen Enden”. In: *Journal für die reine und angewandte Mathematik. In zwanglosen Heften* 57.1, pp. 1–72.

Henderson, A., J. R. James, P. Newham, and G. Morris (1989). “Analysis of gating errors in time domain antenna measurements”. In: *IEE Proceedings H - Microwaves, Antennas and Propagation*. Vol. 136, pp. 311–320.

Hess, D. W. (2010a). “The IsoFilter™ technique: a method of isolating the pattern of an individual radiator from data measured in a contaminated environment”. In: *IEEE Antennas and Propagation Magazine* 52.1, pp. 174–181.

Hess, D. W. (2006). “The IsoFilter™ technique: isolating an individual radiator from spherical near-field data measured in a contaminated environment”. In: *European Conference on Antennas and Propagation (EuCAP)*. Nice, France.

Hess, D. W. and S. McBride (2008). “Evaluation of isofilter™ fidelity in selected applications”. In: *Antenna Measurement Techniques Association Symposium (AMTA)*. Vol. 8. Atlanta, GA.

– (2010b). “Applicability of IsoFilterTM selectivity to antenna diagnostics”. In: *European Conference on Antennas and Propagation (EuCAP)*. Barcelona, Spain.

Hess, D. W. (2011). “A theoretical description of the IsoFilter (TM) rejection curve”. In: *European Conference on Antennas and Propagation (EuCAP)*. Rome, Italy, pp. 3892–3896.

Hill, D. A. (1988). “A circular array for plane-wave synthesis”. In: *IEEE Transactions on Electromagnetic Compatibility* 30.1, pp. 3–8.

– (2009). *Electromagnetic Fields in Cavities: Deterministic and Statistical Theories*. 1st ed. Vol. 35. New Jersey: John Wiley & Sons.

Hofmann, B., O. Neitz, and T. F. Eibert (2019). “On the minimum number of samples for sparse recovery in spherical antenna near-field measurements”. In: *IEEE Transactions on Antennas and Propagation* 67.12, pp. 7597–7610.

Hoop, A. T. de, M. Stoopman, W. A. Serdijn, and I. E. Lager (2013). “Equivalent Thévenin and Norton Kirchhoff circuits of a receiving antenna”. In: *IEEE Antennas and Wireless Propagation Letters* 12, pp. 1627–1629.

Hsiao, Y.-T., Y.-Y. Lin, Y.-C. Lu, and H.-T. Chou (2003). “Applications of time-gating method to improve the measurement accuracy of antenna radiation inside an anechoic chamber”. In: *IEEE Antennas and Propagation Society International Symposium (APSURSI)*. Vol. 3. Columbus, OH.

Hua, Y. and T. K. Sarkar (1989). “Generalized pencil-of-function method for extracting poles of an EM system from its transient response”. In: *IEEE Transactions on Antennas and Propagation* 37.2, pp. 229–234.

Hua, Y. and T. K. Sarkar (1990a). “Matrix pencil and system poles”. In: *Signal Processing* 21.2, pp. 195–198.

– (1990b). “On the total least squares linear prediction method for frequency estimation”. In: *IEEE transactions on acoustics, speech, and signal processing* 38.12, pp. 2186–2189.

– (1991). “On SVD for estimating generalized eigenvalues of singular matrix pencil in noise”. In: *IEEE International Sympoisum on Circuits and Systems (ISCAS)*. Singapore.

Isenberg, C. (1992). *The Science of Soap Films and Soap Bubbles*. 1st ed. New York: Dover Publications.

Isernia, T., G. Leone, and R. Pierri (1994a). “Phaseless near field techniques: formulation of the problem and field properties”. In: *Journal of Electromagnetic Waves and Applications* 8.7, pp. 871–888.

– (1994b). “Phaseless near field techniques: uniqueness conditions and attainment of the solution”. In: *Journal of Electromagnetic Waves and Applications* 8.7, pp. 889–908.

– (1995). “Phase retrieval of radiated fields”. In: *Inverse Problems* 11.1, p. 183.

J., Y. and T. Sarkar (2007). “Interpolation/extrapolation of radar cross section (RCS) Data in the frequency domain using the Cauchy method”. In: *IEEE Transactions on Antennas and Propagation* 55.10, pp. 2844–2851.

Jensen, F. and A. Frandsen (2004). “On the number of modes in spherical wave expansions”. In: *Antenna Measurement Techniques Association Symposium (AMTA)*. Stone Mountain Park, GA.

Jin, J.-M. (2015). *Theory and Computation of Electromagnetic Fields*. 2nd ed. Hoboken, New Jersey: IEEE Press.

Johnson, R. C., H. A. Ecker, and J. S. Hollis (1973). “Determination of far-field antenna patterns from near-field measurements”. In: *Proceedings of the IEEE* 61.12, pp. 1668–1694.

Jørgensen, E., P. Meincke, C. Cappellin, and M. Sabbadini (2010). “Improved source reconstruction technique for antenna diagnostics”. In: *Proceeedings of the 32nd ESA Antenna Workshop*. Nordwijk, the Netherlands.

Jough, R. V. D., M. Hajian, and L. P. Ligthart (1997). "Antenna time-domain measurement techniques". In: *IEEE Antennas and Propagation Magazine* 39.5, pp. 7–11.

Kenig, C. E. (1989). "Restriction theorems, Carleman estimates, uniform Sobolev inequalities and unique continuation". In: *Harmonic Analysis and Partial Differential Equations*. Ed. by J. García-Cuerva. Vol. 1384. Series Title: Lecture Notes in Mathematics. Berlin, Heidelberg: Springer Berlin Heidelberg, pp. 69–90.

Kerns, D. M. (1963). "Analytical techniques for the correctionof near field antenna measurements made with an arbitrary but known measureing antenna". In: *URSI-IRE Meeting*. Vol. 6. Washington DC.

Khare, K. (2007). "Sampling theorem, bandlimited integral kernels and inverse problems". In: *Inverse Problems* 23.4, pp. 1395–1416.

Kim, K. T. (1996). "The translation formula for vector multipole fields and the recurrence relations of the translation coefficients of scalar and vector multipole fields". In: *IEEE Transactions on Antennas and Propagation* 44.11, pp. 1482–1487.

Klinkenbusch, L. (2008). "Brief review of spherical-multipole analysis in radio science". In: *URSI Radio Science Bulletin* 2008.324, pp. 5–16.

– (2009). "On the uniqueness of electromagnetic fields and consequences for inverse-scattering problems". In: *International Conference on Electromagnetics in Advanced Applications*. Torino, Italy.

Knapp, J. and T. F. Eibert (2016). "Algorithmische Echo-Unterdrückung in der Nahfeld- Fernfeld-Transformation von gemessenen Antennenfeldern". In: *Kleinheubacher Tagung*. Miltenberg, Germany.

Knapp, J., A. Paulus, C. Lopez, and T. F. Eibert (2017a). "Comparison of non-convex cost functionals for the consideration of phase differences in phaseless near-field far-field transformations of measured antenna fields". In: *Advances in Radio Science* 15, pp. 11–19.

Knapp, J., A. Paulus, and T. F. Eibert (2017b). "Implementation and evaluation of the utilization of partial knowledge of phase differences in magnitude only near-field far-field transformations". In: *Progress In Electromagnetics Research Symposium (PIERS)*. St. Petersburg, Russia.

Knapp, J. and T. F. Eibert (2017c). "Integral equation based field transformation with effective echo suppression in the near-field by virtual beam forming and field synthesis". In: *Progress In Electromagnetics Research Symposium (PIERS)*. St. Petersburg, Russia.

– (2018a). "Accurate determination of radiation patterns from near-field measurements in strongly reflective environments". In: *European Conference on Antennas and Propagation (EuCAP)*. London, UK.

Knapp, J., R. Morelli, and T. F. Eibert (2018b). "Accurate far-field pattern reconstruction from near-field meaurements with inconvenient probes". In: *Progress In Electromagnetic Research Symposium (PIERS)*. Toyama, Japan.

Knapp, J., A. Paulus, and T. F. Eibert (2018c). "Algorithmic reconstruction of antenna measurement samples from magnitude-only near-field measurements". In: *Kleinheubacher Tagung*. Miltenberg, Germany.

Knapp, J. and T. F. Eibert (2018d). "Fast irregular antenna field transformation algorithm for unmanned aerial vehicle near-field measurements". In: *AMTA Workshop UAV-based Antenna and Field Measurements within the 12th European Conference on Antennas and Propagation (EuCAP)*. London, UK.

Knapp, J., J. Kornprobst, and T. F. Eibert (2019a). “Equivalent source and pattern reconstruction from oversampled measurements in highly-reflective environments”. In: *IET Microwaves, Antennas & Propagation* 13.13, pp. 2232–2241.

Knapp, J., A. Paulus, and T. F. Eibert (2019b). “Investigation on diversity effects for phaseless near-field far-field transformations”. In: *European Conference on Antennas and Propagation (EuCAP)*. Krakow, Poland.

Knapp, J. and T. F. Eibert (2019c). “Near-field antenna pattern measurements in highly reflective environments”. In: *IEEE Transactions on Antennas and Propagation* 67.9, pp. 6159–6169.

Knapp, J., A. Paulus, and T. F. Eibert (2019d). “Reconstruction of squared field magnitudes and relative phases from magnitude-only near-field measurements”. In: *IEEE Transactions on Antennas and Propagation* 67.5, pp. 3397–3409.

Knapp, J., J. Kornprobst, A. Paulus, and T. F. Eibert (2019e). “Time-gating the sources in inverse equivalent source reconstruction problems to eliminate mutual coupling effects”. In: *International Conference on Electromagnetics in Advanced Applications (ICEAA)*. Granada, Spain.

Knapp, J., J. Kornprobst, and T. F. Eibert (2020). “Suppressing undesired echoes by sparsity based time gating of reconstructed sources”. In: *European Conference on Antennas and Propagation (EuCAP)*. Copenhagen, Denmark.

Knapp, J., A. Paulus, J. Kornprobst, U. Siart, and T. F. Eibert (2021). “Multifrequency phase retrieval for antenna measurements”. In: *IEEE Transactions on Antennas and Propagation* 69.1, pp. 488–501.

Koh, J., A. De, T. K. Sarkar, H. Moon, W. Zhao, and M. Salazar-Palma (2011). “Free space radiation pattern reconstruction from non-anechoic measurements using an impulse response of the environment”. In: *IEEE Transactions on Antennas and Propagation* 60.2, pp. 821–831.

Kong, J. A. (1986). *Electromagnetic Wave Theory*. 1st ed. New York: Wiley.

Kornprobst, J. and T. F. Eibert (2018). “A weak-form combined source integral equation with explicit inversion of the combined-source condition”. In: *IEEE Antennas and Wireless Propagation Letters* 17.12, pp. 2174–2178.

Kornprobst, J., J. Knapp, and T. F. Eibert (2019a). “Approximate inverse of the Rao-Wilton-Glisson basis functions Gram matrix via monopolar representation”. In: *IEEE Antennas and Propagation Society International Symposium (APSURSI)*. Atlanta, GA.

Kornprobst, J., J. Knapp, O. Neitz, and T. F. Eibert (2019b). “Measurement-error controlled iterative least-squares solutions of inverse field transformation problems”. In: *Antenna Measurement Techniques Association Symposium (AMTA)*. San Diego, CA,

Kornprobst, J., R. A. M. Mauermayer, O. Neitz, J. Knapp, and T. F. Eibert (2019c). “On the solution of inverse equivalent surface-source problems”. In: *Progress In Electromagnetics Research* 165, pp. 47–65.

Kornprobst, J., O. Neitz, J. Knapp, R. A. M. Mauermayer, and T. F. Eibert (2019d). “Solving inverse equivalent surface source problems by the normal error system of normal equations”. In: *2019 International Conference on Electromagnetics in Advanced Applications (ICEAA)*. Granada, Spain.

Kornprobst, J., J. Knapp, R. A. M. Mauermayer, O. Neitz, A. Paulus, and T. F. Eibert (2021a). “Accuracy and conditioning of surface-source based near-field to far-field transformations”. In: *IEEE Transactions on Antennas and Propagation (Early Access)*, pp. 1–1.

Kornprobst, J., A. Paulus, J. Knapp, and T. F. Eibert (2021b). “Phase retrieval for partially coherent observations”. In: *IEEE Transactions on Signal Processing* 69, pp. 1394–1406.

Korotkova, O. and E. Wolf (2007). “Scattering matrix theory for stochastic scalar fields”. In: *Physical Review E* 75.5, p. 056609.

Kurokawa, K. (1965). “Power waves and the scattering matrix”. In: *IEEE Transactions on Microwave Theory and Techniques* 13.2, pp. 194–202.

Kwon, D.-H. and D. M. Pozar (2009). “Optimal characteristics of an arbitrary receive antenna”. In: *IEEE Transactions on Antennas and Propagation* 57.12, pp. 3720–3727.

Laitinen, T. (2005). “Advanced spherical antenna measurements”. Dissertation. Helsinki University of Technology;

Laitinen, T., P. Kyösti, J.-P. Nuutinen, and P. Vainikainen (2010). “On the number of OTA antenna elements for plane-wave synthesis in a MIMO-OTA test system involving a circular antenna array”. In: *European Conference on Antennas and Propagation (EuCAP)*. Barcelona, Spain.

Larsen, F. H. (1977). “Probe correction of spherical near-field measurements”. In: *Electronics Letters* 14.13, pp. 393–395.

Larsen, F. H. (1984). “Probe-corrected spherical near-field antenna measurements”. In: *IEEE Transactions on Antennas and Propagation* 32.9, pp. 1012–1012.

Las-Heras, F. and T. K. Sarkar (2002). “Radial field retrieval in spherical scanning for current reconstruction and NF-FF transformation”. In: *IEEE Transactions on Antennas and Propagation* 50.6, pp. 866–874.

Leather, P. S. H., J. D. Parsons, J. Romeu, S. Blanch, and A. Aguasca (2004a). “Practical validation of antenna pattern measurement interference cancellation using a correlation technique”. In: *IEEE Antennas and Propagation Society International Symposium APSURSI*. Monterey, CA.

Leather, P. S. H., J. D. Parsons, and J. Romeu (2004b). “Signal processing techniques improve antenna pattern measurement”. In: *IEEE Antenna Measurements and SAR*. Loughborough, UK.

Leibfritz, M. M., M. D. Blech, and T. F. Eibert (2006). “A comparison ofsoftware- and hardware-gating techniques applied to near-field antenna measurements”. In: *Kleinheubacher Tagung*. Miltenberg, Germany.

Leon Fernandez, G., S. Loredo, S. Zapatero, and F. Las Heras Andres (2009). “Radiation pattern retrieval in non-anechoic chambers using the matrix pencil algorithm”. In: *Progress In Electromagnetics Research Letters* 9, pp. 119–127.

Lestari, A. A., A. B. Suksmono, A. Kurniawan, E. Bharata, A. G. Yarovoy, and L. P. Ligthart (2005). “A facility for UWB antenna measurements in time domain”. In: *IEEE International Workshop on Antenna Technology: Small Antennas and Novel Metamaterials*. Singapore, Singapore.

Levitas, B. N. and D. M. Ponomarev (1996). “Antenna measurements in time domain”. In: *IEEE Antennas and Propagation Society International Symposium APSURSI*. Vol. 1. Baltimore, USA.

Levitas, B. N. (2006). “Time domain antenna measurement systems”. In: *3rd International Conference on Ultrawideband and Ultrashort Impulse Signals*. Sevastopol, Ukraine.

Li, Z.-C., H.-T. Huang, and Y. Wei (2011). “Ill-conditioning of the truncated singular value decomposition, Tikhonov regularization and their applications to numerical partial differential equations: Ill-conditioning of the TSVD”. In: *Numerical Linear Algebra with Applications* 18.2, pp. 205–221.

Loredo, S., G. Leon, S. Zapatero, and F. Las-Heras (2009). “Measurement of low-gain antennas in non-anechoic test sites through wideband channel characterization and echo cancellation [Measurements Corner]”. In: *IEEE Antennas and Propagation Magazine* 51.1, pp. 128–135.

Loredo, S., M. R. Pino, F. Las-Heras, and T. K. Sarkar (2004). “Echo identification and cancellation techniques for antenna measurement in non-anechoic test sites”. In: *IEEE Antennas and Propagation Magazine* 46.1, pp. 100–107.

Loredo, S., G. Leon, R. G. Ayestaran, and F. Las-Heras (2011). “Reconstruction of antenna radiation patterns from phaseless measurements in nonanechoic chambers”. In: *IEEE Antennas and Wireless Propagation Letters* 10, pp. 1282–1285.

Love, A. E. H. (1901). “The integrationof the equtions of propataion of electric waves.” In: *Proceedings of the Royal Society of London* 68.442-450, pp. 19–21.

Love, A. W. (2003). “Comment on ”Limitations of the Thevenin and Norton equivalent circuits for a receiving antenna””. In: *IEEE Antennas and Propagation Magazine* 45.4, pp. 98–99.

Ludwig, A. (1971). “Near-field far-field transformations using spherical-wave expansions”. In: *IEEE Transactions on Antennas and Propagation* 19.2, pp. 214–220.

Luo, J., Z. Xie, and M. Xie (2016). “Interpolated DFT algorithms with zero padding for classic windows”. In: *Mechanical Systems and Signal Processing* 70-71, pp. 1011–1025.

Marcuvitz, N. (1951). *Waveguide Handbook*. 1st ed. 21. IET.

Marks, R. J. (1991). *Introduction to Shannon sampling and interpolation theory*. 1st ed. Springer texts in electrical engineering. New York: Springer-Verlag.

Martin, O. J. F., C. Girard, and A. Dereux (1995). “Generalized field propagator for electromagnetic scattering and light confinement”. In: *Physical Review Letters* 74.4, pp. 526–529.

Martin, O. J. F. and N. B. Piller (1998). “Electromagnetic scattering in polarizable backgrounds”. In: *Physical Review E* 58.3, pp. 3909–3915.

Martini, E., G. Carli, and S. Maci (2008). “An equivalence theorem based on the use of electric currents radiating in free space”. In: *IEEE Antennas and Wireless Propagation Letters* 7, pp. 421–424.

Mauermayer, R. A. M. and T. F. Eibert (2017). “Sparse time domain signal representation for echo suppression in antenna measurements”. In: *International Conference on Electromagnetics in Advanced Applications (ICEAA)*. Verona, Italy.

Mauermayer, R. A. M., Y. Weitsch, and T. F. Eibert (2015). “Electromagnetic field synthesis by hierarchical plane wave-based field transformation”. In: *IEEE Transactions on Antennas and Propagation* 63.12, pp. 5561–5572.

Mauermayer, R. A. M. and T. F. Eibert (2016). “Time gating based on sparse time domain signal reconstruction from limited frequency domain information”. In: *Antenna Measurement Techniques Association Symposium (AMTA)*. Austin, TX.

Mautz, J. and R. Harrington (1979). “A combined-source solution for radiation and scattering from a perfectly conducting body”. In: *IEEE Transactions on Antennas and Propagation* 27.4, pp. 445–454.

Migliore, D., F. Soldovieri, and R. Pierri (2000). “Far-field antenna pattern estimation from near-field data using a low-cost amplitude-only measurement setup”. In: *Instrumentation and Measurement, IEEE Transactions on* 49.1, pp. 71–76.

Montgomery, C. G., R. H. Dicke, and E. M. Purcell (1948). *Principles of Microwave Engineering*. 1st ed. McGraw-Hill, New York.

Moon, J.-I., S.-S. Oh, and Y.-B. Jung (2009). “Echo-cancellation technique with recursive data in nonanechoic test sites”. In: *IEEE Antennas and Wireless Propagation Letters* 8, pp. 558–560.

Morales, M. J. L., F. Saccardi, M. S. Castañer, and L. J. Foged (2016). “Comparison of echo reduction techniques for one-single cut antenna measurements”. In: *European Conference on Antennas and Propagation (EuCAP)*. Davos, Switzerland.

Müller, C. (1948). “Die Grundzüge einer mathematischen Theorie elektromagnetischer Schwingungen”. In: *Archiv der Mathematik, Springer* 1.4, pp. 296–302.

– (1954). “On the behavior of the solutions of the differential equation $\Delta U = F(x,u)$ in the neighborhood of a point”. In: *Communications on Pure and Applied Mathematics* 7.3, pp. 505–515.

Neitz, O., R. A. M. Mauermayer, Y. Weitsch, and T. F. Eibert (2017). “A propagating plane-wave-based near-field transmission equation for antenna gain determination from irregular measurement samples”. In: *IEEE Transactions on Antennas and Propagation* 65.8, pp. 4230–4238.

Neitz, O. (2020). “Propagating plane-wave expansions for microwave near-field imaging and radar cross section determination”. PhD Thesis. Munich: Dissertation, Technical University of Munich.

Newell, A. C. (1988). “Error analysis techniques for planar near-field measurements”. In: *IEEE Transactions on Antennas and Propagation* 36.6, pp. 754–768.

Newell, A. C. and G. Hindman (2008). “Scattering reduction in spherical near-field measurements”. In: *IEEE Antennas and Propagation Society International Symposium (APSURSI)*. San Diego, CA.

Oppenheim, A. V. and R. W. Schafer (2010). *Discrete-Time Signal Processing*. 3rd ed. Pearson Higher Education.

Oseen, C. W. (1922). “Die Einsteinsche Nadelstichstrahlung und die Maxwellschen Gleichungen”. In: *Annalen der Physik* 374.19, pp. 202–204.

Paulus, A., J. Knapp, and T. F. Eibert (2016). “Phasenlose Nahfeld-Fernfeld Transformation von gemessenen Antennenfeldern über nicht-konvexe Optimierung”. In: *Kleinheubacher Tagung*. Miltenberg, Germany.

– (2017a). “Phaseless near-field far-field transformation utilizing combinations of probe signals”. In: *IEEE Transactions on Antennas and Propagation* 65.10, pp. 5492–5502.

– (2017b). “Phaseless near-field measurements and transformation for electrically large antennas”. In: *Nationale Konferenz ”Satellitenkommunikation in Deutschland”*. Bonn, Germany.

– (2017c). “Utilizing partial knowledge of phase differences in convex optimization for amplitude-only near-field far-field transformation”. In: *European Conference on Antennas and Propagation (EuCAP)*. Paris, France.

– (2018a). “Nonconvex phaseless near-field far-field transformation for electrically large problems”. In: *European Conference on Antennas and Propagation (EuCAP)*. London, UK.

– (2018b). “Parallel brute-force evaluation of dipole radiation operators on GPUs”. In: *Progress In Electromagnetics Research Symposium (PIERS)*. Toyama, Japan.

– (2018c). “Phasenlose Nahfeld-Fernfeld Transformation mit Neuronalen Netzen”. In: *Kleinheubacher Tagung*. Miltenberg, Germany.

Paulus, A., J. Knapp, J. Kornprobst, and T. F. Eibert (2020a). “Improved-reliability phase-retrieval with broadband antenna measurements”. In: *European Conference on Antennas and Propagation (EuCAP)*. Copenhagen, Denmark.

Paulus, A., J. Knapp, and T. F. Eibert (2020b). “Using broadband signals to enhance the stability of phaseless near-field far-field transformations”. In: *IEEE International Conference on Computational Electromagnetics*. Singapore, Singapore.

Paulus, A., J. Kornprobst, J. Knapp, and T. F. Eibert (2021). “Linear phase retrieval for near-field measurements with locally known phase relations”. In: *European Conference on Antennas and Propagation (EuCAP)*. Düsseldorf, Germany.

Persson, K. and M. Gustafsson (2005). “Reconstruction of equivalent currents using a near-field data transformation-with radome applications”. In: *EMW Publishing, Progress In Electromagnetics Research* 54, pp. 179–198.

Peterson, A. F., C. F. Smith, and R. Mittra (1988). “Eigenvalues of the moment-method matrix and their effect on the convergence of the conjugate gradient algorithm (EM scattering)”. In: *IEEE Transactions on Antennas and Propagation* 36.8, pp. 1177–1179.

Petre, P. and T. K. Sarkar (1992). “A planar near-field to far-field transformation using an equivalent magnetic current approach”. In: *IEEE Antennas and Propagation Society International Symposium APSURSI*. Chicago, IL: IEEE.

– (1996). “Differences between modal expansion and intergral equation methods for planar near-field to far-field transformation”. In: *Progress In Electromagnetics Research* 12, pp. 37–56.

Pierri, R., G. D’Elia, and F. Soldovieri (1999). “A two probes scanning phaseless near-field far-field transformation technique”. In: *IEEE Transactions on Antennas and Propagation* 47.5, pp. 792–802.

Piestun, R. and D. A. B. Miller (2000). “Electromagnetic degrees of freedom of an optical system”. In: *Journal of the Optical Society of America A* 17.5, pp. 892–902.

Pogorzelski, R. J. (2009). “Extended probe instrument calibration (EPIC) for accurate spherical near-field antenna measurements”. In: *IEEE Transactions on Antennas and Propagation* 57.10, pp. 3366–3375.

– (2010). “Experimental demonstration of the extended probe instrument calibration (EPIC) technique”. In: *IEEE Transactions on Antennas and Propagation* 58.6, pp. 2093–2097.

Pozar, D. (2004). “Scattered and absorbed powers in receiving antennas”. In: *IEEE Antennas and Propagation Magazine* 46.1, pp. 144–145.

Quijano, J. L. A., G. Vecchi, M. Sabbadini, L. Scialacqua, B. Bencivenga, F. Mioc, and L. Foged (2011a). “Source reconstruction in advanced processing of antenna measurements”. In: *European Conference on Antennas and Propagation (EuCAP)*. Rome, Italy, pp. 3875–3879.

Quijano, J. L. A. and G. Vecchi (2009). “Improved-accuracy source reconstruction on arbitrary 3-D surfaces”. In: *IEEE Antennas and Wireless Propagation Letters* 8, pp. 1046–1049.

– (2010a). “Field and source equivalence in source reconstruction on 3D surfaces”. In: *Progress In Electromagnetics Research* 103, pp. 67–100.

– (2010b). “Near-and very near-field accuracy in 3-D source reconstruction”. In: *IEEE Antennas and Wireless Propagation Letters* 9, pp. 634–637.

Quijano, J. L. A., L. Scialacqua, J. Zackrisson, L. J. Foged, M. Sabbadini, and G. Vecchi (2011b). “Suppression of undesired radiated fields based on equivalent currents reconstruction from measured data”. In: *IEEE Antennas and Wireless Propagation Letters* 10, pp. 314–317.

Qureshi, M. A., C. H. Schmidt, and T. F. Eibert (2013a). “Adaptive sampling in spherical and cylindrical near-field antenna measurements”. In: *IEEE Antennas and Propagation Magazine* 55.1, pp. 243–249.

Qureshi, M. A., C. H. Schmidt, and T. F. Eibert (2013b). “Efficient near-field far-field transformation for nonredundant sampling representation on arbitrary surfaces in near-field antenna measurements”. In: *IEEE Transactions on Antennas and Propagation* 61.4, pp. 2025–2033.

Qureshi, M. A., C. H. Schmidt, and T. F. Eibert (2013c). “Near-field error analysis for arbitrary scanning grids using fast irregular antenna field transformation algorithm”. In: *Progress In Electromagnetics Research B* 48, pp. 197–220.

Rahola, J. (1996). “Diagonal Forms of the Translation Operators in the Fast Multipole Algorithm for Scattering Problems”. In: *BIT Numerical Mathematics* 36.2, pp. 333–358.

Rao, M. M., T. K. Sarkar, T. Anjali, and R. S. Adve (1999). “Simultaneous extrapolation in time and frequency domains using hermite expansions”. In: *IEEE Transactions on Antennas and Propagation* 47.6, pp. 1108–1115.

Rao, S., D. Wilton, and A. Glisson (1982). “Electromagnetic scattering by surfaces of arbitrary shape”. In: *IEEE Transactions on Antennas and Propagation* 30.3, pp. 409–418.

Razavi, S. F. and Y. Rahmat-Samii (2006). “Phaseless planar near field measurements for scanned beams: Difficulties, a hybrid solution and measured results”. In: *IEEE Antennas and Propagation Society International Symposium APSURSI.* Albuquerque, NM: IEEE, pp. 429–432.

Reddy, J. N. (2013). *An Introduction to Continuum Mechanics, Second Edition*. 2nd ed. Cambridge: Cambridge University Press.

Rengarajan, S. R. and Y. Rahmat-Samii (2000). “The field equivalence principle: Illustration of the establishment of the non-intuitive null fields”. In: *IEEE Antennas and Propagation Magazine* 42.4, pp. 122–128.

Rokhlin, V. (1993). “Diagonal forms of translation operators for the Helmholtz equation in three dimensions”. In: *Applied and Computational Harmonic Analysis* 1.1, pp. 82–93.

Saad, Y. (2003). *Iterative methods for sparse linear systems*. 2nd ed. Philadelphia: SIAM.

Saad, Y. and M. H. Schultz (1986). “GMRES: A generalized minimal residual algorithm for solving nonsymmetric linear systems”. In: *SIAM Journal on Scientific and Statistical Computing* 7.3, pp. 856–869.

Salt, H. (1977). “Practical realization of superdirective arrays”. In: *IET Radio and Electronic Engineer* 47.4, pp. 143–156.

Santiago, X. G., M. Hammerschmidt, S. Burger, C. Rockstuhl, I. Fernandez-Corbaton, and L. Zschiedrich (2019). “Decomposition of scattered electromagnetic fields into vector spherical wave functions on surfaces with general shapes”. In: *Physical Review B* 99.4, p. 045406.

Sarkar, T. K., P. Petre, A. Taaghol, and R. F. Harrington (1997). “An alternative spherical near field to far field transformation”. In: *Progress In Electromagnetics Research* 16, pp. 269–284.

Sarkar, T. K. and O. Pereira (1995). “Using the matrix pencil method to estimate the parameters of a sum of complex exponentials”. In: *IEEE Antennas and Propagation Magazine* 37.1, pp. 48–55.

Sarkar, T. K. and A. Taaghol (1999). “Near-field to near/far-field transformation for arbitrary near-field geometry utilizing an equivalent electric current and MoM”. In: *IEEE Transactions on Antennas and Propagation* 47.3, pp. 566–573.

Sarkar, T. K., M. Salazar-Palma, and E. L. Mokole (2016). “Application of the principle of analytic continuation to interpolate/extrapolate system responses resulting in reduced computations—part a: parametric methods”. In: *IEEE Journal on Multiscale and Multiphysics Computational Techniques* 1, pp. 48–59.

Saxon, D. S. (1955). “Tensor scattering matrix for the electromagnetic field”. In: *Physical Review* 100.6, pp. 1771–1775.

Schanze, T. (1995). “Sinc interpolation of discrete periodic signals”. In: *IEEE Transactions on Signal Processing* 43.6, pp. 1502–1503.

Schejbal, V., O. Fiser, and O. Ondracek (2011). “Comments on “On the power absorbed and scattered by an antenna” [letter to the editor]”. In: *IEEE Antennas and Propagation Magazine* 53.2, pp. 172–174.

Schelkunoff, S. A. (1936). “Some equivalence theorems of electromagnetics and their application to radiation problems”. In: *Bell System Technical Journal* 15.1, pp. 92–112.

– (1943). “A mathematical theory of linear arrays”. In: *The Bell System Technical Journal* 22.1, pp. 80–107.

– (1951). “Kirchhoff’s formula, its vector analogue, and other field equivalence theorems”. In: *Communications on Pure and Applied Mathematics* 4.1, pp. 43–59.

Schmidt, C. H., M. M. Leibfritz, and T. F. Eibert (2007). “Near-field far-field transformation employing plane wave expansion and diagonal translation operators”. In: *URSI International Symposium on Electromagnetic Theory,* Ottawa, Canada.

Schmidt, C. H., S. F. Razavi, T. F. Eibert, and Y. Rahmat-Samii (2010). “Phaseless spherical near-field antenna measurements for low and medium gain antennas”. In: *Advances in Radio Science* 8.B. 2-1/2-2, pp. 43–48.

Schmidt, C. H., D. T. Schobert, and T. F. Eibert (2011a). “Electric dipole based synthetic data generation for probe-corrected near-field antenna measurements”. In: *European Conference on Antennas and Propagation (EuCAP).* Rome, Italy.

Schmidt, C. H., M. M. Leibfritz, and T. F. Eibert (2008a). “Fully probe-corrected near-field far-field transformation employing plane wave expansion and diagonal translation operators”. In: *IEEE Transactions on Antennas and Propagation* 56.3, pp. 737–746.

Schmidt, C. H. and T. F. Eibert (2008b). “Multilevel fst near-field far-field transformation for electically large antennas”. In: *IEEE Antennas and Propagation Society International Symposium (APSURSI).* San Diego, CA,

Schmidt, C. H. and Y. Rahmat-Samii (2009). “Phaseless spherical near-field antenna measurements: Concept, algorithm and simulation”. In: *IEEE Antennas and Propagation Society International Symposium (APSURSI).* Charleston, SC.

Schmidt, C. H. and T. F. Eibert (2011b). “Assessment of irregular sampling near-field far-field transformation employing plane-wave field representation”. In: *IEEE Antennas and Propagation Magazine* 53.3, pp. 213–219.

Schnattinger, G., C. Lopez, E. Kılıç, and T. F. Eibert (2014). “Fast near-field far-field transformation for phaseless and irregular antenna measurement data”. In: *Advances in Radio Science* 12.Young, pp. 171–177.

Schot, S. H. (1992). “Eighty years of Sommerfeld’s radiation condition”. In: *Historia Mathematica* 19.4, pp. 385–401.

Schwebel, S. L. (1970). “Advanced and retarded solutions in field theory”. In: *International Journal of Theoretical Physics* 3.5, pp. 347–353.

Shannon, C. E. and W. Weaver (1998). *The Mathematical Theory of Communication.* 1st ed. Urbana: Univ. of Illinois Press.

Silver, S., ed. (1949). *Microwave Antenna Theory and Design.* 1st ed. OCLC: 233647457. New York: Dover Publ.

Smith, J. O. (2010). *Mathematics of the discrete Fourier transform (DFT): with audio applications*. 1st ed. North Charleston: BookSurge.

Socher, E. and R. Kastner (2013). “An often overlooked term in the application of the Poynting theorem around a receiving antenna”. In: *IEEE Antennas and Propagation Society International Symposium (APSURSI)*. ISSN: 1947-1491. Orlando, FL, pp. 1462–1463.

Socher, E., H. Shannan, and R. Kastner (2014). “On the relationship between the physical aperture and the scattered power from a receiving antenna”. In: *IEEE Antennas and Propagation Society International Symposium (APSURSI)*. Memphis, TN.

– (2015). “On the physical aperture and the power that exits a surface enclosing a receiving antenna”. In: *E-FERMAT* 7.2, pp. 1–6.

Solimene, R., M. A. Maisto, and R. Pierri (2013). “Role of diversity on the singular values of linear scattering operators: the case of strip objects”. In: *Journal of the Optical Society of America A* 30.11, p. 2266.

– (2019). “Sampling approach for singular system computation of a radiation operator”. In: *Journal of the Optical Society of America A* 36.3, p. 353.

Sommerfeld, A. (1912). “Die Greensche Funktion der Schwingungsgleichung”. In: *Jahresbericht der Deutschen Mathematiker-Vereinigung* 21, pp. 309–353.

Song, J., C.-C. Lu, and W. C. Chew (1997). “Multilevel fast multipole algorithm for electromagnetic scattering by large complex objects”. In: *IEEE Transactions on Antennas and Propagation* 45.10, pp. 1488–1493.

Song, J. and W. C. Chew (2001). “Error analysis for the truncation of multipole expansion of vector Green’s functions [EM scattering]”. In: *IEEE Microwave and Wireless Components Letters* 11.7, pp. 311–313.

Song, J. and W. C. Chew (1995). “Multilevel Fast-Multipole Algorithm for Solving Combined Field Integral Equations of Electromagnetic Scattering”. In: *Microwave and Optical Technology Letters* 10.1, pp. 14–19.

Stein, S. (1961). “Addition theorems for spherical wave functions”. In: *Quarterly of Applied Mathematics* 19.1, pp. 15–24.

Steyskal, H. (2010). “On the power absorbed and scattered by an antenna”. In: *IEEE Antennas and Propagation Magazine* 52.6, pp. 41–45.

Stratton, J. A. (1941). *Electromagnetic Theory*. 1st ed. International series in pure and applied physics. OCLC: 536704. New York: McGraw-Hill.

Štumpf, M. (2016). “Receiving-antenna Kirchhoff-equivalent circuits and their scattering reciprocity properties”. In: *IET Microwaves, Antennas & Propagation* 10.9, pp. 983–990.

Stupfel, B. (2004). “A study of the condition number of various finite element matrices involved in the numerical solution of Maxwell’s equations”. In: *IEEE Transactions on Antennas and Propagation* 52.11, pp. 3048–3059.

Stupfel, B. and Y. Morel (2008). “Singular value decomposition of the radiation operator-application to model-order and far-field reduction”. In: *IEEE Transactions on Antennas and Propagation,* 56.6, pp. 1605–1615.

Su, C.-C. (2003). “On the equivalent generator voltage and generator internal impedance for receiving antennas”. In: *IEEE Transactions on Antennas and Propagation* 51.2, pp. 279–285.

Taaghol, A. and T. K. Sarkar (1996). “Near-field to near/far-field transformation for arbitrary near-field geometry, utilizing an equivalent magnetic current”. In: *IEEE Transactions on Electromagnetic Compatibility* 38.3, pp. 536–542.

Tai, C.-T. (1994). *Dyadic Green Functions in Electromagnetic Theory*. 2nd ed. IEEE Press series on electromagnetic waves. Piscataway, NJ: IEEE Press.

Tian, J., L. Zhang, N. Li, and W. Chen (2008). "Time-gating method for V/UHF antenna pattern measurement inside an anechoic chamber". In: *2008 International Conference on Microwave and Millimeter Wave Technology*. Vol. 2. Nanjing, China.

Tian, Z. and S. Gregson (2019). "Examination of the Effectiveness of Mode Orthogonalisation and Filtering for Scattering Suppression in Antenna Measurements Through Computational Electromagnetic Simulation". In: *European Conference on Antennas and Propagation (EuCAP)*. Krakow, Poland.

Tice, T. and J. Richmond (1955). "Probes for microwave near-field measurements". In: *IEEE Transactions on Microwave Theory and Techniques* 3.3, pp. 32–34.

Toivanen, J. T., T. A. Laitinen, and P. Vainikainen (2010). "Modified test zone field compensation for small-antenna measurements". In: *IEEE Transactions on Antennas and Propagation* 58.11, pp. 3471–3479.

Toivanen, J. T., T. A. Laitinen, S. Pivnenko, and L. Nyberg (2009). "Calibration of multi-probe antenna measurement system using test zone field compensation". In:

Toraldo di Francia, G. (1969). "Degrees of Freedom of an Image". In: *Journal of the Optical Society of America* 59.7, p. 799.

Uzkov, A. I. (1946). "An approach to the problem of optimum directive antenna design". In: *Comptes Rendus (Doklady) de l'Academie des Sciences de l'URSS*. Vol. 53. Issue: 1, pp. 35–38.

Van Bladel, J. (2002). "On the equivalent circuit of a receiving antenna". In: *IEEE Antennas and Propagation Magazine* 44.1, pp. 164–165.

– (2007). "Power aspects of the equivalent circuit of an antenna". In: *IEEE Antennas and Propagation Magazine* 49.6, pp. 71–78.

Vipiana, F., P. Pirinoli, and G. Vecchi (2007). "Spectral properties of the EFIE-MoM matrix for dense meshes with different types of bases". In: *IEEE Transactions on Antennas and Propagation* 55.11, pp. 3229–3238.

Waiyapattanakorn, C. and C. G. Parini (1993). "Theoretical and experimental investigations of using time domain gating in antenna pattern measurements". In: *International Conference on Antennas and Propagation*. Edinburgh, UK.

Waterman, P. C. (1965). "Matrix formulation of electromagnetic scattering". In: *Proceedings of the IEEE* 53.8, pp. 805–812.

Wheeler, J. A. and R. P. Feynman (1945). "Interaction with the absorber as the mechanism of radiation". In: *Reviews of Modern Physics* 17.2-3, pp. 157–181.

– (1949). "Classical electrodynamics in terms of direct interparticle action". In: *Reviews of Modern Physics* 21.3, pp. 425–433.

Wigner, E. (1931). *Gruppentheorie und ihre Anwendung auf die Quantenmechanik der Atomspektren*. 1st ed. Wiesbaden: Vieweg+Teubner Verlag.

Wittmann, R. C. (1988). "Spherical wave operators and the translation formulas". In: *IEEE Transactions on Antennas and Propagation* 36.8, pp. 1078–1087.

Yaccarino, R. and Y. Rahmat-Samii (1999). "Phaseless bi-polar planar near-field measurements and diagnostics of array antennas". In: *IEEE Transactions on Antennas and Propagation* 47.3, pp. 574–583.

Yaghjian, A. D., T. B. Hansen, and A. J. Devaney (1997). "Minimum source region for a given far-field pattern". In: *IEEE Transactions on Antennas and Propagation* 45.5, pp. 911–912.

Yaghjian, A. D., T. B. Hansen, and A. J. Devaney (2000). “Determination of the minimum convex source region from the electromagnetic far-field pattern”. In: *Radio Science* 35.2, pp. 417–425.

Yaghjian, A. D. (2002). “Three-dimensional planar surface-current equivalence theorem with application to receiving antennas as linear differential operators”. In: *Radio Science* 37.2.

Yaghjian, A. D. (1977). *Near-field antenna measurements on a cylindrical surface: A source scattering-matrix formulation.* 1st ed. Vol. 696. Department of Commerce, National Bureau of Standards,

– (1986). “An overview of near-field antenna measurements”. In: *IEEE Transactions on Antennas and Propagation* 34.1, pp. 30–45.

Yaroslavsky, L. P. (1996). “Signal sinc-interpolation: A fast computer algorithm”. In: *Wiley Online Library, Bioimaging* 4.4, pp. 225–231.

Yaru, N. (1951). “A note on super-gain antenna arrays”. In: *Proceedings of the IRE* 39.9, pp. 1081–1085.

Yinusa, K. A., C. H. Schmidt, and T. F. Eibert (2012a). “Scattering centers modeling of non-anechoic measurement environments”. In: *Advances in Radio Science* 10.B. 3, pp. 69–73.

Yinusa, K. A. and T. F. Eibert (2013). “A multi-probe antenna measurement technique with echo suppression capability”. In: *IEEE Transactions on Antennas and Propagation* 61.10, pp. 5008–5016.

Yinusa, K. A. (2015). “Echo suppression techniques for near-field antenna measurements”. PhD Thesis. Munich: Dissertation, Technical University of Munich.

Yinusa, K. A., C. H. Schmidt, and T. F. Eibert (2012b). “Modeling of unknown echoic measurement facilities with equivalent scattering centers”. In: *European Conference on Antennas and Propagation (EUCAP).* Prague, Czech Republic.

Yinusa, K. A., R. A. M. Mauermayer, and T. F. Eibert (2014). “Beamforming filtering for planar near-field antenna measurements”. In: *Antenna Measurement Techniques Association Symposium (AMTA).* Tucson, AZ.

Young, J., D. Svoboda, and W. Burnside (1973). “A comparison of time-and frequency-domain measurement techniques in antenna theory”. In: *IEEE Transactions on Antennas and Propagation* 21.4, pp. 581–583.

Journal Publications of the Author

Knapp, J., A. Paulus, C. Lopez, and T. F. Eibert (2017a). “Comparison of non-convex cost functionals for the consideration of phase differences in phaseless near-field far-field transformations of measured antenna fields”. In: *Advances in Radio Science* 15, pp. 11–19.

Knapp, J., J. Kornprobst, and T. F. Eibert (2019a). “Equivalent source and pattern reconstruction from oversampled measurements in highly-reflective environments”. In: *IET Microwaves, Antennas & Propagation* 13.13, pp. 2232–2241.

Knapp, J. and T. F. Eibert (2019c). “Near-field antenna pattern measurements in highly reflective environments”. In: *IEEE Transactions on Antennas and Propagation* 67.9, pp. 6159–6169.

Knapp, J., A. Paulus, and T. F. Eibert (2019d). “Reconstruction of squared field magnitudes and relative phases from magnitude-only near-field measurements”. In: *IEEE Transactions on Antennas and Propagation* 67.5, pp. 3397–3409.

Knapp, J., A. Paulus, J. Kornprobst, U. Siart, and T. F. Eibert (2021). “Multifrequency phase retrieval for antenna measurements”. In: *IEEE Transactions on Antennas and Propagation* 69.1, pp. 488–501.

Kornprobst, J., R. A. M. Mauermayer, O. Neitz, J. Knapp, and T. F. Eibert (2019c). “On the solution of inverse equivalent surface-source problems”. In: *Progress In Electromagnetics Research* 165, pp. 47–65.

Kornprobst, J., J. Knapp, R. A. M. Mauermayer, O. Neitz, A. Paulus, and T. F. Eibert (2021a). “Accuracy and conditioning of surface-source based near-field to far-field transformations”. In: *IEEE Transactions on Antennas and Propagation (Early Access)*, pp. 1–1.

Kornprobst, J., A. Paulus, J. Knapp, and T. F. Eibert (2021b). “Phase retrieval for partially coherent observations”. In: *IEEE Transactions on Signal Processing* 69, pp. 1394–1406.

Paulus, A., J. Knapp, and T. F. Eibert (2017a). “Phaseless near-field far-field transformation utilizing combinations of probe signals”. In: *IEEE Transactions on Antennas and Propagation* 65.10, pp. 5492–5502.

Conference Publications of the Author

Gruber, M. E., J. Knapp, T. M. Dengler, A. Knaak, and T. F. Eibert (2015). “Analysis of a simultaneous clockwise and counterclockwise rotated stirrer in a reverberation chamber”. In: *EMC Europe*. Dresden, Germany.

Knapp, J. and T. F. Eibert (2016). “Algorithmische Echo-Unterdrückung in der Nahfeld- Fernfeld-Transformation von gemessenen Antennenfeldern”. In: *Kleinheubacher Tagung*. Miltenberg, Germany.

Knapp, J., A. Paulus, and T. F. Eibert (2017b). “Implementation and evaluation of the utilization of partial knowledge of phase differences in magnitude only near-field far-field transformations”. In: *Progress In Electromagnetics Research Symposium (PIERS)*. St. Petersburg, Russia.

Knapp, J. and T. F. Eibert (2017c). “Integral equation based field transformation with effective echo suppression in the near-field by virtual beam forming and field synthesis”. In: *Progress In Electromagnetics Research Symposium (PIERS)*. St. Petersburg, Russia.

– (2018a). “Accurate determination of radiation patterns from near-field measurements in strongly reflective environments”. In: *European Conference on Antennas and Propagation (EuCAP)*. London, UK.

Knapp, J., R. Morelli, and T. F. Eibert (2018b). “Accurate far-field pattern reconstruction from near-field meaurements with inconvenient probes”. In: *Progress In Electromagnetic Research Symposium (PIERS)*. Toyama, Japan.

Knapp, J., A. Paulus, and T. F. Eibert (2018c). “Algorithmic reconstruction of antenna measurement samples from magnitude-only near-field measurements”. In: *Kleinheubacher Tagung*. Miltenberg, Germany.

Knapp, J. and T. F. Eibert (2018d). “Fast irregular antenna field transformation algorithm for unmanned aerial vehicle near-field measurements”. In: *AMTA Workshop UAV-based Antenna and Field Measurements within the 12th European Conference on Antennas and Propagation (EuCAP)*. London, UK.

Knapp, J., A. Paulus, and T. F. Eibert (2019b). “Investigation on diversity effects for phaseless near-field far-field transformations”. In: *European Conference on Antennas and Propagation (EuCAP)*. Krakow, Poland.

Knapp, J., J. Kornprobst, A. Paulus, and T. F. Eibert (2019e). “Time-gating the sources in inverse equivalent source reconstruction problems to eliminate mutual coupling effects”. In: *International Conference on Electromagnetics in Advanced Applications (ICEAA)*. Granada, Spain.

Knapp, J., J. Kornprobst, and T. F. Eibert (2020). “Suppressing undesired echoes by sparsity based time gating of reconstructed sources”. In: *European Conference on Antennas and Propagation (EuCAP)*. Copenhagen, Denmark.

Kornprobst, J., J. Knapp, and T. F. Eibert (2019a). “Approximate inverse of the Rao-Wilton-Glisson basis functions Gram matrix via monopolar representation”. In: *IEEE Antennas and Propagation Society International Symposium (APSURSI)*. Atlanta, GA.

Kornprobst, J., J. Knapp, O. Neitz, and T. F. Eibert (2019b). “Measurement-error controlled iterative least-squares solutions of inverse field transformation problems”. In: *Antenna Measurement Techniques Association Symposium (AMTA)*. San Diego, CA,

Kornprobst, J., O. Neitz, J. Knapp, R. A. M. Mauermayer, and T. F. Eibert (2019d). “Solving inverse equivalent surface source problems by the normal error system of normal equations”. In: *2019 International Conference on Electromagnetics in Advanced Applications (ICEAA)*. Granada, Spain.

Paulus, A., J. Knapp, and T. F. Eibert (2016). “Phasenlose Nahfeld-Fernfeld Transformation von gemessenen Antennenfeldern über nicht-konvexe Optimierung”. In: *Kleinheubacher Tagung*. Miltenberg, Germany.

– (2017b). “Phaseless near-field measurements and transformation for electrically large antennas”. In: *Nationale Konferenz ”Satellitenkommunikation in Deutschland”*. Bonn, Germany.

– (2017c). “Utilizing partial knowledge of phase differences in convex optimization for amplitude-only near-field far-field transformation”. In: *European Conference on Antennas and Propagation (EuCAP)*. Paris, France.

– (2018a). “Nonconvex phaseless near-field far-field transformation for electrically large problems”. In: *European Conference on Antennas and Propagation (EuCAP)*. London, UK.

– (2018b). “Parallel brute-force evaluation of dipole radiation operators on GPUs”. In: *Progress In Electromagnetics Research Symposium (PIERS)*. Toyama, Japan.

– (2018c). “Phasenlose Nahfeld-Fernfeld Transformation mit Neuronalen Netzen”. In: *Kleinheubacher Tagung*. Miltenberg, Germany.

Paulus, A., J. Knapp, J. Kornprobst, and T. F. Eibert (2020a). “Improved-reliability phase-retrieval with broadband antenna measurements”. In: *European Conference on Antennas and Propagation (EuCAP)*. Copenhagen, Denmark.

Paulus, A., J. Knapp, and T. F. Eibert (2020b). “Using broadband signals to enhance the stability of phaseless near-field far-field transformations”. In: *IEEE International Conference on Computational Electromagnetics*. Singapore, Singapore.

Paulus, A., J. Kornprobst, J. Knapp, and T. F. Eibert (2021). “Linear phase retrieval for near-field measurements with locally known phase relations”. In: *European Conference on Antennas and Propagation (EuCAP)*. Düsseldorf, Germany.